Πανεπιστήμιο Κρήτης Τμημα Χημειας

University of Crete Chemistry Department

Study of In_2O_3 and ZnO thin films for selective gas sensors applications: Growth effect on the films structure and surface topology as essential factor in metal oxide thin films sensing applications

Ph.D. Thesis

Mirela Petruța Şuchea

Ηρακλειο Νοεμβριος 2009

Πανεπιστήμιο Κρήτης Τμημα Χημειας

University of Crete Chemistry Department

Study of In_2O_3 and ZnO thin films for selective gas sensors applications: Growth effect on the films structure and surface topology as essential factor in metal oxide thin films sensing applications

Mirela Petruța Şuchea

Ηρακλειο 2009

PhD Thesis

Study of In_2O_3 and ZnO thin films for selective gas sensors applications:
Growth effect on the films structure and surface topology as essential factor in metal oxide thin films sensing applications

Mirela Petruța Şuchea

University of Crete
Chemistry Department
Heraklion, Crete, Greece

2009

Η παρούσα διδακτορική διατριβή υλοποιήθηκε στο πλαίσιο του ΠΕΝΕΔ 2003, έργο 03ΕΔ733, με συγχρηματοδότηση κατά 75% από το Ευρωπαϊκό Κοινωνικό Ταμείο (ΕΚΤ) και 25% από Ελληνικούς εθνικούς πόρους.

Motto:

"Though this be madness, yet there is method in't"

(William Shakespeare, Hamlet, Act II, Scene II).

To my friends who always trusted me

and to my family

Abstract

The goal of this thesis is the study In_2O_3 and ZnO thin films for selective gas sensors applications with focus on growth effect on the films structure and surface topology as essential factor in metal oxide thin films. One of the main problems in the field of metal oxide thin film sensors is the impossibility to elaborate a unitary methodology for reproducibility of sensor response in correlation with the surface characteristics. For this, the systematic study of surface characteristics effects on metal oxide thin films sensing involved phenomena plays a major role.

Using DC magnetron sputtering and pulsed laser deposition, nanostructured In_2O_3 and pure or doped ZnO thin films were grown and fully characterized. The study was focused on the morphology of the film and how this affects the photoreduction with UV light and the oxidation by oxidizing gas (ozone) exposure in order to optimize the film properties for gas sensing applications,. For this purpose, different series of samples were grown:

- In_2O_3 series by DC magnetron sputtering varying the following growth parameters: thickness, growth temperature and total pressure and oxygen:argon ratio during the deposition.
- Pure ZnO series by DC magnetron sputtering from metallic and ceramic targets varying the following growth parameters: thickness for different constant growth temperatures, temperature for constant thickness, total pressure and oxygen:argon ratio during the deposition.
- 2% Al doped ZnO by DC magnetron sputtering varying the following growth parameters: thickness and oxygen:argon ratio during growth.
- In doped ZnO thin films by DC magnetron sputtering varying the following growth parameters: thickness and oxygen:argon ratio during growth.
- Pure ZnO series by PLD varying the following growth parameters: thickness and substrate temperature with focus on very thin films (40nm and 100nm series at different growth temperatures).

All films were fully characterized with respect to their structural and surface topology (for understating and optimization of the influences of the growth conditions on the surface properties), optical/electrical response (for understanding and optimization of the photoreduction and oxidation processes) and sensing behavior.

Detailed surface characterization of each film surface was performed and results were collected for further correlation between surface properties and sensing response. Graphical correlations between surface parameters and sensor response ratios were done for each material studied.

Publications during this work:

- *Suchea, M.*, Christoulakis, S., Katharakis, M., Vidakis, N., Koudoumas, E. Influence of thickness and growth temperature on the optical and electrical properties of ZnO thin films (2009) *Thin Solid Films*, 517 (15), pp. 4303-4306.
- Kiriakidis, G., *Suchea, M.*, Christoulakis, S., Moschovis, K., Kitsopoulos, T., Stoemenos, J. Nano-structural and surface characteristics of non-stoichiometric In_2O_{3-x} thin films (2009) *International Journal of Nanotechnology*, 6 (1-2), pp. 208-218.
- Horvath, P., Sadale, S.B., *Suchea, M.*, Christoulakis, S., Voicu, R., Tibeica, C., Bineva, I., Muller, R., Kitsopoulos, T., Kiriakidis, G. ZnO thin films for cantilever coatings: Structural and mechanical properties, observations of photoplastic effect (2008) *Sensor Letters*, 6 (4), pp. 558-563.
- *Suchea, M.*, Christoulakis, S., Tibeica, C., Katharakis, M., Kornilios, N., Efthimiopoulos, T., Koudoumas, E. Structural and morphological properties of thin ZnO films grown by pulsed laser deposition (2008) *Applied Surface Science*, 254 (17), pp. 5475-5480. Cited 2 times.
- Kiriakidis, G., *Suchea, M.*, Christoulakis, S., Horvath, P., Kitsopoulos, T., Stoemenos, J. Structural characterization of ZnO thin films deposited by DC magnetron sputtering (2007) *Thin Solid Films*, 515 (24 SPEC. ISS.), pp. 8577-8581. Cited 6 times.
- Tudose, I.V., Horváth, P., *Suchea, M.*, Christoulakis, S., Kitsopoulos, T., Kiriakidis, G. Correlation of ZnO thin film surface properties with conductivity (2007) *Applied Physics A: Materials Science and Processing*, 89 (1), pp. 57-61. Cited 4 times.
- *Suchea, M.*, Christoulakis, S., Katharakis, M., Kiriakidis, G., Katsarakis, N., Koudoumas, E. Substrate temperature influence on the properties of nanostructured ZnO transparent ultrathin films grown by PLD (2007) *Applied Surface Science*, 253 (19), pp. 8141-8145. Cited 4 times.
- *Suchea, M.*, Christoulakis, S., Katsarakis, N., Kitsopoulos, T., Kiriakidis, G. Comparative study of zinc oxide and aluminum doped zinc oxide transparent thin films grown by direct current magnetron sputtering (2007) *Thin Solid Films*, 515 (16 SPEC. ISS.), pp. 6562-6566. Cited 3 times.
- Kiriakidis, G., Dovinos, D., *Suchea, M.* Sensing using nanostructured metal oxide thin films (2006) *Proceedings of SPIE - The International Society for Optical Engineering*, 6370, art. no. 63700V, .
- *Suchea, M.*, Katsarakis, N., Christoulakis, S., Nikolopoulou, S., Kiriakidis, G. Low temperature indium oxide gas sensors (2006) *Sensors and Actuators, B: Chemical*, 118 (1-2), pp. 135-141. Cited 5 times.
- *Suchea, M.*, Christoulakis, S., Moschovis, K., Katsarakis, N., Kiriakidis, G. ZnO transparent thin films for gas sensor applications (2006) *Thin Solid Films*, 515 (2 SPEC. ISS.), pp. 551-554. Cited 25 times.
- *Suchea, M.*, Katsarakis, N., Christoulakis, S., Katharakis, M., Kitsopoulos, T., Kiriakidis, G. Metal oxide thin films as sensing layers for ozone detection (2006) *Analytica Chimica Acta*, 573-574, pp. 9-13. Cited 4 times.
- Christoulakis, S., *Suchea, M.*, Koudoumas, E., Katharakis, M., Katsarakis, N., Kiriakidis, G. Thickness influence on surface morphology and ozone sensing properties of nanostructured ZnO transparent thin films grown by

PLD (2006) *Applied Surface Science*, 252 (15), pp. 5351-5354. Cited 20 times.

- Ippolito, S.J., Kandasamy, S., Kalantar-Zadeh, K., Wlodarski, W., Galatsis, K., Kiriakidis, G., Katsarakis, N., *Suchea, M*. Highly sensitive layered ZnO/$LiNbO_3$ SAW device with InOx selective layer for NO_2 and H_2 gas sensing (2005) *Sensors and Actuators, B: Chemical*, 111-112 (SUPPL.), pp. 207-212. Cited 9 times.
- *Suchea, M.,* Christoulakis, S., Moschovis, K., Katsarakis, N., Kiriakidis, G. Nanostructured ZnO and ZAO transparent thin films by sputtering-surface characterization (2005) *Reviews on Advanced Materials Science*, 10 (4), pp. 335-340. Cited 9 times.
- Christoulakis, S., *Suchea, M.*, Katharakis, M., Katsarakis, N., Koudoumas, E., Kiriakidis, G. ZnO nanostructured transparent thin films by PLD (2005) *Reviews on Advanced Materials Science*, 10 (4), pp. 331-334. Cited 6 times.
- Kiriakidis, G., *Suchea, M.*, Christoulakis, S., Katsarakis, N. High performance gas sensing materials based on nanostructed metal oxide films (2005) *Reviews on Advanced Materials Science*, 10 (3), pp. 215-223. Cited 10 times.
- *Suchea, M.*, Christoulakis, S., Katharakis, M., Katsarakis, N., Kiriakidis, G. Surface characterization of ZnO transparent thin films (2005) *Journal of Physics: Conference Series*, 10 (1), pp. 147-150. Cited 6 times.
- *Suchea, M.*, Kiriakidis, G. Surface characteristics of In and Zn oxides by atomic force microscopy (2004) *Proceedings of the International Semiconductor Conference, CAS*, 2, art. no. MO.4, pp. 345-348. Cited 2 times.
- Kiriakidis, G., Katsarakis, N., Katharakis, M., *Suchea, M.*, Galatsis, K., Wlodarski, W., Kotzias, D. Ultra sensitive low temperature metal oxide gas sensors (2004) *Proceedings of the International Semiconductor Conference, CAS*, 2, pp. 325-331. Cited 3 times.

Table of contents

Introduction ... 1
1.1 Sensors- Metal oxides gas sensors: The surface ... 7
Sensor definitions ... 7
Metal oxide based gas sensors ... 8
1.2 Materials description ... 17
In_2O_3 lattice and literature review ... 17
ZnO lattice and literature review ... 21
1.3 Conduction mechanisms and models for thin films ... 25
Growth of films ... 25
Surface states ... 27
Surface transport ... 29
Conduction mechanisms ... 30
Oxygen vacancies in semiconducting metal oxides, stoichiometry and non-stoichiometry ... 33
2.1 Physical vapor deposition techniques: Thermal evaporation, DC magnetron sputtering and Pulsed laser deposition ... 41
Thermal evaporation ... 41
DC magnetron sputtering ... 42
Pulsed laser deposition ... 48
2.2 Characterization techniques ... 54
2.2.1. Composition characterization ... 54
2.2.2. Structural characterization ... 59
2.2.3. Surface characterization ... 63
2.2.4. Optical characterization: Ultraviolet-visible spectroscopy ... 76
2.2.5. Electrical characterization: Photoreduction and oxidation ... 79
Annex to AFM surface characterization by AFM ... 80
3. In_2O_{3-x} thin films grown by DC magnetron sputtering ... 89
3.1 Compositional analysis ... 89
3.2 Films structure ... 94
TEM Characterization ... 94
XRD characterization ... 99
3.3 AFM Characterization: Growth parameters effects on film surface morphology ... 101
Thickness effect ... 101
Temperature effect ... 103
Total pressure and growth rate effects ... 106
3.4 Optical properties ... 109
3.5 Electrical properties – sensing ... 114
Conclusions ... 121
References ... 122
Annex 3A: Growth parameters for In_2O_{3-x} thin films grown by DC magnetron sputtering ... 124
4. ZnO thin films grown by DC magnetron sputtering ... 127
4.1 Films structure ... 127
TEM Characterization ... 127
XRD characterization ... 132

4.2 AFM Characterization: Effect of growth parameters on the film surface morphology 140
Thickness effect 140
Temperature effect 142
Total pressure and growth rate effects 144
Partial Pressure of O_2 effects 147
4.3 Optical properties 148
4.4 Electrical properties – sensing 152
4.5 Conclusions 160
References 161
Annex 4A: Growth parameters for ZnO thin films grown by DC magnetron sputtering 162
5. ZnO thin films grown by PLD 165
5.1 Structural characterization 165
TEM characterization 165
XRD characterization 166
5.2 AFM Surface Characterization 171
Thickness effect 171
Growth temperature effect 172
5.3 Optical properties of ZnO films grown by PLD 175
5.4. Electrical properties – sensing 180
References 187
Annex 5A: Growth parameters for ZnO thin films grown by PLD 188
6.1 ZAO thin films grown by DC magnetron sputtering 191
6.2 Si:ZAO thin films grown by DC magnetron sputtering 201
6.3 In:ZnO thin films grown by DC magnetron sputtering 208
6.4 Conclusions 216
References 217
Annex 6A: Growth parameters for doped ZnO thin films grown by DC magnetron sputtering 218
7. Correlations 221
7.2 Considerations for modeling 239
7.3 Sketch of a model 241
7.4 Conclusions 277
Annex 7A Roughness Parameters 278
Annex 7B Shape Measurement Parameters 288
Annex 7C Experimental data for In_2O_{3-x} grown by DC magnetron sputtering. 293
Annex 7D Experimental data for ZnO grown by DC magnetron sputtering. 299
Annex 7E Experimental data for ZnO grown by PLD. 304
Annex 7F Experimental data for doped ZnO grown by DC magnetron sputtering. 309
8. Conclusions 317
Acknowledgements 321

Introduction

Nowadays, material engineering of metal oxide films is one of the most effective methods used for the optimization of the performance of solid state gas sensors. Considerable improvement of sensing parameters such as signal, selectivity, stability and the rate of response can be achieved via the optimization of chemical, structural, bulk and surface properties of the metal oxides used.

There are many types of solid state sensors that can be used for gas detection. Among these, metal oxide based chemiresistors, or conductometric gas sensors are quite a promising family, mainly operating on the basis of surface reactions. These sensors have excellent sensitivity, very short response time, low cost, and very good suitability for the design of portable instruments, which compensate their disadvantages and open great possibilities for those sensors' application in alarm systems, portable instruments and electronic nose.

Many years of research have shown that the gas sensing process in metal oxides is a rather complicated phenomenon, which depends on all metal oxide parameters, such as: thickness, grain size, porosity, grain faceting, agglomerations bulk conductivity, surface architecture, grain network, surface stoichiometry, catalytic reactivity, band gap and so on. Analysis carried out has shown that the influence of the above mentioned parameters on the gas sensing characteristics is based on the change of such film parameters as effective area of intergrain and inter-agglomerate contacts, energetic parameters of adsorption/desorption processes, number of surface sites, concentration of charge carriers, initial surface potential, coordination number of metal atoms on the surface, gas penetrability of sensing matrix, etc.

There are numerous technological approaches, which were used for the optimization of the sensor response with respect to one or other parameter. It has been shown that control of the deposition parameters, post deposition treatments and doping during synthesis or deposition can really influence all important properties of metal oxides for gas sensor applications.

Except these approaches, post-deposition modifications of the metal oxide surfaces have been used for the improvement of the performance of the sensor. As examples, it was proved that:

- Surface modification by noble metals can promote the improvement of sensitivity and decreases the response and recovery times.
- Use of one-dimensional metal oxides can improve the thermal stability of the structure and the properties.
- Doping the metal oxides with transition metals can modify the catalytic reactivity and the morphology of deposited films.

It has been established that the last method for material engineering is the most unpredictable one. Depending on both the concentration of the dopant and the crystallization parameters, various modifications can appear like a structural modification, accompanied by a grain size change, appearance of a second phase in the base oxide, i.e. heterostructures of various forms, and a change of the electrophysical and surface properties. This means that during the trial of finding the proper parameters for metal oxide doping in order to achieve optimal gas sensing characteristics, one should consider the simultaneous change of all basic parameters of the undoped metal oxides.

Considering the results of a rather large research effort regarding the growth and optimization of metal oxides thin films for sensing applications, one can realize that the choice of proper growth methods and relevant parameters, that could guarantee the achievement of necessary physical and structural properties; he has to take into account a great number of requirements. As examples, one should consider the device destination, the nature of detected gas, the required sensitivity, the exploitation conditions, the required rate of the sensor response and so on. The required configuration of a pre-designed sensor is also an important factor influencing the choice of method and growth parameters. As an example one-electrode or two-electrode sensors have different requirements regarding the sensing material resistance for optimal functioning.

In general, the elaboration of a sensors with optimal gas sensing characteristics is a very complicates task. Today, there is no universal model for simultaneous optimization of all parameters of the sensors. In addition, it seems that improvement of one parameter can induce the worsening of another one. For example, in some cases, the smaller the crystallites size is, the higher is the sensitivity, but at the same time the stability of gas sensor parameters is not satisfactory (decrease of the grain size improves the sensitivity but decreases the thermal and temporal stability of the sensor). Therefore, during all stages of the gas sensor design and fabrication one should make a compromise between different parameters and requirements like: sensitivity and stability; selectivity and sensitivity; stability/sensitivity and sensor cost and so on.

Moreover, the comparison of various metal oxides has shown that there is no universal material suitable for application in all types of gas sensors. For example, even the mostly analyzed and used tin and indium oxides have both advantages and disadvantages regarding their application in different gas sensors. The choice of one or other material would be also depending on the exploitation conditions and the requirements for the sensor.

In the light of the above and as a further step towards the development of selective gas sensors with optimum, predefined response, the goal of this work is the correlation between the surface parameters of In_2O_3 and pure or doped ZnO thin films with their ozone sensing response, the films grown by the DC magnetron sputtering and the pulsed laser deposition techniques. One of the main problems in the field of metal oxide thin film sensors is the impossibility to elaborate a unitary methodology for reproducibility of sensor response in correlation with the surface characteristics. For this the systematic study of surface characteristics effects on metal oxide thin films sensing involved phenomena plays a major role.

The thesis has been structured in the following eight chapters:

Chapter 1 is an introductory review about the basics and the progress of gas sensors, an overview of information regarding the two materials used, an overview of the thin films growth and characterization and the available models in the literature regarding the correlation of surface properties with thin films sensing response.

Chapter 2 is dedicated to growth and characterization techniques used.

Chapters 3 to 5 present growth, characterization, and response of In_2O_3, pure ZnO and Al and In doped ZnO thin films grown by DC magnetron sputtering.

Chapter 6 is dedicated to growth, characterization and response of ZnO thin films grown by pulsed laser deposition.

Chapter 7 explains in detail the surface characterization procedure and the parameter considered for each film, bringing together all data collected in this work

regarding both the thin film surface and the ozone sensing response A realistic selection of independent parameters is defined for an experimental data based model of the sensor response, which can correlate the surface structure and topology with the photo- and ozone sensing response. Particular observations are presented for each material, method and parameters group.
Chapter 8 presents the general conclusions and the perspectives of this work.

Chapter 1

Outlines

- **Introductory review of what sensors are and progress on sensors**
- **Overview of information regarding the two materials this study is based on and their applications**
- **Overview of thin films growth and characterization and literature available models for correlation of surface properties with thin films sensing response.**

1.1 Sensors- Metal oxides gas sensors: The surface

Sensor definitions

Without a commonly accepted definition for a sensor and in order to make clear what is designated by the word “sensor”, we will adopt one of the most commonly accepted definitions. A good choice seems to be the definition given by Jacob Fraden in the *Handbook of modern sensors* [1], which states that “a sensor is a device that receives a signal or stimulus and responds with an electrical signal”. The reason why the output of a sensor is limited to an electrical signal is related to the present developments in signal processing, which is exclusively performed with electronic devices. Given this definition, a sensor should be a device that receives a physical, chemical or biological signal and converts it into an electric signal that should be compatible with electronic circuits. This definition may also be supported from the etymological origin of the word sensor. Sensor seems to come from the word *sense*, given that usually sensor devices try to mimic or reproduce human senses’ characteristics. In the biological senses, the output is also an electrical signal that is transmitted to the nervous system. Another term having the same meaning with sensor is transducer. Sometimes transducer is used as a synonym for sensor, as in the case of a series on sensors edited by Göpel *et al.* [2-5]. The word transducer is generally used to designate any device which converts a stimulus into some other form of signal, whether this is electric or not. In this sense a sensor is a transducer that produces only electric output. A sensor may be composed of a series of transducers, responding at the end with an electrical output. In such a case, given the above definition, the last transducer in the series should also be called a sensor. A transducer may also be called sensor element, when it is a part of a sensor. Usually sensors are part of larger complex systems, made by many other transducers, signal conditioners, signal processors, memory devices and actuators. Irrespective of the complexity, the components of a sensor system may be grouped in three different units. The first is the sensor unit, the second is the modifier or signal processor and the third is the output transducer. The second class of components receives the electrical output of the sensors and transforms it into a more suitable form, e.g., it can be amplification, analog to digital conversion or linearization of the signal. The third part converts again the electrical signal into a non-electrical parameter. If the purpose of this last part is the presentation of a result, the output transducer is called a display and the whole setup is a measuring system. If the signal from the output transducer is used to cause some action, the transducer is called an actuator and the whole system is a control system. Both control and measuring systems may be included in a larger group of information processing systems. These systems gather and process data from a variety of sources, in order to produce usable information.
Based on these definitions, one of the most important parts of a sensor is the sensing interface, the part where the targeted gas interacts with the metal oxide surface. These sensors have a quite long history being some of the first developed and their sensing interface consist of a metal oxide layer.

1. Jacob Fraden. Handbook of modern sensors: Physics, designs and applications. AIP Press, second edition, 1997.

2. W. Göpel, J. Hesse, and J. N. Zemel, editors. Fundamentals and general aspects, volume 1 of Sensors: A comprehensive survey. VCH, 1989.
3. W. Göpel, J. Hesse, and J. N. Zemel, editors. Thermal sensors, volume 4 of Sensors: A comprehensive survey. VCH, 1990.
4. W. Göpel, J. Hesse, and J. N. Zemel, editors. Chemical and Biochemical sensors. Part I, volume 2 of Sensors: A comprehensive survey. VCH, 1991.
5. W. Göpel, J. Hesse, and J. N. Zemel, editors. Chemical and Biochemical sensors. Part II, volume 3 of Sensors: A comprehensive survey. VCH, 1992.

Metal oxide based gas sensors

Sensors based on Metal Oxide Semiconductor (MOS) like ZnO and SnO_2 were first developed by Seiyama and Taguchi in the 1960's [1] and tested as detectors for liquid petroleum gases (LPG). As they were highly successful, this sensing approach was explored further. Nowadays MOS sensors are produced in large quantities and have been employed in sensor systems of various kinds. The sensing material has been significantly extended and includes single- (e.g., TiO_2, WO_3, In_2O_3 and other oxides) [2, 3] as well as poli-metalic oxides ($BiFeO_3$, $MgAl_2O_4$, $SrTiO_3$, and $Sr_{1-y}Ca_yFeO_{3-x}$ etc.) [4].The most commonly used MOS film sensors consist of polycrystalline or porous material grown by various chemical or physical techniques. The response is normally measured as the change in resistance between two electrodes following chemical reactions at the surface of the metal-oxide semiconductor. Such modifications in the electrical conductivity have been observed since the earliest studies of semiconducting materials [5, 6].

In brief, the detection mechanism operates as following: in an oxidizing atmosphere, oxygen atoms (resulting from the homolytic decomposition of oxygen molecules in the ambient) or other electron acceptors are adsorbed on the surface of the sensor and trap free electrons from the conduction band of the semiconducting material, a process that leads to an increase of the resistivity. On the contrary, in the presence of a reducing atmosphere, the adsorbed oxygen atoms react with the reducing ambient molecules, releasing the trapped electrons and thus decreasing the resistivity [7].

Regarding the selectivity of these devices, this can be modified accordingly either by doping the metal oxide with noble catalytic metals or by changing the working temperature of the sensing element (250-400ºC), or even by modifying the grain size of the sensing layer.

Some of the advantages of MOS sensors are: a) high sensitivity to most combustible gases including saturated hydrocarbons, NO and CO, although they present poor selectivity between different polar compounds, b) fast response and reliability (simple set-up), c) good resistance to corrosive gases and humidity, d) good mechanical strength and e) low production cost. On the opposite side, their disadvantages are: (a) relatively poor selectivity, which, to some extent, may be improved by dopants and temperature adjustment during the measurement, and (b) relatively high power consuming operation temperature. Today, one of the goals for the sensor technology is the production of sensing systems working at low temperature. Encouraging results are anticipated by current improvements and deployment of Surface Acoustic Wave sensors (SAWs), which now are some of the most commonly used in sensor array systems. Their selectivity and sensitivity towards a certain analyte can be achieved through different sensing layers, chosen according to their strength of interaction with the specific analyte.

The variety of suitable sensing layers allows the tailoring of the sensor towards the needs of a specific application.

It is obvious that the metal oxide layer is the most important component in all these sensors. The physical properties of the metal oxide sensing layer are determined mainly by the applied growth technique and the corresponding parameters. So far, many techniques have been used for the growth of metal oxide thin films and nanostructures, the most commonly used being [8-10]:

- Sol-gel: It is usually based on the precipitation of an insoluble metal compound that can form a gel after its reaction with specific compounds. The obtained gel can lead after thermal decomposition to metal oxide, while, annealing is used to modify the films surface and optimize its properties.
- CVD and spray pyrolysis: These techniques are suitable for the direct preparation of films. They are based on the spraying or flowing of a solution of desired metal salt, such as chloride, on a suitable substrate. The spraying or flowing process is usually done in an air atmosphere and the substrate is heated in order to form the oxide film.
- Aqueous chemical growth method: It is based on the immersion of a substrate in an aqueous solution of a metal compound at temperatures close to 100 ^{o}C for several hours.
- Rheotaxial Growth and its Thermal Oxidation (RGTO): This technique is a two-step process. In the first step, evaporated metal is deposited onto substrates heated to a temperature above the melting point of the metal. Under these conditions, the evaporated metal tends to cluster into small spherical droplets that do not touch each other. In the second step, the metal droplets are thermal oxidized in air at temperatures of the order of 500-700°C, forming polycrystalline metal oxide films.
- Pulsed laser deposition: The metal oxide films are formed by physical vapor deposition of material coming from metal oxide pellets that are irradiated with a pulsed laser beam in a controlled atmosphere.
- Sputtering: It is based on the formation of a metal oxide film by the deposition on a (heated) substrate of material coming from a sputtered metallic or ceramic target in a controlled atmosphere.

Film deposition techniques may also be divided into three categories:

"ultrathin film" deposition processes for thicknesses between 50nm and few μm, a category that includes sputtering, thermal evaporation, chemical vapor deposition (CVD) and pulsed laser deposition (PLD),

"thin-film" deposition processes, such sol-gel, spin coating and spray pyrolysis, for films with thickness bellow 2.0 mm

"thick-film" deposition processes, such as screen printing and tape casting, for films thicker than 10 mm.

Thermal spraying can be used to deposit coatings of metals, ceramics, and cermets thicker than ~50 mm.

In general, there is a close relationship between the gas sensitivity of metal oxides and their surface chemical activity, which in turn depends on the morphology of the material. Today, the great diversity of oxide materials morphologies could be well demonstrated through the variety of self-assembled nanoscale structures that have been recently discovered. For instance nanodiskettes, nanobelts, and other nanoscopic materials have the bulk-like crystalline structure but are only of the order of 10-100 nm in cross-section and up to several millimeters in length. Self-formation of nanostructured metal oxides can also result in nanowires (ZnO [11–

13], In_2O_3 [14], SiO_2 [15–17], Ga_2O_3 [18–20], and GeO_2 [21]), nanobelts (ZnO, SnO_2, Ga_2O_3, In_2O_3, CdO, and PbO_2 [22–25]), and nanorods (MgO [26]). Their surfaces are low index surfaces considered as bulk terminations and thus should exhibit similar properties to single crystal surfaces. Many of these materials have interesting gas sensing properties. Especially, their large surface to volume ratio promotes them to promising materials for well-defined, highly sensitive gas sensors. One fundamental aspect of metal oxide layer sensitivity to different gaseous species is the interaction of a molecule with a solid surface [27–38]. It becomes apparent that as metal oxides often play an important role in chemical processes, surface science studies of well-ordered oxide films or bulk-oxide surfaces are becoming more popular. Recent surface science studies of metal oxides and thin oxide layers on metal substrates, however, indicate that these surfaces can be rather complex [39, 40]. For the same oxide, many different surface structures and compositions exist and the deposited surface phase in each case depends largely on the preparation conditions applied.

Consequently, one can project that also during gas sensing applications, different compositions and structures of the same oxide can be present, depending on the operation conditions. However, not all metal oxide phases can be equally active and thus, one phase can be favored over another by tuning the operation conditions, so that better activation, selectivity, or gas sensitivity may be obtained.

Under the influence of ambient gases, metal oxide layers used in gas sensors may undergo either surface or bulk conductance changes. Usually surface conductance changes are associated with electron transport processes, while bulk conductance changes generally imply ion transport. Depending on the type of charge carrier involved in the sensing processes, these devices may be divided into three different categories: electronic conductance sensors, if the charge carriers are electrons or holes; ion conductance sensors, if the charge carriers are exclusively ions and mixed conductance sensors if the charge carriers are both electrons/holes and ions. Electrochemical sensors belong to the class of the ion conductance sensors. The distinction between electronic, ionic and mixed conduction cannot be done exclusively on the basis of the sensing material because the conduction mechanism may change with temperature or applied electric field. Therefore, individual contributions from electronic and ionic conductivities have to be studied under the specific operating conditions of each device, using proper electron or ion conducting electrodes and measuring procedures that permit an adequate evaluation of local contact influences.

The fabrication of stable three phase boundaries between metals, oxides and gas phase is a common problem in gas sensor development. Usually the electric contacts with the sensing material should be ohmic, should not diffuse into the sensing material and should not interact with the gas phase. An ohmic contact may be defined as a metal-to-semiconductor contact that has a negligible resistance relative to the bulk resistance of the semiconductor [41]. A satisfactory ohmic contact should not significantly degrade the device performance, and should pass the required current with a voltage drop small as compared with the drop across the active region of the device. Diffusion of electrode material into the sensing layer is a common source of long-term drifts. In order to prevent diffusion, a barrier layer may be deposited between the electric contact and the sensing material. Electrode interaction with the gas phase may be used sometimes to improve sensor performance [42], but more frequently, it might be a source of uncontrolled interference to the device output. The interaction mechanisms

between the gas phase and the sensing material involves mainly physisorption, chemisorption, surface defects, bulk defects or three phase boundary processes. Physisorption is the weakest form of adsorption to a solid surface and is essentially maintained by van der Waals interactions. Given the unselective character of van der Waals interaction, sensors based on physisorption processes usually exhibit sensitivity to a wide range of gaseous species. Chemisorption, on the other hand, is a stronger interaction, that shows a higher selectivity. In this kind of interactions, adsorbates form chemical bonds with the surface atoms and thus the electronic structure of both the adsorbate and the surface are modified. Chemisorption is usually promoted by surface defects. The term defect generally corresponds to any region where the microscopic arrangement of the particles differs from that of a perfect crystal. These may be called surface, line or point defects, according to whether the imperfect region is bounded on the atomic scale in one, two or three dimensions [43]. However, since this work is mainly correlated to surface processes, the term surface defect will not be used with the meaning stated above, but as opposed to bulk defects, it will correspond to the defects, whether point or line ones, present on a given surface. It is known that surface atoms usually selfassembly in order to fulfill minimal energy principle requirements, fact which gives the surface quite different properties from the bulk. Furthermore, a surface alone and free of defects, shows an increased reactivity towards the colliding particles and has its own electronic states, which can be different from those of the bulk. On the surface, both line and point defects reveal to be important to gas sensing processes. In the bulk, on the other side, only the point defects are relevant. Discrimination between intrinsic and extrinsic defects is also frequent.

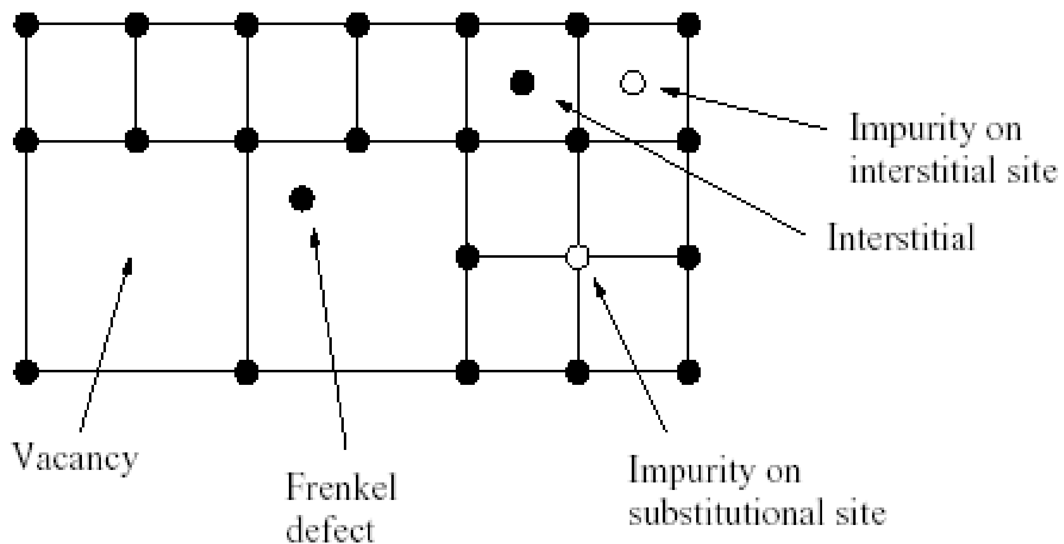

Figure 1.1.1: Types of point defects on a simple crystal lattice

Extrinsic defects are those resulting from the insertion of a foreign particle in the lattice. In this sense, adsorbed atoms may be considered as point defects. The most frequent intrinsic surface defect in n-type semiconducting oxides is a donor-type oxygen vacancy. Other surface defects, important in the gas sensing mechanisms, are impurities or dopants. Their electronic and geometric influence on sensing properties is usually correlated with catalytic behavior [44]. Since many metal oxides are produced in polycrystalline form, surface defects relevant to gas sensing mechanisms include not only the surface in contact with the gas, but also

the size, the shape, the structure and the contact between the grains. Moreover, mobile point defects make possible ion transport in a material. In many cases, non-stable defects may be a source of drifts, but may also be essential to recover the sensor properties after the interaction with the sensed gas. Grain boundaries and crystallites interfere in the charge transport and have been found in some cases to be the key factor that controls the device sensitivity. Finally, instead of impurities at the surface, it is possible to grow a porous catalytic layer over the sensing material in order to improve the sensor performance.
The interaction mechanisms depend not only on the material, but also on the operating conditions of the device. Temperature, for instance, can change adsorption and desorption processes, as well as defect dynamics. At low temperatures, adsorption is favored, while with increasing temperatures desorption starts to dominate. Given the lower binding energies, physisorbed species will desorb before the chemisorbed ones. The effect of temperature on the defect density depends also on the bonding energy between the atoms that form the crystal structure. Surface reactions may be altered by the temperature, the atmosphere composition or the pressure. Usually the reactions involve several different steps, so that it is necessary to know the all the reaction paths of the particles interacting with the surface, in order to understand the whole process. Reactions occurring at the surface of gas sensors mainly fall under the group of heterogeneous catalysis. In a catalyzed reaction, the equilibrium composition of a system is not disturbed, only the rate at which this equilibrium is attained, can be altered [45]. Similarly, the sensor surface should not be altered by the reactions taking place on it. Usually, the surface just provides a better place for a reaction between gaseous species to occur. Furthermore, all the reaction products should desorb during normal sensor operation. Otherwise, the adsorption sites would be blocked and the sensor could no longer used.
In order to get high performance gas sensors, it is necessary to have a good control over the sensing material structure. So far, metal oxides have been produced using several different techniques, either thick-film and ceramic techniques, or thin-film techniques such as thermal evaporation, sputtering or CVD. In general, the reports indicate different response characteristics for gas sensors produced using different techniques. This is to be expected, having in mind that different preparation techniques normally result in different material structure. Usually development and testing of a material starts by studying the characteristic response of a given oxide material without impurities. Afterwards, the preparation conditions or procedures might be changed to achieve a different oxide stoichiometry, defect density crystal structure and morphology. A more common procedure however is to add promoters or a different phase to the structure, in order to change the materials sensing characteristics. The most affected characteristics are usually response time, sensitivity, selectivity and stability.
Metal oxide semiconductors have been used to detect small concentrations of oxidizing, reducing and combustible gases in air. Materials have been grown with sensitivity to: H_2 [42, 46, 47], CO [48–50], O_3 [51-53], H_2S [54-57], NO_x [58-60], PH_3 [61], NH_3 [62-64], CH_4 [65-67], ethanol [68-72] and LPG [73-75]. In the majority of the devices, the detection mechanism of these gases requires oxygen in the atmosphere and is influenced by the presence of water vapors. It may also be observed that with increasing layer temperature, sensitivity reaches a maximum value and then fall towards zero, at higher temperatures [76]. Since the

optimum temperature depends on the gas compound, the operating temperature may be used as a means to change the selectivity of the device. Wide bandgap metal oxides can be activated using also UV radiation. This is the case of metal oxides as In_2O_3 and ZnO, materials which are the subject of this work. Due to their remarkable combination of properties (wide bandgap, transparent in visible spectral region, large variation of intrinsic carrier concentration and electrical mobility in as deposited state, etc) both, In_2O_3 and ZnO, are among the best candidates for miniaturization and edge sensing limits for the next generation of nanoengineered metal oxide gas sensors. Even though there are many studies over the last years on these materials, the sensing mechanism of thin and nanostructured films is not yet completely understood.

1. T. Siyama, A. Kato, K Fujiishi, M. Nagatani, Anal. Chem. 34 (1962) 1502-1503.
2. Zakrzewskagg K 2001, Thin Solid Films 391 229–38
3. Trinchi A, Galatsis K, WlodarskiW and Li Y X 2003 J. IEEE 3 548–53
4. B. Hoffheins, Handbook of Chemical and Biological Sensors, (Institute of Physics, 1996)
5. Many A, Goldstein Y and Grover N B 1965 Semiconductor Surfaces (Amsterdam: North-Holland)
6. Morrisson S R 1977 Chemical Physics of Surfaces (New York: Plenum)
7. Kofstad P 1983 Nonstoichiometry, Diffusion, and Electrical Conductivity in Binary Metal Oxides (New York: Wiley)
8. Semiconductor Sensors in Physico-Chemical Studies: Handbook of Sensors and Actuators 4 (L. Y. Kupriyanov, ed.), Elsevier, Amsterdam (1996);
9. Gas Sensors: Principles, Operation, and Developments (G. Sberveglieri, ed.), Kluwer, Dordrecht (1992).
10. Handbook of Biosensors and Electronic Noses (E. Kress-Rogers, ed.), CRC, Boca Raton, FL (1997).
11. M.H. Huang, Y.Y. Wu, H. Feick, N. Tran, E. Weber, R. Russo, P.D. Yang, Science 292 (2001) 1897.
12. M H. Huang, Y.Y. Wu, H. Feick, N. Tran, E. Weber, P.D. Yang , Adv. Mater. 13 (2001) 113.
13. Y.C. Kong, D.P. Yu, B. Zhang, W. Fang, S.Q. Feng, Appl. Phys. Lett. 78 (2001) 407.
14. C. H. Liang, G.W. Meng, Y. Lei, F. Phillipp, L.D. Zhang, Adv. Mater. 13 (2001) 1330.
15. Y.Q. Zhu, W.K. Hsu, M. Terrones, N. Grobert, H. Terrones, J.P. Hare, H.W. Kroto, D.R.M. Walton, J. Mater. Chem. 8 (1998) 1859.
16. X. C. Wu, W.H. Song, K.Y. Wang, T. Hu, B. Zhao, Y.P. Sun, J.J. Du, Chem. Phys. Lett. 336 (2001) 53.
17. Z.L. Wang, R.P. Gao, J.L. Gole, J.D. Stout, Adv. Mater. 12 (2000) 1938.
18. X.C. Wu, W.H. Song, W.D. Huang, M.H. Pu, B. Zhao, Y.P. Sun, J.J. Du, Chem. Phys. Lett. 328 (2000) 5.
19. H.Z. Zhang, Y.C. Kong, Y.Z. Wang, X. Du, Z.G. Bai, J.J. Wang, D.P. Yu, Y. Ding, Q.L. Hang, S.Q. Feng, Solid State Commun. 109 (1999) 677.
20. C.H. Liang, G.W. Meng, G.Z. Wang, Y.W. Wang, L.D. Zhang, S.Y. Zhang, Appl. Phys. Lett. 78 (2001) 3202.

21. Z.G. Bai, D.P. Yu, H.Z. Zhang, Y. Ding, Y.P. Wang, X.Z. Gai, Q.L. Hang, G.C. Xiong, S.Q. Feng, Chem. Phys. Lett. 303 (1999) 311.
22. Z.W. Pan, Z.R. Dai, Z.L. Wang, Science 291 (2001) 1947.
23. Z.R. Dai, Z.W. Pan, Z.L. Wang, Solid State Commun. 118 (2001) 351.
24. Z.W. Pan, Z.R. Dai, Z.L. Wang, Appl. Phys. Lett. 80 (2002) 309.
25. Z.R. Dai, J.L. Gole, J.D. Stout, Z.L. Wang, J. Phys. Chem. B 106 (2002) 1274.
26. P.D. Yang, C.M. Lieber, Science 273 (1996) 1836.
27. H.-J. Freund, E. Umbach, Adsorption on Ordered Surfaces of Ionic Solids and Thin FilmsSpringer Series in Surface Science, vol. 33, Springer, Berlin, 1993.
28. V.E. Heinrich, P.A. Cox, The Surface Science of Metal-oxides, Cambridge University Press, Cambridge, 1994.
29. C. Noguera, Physics and Chemistry of Oxide Surfaces, Cambridge University Press, Cambridge, 1996.
30. H.-J. Freund, Angew. Chem. Int. Ed. Engl. 36 (1997) 452.
31. C.T. Campbell, Surf. Sci. Rep. 27 (1997) 1.
32. J.P. La Femina, Crit. Rev. Surf. Chem. 3 (1994) 297.
33. M.A. Barteau, J. Vac. Sci. Tech. A 11 (1993) 2162.
34. S.A. Chambers, Surf. Sci. Rep. 39 (2000) 105.
35. D.A. Bonnell, Prog. Surf. Sci. 57 (1998) 187.
36. R.J. Lad, Surf. Rev. Lett. 2 (1995) 109.
37. H.A. Al-Abadleh, V.H. Grassian, Surf. Sci. Rep. 52 (2003) 63.
38. U. Diebold, Surf. Sci. Rep. 48 (2003) 53.
39. W. Weiss, W. Ranke, Prog. Surf. Sci. 70 (2002) 1.
40. S. Surnev, M.G. Ramsey, F.P. Netzer, Prog. Surf. Sci. 73 (2003) 117.
41. Simon M. Sze. Semiconductor Devices: Physics and Technology. John Wiley & Sons, 1985.
42. V. N. Mishra and R. P. Agarwal. Effect of electrode material on sensor response. Sensors and Actuators B [Chemical], 22:121–125, 1994.
43. Neil W. Ashcroft and N. David Mermin. Solid State Physics. Saunders, 1976.
44. W. Göpel and K.-D. Schierbaum. Specific molecular interactions and detection principles, chapter 4. Volume 2 of Göpel et al., 1991.
45. P. W. Atkins. Physical Chemistry. Oxford University Press, fourth edition, 1990.
46. Kyung Hyun Cha, Hee Chan Park, and Kwang Ho Kim. Effect of palladium doping and film thickness on the H_2-gas sensing characteristics of SnO_2. Sensors and Actuators B [Chemical], 21:91–96, 1994.
47. Marta Radecka, Katarzyna Zakrzewska, and Mieczyslaw Rekas. SnO_2–TiO_2 solid solutions for gas sensors. Sensors and Actuators B [Chemical], 47:194–204, 1998.
48. H.-P. Hübner and S. Drost. Tin oxide gas sensors: an analytical comparison of gas sensitive and non-gas-sensitive thin films. Sensors and Actuators B [Chemical], 4:463– 466, 1991.
49. A. Cricenti, R. Generosi, M. A. Scarselli, P. Perfetti, P. Siciliano, A. Serra, A. Tepore, J. Almeida, C. Coluzza, and G. Margaritondo. Pt:SnO_2 thin films for gas sensor characterized by atomic force microscopy and x-ray photoemission spectromicroscopy. J. Vac. Sci. Technol. B, 14(2):1527–1530, Mar/Apr 1996.

50. Fan Lu, Songying Chen, and Shaoyi Peng. Effects of different adsorbed species on ultrafine CO sensors. Sensors and Actuators B [Chemical], 50:220–226, 1998.
51. Seung-Ryeol Kim, Hyung-Ki Hong, Chul Han Kwon, Dong Hyun Yun, Kyuchung Lee,and Yung Kwon Sung. Ozone sensing properties of In_2O_3-based semiconductor thick films. Sensors and Actuators B [Chemical], 66:59–62, 2000.
52. M. Bender, E. Fortunato, P. Nunes, A. Marques, R. Martins, N. Katsarakis, V. Cimalla and G. Kiriakidis , "Highly Sensitive ZnO Ozone Detectors at Room Temperature", Jap. J. Appl. Phys. 42 (2003).
53. G. Kiriakidis, H. Ouacha, and N. Katsarakis , "Nano-structured metal oxide films with room temperature gas sensing properties", *NATO Science Series II: Mathematics, Physics and Chemistry* , Kluwer Academic Publishers, Dordrecht ,Volume 128 , p. 363-382, (2003).
54. Shinji Kanefusa, Masayoshi Nitta, and Miyoshi Haradome. H_2S gas detection by ZrO_2- doped SnO_2. IEEE Transactions on Electron Devices, ED-35(1):65–69, 1988.
55. Jun Tamaki, Tomoki Maekawa, Norio Miura, and Nobotu Yamazoe. CuO–SnO_2 element for highly sensitive and selective detection of H_2S. Sensors and Actuators B [Chemical], 9:197–203, 1992.
56. R. B. Vasiliev, M. N. Rumyantseva, N. V. Yakovlev, and A. M. Gaskov. CuO/SnO_2 thin film heterostructures as chemical sensors to H_2S. Sensors and Actuators B [Chemical], 50:186–193, 1998.
57. V. V. Malyshev and A. V. Pislyakov. SnO_2-based thick-film-resistive sensor for H_2S detection in the concentration range of 1–10 mg m¡3. Sensors and Actuators B [Chemical], 47:181–188, 1998.
58. F. J. Gutiérrez, L. Arés, J. I. Robla, M. C. Horrillo, I. Sayago, J. M. Getino, and J. A. de Agapito. NO_x tin dioxide sensors activities, as function of doped materials and temperature. Sensors and Actuators B [Chemical], 15–16:354–356, 1993.
59. Geraint Williams and Gary S. V. Coles. NO_x response of tin dioxide based gas sensors. Sensors and Actuators B [Chemical], 15–16:349–353, 1993.
60. U. Hoefer, H. Böttner, E. Wagner, and C. D. Kohl. Highly sensitive NO_2 sensor device featuring a JFET-like transducer mechanism. Sensors and Actuators B [Chemical], 47:213–217, 1998.
61. T. Ratcheva, I. Stambolova, and K. Konstantinov. PH_3 detection by SnO_2–ZrO_2 thin films. Sensors and Actuators B [Chemical], 21:199–204, 1994.
62. Dong Hyun Yun, Chul Han Kwon, Hyung-Ki Hong, Seung-Ryeol Kim, Kyuchung Lee, Ho Geun Song, and Ji Eon Kim. Highly sensitive and selective ammonia gas sensor. In Proceedings of the 1997 International Conference on Solid-State Sensors and Actuators, volume 2, pages 959–962, 1997.
63. R. P. Gupta, Z. Gergintschew, D. Schipanski, and P. D. Vyas. YBCO-FET room temperature ammonia sensor. Sensors and Actuators B [Chemical], 63:35–41, 2000.
64. A. Teeramongkonrasmee and M. Sriyudthsak. Methanol and ammonia sensing characteristics of sol–gel derived thin film gas sensor. Sensors and Actuators B [Chemical], 66:256–259, 2000.

65. R. Huck, U. Böttger, D. Kohl, and G. Heiland. Spillover effects in the detection of H_2 and CH_4 by sputtered SnO_2 films with Pd and PdO deposits. Sens. Actuators, 17:355–359, 1989.
66. Soon-Don Choi and Duk-Dong Lee. CH_4 sensing characteristics of K-, Ca-, Mg impregnated SnO_2 sensors. Sensors and Actuators B [Chemical], 77:335–338, 2001.
67. A. Cirera, A. Cabot, A. Cornet, and J. R. Morante. CO–CH_4 selectivity enhancement by in situ Pd-catalysed microwave SnO_2 nanoparticles for gas detectors using active filter. Sensors and Actuators B [Chemical], 78:151–160, 2001.
68. Y. K. Fang and J. J. Lee. A tin oxide thin film sensor with high ethanol sensitivity. Thin Solid Films, 169:51–56, 1989.
69. M. Labeau, B. Gautheron, G. Delabouglise, J. Peña, V. Ragel, A. Varela, J. Román, J. Martinez, J. M. González-Calbet, and M. Vallet-Regi. Synthesis, structure and gas sensitivity properties of pure and doped SnO_2. Sensors and Actuators B [Chemical], 15–16:379–383, 1993.
70. B. Gautheron, M. Labeau, G. Delabouglise, and U. Schmatz. Undoped and Pd-doped SnO_2 thin films for gas sensors. Sensors and Actuators B [Chemical], 15–16:357–362, 1993.
71. Jyh-Jier Ho, Y. K. Fang, K. H. Wu, W. T. Hsieh, C. H. Chen, G. S. Chen, M. S. Ju, Jing-Jenn Lin, and S. B. Hwang. High sensitivity ethanol gas sensor integrated with a solid-state heater and thermal isolation improvement structure for legal drink-drive limit detecting. Sensors and Actuators B [Chemical], 50:227–233, 1998.
72. Tadashi Takada. A new method for gas identification using a single semiconductor sensor. Sensors and Actuators B [Chemical], 52:45–52, 1998.
73. Wan-Young Chung, Chang-Hyun Shim, Soon-Don Choi, and Duk-Dong Lee. Tin oxide microsensor for LPG monitoring. Sensors and Actuators B [Chemical], 20:139–143, 1994.
74. A. R. Phani. X-ray photoelectron spectroscopy studies on Pd doped SnO_2 liquid petroleum gas sensor. Appl. Phys. Lett., 71(16):2358–2360, October 1997.
75. V. A. Chaudhary, I. S. Mulla, and K. Vijayamohanan. Impedance studies of an LPG sensor using surface ruthenated tin oxide. Sensors and Actuators B [Chemical], 55:127– 133, 1999.
76. Th. Becker, S. Ahlers, Chr. Bosch-v.Braunmühl, G. Müller, and O. Kiesewetter. Gas sensing properties of thin- and thick-film tin-oxide materials. Sensors and Actuators B [Chemical], 77:55–61, 2001.

1.2 Materials description

In_2O_3 lattice and literature review

Two crystal structures are known for In_2O_3: body-centered cubic (bcc, Ia3, a = 1.0118 nm) and rhombohedral (rh, R-3c, a = 0.5478 nm and c = 1.451 nm). In the case of bcc-In_2O_3, the physical and optical properties are well known, whereas for rh-In_2O_3, no information is available. Common methods for the deposition of In_2O_3 films and nanostructured layers are evaporation and magnetron sputtering, which usually lead to the growth of In_2O_3 with a poly- or single crystalline bcc structure, independent of the used substrate.
In general, metallic sesquioxides (M_2O_3) crystallize in the corundum type (figure 1.2.1)

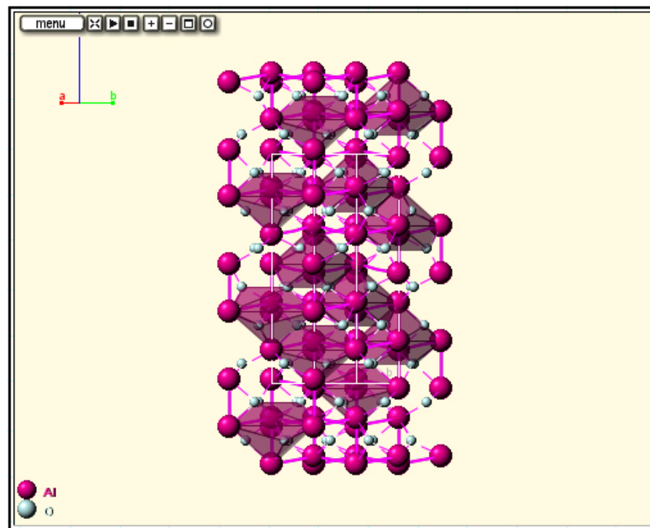

Figure 1.2.1 Corundum type structure

and in the A, B and C modification rare earth structures. The corundum type and the A modification are trigonal, the B modification is monoclinic while the C modification is cubic, Ia3. The C-type rare earth structure (space group Ia3,Th^7, No. 206) is also called bixbyite -type cubic crystals shown in figure 1.2.2.

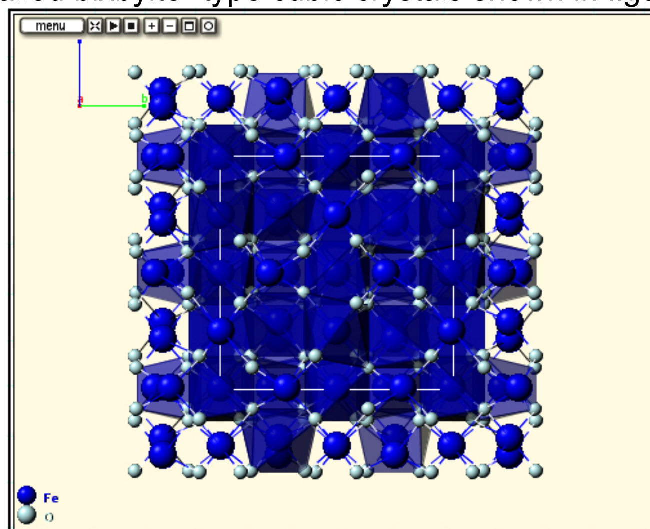

Figure 1.2.2 Bixbyite type cubic structure.

The crystal structure of In_2O_3 has been known since 1930, and since then it has been refined by x-ray diffraction analysis [1-3]

The body centered cubic structure has 80 atoms per unit cell, 32 indium and 48 oxygen atoms (with respect to the 2/3 cation/anion ratio). The 32 indium atoms are in the special positions, 8 In(1) atoms at the b site and 24 In(2) atoms at the d site, while the 48 oxygen atoms are in the general position, at the e sites [4, 6].

According to this structural arrangement, the indium atoms are coordinated by 6 oxygen atoms forming a distorted octahedron, while the oxygen atoms are coordinated by 4 indium atoms forming a tetrahedron, as shown in figure 1.2.3.

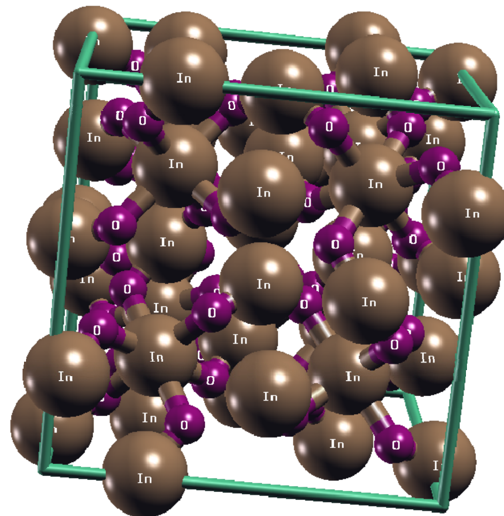

Figure 1.2.3 In_2O_3 unit cell crystalline structure.

The neighboring octahedra are shared with their corners and edges.

The C modification structure is closely related to the fluorite structure and can be derived from it by removing one quarter of the anions and then rearranging the atoms. In the fluorite structure each metal atom is surrounded by eight oxygen atoms, placed at the corners of a cube. Each anion is, in turn, tetrahedrally coordinated. Each cube shares edges with neighboring cubes and the distances between the oxygens is the same. The fluorite structure is shown in figures 1.2.4 a and b.

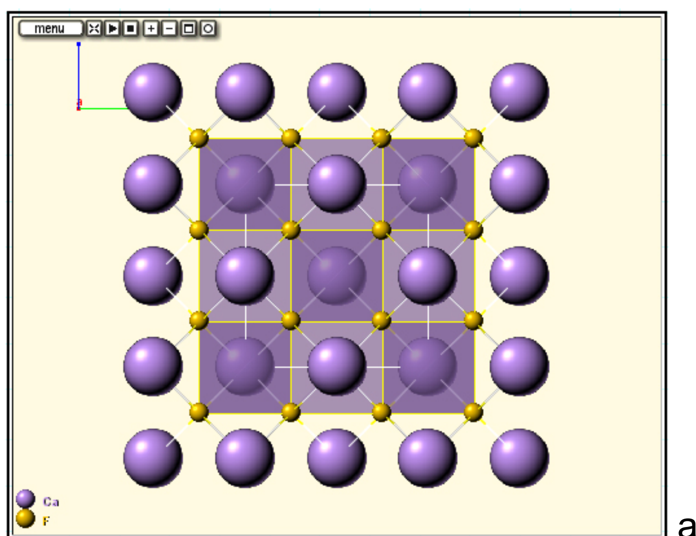

a

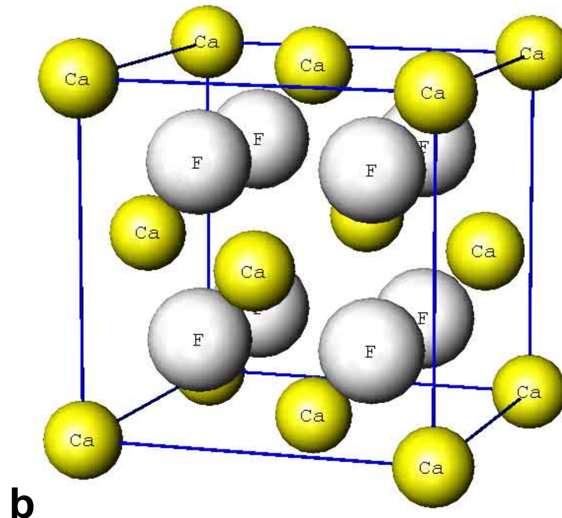

Figure 1.2.4 Fluorite structure: a plane view; b unit cell.

In the C-type structure the cation sublattice is nearly unchanged compared with fluorite structure, but one-fourth of the oxygen atoms in the fluorite structure are missing and the metal ions are surrounded by only six oxygen atoms. The missing oxygen atoms are located either on the face diagonals or body diagonals of the fluorite cubes and they are ordered in such manner that the missing oxygen atoms lie in straight lines through the body diagonals of the cubic structure.
According to the fluorite structure, the lattice of In_2O_3 is formed by a cubic face centered indium sublattice where three quarters of the tetrahedron vacancies between the indium atoms are occupied by oxygen atoms and one quarter remains empty. This means that every fourth anion is missing, so that small shifts of anion take place (~ 4%). The arrangement of these voids is according to a definite pattern which is repeated with a lattice constant of 1.0118 nm, twice the lattice parameter of the cubic face centered indium sublattice. This pattern can be disturbed strongly, especially if the growth of the lattice is done using sputtering at low temperatures.
In_2O_3 in the cubic bixbyite has two non-equivalent six-fold coordinated cation sites. From figure 1.2.3 one can see the two cation sites, which are referred in literature as equipoints "b"and "d". The b site cations have six equidistant oxygen anion neighbors, which lie approximately at the corners of a cube with two anion structural vacancies along one body diagonal. The d site cations are coordinated to six oxygen anions at three different distances, which lie near the corners of a distorted cube with two empty anions along one face diagonal [5, 6].
As prepared, In_2O_3 generally lacks stoichiometry due to oxygen-array vacancies.
At high O_2 vacancies, a vacancy band forms and overlaps E_c at the bottom of the conduction band, producing a degenerate semiconductor. The O_2 vacancies act as doubly ionized donors and contribute with a maximum of two electrons to the electrical conductivity, a fact which can explain the n-type nature of In_2O_3 as semiconductor.

In_2O_3 attracted considerable research effort in the last two decades. It has a direct bandgap of 3.75 eV [7]. The wide bandgap renders In_2O_3 with high optical transparency and makes it an important material for many different applications. In fact, it has been widely used in window heaters, solar cells, and liquid crystal displays [8]. Films of In_2O_3 semiconductor sensors have been successfully used

for the detection of oxidizing gases such as O_3 and NO_2, in a concentration range of ppb to ppm. Takada et al. [9] have first reported ozone sensing properties based on In_2O_3 conductivity measurements, with an optimum operating temperature (for In_2O_3 combined with Fe_2O_3 additives) of around 370 ^oC. Gas-sensing results were also reported by PEML group at IESL FORTH for nanostructured In_2O_3 thin films deposited by the DC sputtering technique, which allows variation of surface properties, the films exhibiting very effective sensing capabilities at low (RT to 100˚C.) temperatures [10]. Earlier conductometric studies [11] indicated that the In_2O_3 films exhibit a rather effective response to ozone after the photoreduction treatment, even at room temperature. This triggers the possibility of employing In_2O_3 films for portable ozone detectors, requiring zero or low power battery support. The deposition parameters, such as oxygen content in the plasma, total plasma gas pressure, substrate temperature, and film thickness, are usually reported to have a decisive role on the properties of these films. Since the sensing mechanism for metal oxides thin films is primarily a surface effect, the technology is now seeking to maximize the surface to volume ratio, a factor that can seriously affect sensing.
Several studies on In_2O_3 nanowire sensing of ethanol, NH_3, NO_2 have been also reported. Ethanol sensor using In_2O_3 nanowires prepared by carbothermal synthesis was fabricated by Chu et al. [12], the response appearing as an increase in the channel conductance. On the other hand, Li et al. have investigated oxidizing gas sensing for NO_2 and NH_3 [13]. Detection of NO_2 down to 5 ppb levels at room temperature has been achieved using a mesh of multiple-wires [14]. Similar to this temperature-dependent change in the sensing response, Li et al. manipulated the carrier concentration and thus the chemical potential by carefully adjusting the oxygen partial pressure during the CVD growth, and observed the reverse sensing behavior [15], i.e., lower (higher) carrier concentration corresponding to lower (higher) chemical potential yielding reducing (oxidizing) sensing performance. Nanostructured In_2O_3 thin sensing layers were also used on SAW sensors as reported by Ippolito et al [16].

1. E. Staritzky: Anal. Chem. 28, 553 (1956)
2. M. Marezio Refinement of the crystal structure of In_2O_3 at two wavelengths: Acta Crystallogr. 20, 723 (1966)
3. M. Marezio, A. Waintal, J. Chenavas, J.J. Capponi and M. Gondrand: Colloq.
4. Int. Centr. Nat. Rech. Sci. 188, 403 (1970)]1
5. “International Tables for X-ray Crystallography”, Vol. I: Symmetry Groups, inp. 315 (eds. N.F.M. Henry and K. Longdale), Kynoch Press, Birmingham, England, 1969
6. Chrisa Xirouchaki Pedersen “Growth and characterization of indium oxide (InO_x) thin films” PhD Thesis, Physics Department University of Crete 1998
7. T. Siyama, A. Kato, K Fujiishi, M. Nagatani, Anal. Chem. 34 (1962) 1502-1503.
8. Zakrzewskagg K 2001, Thin Solid Films 391 229–38
9. Takada, K. Suzuki, M. Nakane, Sensors and Actuators B 13 (1±3) (1993) 404
10. E. Gagaoudakis, M. Bender, E. Douloufakis, N. Katsarakis, E. Natsakou, V. Cimalla and G. Kiriakidis; Sensors and Actuators B. 80 (2001) 155.

11. G. Kiriakidis, M. Bender, N. Katsarakis, E. Gagaoudakis, E. Hourdakis, E. Douloufakis and V. Cimalla, Phys. Stat. Sol. (a). 185 (2001) 27.
12. F. Chu, C.H. Wang, D.L. Jiang, C.M. Zheng, Chem. Phys. Lett. 399 (2004) 461.
13. C. Li, D.H. Zhang, X.L. Liu, et al., Appl. Phys. Lett. 82 (2003) 1613.
14. D.H. Zhang, Z.Q. Liu, C. Li, et al., Nano Lett. 4 (2004) 1919.
15. C. Li, D.H. Zhang, B. Lei, S. Han, X.L. Liu, C.W. Zhou, J. Phys. Chem. B 107 (2003) 12451.
16. S. J. Ippolito, S. Kandasamy, K. Kalantar-Zadeh, W. Wlodarski, K. Galatsis, G. Kiriakidis, N. Katsarakis, M. Suchea, Sensors and Actuators B 111–112 (2005) 207–212,(doi:10.1016/j.snb.2005.07.046.

ZnO lattice and literature review

ZnO crystallizes in two different crystal lattices. The first is the hexagonal wurtzite lattice, which is, among other applications, used in the thin film industry as a transparent conducting oxide or as a catalyst in methanol synthesis [1]. The second structure is more known to the geologist as the rocksalt structure. The rocksalt structure is a spinel phase used for the understanding of the Earth's lower mantle [2]. The crystallographic structure is important for determining the orientation of thin films of ZnO. The hexagonal wurtzite crystal lattice of single crystal ZnO is depicted in figure 1.2.5.

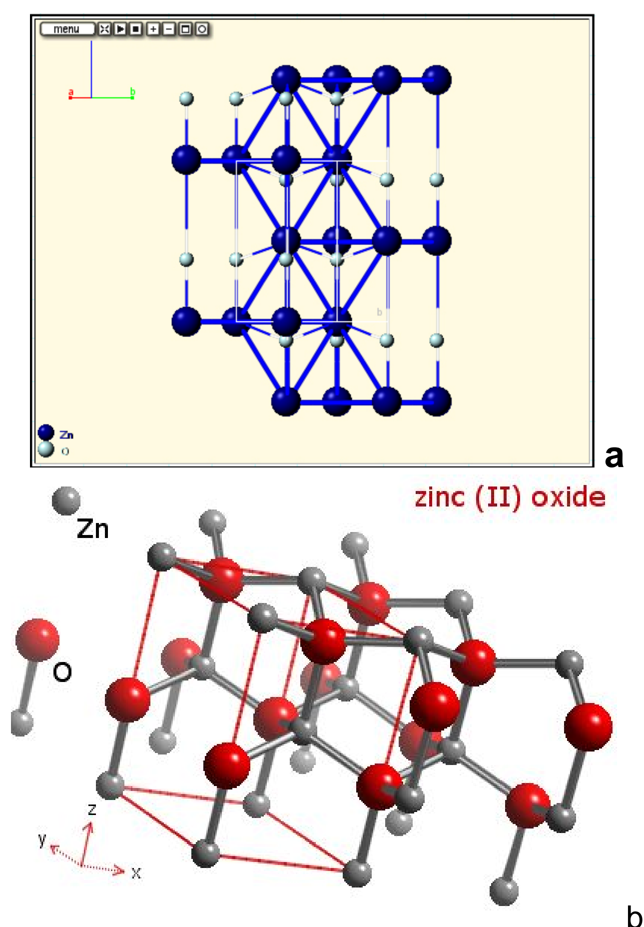

Figure 1.2.5 a and b ZnO hexagonal wurtzite crystalline structure.

Wurzite

The unit cell contains two zinc (Zn) cations and two oxygen (O) anions. The ZnO crystal thus can be viewed as a sequence of O-Zn double layers stacked along the c-axis or (0001) direction (Figure 1.2.6).

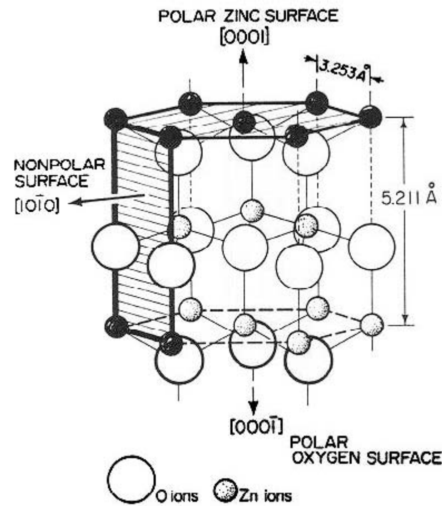

Figure 1.2.6 Unit cell of ZnO hexagonal wurtzite structure, polar and nonpolar surfaces .

The lattice parameters correspond to the second nearest neighbor distance a =3.253 Å and the ratio c/a = 1.602. This structure is well known to exhibit piezoelectric properties with a large electromechanical coupling factor and a low dielectric constant [3]. The crystal structure is normally strongly dependent on the deposition parameters. Table 1.1 summarizes the most significant properties of ZnO.

Crystal system	6mm (wurtzite)
Space group	$P6_3$ mc
Lattice constant	a = 3.253 Å, c = 5.211 Å [Göpel et al., 1982]
Sublimation point	1975 +/- 25°C
Optical transparency	0.4 – 2.5 µm
Refraction index	n_o = 1.9985, n_e = 2.0147 (λ= 6328 Å)
Thermal expansion coefficient	α_{11} = 4.0, α_{33} = 2.1 (10^{-6} /^{o}C)

Table 1.1 Physical properties of a ZnO single crystal [4].

ZnO is naturally an n-type semiconductor of wurtzite structure, with a direct bandgap of about 3.37 eV at room temperature. The native n-type doping is due to the presence of intrinsic defects such as oxygen vacancies and Zn interstitials. They form shallow donor levels with ionization energy of about 30–60 meV.

Some researchers have suggested that the n-type conductivity is due to hydrogen impurity introduced during growth [5, 6].

In the literature various types of dopants, such as group-III (Al [7,8], Ga [9,10], In [10]), group-IV (Sn [10, 11].), group-V (N [12, 13], P [14], As [15,16]), group-VI and transition metal (Co [17], Fe [18], Ni [19], Mn [20]) have been introduced into ZnO nanostructures and films. Doping ZnO by group-III and IV elements has been proved to enhance its n-type conductivity. On the other hand, some groups have investigated the possibility to grow p-type ZnO by incorporating group-V elements,

as an effort to produce reliable Transparent Thin Film Transistors (TTFTs) that could revolutionize the current electronics architectures. In addition, co-doping by N and group-III elements was found to enhance the incorporation of N acceptors in p-ZnO by forming N–III–N complexes [21, 22]. As mentioned above, n-type ZnO is easily realized via substituting group-III and IV elements or incorporating excess Zn.

Oxygen (O_2), ozone (O_3) and nitrogen dioxide (NO_2) are oxidizing gases that were found to be easily detected by ZnO. The ozone sensing properties of nanostructured pure and doped ZnO thin films grown by DC magnetron sputtering and PLD have been recently investigated [23-26].

Tien et al. proposed ZnO nanorod ozone sensors [27]. Because of the higher oxidizing ability of O_3, nanorods sensing response to ozone is dominant in either N_2 or O_2 ambient. Lu and coworkers reported O_2 and NO_2 oxidizing sensing with field-effect transistors made of individual ZnO nanowires [28,29], opening a new field for future ZnO applications. Fan et al. reported sensing response of a single ZnO nanowire exposed to NH_3 at room temperature, manifested by a conductance decrease, while, at 500 K, the conductance presented an increase upon exposure to NH_3. Carbon monoxide (CO) sensing studies carried out at 500 K in synthetic air (20% oxygen) indicated that the admittance of CO into the test chamber results in an increasing of the nanowire conductance. This was suggested to be related to the reaction between CO and the surface adsorbed O_2, which releases the electrons withdrawn by the O_2 adsorption back to the conduction channel [30]. Hydrogen (H_2) detection and storage are also drawing increasing attention due to the demand of solid oxide fuel cell with H_2 as a source. Hydrogen sulfide (H_2S) sensing using hydrothermally prepared ZnO nanorods has been already tested [31, 32]. Finally, Wan et al. demonstrated that H_2S sensitivity down to 50 ppb at room temperature, while humidity (H_2O) sensing has been also tested on Cd-doped ZnO nanowires [33].

1. J.C. Frost, Nature 334 (1988) 577.
2. Liu, L. in High Pressure Research: Applications in Geophysics (eds. Manghnani, M. H., and Akimoto, S.). Academic Press, New York, p245-253 (1977).
3. P. Roth and D. F. Williams, J. Appl. Phys. 52, 6685 (1981).
4. Wasa K., "Basic deposition process and ferroelectric properties of sputtered PLZT thin films", Ferroelectrics 151(1992)343.
5. C.G. Van deWalle, S. Limpijumnong, J. Neugebauer, Phys. Rev. B 6324 (2001) 245205.
6. S.F.J. Cox, E.A. Davis, S.P. Cottrell, et al., Phys. Rev. Lett. 86 (2001) 2601.
7. T. Yamamoto, H. Katayama-Yoshida, Jpn. J. Appl. Phys. Part 2 Lett. 38 (1999) L166.
8. J.G. Lu, L.P. Zhu, Z.Z. Ye, et al., J. Mater. Sci. 41 (2006) 467.
9. J. Zhong, S. Muthukumar, Y. Chen, et al., Appl. Phys. Lett. 83 (2003) 3401.
10. S.Y. Bae, C.W. Na, J.H. Kang, J. Park, J. Phys. Chem. B 109 (2005) 2526.
11. S.Y. Li, P. Lin, C.Y. Lee, T.Y. Tseng, C.J. Huang, J. Phys. D Appl. Phys. 37 (2004) 2274.
12. T. Yamamoto, H. Katayama-Yoshida, Jpn. J. Appl. Phys. Part 2 Lett. 38 (1999) L166.

13. J.G. Lu, L.P. Zhu, Z.Z. Ye, et al., J. Mater. Sci. 41 (2006) 467.],
14. D.K. Hwang, H.S. Kim, J.H. Lim, et al., Appl. Phys. Lett. 86 (2005) 151917.
15. W. Lee, M.C. Jeong, S.W. Joo, J.M. Myoung, Nanotechnology 16 (2005) 764.
16. W. Lee, M.C. Jeong, J.M. Myoung, Appl. Phys. Lett. 85(2004) 6167.
17. J.B. Cui, U.J. Gibson, Appl. Phys. Lett. 87 (2005) 133108.
18. C.X. Xu, X.W. Sun, Z.L. Dong, M.B. Yu, Y.Z. Xiong, J.S. Chen, Appl. Phys. Lett. 86 (2005) 173110.
19. D.A. Schwartz, K.R. Kittilstved, D.R. Gamelin, Appl. Phys. Lett. 85 (2004) 1395.
20. C. Ronning, P.X. Gao, Y. Ding, Z.L.Wang, D. Schwen, Appl. Phys. Lett. 84 (2004) 783.
21. T. Yamamoto, H. Katayama-Yoshida, Jpn. J. Appl. Phys. Part 2 Lett. 38 (1999) L166.
22. J.G. Lu, L.P. Zhu, Z.Z. Ye, et al., J. Mater. Sci. 41 (2006) 467.
23. M Suchea, S Christoulakis, K Moschovis, N Katsarakis and G Kiriakidis, Review on Advanced Materials Science 10 (2005) 335-340 (http://www.ipme.ru/e-journals/RAMS/no_41005/suchea.pdf)
24. G. Kiriakidis, M. Suchea, S. Christoulakis and N. Katsarakis, Review on Advanced Materials Science 10 (2005) 215-223 (http://www.ipme.ru/e-journals/RAMS/no_31005/kiriakidis.pdf)
25. S Christoulakis, M Suchea, E Koudoumas, M Katharakis, N Katsarakis ,G Kiriakidis, Applied Surface Science 2006 in press on line (doi:10.1016/j.apsusc.2005.12.071)
26. M Suchea, S Christoulakis, K Moschovis, N Katsarakis, G Kiriakidis, Thin Solid Films in press on line (doi:10.1016/j.tsf.2005.12.295.
27. L.C. Tien, D.P. Norton, B.P. Gila, S.J. Pearton, H.T.Wang, B.S. Kang, F. Ren, et al., Appl. Phys. Lett. 86 (2005) 243503.
28. Z.Y. Fan, D.W. Wang, P.C. Chang, W.Y. Tseng, J.G. Lu, Appl. Phys. Lett. 85 (2004) 5923.
29. Z.Y. Fan, J.G. Lu, Appl. Phys. Lett. 86 (2005) 123510.
30. Z.Y. Fan, J.G. Lu, IEEE Trans. Nano.,(2006).
31. J.Q. Xu, Y.P. Chen, Y.D. Li, J.N. Shen, J. Mater. Sci. 40 (2005) 2919.
32. C.H. Wang, X.F. Chu, M.W. Wu, Sens. Actuators B Chem. 113 (2006) 320.
33. Q. Wan, Q.H. Li, Y.J. Chen, T.H. Wang, X.L. He, X.G. Gao, J.P. Li, Appl. Phys. Lett. 84 (2004) 3085.

1.3 Conduction mechanisms and models for thin films

Growth of films

Thin films are material layers ranging from fractions of a nanometer to several micrometers in thickness. The steps needed to grow a film by any vapor phase deposition technique are condensation of the vapor on the growing surface (adsorption), surface migration of species, reactions to form the material, coalescence of the reacted material into islands and desorption (re-evaporation) of any product or unused reactant from the surface as shown schematically in figure 1.3.1.

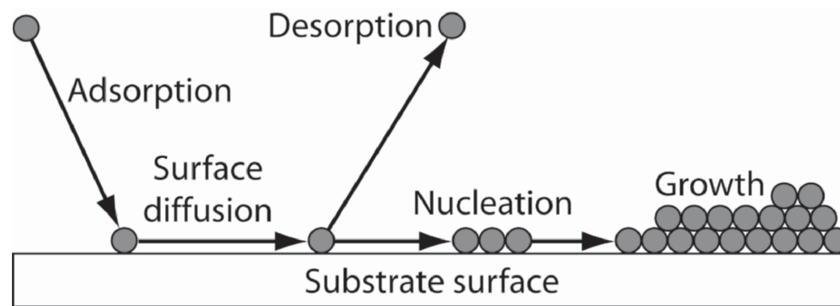

Figure 1.3.1 Schematic representation of growth mechanism.

Nucleation of a thin film is usually described in terms of classical nucleation theory resulting from coalescence of clusters from a random set of atoms on a surface. When atoms are deposited on a film surface, they produce what is generally named a "lattice gas", meaning a low-density gathering of free atoms diffusing randomly among surface lattice sites, occasionally colliding with one another, and presumably sticking together. When adatoms stick together soundly and dimers do not decompose rapidly, nucleation is fast and requires low adatom densities. If adatoms do not stick well enough to the substrate or if single adatoms desorbs much more rapidly than atoms from clusters, it may be difficult to accumulate enough adatoms to form an initial nucleus. This normally leads to a delay in nucleation. If one plots the thickness of a film as a function of time in such a case and extrapolates to zero thickness, it will find out that the extrapolation does not lead to zero time. The nucleation ends as soon as stable nuclei are produced. Denuded zones around nuclei are present, where new clusters are unlikely to form. The greater the adatoms diffusion distance, the larger the denuded zone around a cluster and the larger that cluster will become. However, as these denuded areas shrink, the adatom density within them also decreases and nucleation also becomes less likely there. The formation of denuded zones and the preference for nucleation outside of the existing denuded zones is responsible for the relatively well-organized structure of clusters on the surface. Even clusters that are very large and very stable will lose some atoms. Although the most likely fate for these atoms is to reattach to the cluster that they left from, inevitably, some manage to escape and either form new nuclei or become attached to another cluster. This leads to a gradual process of exchange of atoms among clusters. The process can be rapid or slow in absolute terms or relative to the growth rate of the film. If it is rapid, with or without net growth, the clusters with the greatest stability gain atoms at the expense of the clusters with the lowest stability. This is because their adatom attachment rate relative to the detachment rate is larger than that for

less stable clusters. Thus, the small clusters, which are usually less stable, gradually disappear and the larger, more stable clusters grow. The exchange of atoms leading to growth of large clusters and shrinkage of small clusters is known as coarsening.
The process of coarsening is enhanced if even relatively large clusters can move on the surface and coalesce with one another. This movement is observed experimentally at sufficiently high temperatures. Cluster diffusion results from the fact that atoms may move around the perimeter of the cluster as well as leaving it to join the lattice gas. This results in random transport of atoms from one side of the cluster to the other and, to the movement of its center of mass. The larger the cluster, the more atoms must move in order for it to shift its position. Hence, larger clusters diffuse much more slowly than smaller ones. When two clusters touch, they usually rapidly shift to an equilibrium shape (hemispherical or faceted in most cases) through movement of atoms around the edges.
As the clusters grow, they may also coalesce without diffusion by simply coming into contact. Again, this is usually quickly, followed by clusters reshaping themselves by diffusion across their surfaces. Coalescence eventually leads to complete coverage of the substrate with the growing layer. At this point, there is a tendency for flattening of the surface as much as entropy, atomic transport and surface energy differences from one plane of atoms to another permit. The smoother the surface, the smaller its area is. Ideally, the surface would be atomically smooth, however, the entropy at low temperatures prevents this from happening. The result, near to an ideal general orientation, is a surface consisting of relatively smooth terraces, occasional high points (clusters of adatoms) and various smaller structures including free adatoms. Any real surface will include surface steps that have a much larger radius of curvature than any other feature. As with surface islands on a foreign substrate, atoms may be transferred from small clusters to larger ones on a smooth surface. Ultimately they prefer to transfer to a surface step. Atoms on surfaces will always have preferred locations relative to underlying atoms. The preferred adsorption sites will be on a dangling bond or close to a localized charge. The total energy of the system changes as an atom moves from one site to another on a surface. Generally, from the energy point of view, there will be maxima, minima, and saddle points. The atoms will typically reside at the minima and will move from site to site via saddle points. The nucleation process described above leads to small islands on the surface. With sufficient atomic mobility these may have surface facets. Finally, the orientation of the film atomic planes should be considered. When a grain in a thin film can match its lattice to that of the substrate, there is considerable motivation to do so, as this greatly reduces the density of dangling bonds. Therefore, it is common to find an influence of a crystalline substrate on the texture (the tendency to develop a non-random average grain orientation) of a growing thin film. The ultimate example of this is epitaxy, where the film is fitted to the lattice of a single crystal substrate across a large area.
The most common observation of all is when the film cannot make any satisfactory alignment with the substrate and therefore effectively ignores it. This is also the case for deposition of a thin film on an amorphous substrate. In such a situation, the film typically chooses to put its atoms as close together as possible to maximize bonding among them. This leads to a strong preference for nucleation of grains on a surface. The structure, morphology, and preferred orientation of a thin film as a whole is often very different from that of the nuclei that is formed on the

substrate surface, especially in the case of polycrystalline films. A film that is formed on a very smooth substrate and lowers the surface energy may become a very smooth layer. However, at either very high or very low temperatures, roughening may occur. At low temperatures atoms cannot move far enough from their initial adsorption point to reach the lowest energy points on the surface. Furthermore, if movement across surface steps is difficult, then, the more steps present on the surface, the shorter distance the adatoms can move. These factors can lead to roughening of the surface as time goes on. If one stops growth and allows the surface to anneal, this roughness will gradually heal, since the atoms will have time to approach their lowest energy positions. However, if roughness is allowed to accumulate, defects are often incorporated into the film too. These defects increase the chances of further growth errors to occur. The defects may be also collected together to produce grain boundaries. Thus, at sufficiently low temperature a point will appear where epitaxy breaks down and the film will become polycrystalline or even amorphous.

Surface states

Our ability to predict physical properties of solids most often relies on the fact that they can be approximated by a perfect periodic crystal. Real crystals are ended by surfaces or interfaces and depending on those, different properties are exhibited. Moreover, in many areas of modern technology, especially in the electronics industry, the critical feature sizes are becoming increasingly smaller, since this can induce modified or even novel properties, like in the case of nanostructured metal oxide thin films. This of course implies that the surfaces and interfaces can have an increasing influence on the overall performance of the nanostructured devices. It is therefore important for such cases to accurately characterize the properties of the surfaces and interfaces and thus establish the knowledge necessary to predict the behavior of the device. Apart from the technological aspect to develop better surface characterization methods, surfaces are of fundamental scientific importance, exhibiting a rich and interesting variety of challenging problems. A large number of experimental methods have contributed to the better understanding of crystallographic, chemical and physical properties of surfaces but the performance of a surface as the main player in the functionality is still far from complete understanding. In the particular case of metal oxide nanostructured polycrystalline thin films for gas sensing applications, the contribution of surfaces and interfaces to the sensing mechanism usually dominates the bulk one and yet, there is no systematic and commonly accepted study which could clarify and/or predict how a specific surface topology and structure can affect the device working parameters. For instance, there are plenty of experimental studies highlighting results which prove the direct connection between the thin films nanostructure and their sensing properties, but no quantification of this connection is valid yet in the "market". At the same time, numerous attempts exist on defining theoretical models, including small "real life" conditions, on the other hand, thousand of results being published regarding the influence on gas sensing of film thickness [1], grain size [2], grain distribution [2], features shape [3], roughness [2-5], crystallite shape and size [4], all actually regarding film's surface topography [5] effects, on sensing behavior of metal oxides thin films.
There are also plenty schematic, approximate and some time contradictive trials of explaining these experimental results but nothing might apply at least up to a fair level and at least to similar materials grown by different techniques. More than

that, selectivity using metal oxide sensing layers seems that can be reached only by surface engineering.
In order to understand the difficulties of “choosing” the right model to explain film sensing properties, one should have first a brief overview of different existing approaches. Starting with the textbooks approach, surface states considered as V_0 finite potential as shown in figure 1.3.2, can lead to a set of wave functions with associated allowed electron energies [6]. As for an infinite periodic potential, the allowed energies occupy bands separated by forbidden energy gaps. However, under certain conditions electronic states with energies in the forbidden energy gap appear. These electronic states called surface states, or more specifically, Tamm states, are confined to the surface and their wave functions decay exponentially into the Kronig-Penney model in the delta-Dirac limit terminated by a rectangular vacuum potential crystal (as shown in figure 1.3.2).

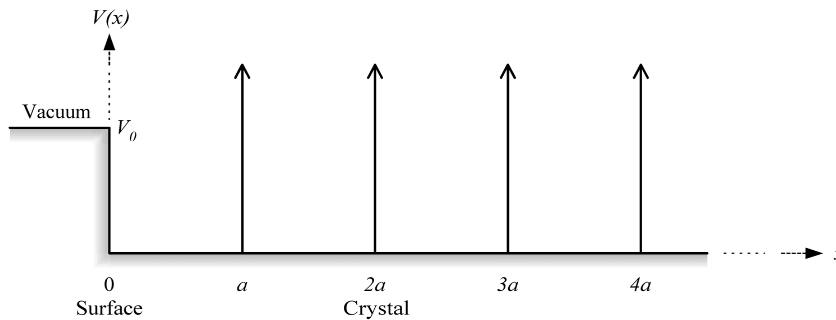

Figure 1.3.2 Kronig Peney model in delta Dirac limit ending in a rectangular vacuum potential associated with the crystal surface.

With *p* denoting the strength of the delta functions, *E* being the electronic energy and *a* and V_0 given in figure, it is found that these states appear only when the so-called existence condition $p - a\sqrt{V_0 - E} > 0$ is satisfied.
This relation may be interpreted in such a way that if the vacuum potential is weak enough, electrons near the surface experience a potential that differs significantly from the potential present deep inside the crystal, causing surface states to develop. More sophisticated models lead to similar relations. For a 1D single state tight-binding model, where only nearest neighbor interactions are included, the existence condition for surface states is [7, 8] $|(\alpha'-\alpha)/\beta|>1$. In this condition, α and α’ are the Coulomb integrals in the bulk and at the surface:
$\alpha = \int \Phi^*(x)H(x-na)\Phi(x)dx$
$\alpha' = \int \Phi^*(x)H(x)\Phi(x)dx$
while β is the resonance integral
$\beta = \int \Phi^*(x)H(x)\Phi(x-a)dx$
where *a* is the lattice constant, *n* is an integer of unity or larger and *x* is taken to be *0* at the center of the surface atom. The atomic orbital is given by Φ (x) while H (x) is the Hamiltonian of the entire crystal. Since $H(x)-H(x-na)=V(x)-V(x-na)$, it can be seen that the existence condition of surface states in tight binding approximation implies that the potential experienced at the surface atoms must differ significantly from that seen by other atoms.
The resulting wave functions are [8]
$\Psi(x) = A\sum e^{-n\mu}\Phi(x-na)$ for $|(\alpha'-\alpha)/\beta|>1$

$\Psi(x) = A\sum(-1)^n e^{-n\mu}\Phi(x-na)$ for $|(\alpha'-\alpha)/\beta|<-1$,

which decay exponentially inside the crystal, as in the Kronig-Penney model.
A different kind of surface states arises from interaction between different atomic orbitals. When isolated atoms are brought together in a crystal, their atomic electron states couple and form continuous energy bands. In some cases the electronic states lie close in energy, and energy bands may overlap as the atoms are brought even closer together. In certain cases the overlapping bands may combine to form hybridized states. These hybridized states further interact to form valence (bonding) and conduction (anti-bonding) bands, equivalent to the bonding and anti-bonding states in molecules. On the crystal surface however, the hybridized states pointing out from the surface have no neighbors to interact with, thus cannot form bonding and antibonding states. Therefore, their energy must lie in the gap between the bonding and antibonding bands formed by the bulk states. These, so-called Shockley states, are localized near the surface similarly to the Tamm states mentioned above. On real crystals, the situation becomes much more complicated than the simple models sketched above.

Surface transport

The presence of surface states gives rise to changes in the conductivity in the vicinity of the surface. The mechanisms responsible for such changes may be one or more of the following:

- The surface states themselves contribute to the electric conduction. The surface states may have a different carrier density and a different band dispersion which in connection with a different scattering probability can result in a modified mobility.
- A different charge neutrality level in the surface states than that of the bulk states may cause a charging of the surface. This results in a potential, needed to align the Fermi levels, which causes a bend of the energy bands, which in turn leads to a change in the carrier density just below the surface, in the so-called space-charge layer.
- New phonon modes, changes in the normal charge distribution and altered topography at the surface may influence the carrier mobility just below the surface. Transport in the space charge layer has been studied intensively in semiconductor device physics [9, 10]

When the transport can be considered parallel to the surface, the conductance contribution from the space-charge layer is relatively easy to derive. If we assume that the carrier mobility in the entire space charge layer is equal to the mobility in the bulk, we just need to calculate the change of the total density of free carriers in the space charge layer. This was conveniently done by Kingston and Neustadter, who found readily the expressions for the excess electron and hole densities when the surface potential is known [11].
Under strong depletion, significant surface state conductance and inversion, it seems plausible to disregard the parallel conduction in the depletion layer and consider the surface and the bulk as two weakly coupled systems. In the case of surface electronic states with significant conductance on a depleted surface, the coupling may be very complicated. Some of the mechanisms involved are:
• Parallel transport in several surface state bands around the Fermi level
• Generation and recombination of the surface state bands

• Thermionic and field emission between bulk and surface electronic states with possible reflections at the surface
• Generation and recombination in the bulk
• Both majority and minority carrier transport in the bulk
• Thermionic and field emission between electrode contacts and the bulk.
Furthermore, the exact surface electronic structure is often not known. In the case of strong inversion, the analysis is quite analogous to that used in semiconductor device physics. Even if the coupling is well described, the calculation is not simple and the system can probably be simulated only numerically.
The analysis of changes in charge carrier mobility near the surface is often very complicated. The effect of surface roughness on the effective mobility of surface excess carrier due to band bending near the surface has been evaluated by Greene et al. [12]. A simpler analysis, giving out almost the same expressions, valid only for depletion and strong accumulation, can be found in reference 13. Later, more simple approximate expressions have been derived by Goldstein et al. [14]. For scattering by fixed surface charges under strong inversion it may be also possible to adopt an approach developed for MOSFET transistors [15].

If no Fermi level pinning is present at the surface, the screening length is given by the bulk extrinsic Debye length [13], given by:

$$L_D = \left(\frac{\varepsilon \varepsilon_0 k_B T}{q^2 (p+n)} \right)^{1/2}$$

where ε and ε_0 are the specific and vacuum permittivity, k_B is Boltzmann constant, T is the temperature, q is the electron charge and n and p are the densities of free electrons and holes respectively. In case of Fermi level pinning by ”metal like” surface states, the scattering potential in the bulk will be a quadrupole potential decreasing as $1/r^3$. The screening in the surface plane is given by the 2D screening length [16] given by:

$$\beta^{-1} = \frac{1}{2}\sqrt{a_B d}$$

where $a_B = 4\pi\varepsilon\varepsilon_0 h^2/m^* q^2$ is the Bohr radius, m* being the effective mass and d is the thickness of the 2D system. The surface screening length is of the order of a few nanometers.
All this information is very useful and applies quite well locally in a very narrow region or for epitaxial growth, but it becomes practically impossible to be used for the explanation/understanding of the behavior of real polycrystalline films.

Conduction mechanisms

The oldest models, regarding conduction mechanism in polycrystalline films, are based on the grain boundary conduction model - developed by Petritz [17] in 1956, which is based on the assumption that the conductivity behavior in polycrystalline films closely approaches that of semiconductors with predominant grain boundary conduction mechanism. The carrier mobility in these films is limited by scattering at the surface and the grain boundaries as well as by normal bulk processes. A model of intergrain boundaries affected by the diffusion of an active gas has been used by Seager and Ginley [18] to explain the changes of conductivity seen in polycrystalline silicon. As found out, diffusion of oxygen down the grain boundaries promoted in these regions significant changes in the density of defect states, resulting in a decrease of conductivity. This model, described extensively by

Seager and Castner for the case of polycrystalline silicon [19], has been adopted until now as the basic approach to explain the conductivity mechanism in polycrystalline metal oxide films. The validity of this model has been confirmed in polycrystalline metal oxide films by experimental results related to the dependence of the conductivity on the temperature, but it cannot explain experimental results when the films are used as sensing layers or when photoreduction is involved.
The main features of this conduction model are: conduction from grain to grain, disturbed by surface barriers which are strongly influenced by chemisorbed oxygen.
The formation of potential barriers at the grain boundaries was proposed by Petritz [17] in 1956, in addition to the normal lattice discontinuity caused by the boundaries. Other models have also been proposed to explain the transport behavior due to the grain boundaries, as that of Volger [20] and Berger [21]. Since then, this subject has been reviewed in detail by Kazmerski [22], while, more trials also appeared using different approaches like the ones of Gardner [23, 24], Bârsan and Weimar [25, 26].
Petritz theory constitutes the basic theoretical analysis of transport mechanisms in polycrystalline semiconducting films. According to this model, grain boundary potential barriers are formed in an n-type semiconductor when the grain boundary region has a lower chemical potential (Fermi level, E_F) for majority carriers, than the grains, due to the density of defect states in this region. These defect states can appear due to the tendency of grain boundaries to act as diffusion whirlpool for impurities. Therefore, these defect states can be treated as trapping centers for majority carriers, resulting in a reduction of their concentration in the boundary region. This in turn causes a flux of majority carriers into the boundary region, creating a space charge build up at these boundaries, which prevents further flux of majority carriers and therefore forms a depletion region for them. This can be presented in a band diagram by an upward bending of the conduction and valence band edges. For a p-type semiconductor respectively, the band edges bend down, toward the Fermi level.
The accumulated negative charge near a joint force the energy bands to be bend upwards by an amount of Φ_B. Since the Fermi energy at equilibrium must be continuous over the grain boundary, the height of the potential barrier, $e\Phi_B$, will be given by the difference of the Fermi's grain-boundary energies. Majority carriers can cross over a grain boundary potential barrier, following two different mechanisms. One is the thermal emission over the barrier and the other is the quantum mechanical tunneling. For the evaluation of electrical characteristics of semiconducting films, most models compare the behavior of the films to that of the bulk crystal. If the bulk crystal was perfect, the conduction carriers could flow unimpeded in a perfect periodic potential. In a real bulk crystal lattice, vibrations, impurities and defects can cause deviations from the ideal behavior, an approach that can be used in polycrystalline thin films analysis, which, however, can result is quite inexact results. The carrier mobility is related directly to the mean free time between collisions, which in turn is determined by the various scattering mechanisms. For bulk crystal behavior in semiconductors, two scattering processes are important: lattice scattering and ionized impurity scattering. In polycrystalline semiconducting films, however, the effect of the grain boundaries should be also considered as an additional scattering mechanism for the carriers. The carriers collide at the grain boundaries and, in a steady state, have an effective mean free path λ_G, constrained by the size of the grains, and a mean

relaxation time τ_G. A simple approach to consider the grain boundaries is represented in figure 1.3.3 **a** and **b** showing schematic representations of polycrystalline thin film structure.

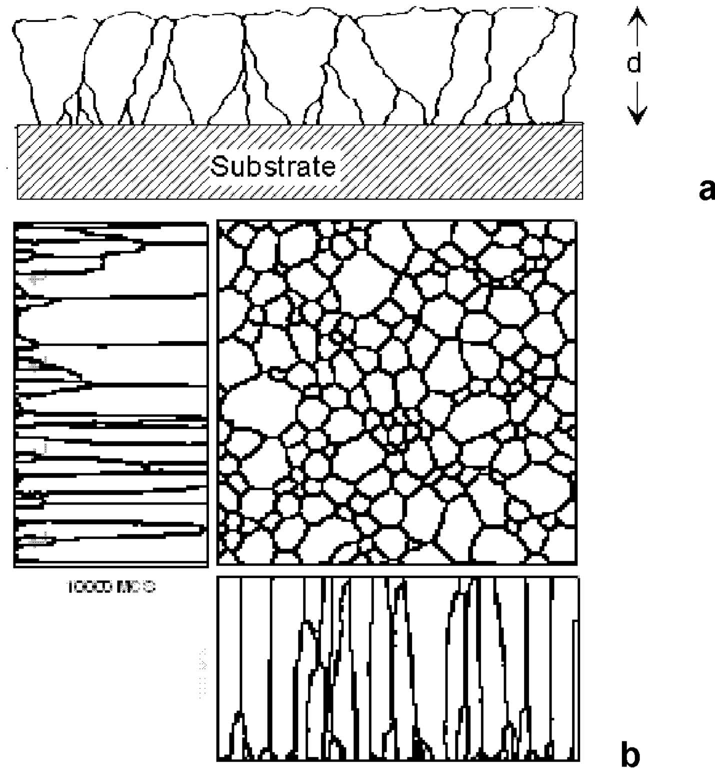

Figure 1.3.3 a schematic representation of cross section in a polycrystalline thin film b plan view and lateral cross sections in a polycrystalline thin film. Grain boundaries are evidenced.

The mobility associated with this mechanism can be expressed as: $\mu_G = q\tau_G / m^* = q\lambda_G / m^* \mathrm{v}$ where m^* is the effective mass of the carriers and v the mean thermal velocity.
According to some models [27], the total resistivity of a polycrystalline film can be expressed as a summation of resistivities corresponding to the different scattering mechanisms. For mobility due to the scattering at the grain boundaries the following expression was proposed:

$$\mu_G = \frac{e\mathrm{v}}{4Nk_BT}\exp\left(-\frac{\Phi_B}{k_BT}\right),$$

where N is the number of surface barriers per unit length of the film thickness (i.e. number of grains), v is the mean thermal velocity of the carriers and Φ_B is the barrier height. This equation shows that the mobility increases with increasing grain size in the film, a fact which should affect the film's electrical conductivity.
It should be also mentioned that in general, any change in the density of the defect states around the Fermi level in the grain boundary region will cause a change in the barrier height Φ_B and correspondingly a change in the mobility and consequently the electrical conductivity. This is actually the working principle of metal oxide resistive gas sensors and basically the grain boundary models remains more or less the basis for the development of any further model. However, this model does not include any considerations for the presence of particular features, of particular structure of film grains or surface topology, which

seem to play deterministic role in the sensing response of nanostructured metal oxide thin films.
If one considers the influence of oxygen on the grain boundary barriers, some topologic surface features involvement may be considered. In accordance with the grain boundary conduction model, oxygen diffuses into a polycrystalline film along the grain boundaries and, from these, into the grains themselves. When a polycrystalline film is exposed to air or to an oxygen atmosphere, the grain boundaries absorb oxygen, resulting in surfaces of the grains covered with many adsorbed oxygen ions. In general, the adsorption of a gas on the surface of a semiconducting film with exchange of charge with the film is called chemisorption. Such a process can either remove or supply majority carriers to the grains. However, when oxygen is chemisorbed on a polycrystalline film, the oxygen adsorbed at the grain boundaries has an additional effect on the electronic transport, except that of the bulk to the grains. As long as the origin for the formation of potential barriers at the grain boundaries is the existence of defect states in the boundary region, it is expected that any increase in the density of these defect states will cause an increase in the barrier height. The diffused oxygen ions act as trapping centers for the electrons in the boundary region, resulting in a reduction of their concentration. Therefore, these oxygen traps are identical to or associated with the defect states that are responsible for the charge build up at the grain boundaries. It is then believed that the barrier height at the grain boundaries is determined by the amount of chemisorbed oxygen. The bulk effect of adsorbed oxygen in polycrystalline films in terms of the band diagram is: oxygen produces a deep surface state below the conduction band, which removes one electron from the conduction band for each oxygen ion chemisorbed. In an n-type semiconductor, the effect of oxygen is to decrease the dark conductivity, while in a p-type semiconductor the chemisorption of oxygen contributes an additional hole to the material and increases the conductivity.
From this, one can consider the grain boundaries in polycrystalline semiconducting films like “sponges” absorbing oxygen and passing it to the grains. This process is associated with the complex nature of the conduction mechanism involved in polycrystalline films. Due to the fact that it is not possible to fabricate a real polycrystalline semiconducting film composed only of high quality bulk material separated by grain boundaries and that real materials contain, in addition to the grain boundaries, stoichiometry deviations, point defects etc, which all can strongly affect the electrical properties, the above mentioned models have very restricted application to very particular cases. In the case of polycrystalline semiconducting metal oxides, point defects which can change the stoichiometry of the material are mainly related to oxygen. These point defects are discussed in the following.

Oxygen vacancies in semiconducting metal oxides, stoichiometry and non-stoichiometry

Both materials used for this study, In_2O_3 and ZnO, are n-type semiconductors. Therefore, the electronic conductivity in these materials is due to a transport of electrons. The n-type conductivity is normally the result of anion deficiency, which usually appears in the form of oxygen vacancies in the crystal lattice. When an oxide M_aO_b contains M and O atoms in the exact ratio a/b, it is said to have a stoichiometric composition. When there is an deviation from the exact a/b ratio, then the material is called nonstoechiometric.

Nonstoichiometry in oxides with respect to the stoichiometric composition may consist of two different types:

- oxygen deficiency
- metal deficiency (or excess oxygen)

Nonstoichiometry in a compound is equivalent to the presence of point defects in the crystal lattice, as compared to that in the stoichiometric conditions. The extent of non-stoichiometry is a direct measurement of the net concentration of the corresponding type of defects in the compound. When a nonstoichiometric oxide is oxygen deficient, the dominant defects may be either oxygen vacancies (oxygen deficit) or interstitial metal ions (excess metal), or even both types of defects. The formation of both oxygen vacancies and interstitial cations leads to the formation of complimentary free electrons. Therefore, oxygen deficient oxides are characterized by n-type conductivity. Respectively, when a non-stoichiometric oxide is metal deficient, the dominant defects may be either metal vacancies or interstitial oxygen atoms (excess oxygen).
When vacancies are present, and thus when atoms in normal sites are missing, part or all of the actual charge of the missing atom may be absent from the vacant site. The process of the formation of an oxygen vacancy in a binary metal oxide has been described in detail by Kofstad [28]. An oxygen vacancy is formed when an oxygen atom in a normal site is removed. In this process, the two negative actual charges, i.e. two electrons, of the oxygen ion are left in the crystal. If both of these two electrons are localized at the oxygen vacancy, the oxygen vacancy has two negative actual charges and the charge is the same as in a perfect crystal. In this case, the oxygen vacancy has zero effective charge. Such vacancies are neutral. If one or both of the localized electrons are excited and transferred away from the neighborhood of the oxygen vacancy, the oxygen vacancy becomes singly or doubly ionized, respectively. Since electrons are removed, the ionized oxygen vacancies will have an effective positive charge with respect to the perfect crystal. The charged oxygen vacancy becomes an electron trapping site, but in this process, one or two electrons are available for conduction. For the conduction to be efficient, it is clear that the volume fraction of traps must be small. Typical free electron concentrations observed in binary oxides are in the region 10^{17} - 10^{21} cm^{-3}. Even at an electron concentration of 10^{21} cm^{-3}, the number of charged oxygen vacancies is expected to be small (about 1%). The oxides used as transparent conductors are all chemically unstable. Consequently, they are relatively easy to be oxidized and reduced.
In an oxygen deficient oxide, where oxygen vacancies are the dominant point defects, the electron concentration depends on the ambient oxygen pressure and it increases with decreasing oxygen pressure. The extent of non-stoichiometry and concentration defects in binary metal oxides depends on the temperature and the partial pressure during fabrication. As the partial pressure of the metal component is usually negligible, as compared with that of oxygen under most of the experimental conditions used, the non-stoichiometry in metal oxides is a result of the interaction with the oxygen in the surrounding atmosphere. In In_2O_3 films, the type of oxygen deficiency observed is usually oxygen vacancies (with respect to 2/3 cation/anion ratio), which act as doubly charged donors, giving electrons to the conduction band. Oxygen vacancies in ZnO can be differently charged, depending on the number of electrons which are removed from the oxide together with the lattice oxygen. When both electrons remain in the vacancy, the local charge is retained (V_O-center). A vacancy with only one electron is usually referred to as

V_o^+-center, while the removal of O^{2-} from the lattice creates a V_o^{2+}-center. Studies of the electronic properties of the differently charged oxygen vacancies in ZnO with quantum chemical methods found that electronic configurations with one or two electrons in the vacancy are stable against a transfer of the electrons into the conduction band. Then, the V_o^{2+}-centers should contain a single unpaired electron.
Taking into account stoichiometry considerations some other models have been also created. The planar models (solving the Poisson equation for the grain boundaries barrier potential in planar geometry and depletion approximation) fail when the grain size becomes comparable to the extension of the depleted region. In this case, indeed, the curvature of the grain plays a relevant role. Some authors considered also solutions of the Poisson equation in spherical symmetry for the potential $\Phi(r)=-E_{CBB}(r)/q$, where $E_{CBB}(r)$ is the conduction band bottom (CBB) energy level at a distance r from the centre of the grain and depletion approximation conditions [29]. Then, some corrections were obtained which include grain size effect, but they also found out that this works only in the particular case of some of their materials and only for the respective grain radius. This was due to the fact that depletion approximation conditions are valid only for the case where the depletion region extent is significantly larger than the Debye length.
All these models presented here together with many more are normally applicable and sustained with particular experiments. None of them includes data from direct surface measurements and experimental grain and grain boundary length/width estimations which are nowadays quite easy to be obtained using modern analytic techniques. The main purpose of the present work is the optimization of film properties for gas sensing application, with focus on the morphology of the films and how this can affect their photoreduction and oxidation response under UV radiation and oxidizing gas respectively. In addition, the work is targeting in a further elaboration of a more general model in a top-down approach from the application to the phenomenology behind it. For this purpose, elaborate surface characterization was performed using Atomic Force Microscopy AFM. AFM was employed, except surface imaging, for the determination of a complete set of morphology parameters (all 44 roughness standard parameters are included in the annex to this work as well as 16 parameters characteristic for grains size, grain distribution on the surface and grain boundaries length), using the Scanning Probe Image Processor (SPIP) image processing software for nano- and micro scale microscopy. Moreover, the optical bandgap of each film and as-deposited, vacuum-photoreduced and oxidized in ozone atmosphere conductivity were measured. Then, a direct correlation between surface morphology and basic or working properties of the films can be deduced. For generalization, two types of materials were studied, polycrystalline In_2O_3 (grown by DC magnetron sputtering) and pure/doped ZnO (grown by DC magnetron sputtering and PLD). This work however is limited to the selection of the most significant parameters for the model and establishes some particular correlations between these parameters.

1 P. Montmeat, R. Lalauze, J.-P. Viricelle, G. Tournier, C. Pijolat, Model of the thickness effect of SnO_2 thick film on the detection properties, Sensors and Actuators B 103 (2004) 84–90.

2 Avner Rothschild and Yigal Komem, The effect of grain size on the sensitivity of nanocrystalline metal-oxide gas sensors J. Appl. Phys. 95, 6374 (2004); DOI:10.1063/1.1728314

3 Jong-Heun Lee, Gas sensors using hierarchical and hollow oxide nanostructures: Overview, Sensors and Actuators B 140 (2009) 319–336

4 Rettig, F., Moos, R., Morphology dependence of thermopower and conductance in semiconducting oxides with space charge regions (2008) Solid State Ionics.

5 Buttá, N., Melli, M., Pizzini, S., Influence of surface parameters and doping on the sensitivity and on the response times of tin oxide resistive sensors, Sensors and Actuators: B. Chemical Volume 2, Issue 2, May 1990, Pages 151-161.

6 S. G. Davison and M. Steslicka, Basic Theory of Surface States, Oxford University Press, Oxford, 1992.

7 S. M. Sze, Semiconductor Devices, Wiley, New York, 1985.,

8 S. G. Davison and M. Steslicka, Basic Theory of Surface States, Oxford University Press, Oxford, 1992.

9 S. M. Sze, Semiconductor Devices, Wiley, New York, 1985.

10 M. Shur, Physics of Semiconductor Devices, Prentice Hall, Englewood Cliffs, 1990.

11 R. H. Kingston and S. F. Neustadter, Calculation of the Space Charge, Electric Field, and Free Carrier Concentration at the Surface of a Semiconductor., Journal of Applied Physics 26, 718—720 (1955).

12 R. F. Greene, D. R. Frankl, and J. Zemel, Surface Transport in Semiconductors, Physical Review 118, 967—975 (1960).

13 S. K. Ghandhi, The Theory and Practice of Microelectronics, Wiley, New York, 1968.

14 Y. Goldstein, N. B. Grover, A. Many, and R. F. Greene, Improved Representation of Calculated Surface Mobilities in Semiconductors. II. Majority Carriers., Journal of Applied Physics 32, 2540—2541 (1961).

15 T. Ando, A. B. Fowler, and F. Stern, Electronic Properties of Two-Dimensional Systems, Review of Modern Physics 54, 437—672 (1982).

16 S. Datta, Electronic Transport in Mesoscopic Systems, Cambridge University Press, Cambridge, 1995.

17 R.L. Petritz: Phys. Rev. 104, 1508 (1956).

18 C.H. Seager and D.S. Ginley: Appl. Phys. Lett. 34, 337 (1979).

19 C.H. Seager and T.G. Castner: J. Appl. Phys. 49, 3879 (1978)

20 J. Volger: Phys. Rev. 9, 1023 (1950).

21 H. Berger: phys. stat. sol. 1, 739 (1961).

22 L.L. Kazmerski: “Properties of Polycrystalline and Amorphous Thin Films and Devices”, in Chap. 3: “Electrical Properties of Polycrystalline Semiconductor Thin Films”, Academic Press, New York, 1980.

23 Gardner, J.W A diffusion-reaction model of electrical conduction in tin oxide gas sensors Semiconductor Science and Technology 4 (5), art. no. 003, pp. 345-350 26,1989.

24 Gardner, J.W A non-linear diffusion-reaction model of electrical conduction in semiconductor gas sensors, Sensors and Actuators: B. Chemical 1 (1-6), pp. 166-170,1990.

25 Bârsan, N. Conduction models in gas-sensing SnO layers: grain-size effects and ambient atmosphere influence (1994) Sensors and Actuators: B. Chemical, 17 (3), pp. 241-246.
26 Nicolae Barsan and Udo Weimar Conduction Model of Metal Oxide Gas Sensors, Journal of Electroceramics, 7, 143–167, 2001.
27 V.F. Korzo and V.N. Chernyaev: phys. stat. sol. (a) 20, 695 (1973).
28 P. Kofstad: “Non-stoichiometry, Diffusion and Electrical Conductivity in Binary Metal Oxides”, Wiley, New York, 1972.
29 M. Cristina Carotta, Alessio Giberti, Vincenzo Guidi, Cesare Malagù, Beatrice Vendemiati, and Giuliano Martinelli, Gas sensors based on semiconductor oxides: basic aspects onto materials and working principles, Mater. Res. Soc. Symp. Proc. Vol. 828 2005 A4.6.1.

Chapter 2

Outlines

- **Growth techniques: DC magnetron sputtering, Pulsed Laser Deposition and thermal evaporation**
- **Characterization techniques: structural, surface, optical, electrical**
- **Annex: Surface profile parameters**

2.1 Physical vapor deposition techniques: Thermal evaporation, DC magnetron sputtering and Pulsed laser deposition

Physical deposition uses mechanical or thermodynamic means to produce a thin film of solid. An everyday example is the formation of frost. Since most engineering materials are held together by relatively high energies, and chemical reactions are not used to store these energies, commercial physical deposition systems tend to require a low-pressure vapor environment to function properly; most can be classified as physical vapor deposition (PVD).
The material to be deposited is placed in an energetic, entropic environment, so that particles of material escape its surface. Facing this source is a substrate surface which collect these particles as they arrive, allowing them to form a solid layer. The whole system is kept in a vacuum deposition chamber, to allow the particles to travel as freely as possible. Since particles tend to follow a straight path, films deposited by physical means are commonly directional, rather than conformal.
There are several physical vapor deposition methods for producing thin films in vacuum and these can be separated into three main groups:

- those involving thermal evaporation, where material is heated in vacuum until its vapor pressure is greater than the ambient pressure,
- those involving ionic sputtering, where high-energy ions strike a solid and knock off atoms from its surface. Ionic sputtering techniques include diode sputtering, ion-beam sputtering and magnetron sputtering
- those involving ablation using laser light pulses for material removal from a target in order to get plasma. One of the most usual technique is Pulsed Laser Deposition (PLD)

All of them are high vacuum techniques.

Thermal evaporation

This method uses high temperature to melt or sublimate the target (source material) into a vapor state. The atoms or molecules of the target are speeding up by high temperature, pass through the vacuum space and condense on the surface of a substrate. Vacuum is required to allow the molecules to evaporate and travel freely in the chamber before condensing on the substrate. As the term "thermal" indicates, high temperature has a key role in this method. "Thermal High Temperature" is a prerequisite for all evaporation technologies, the only difference being the technique used for the heating (evaporation) of the target. Several techniques are used in order to get thermal high temperature; the most often used being the resistive heating. For this technique, a large current passes through a resistor, the target material being at the top or attached to the resistor. The resistor will result in a high temperature and the target material will melt. Traditionally, the resistors are made from W (T_m=3380˚C), Ta (T_m=2980˚C), Mo (T_m=2630˚C) which all present high melting temperature.
The melting temperature of target should be much lower than that of the resistor, so that, when the current passes through, only the target can be melted or vaporized. And then, the atoms can "fly" to the surface of the substrate.

The resistor can have different shapes, depending on the amount of target to be vaporized and the uniformity of evaporation. A wire (filament) was firstly used as resistor, the target (Al, Ag, Au, Cr...) attached to it. In some coating machines and for some target material, a boat or basket shape resistor can be also used.
The advantages of the thermal evaporation are:

- the required equipment is relative simple and cheap.
- the target (source material) can have different shape, depending on the individual needs.

Disadvantages:

- Due to the high temperature, the resistor material can react with the target, degrading the evaporation purity and the thin film quality. Although the method is good for metal targets, the dielectric materials are melting difficult.
- The deposition rate is very low.
- Compound targets may be decomposed by high temperature.
- The hardness of the film is not good and its density is poor.

For the purpose of this thesis, a home made evaporation system was used at IESL FORTH for the deposition of metallic CrNi alloy contacts onto the metal oxide thin films, the contacts required for the electrical measurements.

DC magnetron sputtering

Sputtering as a phenomenon was first observed back in the 1850s but remained a scientific curiosity until the 1940s, when diode sputtering was firstly used to some significant extent as a commercial coating process.
Sputtering is the process whereby atoms or molecules of a material are ejected from a target by the bombardment of high-energy particles.
However, diode sputtering suffering from very low deposition rates had a quite large cost, a fact that limited its use to application where the special benefits of sputtered films were justified. Then, in the mid- 1970s, a magnetically enhanced variant of the diode sputtering emerged and this became known as magnetron sputtering.
Magnetron sputtering is a high-rate vacuum coating technique for depositing metals, alloys and compounds onto a wide range of materials with thicknesses up to millimeter. It exhibits several important advantages over other vacuum coating techniques, a property that led to the development of a large number of commercial applications ranging from microelectronics fabrication to simple decorative coatings. Magnetron sputtering has emerged to complement other vacuum coating techniques such as thermal evaporation and electron-beam evaporation, presenting at the same time many advantages like:

- high deposition rates,
- ease of sputtering any metal, alloy or compound,
- high-purity films,
- extremely high adhesion of films,
- excellent coverage of steps and small features,
- ability to coat heat-sensitive substrates,
- ease of automation,
- excellent uniformity on large-area substrates, e.g. architectural glass.

When power is supplied to a magnetron, a negative voltage of typically -300V or more is applied to the target. This negative voltage attracts positive ions to the target surface inducing at the same time large kinetic energy. Generally, when a positive ion collides with atoms at the surface of a solid, an energy transfer occurs. If the energy transferred to a lattice site is greater than the binding energy, primary recoil atoms can be created, which can collide with other atoms and distribute their energy via collision cascades. A surface atom becomes sputtered if the energy transferred to it on a direction normal to the surface is larger than about 3 times the surface binding energy (approximately equal to the heat of sublimation). Sputtering of a target atom is just one of the possible results of ion bombardment of a surface. The other possibilities are summarized in figure 2.1.1 presented below. Aside from sputtering, the second important process is the emission of secondary electrons from the target surface. These secondary electrons enable the glow discharge to be sustained.

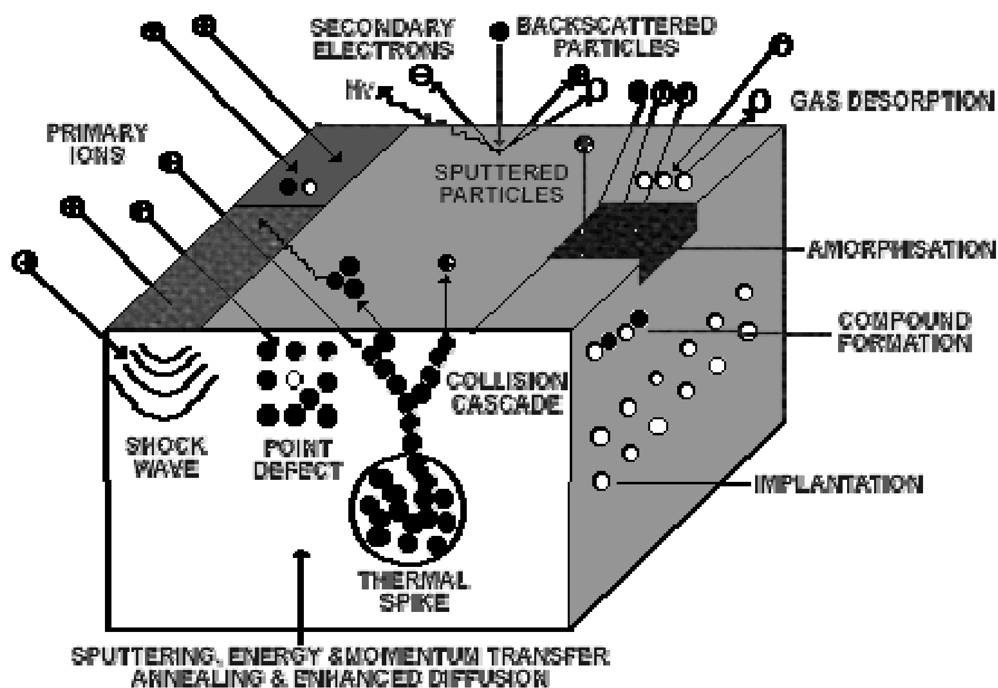

Figure 2.1.1 Effect of target ionic bombardment during sputtering process

The sputter process has almost no restrictions in the type of the target materials, ranging from pure metals where a DC-power can be used to semiconductors and isolators which require either RF-power or pulsed DC. Deposition can be carried out in either non reactive (inert gas only) or reactive (inert and reactive gas) discharges with single or multi-elemental targets.

The gas pressure p and the electrode distance d determine a break-through voltage U_D from which on a self sustaining glow discharge starts following the equation

$U_D = A \times pd/(\ln(pd) + B)$, with A and B constants depending on the materials .

Generally spoken, the ionization probability increases with increasing pressure (and hence the number of ions and the conductivity of the gas also increase), resulting in a decrease of the break through voltage. For a sufficient ionization rate, stable glowing plasma is obtained, wherefrom a sufficient amount of ions of the material is available for sputtering.

To further increase the ionization rate by emitted secondary electrons, a ring magnet below the target is used in the magnetron sputtering. The electrons are trapped in its field, circulating over the targets surface. Due to the longer dwell time of the electrons in the gas, a higher ionization probability is obtained and plasma ignition can appear at pressures, even one hundred times smaller than those for conventional sputtering. As a result of the lower pressure, higher deposition rates can be realized since the kinetic energy at the impact on the substrate is higher due to the fewer collisions occurring for the sputtered material on its way to the substrate. The electron density, and hence the number of generated ions, are maximized for magnetic field parallel to the substrate surface. The highest sputter yield happens on the target area right below this region of the substrate. An erosion zone is formed which follows the form of the magnetic field.
The bombardment of a non-conducting target with positive ions would lead to a charging of the surface and subsequently to a shielding of the electrical field, resulting in a disappearance of the ion current. Therefore, DC-sputtering is suitable for conducting materials, like metals or doped semiconductors.

The Sputtering Parameters

The resulting film properties can be controlled by adjusting the following sputtering parameters:

- The sputtering current I_{sp}, which determines mainly the rate of the deposition process and hence the time available for the particles arriving at the substrate during the growth process for either surface diffusion and agglomeration on existing growth centers or nucleation with other adatoms.
- The applied voltage, which determines the maximum energy carried by the sputtered particles escaping from the target (reduced by the binding energy). Energies of the sputtered particles normally show a broad distribution with a maximum between 1 eV and 10 eV [http://www.pvd-coatings.co.uk/theory-of-pvd-coatings-magnetron-sputtering.htm, Syska paper]. The applied voltage determines also the sputtering yield, which is the number of sputtered particles per incoming ion.
- The pressure p in the sputtering chamber, which determines the mean free path λ of the sputtered material, λ being proportional to 1/p. In combination with the target-substrate distance (TS), the pressure determines the number of collisions each particle encounters before arriving at the substrate. This can influence the porosity of the films. But also the crystallinity and texture can be affected.
- The gas mixture, which can control the stoichiometry of films deposited from a metallic target.
- The substrate temperature, which can have a strong impact on the growth behavior with respect to crystallinity or density of the samples. It can be adjusted between room temperature and 500°C. During sputtering, the substrate temperature may also rise considerably without any external heating, especially during long sputtering times for the deposition of thick films.
- In principle, a bias-voltage up to ±100V can be applied to the substrate, which accelerates electrons or ions either towards the substrate or away from it. Both cases may have an influence on the layer growth.

- Usually substrate and target surface are parallel to each other. A change of the deposition angle (called also: sputtering under oblique incidence) can be achieved by tilting the substrate. This results in a new preferential direction for the film growth and potentially, anisotropic films can be produced.

Thin film growth

In sputtering deposition, as in other standard vacuum deposition processes, the material arrives at the substrate mostly in an atomic or molecular form. Using the kinetic theory of gases it is possible to estimate the frequency with which gas particles impinge on a surface, υ, when the gas phase pressure is p

$υ= p/(2πmkT)^{1/2}$

In the above equation, m is the mass of the gas particles, k the Boltzmann constant and T the temperature. Using this equation for a perfectly smooth surface immersed in air at room temperature and atmospheric pressure, one can estimate that an atom onto the surface will be hit for about 10^9 times per second.
In the case of sputtering, the particles that are involved in the film growth will be the ones evaporated from the target and these will have a much lower collision frequency. The condensed particles may diffuse around the surface, with a motion determined by their binding energy to the substrate, be incorporated into the lattice or evaporate. Given the high collision frequency of the gas particles inside the deposition chamber, the colliding particles will have a non-negligible influence on the adsorbed particles diffusion. The diffusion process may lead to adsorption, particularly at special site edges or other defects, or the diffusing particles may desorb. During these processes, characteristic activation energies have to be overcome. Besides adsorption and surface diffusion, nucleation of more than one adsorbed particle might occur. Inter-diffusion of adsorbed particles with the substrate might appear, leading to smoothing of the film-substrate interface. In thermodynamic equilibrium, all processes take place in the two opposite directions at equal rates. Therefore, in equilibrium no film growth should be observed and layer growth must correspond to a non-equilibrium kinetic process. The final macroscopic state of the system may not be the most stable one, since it is kinetically determined. In general however, certain parts of the overall process may be kinetically forbidden, whereas others may be in local thermodynamic equilibrium. In this case, equilibrium arguments may be applied locally, even though the whole growth process is a non-equilibrium one. Given this fact, a global theory of film growth requires a description in terms of rate equations for each of the processes taking place at the surface. Instead of following a more theoretical atomistic approach, it is possible to deal with the film growth mechanism using a more phenomenological perspective. Usually, three distinct modes of film growth may be considered, each named after the investigators associated with their initial description:

- layer by layer growth mode or Frank-Van der Merve mode;
- island growth mode or Vollmer-Weber mode
- layer plus island growth mode, that is also called Stransky-Krastanov mode;.

In layer by layer growth mode, the interaction between the substrate and the layer atoms is stronger than that between neighboring atoms. Each new layer starts to grow only when the last one is completed. If, on the contrary, the interaction between neighboring atoms is stronger than the overlayer-substrate interaction, the particles will rather form aggregates over the surface, than grow in size and eventually coalesce during film growth. This results in the island growth mode. The layer-plus-island growth mode is an intermediate case where the film in a first stage starts to grow layer by layer and only after some time, the formation of island agglomerates appears. In the island growth mode, each island is usually a single crystal or contains just a few crystals. On a polycrystalline or amorphous substrate, the orientation of each island will be random and the resultant film will be polycrystalline. On single crystal substrates, the islands orientations may be constrained to a given direction by the substrate structure, so that growth and coalescence leads to the formation of a single crystal film. This case is usually known as epitaxy. If surface atoms have high mobility, they have a greater opportunity of finding low energy positions consistent with crystal growth. Knowing that mobility is increased by surface temperature, it is expected that higher substrate temperature will promote crystal growth. The same effect can be achieved by reducing the deposition rate, which gives more time to the adsorbed species to find an energetically favorable lattice position. Epitaxial growth was also found to be promoted by electron or ion bombardment and increased energy of deposited atoms. The environmental conditions around the substrate during magnetron sputtering deposition deserve also to be mentioned, since they will inevitably affect the obtained film structure. In the above description, the effect of the energy of the impinging sputtered atoms was ignored, as well as the effect of other particles hitting on the surface. As an example, contaminants might arrive at the substrate. If these contaminants are chemically active, the contamination will be particularly effective and can be minimized by reducing the contaminant partial pressure. The contaminants may come from an internal source, such as outgassing from a heated part, or by an external source, such as the sputtering gas. If the source is outgassing, the system has to be evacuated to a higher vacuum or the sources of outgassing heated before deposition, in order to reduce the outgassing rate and guarantee a sufficiently low partial pressure of the contaminant during the deposition. On the other hand, if the contaminant comes with the sputtering gas there is no way to reduce its partial pressure without affecting simultaneously the sputtering gas pressure and the deposition process. Thus, it is very important to use high purity sputtering gases. The sputtering gas atoms might also become part of the deposited film. Although the sputtering gas used is usually an inert gas, given its high partial pressure, as compared with that of the sputtered atoms, it is not surprising that some of these atoms can be trapped in the grown film. Inert gas atoms are expected to be only physisorbed, so, if the substrate temperature is increased during deposition, they are more likely to be desorbed just after adsorption. However, there exists an appreciable difference between the interaction of fast gas particles and that of thermal neutrals with the surface. Energetic neutrals may result from the reflection and neutralization of ions that impinge on the target. These neutrals, arriving at the substrate have much higher probability to be embedded in the growing film than thermal neutrals. In fact, it has been observed that nickel films deposited by sputtering in an argon atmosphere have higher argon content than nickel films produced in a similar atmosphere, but using evaporation [Brian N. Chapman. Glow

discharge processes. John Wiley & Sons, 1980]. Positive ions may also impact on the substrate due to the sheath voltage drop near its surface. Negative ions and electrons can only reach the substrate if they have enough energy to cross the space-charge sheath. It is again necessary to distinguish fast from slow particles. Fast negative ions and electrons are produced in the target and accelerated in the target sheath. These fast particles can have a major influence on the structure and properties of the growing film and also cause substrate heating. Finally there are also photons arriving at the substrate. Photons can be produced by ion or electron bombardment on any surface or result from relaxation of excited atoms in the glow. In the former case the photons may have high energy, at most as high as the energy of the bombarding particle. Such energies may be, in a sputtering system, of the same order of the accelerating potential at the target, which is usually higher than 200 eV. The main effect of photon bombardment of the substrate will be electron emission, which may also affect the film growth processes occurring at the substrate.

The sputtering system

The sputtering equipment used for the deposition of the In_2O_3 and pure/doped ZnO thin films related to the present work is a DC planar reactive magnetron sputtering from Alcatel, operated by the PEML Group of IESL-FORTH. Like a typical sputtering deposition system, as seen in figure 2.1.2, it consists of a vacuum chamber, where the deposition process occurs, a pumping system, a gas supply system and a power supply system.

Figure 2.1.2 The Alcatel DC magnetron system @ PEML Group of IESL-FORTH

The deposition chamber is made of stainless steel of cylindrical shape with a base of 0.28 m^2 and a height of 0.4 m. It includes two plane circular sputtering sources (targets) with a diameter of 15 cm each. Permanent magnets are placed at the back of the sputtering sources in a suitable arrangement for the production of the required magnetic field. The sputtering sources are cooled by water circulation during the sputtering process. There is a possibility of changing the sputtering sources according to the type of material to be deposited. At a distance of about 6

cm above the sputtering sources and parallel to them, a substrate holder is placed, for four 1 square inch substrates. The substrate holder can be also heated up to 500˚C during the deposition. The vacuum pumping system consists of a rotary mechanical pump, for pre-pumping, and an oil diffusion pump, for high vacuum, suitably connected. For even higher vacuum, a liquid nitrogen trap is also included in the pumping system. Under these conditions, the chamber can be evacuated to a base pressure of 10^{-7}mbar. Two different gases, i.e. the sputtering gas (Ar) and the reactive gas (O_2), can be simultaneously introduced into the chamber for the deposition process. The gas flow is controlled by mass flow controllers. The pressure of the chamber can be measured by two manometers (pressure gauges), which cover two different regions of pressure. The Pirani type manometer is used for monitoring pressures in the region from atmospheric pressure down to 1 mbar, whereas for lower pressures in the range 10^{-1}–10^{-4} mbar, the Penning type manometer is used. The DC voltage is provided by a DC power supply and through a selector, the voltage can be applied to one of the two targets used for the deposition. There is a possibility of independently controlling of the DC voltage and the DC current. A schematically image of the setup is presented in figure 2.1.3.

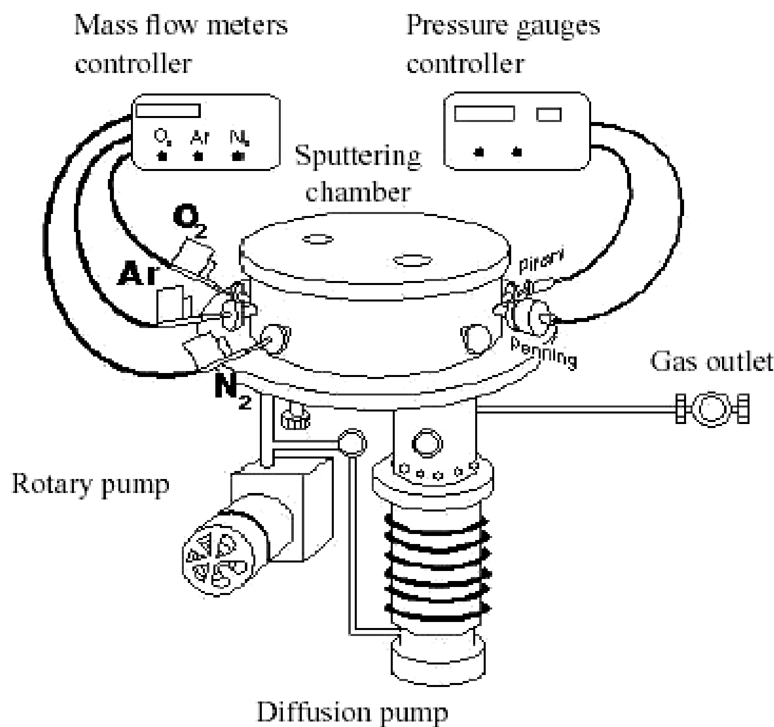

Figure 2.1.3 Schematic representation of the DC magnetron sputtering system.

Pulsed laser deposition

Laser was first demonstrated in 1960 and since then, it has been proved as a powerful tool in many applications. Among other applications, laser is especially useful in material processing. Laser possesses many unique properties such as narrow frequency bandwidth, coherence, directionality and high power density. As a result of this high power density, the laser beam is often intense enough to

vaporize the hardest and most heat resistant materials. Besides, due to its high precision, reliability and spatial resolution, it is widely used in the industry for machining of thin films, modification of materials, material surface heat treatment, welding and micro patterning. Apart from these, multi-component materials can be ablated and deposited onto substrates to form stoichiometric thin films. This last laser application is the so-called pulsed laser deposition (PLD) [1].
In general, the idea of PLD is simple. A pulsed laser beam is focused onto the surface of a solid target. The strong absorption of the electromagnetic radiation by the solid surface leads to rapid increase of the temperature and the evaporation of the target materials. The evaporated materials consist of highly exited and ionized species, which appear as a glowing plasma plume in front of the target surface, if the ablation is carried out in vacuum. Figure 2.1.4 shows some typical plasma plumes produced during PLD process.

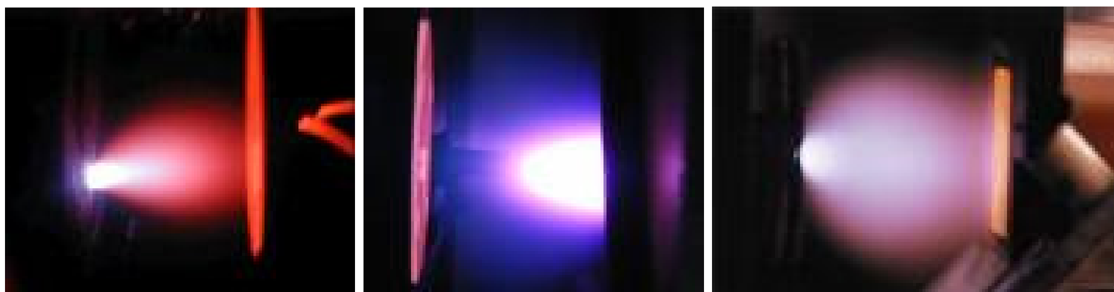

Figure 2.1.4 Typical plasma plumes produced during PLD process.

Indeed, PLD is so straightforward that ones geometric parameters like beam alignment, beam focusing, substrate-target distance are established, only a few parameters, such as laser energy density and pulse repetition rate, need to be controlled during the process in predefined growth environment (pressure, temperature, growth atmosphere). The targets used in PLD are small compared with those required for other sputtering techniques and it is quite easy to produce multi-layered films of different materials by sequent ablation of assorted targets. Besides, by controlling the number of pulses, a fine control of film thickness down to atomic monolayer can be achieved. The most important feature of PLD is however that the stoichiometry of the target can be retained in the deposited films. This is a result of the extremely high heating rate of the target surface (10^8 K/s) due to pulsed laser irradiation. Therefore, PLD leads to the evaporation of the target irrespective of the evaporating point of the individual elements or compounds of the target. Moreover, because of the high heating rate of the ablated materials, laser deposition of crystalline film demands a much lower substrate temperature than other film growth techniques. For this reason, deposition can be performed on semiconductor and integrated circuit without any thermal degradation.

In contrast to the simplicity of the required set-up, the principle of pulsed laser deposition, is a very complex physical phenomenon, involving several physical processes of laser-material interaction during and after the impact of high-power pulsed radiation on a solid target. It includes the formation of the plasma plume with high energetic species, the subsequent transfer of the ablated material

through the plasma plume onto the heated substrate surface and the final film growth process. Thus, PLD generally can be divided into the following four stages.

- Laser radiation interaction with the target
- Dynamic of the ablation materials
- Deposition of the ablation materials on the substrate
- Nucleation and growth of a thin film on the substrate surface

In the first stage, the laser beam is focused onto the surface of the target. At sufficiently high energy densities and short pulse duration, all elements in the target surface are rapidly heated up to their evaporation temperature. Materials are dissociated from the target and ablated out with stoichiometry as in the target. The instantaneous ablation rate is highly dependent on the fluence of the laser radiation on the target. The ablation mechanism involves many complex physical phenomena such as collisional, thermal and electronic excitation, exfoliation and hydrodynamics.
During the second stage, the emitted material tends to move towards the substrate according to the laws of gas-dynamic and presents the forward peaking phenomenon [2]. R. K. Singh [3] reported that the spatial thickness of the material "beam" arriving to the substrate varied as a function of $\cos^n q$, where n>>1. The laser spot size and the plasma temperature have significant effects on the uniformity of the deposited film. The target-to-substrate distance is another parameter that governs the angular spread of the ablated materials. Hanabusa [4] reported that a mask placed close to the substrate could reduce the spreading.
The third stage is important for the quality of thin film. The ejected high-energy species impinge onto the substrate surface and may induce various types of damages to it. The mechanism of the interaction is illustrated in the following figure 2.1.5.

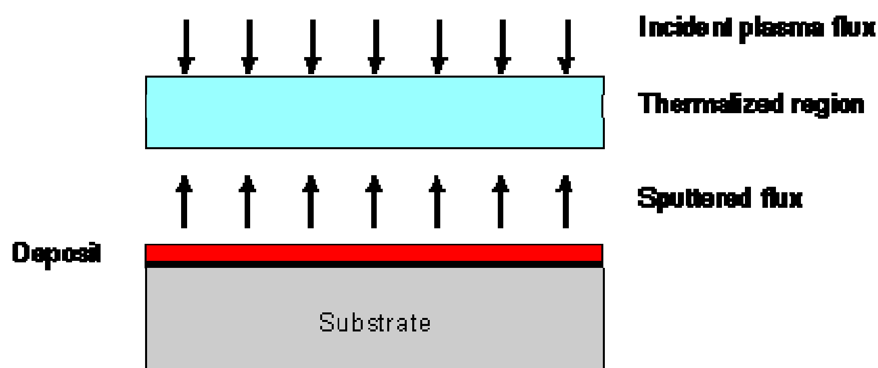

Figure 2.1.5 Schematic diagram of plasma substrate interaction

The energetic species sputter some of the surface atoms and a collision region is established between the incident particle flow and these sputtered atoms. Film grows immediately after this thermalized region (collision region) is formed, the region serving as a source for condensation of particles. When the condensation rate is higher than the rate of particles sputtered from the substrate, thermal equilibrium condition can be reached quickly and film grows on the substrate surface at the expenses of the direct flow of the ablation particles.

Thin film growth

According to the general crystallization kinetics theory, nucleation and growth of crystalline films during PLD deposition process depends on many factors such as the density of deposed species, energy, degree of ionization, and the type of the condensing material, as well as the temperature and the physical-chemical properties of the substrate. The two main thermodynamic parameters for the growth mechanism are the substrate temperature T and the supersaturation D_m the parameters related with the following equation

$$D_m = kT \ln(R/R_e)$$

where k is the Boltzmann constant, R is the actual deposition rate, and R_e is the equilibrium value at the temperature T.
From thermodynamics, the difference between the chemical potentials, $D_m = m_{gaseous\ phase} - m_{crystalline\ phase}$, represents the thermodynamic driving force for the phase transition (in this case crystallization) to occur, and is known as the supersaturation. At equilibrium the chemical potentials of the two phases are equal.
The nucleation process depends on the interfacial energies between the three phases present, the substrate, the condensing material and the vapors. The minimum-energy shape of a nucleus is like a cap, its critical size depending on the driving forces, i.e. the deposition rate and the substrate temperature. For the large nuclei which are a characteristic of small supersaturation, isolate patches (islands) are created on the substrates, which subsequently grow and coalesce together. As the supersaturation increases, the critical nucleus shrinks until its height reaches an atomic diameter and its shape is that of a two-dimensional layer. For large supersaturation, layer-by-layer nucleation will happen for incompletely wetted substrates.
The growth of crystalline films depends on the surface mobility of the adatom (vapor atoms). Normally, the adatom will diffuse through several atomic distances before sticking to a stable position within the newly formed film. The surface temperature of the substrate determines the adatoms surface diffusion ability. High temperature favors rapid and defect free crystal growth, whereas low temperature or large supersaturation crystal growth may be overwhelmed by energetic particle impingement, resulting in disordered or even amorphous structures.
Metev [6] suggested that the N_{99}, the mean thickness at which the growing thin and discontinuous film reach continuity is given by the formula

$$N_{99} = A(1/R)^{1/3} \exp(-1/T),$$

where R is the deposition rate (related to supersaturation), T is the temperature of the substrate and A is a constant related to the materials used.
In the PLD process, due to the short laser pulsed duration (~10 ns) and the small temporal spread (<10 μm) of the ablated materials, the deposition rate can be enormous (~10 μm/s). Consequently a layer-by-layer nucleation is favored and ultra-thin and smooth film can be produced. In addition the rapid deposition of the energetic ablation species causes an increase in the substrate surface temperature. In this respect, PLD tends to demand a lower substrate temperature for crystalline film growth.

For the normal PLD technique, as for other deposition techniques, three modes of film nucleation and initial growth are reported [1]:

- the Frank-Van der Merwe mechanism, which is based on a 2D layer-by-layer growth, occurring when the cohesive energy of the depositing species with the substrate is higher than the cohesive energy among the depositing species;
- the Volmer-Weber mechanism, which occur when the cohesive energy of the depositing species with the substrate is lower than the cohesive energy among the depositing species, resulting in a 3D growth of isolated islands;
- the Stranski-Krastanov mechanism, which is a mixed mode between the previous ones, consisting of island formation after the growth of few 2D layers and occurring because of strain effects due to lattice mismatch between the substrate and the growing film.

The first mechanism results in the growth of a smooth epitaxial film, while the other two modes result in the growth of rough or polycrystalline films or nanostructures.

PLD system

The schematization of a typical PLD system is presented in figure 2.1.6

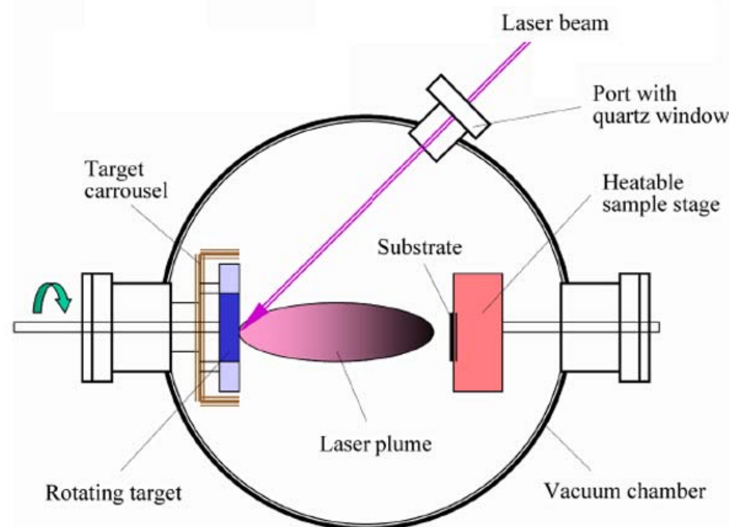

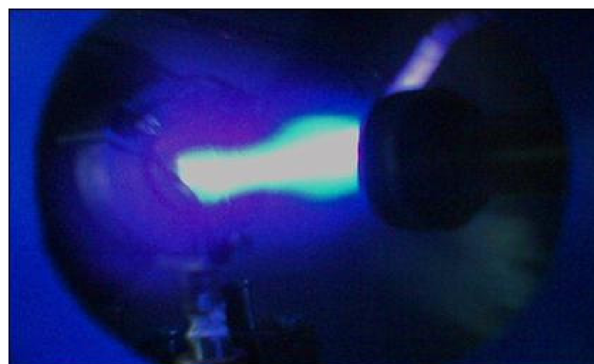

Figure 2.1.6 Schematization of a conventional PLD system. (Image from http://superconductivity.et.anl.gov) and the real plume image

The laser beam is focused onto a target material inside the vacuum chamber, causing the ablation of the material. The ablation can be conducted in vacuum or

in the presence of a background atmosphere of a particular gas. The deposition technique is called simply PLD when the growth takes place in vacuum or an inert atmosphere. The ejected species continue absorbing energy from the laser and eventually interact with the background atmosphere, giving rise to a composite material in which case it is called RPLD – Reactive Pulsed Laser Deposition. The generated plasma plume expands and the material deposits onto a substrate generally placed in front of the target (on-axis configuration). Usually the target holder is rotated and moved to avoid continuous ablation on the same point. The substrate can be heated to the suitable temperature for the desired purpose and moved to gain a uniform thickness of the deposited sample.
The PLD system used for the growth of ZnO thin films in TEI Crete is a typical setup having a deposition chamber equipped with a pump for achieving the desired vacuum level, gas inlets for the control of the deposition atmosphere (O_2, Ar, N_2) rotating target holder, heating system for the substrate during deposition up to 750˚C. A XeCl excimer laser (308 nm), having a pulse width of 25 ns and operating at 10 Hz, was used as the radiation source. The laser beam was focused with a 20 cm focal length quartz lens on the rotating target at a 45˚ angle of incidence, the energy density at the position of the target being around 2 J/cm^2. Sintered ceramic targets of ZnO (99.999%) having 18 mm diameter and 3 mm thickness were used as the target, placed 5.5 cm away from the substrates. The deposition chamber was initially evacuated to 10^{-6} mbar while the growth pressure was kept at 1 mbar by flowing oxygen. The temperature was determined in situ during growth with a thermocouple placed below the substrate.

1 D.B. Chrisey and G.K. Hubler, Pulsed Laser Deposition of Thin Film, John Wiley & Sons, Inc., New York (1994)
2 A. Namiki, T. Kawai, K. Ichige, Surf. Sci. 166, 129 (1986)
3 R.K. Singh, SPIE 2045, 10
4 M. Hanabusa, Mater. Res. Soc. Symp. Proc. 285, 447 (1993)
5 T. J. Goodwin, V. J. Leppert, S. H. Risbud, I. M. Kennedy, and H. W. H. Lee, Appl. Phys. Lett. 70, 3122 (1997),
6 S. Metev, K. Meteva, Appl. Surf. Sci. 43, 402 (1989)

2.2 Characterization techniques

2.2.1. Composition characterization

EDX Analysis

EDX stands for Energy Dispersive X-ray, which is also referred as EDS or EDAX analysis. It is a technique used for identifying the elemental composition of a specimen, or an area of interest on it. An EDX analysis system works in combination with a scanning electron microscope (SEM), operating as an integrated feature.

During EDX analysis, the specimen is bombarded with an electron beam inside the scanning electron microscope. The bombarding electrons collide with the electrons of the specimen atoms, expelling some of them from the material structure. The position of an ejected inner shell electron is eventually occupied by a higher-energy electron from an outer shell. During this process, the transferred electron is releasing energy, resulting in the emission of X-ray radiation, the amount of released energy depending on the initial and the final energy level. The atoms of every element are releasing X-rays of specific energy during this de-excitation process, thus, by measuring the energy of the peaks present in the X-rays released from a specimen; one can identify the element which emitted the X-ray with that specific energy.

The output of an EDX analysis is an EDX spectrum, which is just a plot of how frequently an X-ray of specific energy is received. An EDX spectrum normally displays peaks corresponding to the energy levels from which the X-ray radiation was received. Each of these peaks is uniquely related to an atom, and therefore corresponds to a single element. The more intense a peak in a spectrum, the more concentrated the element is in the specimen. An EDX spectrum plot not only identifies the element corresponding to each of its peaks, but the type of X-ray to which it corresponds as well. For example, a peak corresponding to the amount of energy possessed by X-rays emitted by an electron in the L-shell going down to the K-shell is identified as a K-Alpha peak. The peak corresponding to X-rays emitted by M-shell electrons going to the K-shell is identified as a K-Beta peak. See also figure 2.2.1.

The analytical instrumentation is comprised of an Oxford Instruments INCA Energy X-ray detector and micro-analysis system, integrated in a JEOL CM630 LV SEM at TEI Crete. Image recording is possible via the OI INCA system to hard drive, zip drive or CD writer.

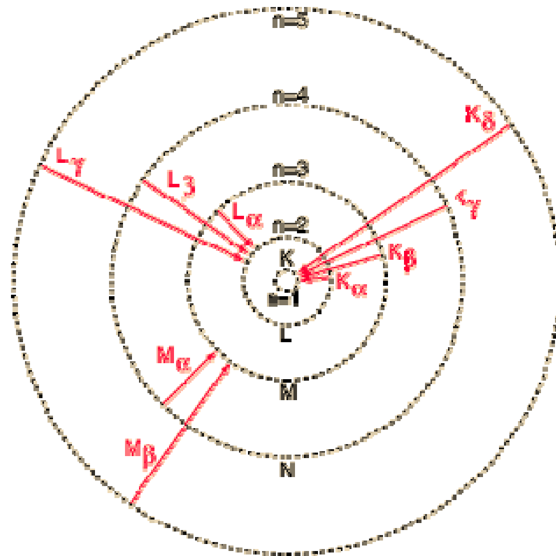

Figure 2.2.1 X-rays generation. Spectral series

Energy dispersive X-ray analysis of almost all minerals and alloys is possible, providing the surface is suitably polished. Detection limits for EDX analysis are variable, but typically are in the range 0.02-0.05%. The software is outputting an energy spectrum. The software also allows multi-element x-ray mapping and line scanning. With modern software, it is possible to collect a series of spectrums for each point (pixel), which can be analyzed by the electron beam probe, as it is scanned across the surface of the specimen. If only one spot is analyzed, quantification of the relative proportions of elements under that spot is possible, which is known as point analysis. If however a line of pixels is analyzed, a line-traverse analysis can be performed which highlights the variation of the proportions of elements with distance along the line. This is known as line scanning. Finally, each pixel in an image can also be analyzed, which illustrates the distribution of a chosen element across the image. This is known as dot-mapping of the elements and can take up some considerable time as the electron probe is required to dwell on each separate point for a pre-determined period of time in order to collect enough data for analysis. In many applications of this technique, this is normally done in conjunction with a backscattered electron image, where each pixel of the image has an exact and corresponding pixel on each of the element maps, which are collected at the same time and at the same resolution. Another reason for choosing this imaging type is that efficient X-ray analysis requires a flat polished surface where there are few obstructions to X-rays leaving the surface of the specimen that may cause contamination of the signal. The software requires calibration against known standards before normal use. Using this powerful tool detailed information regarding films' stoichiometry can be obtained.

SIMS analysis

SIMS ("Secondary Ion Mass Spectrometry") analysis can be used for measuring the atomic composition of solid materials samples. Analysis is performed on plane surfaces, providing profiles of the concentration of the elements as a function of depth. Depths ranging from a few nanometers up to a few tens of microns can be reached. The main feature of this technique is its extreme sensitivity: a secondary ion mass spectrometer can detect, in some cases, one atom of a minor element among several billions (10^9) of matrix atoms (i.e. concentrations near from 10^{13} atoms·cm^{-3}). Although it is a particularly sensitive, technique, this can also be used for measuring the composition of the matrix material with an absolute accuracy of the order of a few percents.
The depth resolution of the profiles can be also very high, approximately 1nm. However, it must be emphasized that is not possible to simultaneously have high sensitivity and high depth resolution, since these two performances are not compatible with each other. In any case, a compromise should be made for optimum results.
This technique is very important in the field of semiconductors for measuring dopants, impurities or major elements concentrations in a wafer as a function of depth. It is implemented for material research, technological process monitoring, reverse engineering and failure study.
During a SIMS analysis, the material under study is bombarded by a beam of accelerated and focused ions. This beam and the corresponding ions are known as "primary" beam and ions. Under typical analysis conditions, the diameter of the primary beam at sample surface (i.e. the probe size) has a value of a few microns. The impact energy of primary ions lies between 0.5 and 15keV, according to the selected conditions. Ar^+, Xe^+ and Cs^+ are the most frequently used primary ions. Ions impact with the sample causes the ejection of surface atoms, so that the primary beam gradually causes a crater on the sample. A spatial scanning is applied to the primary beam so that to homogenize the bombardment and to form a flat-bottomed square crater. The crater covers a surface ranging between 10x10µm^2 to 500x500µm^2. A fraction of ejected atoms is ionized and forms the ions known as "secondary", which are exploited in order to determine the concentrations of elements contained in the sample. Ionic optics limit the detection only to the ions that come from a disc located at the center of the square crater.
In order to avoid charging of the surface, samples are preferable to be conductive. However, insulating materials are also routinely analyzed thanks to specific processes (surface metallization, electrons beam bombardment).
The SIMS analysis is based on the secondary ions detection. Generally, the detected ions are monoatomic. However, it can sometimes be advantageous to detect ions made up of one atom of the analyzed element plus one or several atoms coming from the matrix or the primary beam. Positive and negative ions cannot be detected simultaneously. As a consequence, the analysis conditions have to be adjusted according to the chosen ions polarity. For monoatomic secondary ions, the settings are adjusted to detect positive ions if electropositive elements are searched (for example Al), while they are adjusted to detect negative ions for elements that have a high electronic affinity (for example F). Electropositive or electronegative elements can sometimes be measured by detecting respectively negative or positive ions, but the sensitivity is then considerably decreased. The primary ions nature has an important effect on the

secondary ions polarity. O^{2+} primary ions are generally used to produce positive secondary ions whereas Cs^+ primary ions are used to create negative ions. Cs^+ ions are also used to produce MCs^+ type ions where M can be a metal or a matrix element. This mode is particularly useful to quantify a matrix composition because the ionization efficiency of MCs^+ type species is only little matrix dependant. The depth resolution of a concentration profile depends on:
- the primary ions impact energy. High impact energy leads to a "mixing" of superficial atomic layers which turns out to be the ultimate limiting feature to depth resolution,
- the area the detected ions come from (center of crater only or the whole crater). Indeed, if secondary ions emitted from the crater edges are detected, they tend to scramble the information on depth.

Depth resolution has its drawbacks, since the detection sensitivity is limited by these conditions.

Sometimes, an interfering signal can be superimposed to the signal of the searched ion. This occurs when different ionic species with a very close mass is generated and detected. This phenomenon is called "mass interference". As an example, when one wants to measure a phosphorus concentration into a silicon wafer, a mass interference occurs between 31P and 30Si+1H. When the masses are not too close to each other, they can be separated, but the high mass resolution settings can considerably diminish the transmitted signal, and thus the sensitivity.

Atmospheric elements (H, C, N, O) are present in the vacuum chamber residual atmosphere, even when ultra-high vacuum conditions are adopted. When one wants to measure a very weak concentration of these elements in a sample, the detected signals actually do not correspond merely to the atoms present inside the sample, since the atmospheric atoms adsorbed on the sample surface are also detected. The concentrations below which this phenomenon becomes prevalent are the "detection limits". When the concentrations in the sample are lower than these ones, the analysis can only provide an overvaluation of these concentrations. The detection limits can be lowered by:
- long pumping times before carrying out the analysis,
- high sputtering rate (to the detriment of depth resolution).

Minor and Major element concentrations

A minor element is an element present in small quantity in the sample, at a concentration typically lower than 1% of the total number of atoms. For such a case, the measured signal is considered to be proportional to the element concentration in the material, which can be determined using a standard sample fulfilling the following conditions:

– its matrix must have the same composition as the matrix of the analyzed sample,
– the concentration or the dose (atoms/cm^2) of the required element in the standard must be known.

By measuring under the same conditions the signals of the analyzed sample and the standard sample, one can determine the value of a coefficient named "RSF" (for "Relative Sensitivity Factor") which enables the calculation of a Z element concentration in the analyzed sample using the SIMS formula: $C(Z) = RSF \cdot \frac{S(Z)}{S(ref)}$

where C(Z) is the Z element concentration, S(Z) the signal intensity relative to Z

element and S(ref) the signal intensity relative to the reference species made up of one or several matrix atoms.
A major element concentration is more difficult to be determined than a minor element concentration because of the matrix effect. Matrix effect is due to the fact that ionization rates of atoms are highly dependant on their chemical environment within the analyzed material. As a consequence, when one measures the signal of an ion made up of one matrix atom, this signal is generally not proportional to the element concentration.
The analysis mode known as "MCs^+" makes it possible to reduce considerably (but not completely) the matrix effect. This mode is the one which is generally used to measure matrix compositions. It is necessary then to use a standard made up of the same alloy as the analyzed sample and whose composition is known. If the sample and the standard have sufficiently close compositions, the quantification accuracy can be better than one percent.
The most conventional way to establish the depth scale of a concentration profile is to measure the crater depth using a profilometer and then to deduce one or several sputtering rates according to the results. If the crater crosses several layers whose sputtering rates are different, depths can be determined by taking into account the sputtering rate ratios from a layer to another.
SIMS analysis was performed on In_2O_3 sputtered films, employing a CAMECA IMS 5f system at University of Braunschweig, Germany using the following experimental setup: 3 keV Cs^+ primary ions, Ip = 5 nA, raster 500x500 µm, sputter rate 0.02 nm/s based on the determination of crater depth by profilometry, CsM^+ (M=element of interest) molecular secondary ions, accepted area of Ø=120 µm in the center of the raster field.

2.2.2. Structural characterization

X-ray diffraction

This technique allows the identification and the study of crystalline materials by using the phenomenon of diffraction. Briefly, diffraction occurs when penetrating radiation, such as X-rays, enters a crystalline structure and is scattered. The direction and intensity of the scattered (diffracted) beams depends on the orientation of the crystal lattice with respect to the incident beam. Any face of a crystal lattice consists of parallel rows of atoms separated by a unique distance (d-spacing), which are capable of diffracting X-rays. In order for a beam to be fully (100%) diffracted, the distance it travels between the rows of atoms at a specific angle of incidence must be equal to an integral multiple of the wavelength of the incoming radiation. d spacing greater or lesser than the wavelength of the incoming X-ray beam at the angle of incidence will result in a diffracted beam of less intensity. The resulting XRD analysis is presented graphically as a set of peaks with their intensity on the Y-axis and the goniometer angle of incidence on the X-axis. The exact angle position and the intensity of a set of peaks are unique for a specific crystal structure and a comparison with data from standard tables, such as JCPDS spectra published by the American Society for Testing and Materials, provides valuable information about the crystalline structure and the composition of materials. If the sample is powdered, it can provide, theoretically, all possible orientations of the crystal lattice; the goniometer provides a variety of angles of incidence, and the detector measures the intensity of the diffracted beam.

Besides, XRD can be used to determine the crystallite size of a sample, which is a key point in the field of gas sensors based on metal oxides. Nano-sized crystals are generally too fine to be measured by other techniques, except transmission electron microscopy (TEM). However TEM is complex and time consuming, requires very expensive equipment and sample preparation by destructive methods, while, it is difficult to measure more than a few hundred particles per sample, Moreover, measurements requiring several days of intensive effort, result in an accurate mean crystallite size for a sample, but a not accurate distribution of sizes. Measurement of crystallite size distributions by X-ray diffraction (XRD) solves these difficulties. An X-ray scan of a sample can be performed automatically in a few minutes to a few hours time and the resulting XRD peaks correspond to average diffraction effects from billions of individual nano-sized crystals. The simplest approach for the determination of the crystallite size is to use the peak width at half maximum (FWHM) and the Scherrer equation. However, the crystallite size measured by XRD may be related to the size of the individual crystals of the metal oxide film in the sample, rather than to the size of particles formed from the agglomeration of these crystals. Moreover, when the Scherrer equation is used, crystalline defects can mislead the measurement of the crystallite.

The position of the diffraction peaks and the corresponding d-spacings provide information about the location of the lattice planes in the crystal structure. Each peak corresponds to a d-spacing representing a family of lattice planes. Each peak also has an intensity which differs from that of other peaks in the pattern and reflects the relative strength of the specific diffraction. In a diffraction pattern, the

strongest peak is, by convention, assigned to an intensity value of 100, the other peaks being scaled relative to that value. Although the peak height may be used as a qualitative measure of the relative intensity, a most accurate measure of the intensity relationships in a pattern can be obtained by measuring the area under the peaks (minus background). Variations in measured intensity are related mainly to variations in the scattering intensity of the components of the crystal structure and their arrangement in the lattice. Some of the most dramatic variations are related to the interference between diffractions produced in the lattice; these can produce systematic extinctions or greatly reduced intensities of peaks from certain lattice planes.

For crystallites of large size (i.e., thousands of unit cells), the normal diffraction will produce diffraction peaks only at the precise location of the Bragg angle. This is because of the canceling of diffractions by incoherent scattering at other angles by the lattice planes within the large crystal structure. If the crystallite size is smaller (so that there are insufficient lattice planes to effectively cancel all coherent scattering at angles close to the Bragg angle), the net result will be a broadening of the diffraction peak around the Bragg angle. The phenomenon of widening of diffraction peaks is therefore related to incomplete "canceling" of small deviations from the Bragg angle in small crystallites and is known as particle size broadening. The crystallite size broadening (β) of a peak can usually be related to the mean crystallite dimension (d) by the Scherrer equation:

$d=K\lambda/(\beta^2- \beta o^2)^{1/2}\cos\theta$

where β and βo are the peak width at half maximum in radians and the width introduced by instrumental broadening, K=180/π, (λ=0.154056 nm for Kα1 of Cu) and θ is obtained from the peak position.

Particle size broadening is not significant at sizes above 1 µm, and is trivial to un-measurable at sizes bellow 0.01 µm. When all parameters are known (i.e.FWHM values for crystallites of known size around 1 µm or larger), the relationship above may be used to calculate crystallite sizes as small as 10 Å if no stresses are present in the structures.

It is interesting to consider the particle size broadening when studying the diffraction pattern obtained from amorphous materials. Typically these materials (like glass and plastics) will give an extremely broad peak over an angular range that will look like a "hump" in the background. One can think of this "hump" as an extreme example of particle size broadening, where the short range ordering is on the order of a few angstroms. Residual Stress and Strain in a material can produce two types of diffraction effects. If a tensile or compressive strain is uniform, it is called macrostrain and the unit cell distances will become larger respectively smaller, resulting in a shift in the pattern of the diffraction peaks. Macrostrain causes the lattice parameters to change in a permanent (but possibly reversible) manner resulting in this peak shift. In contrast, microstrains are produced by a distribution of tensile and compressive forces, resulting in a broadening of the diffraction peaks. In some cases, some peak asymmetry may be also the result of a microstrain. Regarding microstress in crystallites, this may come from dislocations, vacancies, shear planes, etc, its effect generally being a distribution of peaks around the unstressed peak location and a crude broadening of the peak in the resultant pattern.

All In_2O_3 and ZnO thin films included in this study were characterized by XRD, using an X-ray workstation including a high flux Rigaku D/max-2400 generator capable of producing simultaneously two X-ray beams. The characteristics of the

generator are: rotating anode with changeable target material capability, horizontal tube with 2 Be windows and electromagnetic shutters, line and point focus, 12 kW maximum power output, 60 kV maximum voltage, 200 mA maximum current and 0.5x10 mm^2 focal spot size. Two instruments were attached to the generator: a small-angle X-ray scattering camera (2j range: -3° to +3°, slit collimation) with a position sensitive detector (100 mm effective length, 10 mm window height), and an X-ray diffractometer (2j range: -60° to +158°).

Transmission electron microscopy

The Transmission Electron Microscope (TEM) was the first type of Electron Microscope developed and its operation is similar to that of the Light Transmission Microscope except the use of a focused electron beam instead of a light beam in order to "see through" a specimen. It was first developed by Max Knoll and Ernst Ruska in Germany in 1931 and its operation was based on the dispersion of electrons, focused by condenser lenses, colliding with the sample. An image was obtained from electrons less dispersed, which was then successively magnified by electromagnetic lenses and finally projected onto an electron sensitive film or a screen.

Since then, many TEM techniques have been developed in such a way that today TEM is much more than just a characterization method, being an independent scientific, very challenging field. The existing TEM techniques are:

- Bright field (BF)
- Dark field (DF)
- Selected-area diffraction (SAD)
- High-resolution TEM (HRTEM)
- Convergent beam electron diffraction (CBED)/Large angle CBED (LACBED)
- Scanning TEM (STEM)
- Energy-dispersive X-ray (EDX) spectroscopy
- Electron energy-loss spectroscopy (EELS)
- Energy-filtered TEM (EFTEM)
- SPINNING STAR (precession diffraction)
- Cathodoluminescence (CL)
- Tomography
- In-situ (heating/cooling, traction)

Conventional TEM under bright and dark field conditions was used for characterization and understanding of the intimate structure of the thin films as well as their growth mechanism.

Bright field (BF) characterization

It is based on imaging the sample under broad electron beam illumination, and selecting with an objective aperture only undiffracted electrons for the image formation (e.g. to improve image contrast and focusing). BF images contain mass-thickness and diffraction contrasts. In crystalline specimens, one may observe thickness fringes, bend contours, grain boundaries, crystalline defects such as dislocations, twins, or stacking faults, and second phases. Generally BF imaging requires minimal set up, and is, for instance, useful for specimen inspection and for imaging size and morphology of nanostructured materials.

Dark field (DF)

An objective aperture is used and the sample is tilted, so that only crystal(s) fulfilling a particular diffraction condition can contribute to the TEM image.

Aberrations from the perfect crystal, such as dislocations or second phases, do not fulfill the diffraction condition, and are discriminated as dark sections on the image. Commonly, it requires a 2-beam set up, in which one lattice place diffracts very strongly, in order to obtain maximum image intensity. DF imaging is used, for example, for imaging crystalline defects, twinning and second phase precipitates and for determining dislocation types and Burger's vectors. It is also useful for imaging size, shape and distribution of nanocrystals by selecting only a proportion of the nanocrystals to contribute to the image.

Selected-area diffraction (SAD)

A diffraction pattern is constructed under broad, parallel electron illumination. An aperture in the image plane is used to select the diffracted region of the specimen, giving site-selective diffraction analysis. SAD patterns are a projection of the reciprocal lattice, with lattice reflections appearing as sharp diffraction spots. By tilting a crystalline sample to low-index zone axes, SAD patterns can be used to identify crystal structures and measure lattice parameters. SAD is essential for setting up DF imaging conditions. Other uses of SAD include analysis of: lattice matching, interfaces, twinning and certain crystalline defects. SAD of nanocrystals gives ring patterns analogous to those from X-ray powder diffraction, and can be used to identify texture and discriminate nanocrystalline from amorphous phases. While SAD can obtain diffraction information from relatively small volumes, CBED is necessary for diffraction on the nanometre scale. SAD patterns of In_2O_3 and ZnO films were used to prove XRD analysis conclusions in order to avoid the misinterpretation due to problems associated with polycrystalline samples characterization.

High resolution TEM (HRTEM) is a powerful technique for the detailed structural study of the nanocrystalline samples. High-resolution TEM in general refers to an imaging in which lattice fringes (i.e. crystallographic planes) are observed or atomic resolution is achieved. Unlike BF or DF TEM, HRTEM images are formed from a number of diffracted beams; this multi-beam approach is known as phase-contrast imaging, and is necessary to construct an image of the crystal lattice. HRTEM provides access plenty of information about the sample, so that someone can analyze crystalline defects and interfaces at the atomic scale and observe and verify devices, multilayers, nanocrystals and nanostructures. The technique typically requires very thin specimens free of preparation artifacts. Additionally, correct interpretation of HRTEM images may depend upon image simulation. HRTEM characterization was performed on some of the films included in this work.

2.2.3. Surface characterization

Scanning electron microscopy

The SEM's principle is scanning the surface of a specimen with finely focused electron beam in order to produce an image of the surface. The first published description of SEM appeared in 1935 by the German physicist Dr. Max Knoll. Although another German physicist, Dr. Manfred von Ardenne, performed in 1937 some experiments with what one could call a scanning electron microscope, it was not until 1942 that three Americans, Dr. Zworykin, Dr. Hiller and Dr. Snijder first described a true SEM with a resolving power of 50 nm and magnification of 8000 times. The Scanning Electron Microscope (SEM) is a microscope that uses electrons to form an image and there are many advantages to use it instead of other instruments. SEM has a large depth of field, which allows a large amount of the sample to be in focus at one time. SEM also produces images of high resolution, which means that closely spaced features can be separately examined at a high magnification. Nowadays SEMs can have resolving power of 1 nm and magnify over 400000 times.
Basically, during SEM operation, a beam of electrons is generated in an electron gun (cathode, located at the top of the column). This beam is attracted to the anode, condensed by a condenser lens and focused at a very fine point on the sample by the objective lens. The electron beam hits the sample, producing, among others, secondary and backscattered electrons from the sample. These electrons are collected by a secondary electron or a backscattered electron detector, converted to a voltage, and amplified.
Electron beam interaction with a sample is what makes electron microscopy possible. The energetic electrons in the microscope strike the sample and various reactions can occur, presented in figure 2.2.2.

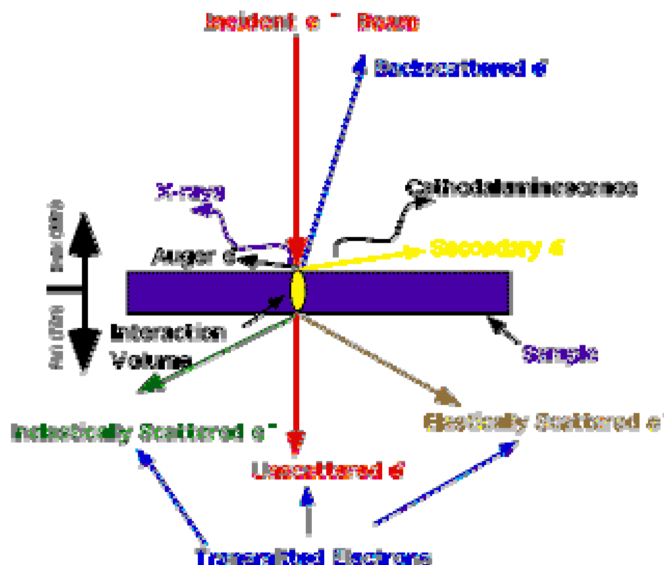

Figure 2.2.2. Schematic illustration of specimen-electron beam interaction

The types of signals collected in a SEM apparatus include secondary electrons, back scattered electrons (BSE), x-rays, light (cathodoluminescence), specimen current and transmitted electrons, all signals resulting from interactions of the electron beam with atoms at or near the surface of the sample.. These types of

signal all require specialized detectors that are not usually all present in a single apparatus. In the most common or standard detection mode, secondary electron imaging or SEI, SEM can produce very high-resolution images of a sample surface, revealing details about 1 to 5 nm in size. Due to the way these images are created, SEM micrographs have a very large depth of field, yielding a characteristic three-dimensional appearance useful for understanding the surface morphology of a sample. Back-scattered electrons (BSE) are beam electrons that are reflected from the sample by elastic scattering. BSE are often used in analytical SEM along with the spectra made from the characteristic x-rays. Because the intensity of the BSE signal is strongly related to the atomic number (Z) of the specimen, BSE images can provide information about the distribution of different elements in the sample. Preparation of the samples is relatively easy since the SEM only requires the sample to be conductive. Also nonconductive samples can sometimes be observed in the traditional SEM, using low beam energies to avoid charging or in novel SEM systems operated at low vacuum. The combination of higher magnification, greater resolution, larger depth of focus and easiness of sample preparation makes SEM one of the most powerful surface characterization tools.
SEM characterization of some samples was carried out using a JEOL JSM-6510 LV equipped an INCA Energy x-rays detector for EDX analysis.

Atomic force microscopy AFM (Scanning probe microscopy SPM)

In 1981, a new revolutionary method of microscopy known as scanning probe microscopy (SPM) was invented and its applications have been increasing exponentially in diverse fields of life, physical sciences, engineering and technology. The development of this technique resulted in a Nobel Prize. Gerd Binnig and Heinrich Rohrer, both from IBM in Zurich, won the Nobel prize in 1986 for the invention of the Scanning Tunneling microscope. Later, this technique gave birth to a family of scanning probe microscopy (SPM) instrumentations, their approach to solve the problem of imaging nanoscale objects being novel. Their solution for nanoscale imaging was to literally feel the surface of the object with a very sharp probe, while very fine control on the movement of the probe was made possible by advances in piezoelectric technology. G. Binnig, C.F. Quate and C.H. Gerber developed the Atomic Force Microscope, in 1986, which could also be used to explore samples that are not electrically conductive.
A large number of SPM variants have been developed based on the detection of forces between the probe tip and a sample. A variety of tip-surface interactions may be investigated by an atomic force microscope (AFM), depending on the separation between tip and sample. At short distances, the tip predominantly experiences interatomic forces: the very short range (~ 0.1 nm) Born repulsive forces and the longer range (up to 10 nm) van der Waals forces. Further away from the surface, where the van der Waals forces decay rapidly and become negligible (100-500 nm above the surface), long-range electric, magnetic and capillary forces are still significant and can be probed. At distances of a few nanometers, van der Waals (VdW) forces are sufficiently strong to move macroscopic objects, such as AFM cantilevers (to which the scanning tip is attached). VdW forces are usually attractive and rapidly increase as atoms/molecules approach one another. When lifting the probe by at least one nanometer from the sample surface, only long-range interactions remain. The

relevant forces result in general from van der Waals interactions, electro- and magnetostatic interactions, and, under ambient conditions, often from the formation of liquid capillaries. Then, the information of the atomic or nanoscale surface structure gets completely lost.
While VdW forces are relatively small and capillary forces can be avoided by either choosing a sufficiently large working distance or by working on clean surfaces, electro- and magnetostatic interactions can yield relatively strong forces. This can provide important information about the electrical or magnetic charge distribution in the near-surface regime of the sample. Since these charge distributions can vary significantly, the lateral variations as well as the range of the resulting interactions can be very different on different samples. Near-field operation means, in this context, that only charges in the probe and the sample within a certain volume around the probe apex contribute to contrast formation. In other words, if the static interaction is modeled in terms of a multipole expansion of the charge distribution, one usually finds monopole, dipole, and higher contributions which all have to be taken into account up to a certain degree. Thus, for the magnetostatic interaction it is very frequently found that the resulting forces are not simply dipole forces but that the monopole term dominates the contrast formation.
VdW interactions consist of three components: polarization, induction and dispersion forces. For two identical interacting gas molecules, for example, the VdW potential (U_{VdW}) can be expressed as the sum of these three components as:

$$U_{VdW} = -\left(\frac{1}{4\pi\varepsilon_0}\right)^2 \left(\frac{\mu^4}{3kT} + 2\mu^2\alpha + \frac{3}{4}\alpha^2 \bar{h}\omega\right) \cdot \frac{1}{z^6} \approx -\frac{C_1}{z^6}$$

where ε_0 is the permittivity of vacuum, T is the temperature, μ is the permanent dipole moment, α is the polarizability of the molecules, $\bar{h}\omega$ is the ground state energy of electrons, z is the distance between the interacting molecules and C_1 is a constant, known as the London coefficient. Dispersion forces (London forces) generally dominate over orientation and induction forces (except in the case of strongly polar molecules). Since dispersion forces originate from the instantaneous fluctuations of electrons around the nuclei, they act between all materials (such forces are also called instantaneous-dipole - induced-dipole forces.). If the probe further approaches the sample and the electronic wavefunctions of the outermost probe atoms and sample atoms start to overlap, strong repulsive forces arise. These forces, also called Born repulsive forces, are characterized by having very short range and increase very sharply as two molecules come together. The repulsive potential is most often expressed as a power-law potential:

$$U_{rep} = \frac{C_2}{z^{12}}$$

The total intermolecular pair potential is obtained by summing the attractive (Eqn. 1) and repulsive (Eqn. 2) potentials. The expression is the well-known Lennard-Jones potential:

$$U = \frac{C_2}{z^{12}} - \frac{C_1}{z^6}$$

where C_1 and C_2 are the corresponding coefficients for the attractive and repulsive interactions.
Describing the AFM tip and sample interactions, the attractive and repulsive potential pairs have to be summed for all interacting atoms with considerations on the local geometry, material properties and the non-additive characteristics of the

VdW interactions. In practice, an experimental force vs. distance curve is applied, that can be registered by AFM while approaching the tip towards the sample. Typical variation of the tip-sample interaction force with the separation in between them is shown in figure 2.2.3.

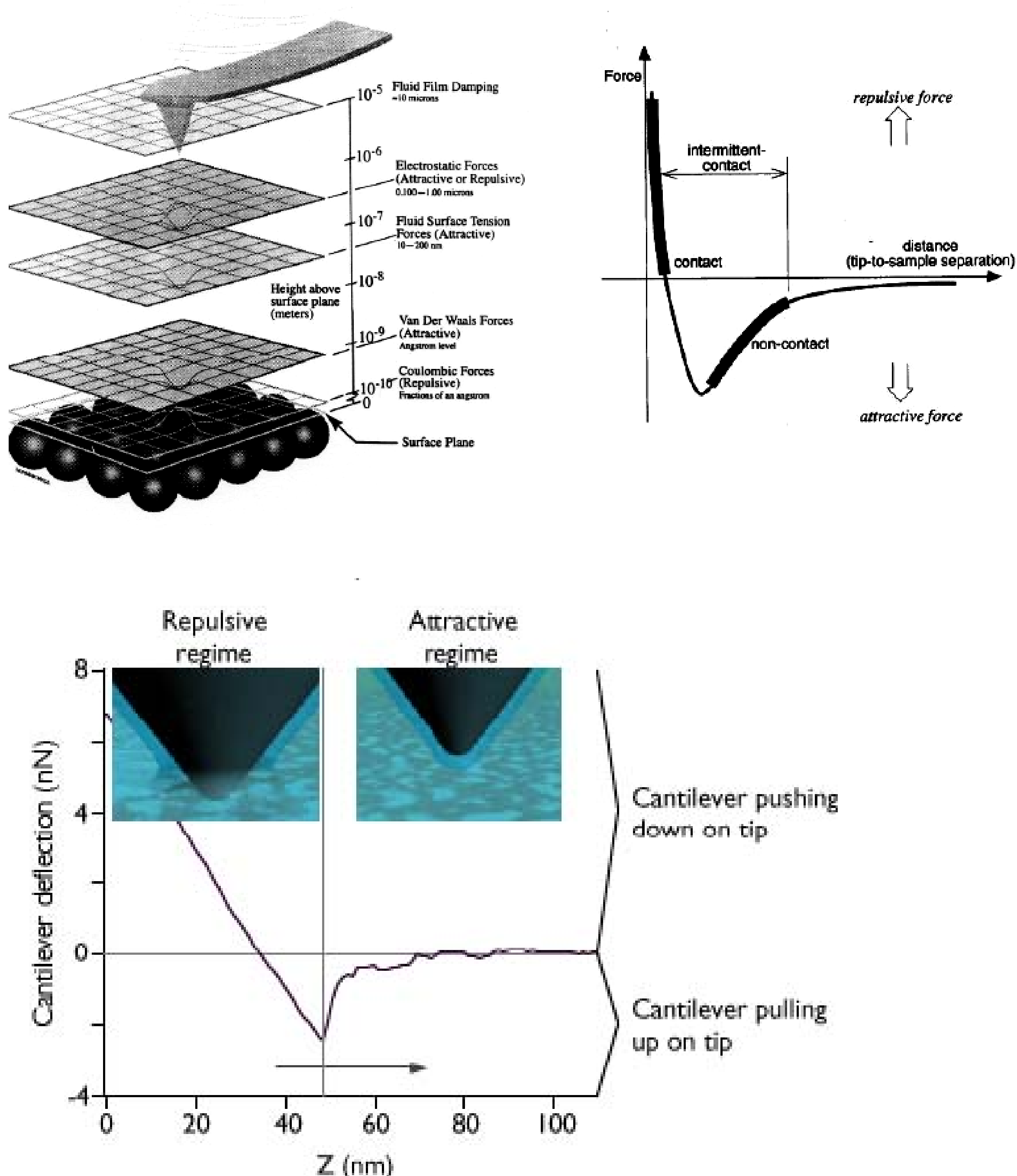

Figure 2.2.3 Typical variation of the tip-sample interaction force with the separation in between them

The VdW potential between two macroscopic bodies, for example a sphere (like the AFM tip end) and a plane (the sample surface), can be approximated as:

$U_{VdW} = -\left(\frac{AR}{6z}\right)$ and the VdW force as: $F_{VdW} = -\frac{dU_{VdW}}{dz} = -\frac{AR}{6z^2}$

where R is the radius of the sphere and A is the Hamaker constant, $A = \pi^2 C_1 \rho_1 \rho_2$, that characterizes the properties of the interacting materials (and was more precisely given by Lifshitz). C_1 is the London coefficient and ρ_1 and ρ_2 are the densities of the interacting bodies.
A model concerning repulsive forces between macroscopic objects was formulated by Hertz more than hundred years ago. According to this, the indentation force acting when a sphere is pressed onto a flat surface can be given as

$$F_{ind} = \sqrt{K^2}\sqrt{Rd^3}$$

where K is the effective elastic modulus (Young's module and Poisson coefficients of the tip and the sample) and d the indentation depth. However, since Hertzian mechanics assumes that there are no adhesion or surface forces (i.e., no attraction whatsoever), it is not the best model for describing a typical AFM experiment.
Operation modes in AFM can be discussed in terms of the applied force regimes (contact, non-contact and intermittent-contact, as shown in figure above) or in terms of the force sensing technique employed (deflection or quasistatic (DC) mode and vibrational or dynamic (AC) mode). The operating modes of AFM can be discussed in more detail theoretically.
Force detection and AFM imaging
The underlying principle of AFM is that the interactions between the sample and the edge of a probe tip, which is mounted on a cantilever, result in a response in the cantilever, notably a deflection.

In the continuous contact mode, also known as repulsive mode, an AFM tip makes a soft "physical contact" with the sample (see figure 2.2.4 a). The sharp probe tip, often a pyramidal-shaped etched silicon nitride tip, is attached to the end of a V-shaped spring cantilever with a low spring constant, typically between 0.06 N/m and 0.6 N/m. As the scanner gently traces the tip across the sample, the contact force causes the cantilever to deflect to accommodate changes in topography. In the standard constant force mode (figure 2.2.4 b), a feedback system maintains the cantilever deflection at a constant level (which corresponds to a constant force according to Hooke's law). The setpoint, a parameter which is defined by the user, defines the force that will be exerted on the surface by the tip (which can be as low as ~ 0.1 nN). A common way to measure the cantilever deflection is by utilizing a laser beam which is reflected at the back of the cantilever via a mirror, into a position-sensitive photo detector. The laser beam which bounces off the cantilever functions as an optical lever arm, amplifying in this way the deflection. As the sample is scanned under the tip, the x, y and z position of the sample surface with respect to the tip is determined by a piezoelectric tube scanner. The movement of the sample in the z-direction, that is needed to keep the deflection at its constant setpoint level, is registered during x-y scanning, and a three dimensional map is constructed which is closely related to the topography of the surface.
Frictional force (figure 2.2.4 c), exerted by the sample on the tip as it sweeps over the sample, may significantly contribute to the topographical image. Surface

domains with different frictional properties may appear as topographical features in the image. The use of a four-segment photodetector gives the advantage of being able to distinguish friction from topography, and with such a setup, lateral force microscopy can be performed.

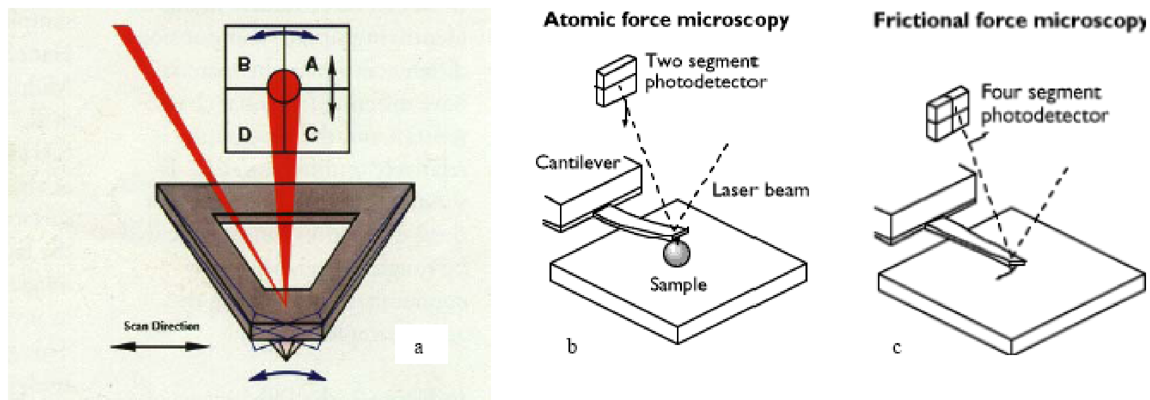

Figure 2.2.4 a Laser beam deflection on the tip; b tip movement in standard constant force mode; c tip movement in frictional force microscopy.

Contact mode successfully performed many pioneering AFM applications. However, it suffers from several drawbacks. The constant downward force of the tip onto the surface is not always low enough to avoid damaging certain sample surfaces. These include not only biological and most polymer surfaces, but even many seemingly harder materials, which are not completely resistant to such damage. In ambient operation, there is often a lack of force control in the desired range. The main reason for this is that in a typical atmospheric ambient environment, surfaces are always covered by 10-30 mono layers of adsorbed water vapor, hydrocarbons and/or other contaminants. When the tip comes in close proximity to the surface, the capillary action pulls the tip down towards the surface. This leads to increased normal and lateral forces, when scanning in the continuous contact mode. Interaction forces as well as certain nanomechanical properties of the surface can be estimated by plotting so called force-distance curves. While topographic imaging uses the up-and-down deflection of the cantilever, friction imaging (or “lateral force imaging” or “lateral deflection imaging”) uses torsional deflection. If the scanner moves the sample perpendicular to the long axis of the cantilever, friction between the tip and samples causes the cantilever to twist.

Lateral deflections of the cantilever usually arise from two sources (see figure 2.2.5):

• changes in friction (figure 2.2.5 a) and
• changes in slope (figure 2.2.5 b).

In the first case, the tip may experience different frictions as it traverses inhomogeneities, causing the cantilever to twist more or less strongly. In the second case, the cantilever may twist when it reaches steep slope. To separate one effect from the other, normal topographical images should be collected simultaneously.

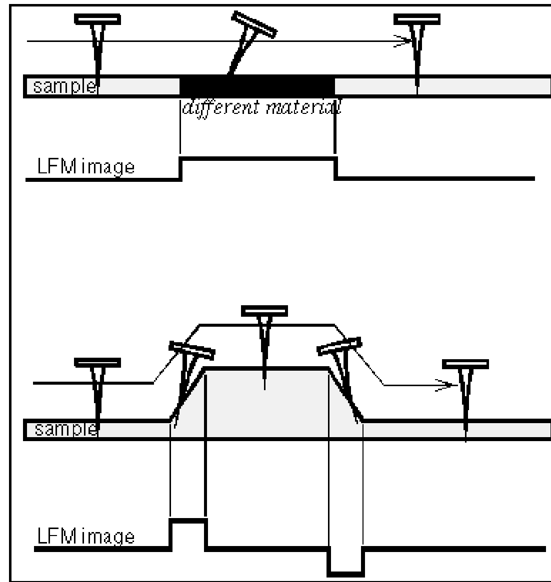

***Figure 2.2.5 The two sources of lateral deflections: a: Changes in friction, b: Changes in slope*.**

Tapping mode (TM) AFM successfully overcomes many drawbacks of the contact-mode. In tapping mode, to diminish lateral and normal forces exerted by the tip on the sample, the tip is brought only intermittently into contact with the surface during scanning. The basic idea is that the cantilever is brought into oscillation, and changes in oscillation amplitude or phase are detected as the vibrating tip sweeps across and interacts with the surface.
TM-AFM operation can be simulated as a driven, damped harmonic oscillator with an additional term to describe the interaction between the tip and the sample. The motion is expressed in terms of the displacement of the tip d(t), and the position of the root of the cantilever z(t), as depicted in figure 2.2.6.

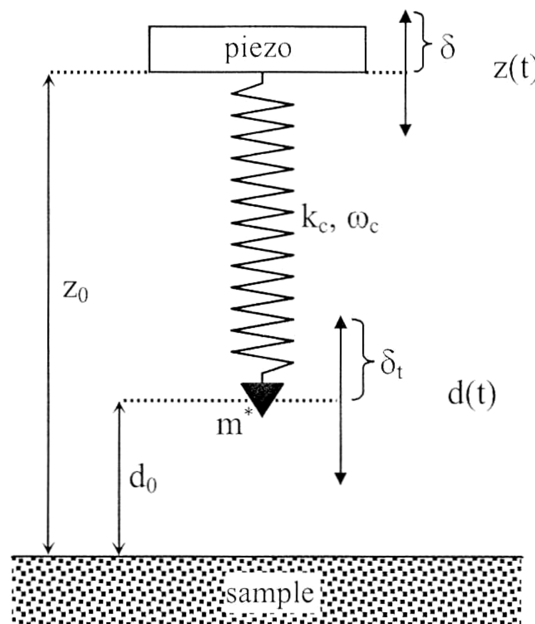

Figure 2.2.6 Driven, damped harmonic oscillator model system can be applied for the description of the tapping-mode AFM operation.

The cantilever is treated as a massless spring of spring constant k_c and eigenfrequency f_c that is loaded by a tip of effective point mass m^*. The equation of motion can be given as

$$m^* \frac{\partial^2 d(t)}{\partial t^2} = k_c (z(t) - d(t)) + \frac{m^* \omega_c}{Q} \left(\frac{\partial z(t)}{\partial t} - \frac{\partial d(t)}{\partial t} \right) + F_{ts}(d, \frac{\partial d}{\partial t})$$

The term $F_{ts}(d, \frac{\partial d}{\partial t})$ contains the unique physics of the intermittent contact mode and represents the interaction between the tip and the sample. Q is the quality factor of the cantilever. (Q is defined as the ratio of the peak height of the root-mean-square (RMS) amplitude curve at resonance to the peak full-width-at-half-maximum.)

The cantilever is driven through z(t) as $z(t) = z_0 + \delta \cdot \sin(\omega t)$, where δ is the drive amplitude and f the drive frequency. z_0 is the mean distance between the base of the cantilever and the sample surface and it is used to regulate the setpoint amplitude. After a short transient, the oscillation of the tip can be expressed as: $d(t) = d_0 + \delta_t \cdot \sin(\omega t + \alpha)$ where d_0 is the mean distance between the tip and the sample surface, δ_t is the amplitude and α is the phase.

In TM-AFM, the tip is mounted on a rigid cantilever (k_c = 20- 50 N/m) that is oscillated vertically at a relatively high amplitude (10-100 nm) using a piezoelectric crystal. The oscillation frequency is set close to the mechanical resonance frequency of the cantilever (f_c ~200-400 kHz). Typical operation parameters give the cantilever enough energy to avoid being trapped by attractive forces. The movement of the tip goes through non-contact and contact tip-sample conditions and the two regimes are separated by the interatomic distance (a_0). For distances larger than a_0 the attractive tip-sample interaction (F_{ts}) can be calculated through the VdW force between a sphere and a flat surface according to a previous equation. At distances smaller than a_0, repulsive forces come into play and the description of F_{ts} in this regime is not that simple. Several continuum contact mechanical models have been proposed, where both elastic and inelastic tip-sample interactions are considered as the tip touches the surface.

During tapping mode imaging, the vibrational characteristics - frequency, amplitude and phase - of the oscillating tip are measured. In principle a feedback regulation can be based on the detection of any of these parameters, since via oscillator equation, these all are sensitive to changes of the tip-sample interactions. Most often, it is the RMS oscillation amplitude that is measured, using the same detection device as shown for the contact mode (see figure 2.2.7). While the sample is scanned under the vibrating tip, a feedback loop adjusts the tip-sample separation to maintain constant cantilever amplitude at a setpoint level determined by the user. A topographical image of the surface is created by recording the feedback signal which regulates the vertical movements of the sample during scanning (and therefore contains height information), and plotting it as a function of the horizontal position, determined by the x and y positions of the piezoelectric tube scanner.

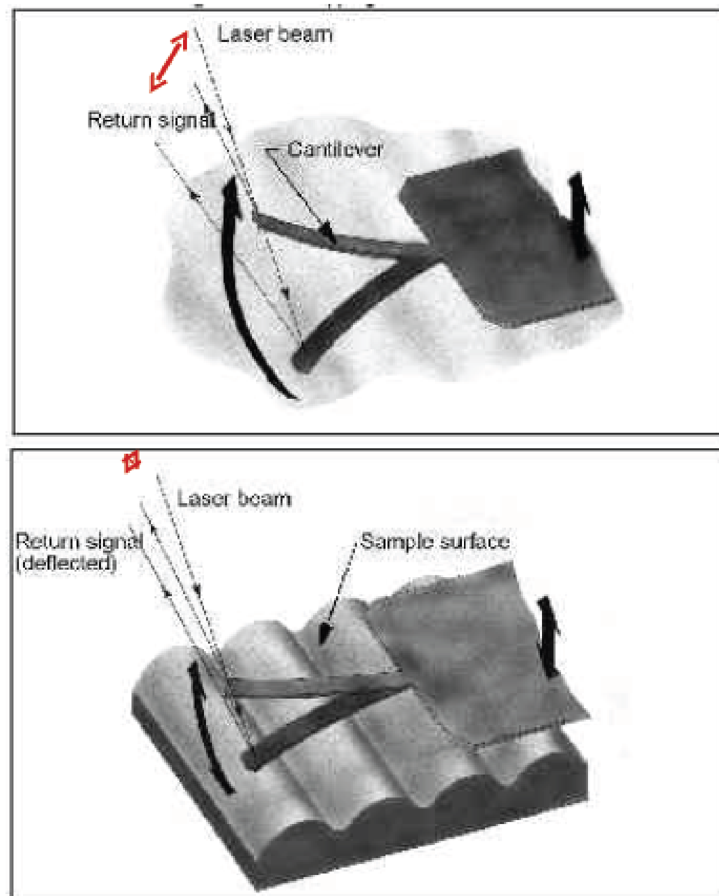

Figure 2.2.7 cantilever movement in tapping mode

An alternative (maybe more picturesque) way of understanding the operation of the tapping mode is by considering, that under the influence of the force gradient $\partial F_{ts}/\partial z$ near the surface, the cantilever behaves as it would have a modified spring constant $k_c^{'} = k_c - \frac{\partial F_{ts}}{\partial z}$.

As the tip approaches the sample, the change in the apparent spring constant will modify the cantilever resonance frequency too, since:

$$\omega_c = \sqrt{k_c / m_{eff}}$$

and therefore the frequency will be

$$\omega^{'} = \omega_c \sqrt{1 - \frac{1}{k_c}\frac{\partial F_{ts}}{\partial z}}.$$

The modification of the resonance frequency will result in a change in the probe's oscillation amplitude and the phase shift as well. The frequency dependence of the oscillation amplitude and the phase is illustrated bellow in figure 2.2.8:

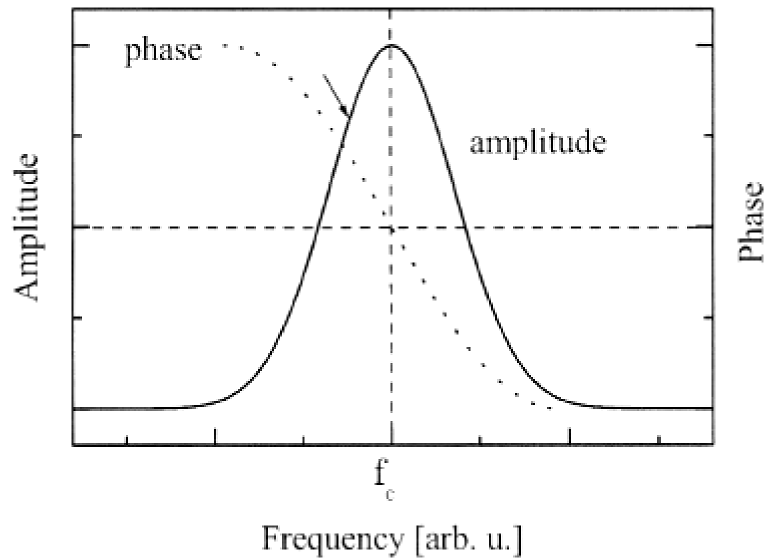

Figure 2.2.8 Frequency response of a typical TM-AFM cantilever. The amplitude of the tip vibration as a function of the driving frequency exhibits a peak that indicates the resonant frequency. The dashed line shows the phase of the tip oscillation. The arrow indicates a typical choice of drive frequency during TM-AFM operation.

The AFM system

A generic AFM comprises the following components:

- Scanning System
- Probe
- Probe Motion Sensor
- Controller Electronics
- Noise Isolation
- Computer

The AFM system in Crete University AFM Multimode III from Digital Instruments:

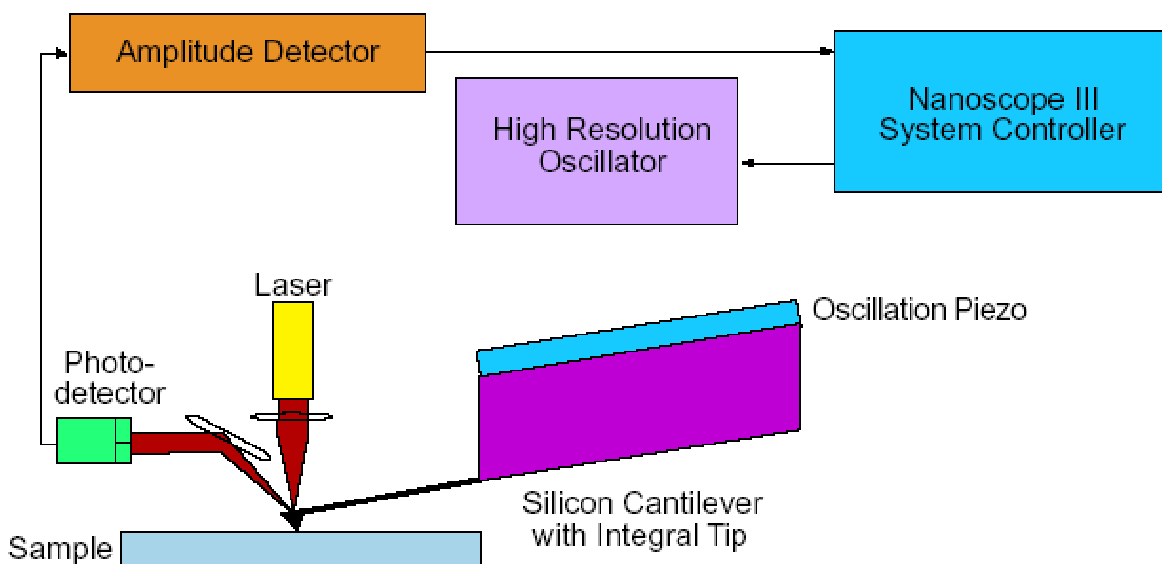

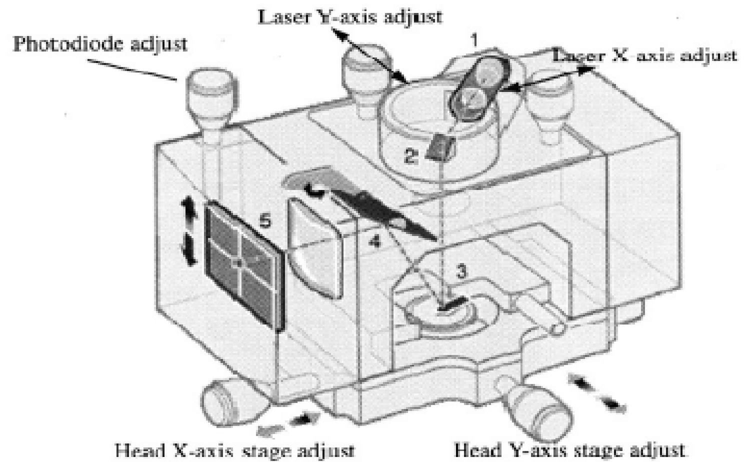

Most materials can be investigated by this technique because, regardless of the material, a repulsive force results when the tip and the surface are nudged closed enough together.

Probes

All AFMs use a sharp mechanical tip (probe) to “feel” the surface of the sample by detecting the forces acting between tip and sample surface or the amount of tunneling current flowing between them.

AFM Tips and Cantilever

The tips are commonly fabricated from silicon, silicon nitride or diamond (for hardness testing only) and are left bare or coated with a special material (metal for electric force microscopy - EFM and rare-earth boride for magnetic force microscopy - MFM) to suit a particular application. The tip is mounted on a thin cantilever whose deflections provide a measure of the interaction forces.
Currently commercially available AFM tips are microfabricated in three geometries, namely: (1) conical, (2) tetrahedral and (3) pyramidal. Conical tips can be made sharp with a high aspect ratio (the ratio of tip length to tip diameter) making them especially useful for imaging features that are deep and narrow. Conical tips with diameters of 5 nm can be made, but they are easily broken. The pyramidal and tetrahedral tips have lower aspect ratios with tip diameter ranging 10nm to 50 nm. These tip configurations are duller, but more durable.

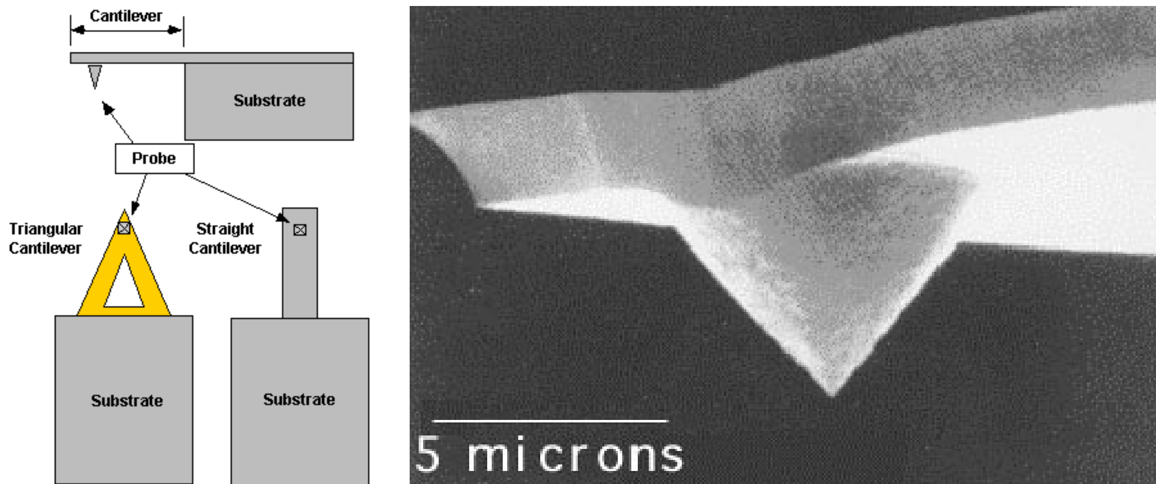

Scanners

At present no mechanical motors can achieve precise, reproducible movement at the atomic scale. The scanning probe microscopes utilize the phenomenon of piezoelectricity to move the tips relative to the sample surface, at the atomic scale. A scanner fabricated from ceramic, piezoelectric component, typically made from sintered ceramic lead zirconium titanate (PZT), is used to move the probe and the sample relative to each other in all three (x, y, z) directions. An electrical voltage is applied to the piezoelectric component to make the scanner mechanically expand. The typical expansion coefficient for piezoelectric components ranges from 0.1 nm / Volt up to 300 nm / Volt.

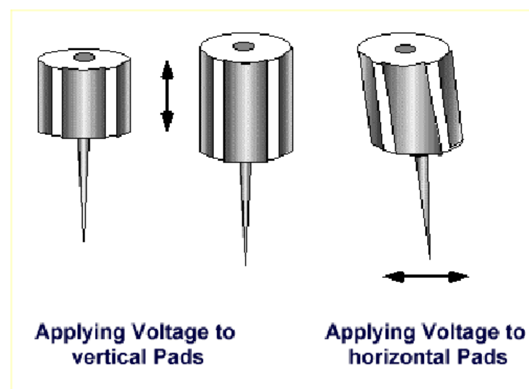

As a result of these mechanical movements, the tip can be rastered over the sample, as shown schematically below.

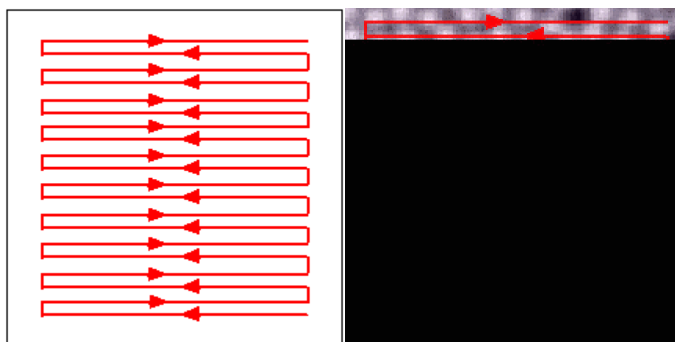

As the tip is rastered over the sample surface, the lateral (x, y) location and the height or property value at that position (z) is recorded. Once the z-profile for each of the raster lines are put together, an image of the surface can be constructed and visualized.

AFM working modes

Based on the above presented information, AFM has four basic operation modes:

- Contact Mode (strong repulsive force of interaction –constant force or constant distance)
- Non contact mode (weak attractive force of interaction- vibrating probe)
- Tapping mode (strong repulsive force of interaction – vibrating probe)
- Lateral force mode (frictional forces exert a torque on the scanning cantilever)

Each of those modes has its own specific features and actually the possibilities on characterization using such systems become more effective.

In the present work, AFM characterization played the most important role since the main focus of this thesis was on the correlation of the surface topography with film functionality. AFM measurements were performed in air at room temperature (RT) using a Digital Instrument AFM with Nanoscope III controller in tapping mode. Ultra-sharp silicon cantilevers (NSC15 series, 125 mm long, spring constant ~ 40 N/m, resonant frequency ~200-400 kHz) were used. The images were collected at 512 × 512 pixels per image at a scan rate of 1 Hz. In the present study, characterization of all films with AFM was followed by a detailed analysis and processing of data using the Scanning Probe Image Processor, SPIP, on the captured ascii images.

2.2.4. Optical characterization: Ultraviolet-visible spectroscopy

The optical constants, which are necessary in order to describe the optical properties of transparent semiconducting films, are briefly presented here. The basic idea of all the optical properties is the interaction of visible, UV and NIR electromagnetic radiation with the electrons of materials. Electromagnetic radiation propagates differently in materials than in free space because of the presence of radiation-matter interactions. As a result, there is a change in the wave velocity and intensity of the radiation, described by the complex index of refraction, which is defined as n_c=n-ik, where n is the real index of refraction and k is the index of absorption, which is also known as the extinction coefficient.
The mechanisms of light losses in transparent conducting films are absorption, reflection and scattering. Charge carrier absorption, absorption by bound charges and molecular scattering are mechanisms related to the material of a film. Similar types of absorption also occur in the substrates, but this will not be considered, as its effect is always subtracted from the optical data. Finally, reflections occur at the air-film, film-substrate and substrate-air interfaces.
When light passes through an absorbing film, the ratio of the transmitted light intensity I over the incident light intensity I_0, is given by a well known exponential equation (Lambert law):

$$I = I_0 e^{-ad}$$

where d the thickness of the film and a is the absorption coefficient, related to the extinction coefficient k with the equation:

$a = \frac{4\pi k}{\lambda}$, λ being the wavelength of the light.

Fundamental absorption and optical gap determination
The fundamental absorption is related to the band-to-band transitions in a polycrystalline semiconductor, i.e., to the excitation of an electron from the valence band to the conduction band. Therefore, the fundamental absorption can be used to determine the energy gap of the semiconductor. The kinetic energy of a conduction electron can be expressed as: $E = \frac{p^2}{2m_e}$, where p is the crystal momentum and m_e is the electron effective mass. But $p = \bar{h}$ k where k is the wave vector, which in the case of a semiconductor is called the “crystal momentum vector”. Then $E = \frac{\bar{h}^2 k^2}{2m_e}$
A similar expression can be written for holes in the valence band, with an effective mass m_h The photon absorption process in a semiconductor is described by the absorption coefficient a(hv) which for a given photon energy hv is proportional to the probability P_{if} of the transition from the initial state i to the final state f and to the density of electrons in the initial state n_i and also to the density of available (empty) final states n_f. For an accurate result, the probability must be summed for all the possible transitions between states separated by an energy difference

equal to hv [J.I. Pankove: “Optical Processes in Semiconductors”, Dover, New York, 1971]: $a(h\nu) = A\sum P_{f_i} n_i n_f$

For simplicity, it is assumed that all lower states are filled and all upper states are empty. The dependence of the absorption coefficient a on the photon energy hv is different for direct and indirect transitions. In direct transitions, both the top in the valence band and the bottom in the conduction band occur at the same crystal momentum k = 0, so that a transition from the valence band to the conduction band is vertical and does not require a change in the crystal momentum for the electron. In indirect transitions, the bottom of the conduction band occurs for some nonzero value of k and in this case a transition between the two bands requires not only a change in energy (≥ Eg) but also some change in the crystal momentum. This transition is a two-step process, because one photon cannot provide a change in the momentum. This change is accomplished by a phonon interaction. However, we limit this discussion to the case of direct transitions, since both In_2O_3 and ZnO are well known as a semiconductor with allowed direct transitions.

For direct transitions from state i to state f, the transition probability P_{if} is independent of photon energy, so it can be taken as a constant. Every initial state at energy E_i is associated with a final state at energy E_f through the relation: $E_f = h\nu - |E_i|$

For parabolic bands,

$E_f - E_g = \frac{\bar{h}^2 k^2}{2m_e}$ and $E_i = \frac{\bar{h}^2 k^2}{2m_k}$

$h\nu - E_g = \frac{\bar{h}^2 k^2}{2}\left(\frac{1}{m_e} + \frac{1}{m_h}\right) = \frac{\bar{h}^2 k^2}{2}\frac{1}{m_r}$ where m_r is the reduced mass.

The density of directly associated states using the previous equations can be written

$$N(h\nu)d(h\nu) = \frac{8\pi k^2 dk}{(2\pi)^3} = \frac{(2m_r)^{3/2}}{2\pi \bar{h}^2}(h\nu - E_g)^{1/2} d(h\nu)$$

Using the expression for the transition probability from state i to state f P_{if}, the absorption coefficient expression will be given by:

$$a(|h\nu|) = A^*(h\nu - E_g)^{1/2}$$

where hv and E_g are expressed in eV. Such a plot, by extrapolation to a = 0, gives the value of E_g.

This study presents only In_2O_3 and ZnO thin films characterization.

In the case of both metal oxides studied, the absorption radiation range corresponding to their bandgap is in UV-Vis spectral region.

For optical characterization of the films, a Varian Cary 50 - UV/Vis-Spectrometer (see figure 2.2.9) was used, equipped with a full spectrum Xe pulse lamp, a Czerny-Turner 0.25 m monochromator and dual Si diode detectors. The maximum scan rate of this spectrometer is 24000 nm/min, resulting the requirement of 3 seconds to scan the wavelength range from 190 to 1100 nm. The spectral bandwidth is fixed at 1.5 nm, while the wavelength accuracy is +/-0.5 nm at 541.9 nm.

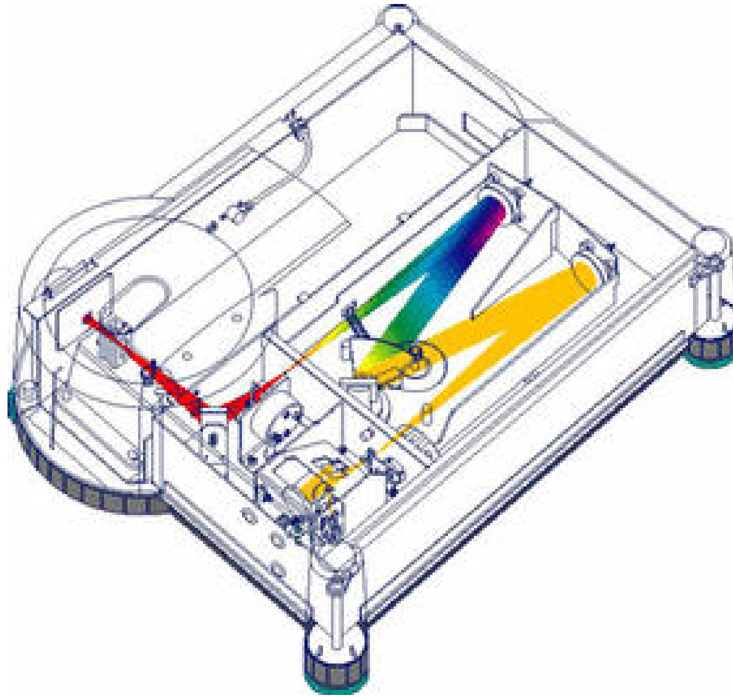

Figure 2.2.9 Varian Cary 50 - UV/Vis-Spectrometer

Optical measurements can be done in reflection as well as in transmission mode. Using Corning glass substrates, we are able to determine the optical properties of a thin film like optical band-gap energy and absorption coefficient. The optical energy gap E_{gap} was derived assuming a direct transition between the edges of the valence and the conduction band, for which the variation in the absorption coefficient with the photon energy hv is given by:
$\alpha(h\nu)=A(h\nu-E_{gap})^{1/2}$ as defined before.
In this equation, E_{gap} denotes the optical energy gap between the valence and the conduction band. "Tauc" plots of α^2 versus hv give by extrapolation of the linear region of the resulting curve, the optical band gap value E_{gap}.

2.2.5. Electrical characterization: Photoreduction and oxidation

The apparatus used for the photoreduction and oxidation of the In_2O_3 and ZnO films in the present work was a homemade glass chamber (as described in C. Xirouchaki, Ph.D. Thesis - Crete, 1998) pumped down by a rotary pump. A schematic illustration of the system is shown in figure 2.2.10.

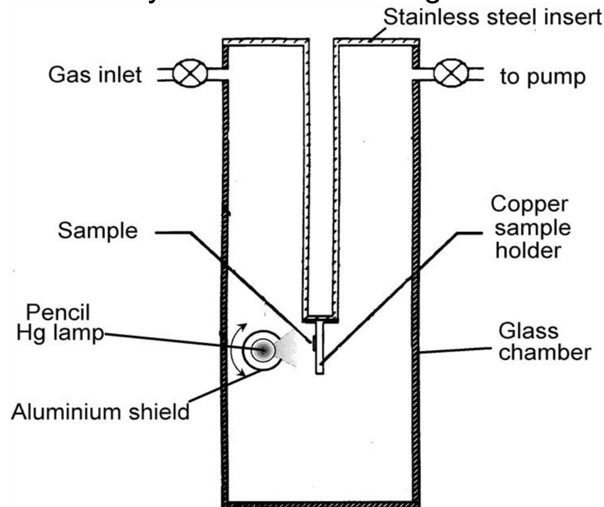

Figure 2.2.10 Schematic representation of setup for photoreduction-oxidation films measurements

A small short-wavelength pencil mercury lamp from Edmund Scientific Co., with an average intensity of 4 mW/cm^2 at λ = 254 nm, was used as the UV light source, placed at a distance of 3 cm from the samples. For the photoreduction process, the samples were exposed directly to the UV light in vacuum. Oxidation was carried out in the same chamber, the samples exposed to ozone produced by the UV light source in 600 Torr of O_2, being shielded at the same time from a direct exposure to the UV light. A field of about 1 V/cm was applied to the samples and the current through the samples was measured with a Keithley picoameter. For the determination of the conductivity of the In_2O_3 and ZnO films deposited onto Corning 1737 glass substrates, thermally evaporated NiCr electrodes were used. The conductivity values of the films after photoreduction and oxidation cycles were calculated from the measured current values I, and the dimensions of the samples, using the equation: $\sigma = \frac{Is}{Vad}$, where V is the applied voltage, d is the thickness of the sample in Å, while s and a are the dimensions of the sample in mm as shown in figure 2.2.11

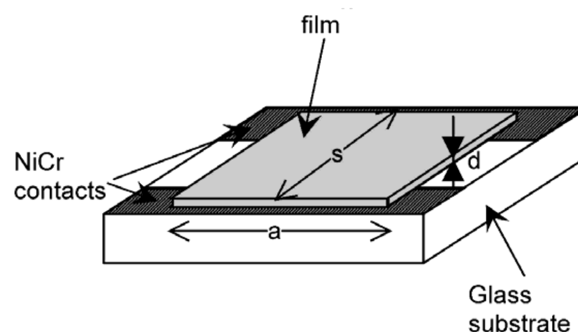

Figure 2.2.11 Schematic representation of o thin film with contacts.

Annex to AFM surface characterization by AFM

Surface Profile Parameters

Roughness Amplitude Parameters

Ra - Average Roughness

Average roughness is also known as Arithmetic Average (AA), Center Line Average (CLA) and Arithmetical Mean Deviation of the Profile. The average roughness is the area between the roughness profile and its mean line, or the integral of the absolute value of the roughness profile height over the evaluation length: $R_a = \frac{1}{L}\int_0^L |r(x)|dx$. When evaluated from digital data, the integral is normally approximated by a trapezoidal rule: $R_a = \frac{1}{N}\sum_{n=1}^{N}|r_n|$. Graphically, the average roughness is the area (shown below in figure 2.a1) between the roughness profile and its center line divided by the evaluation length (normally five sample lengths are used, with each sample length equal to one cutoff).

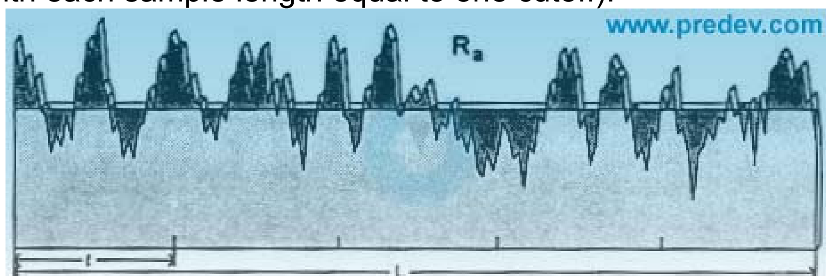

Figure 2. a1

The average roughness is by far the most commonly used parameter in surface finish measurement. The earliest analog instruments for determining roughness were measuring Ra by moving a stylus continuously back and forth over a surface and integrating (finding the average) electronically. The main reason why Ra has such a long history is that It is fairly easy to take the absolute value of a signal and then to integrate it using only analog electronics.

An older means of specifying a range for Ra is RHR. This is a symbol on a drawing specifying a minimum and maximum value for Ra.

Ra cannot tell the whole story about a surface. For example, in figure 2.a2, three surfaces are presented, all having the same Ra. One can easily see by eyes that these are quite different surfaces. As a result, in some applications they will perform very differently as well.

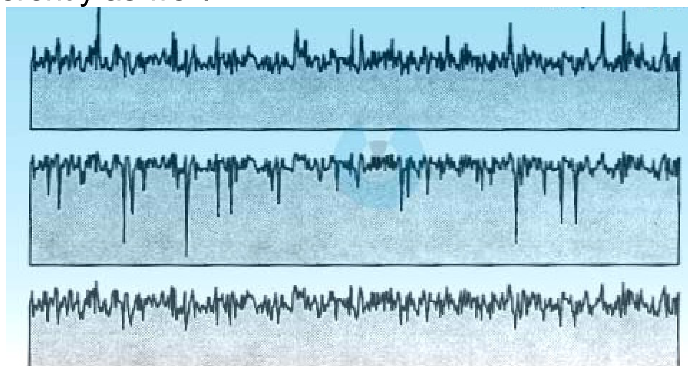

Figure 2. a2

These three surfaces all have the same Ra, even though the eye immediately distinguishes their different general shapes. The following three surfaces presented in figure 2.a3 also all have the same Ra.

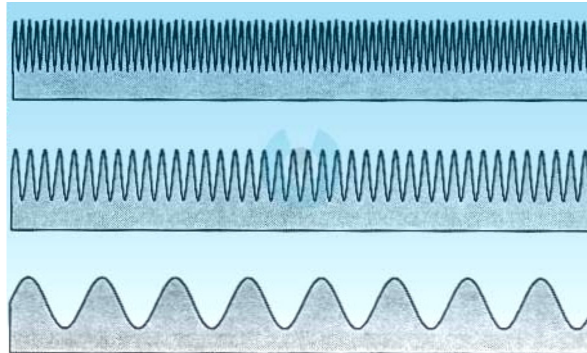

Figure 2. a3

If someone wants to distinguish surfaces that differ in shape or spacing, he needs to calculate other parameters for each surface that measure peaks and valleys and profile shape and spacing. The more complicated the shape of the surface, and the more critical the corresponding function, more sophisticated parameters are required beyond Ra to describe the case.

Rq - Root-Mean-Square Roughness

The root-mean-square (RMS) average roughness of a surface is calculated from another integral of the roughness profile:

$$\mathrm{RMS} = \sqrt{\frac{\sum_{i=1}^{N}\left(z_i - z_{ave}\right)^2}{N}},$$

where z_i is the current value of z, z_{ave} is the mean value of z in the scan area and N is the number of points.

For a pure sine wave of any wavelength and amplitude, RMS is proportional to Ra, being about 1.11 times larger. Some instruments use this approximation to calculate Ra with analog electronics and then multiply by 1.11 to get RMS. However, real profiles are not simple sine waves and the approximation often fails dramatically. There is no reason to make the approximation that RMS is proportional to Ra. Modern instruments either digitize the profile to determine RMS or do not report RMS.

Rt, Rp, and Rv

The peak roughness Rp corresponds to the height of the highest peak in the roughness profile. over the evaluation length (p1 in figure 2.a4). Similarly, Rv is the depth of the deepest valley in the roughness profile, over the evaluation length (v1 in figure 2.a4). The total roughness, Rt, is the sum of Rt and Rv, that is, the vertical distance from the deepest valley to the highest peak.

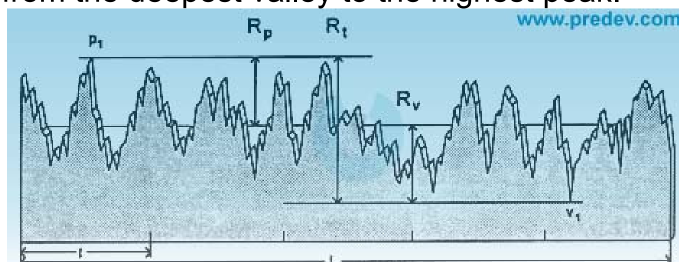

Figure 2. a4

$R_v = |\min[r(x)]|$ 0<x<L

$R_p = |\max[r(x)]|$ 0<x<L

$R_t = R_v + R_p$

These three extreme parameters are useful in finding unusual conditions, like a sharp spike or burr on the surface that would be detrimental to a seal or a crack or scratch that might be indicative of poor material or poor processing.

Rtm, Rpm and Rvm

These three parameters correspond to mean values, since they are averages of a number of sample lengths. For example, we define the maximum height for the i-th sample length as Rpi, Rvi the depth of the deepest valley in the i-th sample length and Rti is the sum of Rvi and Rpi. These three parameters have some of the same advantages as Rt, Rp, and Rv for finding extremes in the roughness, but they are not so sensitive to single unusual features.

Rymax (or Rmax) - Maximum Roughness Height within a Sample Length

Ry and Rmax are other names for Rti. Rmax is the older American name, Ry being the newer ISO and American name. Ry is the maximum peak to lowest valley vertical distance within a single sample length. For a standard five cutoff trace, there are five different values of Ry.

Rymax(ISO) - Maximum Ry

Rymax is an ISO parameter defined as the maximum of the individual or Rmax (i.e. Rti) values.

Rz(DIN)

Rz(DIN), i.e. Rz according to the German DIN standard, is just another name for Rtm in the American nomenclature. (over five cutoffs)

Rz(ISO)

Rz(ISO) is the sum of the height of the highest peak plus the lowest valley depth within a sampling length. Figure 2.a5 shows an intuitive representation of this.

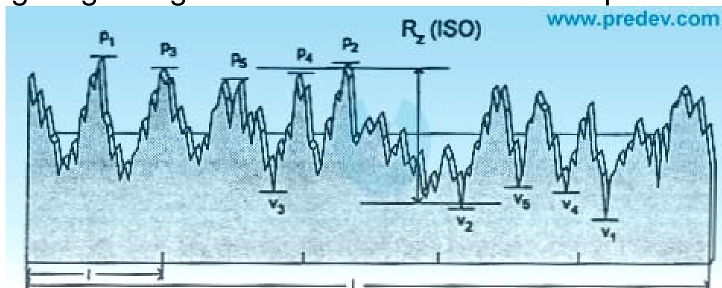

Figure 2. a5

R3zi - Third Highest Peak to Third Lowest Valley Height

The parameter R3zi is the height from the third highest peak to the third lowest valley within one sample length as shown in figure 2.a6.

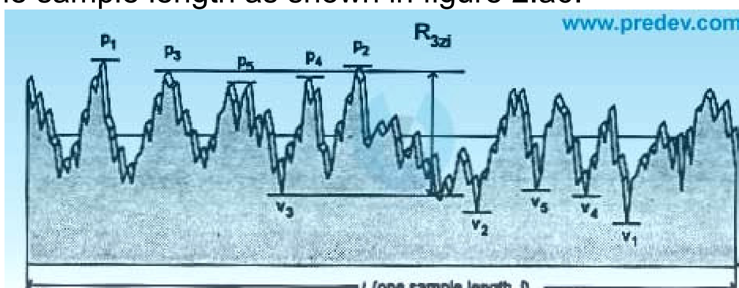

Figure 2. a6

Roughness Spacing Parameters

Pc - Peak Count

Peak count is a number giving the number of peaks per length of a trace in a profile. For the calculation of Pc, a "peak" is defined relative to an upper and lower threshold. Usually this is a single number, the "peak count threshold" given by the distance from a lower threshold up to an upper threshold, centered on the mean line as presented in figure 2.a7. A peak must cross over the upper threshold and go below the lower threshold in order to be counted.

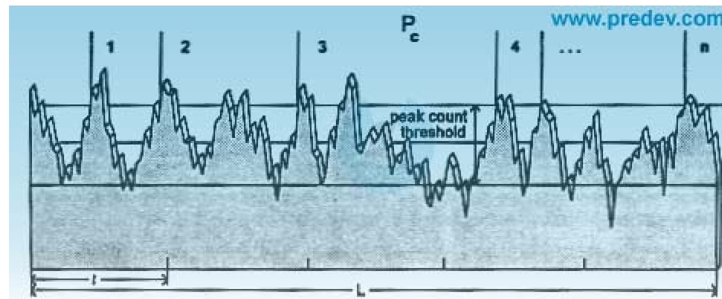

Figure 2. a7

Peak count is the number of peaks in the evaluation length divided by the evaluation length,(or by the distance from the beginning of the first peak to the end of the last peak). Pc is thus reported as [peaks/in] or [peaks/cm]. Some instruments allow the thresholds to be centered on a height that differs from the mean line. This is nonstandard but may be convenient. For example, a pair of thresholds that count low peaks accompanied by deeper valleys may be appropriate for plateau surfaces. The value obtained for Pc depends quite heavily on the peak count threshold for most surfaces. The figure 2.a8 shows peak count versus threshold for a ground surface and a turned surface as representative samples. For the ground surface the parameter shows no stability. For the turned surface there is a bit of flattening out at a threshold of about 40 µin, but even for this surface Pc shows a wide variation with threshold.

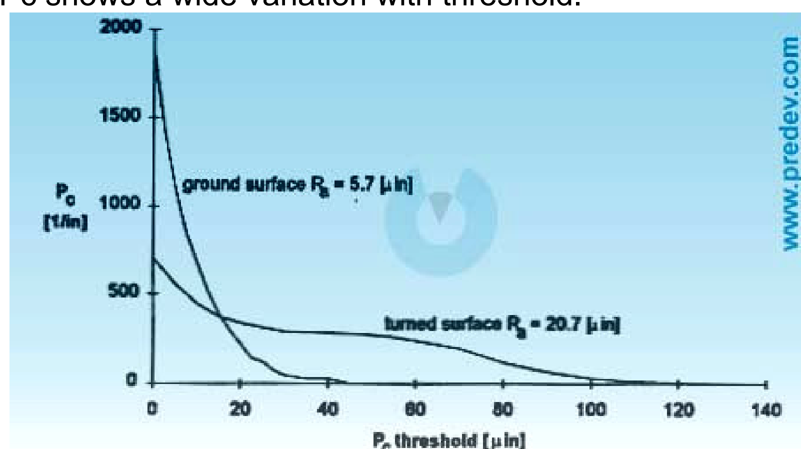

Figure 2. a8

HSC - High Spot Count

High spot count, HSC, is similar to peak count except that a peak is defined relative to only one threshold (see figure 2.a9). High spot count is the number of

peaks per inch (or cm) that cross over a certain threshold. A "peak" must cross over the threshold and then go back below it.

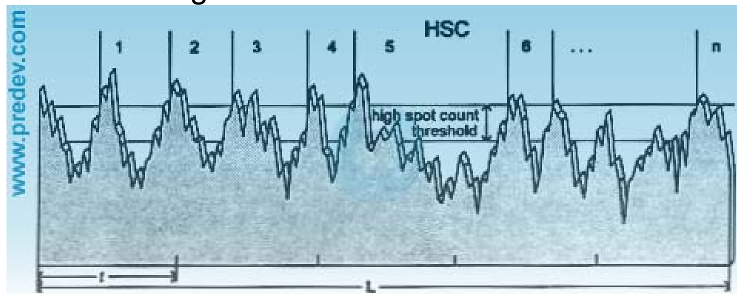

Figure 2. a9

Sm - Mean Spacing

Sm is the mean spacing between peaks, the peaks defined relative to the mean line. For a peak to exist, the height must cross over the mean line and then go back below it as can be observed form intuitive representation in figure 2.a10.

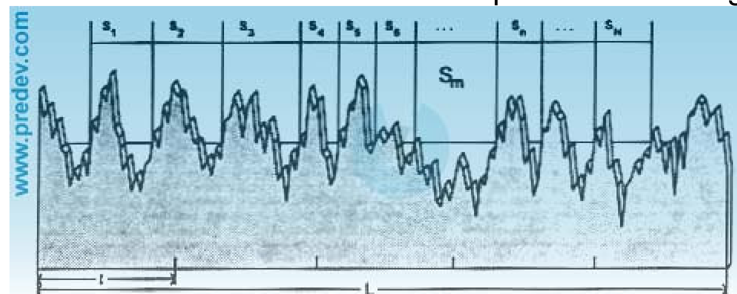

Figure 2. a10

λa - Average Wavelength

The average wavelength of the surface is defined as follows: $\lambda_a = 2\pi \frac{R_a}{\Delta_a}$

This parameter is analogous to Sm, since it measures the mean distance between features, but it is weighted by the amplitude of the individual wavelength, whereas Sm can find the predominant wavelength.

Statistical Analysis

The Amplitude Distribution Function

The amplitude distribution function (ADF) is a probability function that gives the probability that a profile of the surface has a certain height, z, at any position x. Ordinarily, ADF is computed for the roughness profile, although the texture or even primary profiles might be used in specialized applications.

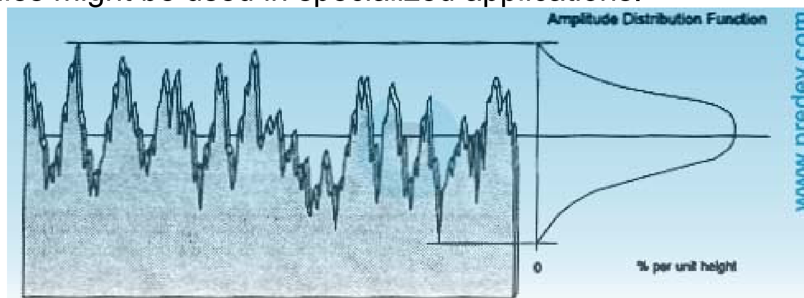

Figure 2. a11

ADF has a characteristic bell shape, like many probability distributions, and indicates "how much" of the profile lies at a particular height, in a histogram sense as shown in figure 2.a11. It is the probability that a point on the profile at a randomly selected x value lies at a height within a small neighborhood of a particular value z.

The Bearing Ratio Curve

The Bearing Ratio Curve (see figure 2.a12) is related to the ADF, since it is the corresponding cumulative probability distribution and sees much greater use in surface finish. The bearing ratio curve is the integral (from the peak to valley) of the ADF. Other names used for the bearing ratio curve are: the bearing area curve (this is becoming outdated due to the increased used of other topographical methods), the material ratio curve, or the Abbott-Firestone curve.

Physical Significance of the Bearing Ratio Curve

The bearing ratio curve mathematically is the integral of the amplitude distribution function. It is a cumulative probability distribution. Ordinarily, the integral is performed from the highest peak downward, so each point on the bearing ratio curve has the physical significance of showing what linear fraction of a profile lies above a certain height (compared to the ADF which tells how much of a surface lies at a given height).

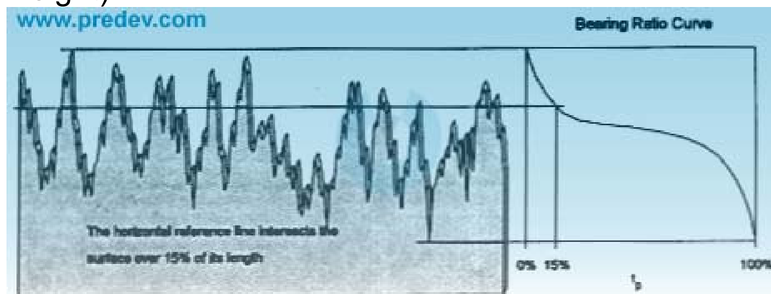

Figure 2. a12

In order to describe the Bearing Ratio Curve, several parameters are used. One of the most usual is Bearing Ratio Parameters is the *Surface bearing index, S_{bi}* which is the ratio of the RMS deviation over the surface height at 5% bearing area.

$$S_{bi} = \frac{\mathrm{RMS}}{Z_{0.05}} = \frac{1}{h_{0.05}} ,$$

where $h_{0.05}$ is the normalized surface height at 5% bearing area. A larger surface bearing index indicates a good bearing property. For a Gaussian height distribution, S_{bi} approaches 0.608 with increasing number of pixels.

Other advanced statistic parameters

The **Surfaces Area Ratio**, S_{dr}, expresses the ratio between the real surface area (taking the z height into account) and the area of the corresponding flat xy plane:

$$S_{dr} = \frac{S_{3A}}{S_{2A}} = \frac{\left(\sum_{k=0}^{M-2}\sum_{l=0}^{N-2} A_{kl}\right) - (M-1)(N-1)\delta x \delta y}{(M-1)(N-1)\delta x \delta y} 100\% \text{ , where}$$

$$A_{kl} = \frac{1}{4}\left[\sqrt{\delta y^2 + \left(z_{k,l} - z_{k,l+1}\right)^2} + \sqrt{\delta y^2 + \left(z_{k+1,l} - z_{k+1,l+1}\right)^2}\right] \cdot \left[\sqrt{\delta x^2 + \left(z_{k,l} - z_{k+1,l}\right)^2} + \sqrt{\delta x^2 + \left(z_{k,l+1} - z_{k+1,l+1}\right)^2}\right] .$$

For a totally flat surface, the real surface area and the area of the flat xy plane are the same resulting in S_{dr} = 0 %. In general, small values of Sdr indicate surfaces quite flat.
The **Fractal Dimension**, S_{fd} is calculated for the different angles by analyzing the Fourier amplitude spectrum. For different angles, the Fourier profile is extracted and the logarithm of the frequency and amplitude coordinates is calculated. The fractal dimension for each direction is then calculated as 2.0 minus the slope of the log - log curves.
From a usual AFM study, one can obtain the most complete characterization of the surface. Except the many parameters regarding surface profile described above, grain distributions, grains dimensions, features sizes, as well as coverage types and percentages can be obtained in addition to the already mentioned informational package on surface physical properties contained in the tip-surface interaction control.

Chapter 3

In_2O_{3-x} thin films grown by DC magnetron sputtering

Outlines

- **Growth**
- **Characterization: structural, surface, optical, electrical**
- **Particular correlations of different parameters**
- **Annex 3A: Growth conditions table**

3. In_2O_{3-x} thin films grown by DC magnetron sputtering

Following the main research topic of PEML group at IESL FORTH [1-10], different In_2O_{3-x} series were grown by DC magnetron sputtering and their properties were analyzed. In particular, the influence of thickness, growth temperature, total pressure and oxygen:argon ratio during growth on the properties of the films was investigated. Complete surface characterization of each film was performed and the surface characteristic parameters and the grain size were determined. A list of the grown films, their growth conditions and their sensing response can be found in the table inserted to the end of this chapter as Annex A.
The effect of DC magnetron growth parameters (thickness, substrate temperature, total pressure and oxygen partial pressure) of In_2O_{3-x} thin films on theirs physical properties, surface and sensing was systematical studied. The results made the subject of some publications and presentations in international symposia as mentioned in the attached list of publications [11-25]. The following discussion will be developed in a particular way regarding effect of each growth parameter on each studied property.

3.1 Compositional analysis

EDX analysis of In_2O_{3-x} films grown by DC magnetron sputtering from 99.999% pure In metallic target under the following deposition parameters: total sputtering pressure $8x10^{-3}$ mbar, substrate temperature 27^oC (RT) and thickness of about 150nm. The results presented in the table 3.1 indicated that increasing the oxygen partial pressure in the plasma content during deposition causes a small decrease of the x value. As expected the O/In ratio variation the stoichiometry is improving getting closer to the theoretical value of 1.5 as the oxygen partial pressure in the DC magnetron chamber is increasing.

O_2%	In [at%]	O [at%]	O/In
50%	46	54	1.2
40%	46	54	1.2
60%	44	56	1.3
80%	43	57	1.3
100%	42	58	1.4

Table 3.1 Material stoichiometry variation with oxygen concentration in plasma composition

EPMA (Electron Probe Micro Analysis) was also carried out at University of Braunschweig, Germany using a CAMECA SX50 EPMA system under conditions E_0=5 keV and depth of analysis < 150 nm. Available standards of InP (for In) and SnO_2 (for O) were used for quantification purposes.
In_2O_{3-x} in its stoichiometric form (In_2O_3) normally behaves as an insulator, while in its non-stoichiometric form (In_2O_{3-x}), it appears to have semiconducting properties. Film stoichiometry was investigated by EPMA and the average of 15 points (spot ~Ø=10 µm) of analysis on each sample is presented in table 3.2.

Sample	In [at%]	O [at%]	In/O atomic ratio	Formula
In_2O_{3-x} non-conductive	40.5	59.5	0.68	$In_2O_{2.94}$
In_2O_{3-x} conductive	40.8	59.2	0.69	$In_2O_{2.90}$

Table 3.2: Film stoichiometry investigated by EPMA

As non-conductive In_2O_{3-x} we considered the as deposited film, while, conductive In_2O_{3-x} the film after UV exposure. Within the precision of the EPMA experiments, the “bulk“ composition of the coatings had to be regarded as identical. As can be seen, the composition is very close to the stoichiometry of In_2O_3.

Finally, SIMS (Secondary Ion Mass Spectrometry) was performed using a CAMECA IMS 5f system with the following experimental conditions: 3 keV Cs^+ primary ions, Ip = 5 nA, raster 500x500 µm, sputter rate 0.02 nm/s, a value based on the determination of the crater depth by profilometry, CsM^+ (M=element of interest) molecular secondary ions and accepted area of Ø=120 µm in the center of the raster field.

For the SIMS measurements, the calibration of the concentration axis in respect with In and O was carried out assuming the “bulk“ stoichiometry (i.e., for a depth < 20 nm) of $In_2O_{2.94}$ (C_{In} / C_O = 0.68) corresponding to the results of EPMA. The concentrations of the impurity elements (H, C, N, Si) are rough estimations based on the sensitivity factors derived from a coating standard of Si-C:H:N:O. Fig. 3.1.1a and 3.1.1b show that the sample, in both non-conductive and conductive states is homogeneous in depth.

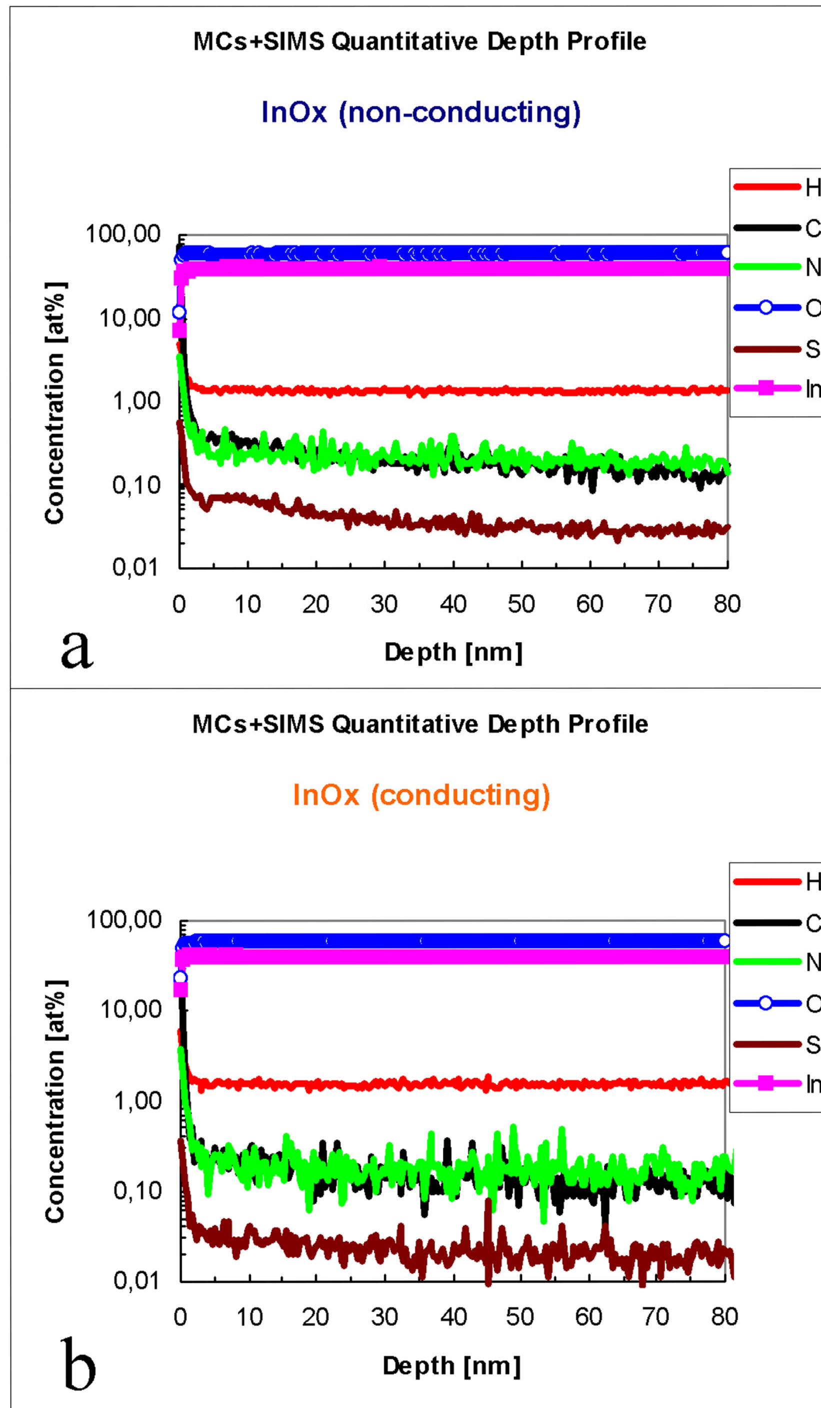

Figure 3.1.1. SIMS compositional characterization of "non-conducting"(a) and "conducting"(b) In_2O_{3-x}.

The curves of Figure 3.1.1a and 3.1.1b indicate that there is no visible difference between "non-conducting" and "conducting"In_2O_{3-x}, including the level of impurity elements.

Fig. 3.1.2a and 3.1.2b can give a „closer look" to the In and O concentrations in the near-surface region. Within a depth of 0-5 nm, a small difference between "non-conducting" and "conducting"In_2O_{3-x} can be detected.

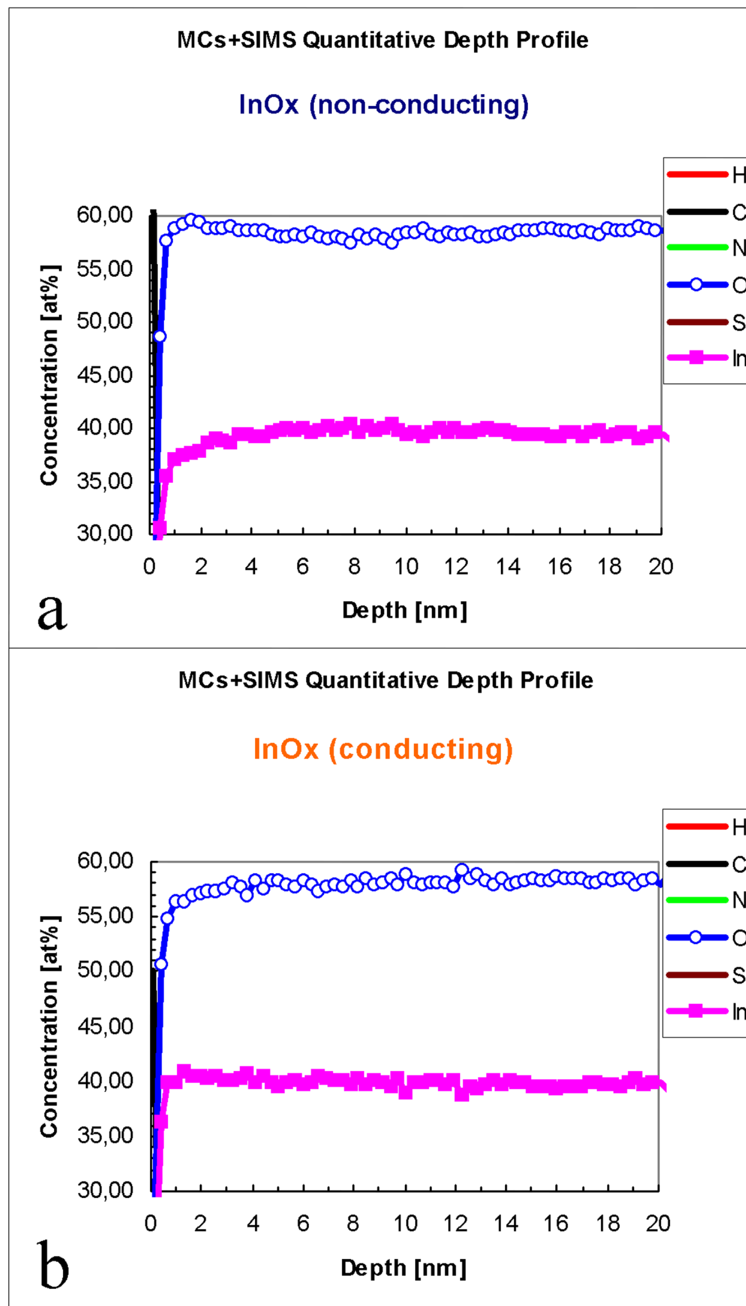

Figure 3.1.2 A „closer look" to the In and O concentrations in the near-surface region. Within a depth of 0-5 nm a small difference between "non-conducting"(a) and "conducting"(b) In_2O_{3-x} can be seen.

This difference becomes clearly visible when the In:O atomic ratio of both samples is plotted as a function of depth (figure 3.1.3).

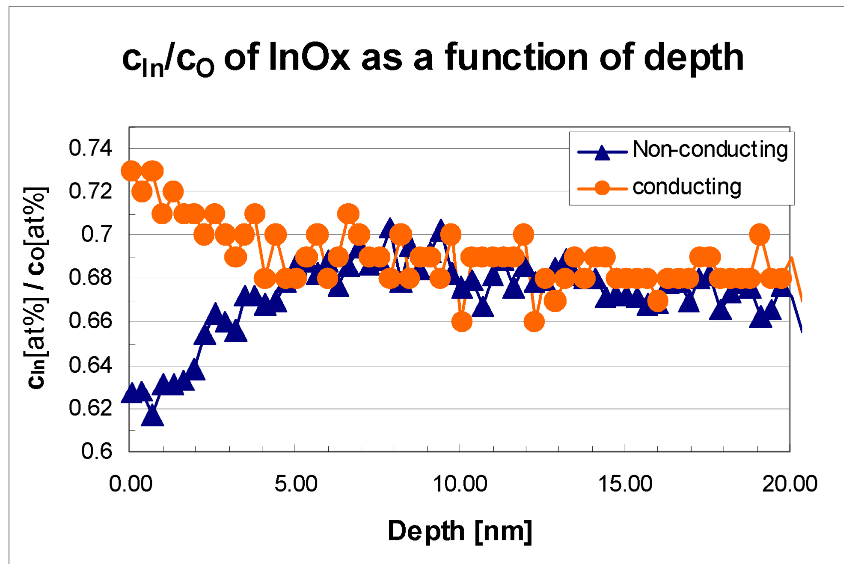

Figure 3.1.3. In:O atomic ratio of both, "non-conducting" and "conducting" In_2O_{3-x} samples plotted as a function of depth.

As compared with the "bulk"(> 10 nm) composition (In:O=0.68, =$In_2O_{2.94}$), the "non-conducting" sample exhibits an excess of O (2nm: In:O~0.65, ~$In_2O_{3.08}$) within the first 5 nm, whereas the "conducting" sample shows a deficit of O (2nm: In:O~0.70, ~$In_2O_{2.86}$).
These results prove that sensing phenomena on In_2O_{3-x} thin films is mostly a surface effect. The UV photoreduction of In_2O_{3-x} which reflects in the conductivity increase is connected with surface stoichiometry change in a depth directly connected with the oxygen diffusion rate from the bulk. This explains why In_2O_{3-x} is one of the most suitable materials for sensing of both reducing and oxidizing gases.

3.2 Films structure

TEM Characterization

Indium Oxide film on Si substrate
In_2O_{3-x} films deposited on Si were examined using TEM, XTEM and SAD.
Figure 3.2.1a is the XTEM micrograph of such as film.

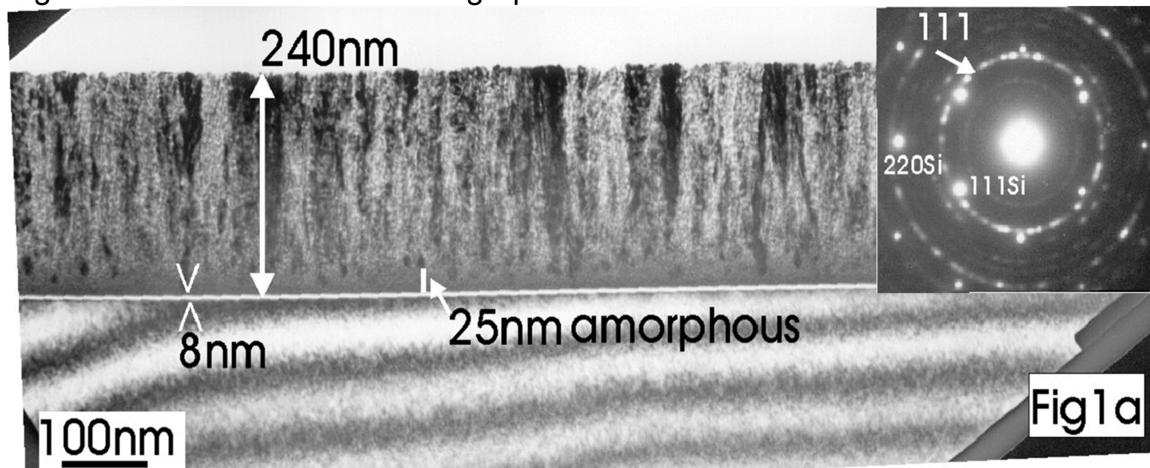

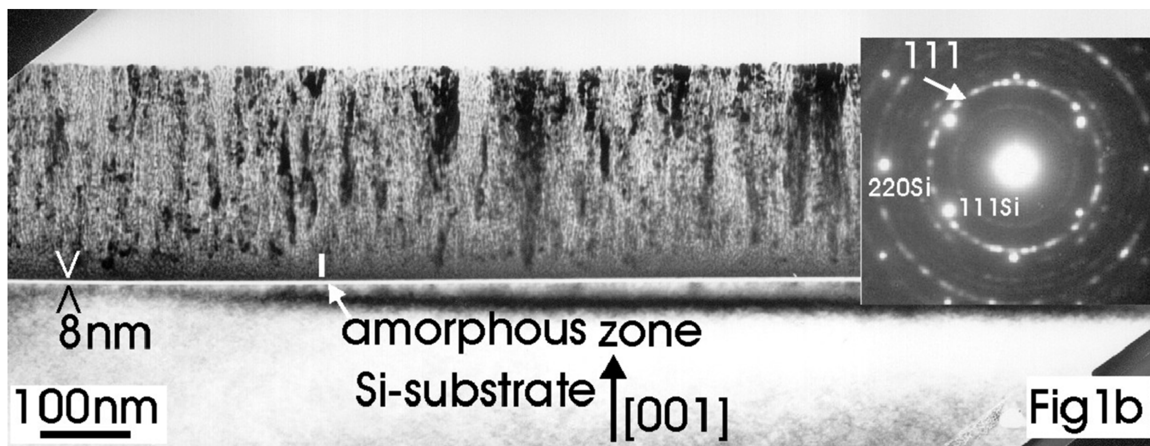

Figure 3.2.1: a) XTEM micrograph: the Si wafer has [001] orientation; film thickness is 240nm and the crystallites are columnar. Between the Si and the In_2O_{3-x} film a very thin amorphous layer about 8 nm is observed. It can be supposed that this is a SiO_2 layer. b) XTEM micrograph on a different area.

The Si wafer has a [001] orientation, the thickness of the film as it can be seen in the image is 240 nm and the crystallites are columnar. Between the Si and the In_2O_{3-x} film, a very thin amorphous layer of about 8nm thickness is observed, which can be attributed to. SiO_2. Similar behavior is observed in figure.3.2.1b, which corresponds to a different area of the film. It is evident from figure 3.2.1a and 1b that the first 25 nm of the deposited In_2O_{3-x} remain amorphous and the crystallization starts after this thickness.
The formation of crystalline In_2O_{3-x} was confirmed by considering the diffraction patterns from the In_2O_{3-x}/Si interface, where the diffraction rings from the polycrystalline In_2O_{3-x} are superimposed with the diffraction spots of the Si

substrate, as shown in the inset in Figure.1b. As a result, the diffraction rings of In_2O_{3-x} were indexed, having as reference the Si spots. Especially, the [111] In_2O_{3-x} ring was found more intense perpendicular to the Si-substrate, revealing a preferred [111] orientation of the In_2O_{3-x} grains. The presence of amorphous In_2O_{3-x} near the In_2O_{3-x}/Si interface was also shown at higher magnification in figure 3.2.2a. Rows of vacancies are observed between the grains shown by arrows in figure 3.2.2a. The mean width of the columnar grains was estimated to be 20 nm, a value evident from the dark field (DF) micrograph in figure 3.2.2b, which was taken from the [111] diffraction In_2O_{3-x} ring.

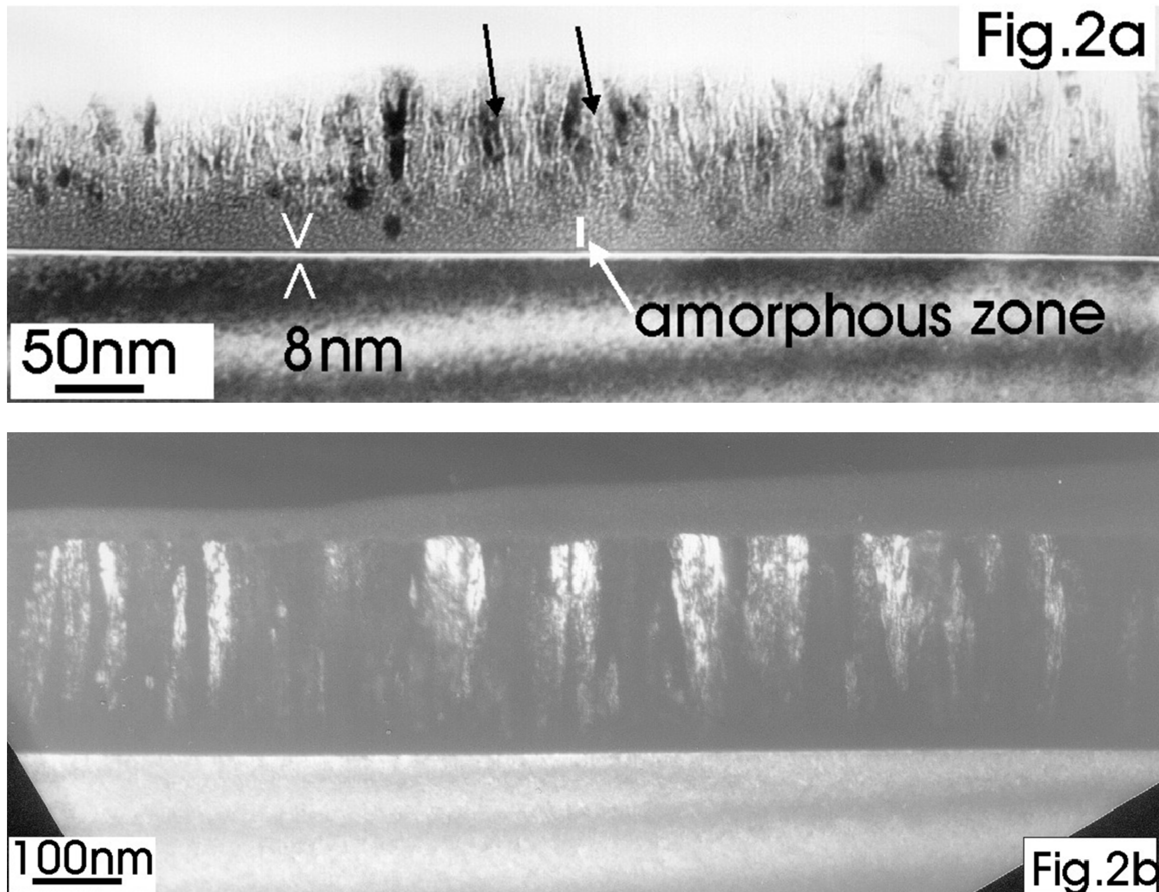

Figure 3.2.2. a) High magnification image on amorphous In_2O_{3-x} near the In_2O_{3-x}/Si interface. Rows of vacancies are observed between the grains shown by arrows. b) Dark field (DF) micrograph taken from the [111] diffraction In_2O_{3-x} ring. The mean width of the columnar grains was estimated to be 20 nm.

The In_2O_{3-x} films were also studied by PVTEM, after thinning the Si-substrate from the backside, first by mechanical ground and then by Ar ion thinning, leaving the uppermost part of the In_2O_{3-x} film intact. The morphology of the film is shown in figure 3.2.3a, the corresponding diffraction pattern presented in the inset. The diffraction rings were found to be the same as those in the inset of figure 3.2.1b.

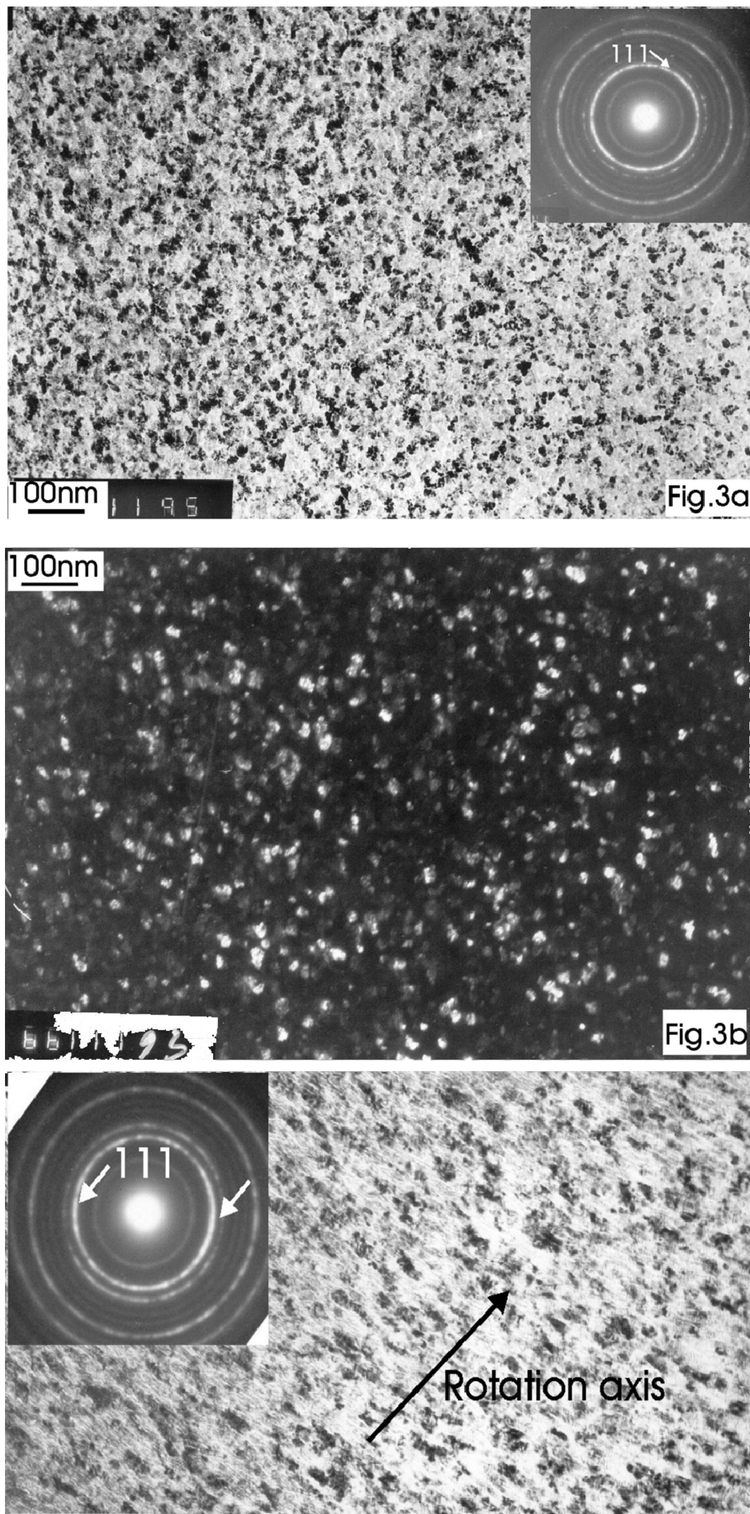

Figure 3.2.3. a) PVTEM micrograph:. Inset: diffraction pattern b) DF micrograph taken from the [111] ring. c) Rotating the specimen by 45° around the indicated axis, the grains were found elongated, revealing a columnar character for the grains. Inset diffraction pattern: [111] diffraction ring was split into two more intense arcs.

The mean width of the grains, estimated from figure 3.2.3a, was also 20 nm. This was also confirmed from the DF micrograph taken from the [111] ring, shown in figure 3.2.3b. Rotating the specimen for 45° around the axis shown in figure

3.2.3c, the grains were found elongated, revealing a columnar character of the grains. Also the [111] diffraction ring was split into two more intensive arcs, as shown in the corresponding diffraction pattern in the inset of figure 3.2.3c.
It the case of the specimens prepared for PVTEM characterization, a part of the In_2O_{3-x} film was also etched from the backside, so that the remaining thickness was of the order of 100nm. For this reason, specimens were prepared for PVTEM observation without thinning the specimen by ion beam. Instead, only chemical etching was used (etching the Si substrate with a solution of HNO_3 and HF). In this case, thick areas including the In_2O_{3-x} film and a thin layer of non-etched Si substrate were studied by PVTEM, as shown in figure 3.2.4a. Therefore, partial etching is preferable at the grain boundaries, which have a large portion of vacancies, as we have seen in figure 3.2.2a, cannot be excluded. This explains the fingerprint morphology of the film shown in Figure.4a. The corresponding DF micrograph is shown in Figure 4b.

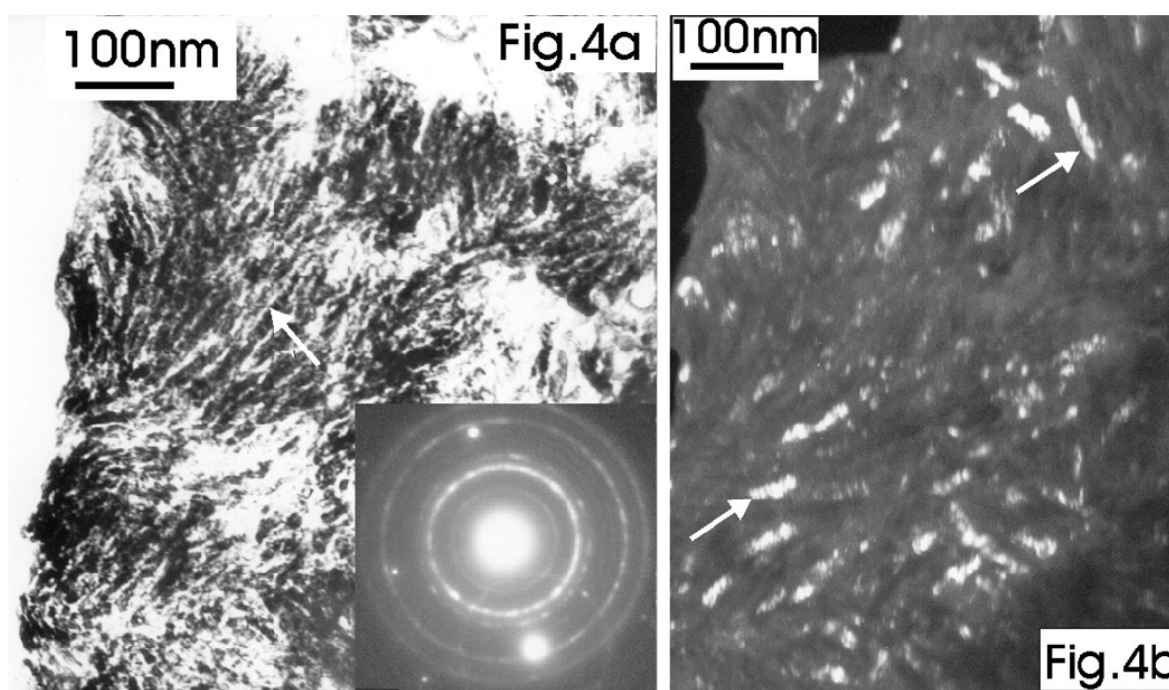

Figure 3.2.4. a) PVTEM fingerprint morphology of film on Si prepared by chemical etching. b) the corresponding DF micrograph.

Due to the superposition of the In_2O_{3-x} film and the Si-substrate, the related diffraction pattern shown in the inset of figure 3.2.4a, includes both Si spots and rings from the In_2O_{3-x} film. These are exactly the same as in the diffraction rings of the In_2O_{3-x} film thinned by Ar ion beam.

Indium Oxide film on NaCl substrate
Film preparation was very simple by dissolving the NaCl and picking-up the In_2O_{3-x} film on a copper grid; only specimens for PVTEM observation can be prepared by this method. The thickness of these films is estimated to be about 150nm. The morphology of the grains is shown in figure 3.2.5a and is very similar to that observed in figure 3.2.3a and 3.2.3b.

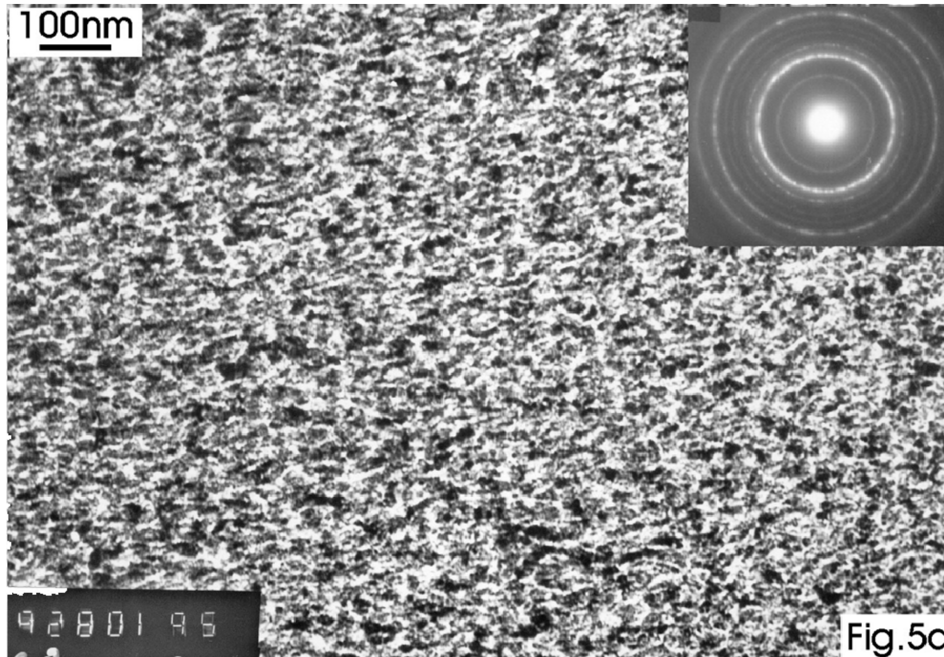

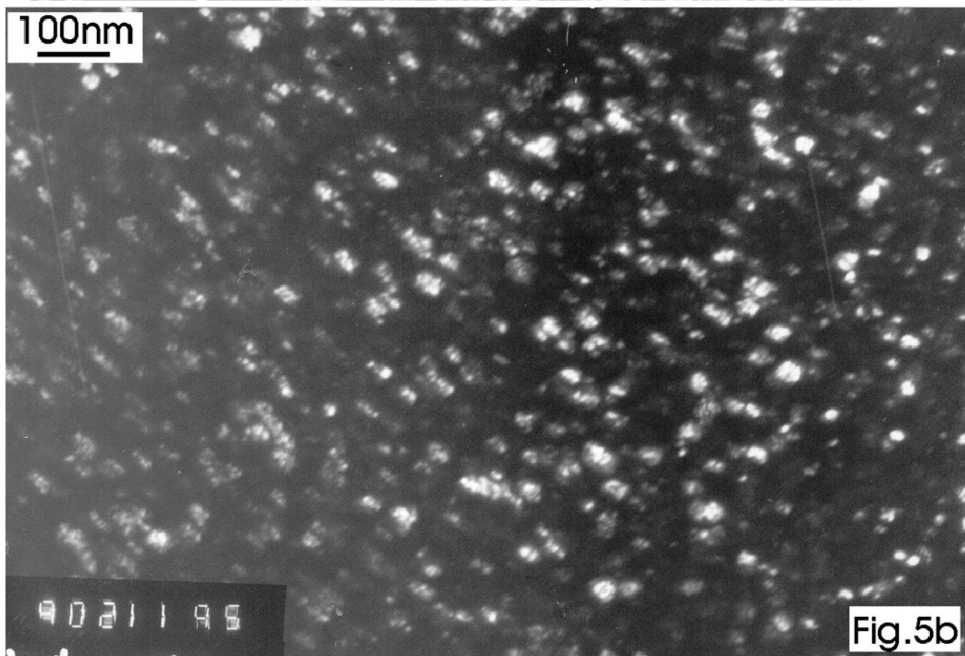

Figure 3.2.5. a) PVTEM observations for indium oxide films on NaCl substrate. Inset: diffraction pattern coincides with the already observed In_2O_{3-x}. b) DF micrograph from the same specimen.

The diffraction pattern coincides with that already observed for the other In_2O_{3-x} cases. The DF micrograph from the same specimen is shown in figure 3.2.5b. The mean width of the grains is estimated to be around 22 nm.
From this characterization the general observations for In_2O_{3-x} films grown by DC magnetron sputtering are;
The In_2O_{3-x} were polycrystalline with a columnar mode of growth
The films were amorphous in the early stage of growth and after a critical thickness, they become crystalline. This behavior can be attributed to the incubation time, which is needed in order to generate nucleation centers at a given temperature in an amorphous material.

The incubation time at a given deposition temperature can be determined if one knows the deposition rate and the critical thickness for the starting of the crystallization.
The observation of the same morphology for films deposited on Si and NaCl substrates ensures that the procedure for the TEM specimen preparation of the In_2O_{3-x} films on Si does not affect the structure of the films.

XRD characterization

XRD studies showed that films thinner than 42 nm are amorphous, while films thicker than 100 nm are polycrystalline, with tendency of texturing, having preferential orientation the [222] of the bcc In_2O_3 crystalline structure. Some films with larger thickness showed also contribution from crystallites with [400] and [440] orientations of the same structure. Obviously, an improvement in crystallinity was noticed with increasing thickness due to the fact that for higher thicknesses the deposition time is larger and the material can build up in the proper structure. Figure 3.2.6 shows a typical evolution of X-ray diffractograms with increasing thickness for In_2O_{3-x} grown by DC magnetron sputtering from 99.999% pure In metallic target under the following deposition parameters: pressure $8x10^{-3}$ mbar, oxygen concentration in the plasma 100%, growth rate 5.6 nm/min and substrate temperature 27°C (RT).

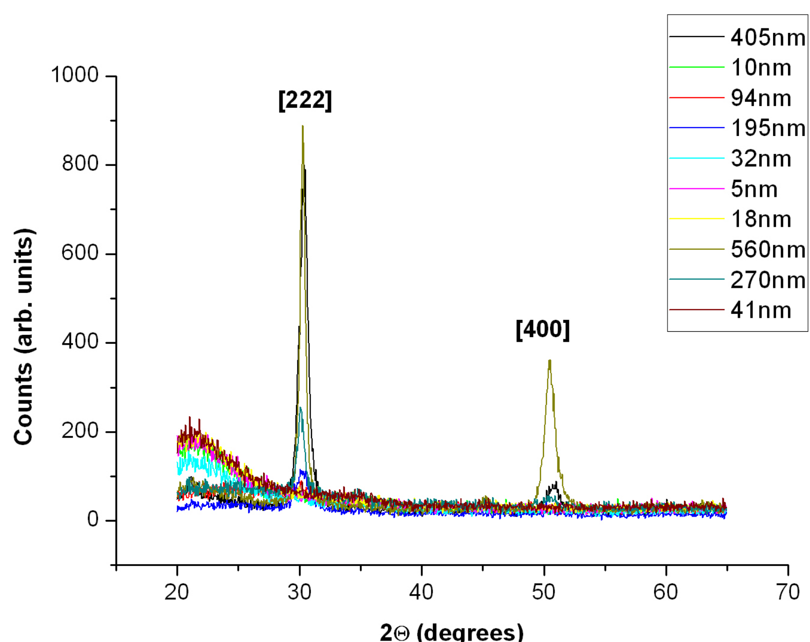

Figure 3.2.6 Typical variation of X-ray diffractograms with thickness for In_2O_{3-x} grown by DC magnetron

Heating during deposition was found to improve films crystallinity as can be clearly noticed from figure 3.2.7, which presents a typical evolution of X-ray diffractograms with increasing substrate temperature during growth for In_2O_{3-x} grown by DC magnetron sputtering under the same conditions as in the previous figure, the thickness being kept constant at 151nm.

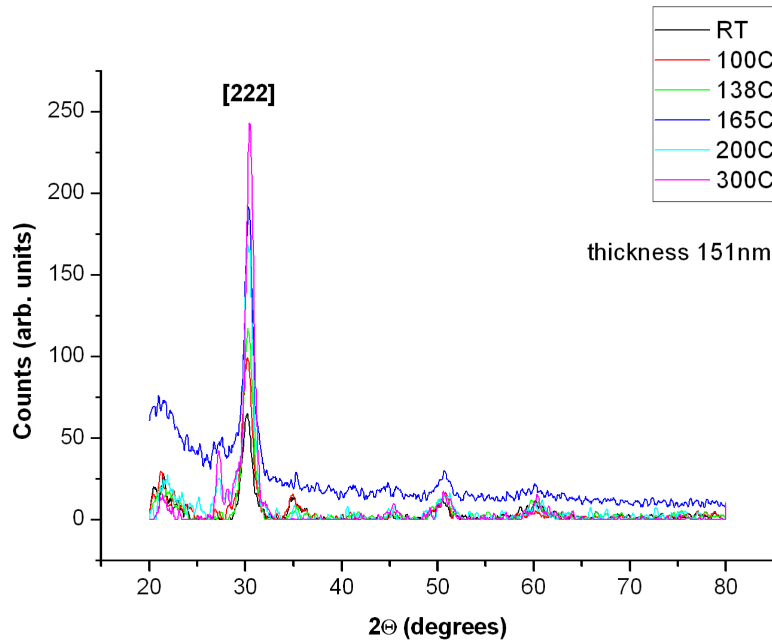

Figure 3.2.7 Typical dependence of X-ray diffractograms on substrate temperature during growth for In_2O_{3-x} grown by DC magnetron sputtering

Decreasing the sputtering pressure was found to induce a slightly decrease of the crystallinity due to the high deposition rate which decreases the deposition time and does not allow the lattice formation. Finally, unexpected, the diffraction peak intensity was increasing when the oxygen content in the plasma was decreased. Typical evolution of the X-ray diffractograms with decreasing the oxygen partial pressure in plasma content during deposition for In_2O_{3-x} grown by DC magnetron sputtering under the same conditions other as before presented and a thickness of about 151nm are presented in figure 3.2.8.

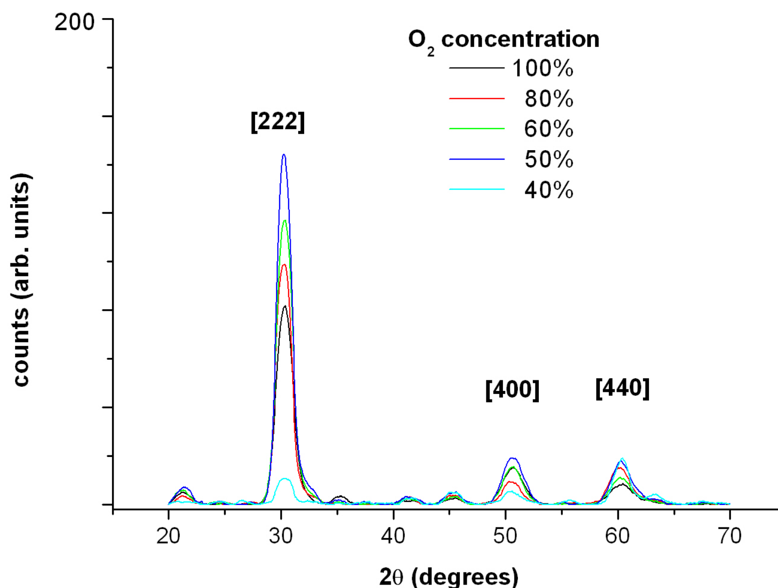

Figure 3.2.8 Typical evolution of the X-ray diffractograms with decreasing the oxygen partial pressure in plasma content during deposition for In_2O_{3-x} grown by DC magnetron sputtering

3.3 *AFM Characterization: Growth parameters effects on film surface morphology*

Thickness effect

AFM characterization of films with different thickness deposited onto Corning 1737F glass substrates revealed a granular, polycrystalline morphology. Figure 3.3.1 presents the variation of the surface roughness (RMS) (circles) and the surface grain radius (triangles) with film thickness, the values determined from the AFM measurements.

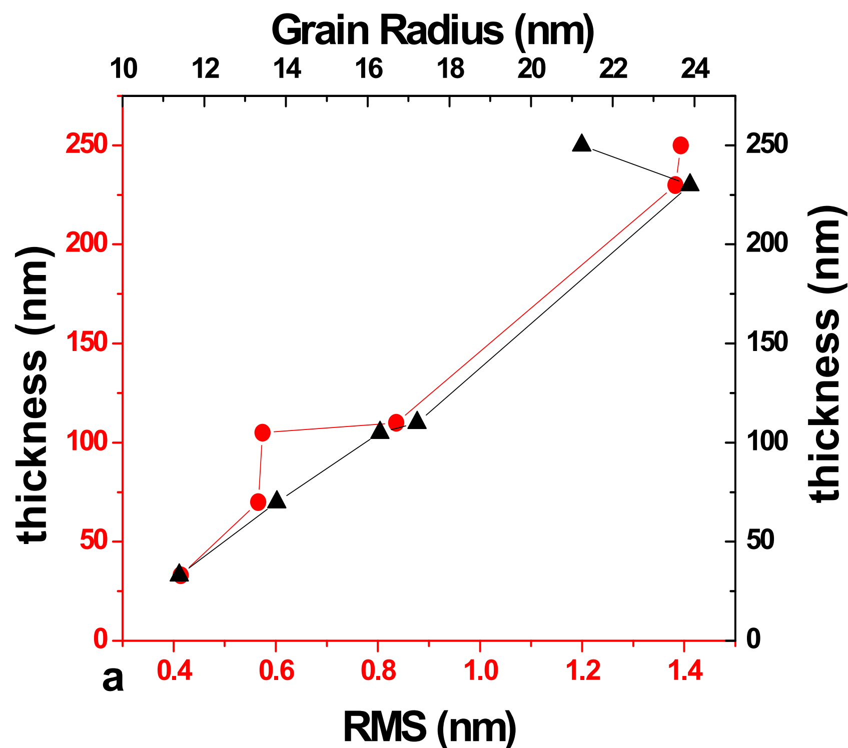

Figure 3.3.2 RMS variation with film thickness for In_2O_{3-x} thin films grown by DC magnetron sputtering.

The films were grown by DC magnetron sputtering from 99.999% pure In metallic target under deposition parameters: pressure 8x10^{-3} mbar, oxygen concentration in the plasma 100%, growth rate 5.6 nm/min and room temperature. From this investigation, it was found that both the average lateral grain size and the surface roughness increased with increasing film thickness due to the increased crystallinity of the films as proved by XRD. In figure 3.3.2, images and the corresponding distribution of the surface grain height of films with a thickness of: a) 33 nm, b) 70 nm, c)100 nm and d) 230 nm are shown (scan size 2x2 μm). For the specific growth conditions and a thickness variation from 30 nm to 250 nm, the mean grain radius was found increasing from 13 nm to 24 nm, the respective RMS

value also increasing from 0.4 nm to 1.3 nm. These variations can be correlated with the film crystal formation as was seen in the XTEM analysis. In the case of thinner films, the growth time is shorter and the surface reveals an inhomogeneous distribution of smaller grains. At longer deposition periods, small grains aggregation was leading to the formation of larger grains with a subsequent increase in the measured lateral grain size and an overall rougher surface (figures 3.3.1 and 3.3.2).

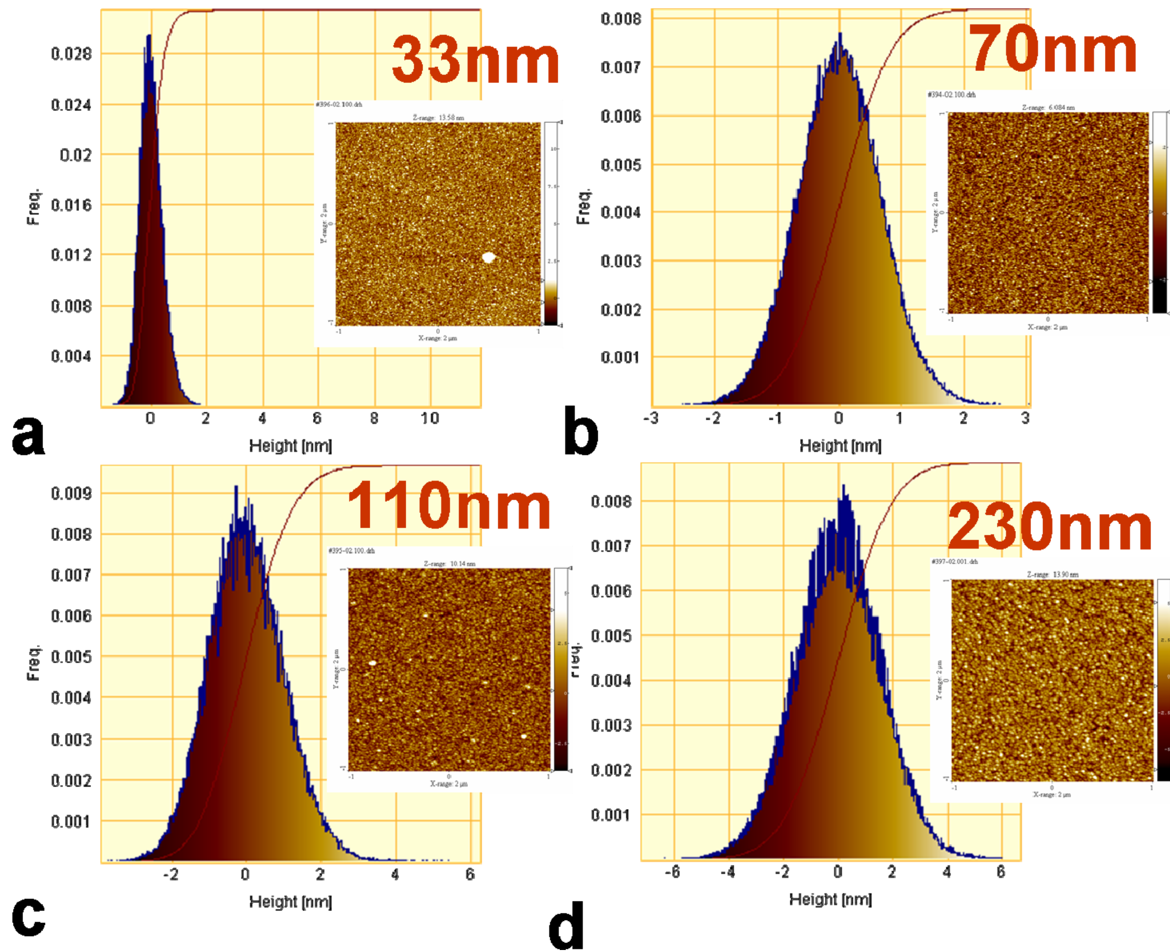

Figure 3.3.2 Grain height distribution and 2-D images of films with thickness a) 33 nm, b) 70 nm, c) 100 nm, d) 230 nm (scan size 2x2 μm) are shown.

For comparison, another thickness series was grown at higher deposition pressure ($15x10^{-3}$ mbar), keeping all other growth parameters the same. As was found out, similar dependence exists with increasing thickness, RMS varying from 0.52 nm, for a thickness of 20 nm, up to 2.15 nm for 615nm thickness. For the same range of thickness, the mean grain radius was varying from 13.24 nm up to 29.25 nm. The dependence of RMS and mean grain radius on thickness at this deposition pressure are shown in figure 3.3.3 a and b and AFM 3D images of the films with thickness from 20 to 200nm (scan size 2x2μm) are presented in figure 3.3.4.

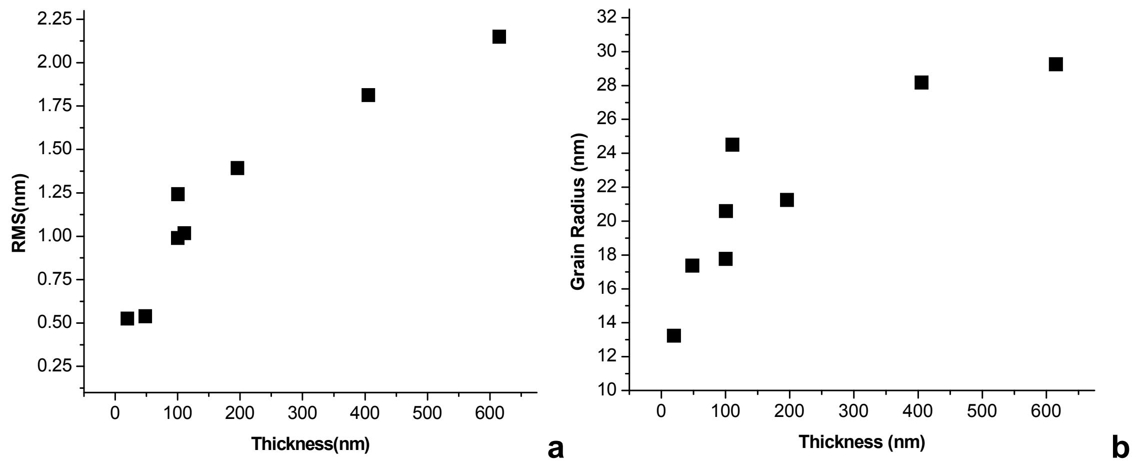

Figure 3.3.3 a RMS variation b Grain radius variation with film thickness for films grown at 15x10^{-3} mbar pressure.

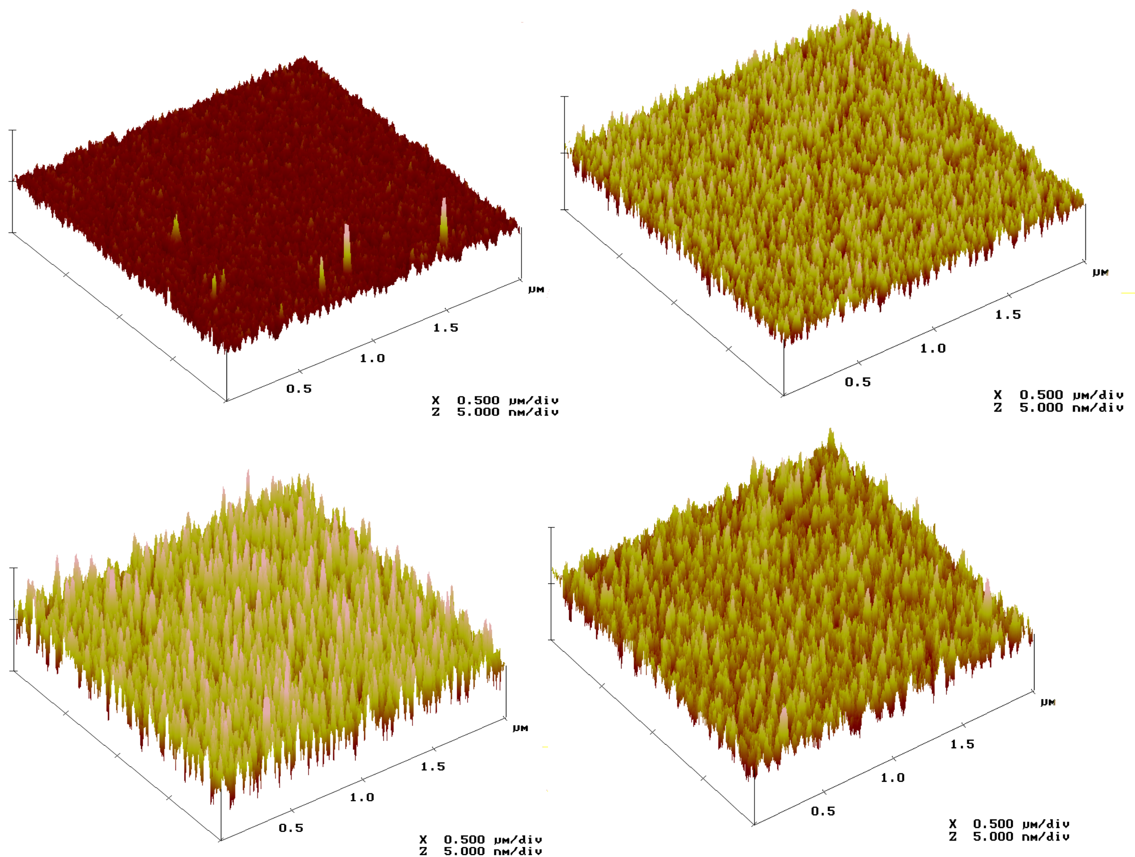

Figure 3.3.4 3-D images of films with a thickness of a) 20 nm, b) 50 nm, c) 100 nm and d) 200nm are presented (scan size 2x2 μm) grown at 15x10^{-3} mbar pressure.

Temperature effect

The effect of deposition temperature on the films surface morphology was also analyzed. In figures 3.3.5a, b and 3.3.6 a, b are shown examples of the evolution of typical surface parameters with temperature (from room temperature up to 300

°C) at two different growth pressures during growth for In_2O_{3-x} grown by DC magnetron sputtering from 99.999% pure In metallic target under the following deposition parameters: pressure $8x10^{-3}$ and $15x10^{-3}$mbar respectively, oxygen concentration in the plasma 100%, growth rate 5.6 nm/min and 130nm thickness.

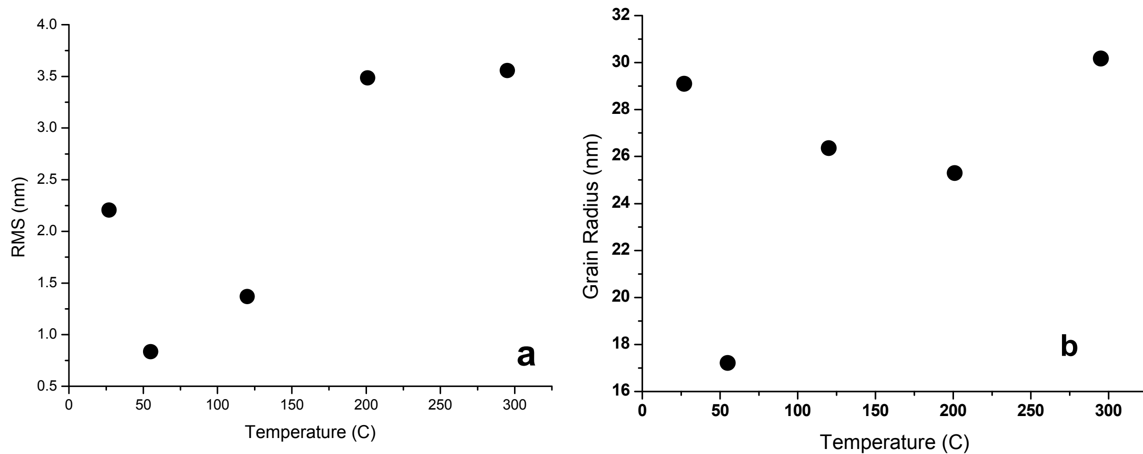

Figure 3.3.5 a RMS variation b Grain radius variation with growth temperature for films with a thickness 130nm grown at 100% oxygen, $8x10^{-3}$ mbar pressure

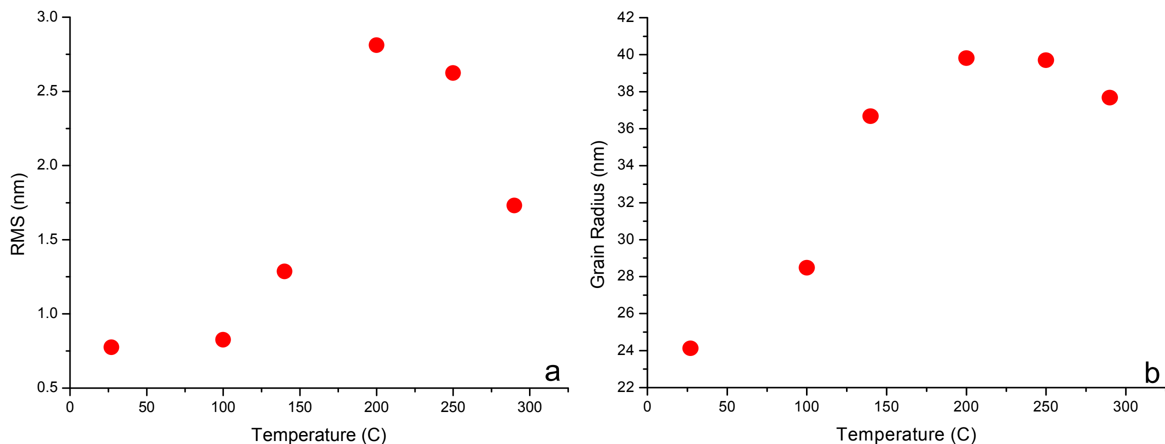

Figure 3.3.6 a RMS variation b Grain radius variation with growth temperature for films with a thickness 130nm grown at 100% oxygen, $15x10^{-3}$ mbar pressure

As can be seen in figures 3.3.5 and 3.3.6, all surfaces exhibit
a granular structure with the mean grain size varying between 17 and 30nm with increasing temperature at low growth pressure, the range becoming 24 to 37 nm for higher pressure. RMS also showed an increasing trend, being smaller for higher growth pressure. These are obvious also from AFM 2D images of 130nm films grown at different temperature RT, 200 and 300˚C for the higher pressure presented in figure 3.3.7.

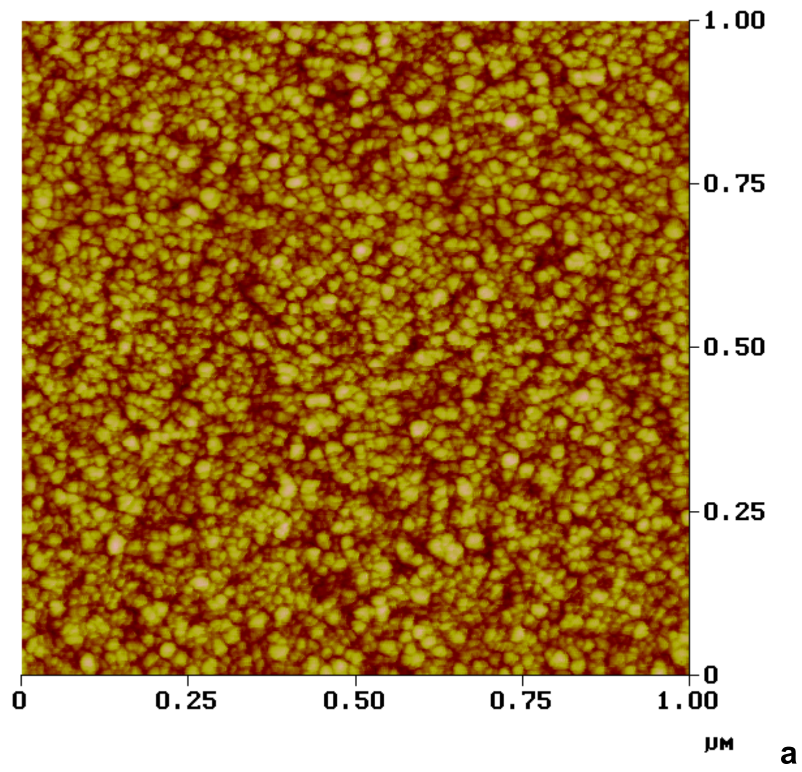
1.00
0.75
0.50
0.25
0
0
0.25
0.50
0.75
1.00
μm
a

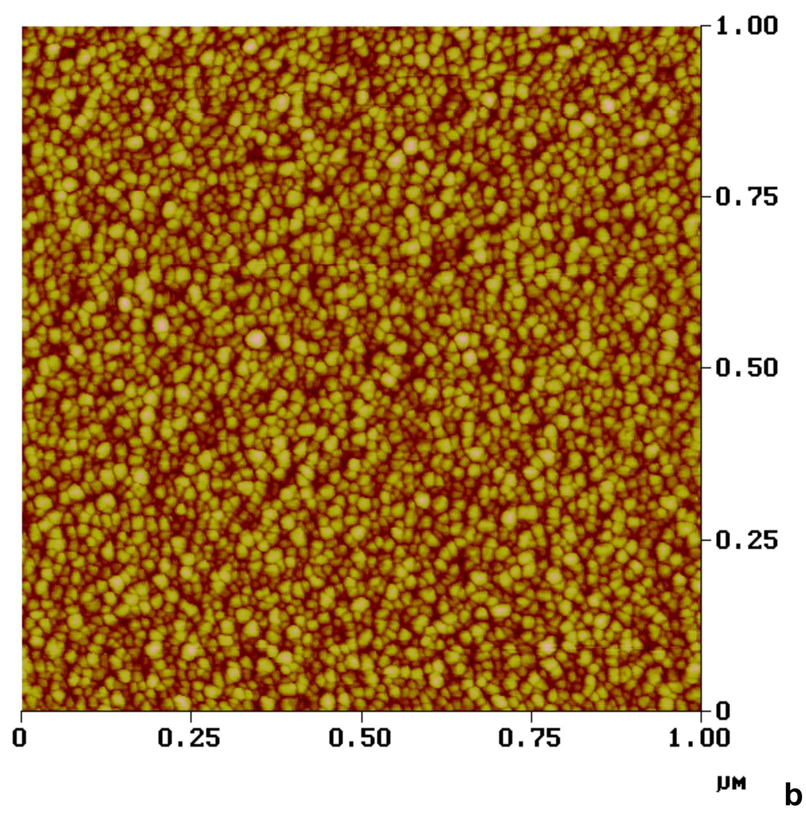
1.00
0.75
0.50
0.25
0
0
0.25
0.50
0.75
1.00
μm
b

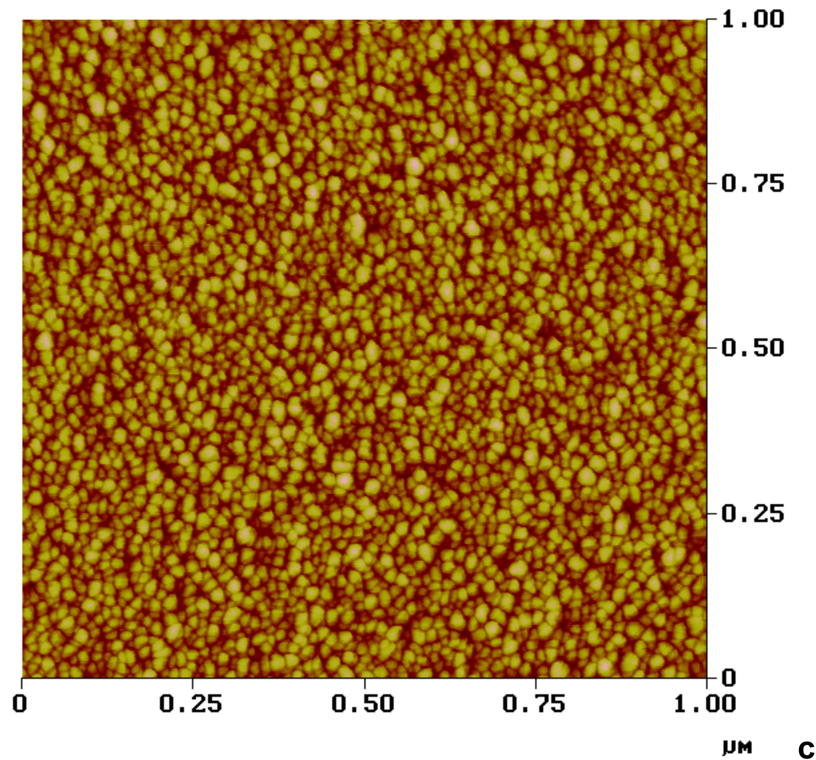

Figure 3.3.7 AFM 2D images of 130nm films grown at different temperatures a RT, b 200˚C and c 300 ˚C at 15x10^{-3} mbar pressure (scan size 1x1μm).

Total pressure and growth rate effects

Changing the total pressure during the deposition, its effect on the sample topology was determined, the corresponding surface parameters presented in Table 3.3. The total pressure during the deposition is correlated with the growth rate, the lowest growth rate corresponding to the highest deposition pressure. The other deposition parameters were: room temperature for the substrate, oxygen concentration 100%, film thickness 100nm.

Growth Rate (nm/min)	Pressure (μbar)	Grain Radius (nm) ± 0.01nm	RMS (nm) ± 0.01nm
6.00	5	23.96	0.85
5.55	8	17.75	0.99
5.00	15	21.48	1.82
2.40	30	31.28	2.61
1.97	50	33.17	3.67

Table 3.3 Total pressure and growth rate effect on films surface parameters

The dependence of RMS and grain size on the total pressure during the deposition appeared to have a more or less linear behavior, as shown in figure 3.3.8 a, b, c, and d.

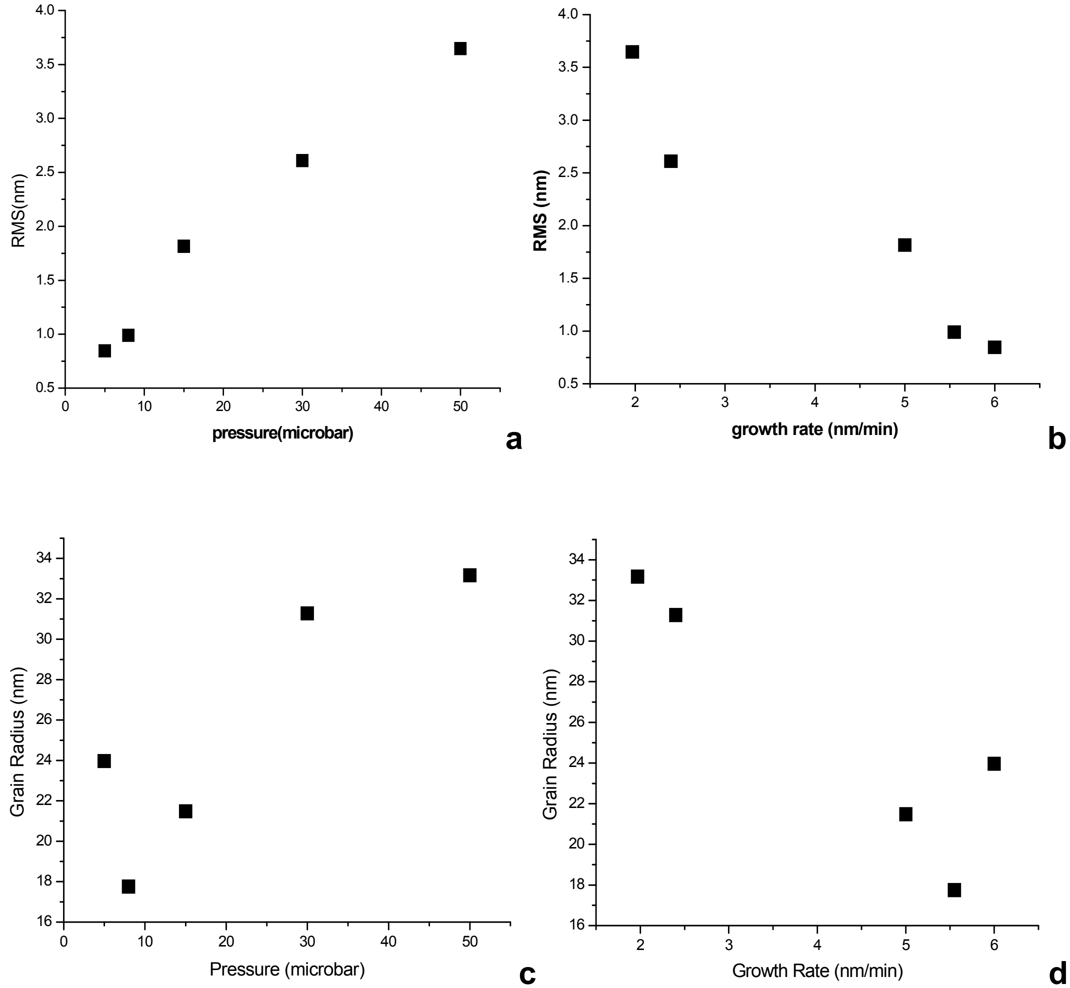

Figure 3.3.8 a RMS variation with pressure b RMS variation with growth rate c Grain radius variation with pressure d grain radius variation with growth rate for In_2O_{3-x} films grown by DC magnetron sputtering at different total pressures

As shown in figure 3.3.8, the surface roughness and grain radius is increasing when the total pressure increases and decreasing when the growth rate increases. Finally the surface aspect changes with total pressure are presented in figure 3.3.9.

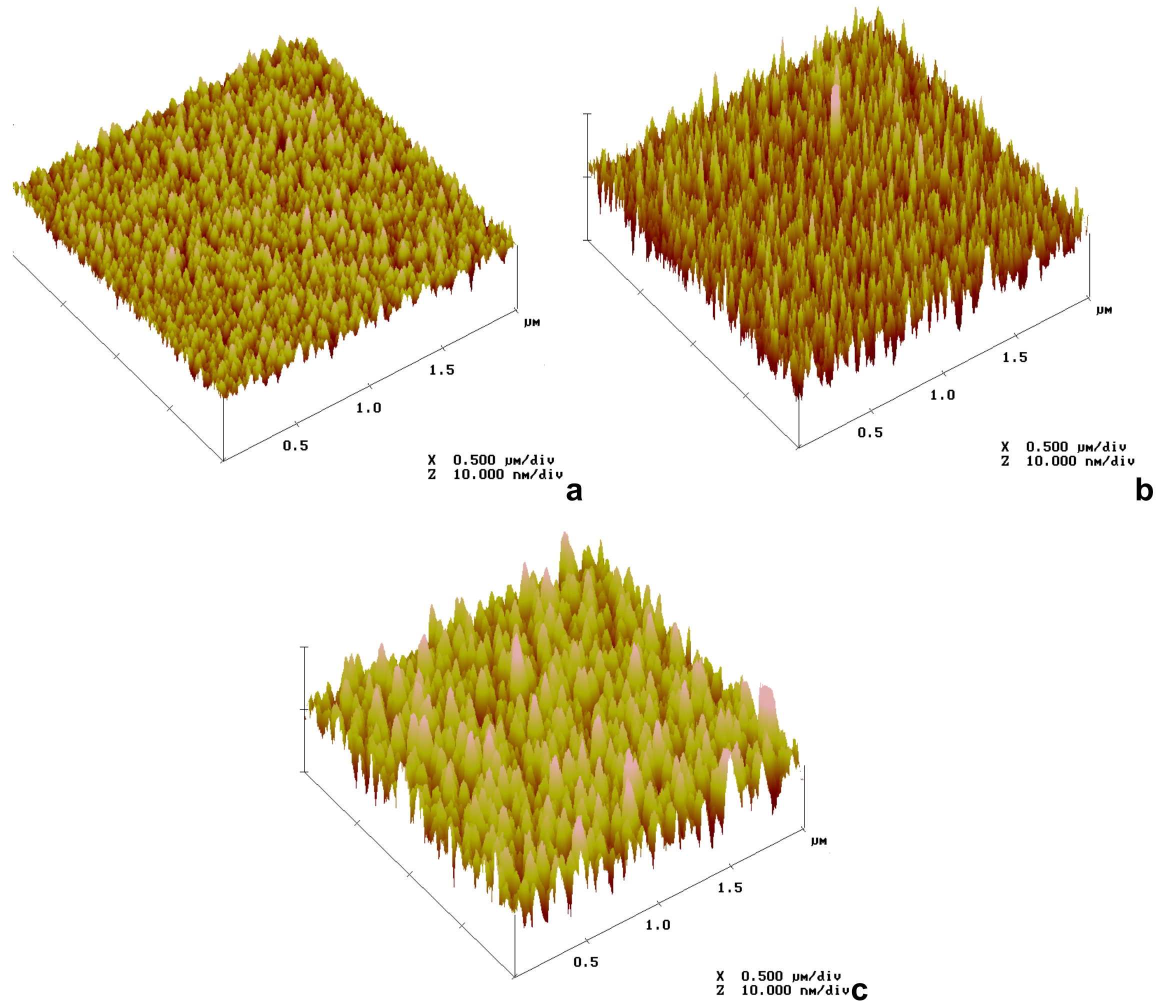

Figure 3.3.9. AFM 3-D images of In_2O_{3-x} films growth at different deposition pressures a - p=5 mbar, b - p=15 mbar, c - p=30 mbar.

These results prove that increased total pressure during DC magnetron sputtering film growth is strongly reflected in films surface formation. The main effect is the increase of surface grain lateral size associated with local surface roughening. This is in concordance with XRD observation and can be explained considering the decreased growth rate and the increased deposition time which allows material structuring.

3.4 Optical properties

The optical transmittance of the films was measured using the Varian Cary50 UV/Visible spectrophotometer with the Varian data analysis tools. The as-deposited In_2O_3 thin films were found to be highly transparent in the visible wavelength region, with an average transmittance of 80-90%, the absorption edge in the UV region depending on film growth conditions. The optical energy gap E_g was then derived from the transmission curves, assuming a direct transition between the edges of the valence and the conduction band. Then, the variation in the absorption coefficient with the photon energy hν is given by $\alpha(h\nu) = A\sqrt{h\nu - E_g}$. "Tauc" plots of α^2 versus hν helped in the determination of the optical band gap value E_g, by extrapolation of the linear region of the resulting curve. The calculated values of the direct optical energy gap for the In_2O_3 thin films were determined to be in the range 3.3 to 3.75 eV, the actual value depending on the growth conditions. The effect of thickness, total pressure during growth and growth temperature on the films optical properties are shown in the following figures. The variation of the optical energy gap as a function of previously mentioned deposition parameters is also presented.

The first two figures 3.4.1 and 3.4.2 present the UV-Vis optical transmittance and the calculated optical band gap energy as a function of thickness, for films grown at different total pressure. It is obvious that the mean optical transmittance in the visible spectral region slightly decreases as thickness increases (accordingly with light absorption law in solid material $T=e^{-\alpha d}$, where α is the medium light absorption coefficient and d is the film thickness), becoming slightly higher for films grown at higher pressure due to improved crystallinity (proved by XRD) which reflect in reduced scattering effects.

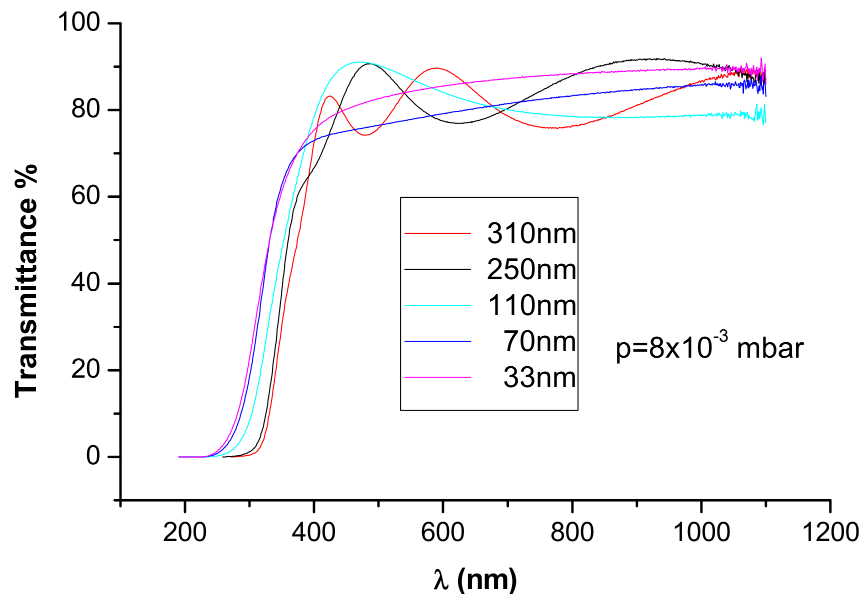

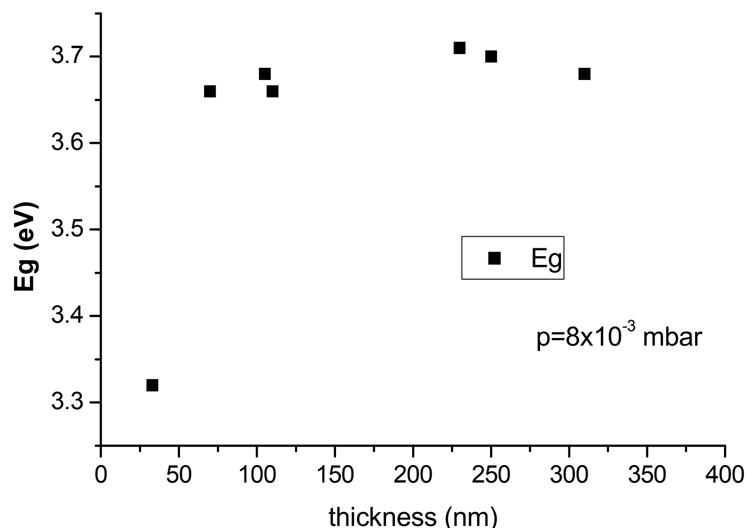

Figure 3.4.1 UV-Vis optical transmittance of In_2O_{3-x} thin films grown at $8x10^{-3}$ mbar total pressure and their calculated optical bandgap energy variation with thickness

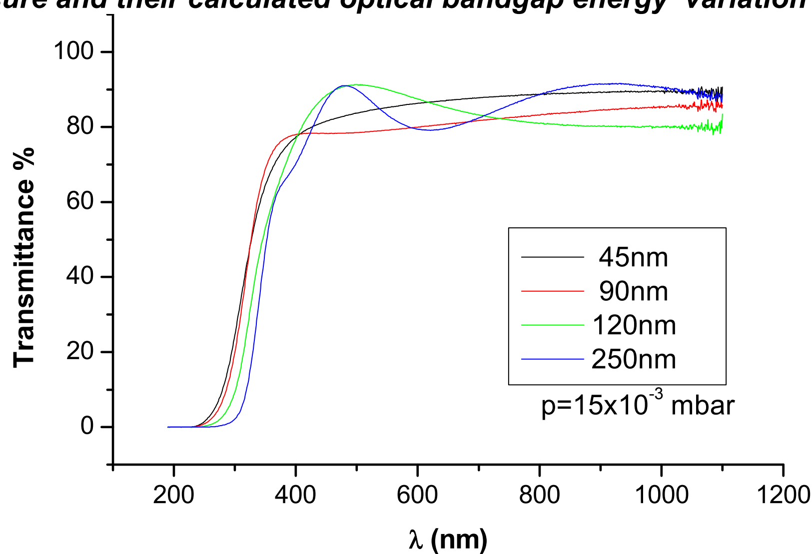

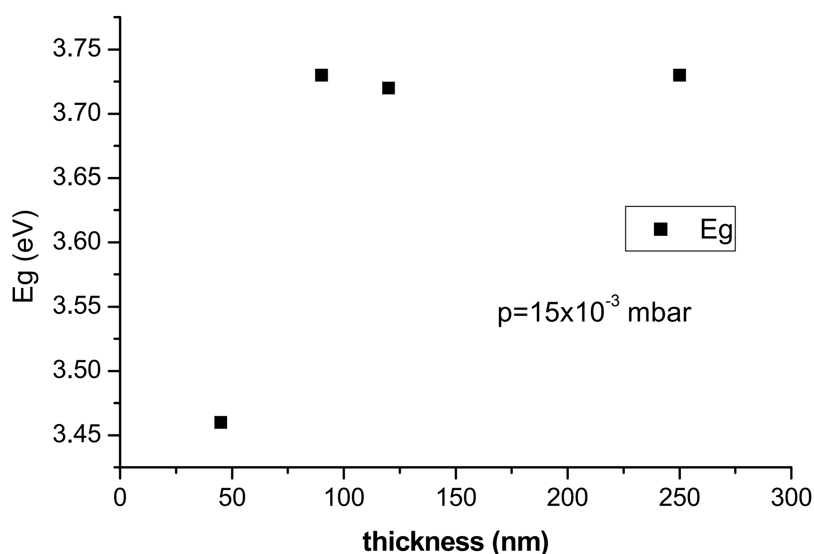

Figure 3.4.2 UV-Vis optical transmittance of In_2O_{3-x} thin films grown at $15x10^{-3}$ mbar total pressure and their calculated optical bandgap energy variation with thickness

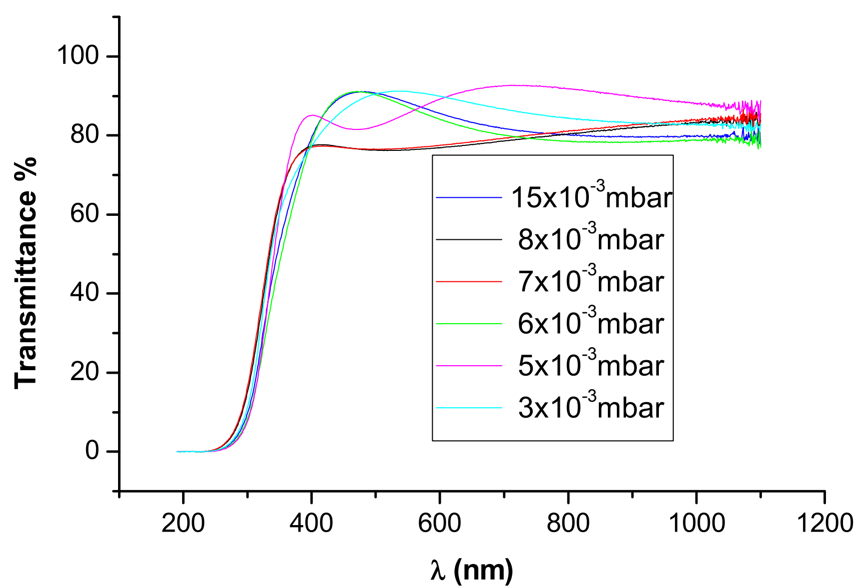

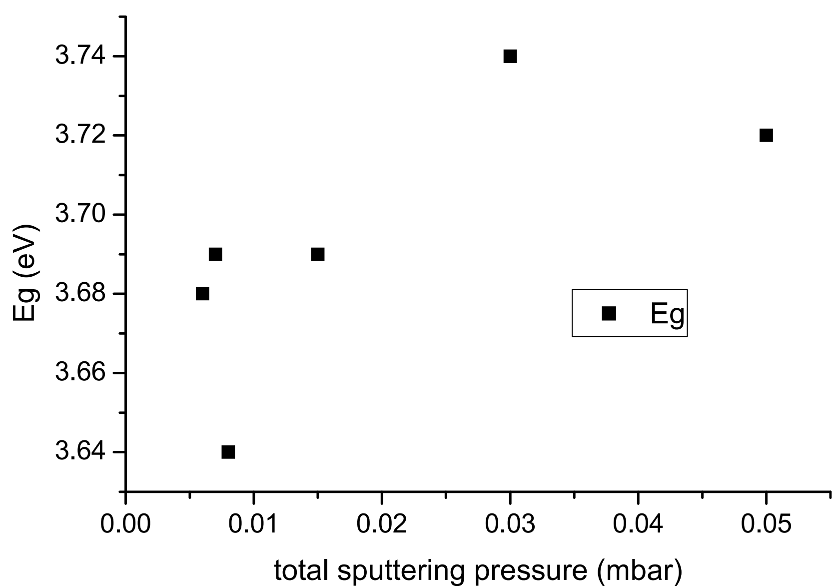

Figure 3.4.3 UV-Vis optical transmittance of In_2O_{3-x} thin films grown at different total pressure and their calculated optical bandgap energy.

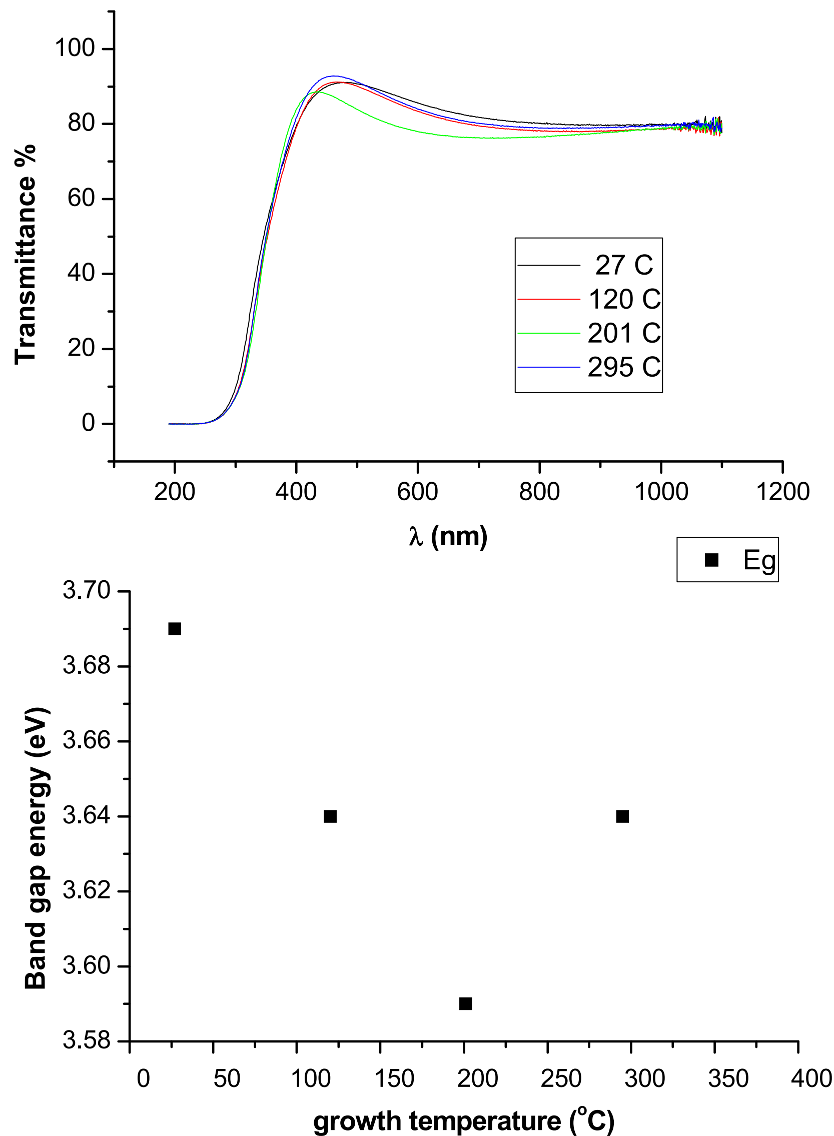

Figure 3.4.4 UV-Vis optical transmittance of In_2O_{3-x} thin films grown at different substrate temperature and their calculated optical bandgap energy.

As can be observed, the energy gap varies slightly with growth temperature, a response attributed to the variation of the bulk improved crystallinity (from XRD) with temperature.

It has been suggested in the literature [Hamberg, 1986, J. Appl. Phys. 60, R123] that two concurring phenomena affect the optical band gap. First, the well-known Burstein-Moss shift (BM shift), which depends on the shape of the band edge and leads to an increase of the optical energy gap due to the filling of the lowest levels of the conduction band with charge carriers in degenerate semiconductors. The observed energy gap is then

$$E_{gap} = E_{gap,0} + \Delta E_{BM}$$

For parabolic band edges, ΔE_{BM} is given by

$$\Delta E_{BM} = \frac{\hbar}{2m_{vc}^{*}}(3\pi^2 n)^{2/3}$$

The second phenomenon, which is responsible for band gap shrinkage due to increased tailing of the absorption edge, is attributed to the merging of the donor states with the conduction band in the vicinity of the semiconductor-metal transition [Roth, 1982, Phys. Rev. B 25, 7836] and to electron-electron interactions [Gupta, 1989, Thin Solid Films 176, 33]. The observation of a decreasing band gap with increasing substrate temperature leads to the assumption that the effect of band merging probably plays a dominant role in the films studied here, presumably caused by building up a donor band below the conduction band edge for films deposited at elevated temperatures. A detailed analysis of the transport properties could provide further insight to the observed behavior.

3.5 Electrical properties – sensing

As explained in the previous chapter dedicated to the conduction mechanisms in metal oxide thin films, the gas detection is based on the interaction of the gaseous species with the surface of the semiconducting sensitive layer. As a consequence of this surface interaction, charge transfer takes place between absorbed species and the semiconducting material. The experiments done in order to analyze the photoreduction-oxidation of all grown thin films for the sensing application were also presented.
The conductivity of the as-deposited DC magnetron sputtered In_2O_{3-x} thin films was found to range from 3.39×10^{-9} up to 33.5 Ω-1cm-1, its values depending on the deposition conditions. An increase up to seven orders of magnitude is observed after the exposure of the films to ultraviolet (UV) light in vacuum, the corresponding decrease after ozone exposure being usually lower, a fact connected to possible irreversible surface photoeffects.
A typical photoreduction-oxidation curve of a metal oxide thin film is shown in the figure 3.5.1.

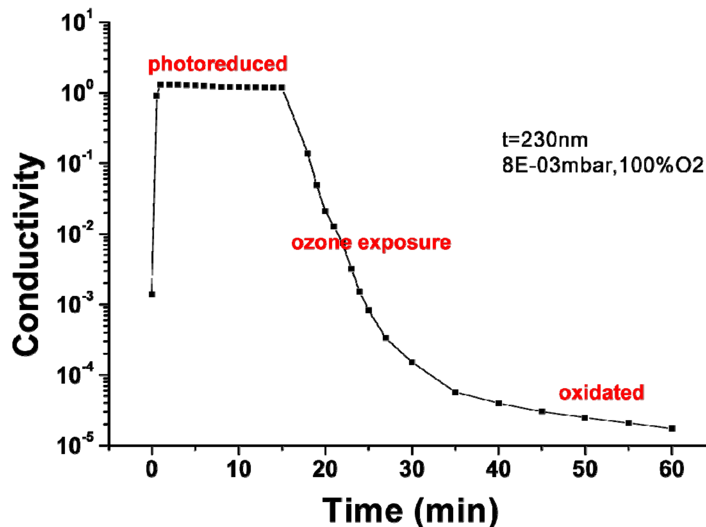

Figure 3.5.1 Typical conductivity curve for photoreduction-oxidation of In_2O_{3-x} thin films. The photoreduced state corresponds to maximum conductivity, while the oxidized state corresponds to minimum conductivity

For the purpose of the present thesis, we define the ratio $\sigma_{max}/\sigma_{final}$ (conductivity in equilibrium photoreduced state divided by fully oxidized with ozone final equilibrium state) as film's ozone sensitivity. The influence of the growth conditions on the conductivity of the films was rigorously studied and the obtained values are included at the end of chapter 7 as table in Annex 7C. The purpose of this trial was to obtain a complete set of data regarding the correlation between the growth conditions and the sensing properties for the grown films, which can be used for modeling.
It was observed and confirmed that the photoreduction treatment results in an increase of conductivity up to around six orders of magnitude for the temperature and the thickness series (figure 3.5.2) and up to almost seven orders of magnitude for the total deposition pressure series, a fact which confirms the stronger effect of the sputtering pressure on the film stoichiometry, also observed from XRD

analysis. Increasing film thickness results in a decrease of the ozone sensitivity, as can be seen in figure 3.5.3, for the thickness series In_2O_{3-x} films grown by DC magnetron sputtering from 99.999% pure In metallic target under the following deposition parameters: pressure $8x10^{-3}$ mbar, oxygen concentration in the plasma 100%, growth rate 5.6 nm/min, at RT.

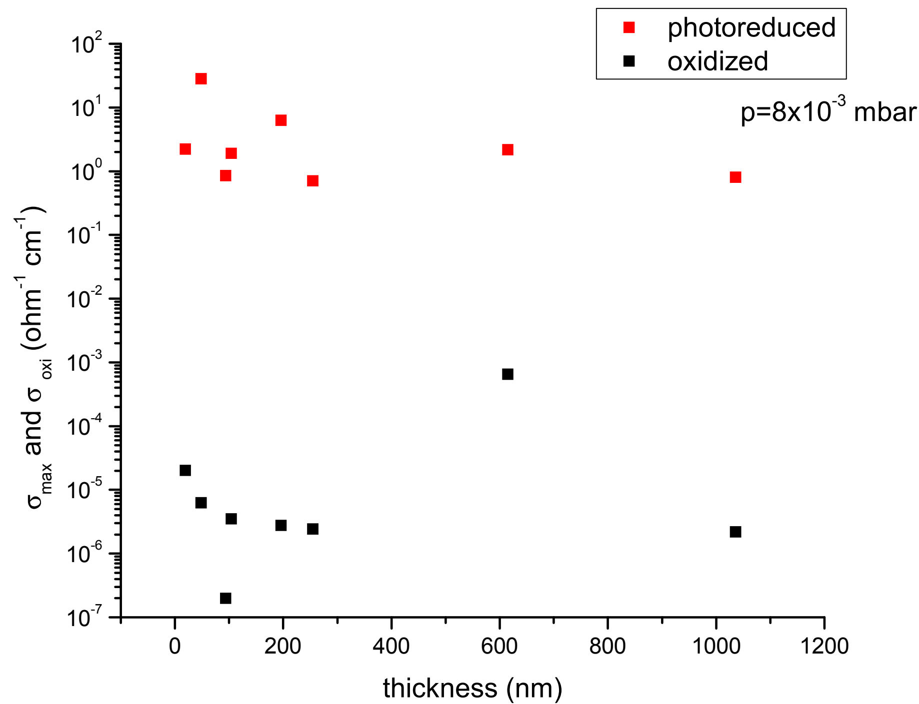

Figure 3.5.2 Maximum conductivity (photoreduced) and minimum conductivity (oxidized) variations as functions of film thickness

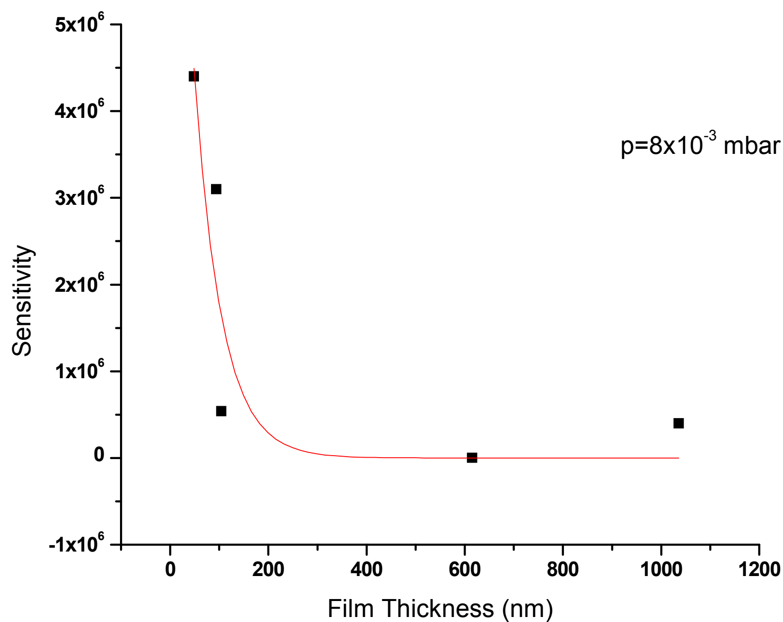

Figure 3.5.3 Ozone sensitivity as functions of film thickness

Considering the influence of surface RMS and grain size on the conductivity changes, parameters determined from AFM measurements, sensitivity was found increasing with increasing RMS, the opposite appearing for the grain radius case as shown in figure 3.5.4 a and b for the thickness serie considered also previously.

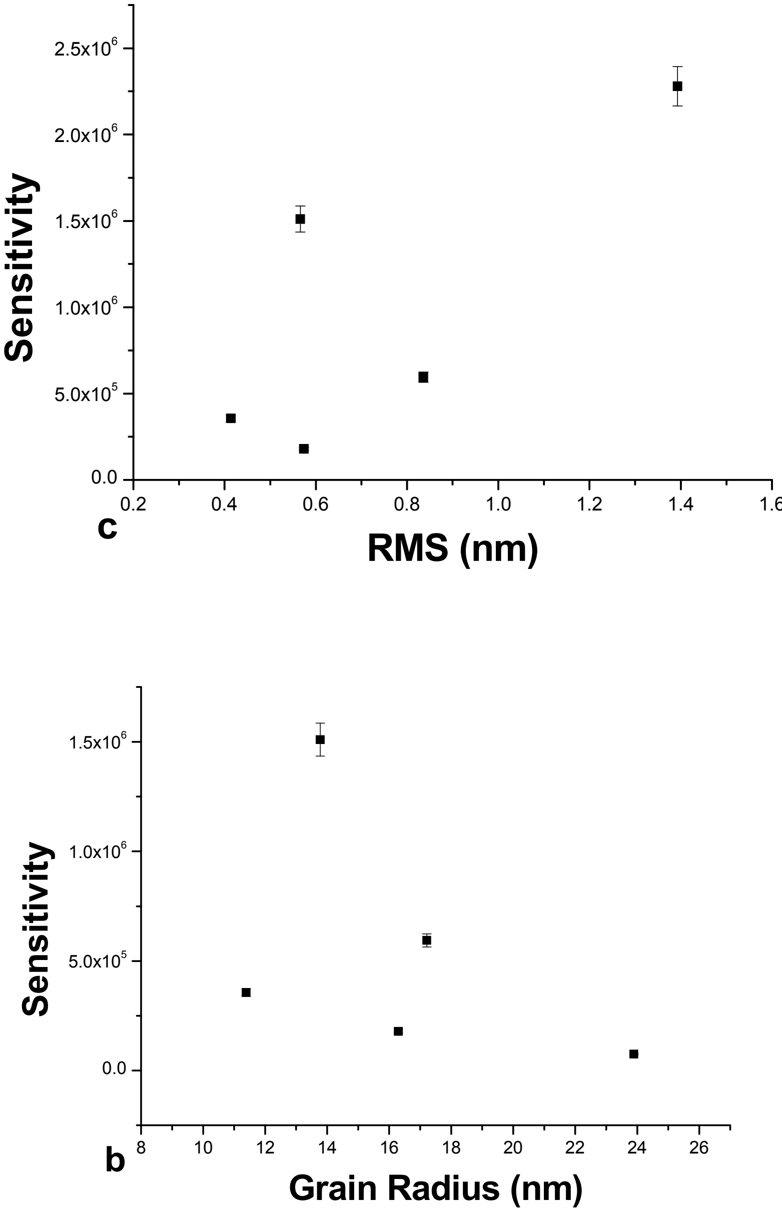

Figure 3.5.4 Ozone sensitivity as functions of a RMS and b grain radius

The observed correlation between the film sensitivity and the surface parameters can be explained particularly for this case using the conduction model of metal oxide gas sensors approximation, given by Barsan et al. According to this model, for small grains and narrow necks, when the mean free path of free charge carriers becomes comparable with the dimension of the grains, the surface influence on the mobility becomes dominant over bulk phenomena. In the presence of the ionic species on the surface, after UV photoreduction, the electronic concentration in the surface states increases. The surface states concentration is correlated with the roughness and grain size via surface-to-volume ratio.

The sensing behavior of films grown at different substrate temperatures are shown in figure 3.5.5.

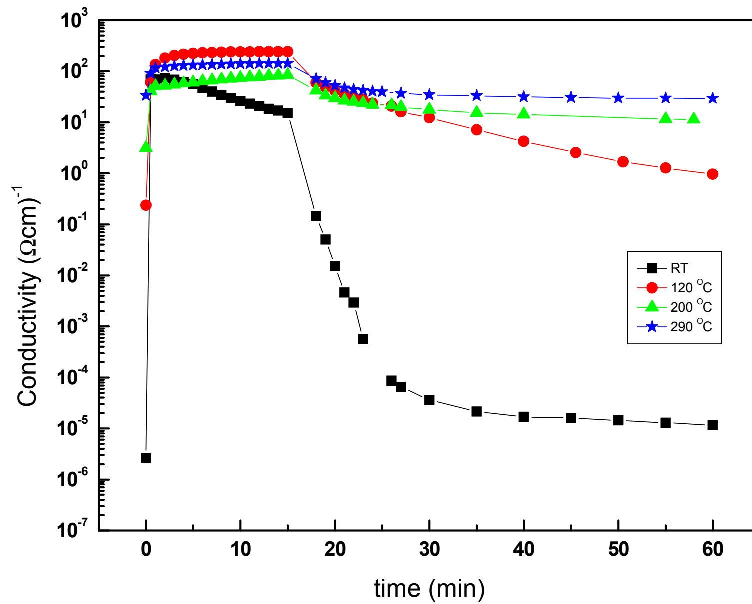

Figure 3.5.5 Photoreduction-oxidation cycles for 130nm thin films grown at different substrate temperatures

Figure 3.5.6 a show that, due to improved stoichiometry, as the deposition temperature increases the ozone sensitivity decreases. The stoichiometric In_2O_3 is an insulator and loses a very small quantity of oxygen during the photoreduction. This is directly reflected in the photoreduced state conductivity. With temperature increase, the grain radius also increases (see figure 3.5.6 b), resulting in a decrease of the ozone sensitivity.

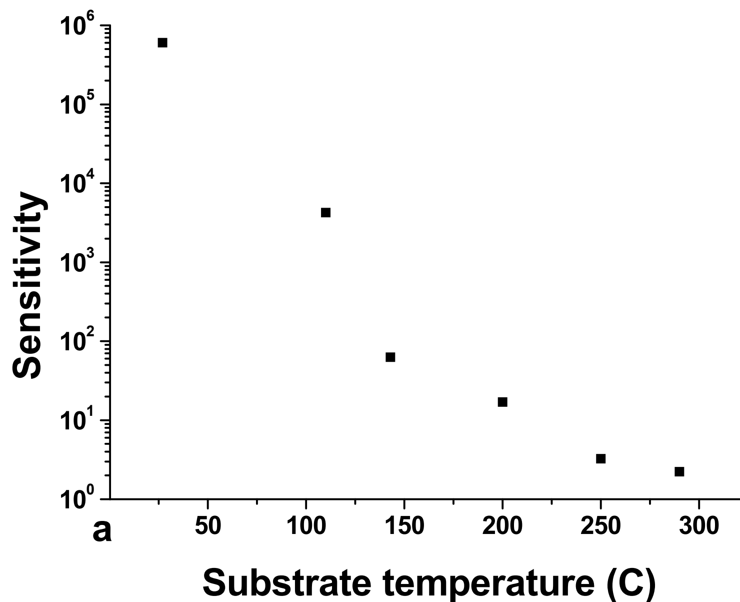

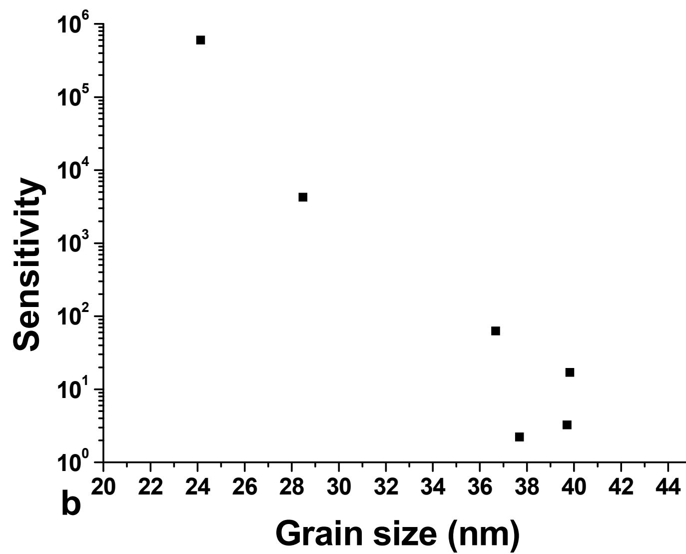

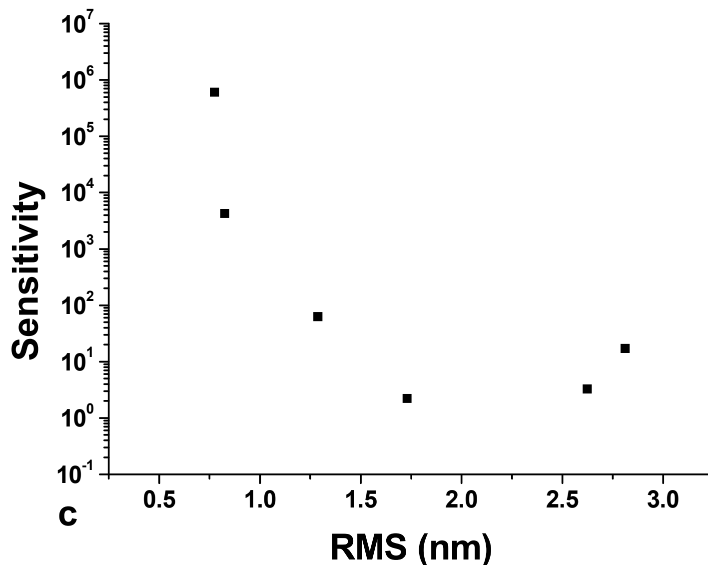

Figure 3.5.6 Ozone sensitivity variations with a substrate temperature; b grain size; c RMS for an 130nm thin films serie.

Similarly, increased film RMS was found causing a decrease in the ozone sensitivity as shown in figure 3.5.6 c.

Moreover, the following figures present a correlation between the films' sensitivity and the total pressure in the sputtering chamber (and consequently with the growth rate). An example of maximum and minimum conductivities variations with total pressure are presented in figure 3.5.7.

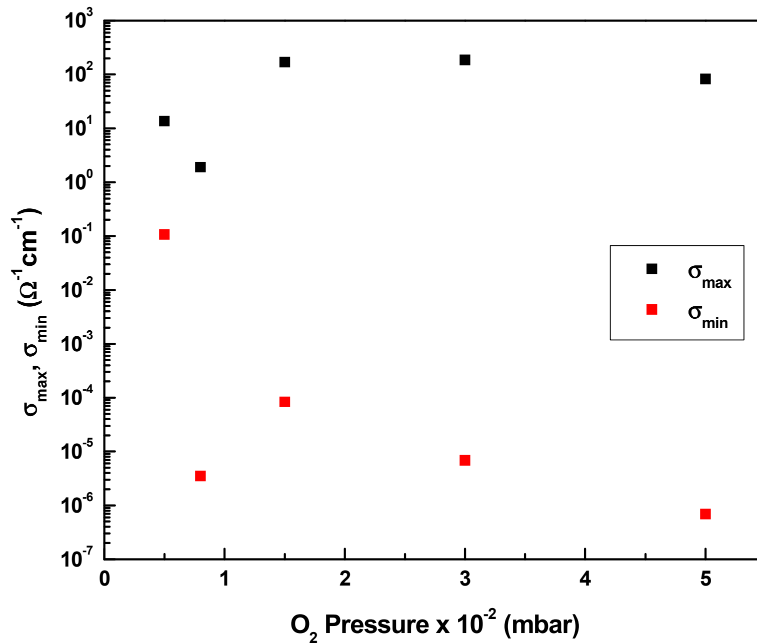

Figure 3.5.7 Maximum conductivity (photoreduced) and minimum conductivity (oxidized) variations as functions of total pressure.

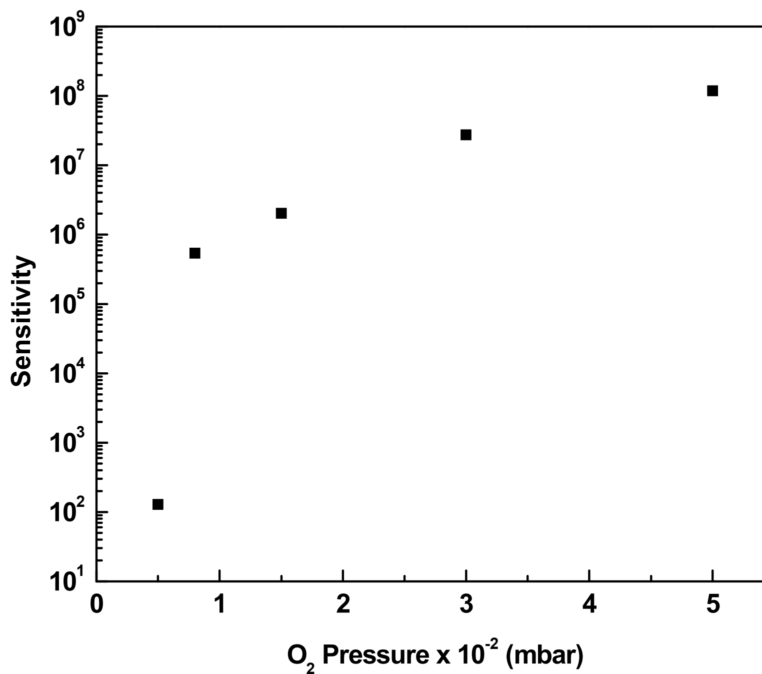

Figure 3.5.8 Ozone sensitivity variation as functions of total pressure.

Ozone sensitivity shows an increasing trend as oxygen total pressure during growth increases. This can be seen from figure 3.5.8 and it can be correlated with surface parameters variation.

The influence of the total pressure, the growth rate and the surface parameters (grain radius and RMS) on the ozone sensitivity is presented in the graphs included in figure 3.5.9 a, b, c and d.

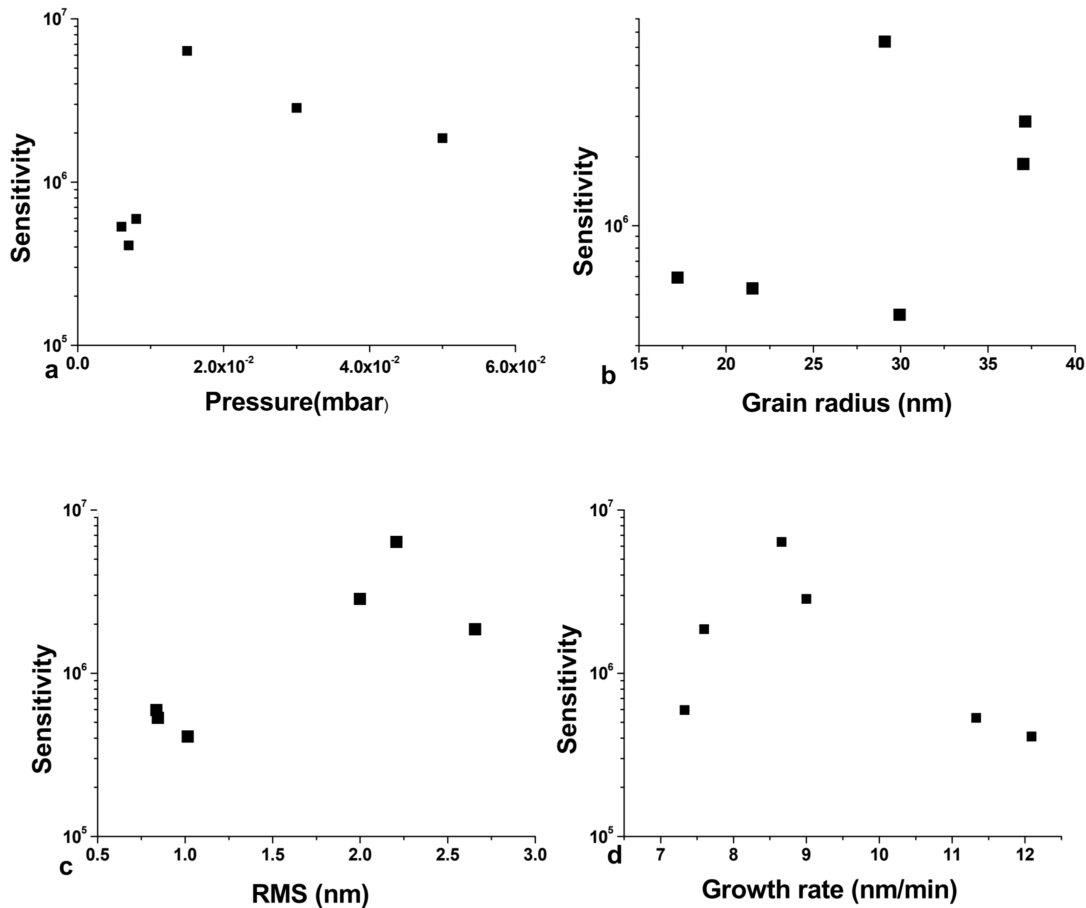

Figure 3.5.9 The influence of a the total pressure; b grain radius; c RMS and d growth rate on the ozone sensitivity

As can be seen from figure 3.5.9, there is a distinct different behavior between the sensitivities for films grown at pressures below and over 10^{-2} mbar. This can be attributed to their grain size and RMS values. Indeed, the lower pressure films show lower RMS and grain size than the higher-pressure ones (see figures 3.5.9 b and c). The grain size local variation within the two mentioned groups of films shows an increase of sensitivity with decreasing grain size according with the previous sensitivity-grain size correlations. The surface RMS correlation with ozone sensitivity follows the same trend with the grain size- sensitivity correlation shown in c.

Conclusions

This chapter was dedicated to the deposition and the properties of In_2O_{3-x} grown by DC magnetron sputtering in different growth conditions. The results can be summarized as following:

- DC magnetron thin films grown at room temperature in various conditions were nonstoichiometric, oxygen deficient.
- All films were amorphous in the early stage of growth becoming polycrystalline with columnar bulk structure and texturing on preferential orientation [222] of bixbyite crystalline structure after the critical thickness, corresponding to the incubation time, was reached. In some cases, [400] and [440] lattice plans showed a small tendency of growth.
- All films had homogenous surface with narrow grain size distribution and RMS bellow 3 nm even for films with large thickness.
- Growth conditions control the surface texturing and roughening as well as bulk crystallite growth.
- Photoreduction and oxidation with ozone experiments leads to the conclusion that both, photoactivation and oxidation processes are strongly surface correlated and sensing behavior can be controlled via surface engineering.
- The partial correlation in particular cases of films grouped according to the growth conditions clearly indicated that a larger correlation between surface morphology and sensing action exists.
- All films showed high transmittance in visible spectral range (~80%) and optical band gap energies smaller than the theoretical values for In_2O_3 but in a good accordance with this. The lower values of band gap can be associated with Burnstein-Moss effect due to presence of ionized oxygen vacancies acting as donor impurities.

References

1 G. Kiriakidis, N.Katsarakis ,M.Bender, E.Gagaoudakis and V.Cimalla, “InOx Thin Films, Candidates for Novel Chemical and Optoelectronic Applications”, Materials Physics and Mechanics” Vol 1 No2, pp. 83-97, 2000.

2 C. Xirouchaki, K. Moschovis, E. Chatzitheodoridis, G. Kiriakidis, H. Boye, P. Morgen, "Structural and chemical characterization of as-deposited microcrystalline indium oxide films prepared by DC reactive magnetron sputtering", Journal of Electronic Materials, Vol.28, No.1 p 26-34, 1999.

3 G. Kiriakidis, M. Bender, N. Katsarakis, E. Gagaoudakis, E. Hourdakis, E. Douloufakis and V. Cimalla. "Ozone sensing properties of polycrystalline Indium Oxide films at room temperature" Phys. Stat. Sol. Vol. 185, No 1, 2001.

4 M. Bender, N. Katsarakis, E. Gagaoudakis, E. Hourdakis, E. Douloufakis and V. Cimalla, G. Kiriakidis. “ Dependence of the Photoreduction and Oxidation Behaviour of Indium Oxide Films on Substrate Temperature and Film Thickness “.Journal of Applied Physics V 90,N 10, P 5382-5387, 2001.

5 E. Gagaoudakis, M. Bender, E. Douloufakis, N. Katsarakis, E. Natsakou, V. Cimalla, G. Kiriakidis. “The Influence of Deposition Parameters on Room Temperature Ozon Sensing Properties of InOx Films”. Sensors and Actuators B, 80, p155-160, 2001.

6 N. Katsarakis, M. Bender, L. Singleton, G. Kiriakidis, and C. M. Soukoulis, “Two-dimensional metallic photonic band-gap crystals fabricated by LIGA”, Microsystem Technologies 8, 74 (2002).

7 M. Bender, N. Katsarakis, G. Kiriakidis, I. A. Ovid’ko, and A. B. Reizis, “Physical mechanisms of enhanced conductivity in irradiated InOx nanocrystalline films”, Mater. Phys. Mech. 5, 11 (2002).

8 G. Kiriakidis, H. Ouacha, and N. Katsarakis, “Nano-structured metal oxide films with room temperature gas sensing properties”, NATO Science Series II: Mathematics, Physics and Chemistry, Kluwer Academic Publishers, Dordrecht ,Volume 128, p. 363-382, , (2003).

9 G.Kiriakidis, H. Ouacha and N.Katsarakis, “InOx Nanostructured Thin Films: Electrical and Sensing Characterization”, Rev. Adv. Mater. Sci. 4, p32-40 (2003)

10 N. Katsarakis, M. Bender, V. Cimalla ,E. Gagaoudakis and G. Kiriakidis, “ Ozone sensing properties of DC-sputtered, c-axis oriented ZnO films at room temperature” Sensors and Actuators B 96, 76-81 (2003).

11 Kiriakidis, G.”Near surface characteristics of highly sensitive metal oxide thin films” (2005) Materials Research Society Symposium Proceedings, 828, art. no. A1.5, pp. 37-49.http://www.scopus.com/cto2/print.url2

12 G. Kiriakidis, N. Katsarakis, M. Suchea, S. Christoulakis, K Moschovis, “Low cost metal oxide ozone detector for food processing”, Science, Processes, and Food Technologies, vol. XI (CNCSIS publication)

13 M. Suchea, G. Kiriakidis, C. Mateescu, “Nanostructured materials and microdevices for food and agricultural applications” Review Paper, Science, Processes, and Food Technologies, vol. XI (CNCSIS publication)

14 M. Suchea, G. Kiriakidis, "Atomic Force Microscopy Analysis of Polycrystalline Indium Oxide Thin films", Proceedings of 19-th Panhellenic Conference in Solid State and Materials Science, 2003, p. 389-392.

15 G. Kiriakidis, N. Katsarakis, K. Moschovis, E. Gagaoudakis, M. Suchea, S. Christoulakis, M. Katharakis, “InO_x Thin Film Gas Sensor“ (“Αισθητήρας αερίων από λεπτά υμένια InO_x”), 20th Panhellenic Conference on Solid State Physics & Materials Science (XX ΠΣΣΥ), Ioannina – Greece, September 26-29, 2004, (in Greek)

16 N. Katsarakis, M. Suchea, M. Nikolopoulou, S. Christoulakis, K. Moschovis, E. Gagaoudakis, M. Katharakis, G. Kiriakidis “Conductivity Change of InO_x Thin Films in function of thickness” (“Μεταβολή Αγωγιμότητας Υμενίων InO_x Συναρτήσει του Πάχους και της Έκθεσης σε UV”), 20th Panhellenic Conference on Solid State Physics & Materials Science (XX ΠΣΣΥ), Ioannina – Greece, September 26-29, 2004 (in Greek).

17 M. Suchea, G. Kiriakidis, “Correlation of Surface Characteristics of In and Zn Oxides by AFM”, 2004 International Semiconductor Conference. CAS 2004 Proceedings (IEEE Cat. No.04TH8748), 2004, Vol. 2, p. 345-348

18 G.Kiriakidis, N.Katsarakis, M. Katharakis, M. Suchea, K. Galatsis, W. Wlodarski, D. Kotzias, "Ultra Sensitive Low Temperature Metal Oxide Gas Sensors", 2004 International Semiconductor Conference. CAS 2004 Proceedings (IEEE Cat. No.04TH8748), 2004, Vol. 2, p. 325-333.

19 Kiriakidis, G., Dovinos, D., Suchea, M. Sensing using nanostructured metal oxide thin films (2006) Proceedings of SPIE - The International Society for Optical Engineering, 6370, art. no. 63700V.

20 S. J. Ippolito, S. Kandasamy, K. Kalantar-Zadeh, W. Wlodarski, K. Galatsis, G. Kiriakidis, N. Katsarakis, M. Suchea, “Highly Sensitive Layered $ZnO/LiNbO_3$ SAW Device with InO_x Selective Layer for NO_2 and H_2 Gas Sensing” Sensors and Actuators B 111–112 (2005) 207–212,(doi:10.1016/j.snb.2005.07.046)

21 G. Kiriakidis, M. Suchea, S. Christoulakis and N. Katsarakis, “High performance gas sensing materials based on nanostructured metal oxide films”, Review on Advanced Materials Science 10 (2005) 215-223 (http://www.ipme.ru/e-journals/RAMS/no_31005/kiriakidis.pdf)

22 Ippolito, S.J., Kandasamy, S., Kalantar-Zadeh, K., Wlodarski, W., Galatsis, K., Kiriakidis, G., Katsarakis, N., Suchea, M. Highly sensitive layered ZnO/LiNbO3 SAW device with InO_x selective layer for NO_2 and H_2 gas sensing (2005) Sensors and Actuators, B: Chemical, 111-112 (SUPPL.), pp. 207-212. Cited 9 times.

23 Suchea, M., Katsarakis, N., Christoulakis, S., Katharakis, M., Kitsopoulos, T., Kiriakidis, G. Metal oxide thin films as sensing layers for ozone detection (2006) Analytica Chimica Acta, 573-574, pp. 9-13. Cited 4 times.

24 Suchea, M., Katsarakis, N., Christoulakis, S., Nikolopoulou, S., Kiriakidis, G. “Low temperature indium oxide gas sensors” (2006) Sensors and Actuators, B: Chemical, 118 (1-2), pp. 135-141. Cited 5 times.

25 Kiriakidis, G., Suchea, M., Christoulakis, S., Moschovis, K., Kitsopoulos, T., Stoemenos, J. “Nano-structural and surface characteristics of non-stoichiometric In_2O_{3-x} thin films” (2009) International Journal of Nanotechnology, 6 (1-2), pp. 208-218.

Annex 3A: Growth parameters for In_2O_{3-x} thin films grown by DC magnetron sputtering.

RUN	% O_2	PO_2 (mbar)	ISP (A)	time (s)	T (°C)	d (nm)	growth rate
1	100	0.008	0.60	1260	300	151.4	0.12
2	100	0.008	0.60	1257	138	151.7	0.12
3	100	0.008	0.60	1225	200	152	0.12
4	100	0.008	0.60	1260	165	151.8	0.12
5	100	0.008	0.60	1296	25	151.9	0.12
6	100	0.008	0.60	1262	100	151.7	0.12
7	100	0.008	0.45	4320	25	405.4	0.09
8	100	0.008	0.44	6600	25	615	0.09
9	100	0.008	0.44	1080	25	100.5	0.09
10	100	0.015	0.45	1200	25	100.5	0.08
11	100	0.050	0.45	1020	25	101.6	0.10
12	100	0.030	0.45	2550	25	100.8	0.04
13	100	0.050	0.45	3075	25	100.5	0.03
14	100	0.008	0.45	540	25	48.3	0.09
15	100	0.008	0.45	240	25	19.4	0.08
16	100	0.008	0.45	2100	25	195.9	0.09
17	100	0.008	0.45	1080	25	100.3	0.09
18	100	0.008	0.45	1200	25	110.8	0.09
19	100	0.015	0.15	5700	25	94	0.02
20	100	0.006	0.44	540	25	101.7	0.19
21	100	0.007	0.44	516	25	103.6	0.20
22	100	0.008	0.44	720	25	103.1	0.14
23	100	0.008	0.44	480	25	70	0.15
24	100	0.008	0.44	900	25	133	0.15
25	100	0.008	0.44	240	25	34	0.14
26	100	0.008	0.44	1800	25	270.1	0.15
27	100	0.015	0.45	900	25	129.9	0.14
28	100	0.015	0.45	900	137	130.6	0.15
29	100	0.015	0.45	900	210	130.7	0.15
30	100	0.015	0.45	900	290	130.2	0.14
31	100	0.015	0.45	240	37	31.8	0.13
32	100	0.015	0.45	480	37	67.4	0.14
33	100	0.015	0.45	900	38	133	0.15
34	100	0.015	0.45	1800	49	274	0.15
35	100	0.030	0.45	900	49	94.1	0.10
36	100	0.050	0.45	1500	51	104.3	0.07
37	100	0.015	0.15	660	35	41.3	0.06
38	100	0.015	0.45	570	58	132.9	0.23
39	100	0.015	0.45	570	110	133.7	0.23
40	100	0.015	0.45	570	154	135.7	0.24
41	100	0.015	0.45	540	206	134.7	0.25
42	100	0.015	0.45	570	250	137.6	0.24
43	100	0.015	0.45	600	290	137.6	0.23
44	100	0.008	0.44	600	59	147.4	0.25
45	80	0.008	0.44	540	61	145.1	0.27
46	60	0.008	0.44	390	59	148.4	0.38
47	40	0.008	0.44	330	53	150	0.45

Chapter 4

Pure ZnO thin films grown by DC magnetron sputtering

Outlines

- **Growth**
- **Characterization: structural, surface, optical, electrical**
- **Particular correlations of different parameters**
- **Annex 4A Growth parameters of ZnO films by DC magnetron sputtering.**

4. ZnO thin films grown by DC magnetron sputtering

Various ZnO series were grown by DC magnetron sputtering under different sputtering conditions and analyzed. Special attention was paid to the influence of thickness, growth temperature, total pressure during the deposition and oxygen:argon ratio during growth on the properties of the films. Complete surface characterization of each film was performed and surface characteristic parameters and grain sizes were determined. A list of the grown films and their growth conditions can be found in Table annex A at the end of this chapter.

4.1 Films structure

TEM Characterization

All depositions of the ZnO films were carried out in the Alcatel DC magnetron sputtering system using a 99.999% pure Zn metallic target under the following deposition parameters: pressure during growth $8x10^{-3}$ mbar, oxygen concentration in the plasma 100%, growth rate 9.6 nm/min, plasma current 0.24 at room temperature. The base pressure in the chamber was 5×10^{-7} mbar. Films of different thickness were deposited onto Corning 1737F glass substrates with electrical contacts, as well as on NaCl and silicon substrates.

The structure of the ZnO film was examined using conventional TEM and high-resolution TEM (HRTEM). For the specimen preparation for the cross-section TEM (XTEM) two strips of the sample were cut along the [220] direction of the Si substrate, glued together face to face on the (001) plane and then mechanically thinned down to a thickness of 25µm by Ar ion milling with energy of 4kV, at a very low incident angle of 4°, suitable to avoid artifacts due to amorphisation induced by the argon ions. This process was required for electron transparency. For the conventional TEM characterization, a JEM 120 CX was used, while, for the HRTEM investigation the model JEM 2010 having 0.194nm point to point resolution was employed. The obtained morphology of the films as a function of film thickness is presented in the four XTEM micrographs shown in figures 4.1a, 4.1b, 4.1c, 4.1d.

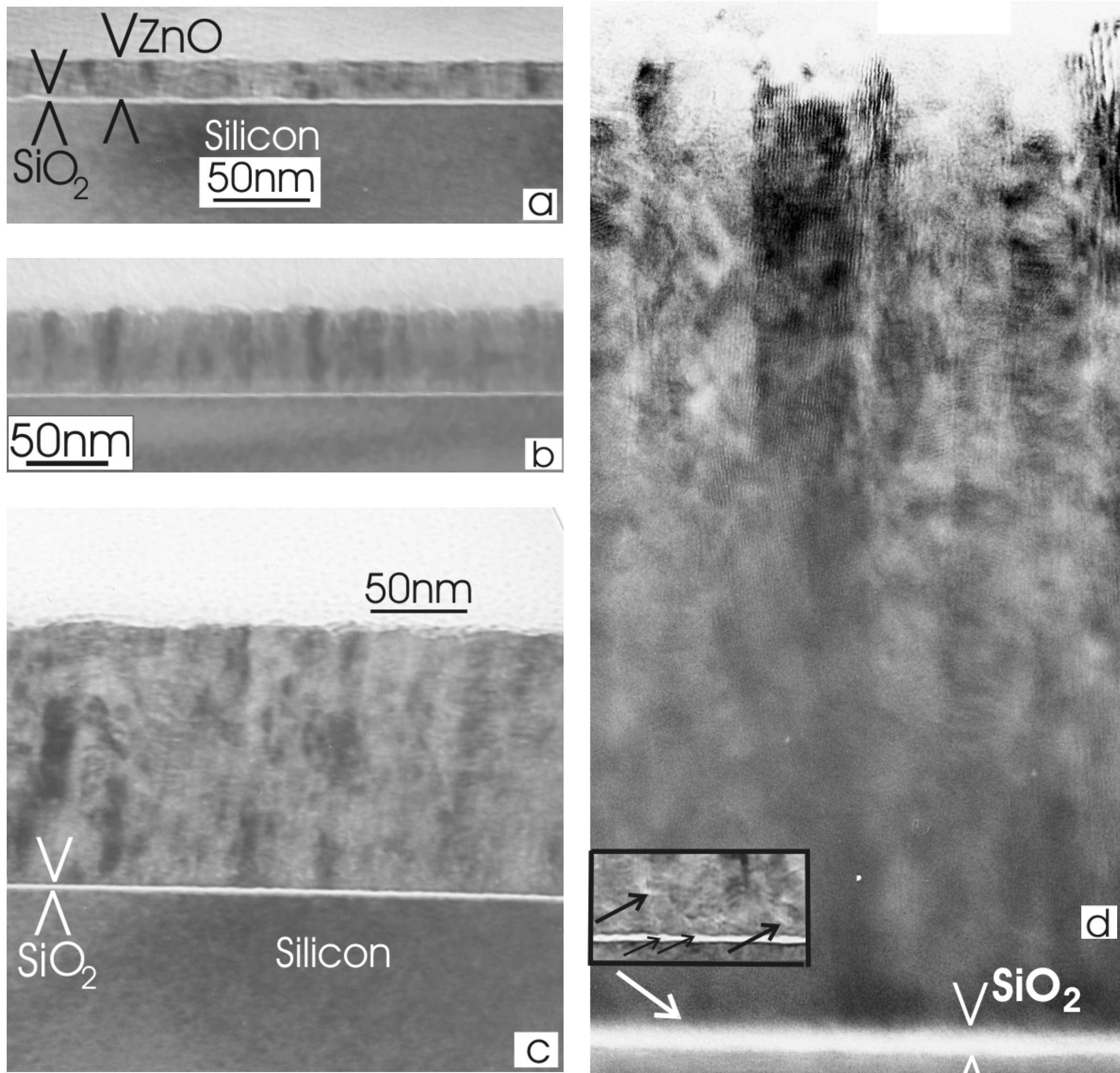

Figure 4.1.1 XTEM micrographs from ZnO films deposited at thickness: a) 19nm, b) 49nm, c) 132nm and d) 270nm

The thinnest films were found to consist of small grains, having a mean diameter of 20nm, denoted by the arrows in figure 4.1a. The surface of the films was extremely smooth, exhibiting roughness less than 1 nm, a behavior also confirmed by AFM measurements. As the film grows, a columnar morphology of the grains is evident, shown in figure 4.1.1b for the case of the 49nm film. Figure 4.1.1c, corresponding to the 132nm film, indicates that the columnar morphology is even more pronounced with increasing thickness as obviously shown also for the 270nm films presented in figure 4.1.1c. It was noticed that the interface between the Si substrate and ZnO film consist in an about 3nm thin layer of amorphous SiO_2 which can be attributed to wafer oxidation before deposition.
Moreover, the grains exhibit a strong preferential orientation, as indicated by the related diffraction pattern in figure 4.1.2.

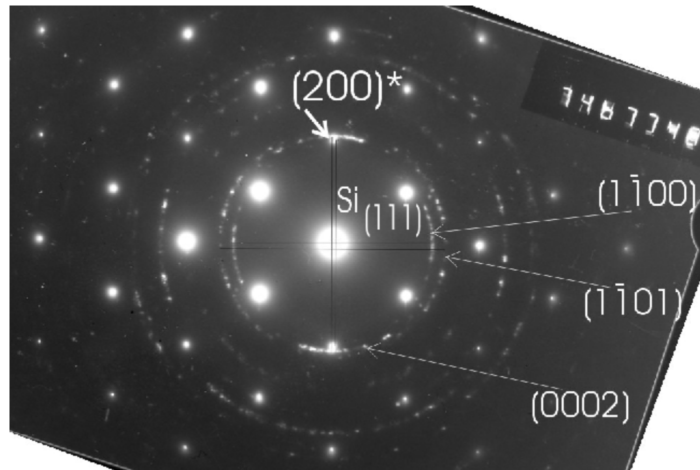

Figure 4.1.2 Diffraction pattern of the ZnO film with a thickness of 132nm and the silicon substrate. ZnO exhibits strong preferred orientation.

As visible in figure 4.1.2 the diffraction rings are degenerating to arcs, revealing the strong preferred orientation. The arcs are superimposed with the diffraction spots of the (110) section of the Si substrate. This configuration permits the indexing of the arcs with high accuracy, the film identified to have the hexagonal form of the ZnO. The most intensive arc is the (0002) one, which is close to the double diffracted (200)* silicon spot. This shows that the ZnO grains are grown preferentially along the [0001] direction, which is almost perpendicular to the plane of the Si wafer. Measuring the length of the (0002) diffraction arc in figure 4.1.2, it was found that the columnar grains deviate from the normal to the wafer by $\pm 8^o$. The mean width of the columnar grains remains the same as in the case of the lower thickness film, and it is of the order of 20 nm. The second most intense arc is the $(1\bar{1}00)$, which forms an angle of 90° with the (0002) arc. The columnar grains are extended from the SiO_2 interface up to the film surface. It was also noticed that near the SiO_2 surface, small grains were present not exhibiting the columnar structure. The columnar structure is also evident in the dark field (DF) micrographs, taken from the (0002) and the $(1\bar{1}00)$ arcs, as shown in figure 4.1.3a and 4.3b, respectively.

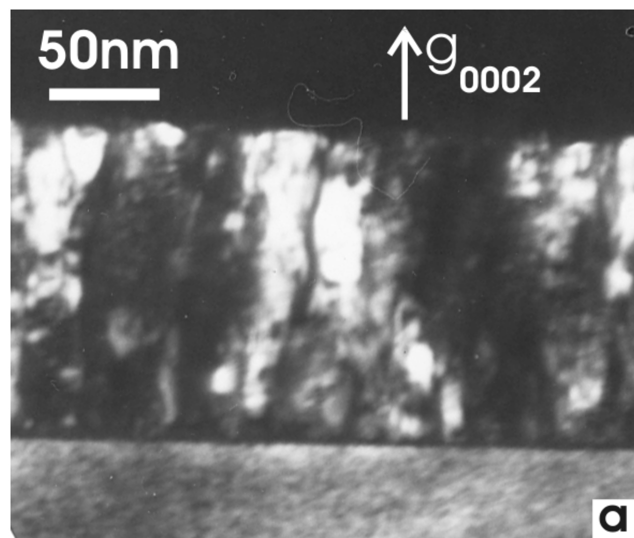

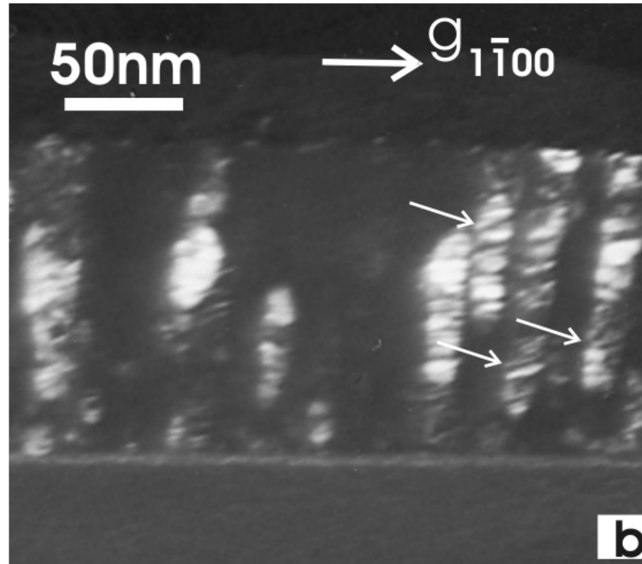

Figure 4.1.3 Dark field micrograph taken: a) from the (0002) arc, b) from the $(1\bar{1}00)$ ***arc.***

Under the $(1\bar{1}00)$ diffraction condition, bands of ingrain planar defects are evident, denoted by arrows in figure 4.1.3b. These planar defects are perpendicular to the long axis of the columnar grains. The burgers vector $\bar{b}$ of these planar defects must be component parallel to the $[1\bar{1}00]$ direction. This is supported by the fact that these defects are invisible in the DF micrographs taken with the (0002) arc, perpendicular to the $[1\bar{1}00]$ direction, satisfying the invisibility criterion $\bar{b}.\bar{g} = 0$, where $\bar{g}$ is the vector of the reciprocal lattice for the operating reflection. Therefore, since the defects are invisible for the reflection $\bar{g}_{(0002)}$, as is evident from the DF micrograph of figure 4.1.3a, the burgers vector $\bar{b}$ must be perpendicular to it, namely parallel to the basal plane. Additional information about these defects will be presented in the high resolution XTEM (HRXTEM) observations. The overall morphology of the 270nm thick film was shown in figure 4.1.1d. It is evident that long columnar grains derive from the ZnO/SiO_2 interface. The roughness at the surface increases slightly as the film thickness increase, remaining always below 2.5nm, a value in good agreement with the AFM measurements. Small voids are observed at the ZnO/SiO_2 interface, also between the grains, denoted by arrows in the inset of Fig.1d. The same film was also examined by HRTEM in an effort to understand the growth mechanism of ZnO thin films and the strong thickness effects on physical properties of the film noticed in earlier work. As shown in the HRXTEM micrograph in figure 4.1.4, large grains along the c-axis, that is almost perpendicular to the interface, are observed.

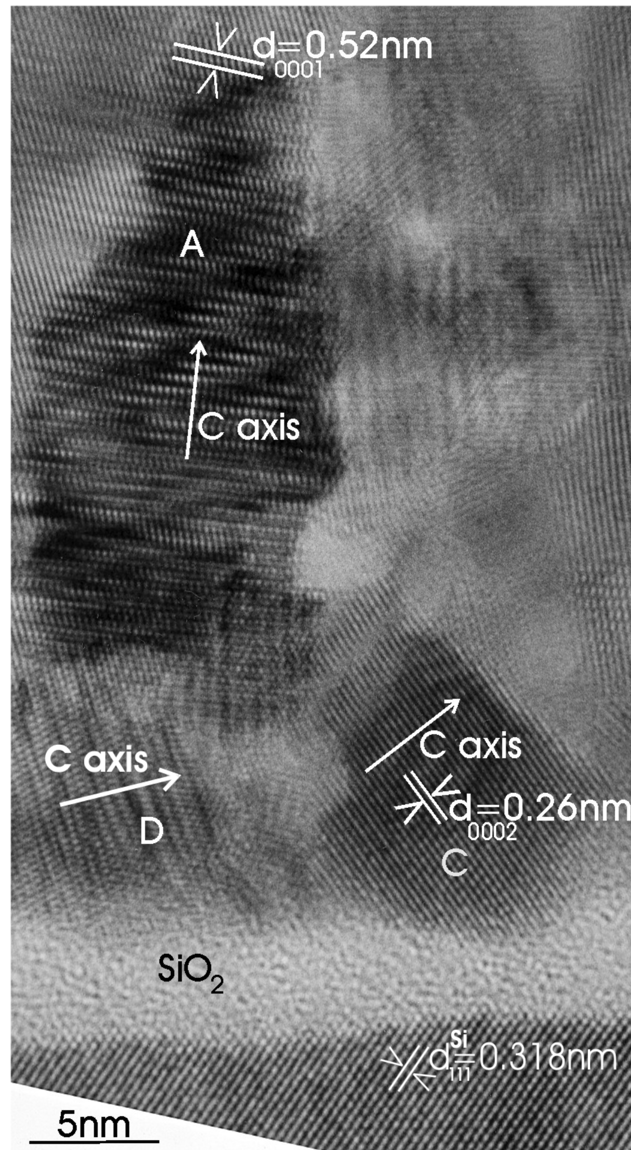

Figure 4.1.4 HRXTEM micrograph from the ZnO/SiO$_2$ interface for a ZnO film with a thickness of 270nm, revealing the early stage of growth.

The periodicity of the lattice planes was determined with high precision by comparing their spacing with the (111) d-lattice spacing of the Si substrate, which is 0.318nm. Lattice planes of the (0002) type with d_{0002} = 0.260 nm were determined. Most of the grains had already a columnar form from the early stage of growth along the c-axis, which exhibits the fastest rate of growth, almost perpendicular to the interface, as shown in Fig.4. In between, there were smaller grains, denoted by the letters C and D, having their c-axis almost parallel to the interface, which prevent their growth close to the interface. Therefore the columnar growth is the result of a growth – death competition between the grains. Significant distortion of the lattice planes is frequently observed due to internal stress, as shown in figure 4.1.5.

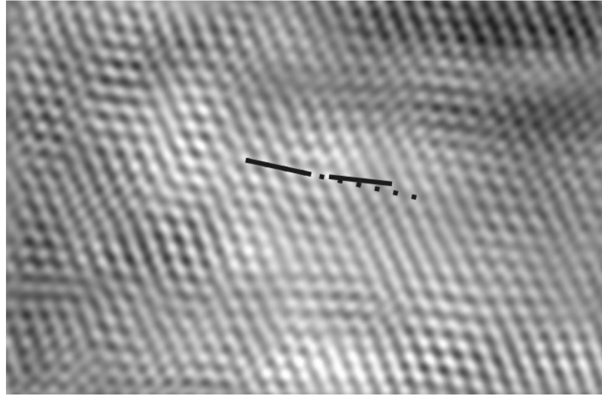

Figure 4.1.5 Lattice plane of the ZnO grains significantly distorted.

Planar defects perpendicular to the c-axis, like these shown in figure 4.1.3b, were also observed, related to insertion of extra planes, suggesting intrinsic Stacking Faults (SFs), as shown in figure 4.1.6.

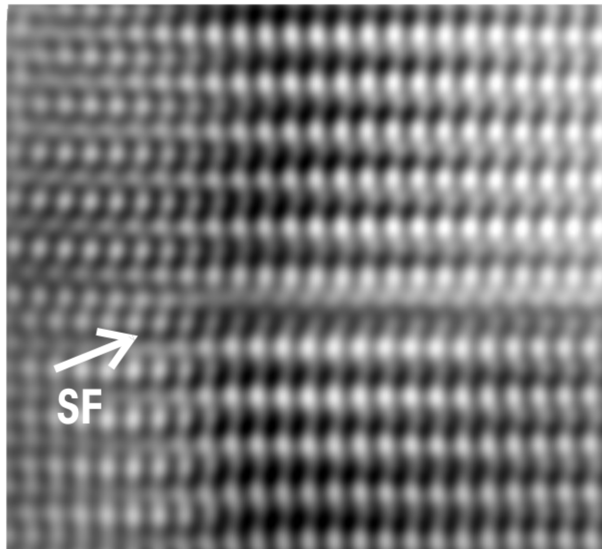

Figure 4.1.6 Intrinsic Stacking Faults (SF) frequently formed in the ZnO grains

The above insight into the columnar growth and the morphology of our films is very important for their electrical and mechanical properties, which could be not fully explained before this structural analysis. As a conclusion, since both, surface roughness and the observed average bulk grain size of about 20nm remain unaffected by the film thickness, this should reflect on all structural related film properties (for films grown at RT).

XRD characterization

XRD studies have shown that all ZnO films grown by DC magnetron sputtering are polycrystalline with tendency of texturing and preferential orientation [002] (along c axis) of the ZnO wurzite crystalline structure. Some thicker films showed also contribution from crystallites with the [004] orientation of the same structure. An improvement was noticed in crystallinity with increasing thickness. Figure 4.1.7 shows typical evolution of X-ray diffractograms with increasing thickness for ZnO

grown by DC magnetron sputtering from 99.999% pure Zn metallic target under deposition parameters: 1Pa pressure, oxygen concentration in the plasma 100%, flow rate 10sccm and substrate temperature 27°C (RT).

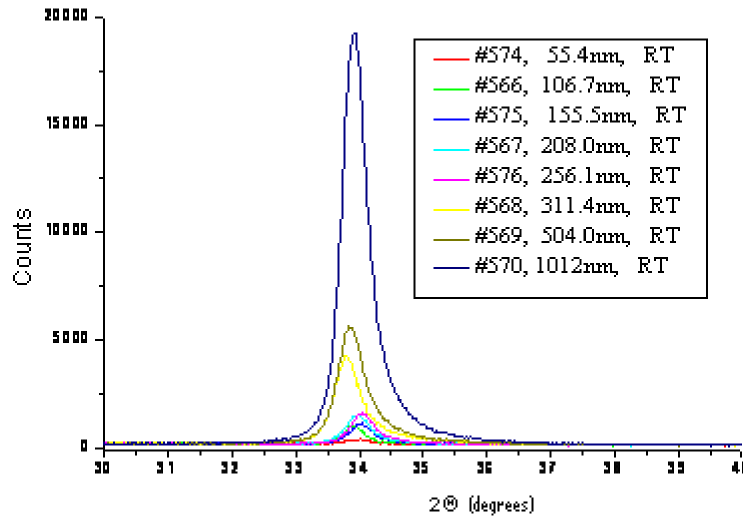

Figure 4.1.7 Typical evolutions of X-ray diffractograms with increasing thickness for ZnO grown by DC magnetron sputtering.

From figure 4.1.7 it is obvious that the larger the film thickness the better the contribution form [002] crystalline orientation of wurzite structure. Estimation of full with at half maximum (FWHM) for this peak and estimation of mean value of bulk crystallite size using Scherrer formula presented in the experimental chapter of this thesis are presented in figure 4.1.8.

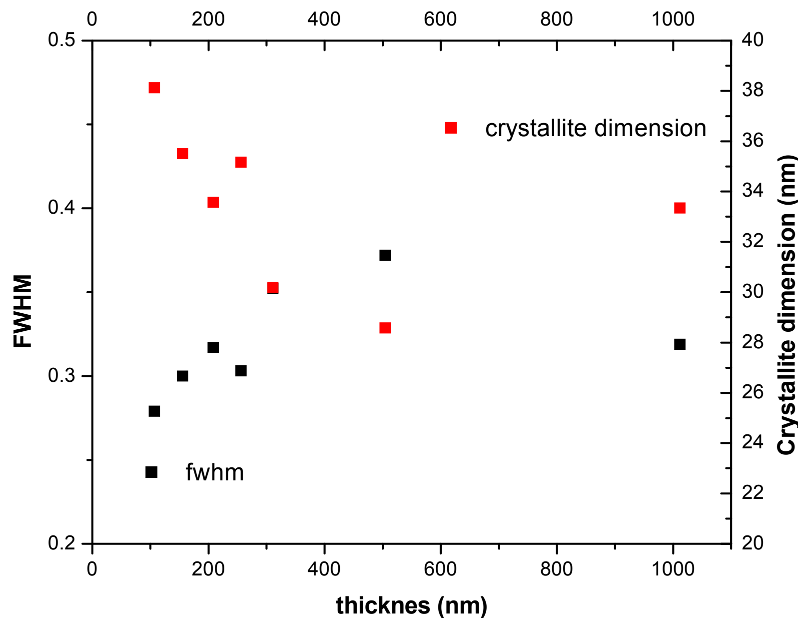

Figure 4.1.8 Full width at half maximum (FWHM) for [002] peak in XRD's and estimation of mean value of bulk crystallite size from Scherrer formula as a function of film thickness.

It is noticed that for very thin films when the thickness is increasing a decrease of mean crystallite size occurs after the thickness reaches 200nm the opposite is happening. The same behavior was noticed for ZnO films grown by PLD and is

make the subject of future studies being in contradiction with existing growth theory and models.

Heating during deposition seems to improve the films crystallinity, as can be noticed in figures 4.9 a, b which present typical evolution of X-ray diffractograms with increasing substrate temperature during growth for different thicknesses and at constant thickness.

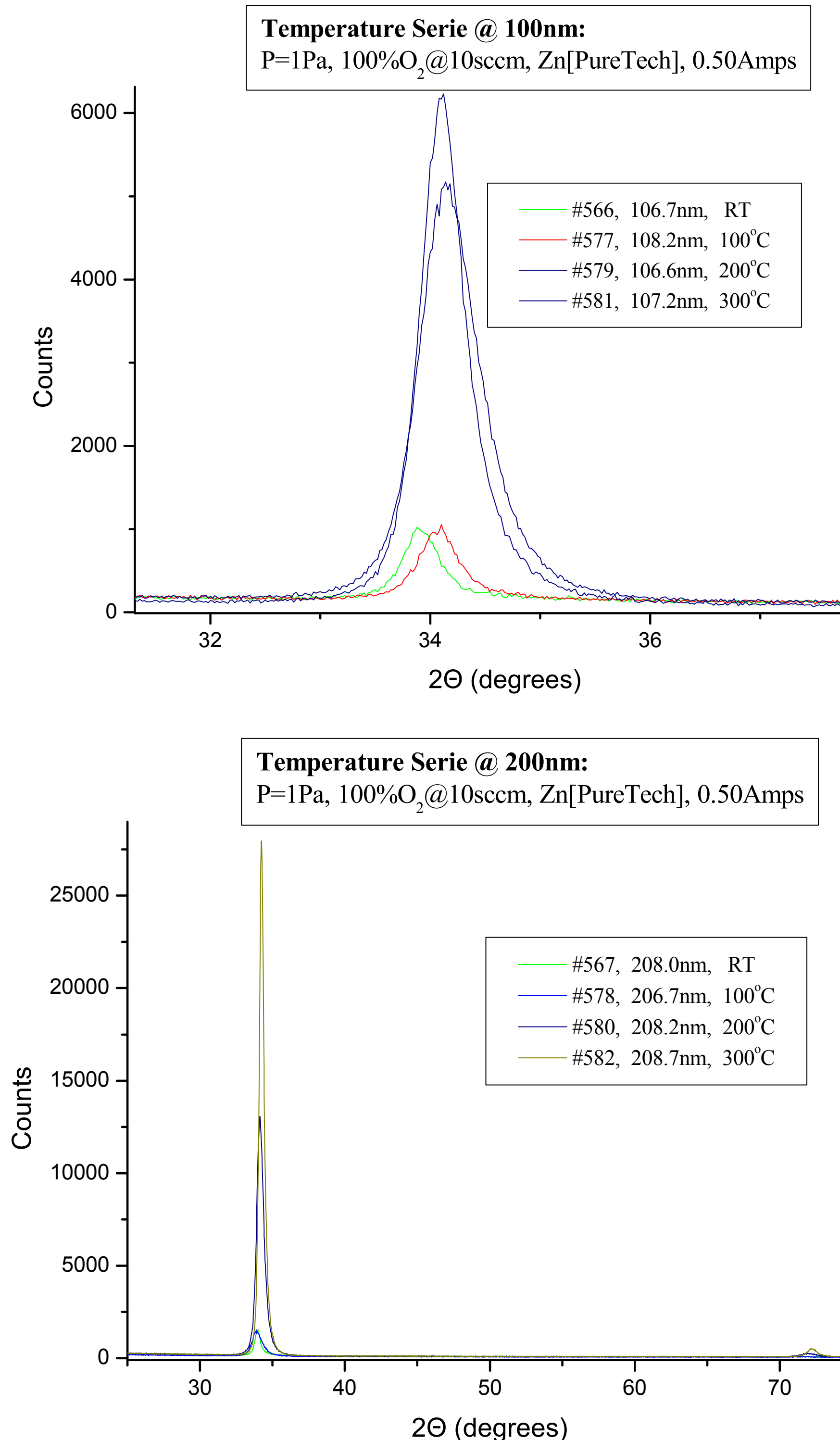

Figure 4.1.9 Typical evolution of X-ray diffractograms with increasing substrate temperature during growth for two different thicknesses a 100nm and b 200nm

Decreasing of the films crystallinity was also observed with decreasing sputtering pressure, due to an increase of growth rate which makes the deposition time shorter and does not allow the ZnO to form a perfect lattice, as can be seen in figure 4.1.10.

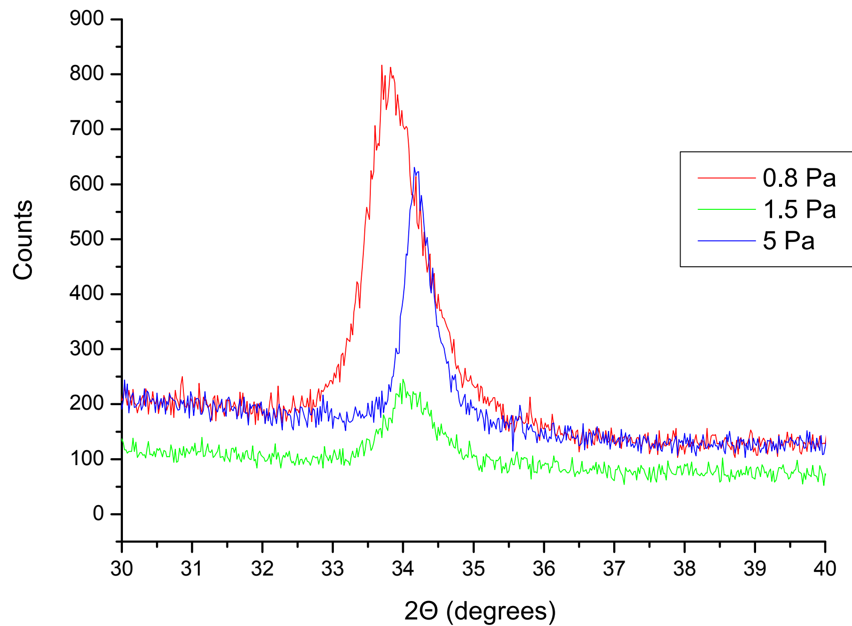

Figure 4.1.10 Typical evolution of X-ray diffractograms with increasing total pressure during growth

The crystallinity was found improved with decreasing oxygen content. Typical evolution of X-ray diffractograms with decreasing the oxygen partial pressure in the plasma content during deposition is presented in the figure 4.1.11 a and b.

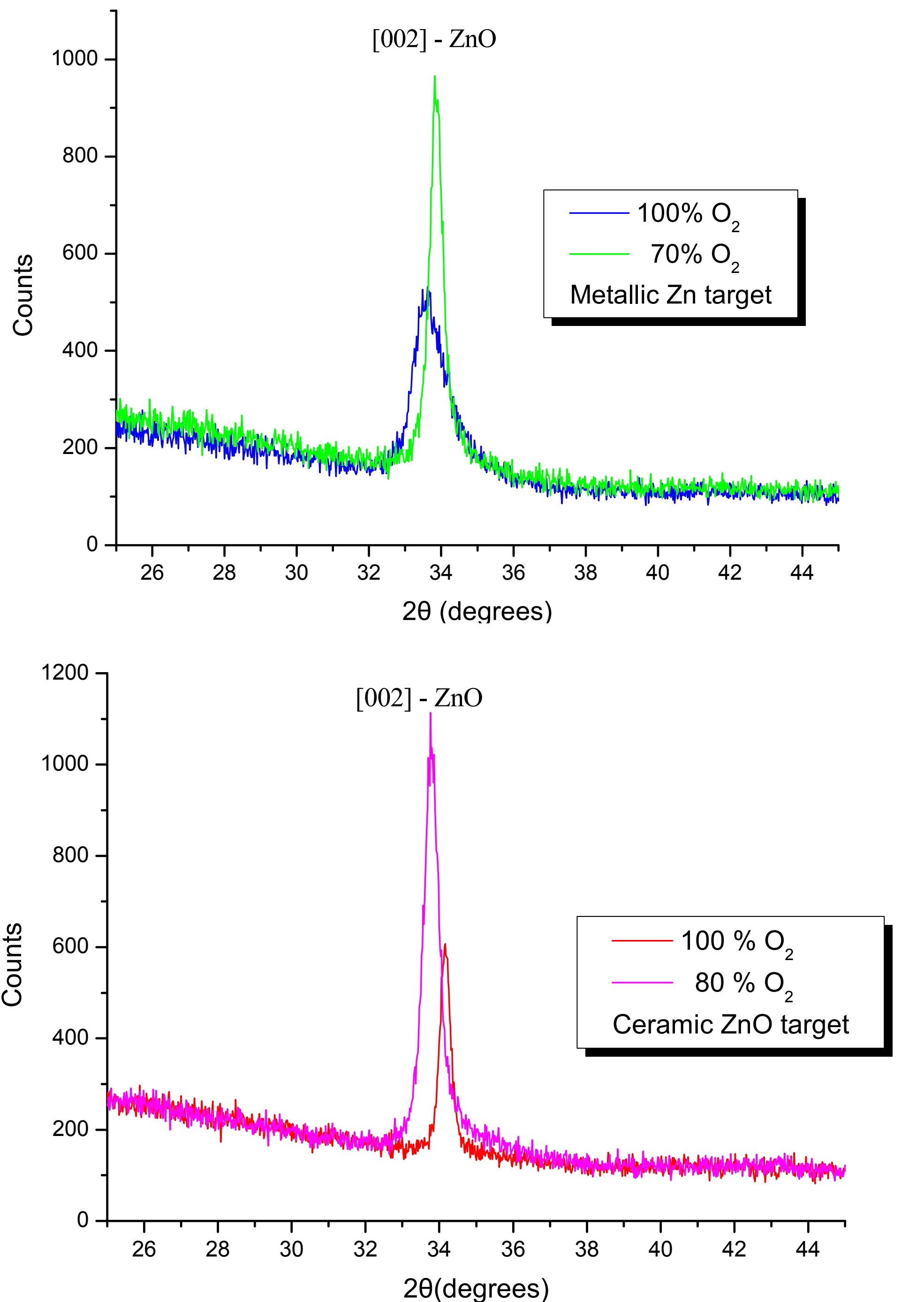

Figure 4.1.11 Typical evolution of X-ray diffractograms with increasing the oxygen partial pressure during growth for films grown from a metallic target, b ceramic target.

Similar behavior was recorded for both films grown from metallic Zn and ceramic ZnO targets under similar growth conditions, that is, an improved crystallinity and a clear tendency of peak narrowing as the oxygen contend was decreasing.

From the XRD diffractograms, the variation of the lattice constant as a function of the film thickness and the substrate temperature during growth was studied. As shown in figure 4.1.12 a and b, $c_{lattice}$ for all films has a value smaller than that of

the unstressed ZnO (powder), c_{powder} = 5.408Å. For very thin films grown at low temperatures (<200˚C), as thickness increases, the c value seem to decrease. At thickness of about 250nm, the lattice constant values are getting larger, having the same decreasing trend as thickness enlarges further. Analyzing $c_{lattice}$ variation with temperature, from RT up to 300˚C and different thicknesses (see figure 4.1.12b), it was found out that temperature induces a decrease of $c_{lattice}$ for all studied thickness series.

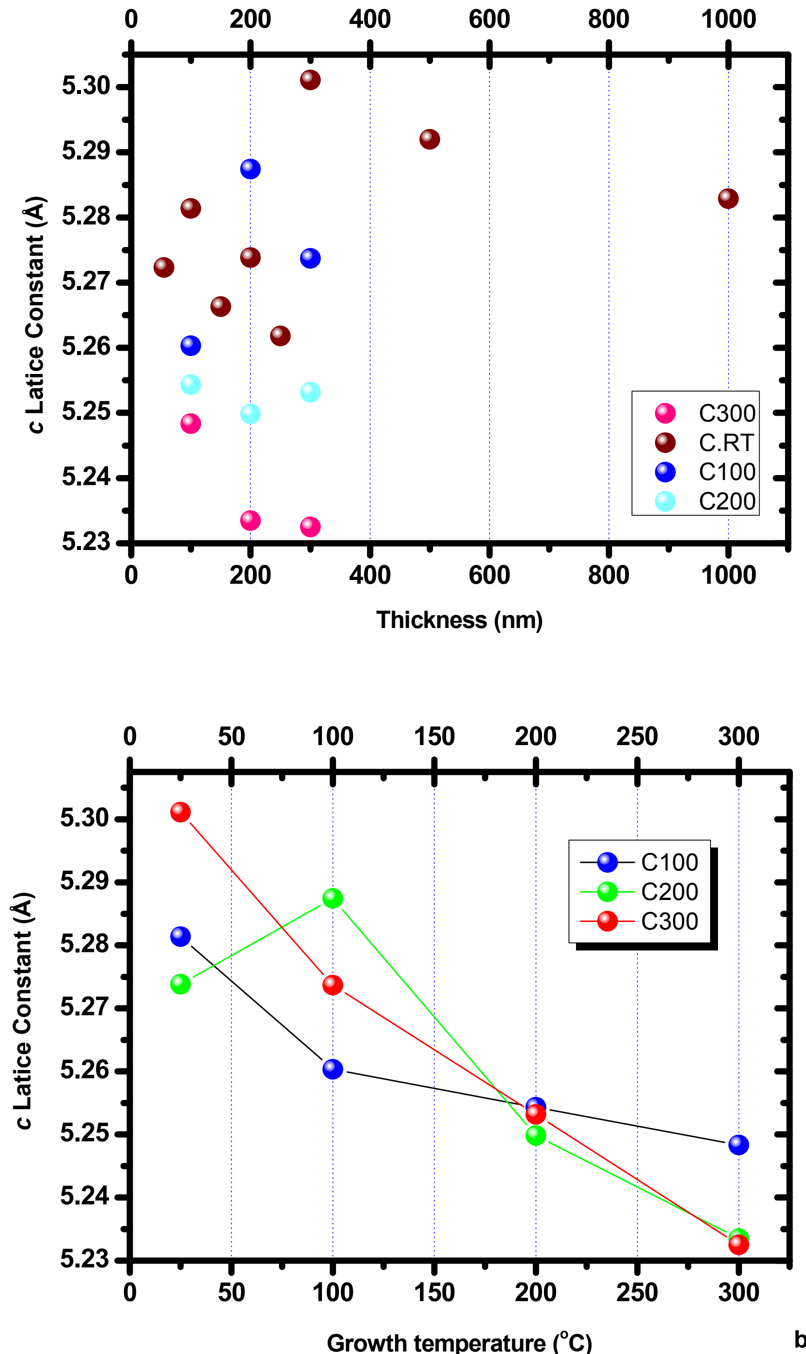

Figure 4.1.12 c-lattice constant variation with a film thickness and b growth temperature.

Finally, the residual stress in the plane of the film (supposed uniform bi-axial stress) were determined using the following two procedures [1],[2]:

A) $\sigma_{film} = [E_{film} (2\theta-2\theta_0)]/[4v_{film} \, tg(\theta_0)]$ (1)

where $2\theta_0 = 34.42^o$ is the diffraction angle of the bulk ZnO (002) peak, and 2θ is the measured diffraction angle for the sample. In these calculations it was considered a Young's modulus of E_{film} = 170 GPa and Poisson's ratio of v_{film} = 0.36.

B) $\sigma_{film} = [C_{13}-C_{33}(C_{11}+C_{12})/2C_{13}][(c_{film}-c_{powder})/c_{powder}]$ (2)

where the elastic stiffness constants of ZnO were taken as following:

C_{11}=208.8 GPa, C_{12}=119.7 GPa, C_{13}=104.2 GPa, C_{33}=213.8 GPa.

As lattice constant of the unstressed ZnO (powder was taken c_{powder} = 5.408Å, while, the lattice constants of stressed films, c_{film}, were derived from the above XRD spectra. The results of this estimation are shown in figure 4.1.13 a and b.

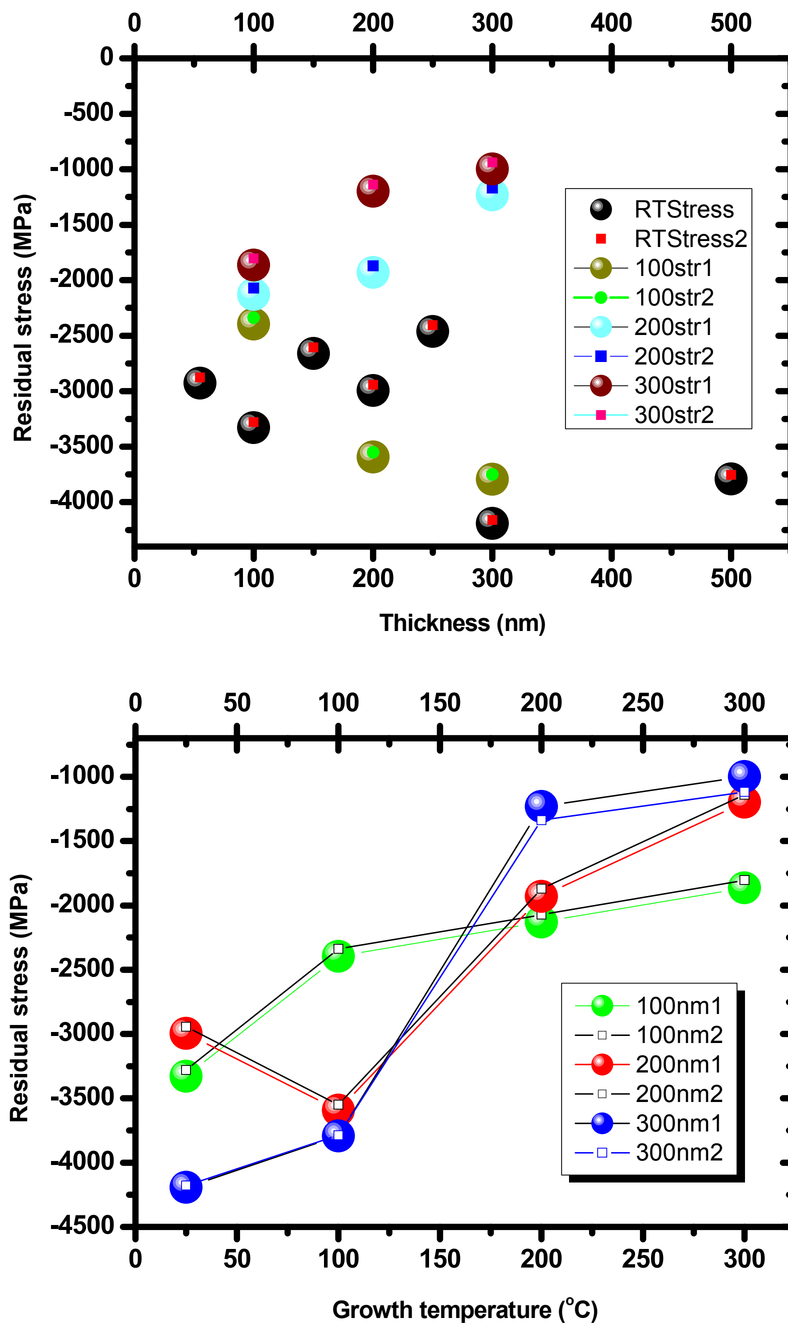

Figure 4.1.13 residual stress variation with a film thickness and b growth temperature for different ZnO thin films series.

The estimated values prove that ZnO thin films grown by DC magnetron sputtering are under compressive residual stress. The values are about three orders of magnitude smaller than previously reported in literature for similar growth method [2].

References:

1 A. Cimpoiasu, N. M. van der Pers, Th. H. de Keyser, A. Venema, M. J. Vellekoop, “Stress control of piezoelectric ZnO films on silicon substrates”, Smart Materials and Structures, Volume 5, Issue 6, pp. 744-750 (1996)

2 S. Maniv, W. D. Westwood, E. Colombini, “Pressure and angle of incidence effects in reactive planar magnetron sputtered ZnO layers”, Journal of Vacuum Science and Technology, 20 (2), pp. 162-170 (1982)

4.2 AFM Characterization: Effect of growth parameters on the film surface morphology

Thickness effect

AFM characterization of ZnO thin films with different thickness deposited by DC magnetron sputtering onto Corning 1737F glass substrates surfaces revealed a granular, polycrystalline morphology. The films were grown from Zn metallic target at RT, in 100% O_2 atmosphere, total sputtering pressure 0.01 mbar, the thickness varying from 100 nm to 1012 nm. As shown in the following 3D 2x2µm scan size AFM images included figure 4.2.1, the films surface is evolving from small not well formed grains, with a z-range smaller than 5nm, to well formed large grains having a z-range of about 40nm, at a thickness of 1µm. It is also clear that as the thickness becomes larger than 200nm, the grains start agglomerating.

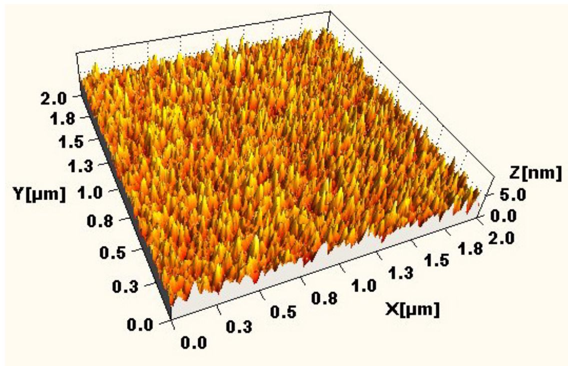

100nm

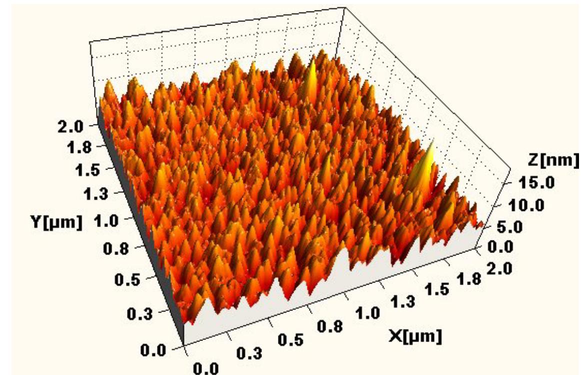

155nm

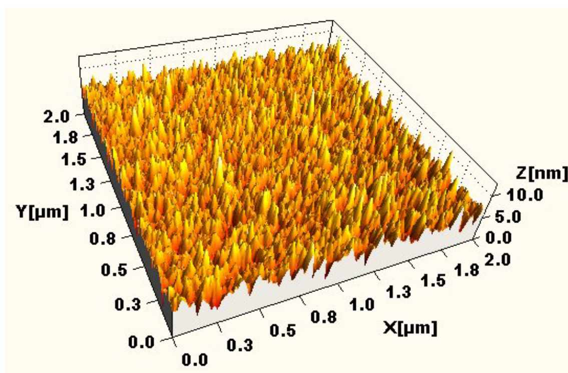

208 nm

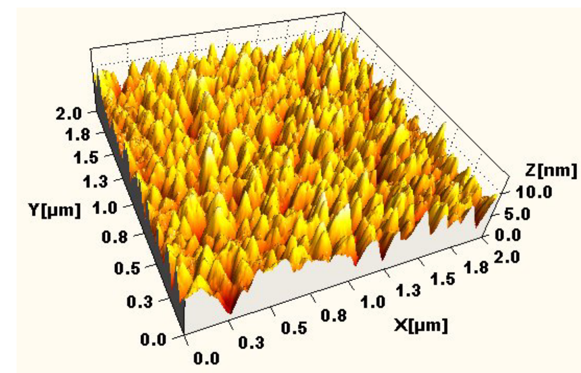

256 nm

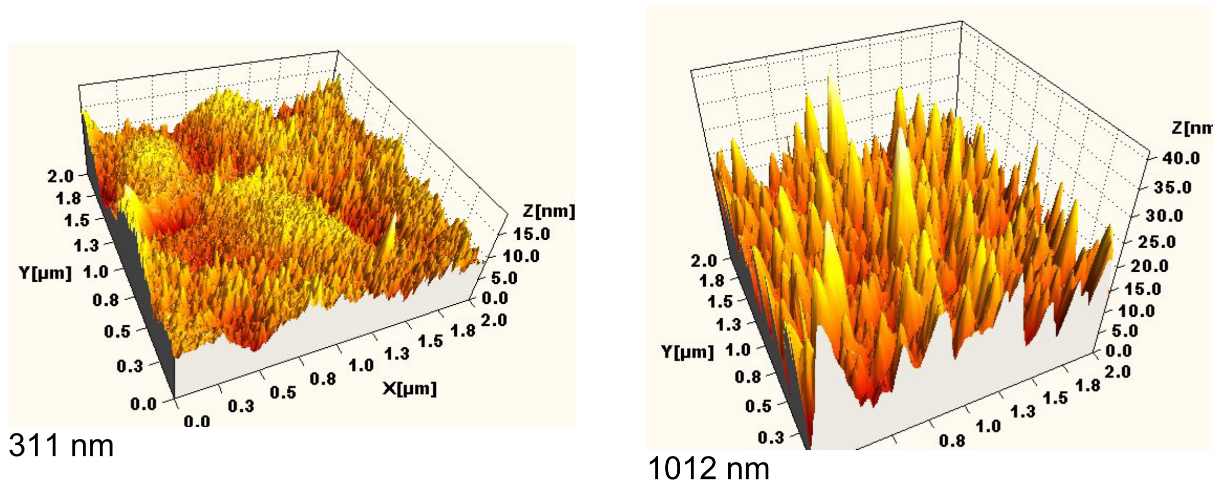

Figure 4.2.1 Thickness effect on surface morphology evolution for ZnO films grown by DC magnetron sputtering.

The evolution of the surface parameters with thickness was also studied. An analytical description of all parameters and their dependence on all growth conditions will be the subject of a later chapter. For this chapter, only the variations of RMS, SDR and grain radius with thickness will be presented.

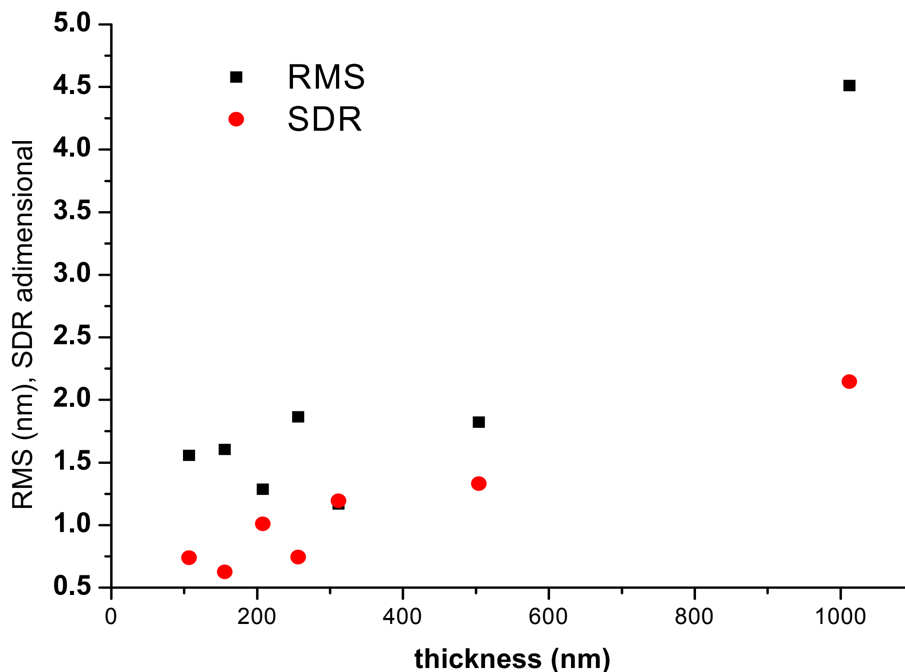

Figure 4.2.2 Thickness effect on RMS and SDR surface parameters evolution for ZnO films grown by DC magnetron sputtering.

From figure 4.2.2, an increasing trend of both RMS and SDR with increasing film thickness is obvious. Moreover, the evolution of grain radius with increasing thickness is shown bellow (figure 4.2.3)

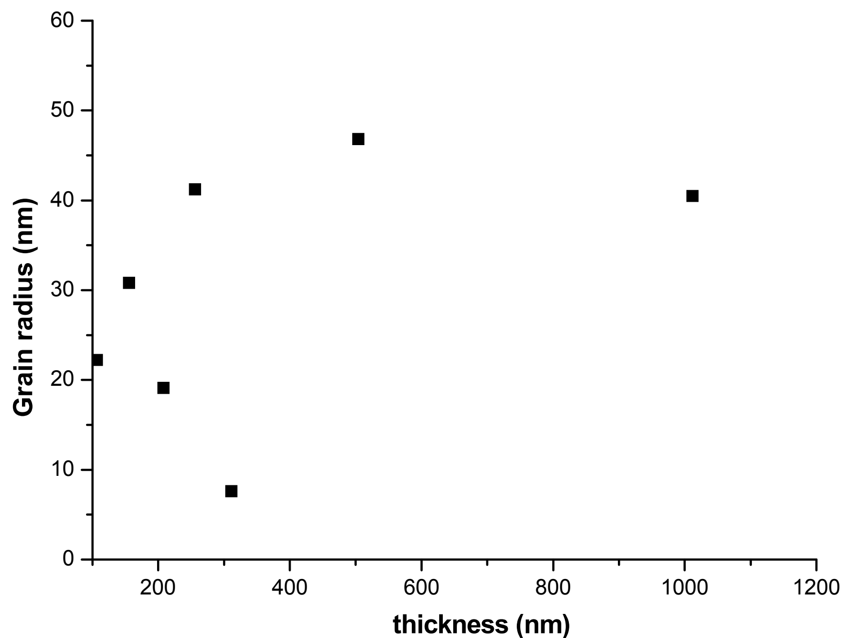

***Figure 4.2.3 Thickness effect on surface grain mean radius for ZnO films grown by DC magnetron sputtering*.**

As can be observed, the mean grain radius does not depend monotonically on thickness but it follows a behaviour also indicated in the AFM images. This variation apparently is not affecting the increase of RMS and SDR. The decrease of crystallite dimensions in the first stage of growth was also noticed from XRD characterization for ZnO thin films grown by both DC magnetron sputtering and PLD.

Temperature effect

Surface evolution with substrate temperature during growth was also studied by AFM. Figure 4.2.4 presents 2d images of ZnO thin films grown by DC magnetron sputtering in 100% O_2 environment, total pressure of 0.01mbar, two thicknesses of 100 and 200nm respectively and three temperatures, RT, 100 ˚C and 200 ˚C

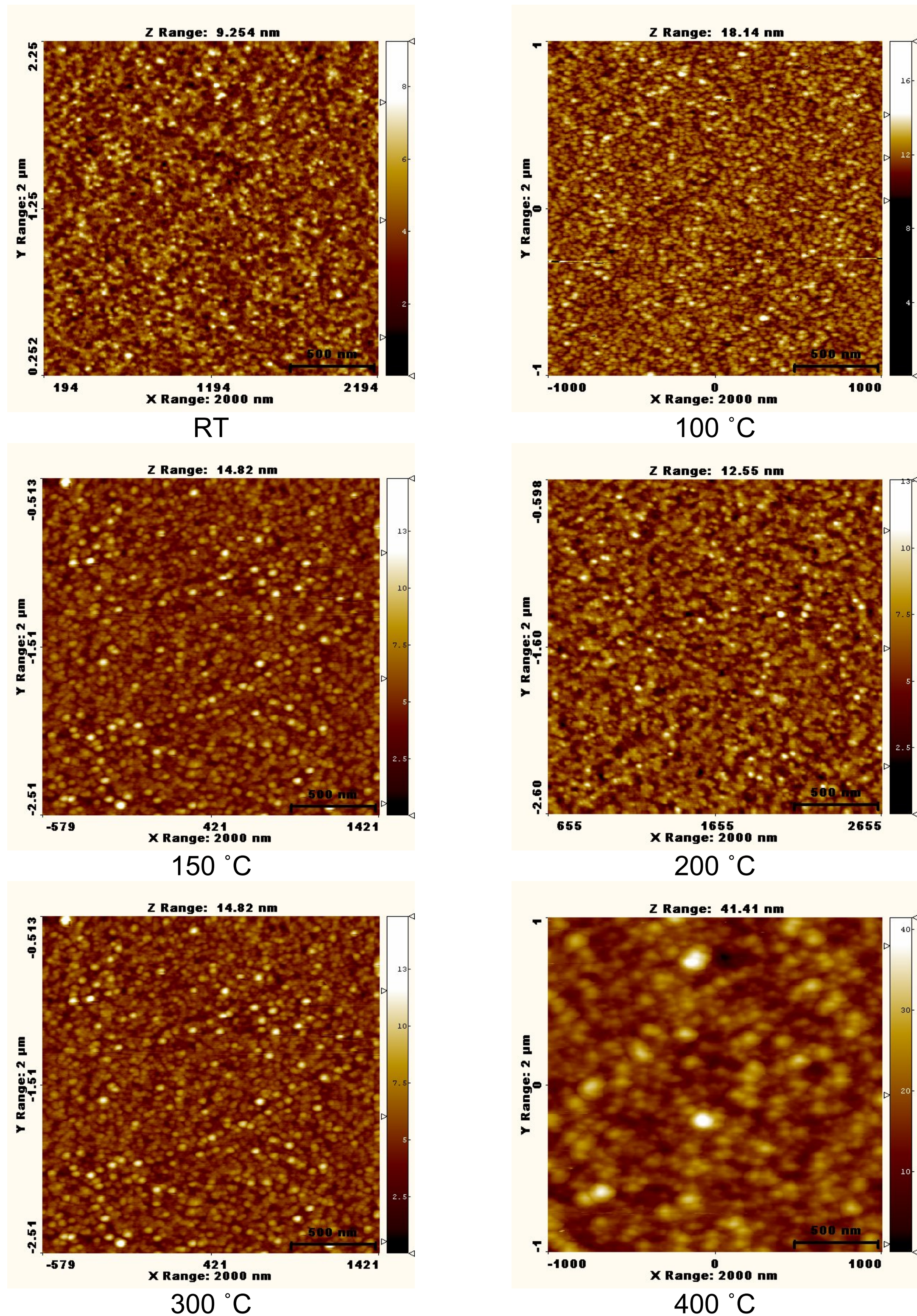

***Figure 4.2.4 Growth temperature effect on surface morphology evolution for ZnO films grown by DC magnetron sputtering*.**

As the substrate temperature increases, the surface grain size tends to increase and become more homogeneously dimensional as visible from figure 4.2.4. The surface RMS and SDR slightly decreases. This behavior is clearly shown in figure 4.2.5, for the 100nm thickness thin films.

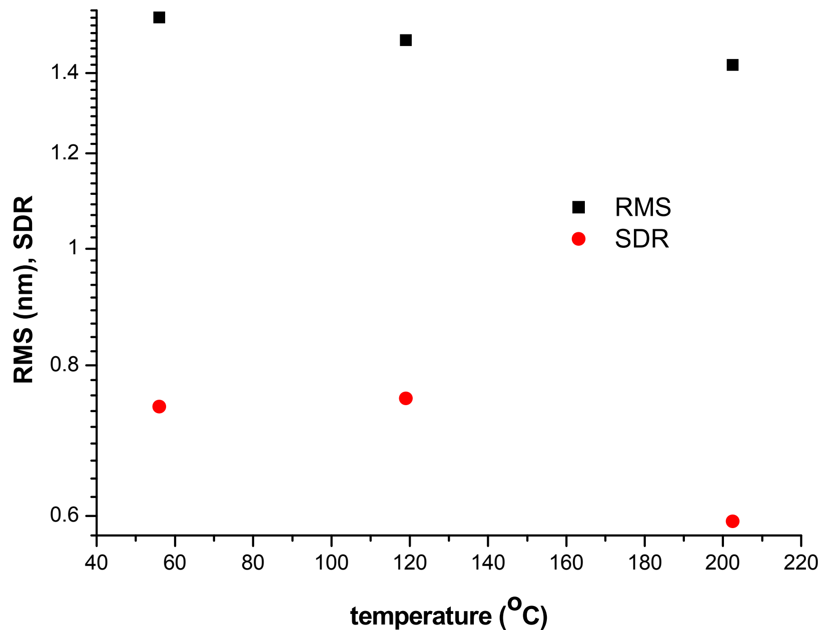

Figure 4.2.5 Substrate temperature effect on RMS and SDR surface parameters evolution for ZnO films grown by DC magnetron sputtering.

Total pressure and growth rate effects

Changing the total pressure during the deposition, its effect on the sample topology was examined and shown in figure 4.2.6, for films grown at 0.008, 0.03, 0.05 mbar, by DC magnetron sputtering from metallic Zn target in 100%O_2 atmosphere at RT, the films having a thickness of about 100nm. A clear structuring of the surface appears as the pressure increases. Regarding grain radius, this increases almost linearly with increasing pressure, as shown in figure 4.2.7. Finally, RMS and SDR increase too with pressure as shown in figure 4.2.8. These dependences can be associated with the decrease of the growth rate as the pressure increases. The slower the growth processes, the larger the time for the formation of the crystalline grains and the improvement of the surface quality.

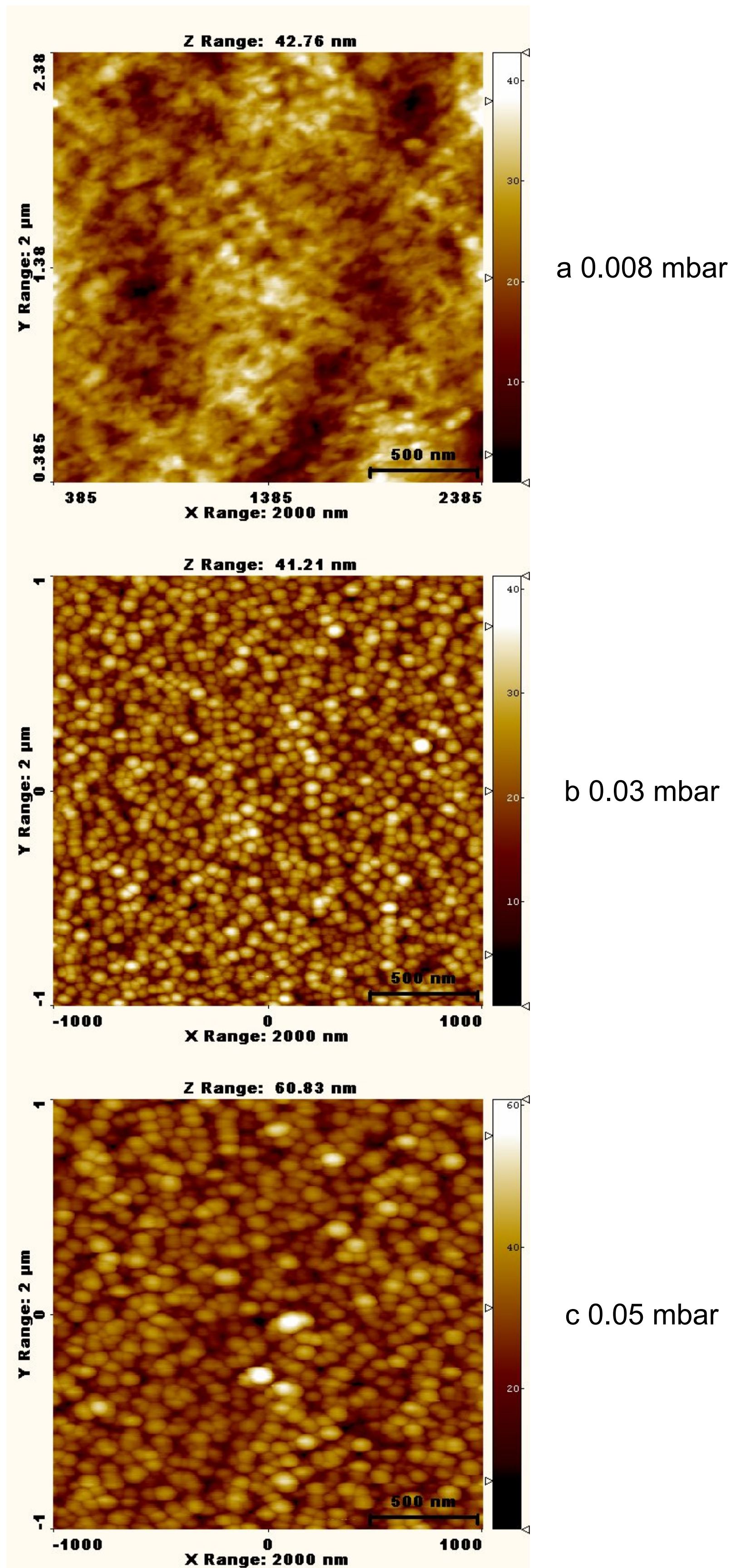

Figure 4.2.6 Total pressure effect on surface morphology evolution for ZnO films grown by DC magnetron sputtering.

From figure 4.2.6 it is obvious the strong effect of total pressure during growth on film's surface morphology. As the pressure increases the surface structuring to homogeneous and well formed grains it is evident.

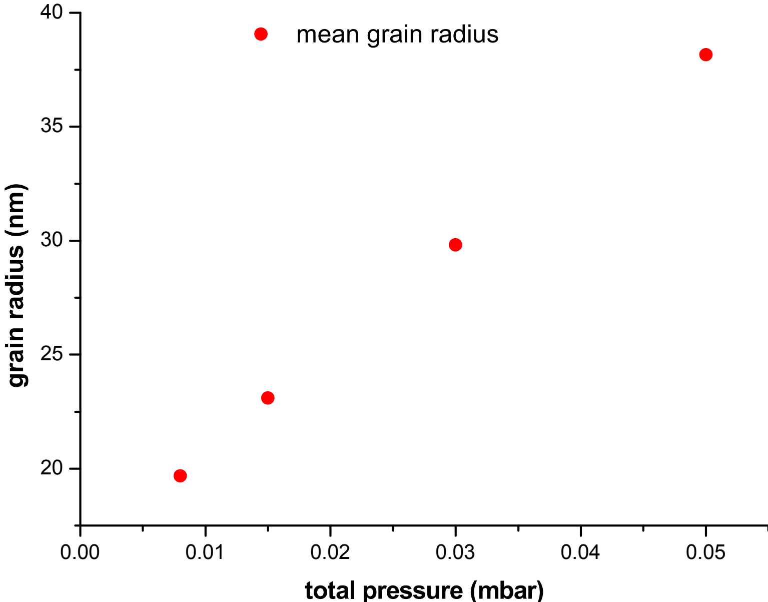

***Figure 4.2.7 Total pressure effect on surface grain mean radius for ZnO films grown by DC magnetron sputtering*.**

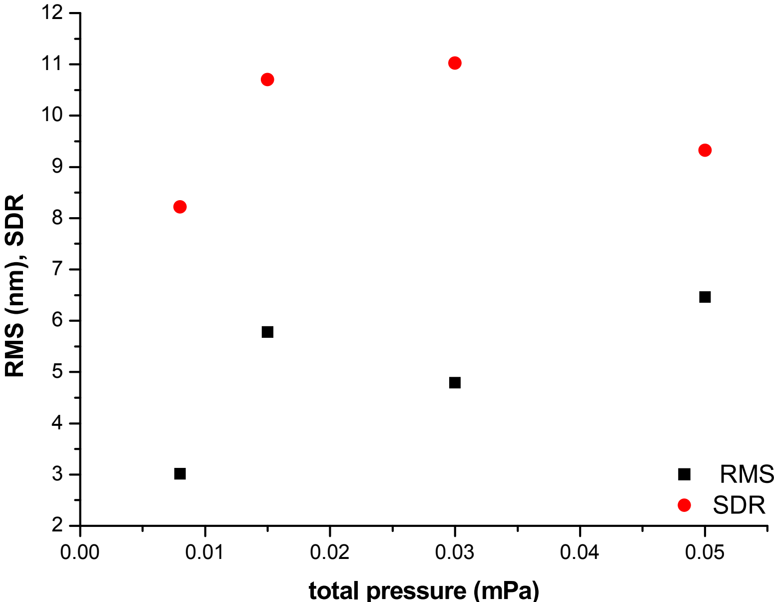

***Figure 4.2.8 Total pressure effect on RMS and SDR surface parameters for ZnO films grown by DC magnetron sputtering*.**

Partial Pressure of O_2 effects

Finally, the effect of O_2 partial pressure on the surface evolution was studied for ZnO thin films grown by DC magnetrons sputtering. The deposition parameters were: total pressure 8x10^{-3} mbar, substrate temperature 27°C (RT) and film thickness of about 100nm, while, the depositions were done for two different plasma current settings (I=0.44A and I=0.25A). AFM characterization of the films revealed that grain size increases as the O_2 partial pressure decreases for both I=0.44A and I=0.25A. In contrast, the roughness increases in the case of higher plasma current I=0.44A, not presenting a clear variation in the case of lower plasma current I=0.25A, as shown in the tables. The plasma current is correlated with the growth rate in the sense that high plasma current corresponds to high deposition rate. Also, the growth rate increases when the O_2 concentration decreases. Some representative results are presented in the following tables 4.2.1 and 4.2.2.

Table 4.2.1 I=0.44A

O_2 Conc (%)	Growth Rate (nm/min)	Grain Radius $\pm$ 0.01 (nm)	RMS $\pm$ 0.01 (nm)
100	21.0	37.47	1.82
73	22.2	24.12	1.33
60	24.0	26.69	2.32
50	25.2	31.37	3.43

Table 4.2.2 I=0.25A

O_2Conc (%)	Growth Rate (nm/min)	Grain Radius $\pm$ 0.01 (nm)	RMS $\pm$ 0.01 (nm)
100	10.8	49.99	2.71
73	12.6	23.18	5.24
60	13.8	34.64	1.74
50	14.4	36.37	2.86

AFM images for films grown at I=44A are shown in the images of figure 4.2.9. The surface grain size and roughness decrease as the oxygen partial pressure decreases.

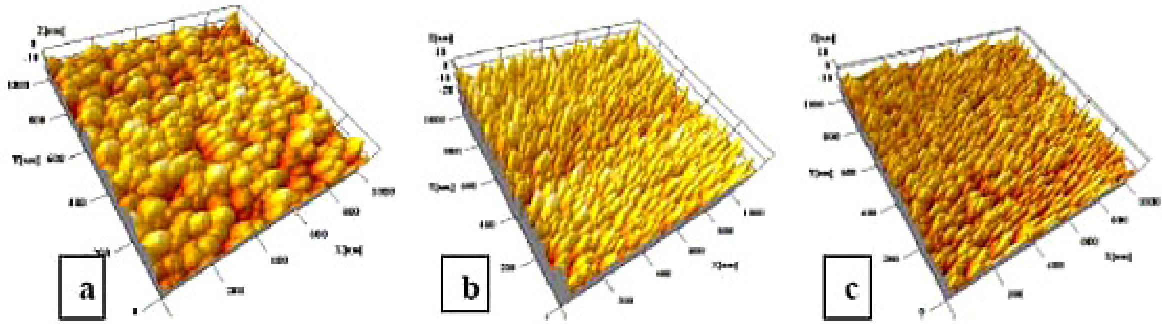

Figure 4.2.9 Total pressure effect on surface morphology evolution for ZnO films grown by DC magnetron sputtering.

4.3 Optical properties

The optical transmittance of the films was measured using the Varian Cary50 UV/Visible spectrophotometer with the Varian data analysis tools, a procedure similar to that for the case of In_2O_{3-x} thin films. The as-deposited ZnO thin films were found to be highly transparent in the visible region with an average transmittance of 80-90%, the absorption edge in the UV region depending on film growth conditions.

The following figures present the UV-Vis optical transmittance as a function of thickness (figure 4.3.1a), growth temperature (figure 4.3.1b), total pressure (figure 4.3.1c) and oxygen content in the plasma (figure 4.3.1d). As can be seen, the mean optical transmittance in the visible region decreases slightly as thickness increases and it is improved at higher total pressure.

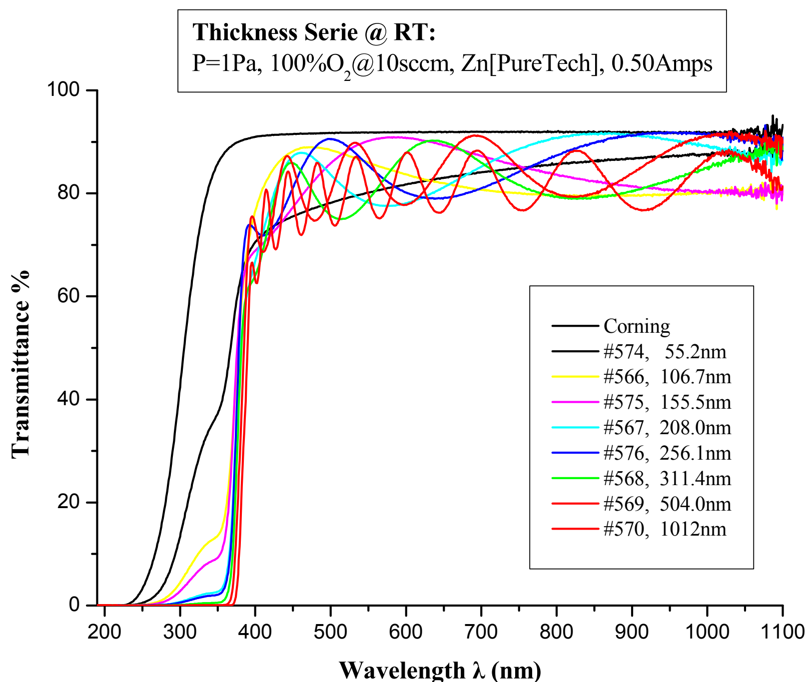

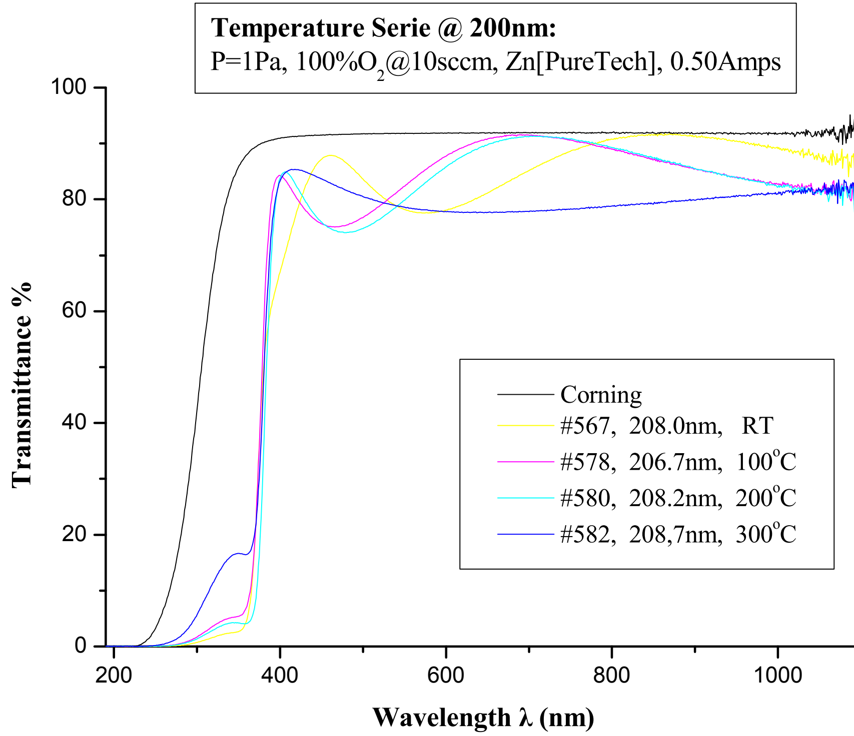

b

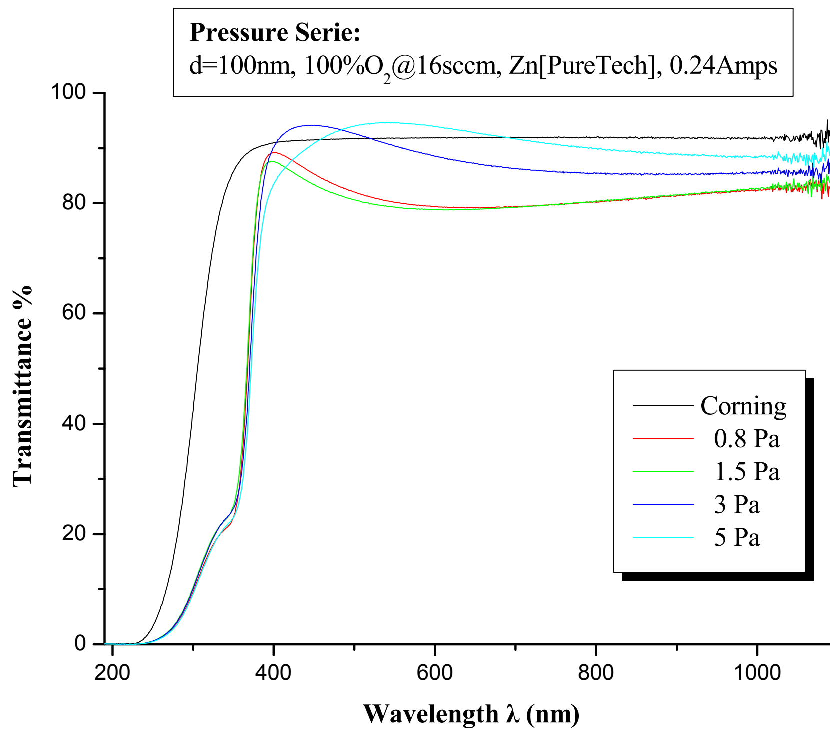

c

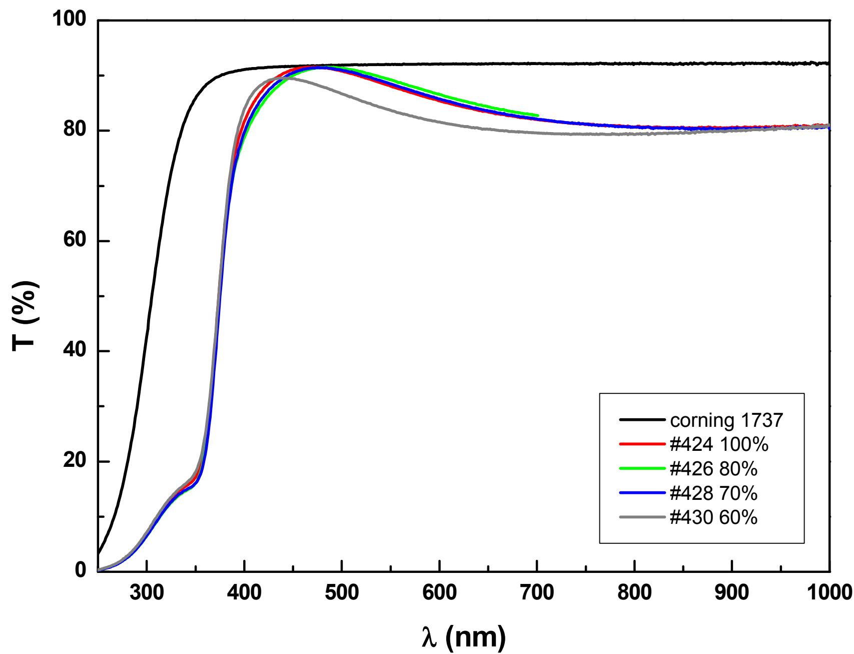

d

Figure 4.3.1 UV-Vis optical transmittance as a function of a thickness, b growth temperature, c total pressure and d oxygen content in the plasma.

For the above UV-vis transmittance spectra, the optical energy gap E_g was derived for all films, assuming a direct transition between the edges of the valence and the conduction band. Then, the variation in the absorption coefficient with the photon energy hv is given by the equation

$$\alpha(h\nu) = A\sqrt{h\nu - E_g} \ .$$

"Tauc" plots of α^2 versus hv can be used for the determination of the optical band gap value $E_{g,}$ by extrapolation of the linear region of the resulting curve. The values of the direct optical energy gap for the ZnO thin films were determined to be in the range 3.3 to 3.36 eV, the actual value depending on the growth conditions.

An example of the effect of oxygen partial pressure in the sputtering plasma for both metallic and ceramic targets on the optical properties of the films is shown in figure 4.3.2 for ZnO series with 100 nm thickness.

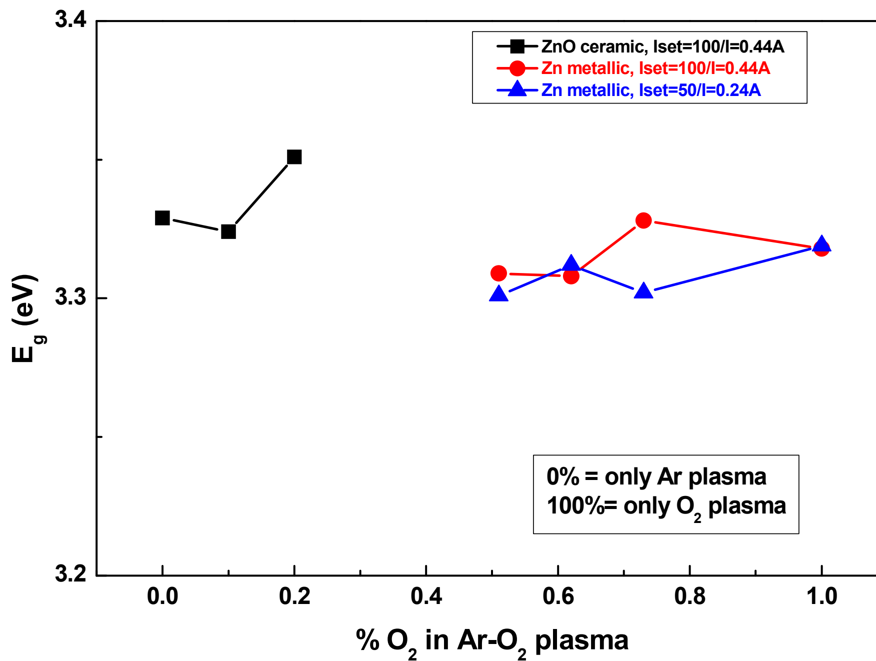

Figure 4.3.2 Optical band gap energy as a function of the oxygen content in the plasma for films grown from metallic and ceramic targets.

More than this it was found that the optical energy gap varies slightly with growth temperature, a response attributed to the variation of the film structure with oxygen partial pressure as well as to the variation of the defect concentration. Surface may also affect the optical properties of the films. As an example, the variation of RMS, obtained from the AFM analysis, and the calculated optical band gap energies for the same films as a function of Ar partial pressure is presented in figure 4.3.3. As can be seen, the optical and the morphology parameters are correlating.

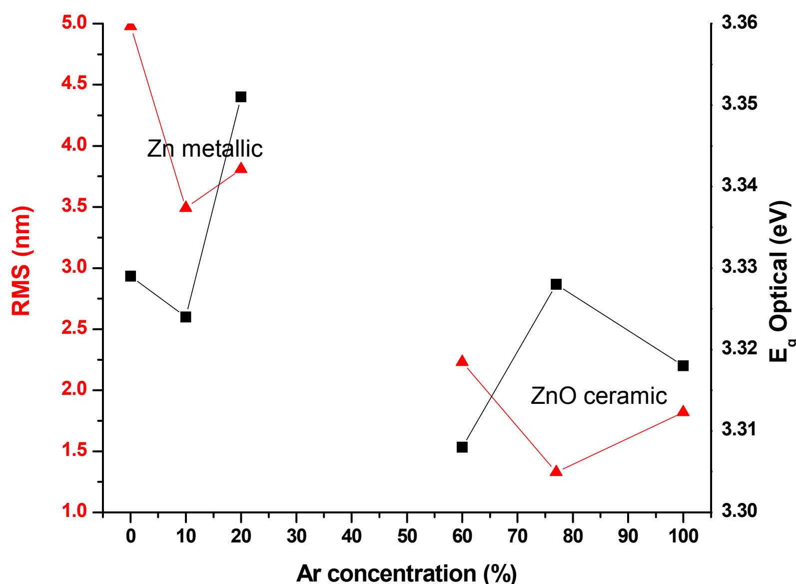

Figure 4.3.3 Optical band gap energy and RMS as a function of the oxygen content in the plasma for films grown from metallic and ceramic targets.

4.4 Electrical properties – sensing

The effects of growth conditions on the conductivity and the conductivity change under photoreduction and oxidation treatments for all grown films were rigorously studied. A table containing these values has been included at the end of chapter 7 as table annex 7D.

Unlike the case of In_2O_3 where all as deposited films were insulating, the conductivity of as-deposited DC magnetron sputtered ZnO thin films was found to vary in a very large interval from $6.43x10^{-11}$ up to 10^{-01} Ω-1cm-1, its value determined mainly by the deposition conditions. Moreover, this was found to increase up to seven orders of magnitude after the exposure to ultraviolet (UV) light in vacuum. The corresponding decrease after ozone exposure was found relatively lower than the photoreduction increase, a fact which can be connected with irreversible surface photoeffects

An example of the dependence of the conductivity of the as-deposited films on the O_2 partial pressure at two different sputtering current values are shown in figure 4.4.1. As can be seen, increasing oxygen contend in the plasma induces an increase in the as-deposited conductivity, this however, remaining unaffected by the sputtering current

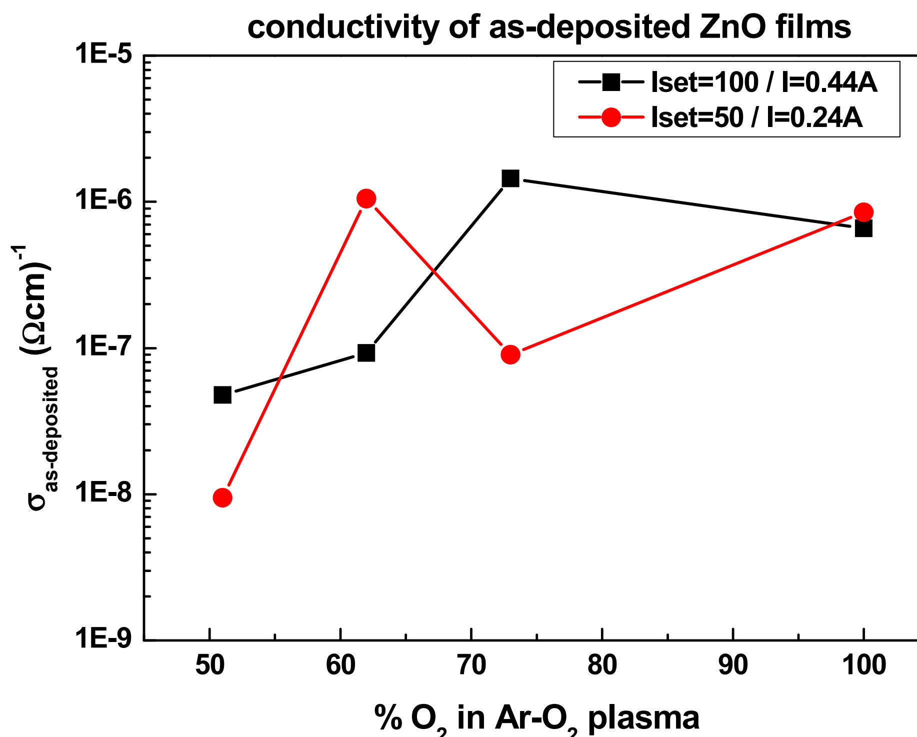

Figure 4.4.1 Example of the dependence of the conductivity of the as-deposited films on the O2 partial pressure at two different sputtering current values.

A comparison of the as-deposited conductivity for the ZnO films sputtered from Zn metallic and ZnO ceramic targets is presented in figure 4.4.2.

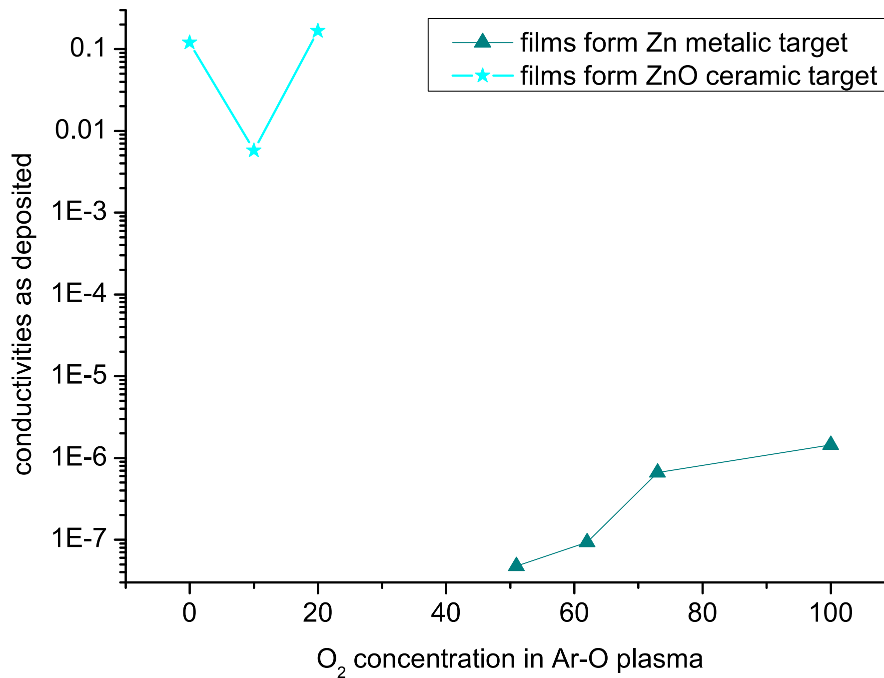

Figure 4.4.2 Example of the dependence of the conductivity of the as-deposited films on the nature of the target.

As can be seen, films grown from ceramic ZnO targets have much higher as-deposited electrical conductivity. However, as it will be reported next, the films from ceramic targets exhibit smaller response in photoactivation and oxidation processes.

Regarding the conductivity changes under photoreduction and ozone oxidation treatments; these were examined as a function of various growth parameters. Initially, the effect of oxygen partial pressure in the plasma was studied for two values of the current and ceramic/metallic targets. In this work, the film's sensitivity is by definition the ratio between the conductivity in an equilibrium photoreduced state and the conductivity in fully oxidized with ozone final equilibrium state ($\Delta=\sigma_{max}/\sigma_{final}$). The results are shown in figures 4.4.3 a and b for two different plasma currents in the case of metallic Zn target and 4.4.4 for growth from ceramic ZnO target in similar conditions. As can be seen, a maximum sensitivity of about 10^6 was found for films grown from metallic targets at 100% oxygen atmosphere and a current intensity of 0.44 A.

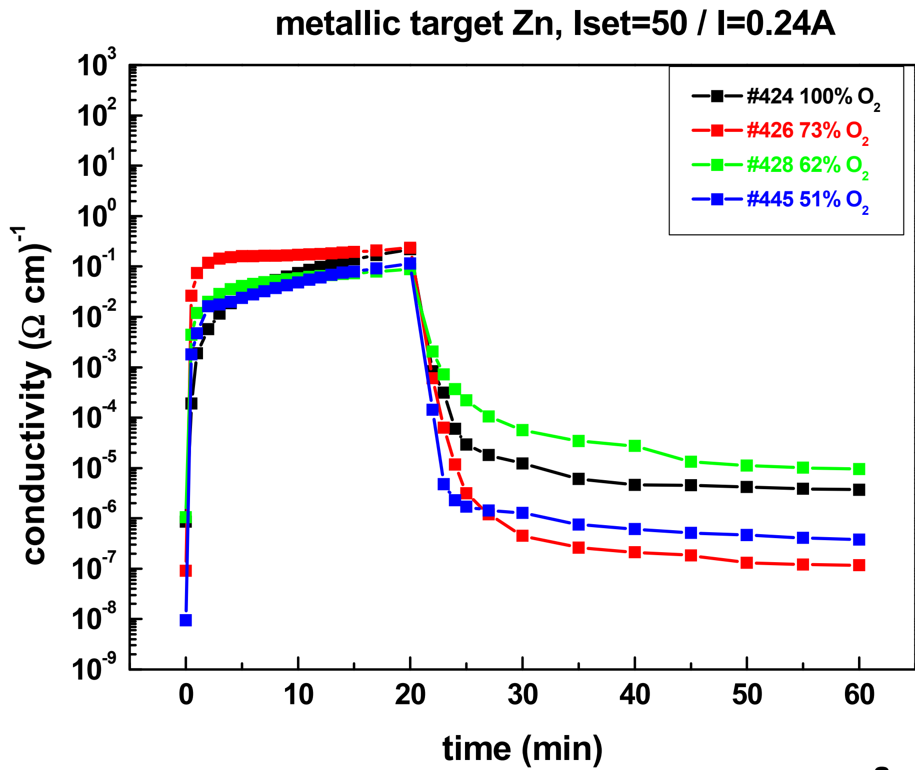

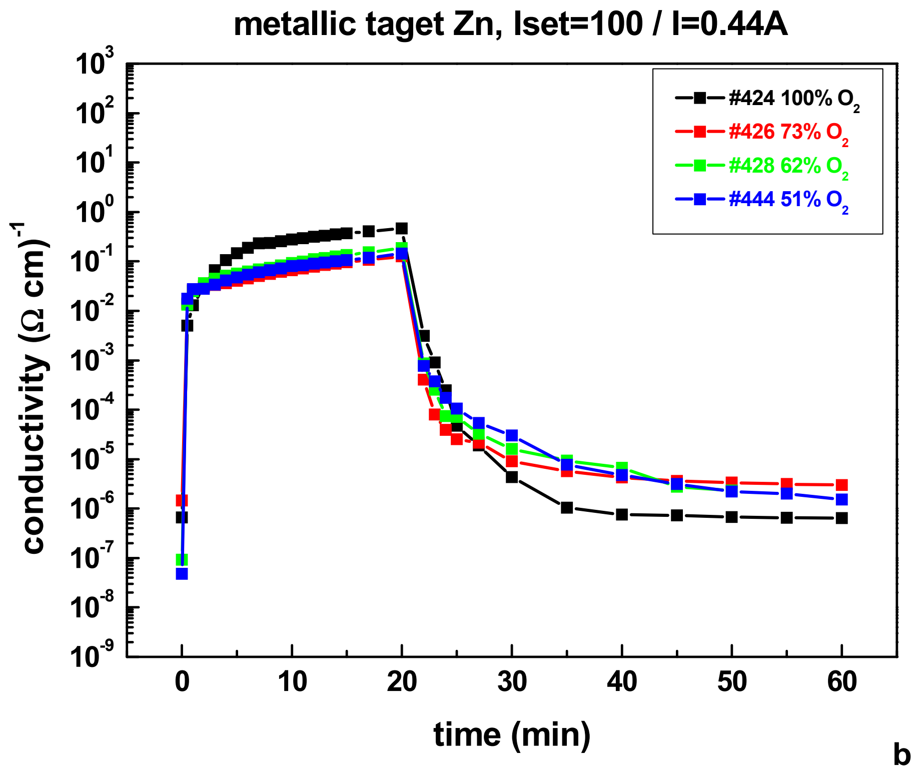

Figure 4.4.3 Dependence of conductivity changes under UV and ozone exposure on oxygen partial pressure during growth for films grown from Zn metallic target at a I=0.24A and b I=0.44A.

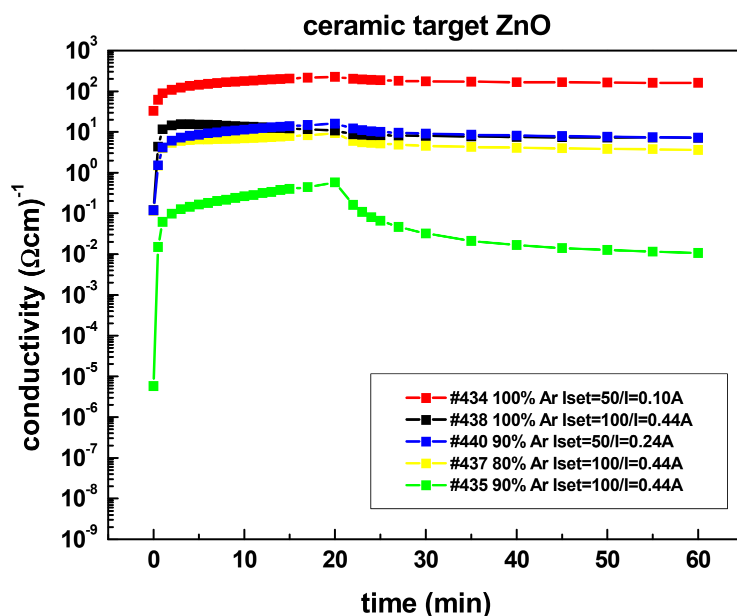

Figure 4.4.4 Dependence of conductivity changes under UV and ozone exposure on oxygen partial pressure during growth for films grown from ZnO ceramic target at I=0.24A and I=0.44A.

In addition, the effect of film thickness on the conductivity of the films and their sensitivity was examined. The systematical dependence of film sensitivity for a thickness series grown by DC magnetron sputtering from 99.999% pure Zn metallic target, pressure $8x10^{-3}$ mbar, oxygen concentration in the plasma 100%, growth rate 9.6 nm/min and RT is presented in figure 4.4.5. As shown, increasing thickness results in a decrease of the ozone sensitivity.

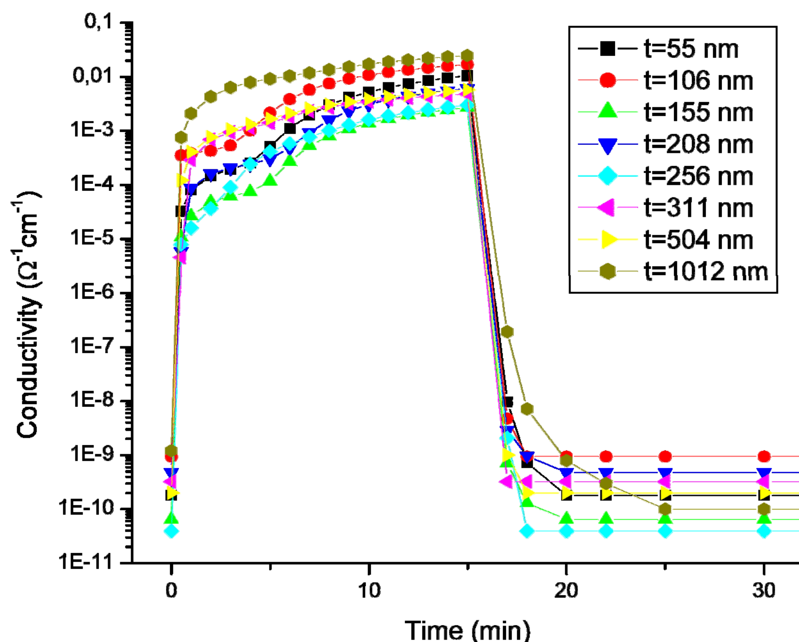

Figure 4.4.5 Dependence of conductivity changes under UV and ozone exposure on thickness.

Using the photoreduction – ozone oxidation cycles presented before, the minimum and maximum conductivity as well as the ozone sensitivity of the films were determined as a function of various growth parameters. Figure 4.4.6 presents the influence of the oxygen content in the plasma and the plasma current on the maximum and the minimum conductivity.

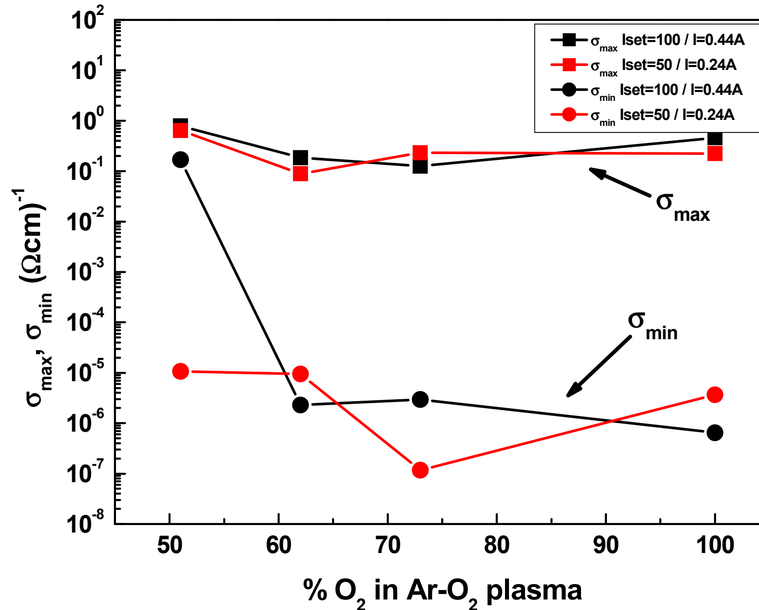

Figure 4.4.6 Dependence of conductivity changes under UV and ozone exposure on oxygen partial pressure and plasma current.

The effect of oxygen partial pressure during growth connected with the nature of the target used was investigated. Figure 4.4.7 presents some results in this sense. It is noticeable that films from ceramic targets exhibit smaller response in photoactivation and oxidation processes.

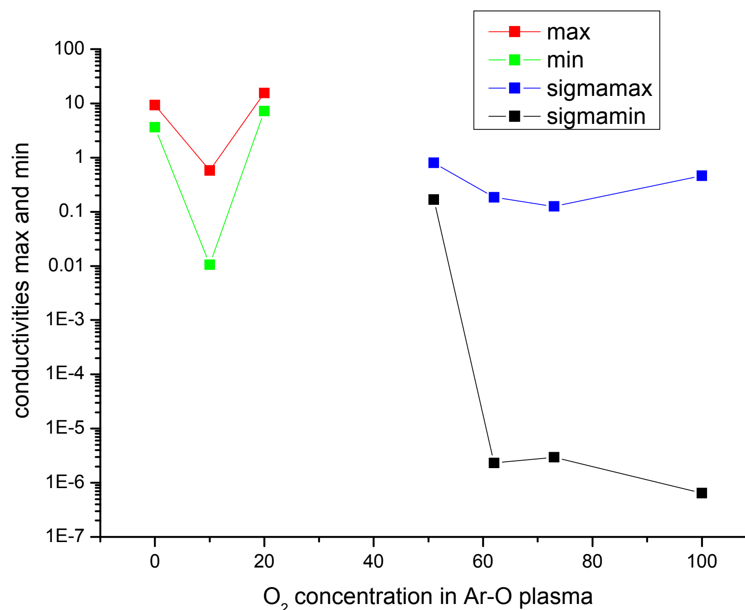

Figure 4.4.7 Dependence of conductivity changes under UV and ozone exposure on oxygen partial pressure and target nature.

Study of sensitivity changes versus surface RMS and grain size, determined from AFM measurements for ZnO grown by DC magnetron sputtering at RT, showed that as RMS and grain radius increase, the sensitivity also increased, as presented in figure 4.4.8 and 4.4.9. Similar increase of the conductivity change was observed with increasing surface area ratio (SDR), at least for values larger than 1 as shown in figure 4.4.10.

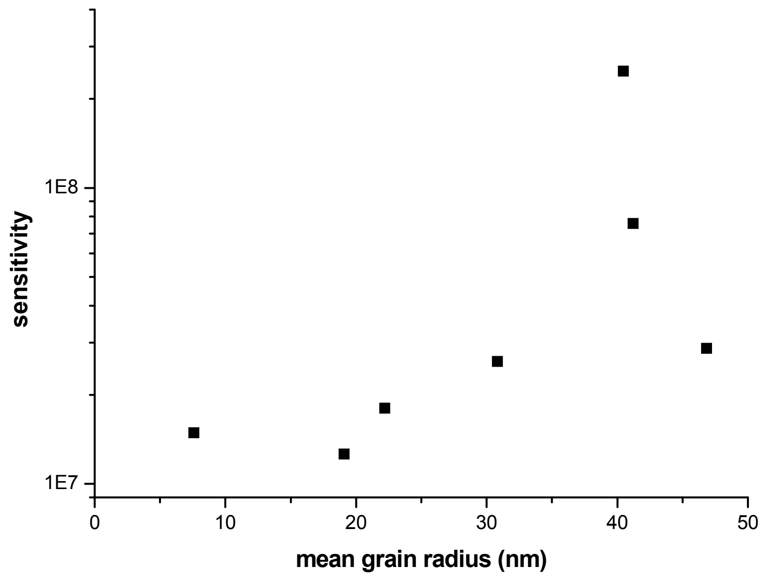

Figure 4.4.8 Dependence of conductivity changes under UV and ozone exposure – sensitivity on mean surface grain radius.

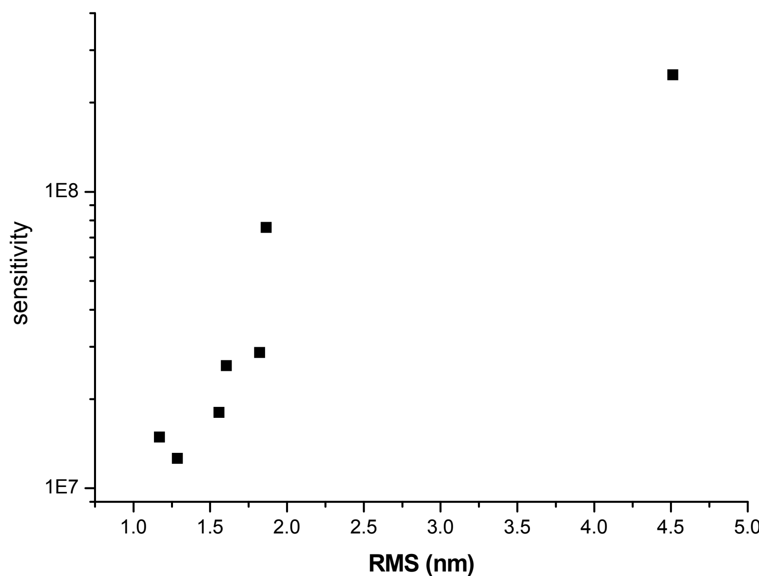

Figure 4.4.9 Dependence of conductivity changes under UV and ozone exposure – sensitivity on surface RMS.

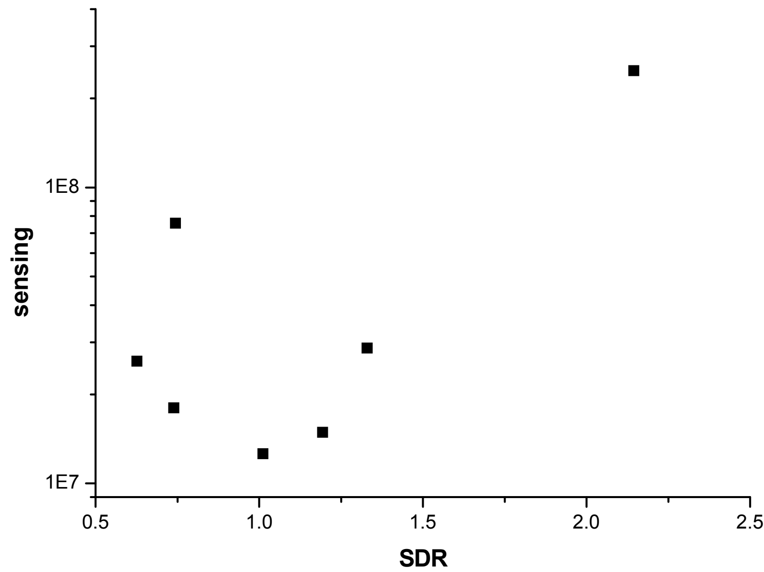

Figure 4.4.10 Dependence of conductivity changes under UV and ozone exposure – sensitivity on SDR.

As an example, that proves the correlations of the growth parameters with the surface sensitivity for ZnO films (grown using DC magnetron sputtering), is presented the effect of thickness variation on the surface parameters and the response of the film (figure 4.4.11). The figure shows the evolution of the measured roughness values (Ra and Rq) along with the film response Δ. One can see a strong correlation of Δ with the film surface roughness even for the smaller thickness range. However, these are parameters determined by height variation on the surface and they do not include enough information on surface geometry such as grain shape and size.

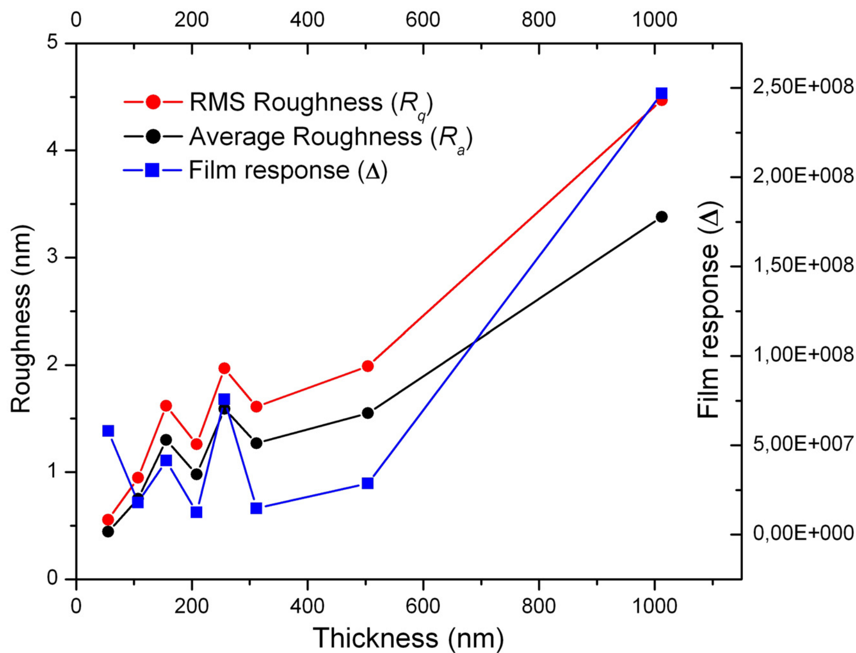

Figure 4.4.11 Dependence of RMS parameters Rq and Ra and sensing response on film thickness.

For a more accurate description of the surface morphology, additional parameters such as skewness, surface area ratio and fractal dimension are needed. In figure 4.4.12, one can see that particularly for thicknesses bellow 500 nm, the skewness changes contrary to the film response (Δ) indicating that the peakyness of the surface becomes dominant over the valleys and pits, suggesting a sensing mechanism predominately controlled by the valley structures of the film.

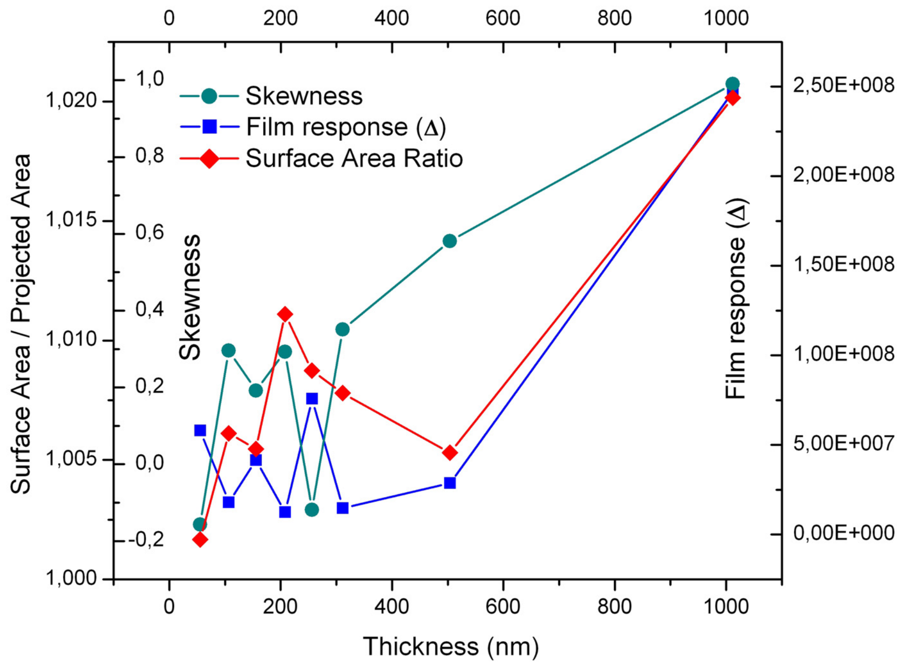

Figure 4.4.12 Dependence of SDR and skewness and sensing response on film thickness.

This is in a good agreement with the theory of the grain boundary controlled conduction process. With decreasing skewness, the grain boundaries of structures rich in valleys become more exposed to the ambient and this change can cause a decrease in the electron concentration in the surface layer and a consequent increment in the height of the intergrain barriers. However, for thicker films (>500 nm) the conductivity response Δ was found to be independent or much less influenced by the skewness and more influenced by the surface area ratio, although roughness still remained a good indicator of Δ, in this thickness range. This may be attributed to a change in the contribution of grain boundaries over surface depleted area adsorption theory in the conduction mechanism above a specific thickness. This approach proves once more the insufficiency of existing models for coherent conductivity mechanism in polycrystalline metal oxide thin films and the importance of surface involvement in the evaluations.
The correlations chapter will present in more details the influence of the whole set of growth parameters on the surface parameters and their subsequent effect on the conductivity changes for ZnO thin films.

4.5 Conclusions

This chapter was dedicated to the growth and the properties of ZnO thin films grown by DC magnetron sputtering in different growth conditions. The results can be resumed to the following highlights:

Pure ZnO series were grown by DC magnetron sputtering using Zn metallic and ZnO ceramic targets. The influences of the growth parameters (thickness keeping the growth temperatures constant, growth temperature keeping the thickness constant, total pressure during the deposition, oxygen:argon ratio during growth.) on the properties of the films was examined. It was proved that:

- All films are polycrystalline (even the thinnest ones grown at room temperature) with columnar grains and textured with preferential orientation along [002] crystalline direction of the wurzite structure.
- Films grown from ceramic targets have higher stoichiometry than films grown from metallic targets.
- Surface and surface parameters are determined by growth conditions.
- Optical transmittance in UV-Vis spectral region showed that all films are highly transparent, having an average 70-90% transmittance in the visible range. From the UV absorption minima, corresponding to direct transition across the band gap, the band gap energy was estimated and found to be in the range 3 to 3.36 eV, values smaller than that of the bulk value 3.37eV. This difference can be attributed to nonstoichiometry, defects and presence of stress in the films structure.
- All films were examined under photoreduction and ozone oxidation cycles and the results were compared and correlated with the evolution of the growth parameters and the changes of the surface parameters accordingly. It was proved that there is an obvious connection between surface and conductivity and that a systematical analysis based on experimental results may lead to the selection of most significant surface parameters that can be used for a more general correlation of surface properties with films sensing.

References

- M. Suchea, G. Kiriakidis, “Correlation of Surface Characteristics of In and Zn Oxides by AFM”, 2004 International Semiconductor Conference. CAS 2004 Proceedings (IEEE Cat. No.04TH8748), 2004, Vol. 2, p. 345-348
- M. Suchea, M. Katharakis, S. Christoulakis, N. Katsarakis, G. Kiriakidis, “Surface Analysis of ZnO Transparent Thin Films”, MMN2004 International Conference, Athens, 14-17 nov.2004, to be published in IOP J. Physics: Conference Series
- Kiriakidis, G., Suchea, M., Christoulakis, S., Katsarakis, N. High performance gas sensing materials based on nanostructed metal oxide films (2005) Reviews on Advanced Materials Science, 10 (3), pp. 215-223. Cited 6 times.
- Suchea, M., Christoulakis, S., Moschovis, K., Katsarakis, N., Kiriakidis, G. ZnO transparent thin films for gas sensor applications (2006) Thin Solid Films, 515 (2 SPEC. ISS.), pp. 551-554. Cited 11 times.
- Kiriakidis, G., Dovinos, D., Suchea, M. Sensing using nanostructured metal oxide thin films (2006) Proceedings of SPIE - The International Society for Optical Engineering, 6370, art. no. 63700V.
- Suchea, M., Christoulakis, S., Katsarakis, N., Kitsopoulos, T., Kiriakidis, G. Comparative study of zinc oxide and aluminum doped zinc oxide transparent thin films grown by direct current magnetron sputtering (2007) Thin Solid Films, 515 (16 SPEC. ISS.), pp. 6562-6566.
- Kiriakidis, G., Suchea, M., Christoulakis, S., Horvath, P., Kitsopoulos, T., Stoemenos, J. Structural characterization of ZnO thin films deposited by DC magnetron sputtering (2007) Thin Solid Films, 515 (24 SPEC. ISS.), pp. 8577-8581.
- Tudose, I.V., Horváth, P., Suchea, M., Christoulakis, S., Kitsopoulos, T., Kiriakidis, G. Correlation of ZnO thin film surface properties with conductivity (2007) Applied Physics A: Materials Science and Processing, 89 (1), pp. 57-61.

Annex 4A: Growth parameters for ZnO thin films grown by DC magnetron sputtering.

RUN	% O2	pressure (mbar)	timp(sec)	medium temp	thickness (nm)	growth rate nm/sec
1	100	8.00E-03	4800	93.5	3700	7.71E-01
2	100	8.00E-03	8460	99.5	2800	3.31E-01
3	80	8.00E-03	3900	107	1540	3.95E-01
4	100	8.00E-03	1800	25	881	4.89E-01
5	80	8.00E-03	1620	66	1002	6.19E-01
6	100	8.00E-03	300	56	106	3.53E-01
7	100	8.00E-03	570	41	106	1.86E-01
8	73.40	8.00E-03	300	54.5	111	3.70E-01
9	73.40	8.00E-03	540	45.5	110	2.04E-01
10	61.67	8.00E-03	270	47	108.8	4.03E-01
11	61.67	8.00E-03	375	43.5	95.5	2.55E-01
12	50.85	8.00E-03	190	51	106.8	5.62E-01
13	50.85	8.00E-03	420	38.5	101.7	2.42E-01
14	0	8.00E-03	150	49	107.7	7.18E-01
15	0	8.00E-03	720	36.5	106.1	1.47E-01
16	10	8.00E-03	180	51.5	107.6	5.98E-01
17	10	8.00E-03	80	40	22.7	2.84E-01
18	20	8.00E-03	180	47	108.5	6.03E-01
19	0	8.00E-03	150	48.5	104.5	6.97E-01
20	10	8.00E-03	270	48	105.9	3.92E-01
21	50.85	8.00E-03	240	44.5	104.5	4.35E-01
22	50.85	8.00E-03	390	42.5	105.6	2.71E-01
23	100	8.00E-03	680	40.5	102	1.50E-01
24	100	8.00E-03	150	36.5	22.4	1.49E-01
25	100	8.00E-03	340	35.5	51.8	1.52E-01
26	100	8.00E-03	960	45.5	152.7	1.59E-01
27	100	8.00E-03	1260	48	202	1.60E-01
28	100	8.00E-03	1690	36	301.7	1.79E-01
29	100	8.00E-03	3070	55.5	502.5	1.64E-01
30	100	1.50E-02	670	44.5	102.6	1.53E-01
31	100	3.00E-02	870	43	102.2	1.17E-01
32	100	5.00E-02	1220	44	102.2	8.38E-02
33	100	8.00E-03	4800	115	4960	1.03E+00
34	100	8.00E-03	4800	93	2498	5.20E-01
35	100	8.00E-03	300	48.5	95.3	3.18E-01
36	90	8.00E-03	300	109.5	101.7	3.39E-01
37	80	8.00E-03	240	40	102.9	4.29E-01
38	70	8.00E-03	240	40	100.3	4.18E-01
39	100	1.00E-02	360	56	106.7	2.96E-01
40	100	1.00E-02	700	61	208	2.97E-01
41	100	1.00E-02	990	62.5	311.4	3.15E-01
42	100	1.00E-02	1620	70.5	504	3.11E-01
43	100	1.00E-02	3180	81.5	1012	3.18E-01
44	100	1.00E-02	360	71	101.9	2.83E-01
45	100	1.00E-02	500	57	155.5	3.11E-01
46	100	1.00E-02	780	65.5	256.1	3.28E-01
47	100	1.00E-02	340	119	108.2	3.18E-01
48	100	1.00E-02	620	132	206.7	3.33E-01
49	100	1.00E-02	360	202.5	106.6	2.96E-01

Chapter 5

Pure ZnO thin films grown by PLD

Outlines

- **Growth**
- **Characterization: structural, surface, optical, electrical**
- **Particular correlations of different parameters**
- **Annex 5A: growth parameters of ZnO films by PLD**

5. ZnO thin films grown by PLD

The pulsed laser deposition technique was also used to produce zinc oxide thin films with different thickness at different substrate temperature during growth onto silicon and Corning glass substrates in the growth conditions presented in table Annex 5.A.

5.1 Structural characterization

TEM characterization

ZnO films grown by PLD from ceramic ZnO targets were analyzed by TEM. As observed, the films were polycrystalline, exhibiting columnar grains as shown in the bright field (BF) micrograph in figure 5.1.1a, as well as in the dark field (DF) micrograph in figure 5.1.1b. The film presented was deposited on Si, had a thickness of 48nm and the mean diameter of the columnar grains was determined to be 25nm. Therefore, the films deposited with PLD have relative larger width of grains as compared with those grown by DC magnetron sputtering.

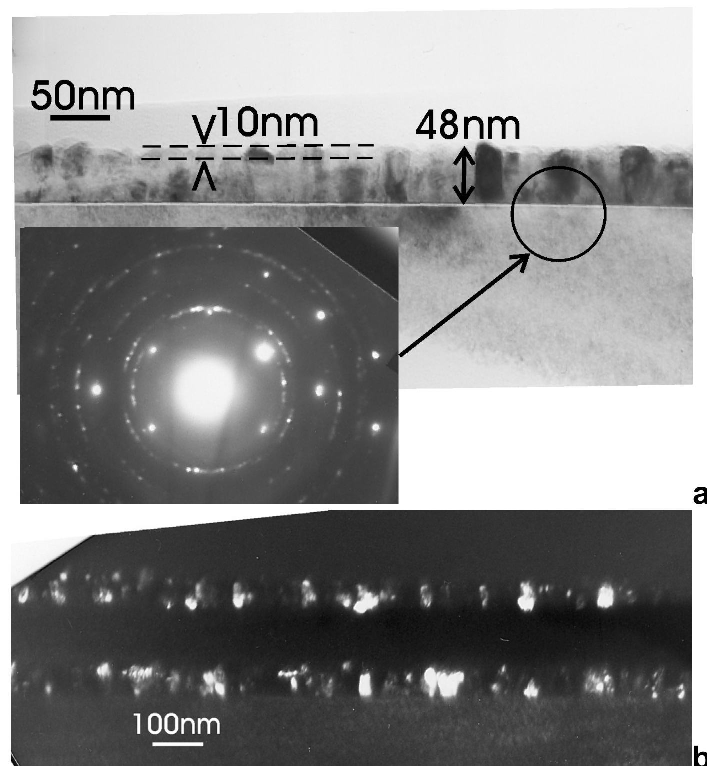

Figure 5.1.1 TEM images of ZnO thin film grown by PLD a bright field (BF) micrograph b dark field (DF) micrograph.

The films had the wurtzite hexagonal structure, as was evident from the corresponding diffraction pattern, shown in inset of figure 5.1.1a. In this figure the spots from the single crystalline Si substrate are superimposed to the diffraction rings of the polycrystalline ZnO. Therefore, taking as reference the Si spots, it was possible to index with high accuracy the rings of the ZnO film.

The films were also found to exhibit strong preferred orientation, the columnar grains being along the c-axis, which is perpendicular to the plane of the Si-substrate, as shown in figure 5.1.1a. This preferred orientation of the columnar grains was deduced considering the details of the diffraction pattern, since the intensity around each ring of the ZnO was not constant. There were certain directions with higher intensity, giving the impression of arcs instead of rings, as is evident in inset of Fig.1a. As a result, the intensity of the (0002) ZnO ring was higher (arc) along the [001] crystallographic direction of the Si-substrate. Also the rings [1 0 -1 0] and [1 1 -2 0] were also exhibiting strong intensity (arcs) perpendicular to the plane of the Si-substrate. According to the diffraction theory, this reveals a strong preferred orientation of the columnar grains, their c-axis being perpendicular to the Si-substrate.
Moreover, it was observed that the ZnO films were not actually deposited on the Si substrate, but on a 2nm thin amorphous layer, probably native SiO_2, as shown in figure 5.1.1a.

XRD characterization

XRD measurements revealed that all films were polycrystalline, presenting a highly preferential orientation of the crystallites along the (002) basal plane of wurtzite ZnO, implying c-axis uniformly perpendicular on the surface even for films grown at RT, a result consistent with the TEM observations. The (004) plane of wurtzite ZnO was also recorded; the intensity of the corresponding peak being rather low. An example of the growth parameter influence on the crystal structure is presented in figure 5.1.2, which shows a thickness series (films with thickness from 100 to 400 nm) grown at 350˚C onto Corning 1737 glass substrate.

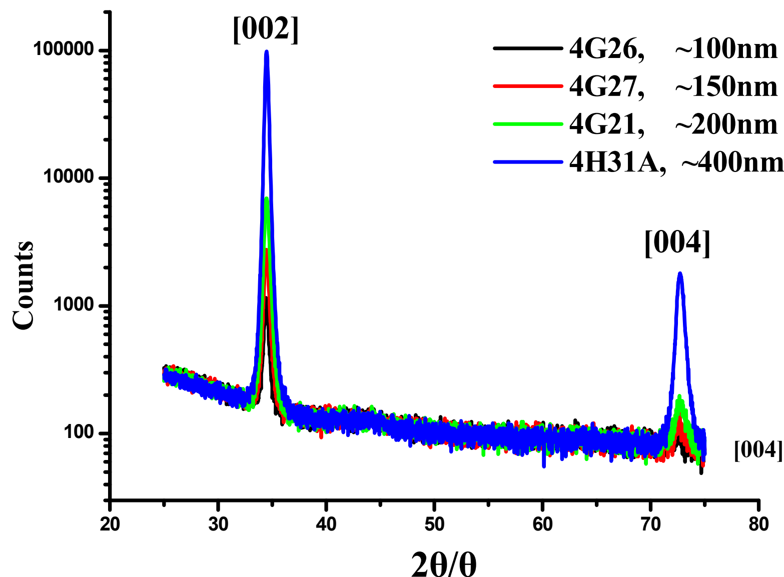

Figure 5.1.2 Typical XRD diffractograms of ZnO thin films grown by PLD. The image presents a thickness series (films with thickness from 100 to 400 nm) grown at 350˚C onto Corning 1737 glass substrate.

As shown, increasing thickness results in more intense and narrower peaks, a behavior indicating better crystallinity of the grown films. The narrowing of the diffraction peaks (FWHM) with increasing thickness can be correlated with a increasing of the grain size, a result also observed by AFM analysis.
From the [002] peak narrowing, the crystallite dimension for each film was estimated using Scherrer formula (**$d=K\lambda/(\beta^2- \beta o^2)^{1/2}\cos\theta$** where β and βo are the peak width and the width introduced by instrumental broadening, K=180/π, λ=0.154056 nm, θ is obtained from the peak position). The variation of the crystallite dimension as a function of the film thickness is shown in figure 5.1.3. It is evident that increasing film thickness up to a value of 200 nm results in a decrease of the crystallite dimension, while, for even larger thicknesses, the crystallite dimension increases.

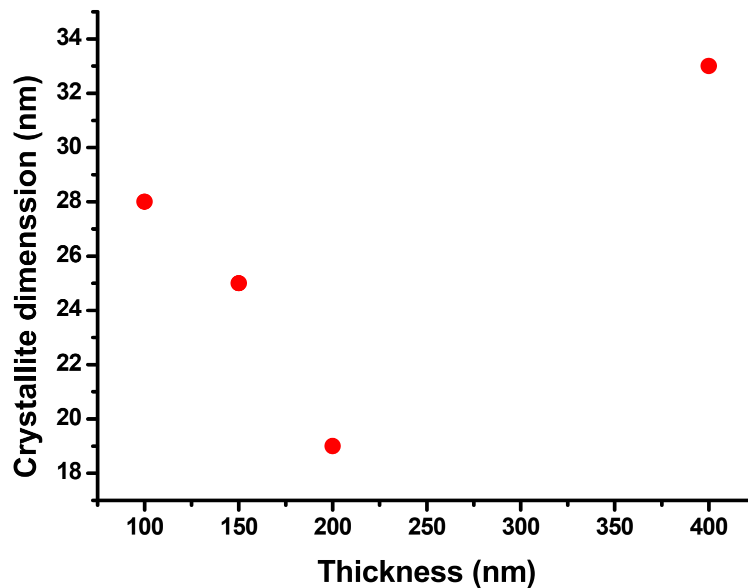

Figure 5.1.3 Mean crystallite variation with film thickness calculated from the diffractograms presented in the previous image using Scherrer's formula.

A shift towards higher diffraction angles of the (002) peak was also observed with increasing thickness, as well as a crude peak broadening as the thickness was decreasing. These observations can be attributed to the presence of microstress into the films. Microstresses are normally produced by a distribution of tensile and compressive forces, resulting in a broadening of the diffraction peaks. Microstress in crystallites may come from dislocations, vacancies, shear planes, etc.
To compute the residual stress in the plane of the film (supposing uniform bi-axial stress) two methods were used and compared as explained in the previous chapter.
The lattice constant of unstressed ZnO (powder) was assumed to be c_{powder} = 5.408Å, while the lattice constants of the stressed films, c_{film}, were derived from the XRD diffractograms. The dependence of lattice constant c_{film} on the film thickness is shown in figure 5.1.4.

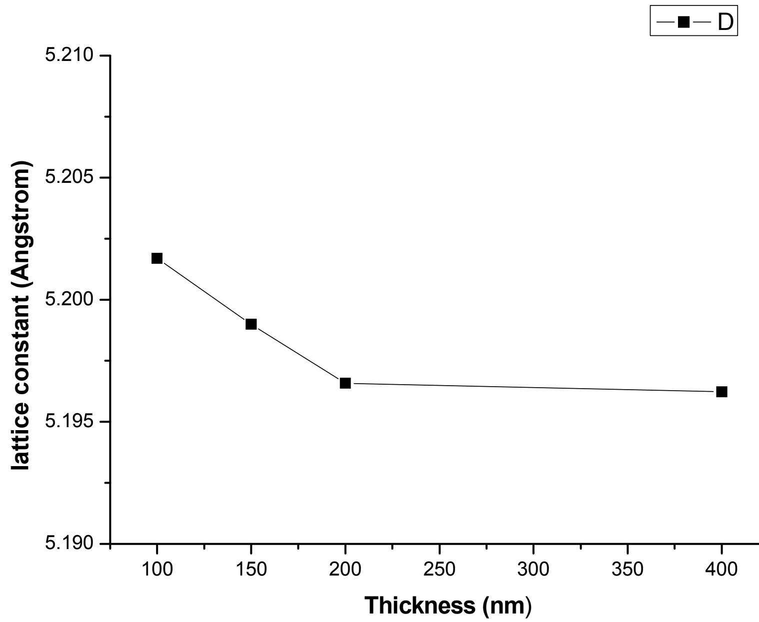

Figure 5.1.4 c constant lattice variation with film thickness calculated from the diffractograms presented in figure 5.1.2.

It is clear that increasing of the films thickness induces a slight decrease of the lattice constant. The results of the stress calculations and its dependence on the film thickness are presented in figure 5.1.5. As can be observed, increasing film thickness results in an increase of the tensile stress in the films. Moreover, one can see that the results of the two computations are in a fair agreement.

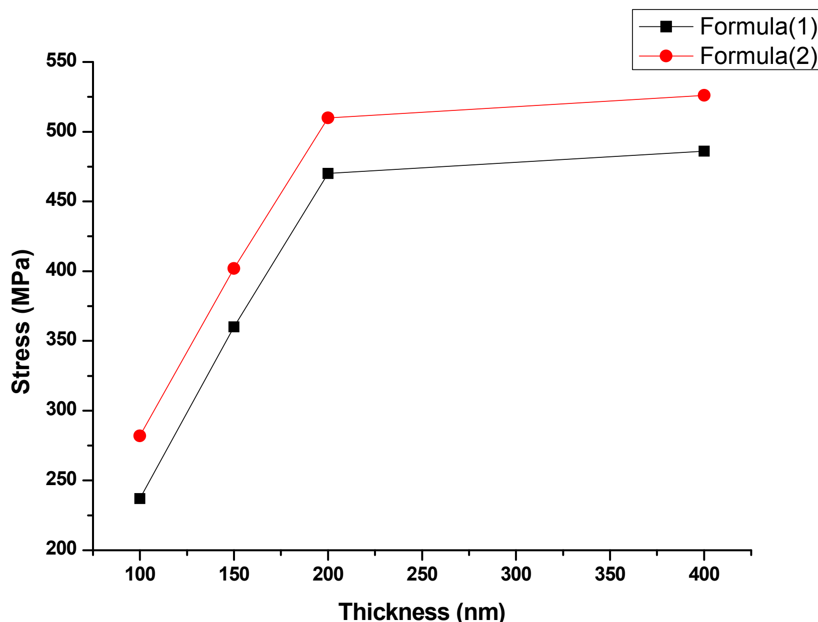

Figure 5.1.5 Microstress variation with film thickness calculated according to formulas (1) and (2).

The effect of the growth temperature on the films structure was also studied. Figure 5.1.6 presents the XRD curves of a series of films having 100nm thickness,

grown at different temperatures ranging from RT up to 650˚C. Increasing temperature induces an increasing of the (002) peak intensity and a shift of the peak position towards higher angles. Increased intensity of the (002) XRD peak means improved crystallinity while, variations of the crystalline lattice strain can result in the observed peak shift. The shift was from 34.281 to higher angles up to 34.502 (the theoretical position of the peak is at 34.42).

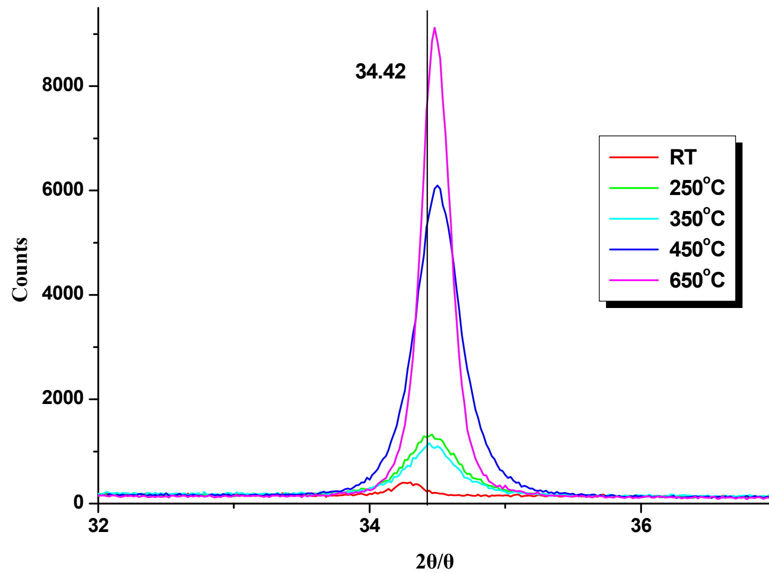

Figure 5.1.6 Growth temperature effect on XRD diffractograms of ZnO thin films grown by PLD, 100 nm serie, the plot is focused on [002] peak..

Using the FWHM of the XRD curves presented in figure 5.1.6, the crystallite dimension was calculated using the Scherrer formula. The corresponding results are shown in figure 5.1.7. The temperature effect on [002] peak broadening, with respect to the theoretical diffraction line, is shown also in this figure as FWHM variation.

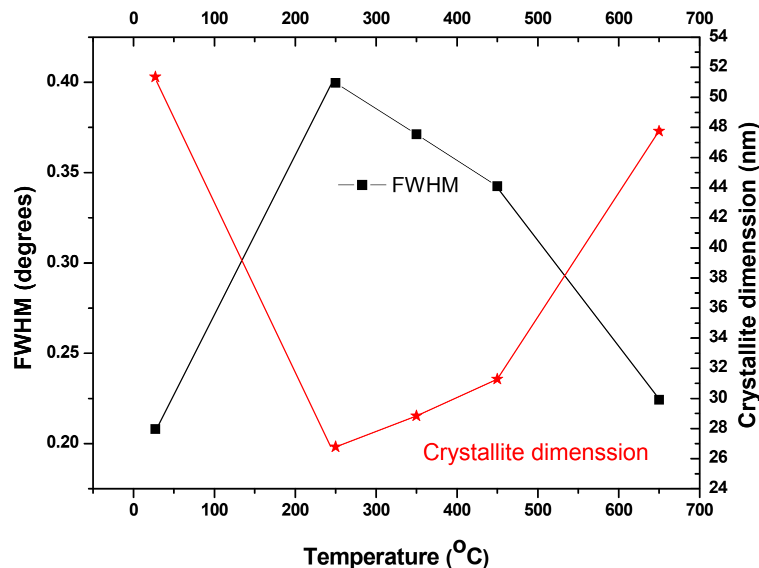

Figure 5.1.7 Mean crystallite variation and FWHM of [002] peak with substrate growth temperature calculated from the diffractograms presented in the previous image using Scherrer's formula.

Increasing of the temperature leads to an increase of the crystallite dimension, for films grown at RT crystallite dimension is not following this rule. It is clear that increasing growth temperature results in an increase of the crystallite dimensions, therefore an improved crystallinity. Only films grown at RT deviate from this behaviour. It is interesting to note that the crystallite dimension at RT growth (~50nm) is similar to the surface grain size (determined from the AFM measurements), while at higher temperatures surface grain size is always bigger than the crystallite dimension, a difference that can be explained by grain-subgrain structure of surface.
The lattice constant c_{film} of the films was also determined for various growth temperatures and is shown in figure 5.1.8.

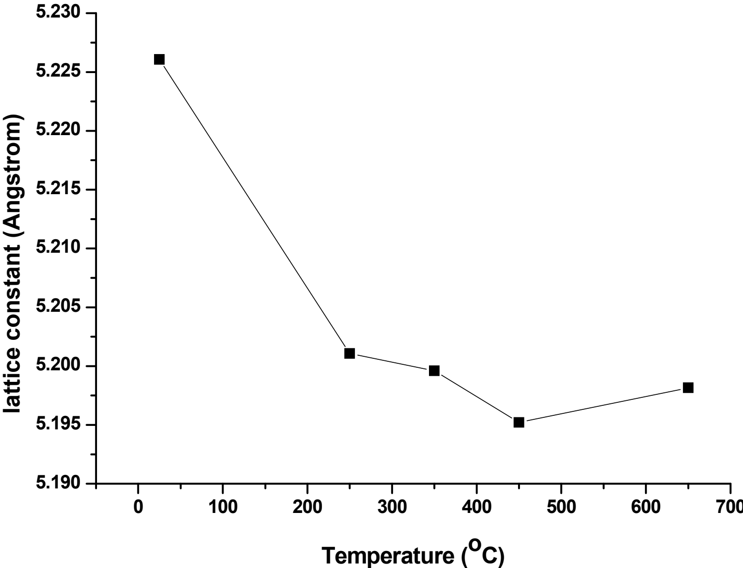

Figure 5.1.8 c constant lattice variation with substrate growth temperature calculated from the diffractograms presented in figure 5.1.6.

It is clear that increasing of growth temperature reflects in a decrease of lattice constant. The results of the stress calculations and its dependence on the growth temperature are presented in figure 5.1.9.

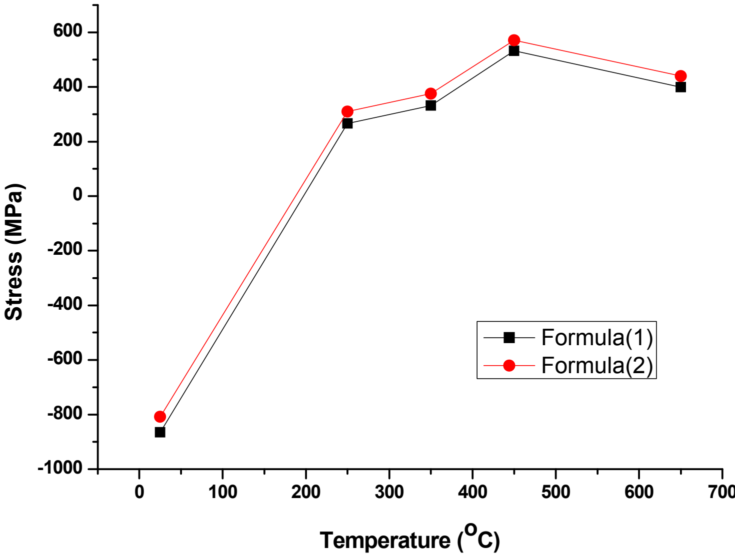

Figure 5.1.9 Microstress variation with substrate growth temperature calculated according to formulas (1) and (2).

According to these results, an increase of the growth temperature induces a transition from compressive stress at RT to tensile stress for elevated temperatures. Temperatures larger than 450ºC are causing a lattice stress relaxation, a fact proved by the slightly lower stress values for the films grown at 650ºC. Finally, films grown at RT appeared to exhibit rather low crystal quality, a behavior that can be attributed to the initial stages of the film growth. The increase of the growth temperature increases the diffusion rate for oxygen and zinc atoms trough the surface leading to a decrease of the oxygen and zinc vacancies. As a result, the density of the defects is reduced and highly crystalline films are deposited. As a consequence, the peak corresponding to preferential orientation (002) gains significantly in intensity with increasing temperature, shifting slightly at the same time to higher angles. Comparing stress values in PLD growth ZnO thin films with the ones estimated for DC magnetron sputtering it can be concluded that in the case of PLD films lattice is far more relaxed while the DC magnetron sputtered films are under compressive microstress even at elevated growth temperatures.

5.2 AFM Surface Characterization

Thickness effect

Surface characterization performed with AFM of thin films grown by PLD, revealed variations in the sample topography as a function of the thickness. AFM images for films with a thickness of 100, 150, 200 and 400 nm are presented in figure 5.2.1. With increasing thickness, the roughness of the ZnO samples was increasing from about 0.60 nm to 13.95 nm, a variation connected with the film crystal formation. In the case of thinner films, the growth time is shorter and the surface has a more homogeneous distribution of small grains (30-40nm). At longer deposition periods, the small grains aggregate, which leads to the formation of larger grains, with a subsequent increase in the measured lateral grain size and an overall rougher surface. As the thickness increases, the AFM images reveal that the surface grain size also increases, at least for films with thicknesses lower than 200nm. Also, the results indicated equiaxed grain microstructure, where the grain size is proportional to film thickness. Grain shape was also varying, particularly as a function of grain size as visible in figure 5.2.1.

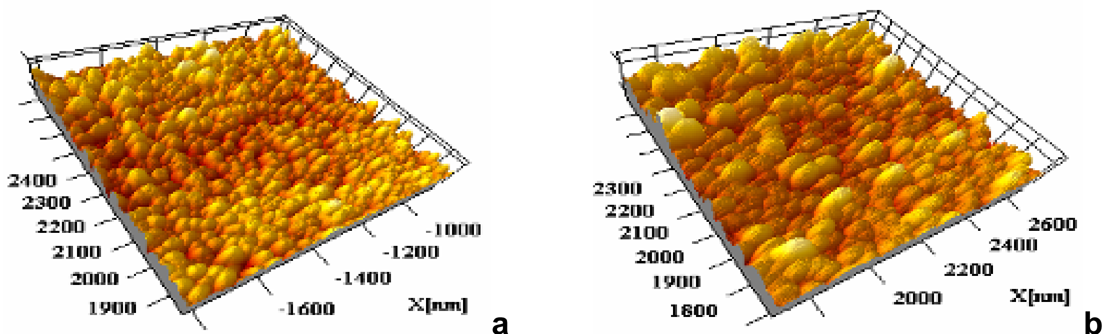

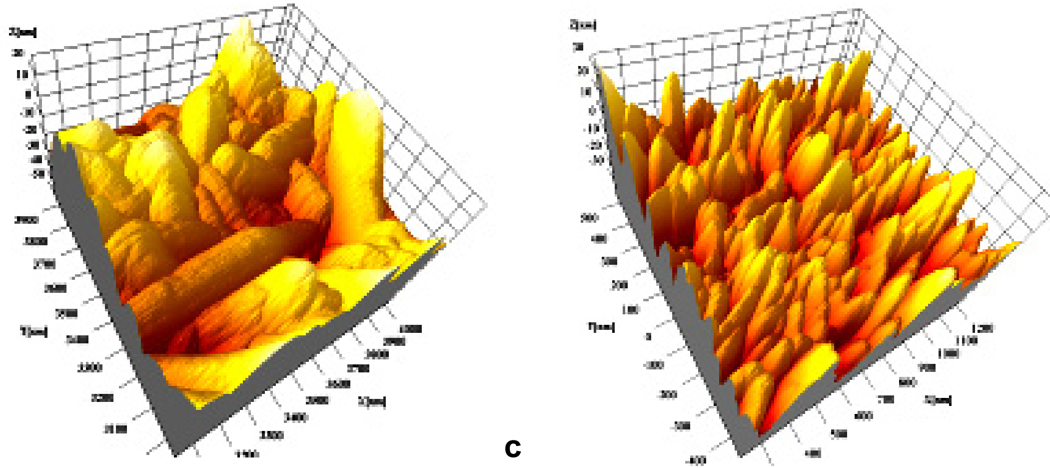

Figure 5.2.1. 3D images of 1x1 μm scan size on surfaces of thin films with 100nm, 150nm, 200nm, 400nm thickness

The variation of the RMS roughness of these films with thickness is shown in figure 5.2.2, which indicates an increase from about 0.60 nm to 13.95 nm.

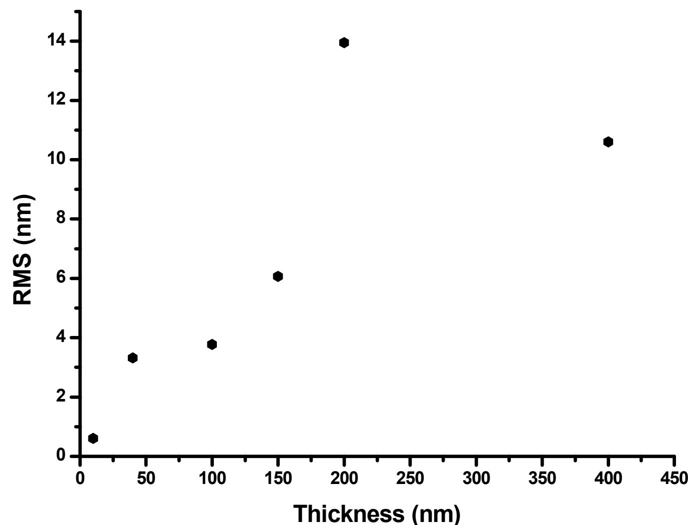

Figure 5.2.2. Variation of the RMS roughness of films with the thickness.

Maximum RMS value was found for the film with 200nm thickness, where "spaghetti" like nanostructures were present on the surface (figure 5.2.1 c). Features dimensions on the ZnO thin films prepared by PLD were varying from 10 nm to 1μm and they could be well controlled though the deposition parameters. For films with larger thickness, a mean grain radius could not be defined due to the non regulated shape of the grains and dimensional inhomogeneity, as shown in figure c, d.

Growth temperature effect

The effect of growth temperature on the surface properties of ZnO thin films grown by PLD was also studied. As examples, results related to some estimated of surface parameters are presented for two temperature series with thicknesses 40 and 100nm.

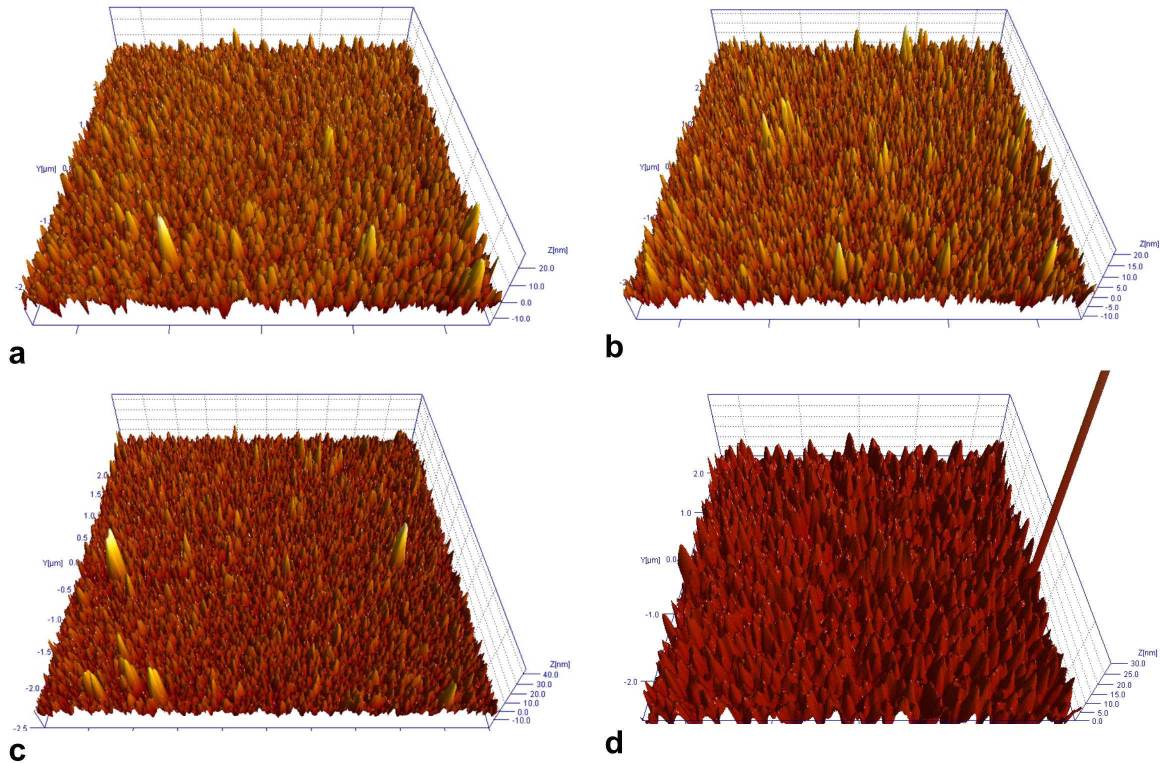

Figure 5.2.3 . 3D images of 5x5 µm scan size on surfaces of thin films grown at(a) room temperature, (b) 150 ˚C (c) 450 ˚C (d) 650 ˚C.

Images presented in figure 5.2.3 present the AFM 5x5 µm scan size images of ZnO thin films deposited at (a) room temperature, (b) 150 °C (c) 450 °C (d) 650 °C. As clearly shown in these 3D representations, homogeneous surfaces with shaped grains are obtained in all cases. Grain diameters were measured to be about 40-50nm for growth at room temperature, increasing up to 90 nm for 650 °C. With increasing temperature, an evolution from grains to grain agglomeration structures occurs and, at 650°C, wall-like structures are present. The roughness of the grown films was found to be slightly dependent on the deposition temperature, being in the range 2 to 4 nm for the films grown on silicon substrate and slightly larger for the ones on Corning 1737F glass substrates.

For a more detailed characterization of the evolution of the film surface as a function of the growth temperature, the surface characteristic parameters SDR, SBI and SFD were determined and figure 5.2.4 a, b presents their variation with temperature. SDR presents a decreasing tendency with increasing growth temperature, a behaviour indicating that high temperatures favour improvement of surface planarity. On the other hand, increasing growth temperature induces a general increase of SFD which can be associated with surface texturing. Finally, SBI varies slightly from 0.525 to 0.601, values close to 0.608 which corresponds to a Gaussian ideal distribution as a measure of surface homogeneity improvement.

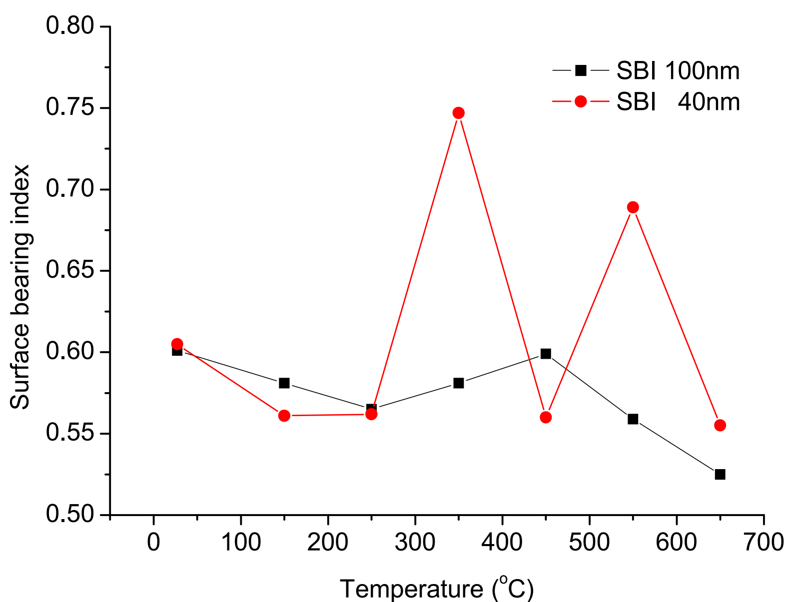

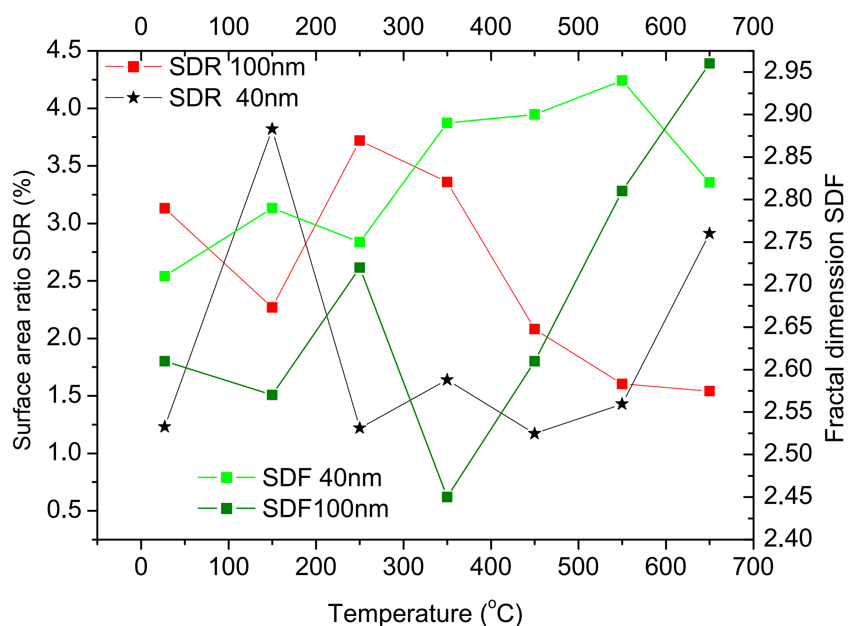

5.2.4. Variation of SBI (a), SDR and SFD (b) of PLD grown ZnO films with substrate temperature during growth.

Detailed and complete evaluation of the surface parameters as well as their correlation with the conductivity and the sensing response for all films grown by PLD will be presented in chapter 7.

5.3 Optical properties of ZnO films grown by PLD

Figure 5.3.1 presents the UV-visible transmission spectra of some of the as-deposited ZnO thin films as a function of (a) the film thickness for films grown at 350 °C and (b) the growth temperature for films with a thickness of 100 nm.

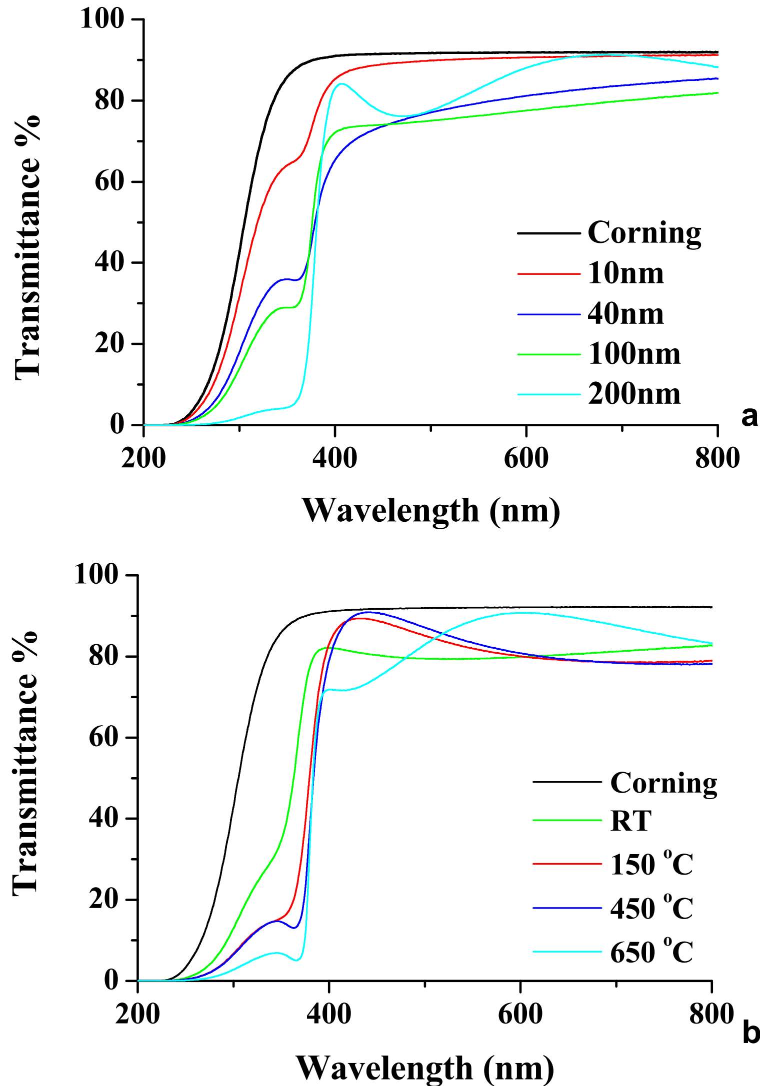

Figure 5.3.1. UV-visible transmission spectra of ZnO thin films as a function of (a) the film thickness for films grown at 350 °C and (b) the growth temperature for films with a thickness of 100 nm.

The films were found to be highly transparent in the visible wavelength region with an average transmittance of 80-90%, with a fall off for wavelengths shorter than 380 nm, a behavior characteristics of high quality ZnO films. The position and the shape of the absorption edge observed for wavelengths below 380 nm were found depending on the film thickness and growth temperature. In order to better investigate the influence of the growth parameters on the absorption edge, we used the recorded transmission spectra for the determination of the optical energy gap E_{gap}, assuming a direct transition between the edges of the valence and the

conduction band. Under these conditions, the variation of the absorption coefficient α with the photon energy hv can be given by the equation:
$\alpha(hv)=A(hv-E_{gap})^{1/2}$

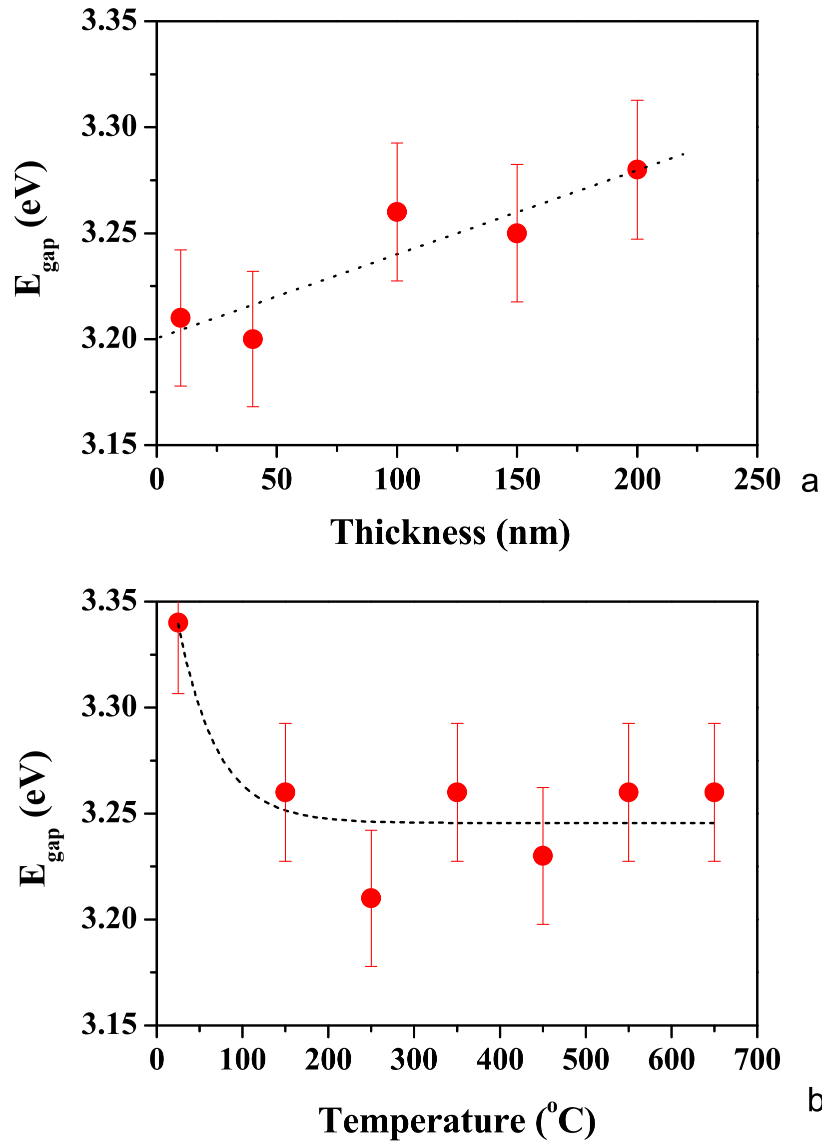

Figure 5.3.2 Optical bandgap energy as estimated from the UV-visible transmission spectra of ZnO thin films as a function of (a) the film thickness and (b) the growth temperature.

The optical band gap value E_{gap} can then be extrapolated from the linear region of "Tauc" plots of α^2 as a function of hv as shown in figure 3.3.3 a and b. The determined values of the direct optical energy gap for the as-deposited ZnO films were found to be in the range 3.20 to 3.35 eV, its value depending on the thickness of the film and the growth temperature. Figure 5.3.2 depicts the variation of the optical energy gap as a function of (a) the thickness of film and (b) the growth temperature. As can be seen, the energy gap increases slightly with increasing thickness, approaching a value of 3.27 eV for large thicknesses. In contrast, increasing growth temperature results in a slight decreasing of the

energy gap, this approaching a value of 3.27 eV for temperatures larger than 300 °C.

Except the normal absorption edge related to the transition between the valence and the conduction bands, an additional absorption band was also recorded in the wavelength region around 360 nm (3.44 eV). For low deposition temperatures, the band appears as a shoulder, becoming clear for temperatures higher than 250 °C. Figures 5.3.4 a and 5.3.4 b present the dependence of the maximum of this absorption band on the substrate temperature and the film thickness. As can be seen, the band is red shifted with increasing growth temperature, approaching a value of 3.4 eV for temperatures larger than 500 °C. In contrast, increasing film thickness results in a significant blue shift, only the film of 40 nm deviating from this behaviour.

As was shown, the band gap energy calculated from Tauc plots for two different temperature series with different thicknesses is varying around 3.24 eV, being much smaller than the theoretical value 3.37eV. The films grown at RT have the biggest calculated band gap of 3.34eV, but at the same time, they do not show the additional absorption peak.

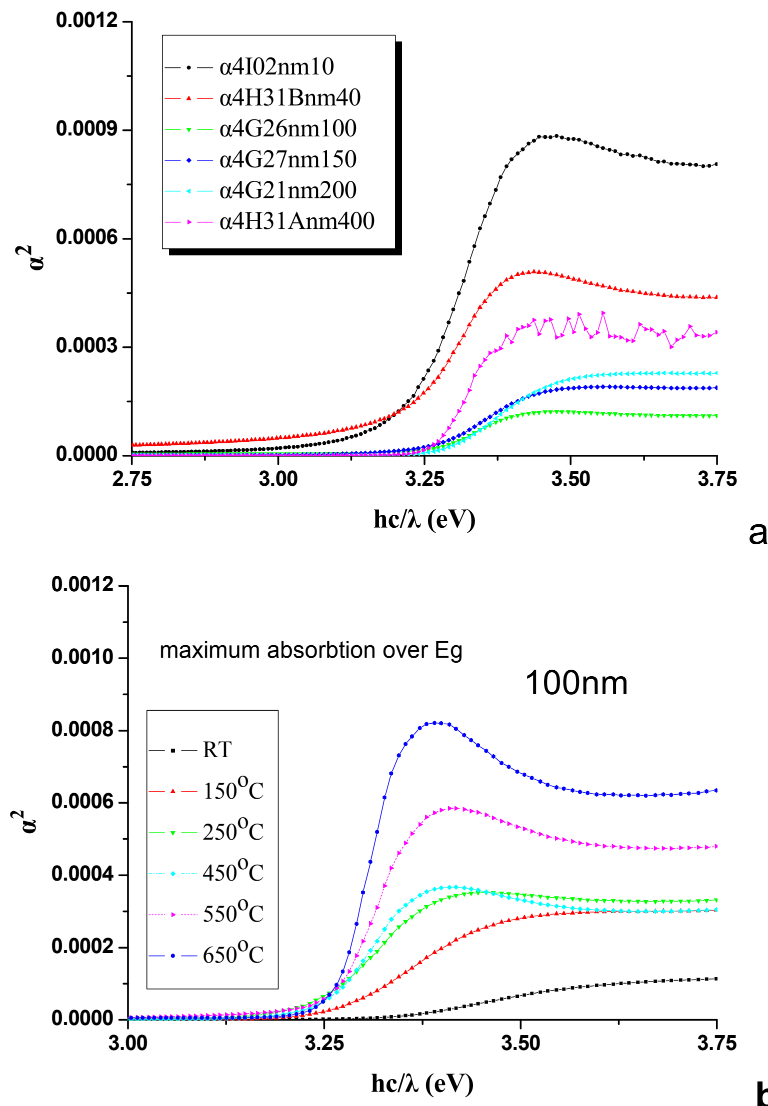

Figure 5.3.3 α^2, as estimated from UV-visible transmittance spectra of ZnO thin films, as a function of energy. The effect of: (a) film thickness and (b) growth temperature.

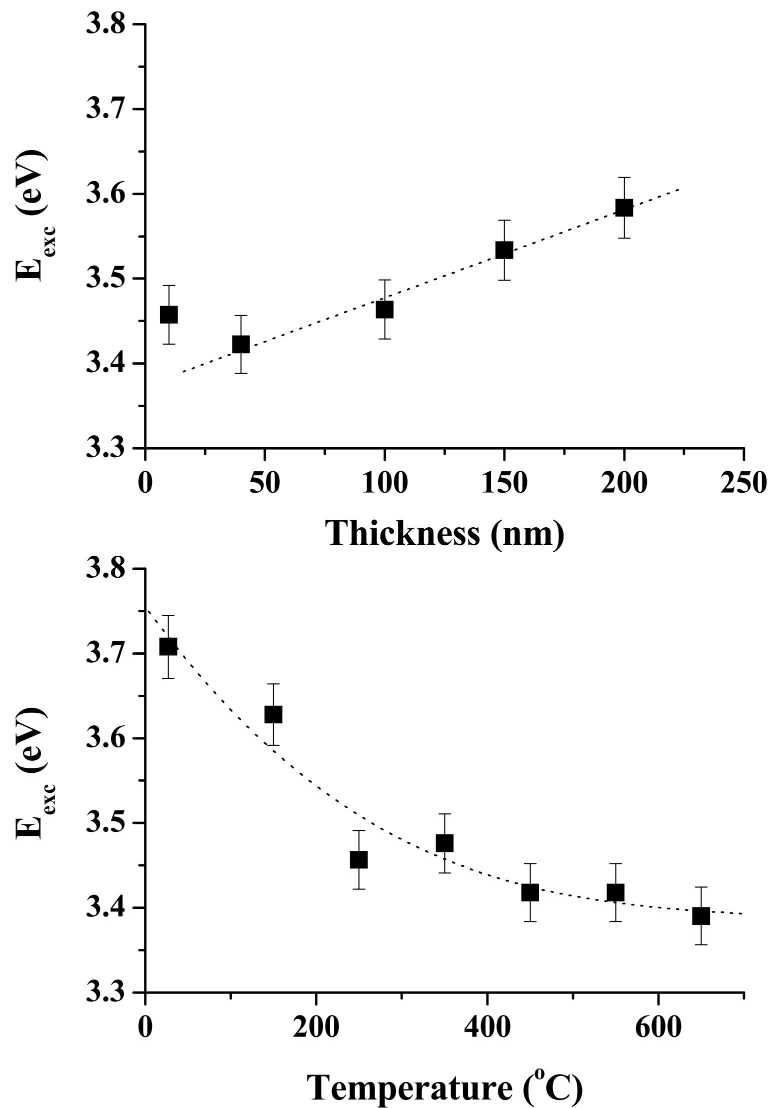

Figure 5.3.4 Additional absorption band energy as estimated from the UV-visible transmission spectra of ZnO thin films as a function of (a) the film thickness and (b) the growth temperature.

From the above results, it seems that additional peak intensity (height) is influenced globally by film thickness (it reduces when thickness increases) and locally by growth temperature. The global influence of temperature seems to manifest stronger on the position of peak. As temperature increase from RT to 450°C, the energy corresponding to this additional absorption band decreases (red shift) reaching a kind of saturation at 3.39eV in both cases.
The influence of the growth temperature on the optical parameters was also investigated with very thin ZnO films, having a thickness of 40 nm. The variation of position of the energy gap and the additional absorption band are presented in figures 5.3.5 a and b. As can be seen, the dependence of the maximum of the additional absorption band on temperature is similar for both thickness series. In contrast, in the case of the energy gap for the 40 nm thick films, this remains more or less constant with varying growth temperature.

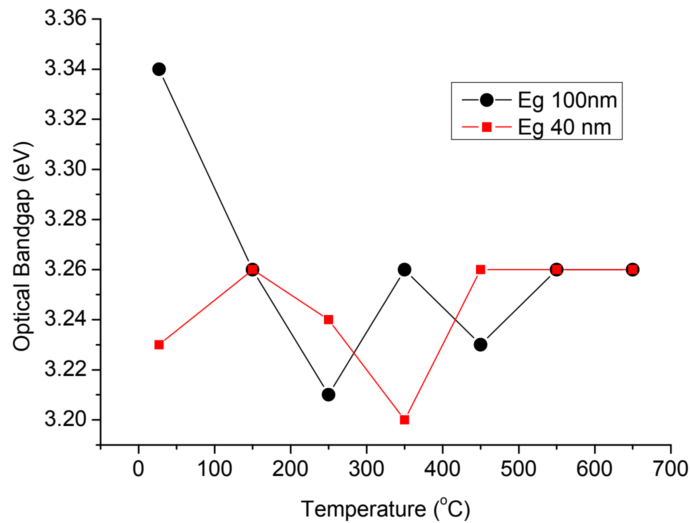

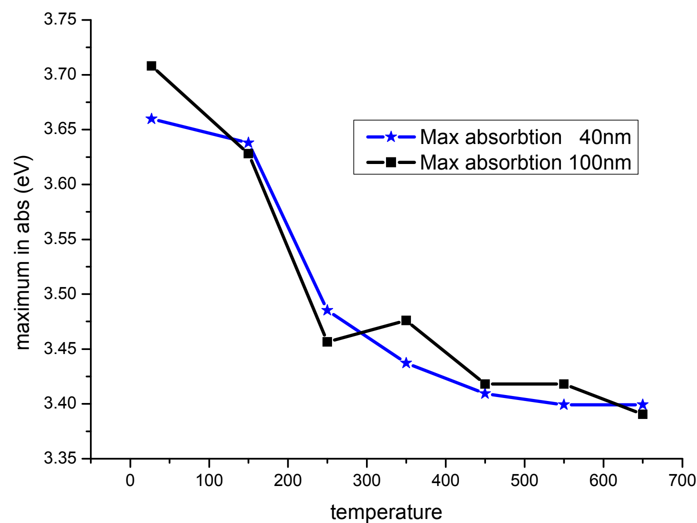

Figure 5.3.5 a Optical bandgap energy and b additional absorption band energy of ZnO thin films with 40nm and 100nm thickness as a function of the growth temperature.

The study of the additional absorption band and the reproducibility on its maximum variation with temperature for both thicknesses for ZnO films grown by PLD together with the presented results concerning ZnO films grown by DC magnetron sputtering already presented in the previous chapter may become the subject of further research for deeper understanding of nanostructured materials optical properties. It may prove also having a significant role in films photoreduction process with UV light (λ=254nm). At this point is not possible to explain on theoretical bases and predictions even the presence of such an absorption in the spectrum. Experimentally this absorbtion was observed also by other researchers for ZnO and GaN, both wide band gap materials and only mentioned as appearing. A possible explanation bases on the assumption that it is the first exciton absorption edge.

5.4. Electrical properties – sensing

The effects of the growth conditions on the conductivity value of ZnO films grown by PLD were rigorously studied, the corresponding values included in the table at the end of this section.

The conductivity of the as-deposited ZnO thin films was determined to be in the range from 8.75x10-5 up to 102 Ω-1cm-1, the actual value depended on the deposition conditions. The conductivity was found increasing up to five orders of magnitude after the exposure of the films to ultraviolet (UV) light in vacuum. Moreover, after ozone exposure of the films, the reduction in the conductivity was slightly lower, a fact which can be connected with irreversible surface photoeffects, also noticed in the case of ZnO from DC magnetron sputtering and In_2O_{3-x}. As examples of the conductivity of as deposited films and its dependence on the substrate temperature during growth and the film thickness are shown in the figures 5.4.1 and 5.4.2.

Figure 5.4.1 presents the variation of the conductivity of the as deposited ZnO films as a function of the film thickness. As can be seen, for films thicker than 100 nm, increasing thickness improves the conductivity of the films. Only the 40 nm film seems to deviate from this behavior. The observed increase in the conductivity can be correlated with the decreased concentration of grain boundaries in thicker films due to the presence of bigger grains and improved crystallinity, which can reduced scattering processes and increase the conductivity. In addition, the increasing of the thickness can lead to higher concentration of intrinsic defects and thus to an increased conductivity.

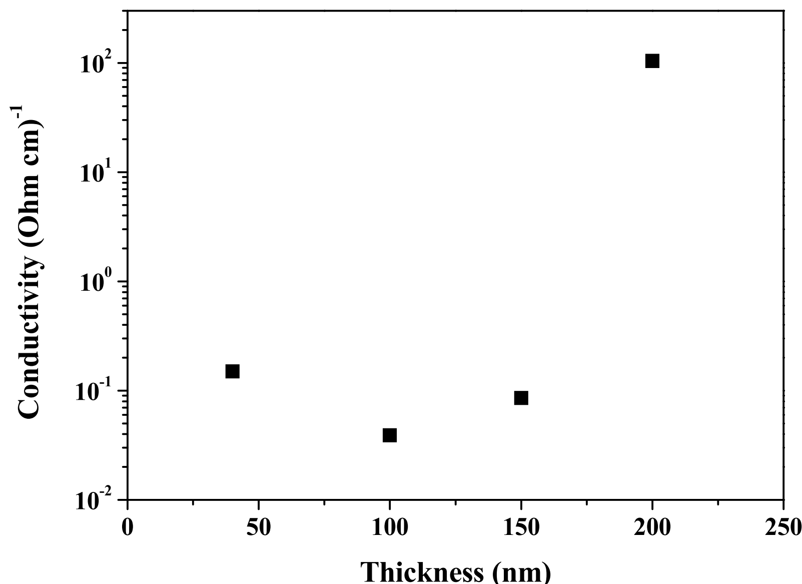

Figure 5.4.1 Conductivity of the as deposited ZnO films as a function of the film thickness.

Figure 5.4.2 presents the variation of the conductivity of ZnO film with thicknesses of 40 and 100 nm. As can be seen, for films deposited in the range of temperature between 150 and 650 ˚C, the conductivity presents a monotonous decreasing, a behavior consistent with that reported in literature [1,2]. The RT film however seems to deviate from this behavior, its conductivity being quite small. The

decrease of the conductivity can be simply attributed to the improved stoichiometry of the ZnO films with increasing temperature, since this improvement can induce a decrease in the concentration of the intrinsic defects.

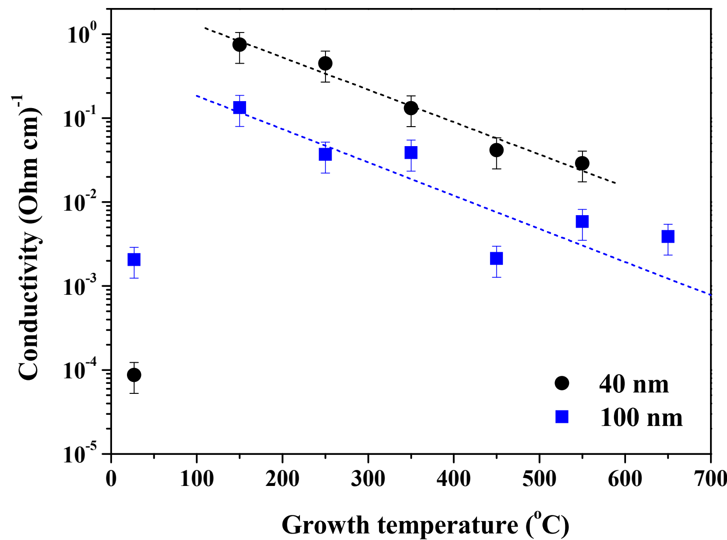

Figure 5.4.2 Conductivity of the as deposited ZnO films as a function of growth temperature.

As mentioned earlier, the photoreduction/oxidation treatment of the ZnO films resulted in an increase/decrease of the conductivity. For the case of the thickness series films, an increase of about three orders of magnitude was recorded under photoreduction, while, under ozone oxidation, the maximum reduction of the conductivity was to two orders of magnitude. This behavior is clearly seen in figure 5.4.3, which shows one photoreduction and ozone oxidation cycle for the ZnO films with a thickness of 40, 100, 150 and 200 nm.

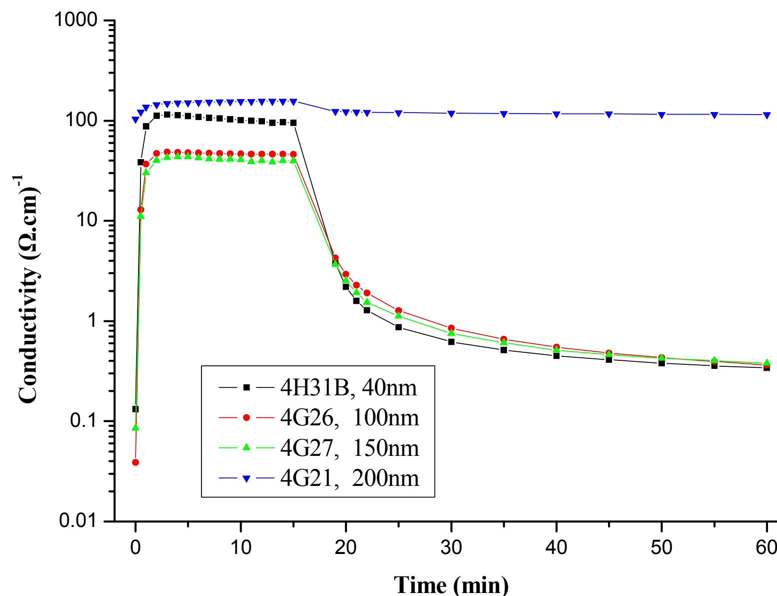

Figure 5.4.3 Photoreduction and ozone oxidation cycle for the ZnO films with a thickness of 40, 100, 150 and 200 nm.

In the case of 200 nm thick film, the conductivity change was very small, a fact which can be attributed to the presence of nanorods on the surface thus to a improved surface crystallinity and stoichiometry leading to lower oxygen vacancies concentration even if it has the highest RMS value. The roughness compared with conductivity changes for the 40, 100 and 150nm thick, shows the strong influence of film topology on film sensitivity and permits optimization of ozone sensitivity though growth parameters. An example regarding the film sensitivity correlation with surface parameters for thickness serie is shown bellow. Complete results will be presented in the correlations chapter.

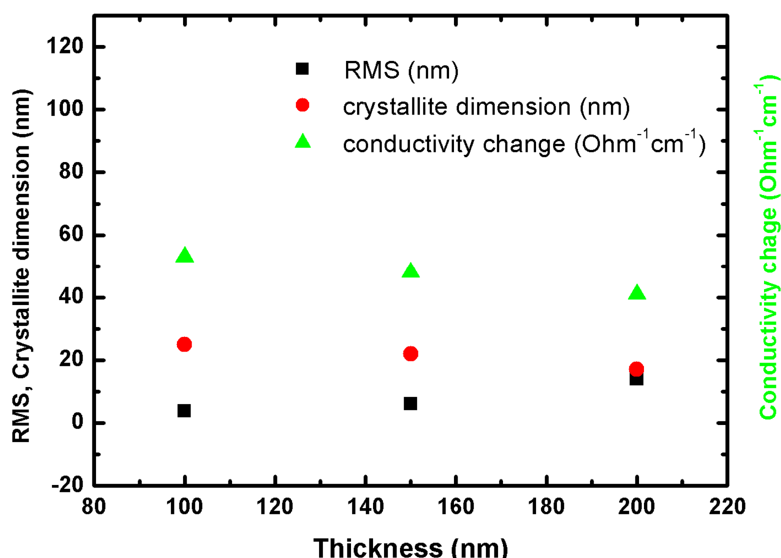

Figure 5.4.4 Conductivity changes correlation with RMS surface parameter and crystallite dimensions for a thickness serie ZnO PLD grown thin films.

Comparing the variation of the conductivity changes with those of the surface RMS from the AFM measurements (Figure 5.5.4, square points), it can be seen that as the RMS is increasing, the conductivity changes are decreasing. The bulk crystallite dimensions also decrease with increasing film thickness (Figure 5.5.4, circular points). The lateral grain size variation with thickness observed by AFM (grain size dimensions increasing with thickness) can be due to the possible formation of surface grains by agglomeration of a number of smaller crystallites.
Therefore the effect of the thickness on the film sensitivity is a result of structural surface properties and, as the thickness increases the ozone sensitivity decreases.

The results of the photo-reduction and oxidation treatments of two series of ZnO films deposited by PLD at different substrate temperature are presented in Figures 5.4.5 a and b. As can be seen, the reduction of the as-deposited films resulted in a 5 to 8 orders of magnitude increase of conductivity, the actual response depending on growth temperature. The subsequent oxidation in ozone leads in a drop of conductivity by 1 to 6 orders of magnitude, a behavior completely reversible through many cycles of photo-reduction and oxidation.

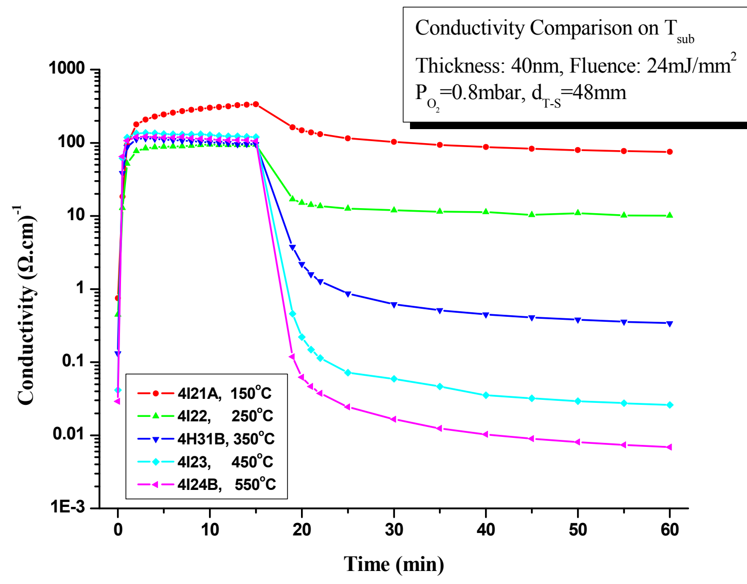

a

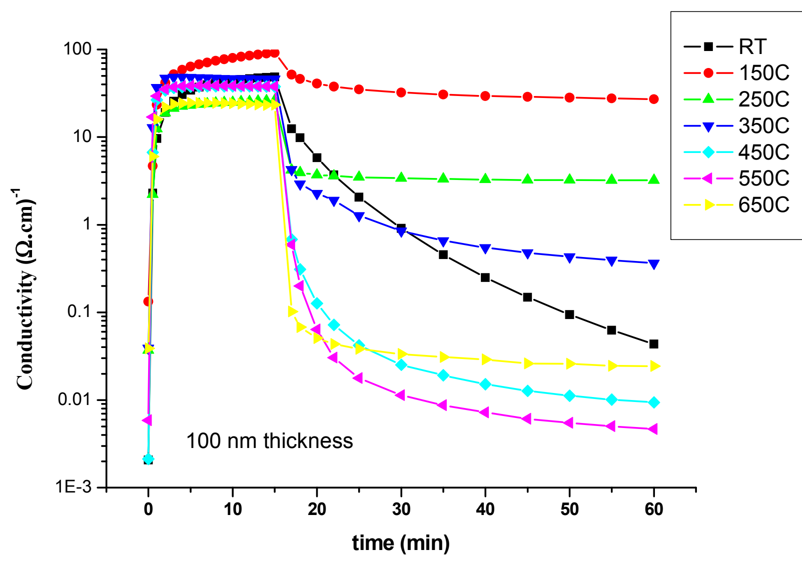

b

Figure 5.4.5 Photoreduction and ozone oxidation cycles for the ZnO films with a thickness of a 40nm, b 100nm, grown at different substrate temperatures.

The dependence of the conductivity changes on the growth temperature can be attributed to the improved evolution of the surface of the films with temperature.
This can be seen in figure 5.4.6, which presents the variation of conductivity changes under ozone exposure with that of the parameter SFD, SDR and SBI, obtained from the AFM measurements. As can be seen, SBI correlates better with the conductivity changes.

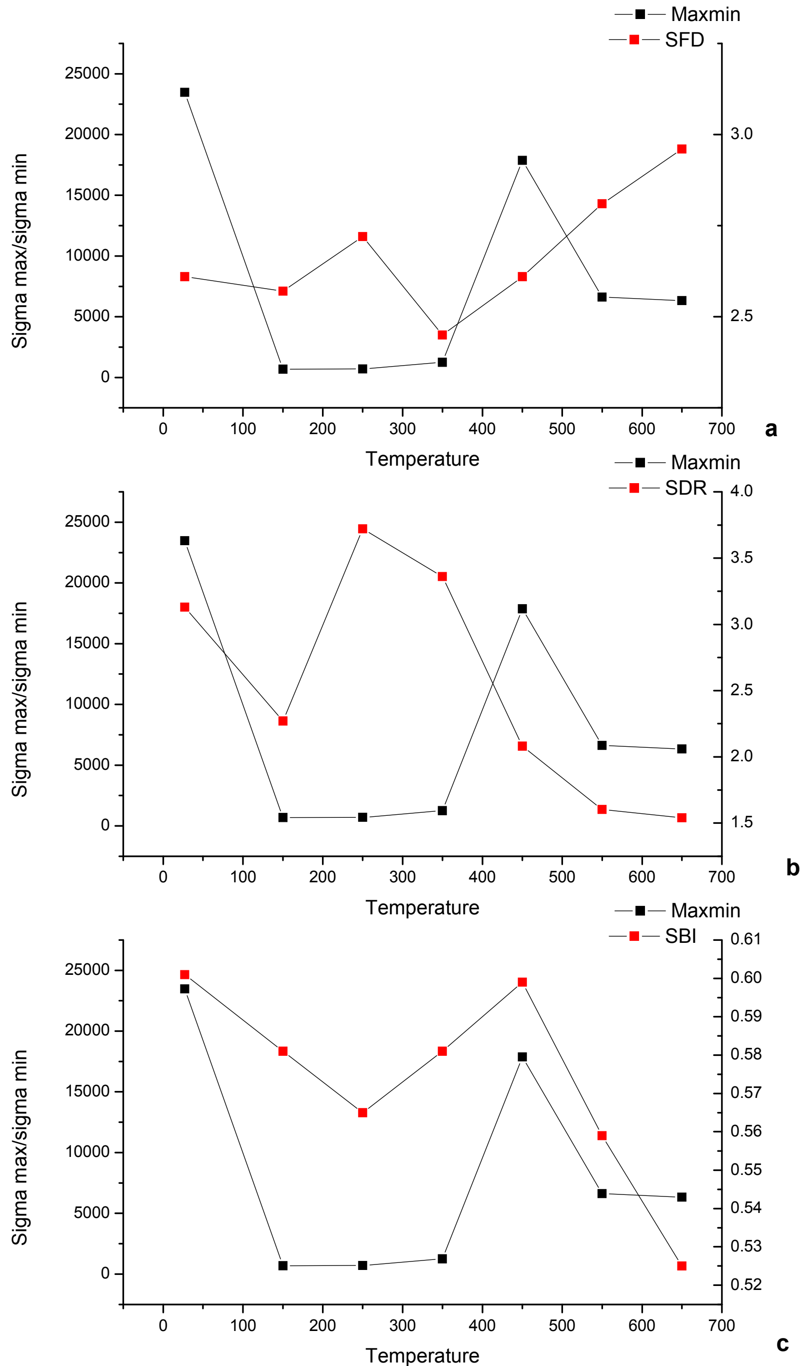

Figure 5.4.6 Variation of conductivity changes under ozone exposure with that of the parameter a SFD, b SDR and c SBI, obtained from the AFM measurements.

The influence of the growth temperature on the conductivity change under photo-reduction and oxidation can be attributed on the alterations of the film surface morphology. In the initial stages of the film growth, various processes can occur such as collision fragment deattachment, cluster nucleation, trapping on surface by defects. The key issue is the mobility of the atoms deposited on the surface. At certain temperatures, only the processes exceeding a certain energy threshold are possible, at lower temperatures being inhibited. In other words, the closer the temperature of the substrate is to the melting temperature of the film, the more film

relaxation channels are energetically accessible. At low substrate temperatures (RT), the film growth enables metastable structures due to athermal growth. This may be the reason for the inconsistent behavior of RT grown film which can be associated with the lack of stoichiometry. At higher temperatures, film grain boundaries gain mobility and the surface diffusion and recrystallisation occurs more efficiently, inducing improved structural properties.
These results and correlations made the subject of some publications during this work as shown in the references at the end of this chapter.

1 J. L. Zhao, X. M. Li, J. M. Bian, W. D. Yu, X. D. Gao, J. Cryst. Growth, 276 (2005) 507-512.

2 J. Zou, S. Zhou, C. Xia, Y. Hang, J. Xu, S. Gu, R. Zhang, J. Cryst. Growth, 280 (2005) 185-190.

5.5 Conclusions

This chapter is dedicated to the growth and the properties of pure ZnO thin films grown by PLD under different growth conditions. The films were grown from sintered ceramic targets and the investigation concerned the influence of thickness (for constant growth temperature) and growth temperature (for constant thickness) on the properties of the films. The results can be summarized as following:

- All films were polycrystalline (even the thinnest ones, or the ones grown at room temperature) with columnar grains and textured with preferential orientation along [002] crystalline direction of the wurzite structure.
- Films grown by PLD seem to have higher stoichiometry than films grown by DC magnetron sputtering.
- UV-Vis optical transmittance showed that all films are highly transparent (80-90% transmittance) in visible spectral region. From the UV absorption minima, corresponding to direct transition across the bangap, the energy gap was estimated, being for all films smaller than that of the bulk value, 3.37eV. The energy gap was found increasing slightly with increasing thickness, the opposite appearing with increasing growth temperature. Moreover, an excitonic band was observed, the position of its maximum depending also on the film thickness and the growth temperature.
- Regarding the electrical properties of the as-deposited films, increasing substrate temperature was found to induce a decrease in the conductivity, the opposite appearing with increasing thickness. Only films grown at RT of having quite small thickness were found to deviate from this behavior.
- It was proved that there is a connection between surface topography and conductivity change under photoreduction and ozone oxidation. Therefore, a systematic analysis based on experimental results may lead to the selection of the most significant surface parameters, which can be used for more general correlations of the properties of the films with their sensing response.

References

- M. Suchea, M. Katharakis, S. Christoulakis, N. Katsarakis, G. Kiriakidis, “Surface Analysis of ZnO Transparent Thin Films”, 2005 *J. Phys.: Conf. Ser.* 10 147-150
- S Christoulakis, M Suchea , M Katharakis, N Katsarakis , E Koudoumas and G Kiriakidis, “ZnO nanostructured transparent thin films by PLD” Review on Advanced Materials Science 10 (2005) 331-334 (http://www.ipme.ru/e-journals/RAMS/no_41005/christoulakis.pdf)
- G. Kiriakidis, M. Suchea, S. Christoulakis and N. Katsarakis, “High performance gas sensing materials based on nanostructured metal oxide films”, Review on Advanced Materials Science 10 (2005) 215-223 (http://www.ipme.ru/e-journals/RAMS/no_31005/kiriakidis.pdf)
- S Christoulakis, M Suchea, E Koudoumas, M Katharakis, N Katsarakis ,G Kiriakidis, “Thickness influence on surface morphology and ozone sensing properties of nanostructured ZnO transparent thin films grown by PLD”, Applied Surface Science 2006 (doi:10.1016/j.apsusc.2005.12.071)
- Christoulakis, S., Suchea, M., Koudoumas, E., Katharakis, M., Katsarakis, N., Kiriakidis, G “Thickness influence on surface morphology and ozone sensing properties of nanostructured ZnO transparent thin films grown by PLD” (2006) Applied Surface Science, 252 (15), pp. 5351-5354. Cited 20 times.
- Suchea, M., Christoulakis, S., Katharakis, M., Kiriakidis, G., Katsarakis, N., Koudoumas, E. ”Substrate temperature influence on the properties of nanostructured ZnO transparent ultrathin films grown by PLD” (2007) Applied Surface Science, 253 (19), pp. 8141-8145. Cited 4 times.
- Suchea, M., Christoulakis, S., Tibeica, C., Katharakis, M., Kornilios, N., Efthimiopoulos, T., Koudoumas, E. “Structural and morphological properties of thin ZnO films grown by pulsed laser deposition” (2008) Applied Surface Science, 254 (17), pp. 5475-5480. Cited 2 times.
- Suchea, M., Christoulakis, S., Katharakis, M., Vidakis, N., Koudoumas, E. “Influence of thickness and growth temperature on the optical and electrical properties of ZnO thin films” (2009) Thin Solid Films, 517 (15), pp. 4303-4306.

Annex 5A: Growth parameters for ZnO thin films grown by PLD.

run	dts	ts	ss	fluence	puls no.
1	47	360	8	21	5.4E+03
2	47	360	8	22	5.4E+03
3	47	360	8	23	5.4E+03
4	48	360	8	24	6.0E+03
5	48	360	8	24	6.0E+03
6	48	360	8	24	6.0E+03
7	48	350	8	24	1.0E+03
8	48	350	6	31	5.0E+02
9	48	350	6	31	5.0E+02
10	48	350	8	24	7.5E+02
11	48	350	8	24	7.5E+02
12	48	350	10	19	4.0E+02
13	48	350	10	19	4.0E+02
14	48	350	7	23	2.0E+03
15	48	350	7	23	2.0E+02
16	48	350	8	24	5.0E+01
17	48	23	8	24	2.0E+02
18	48	150	8	24	2.0E+02
19	48	23	8	24	5.0E+02
20	48	450	8	24	2.0E+02
21	48	550	8	24	4.0E+02
22	48	550	8	24	2.0E+02
23	48	650	8	24	2.0E+02
24	48	350	8	24	1.0E+03
25	48	350	6	31	5.0E+02
26	48	450	10	19	5.0E+02
27	48	450	10	19	5.0E+02
28	48	110	10	21	5.0E+02
29	48	100	10	21	5.0E+02
30	48	21	8	24	5.0E+02
31	48	21	8	24	5.0E+02
32	48	150	8	24	5.0E+02
33	48	150	8	24	5.0E+02
34	48	250	8	24	5.0E+02
35	48	250	8	24	5.0E+02
36	48	450	8	24	5.0E+02
37	48	450	8	24	5.0E+02
38	48	550	8	24	5.0E+02
39	48	550	8	24	5.0E+02
40	48	650	8	24	5.0E+02
41	48	350	8	24	1.0E+03
42	48	350	8	24	5.0E+02
43	48	350	8	24	5.0E+02
44	51	350	8	22.5	1.0E+03
45	51	350	8	22.5	1.0E+03

Chapter 6

The effect of doping on physical properties of ZnO transparent thin films grown by DC magnetron sputtering

Outlines

- **Growth of Al, In and AlSi doped zinc oxide transparent thin films were prepared onto silicon and Corning glass substrates by DC magnetron sputtering using metallic and ceramic targets under similar deposition conditions**
- **Characterization: structural, surface, optical, electrical**
- **Particular correlations of different parameters comparison with undoped ZnO grown by DC magnetron sputtering.**
- **Annex 6A Growth parameters for doped ZnO films grown by DC magnetron sputtering.**

6.1 ZAO thin films grown by DC magnetron sputtering

Zinc oxide (ZnO) and aluminum zinc oxide (ZAO) transparent thin films with different thicknesses were prepared onto silicon and Corning glass substrates by DC magnetron sputtering using metallic and ceramic targets. In the case of the ZAO films Al-doped metallic (ZnAl2%*) and ceramic (ZnAl2%O) targets were employed. The deposition was carried out using the Alcatel DC magnetron sputtering system, already presented in the experimental section. Films with a thickness of about 100nm were grown onto the Corning 1737F glass and silicon substrates in an oxygen-argon atmosphere, the deposition parameters being: total pressure 8×10^{-3} mbar and substrate temperature 27 ^{o}C (RT). Finally, the depositions were done for two different plasma current settings, 0.44 A and 0.25 A.

XRD characterization showed that all films are polycrystalline with preferential orientations the [002] and the [103] basal plane reflections of wurtzite ZnO, for the case of the ZnO films and the [002] for the ZAO ones. Some typical diffractograms are presented in figure 6.1.1a. For the metallic targets, the [002] peak was found shifted to lower angles, the crystallinity of the films being decreased. The [002] diffraction peak position approaches but never reaches that of the bulk ZnO, which has a value of 34.42°. Best results were obtained for films grown from a ceramic target, the interplanar distance approaching the theoretic value for fully stoichiometric ZnO.

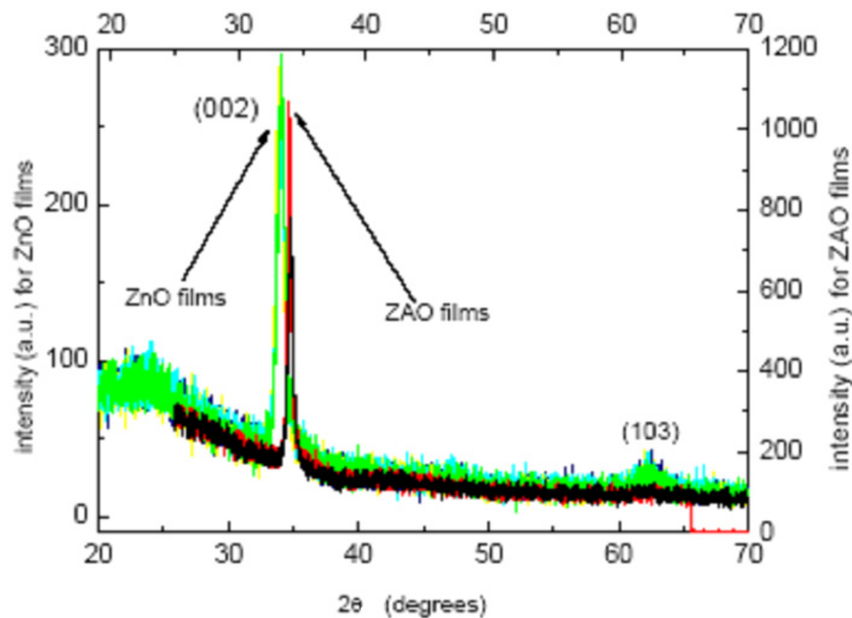

A

* The dopants are mentioned as atomic percentage in the respected dominant material (eg. ZnAl2 corresponds to 2% metallic Al atoms in metallic Zn, when ZAO2 corresponds to 2% Alumina (Al_2O_3) in ceramic ZnO targets)

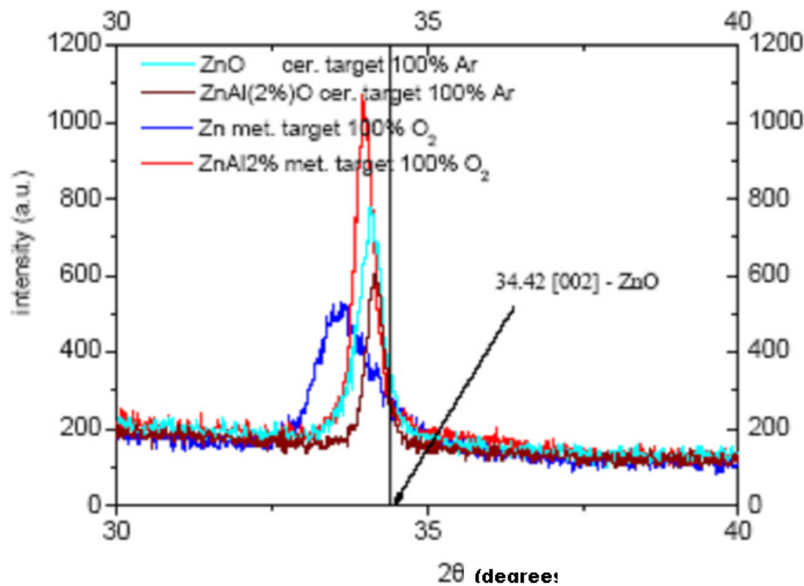

b

Figure 6.1.1 XRD diffractograms of ZnO and ZAO films a general behavior, b closer look at the peak corresponding to [002] orientation.

The ZAO films exhibited only the [002] peak in the displayed 2θ/ω region, with no metallic Zn or Al characteristic peaks present, while the ZnO films are found to be composed of mixed crystallites with orientations of [002] and [103]. The characteristic parameters given by XRD from the [002] plane were used to characterize the features of the ZnO and ZAO films shown in figure 6.1.1b. The 2θ/ω diffraction angle ranges from 33.669° for ZnO films grown from Zn metallic target, to 34.16° for ZnO films grown from ceramic target, the corresponding full width at half maximum (FWHM) being from 0.862° to 0.304°. In the case of the ZAO films, the 2θ/ω diffraction angle ranges from 33.980°, for films grown from ZnAl2% metallic target, to 34.085°, for films grown from ceramic target, the corresponding full width at half maximum (FWHM) being from 0.317° to 0.402°. In all cases, the 2θ/ω diffraction peak position approaches, but never reaches that of the bulk ZnO, which has the value of 34.42 °. Obviously, the films show [002] textures and the [002] peak shifts to lower angle for the case of metallic targets, which correspond as well to a decreased film crystallinity, indicated by both the lower peak intensity and a crude peak broadening. Cebulla et al [1] attributed the shift to lower diffraction angles to a significant increase of compressive stress, with a decrease of the oxygen concentration. This leads to the presence of higher oxygen vacancies, a fact which can explain the shift from the extreme value of 33.669° for ZnO films grown from Zn metallic target in high O_2 concentrations, to a more optimum value of 34.16° for ZnO films grown from ceramic target in high concentrations of Ar. Kuroyanagi et al. [2] attributed the shifts towards lower angles from the [002] plane for the case of the Al doped ZnO films, grown by ionized deposition, to the ionization of ZnO rather than the Al doping. Gupta et al. [3] have observed that sputtered ZAO films are in a uniform state of stress with tensile components parallel to c axis that could also result in a shift towards lower diffraction angle. These observations are in line with what was observed in this work for ZAO films. Films grown under different O_2:Ar plasma concentrations did not show any significant variations in the XRD diffractograms.

AFM images of the surfaces of ZnO and ZAO thin films deposited at room temperature from metallic and ceramic targets, under varying Ar/O_2 flow ratios, are shown in figure 6.1.2.

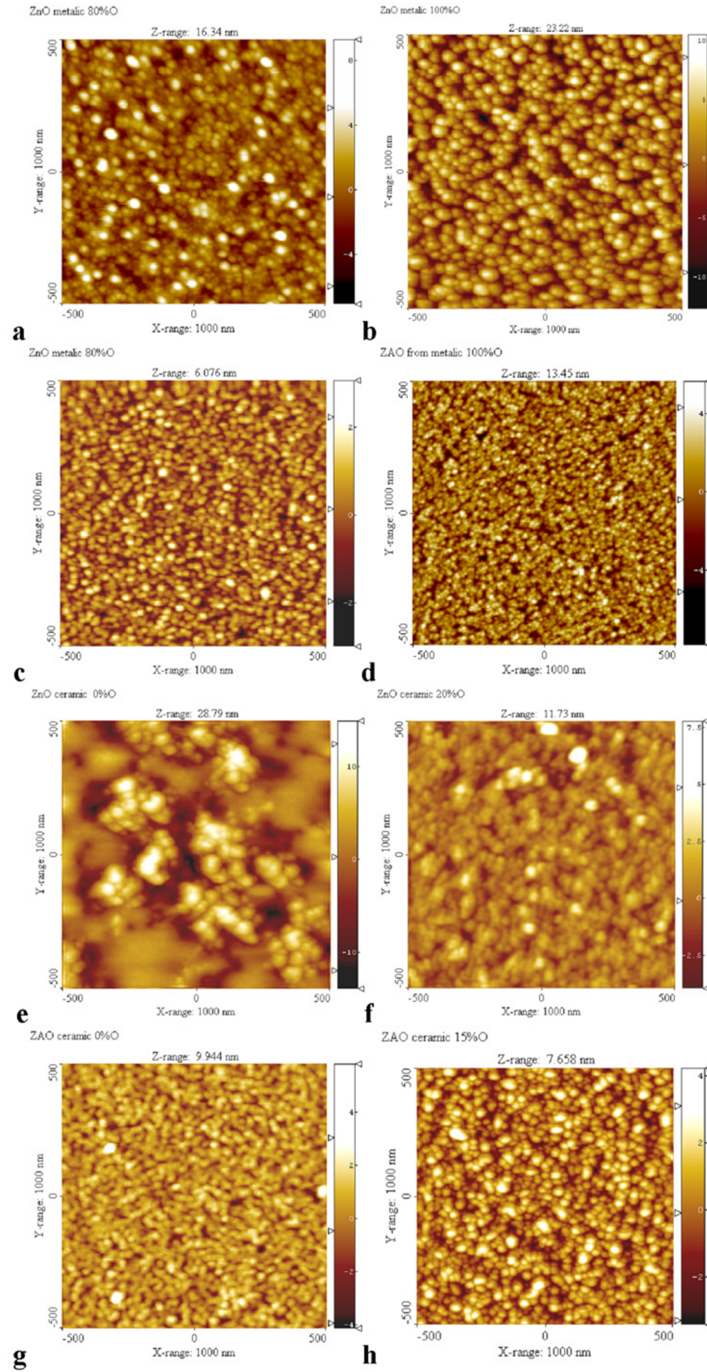

Figure 6.1.2 1×1 µm scan size 2D AFM images of films grown: (a) from Zn metallic target in 80% O_2 concentration, (b) from Zn metallic target in 100% O_2, (c) from ZnAl2% metallic target in 80% O_2 concentration, (d) from ZnAl2% metallic target in 100% O_2, (e) from ZnO ceramic target in 0% O_2, (f) from ZnO ceramic target in 20% O_2 (g) from ZAO ceramic target in 0% O_2, (h) from ZAO ceramic target in 15% O_2.

AFM characterization for the films deposited from a metallic target (figure 6.1.2a, 6.1.2b for ZnO and 6.1.2c, 6.1.2d for ZAO) revealed a granular, polycrystalline morphology, the grain size decreasing and the roughness increasing as the oxygen partial pressure in the plasma was decreased. In the case of films grown

from a ZnO ceramic target (figures 6.1.2e, 6.1.2f) the surface had a complete different morphology, being dominated by grain agglomerations and very tall features, while, films grown from ZAO ceramic target presented a very smooth and homogeneous surface, as shown in figures 6.1.2g, 6.1.2h. The grain size, derived with the SPIP software from the AFM measurements, was found varying from 50 to 20 nm, for ZnO deposited from a metallic target when O_2:Ar ratio in the plasma was varied. In the case of ZnO films deposited from a ceramic target, the dimensions of the agglomerates were varying from 500 to 50 nm, the corresponding subgrain dimensions being in the range of 10-50 nm for the same O_2:Ar ratio variation. For ZAO films grown from ZnAl2% metallic target, the grain size was found to vary from 75 to 30 nm while for ZAO films grown from a ceramic target from 15 to 40 nm. In general, the overall surface of the ZAO films was formed by smaller and more homogeneous grains, as compared to that of the ZnO films. The above mentioned microstructural differences can be directly attributed to the film growth rate variation. The growth rate increases when the O_2 partial pressure decreases due to the presence of Ar atoms in the plasma. In the case of growth from a metallic target, films deposited at higher O_2 ratio (figures 6.1.2a, c) presented bigger, better-formed grains, whereas those deposited at higher Ar ratio (figures 6.1.2b, d) had a uniform, smaller size grain distribution. These observations may be attributed to the introduction of oxygen in the plasma, which could also generate high-energy oxygen neutral atoms. It is generally believed that the formation of grain agglomerations in film deposited under the presence of oxygen might be due to re-sputtering of high-energy neutral oxygen atoms [4]. As oxygen content in the plasma increases, the re-sputtering effect by high-energy neutral oxygen atoms can also increase. Subsequently, it might accelerate the grain growth (or aggregation of particles) and thus change the surface topology of the film at the initial stage of the film growth. For films grown from a ceramic target, the growth rate had a remarkable increase as compared to that of the metallic target case, for both ZnO and ZAO, due to the high Ar ion concentration in the plasma. The surface roughness variations of the ZnO and ZAO thin films deposited at different O_2/Ar ratio are shown in figure 6.1.3.

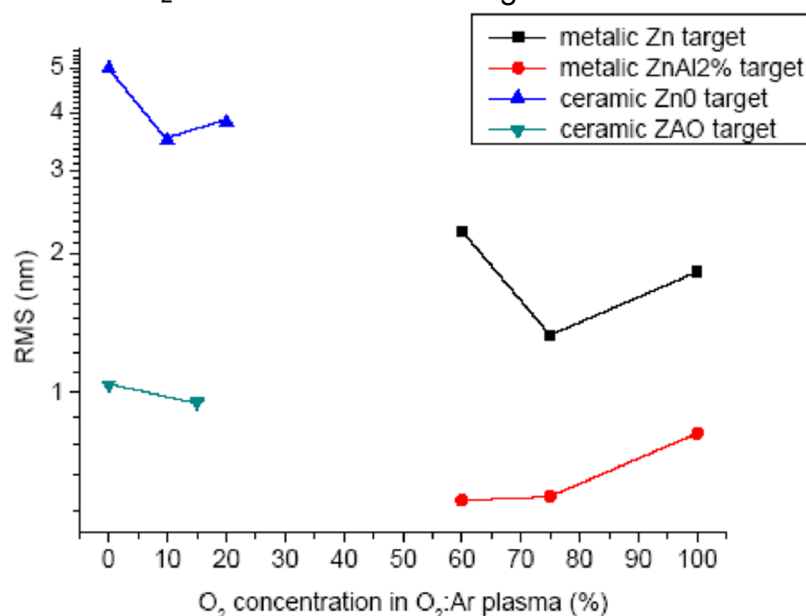

Figure 6.1.3 The surface roughness variations of the ZnO and ZAO thin films deposited at different O_2/Ar ratio.

The scan area for the determination of the surface roughness was 5x5 μm. It can be observed that the surface roughness (RMS) of the ZAO films is generally much smaller than that of the ZnO ones. This indicates the role of Al dopant as a mineralizer or surfactant that can significantly improve the texture of the layers.

The effect of the O_2: Ar ratio in the plasma on the optical properties of the films was also investigated. Figure 6.1.4 shows the normalized UV-VIS transmittance of different films grown from the four different targets mentioned before on Corning glass at RT.

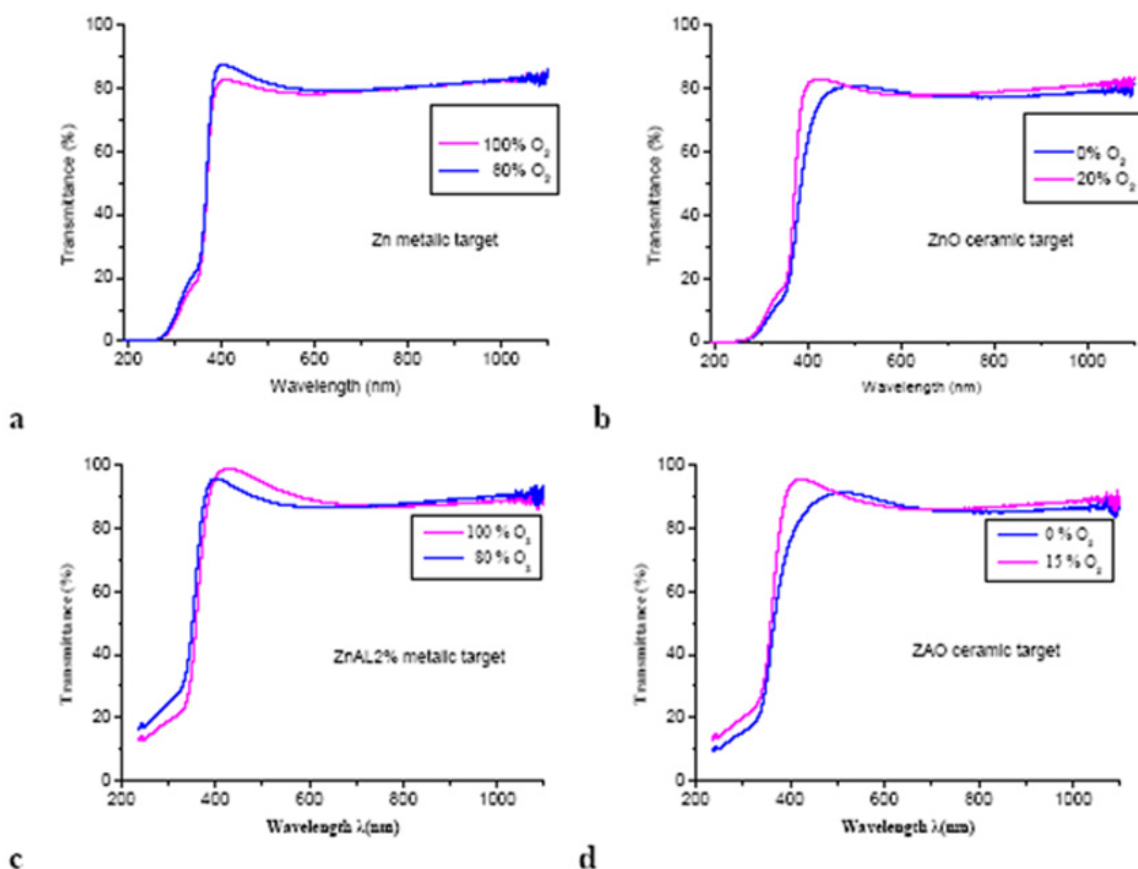

Figure 6.1.4 Variation of the UV-VIS transmittance with O_2 concentration in the plasma for films grown: (a) from Zn metallic target, (b) from ZnO ceramic target (c) from ZnAl2% metallic target (d) from ZAO ceramic target.

All films were found to exhibit a transmittance higher than 80% in the visible spectral region and a sharp absorption edge. As shown in figure 6.1.5a the transmission of all films grown from ceramic targets was observed to increase slightly when the O_2 concentration in the plasma was increasing. In the case of metallic target, the variation in the transmission, as a function of the O_2 content in the plasma, did not show any significant trend. However, notable changes on the UV-VIS transmittance were recorded when Al was introduced in the ZnO films, since ZAO films grown from both metallic and ceramic targets were found to exhibit higher transmittance in visible region. Therefore, Al-doping enhances the optical transmittance of the ZnO films to values of the order of 90%, which make them suitable for use as glass window coating material.

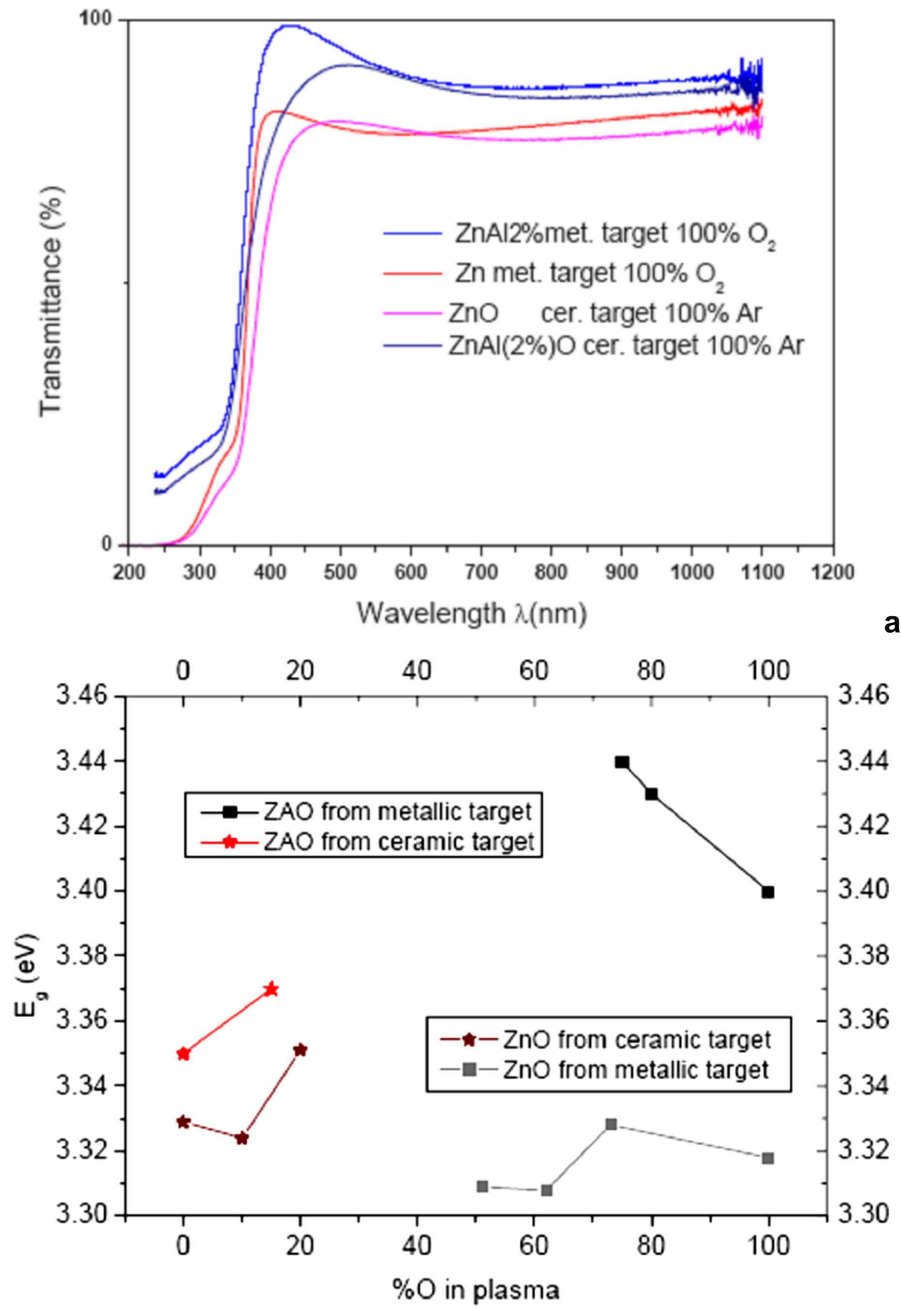

Figure 6.1.5 a UV-VIS transmittance comparison of films grown from Zn metallic target, ZnO ceramic target, ZnAl2% metallic target and ZAO ceramic target b Optical bandgap variation with O_2/Ar ratio in plasma.

The optical band gap was calculated and it is in the range of 3.31 to 3.35 eV for ZnO films and from 3.35 to 3.43 eV for ZAO films. The optical band gap was dependent on the O_2/Ar ratio in the plasma; since this was generally increasing with increasing O_2 contend in the plasma, as shown in figure 6.1.5b. Moreover, the optical band gap of the ZAO films was found to have slightly higher values than that of ZnO. It is known that the conduction electrons in ZnO films are supplied from donor sites, associated with oxygen vacancies or excess metal ions. In general the conduction characteristics of ZnO are primarily dominated by electrons generated from O_2 vacancies and Zn interstitial atoms, which determine the shift of

the optical band gap to values smaller than the bulk one, 3.37 eV. The increase of the band gap with O_2 concentration can be associated with the decrease of the growth rates for all targets leading to a relative improved stoichiometry, therefore a closer value of the energy gap of the film to that of the bulk material. For ZAO films, the contribution from Al^{3+} ions on substitutional sites of Zn^{2+} ions and Al interstitial atoms determines the widening of the band gap, caused by an increase in the carrier concentration. As presented in the characterizations techniques chapter, Burstein–Moss effect [1] is due to the Fermi level moving into the conduction band. According to the Burstein–Moss effect, the broadening of the optical band gap is given by:

$$\Delta Eg = \left(\frac{\hbar^2}{2m_{vc}^*}\right)\left(3\pi^2 n\right)^{2/3},$$

where ΔE_g is the shift of doped semiconductor compared to undoped semiconductor, m_{vc}* is the reduced effective mass, ħ is Plank constant, and n is carrier concentration. According to this equation the band gap would increase with increasing carrier concentration. However, the band gap obtained for our ZAO films does not accurately follow the equation, being much smaller than predicted (~3.9 eV) from the Burstein–Moss theory for about 2 % Al doped films [5, 6]. This difference can be attributed to the merging of an impurity band into the conduction band, thereby shrinking the band gap and compensating the Burstein–Moss effect and it is in line with previous observations [5].

Finally, the effect of O_2/Ar gas ratio on the conductivity changes under ozone exposure was studied for two plasma currents. Results showed that the film conductivity and its modifications are depended on the O_2/Ar ratio. The photoreduction treatment resulted in an increase of the conductivity of up to six orders of magnitude for the ZnO thin films and up to five orders of magnitude for the ZAO ones. Subsequent ozone oxidation was found to lead to conductivity changes of up to six orders for the ZnO films and up to four orders for ZAO films, as shown in figures 6.1.6a and b.

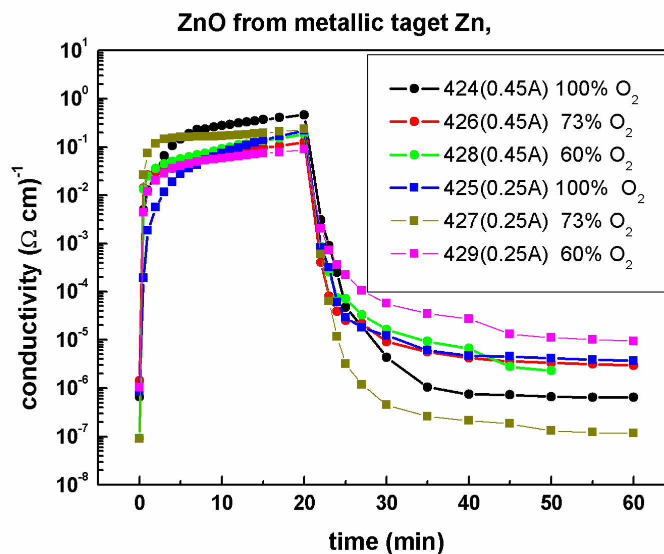

a

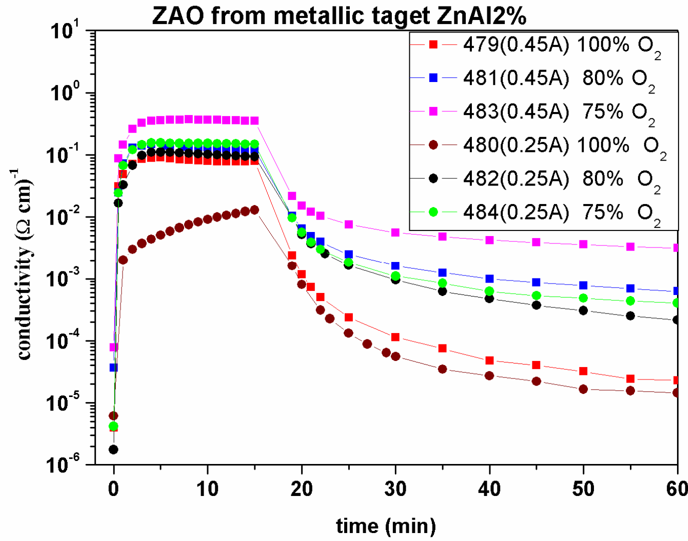

Figure 6.1.6 The effect of O_2/Ar gas ratio on the conductivity changes under UV subsequent ozone exposure for two plasma currents a for ZnO and b for ZAO

The behavior observed in figures 6.1.6a and b was completely reversible through many cycles of photoreduction and oxidation treatments. It is significant to note that the as-deposited ZAO films were exhibiting conductivity systematically higher than that of ZnO films, due to the presence of the Al dopant, as shown in figure 6.1.6. To a lesser degree, Al was also affected the conductivity of the films at the photoreduced state (i.e. after UV illumination). Moreover, ZAO films demonstrated more stable and relatively higher conductivity values at the phororeduced state, regardless of the deposition rates. Subsequent ozone exposure was found to lead to a decrease of the conductivity, to values however higher than those of the as deposited films, possibly due to annihilation of some oxygen vacancies. In conclusion all ZAO films exhibited reduced sensitivity to ozone exposure.

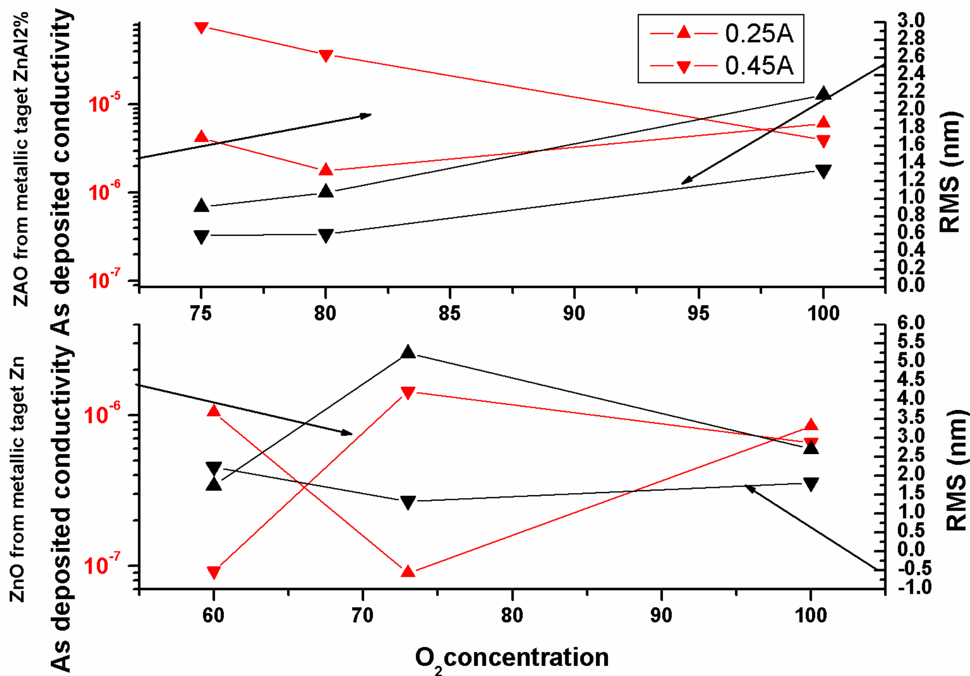

a

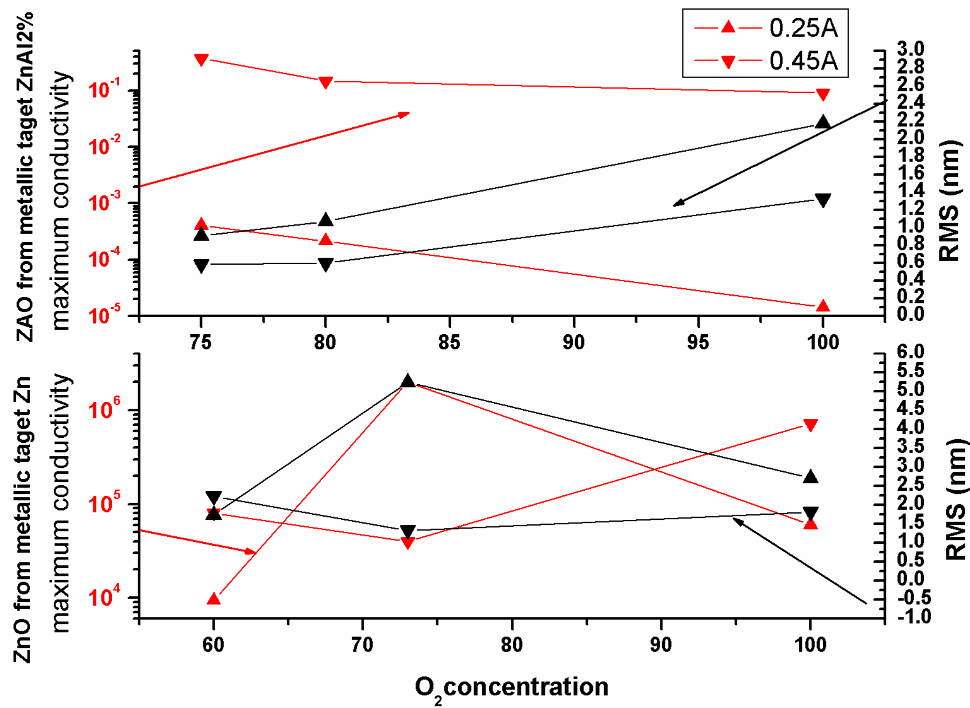

b

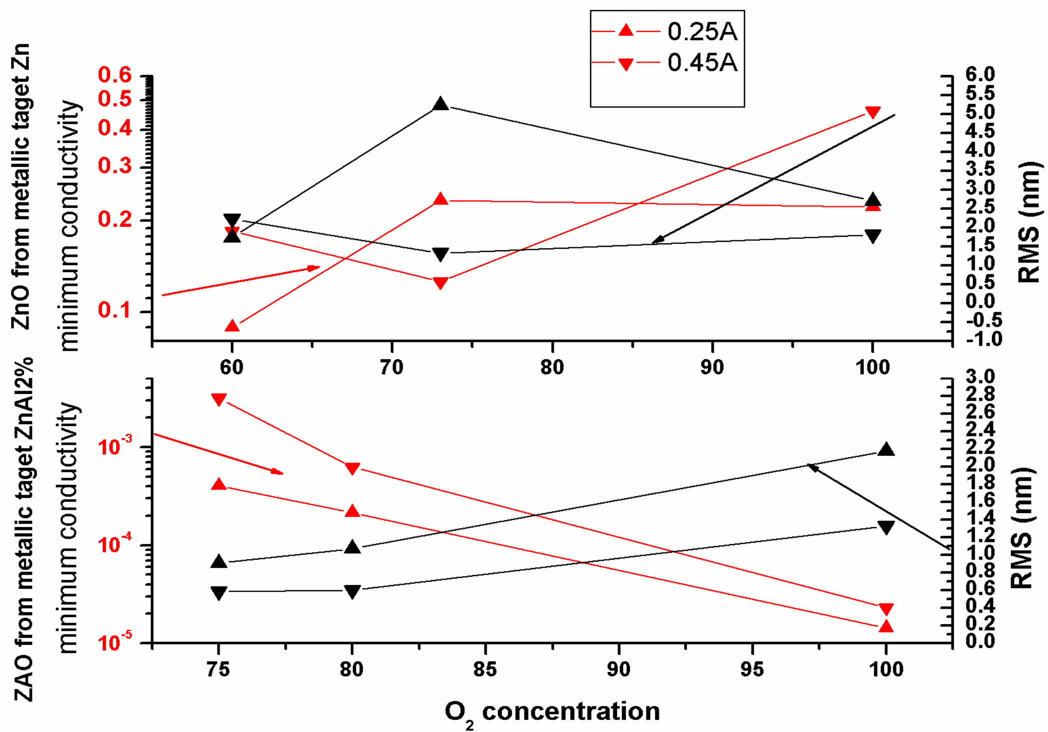

C

Figure 6.1.7 conductivity change with that of the surface RMS from AFM measurements.

Comparing the conductivity change with that of the surface RMS from AFM measurements (figures 6.1.7 (a), (b), (c)), it can be seen that these are correlating,

in the sense that in most of the cases, as the RMS increases, the conductivity decreases. Figures 6.1.7 (a), (b), (c) show also the variation of the RMS and the conductivity change as a function of the O_2 concentration during growth. As the O_2 concentration decreases, the RMS of the ZAO thin films decreases, while, for the case of the ZnO thin films, RMS has not a monotonically variation.

1 R. Cebulla, R. Wendt, and K. Ellmer, J. Appl. Phys. 83, (1998), p.1087.

2 Kuroyanagi, J. Appl. Phys. 66, (1989), p.5492.

3 V. Gupta and A. Mansingh, J. Appl. Phys. 80, (1996), p.1063.

4 S. Mishra,C. Ghanshyama, N. Rama, R.P. Bajpai and R.K. Bedi, Sensors and Actuators B 97 (2004) p. 387.

5 Z. C. Jin, I. Hamberg, and C. G. Granqvist, J. Appl. Phys. 64, (1988), p.5117.,

6 K. C. Park, D. Y. Ma, and K. H. Kim, Thin Solid Films 305, (1997), p.201.

6.2 Si:ZAO thin films grown by DC magnetron sputtering

A 2% Al_2O_3 and 1000 ppm Si-doped zinc oxide (Si:ZAO) ceramic target was used for the growth of thin films by DC magnetron sputtering technique. X-ray diffraction (XRD), atomic force microscopy (AFM), and UV-VIS transmission studies were conducted in order to investigate the physical properties of the deposited films as a function of the deposition parameters.

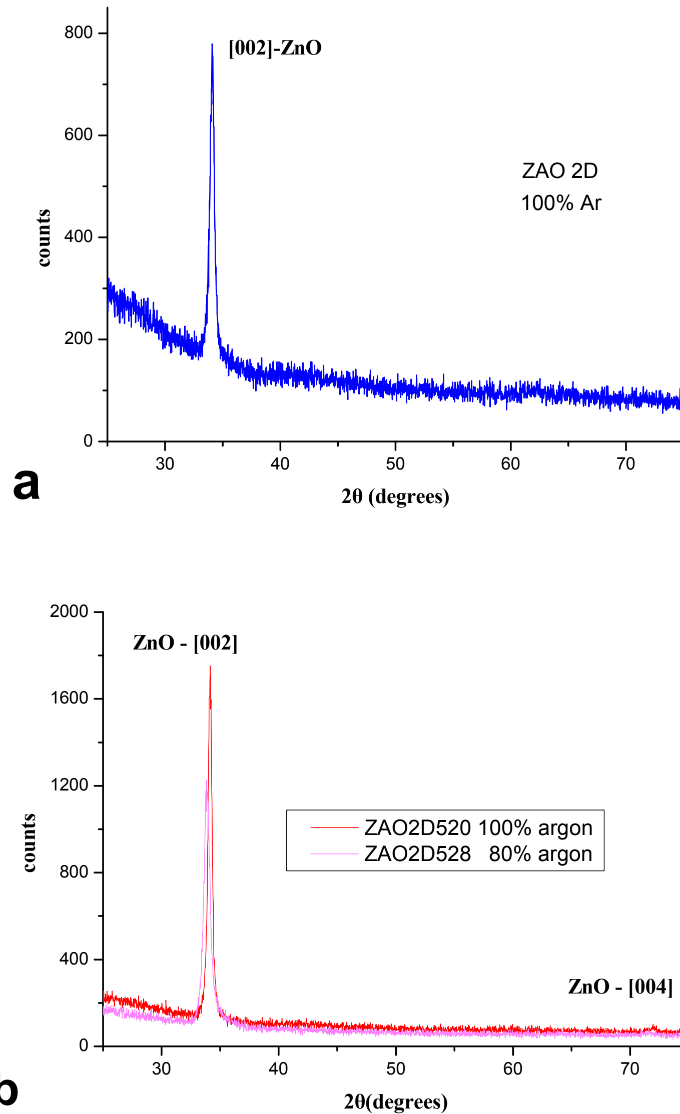

Figure 6.2.1 The x-ray diffractograms of a) ZAO film and b) Si:ZAO deposited on Corning glass.

The general characteristics for all this films were:

- ✓ The films are dominated by the hexagonal ZnO (002) plane confirming the strong (002) textures.
- ✓ The 2θ peak position of the ZAO films was found to be around 34.08°, the corresponding peak for the Si: ZAO films being at about 34.2°

- ✓ The 2θ diffraction peak position approaches, but never reaches that of the bulk ZnO, which has a value of 34.42 °.
- ✓ The shift of the [002] peak to lower angles with respect ZnO [002] position for perfect crystalline structure can be due to tensile stress induced in the presence of the dopant.
- ✓ Film crystallinity seems to be improved by adding Si (higher intensity of the [002] peak). Increase of the oxygen partial pressure leads a decrease of the intensity of the [002] peak.

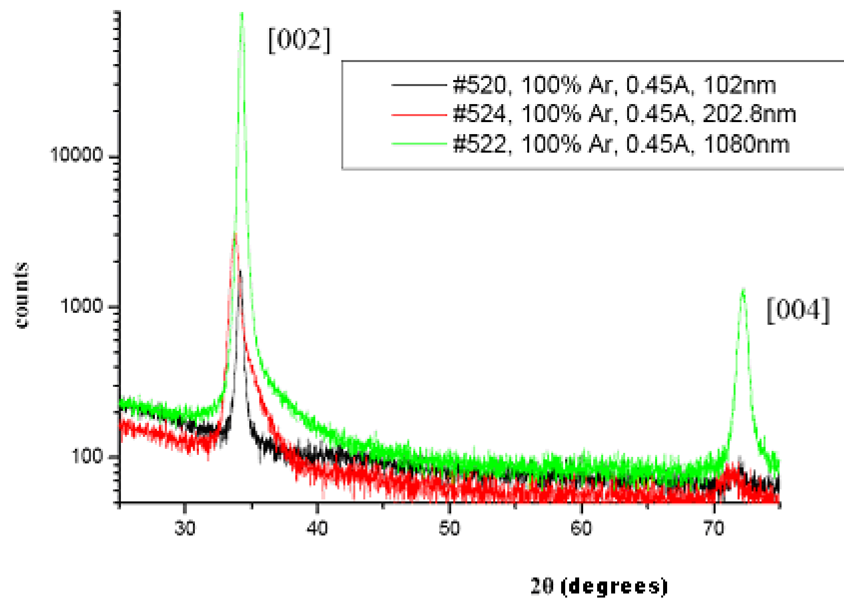

✓

Figure 6.2.2 X-rays diffractograms for Si:ZAO films with different thickness grown in 100%Ar atmosphere at RT.

Figure 6.2.2 presents XRD diffractograms for Si:ZAO films with different thickness grown in 100%Ar atmosphere at RT.

Then, the surface topology and the optical transmission of films grown from Si:ZAO ceramic target were investigated for various thicknesses and various oxygen partial pressures in the sputtering atmosphere.

AFM characterization

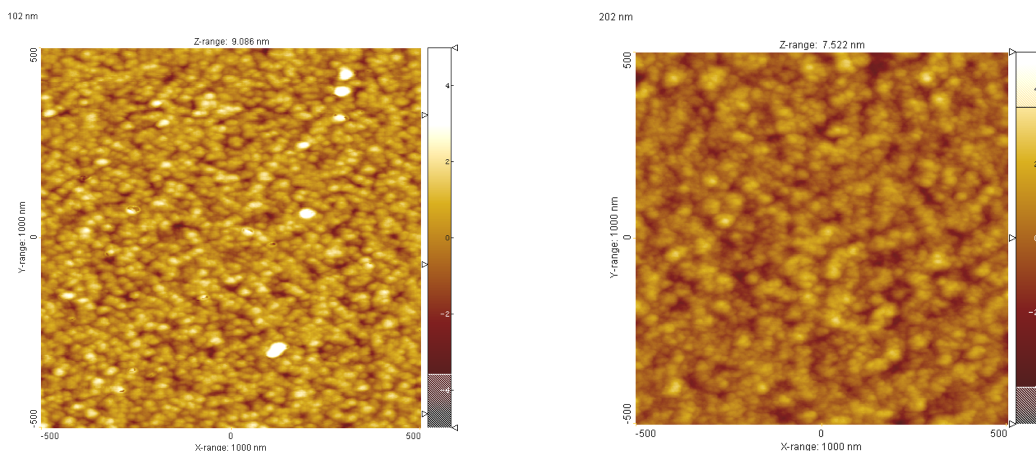

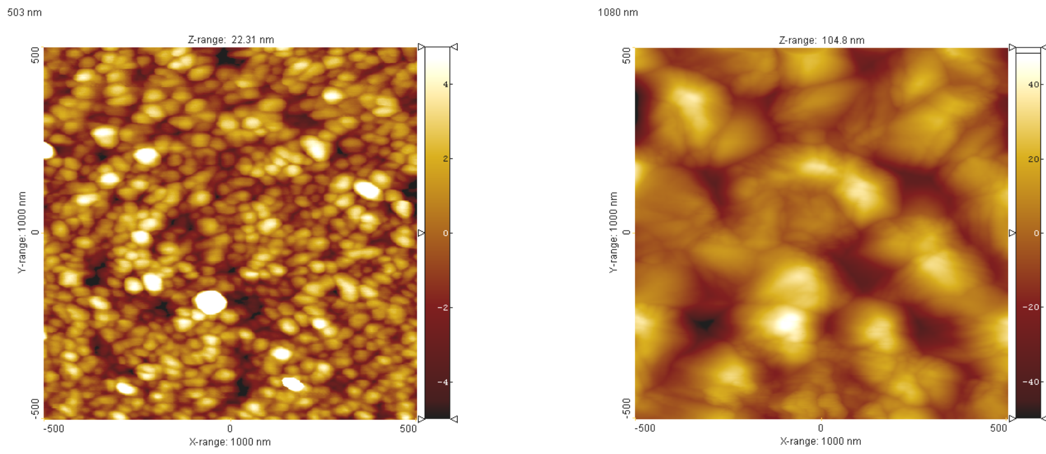

Figure 6.2.3 Film's surface topology for Si:ZAO thin films with different thickness

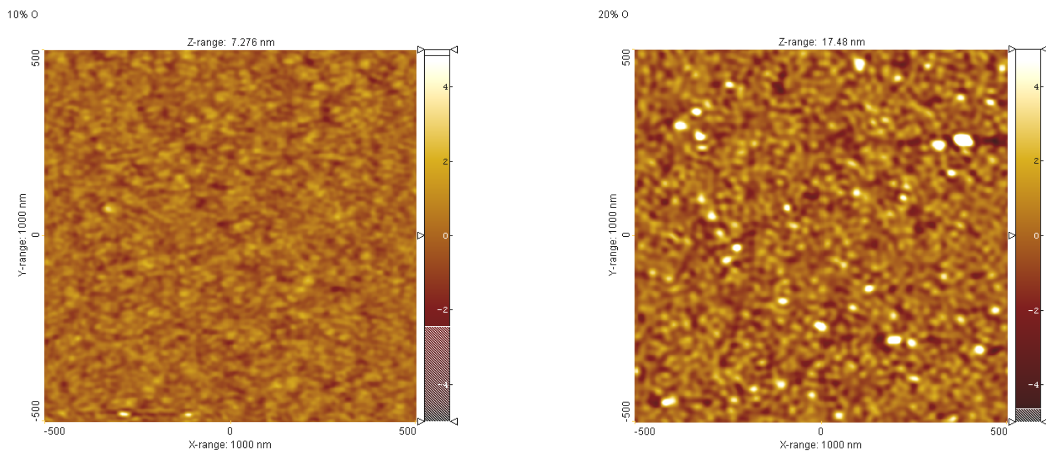

Figure 6.2.4 AFM images for films grown at 10% O_2 and 20%O_2 in plasma during growth.

The AFM characterization showed that:

- ✓ All Si:ZAO films exhibits granular surface structure.
- ✓ Surfaces are very smooth, the films exhibiting an RMS roughness smaller than 1 nm for a thickness of about 100 nm.
- ✓ Increasing thickness leads to grain aggregations as it can be seen in figure 6.2.3 at the same time, RMS also increases, as indicated in figure 6.2.5a.
- ✓ Increasing O_2 partial pressure during the growth was found to cause a decrease in the RMS roughness, as indicated in figure 6.2.5b.

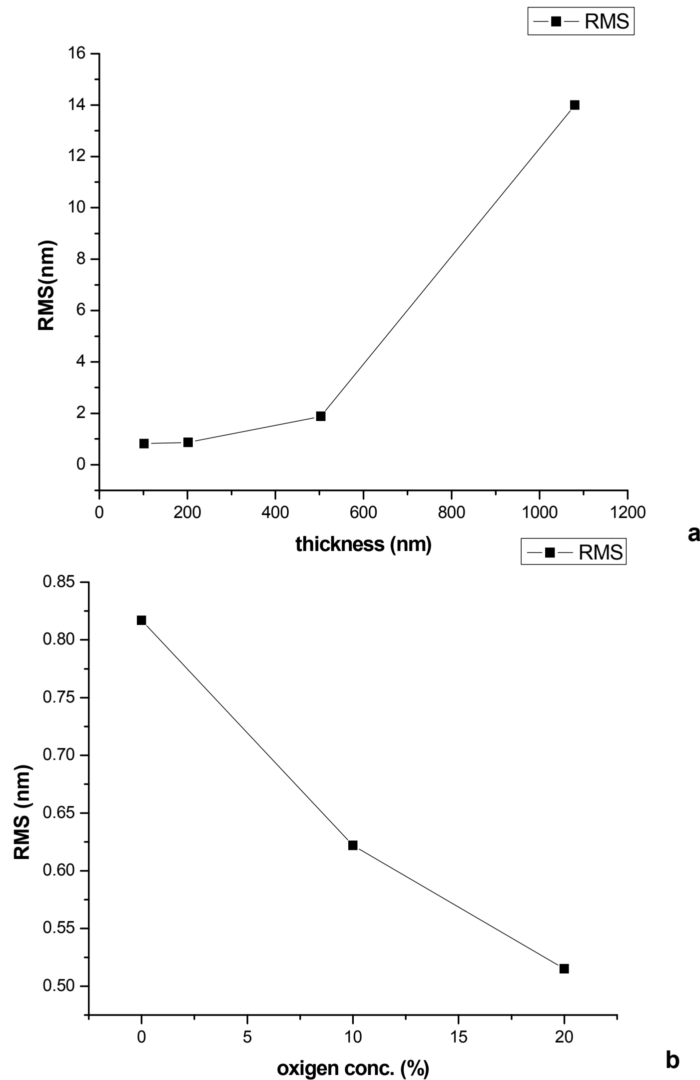

Figure 6.2.5 RMS variation with a thickness b oxygen concentration in plasma for Si:ZAO thin films

The effect of thickness, O_2 partial pressure and current intensity on the optical properties of films sputtered from a Si:ZAO ceramic target were then studied.

Si doping of ZAO target produced a small increase of the optical transmission, as compared with that of thin films grown from a pure ZAO ceramic target. Decrease of the argon/oxygen ratio in the plasma was found to cause a small decrease in the films' transmission.

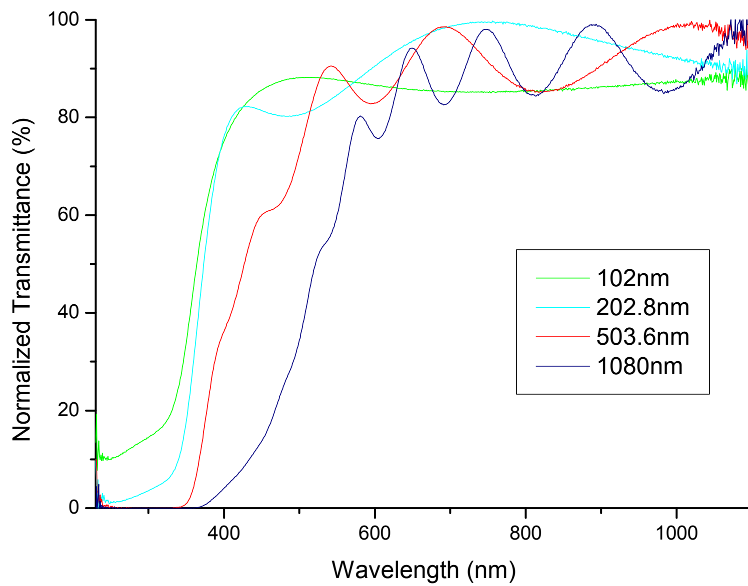

Figure 6.2.6 Optical transmittance variations with the thickness for the Si:ZAO films grown in 100%Ar atmosphere at RT. Even the 1 μm film is still highly transparent in VIS region, at least for wavelengths longer than 600 nm.

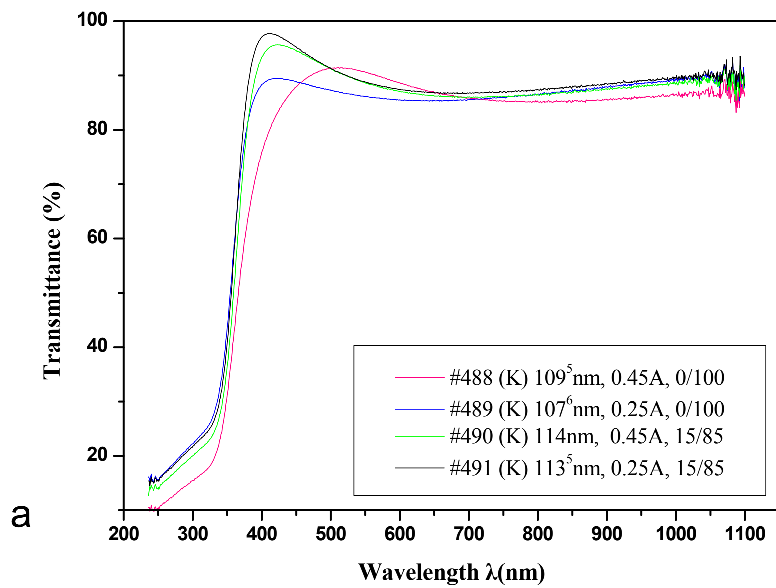

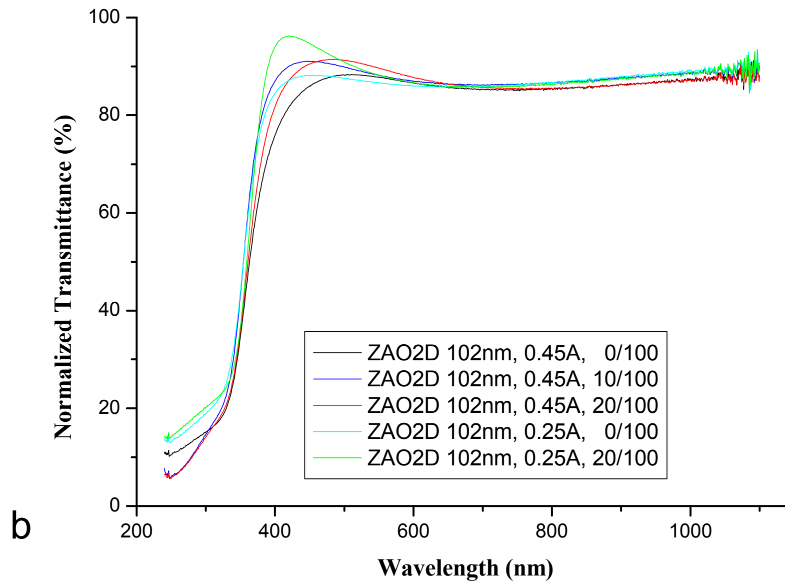

Figure 6.2.7 Transmission in the visible region UV-VIS transmittance of a) ZAO and b) Si:ZAO films grown on at different plasma current and O_2/Ar ratios.

All films were found to exhibit high transmittances in the visible region and a sharp absorption edge. Moreover, the optical transmission in visible spectral range:

- ✓ Increases slightly when the O_2 concentration in O_2/Ar plasma increases.
- ✓ Si:ZAO films exhibit higher transmittance in visible region. Si-doping enhances the optical transmittance of the ZnO films to values of the order of 90%.

Finally, electrical measurements were performed for Si:ZAO thin films of about 100 nm thickness grown at different O_2:Ar plasma concentrations and two different sputtering currents, the results shown in figure 6.2.8.

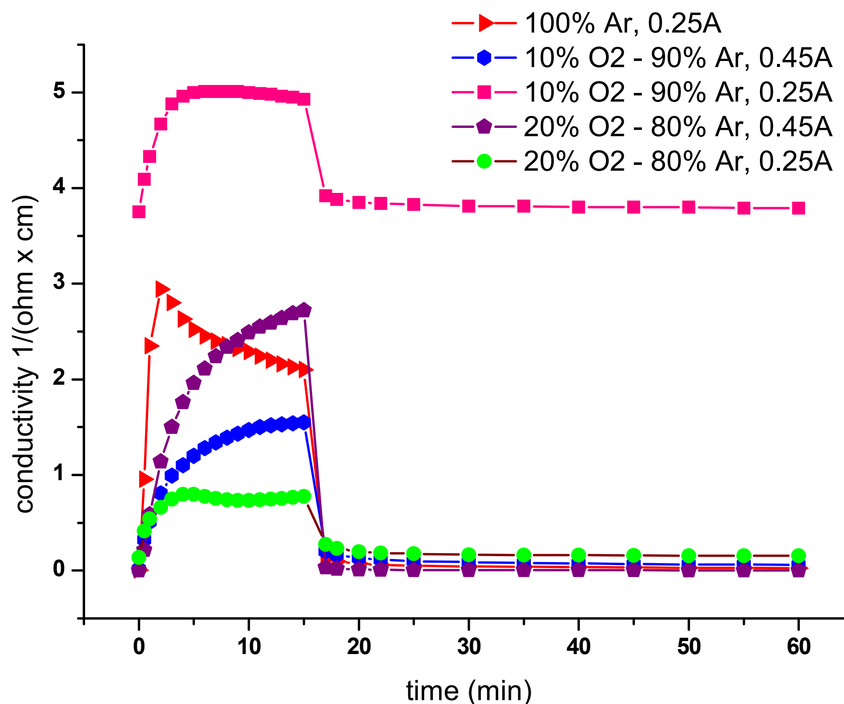

Figure 6.2.8 Conductivity change under UV-ozone subsequent exposure for Si:ZAO thin films

A relative increase of electrical conductivity of the as-deposited Si:ZAO films was observed, as compared with that of ZAO films grown under similar conditions. However, photoreduction–oxidation treatment was found to lead to very low variations in the conductivity, bellow an order of magnitude. Therefore, these films are not promising for gas sensing.
More detailed analysis of photoreduction-oxidation results will be included in the following chapter related to correlations.

6.3 In:ZnO thin films grown by DC magnetron sputtering

In:ZnO films were deposited by DC magnetron sputtering from a ZnIn5 (5% In-doped Zn) metallic target for two plasma currents 0.25 and 0.45 A in 100%, 90% and 80% O_2/Ar plasma atmosphere with a 100nm thickness at RT.
The films were deposited onto silicon and glass substrates in an oxygen-argon atmosphere.

XRD characterization
The In:ZnO films were found to exhibit low crystallinity and a small tendency of texturing in the wurtzite ZnO c-axis orientation, as was observed in the case of pure ZnO thin films grown under similar experimental conditions.

Examples of the effect of the growth parameters on structure of the films are presented in figures 6.3.1 and 6.3.2. More specifically, the effect of the plasma current intensity and the O_2:Ar partial pressure in plasma during deposition was examined. As shown in figure 6.3.1, an increase of the sputtering current intensity leads to a decreased intensity and the broadening of the [002] peak, associated to a lower crystallinity.

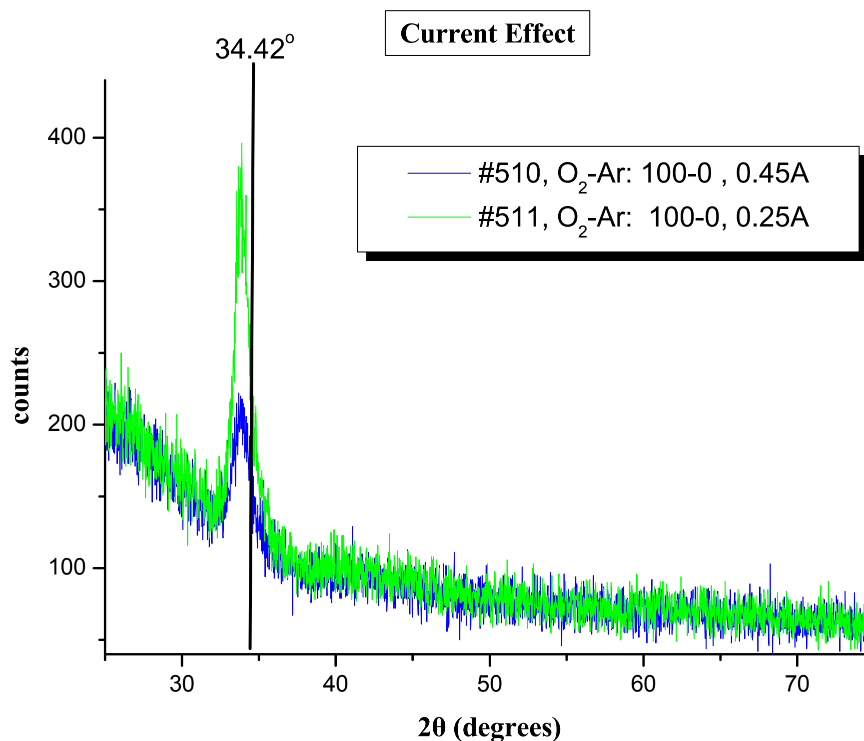

Figure 6.3.1 Typical X-rays diffractograms of IZO films grown at two different plasma currents intensities in 100% O_2 atmosphere.

The effect of the O_2:Ar ratio in the plasma for both plasma current intensities is presented in figures 6.3.2 a and b. As the oxygen concentration decreases, the [002] peak is improved shape and intensity for both current intensities. It is also noticed that all films show a large shift to lower diffraction angles for the [002] peak with respect to that of the bulk, a fact which can be attributed to stress/strain presence in the bulk of the films.

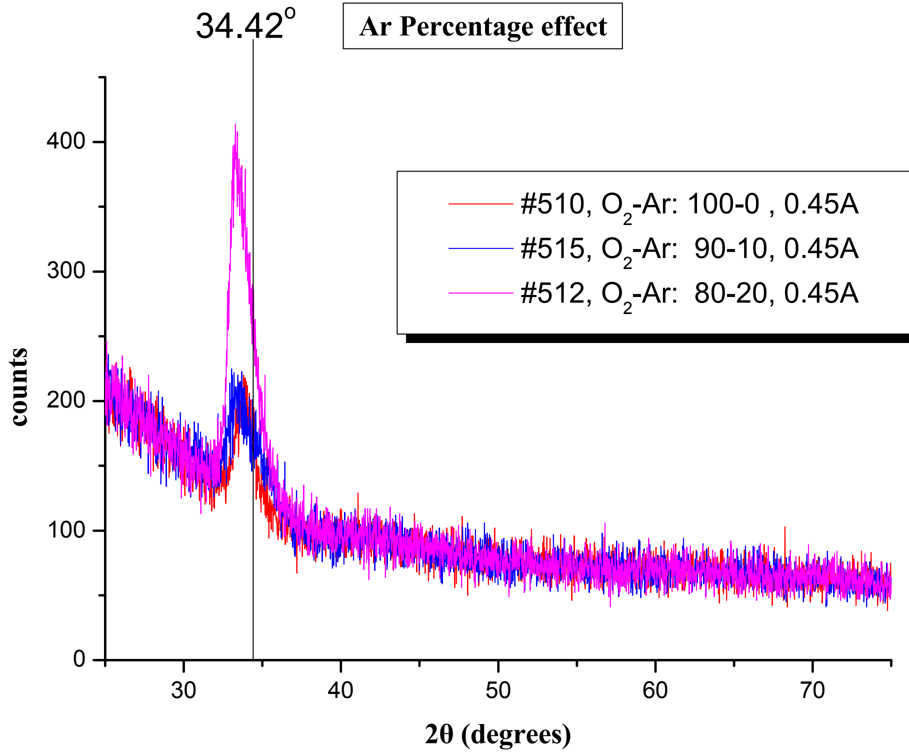

a

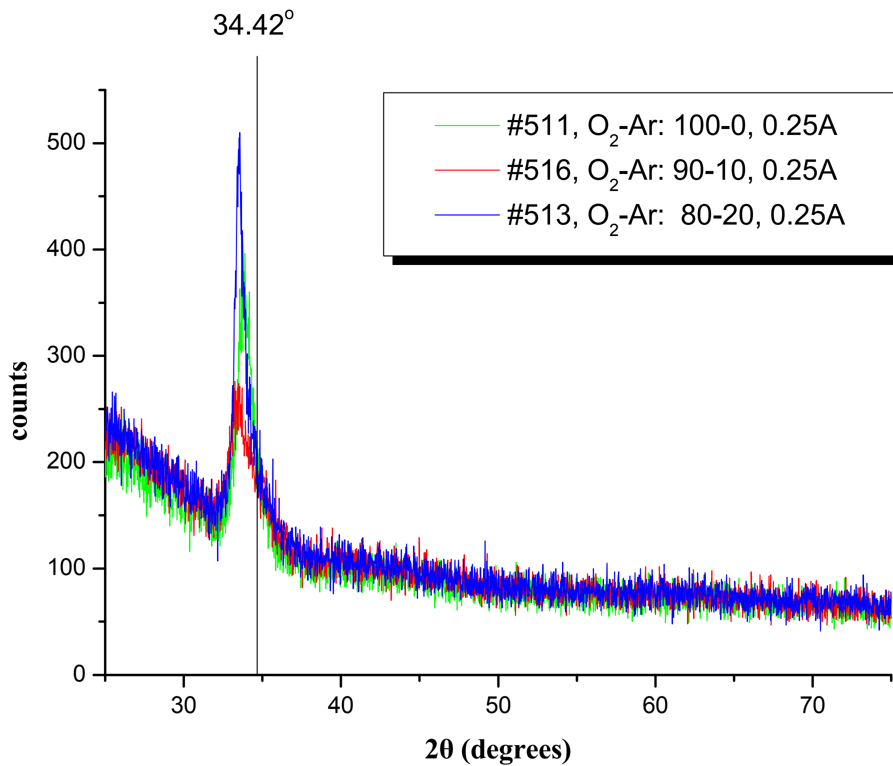

b

Figure 6.3.2 The effect of the O_2:Ar ratio in the plasma on X-rays diffractograms for both plasma current intensities a 0.45A and b 0.25A.

Optical microscopy, SEM and EDX were also performed, in order to correctly characterize the In:ZnO surfaces. The presence of almost circular splashes with diameter of few tens of μm was observed on the films surface. An example of an

optical microscopy image of such a splash onto In:ZnO surface is presented in figure 6.3.3.

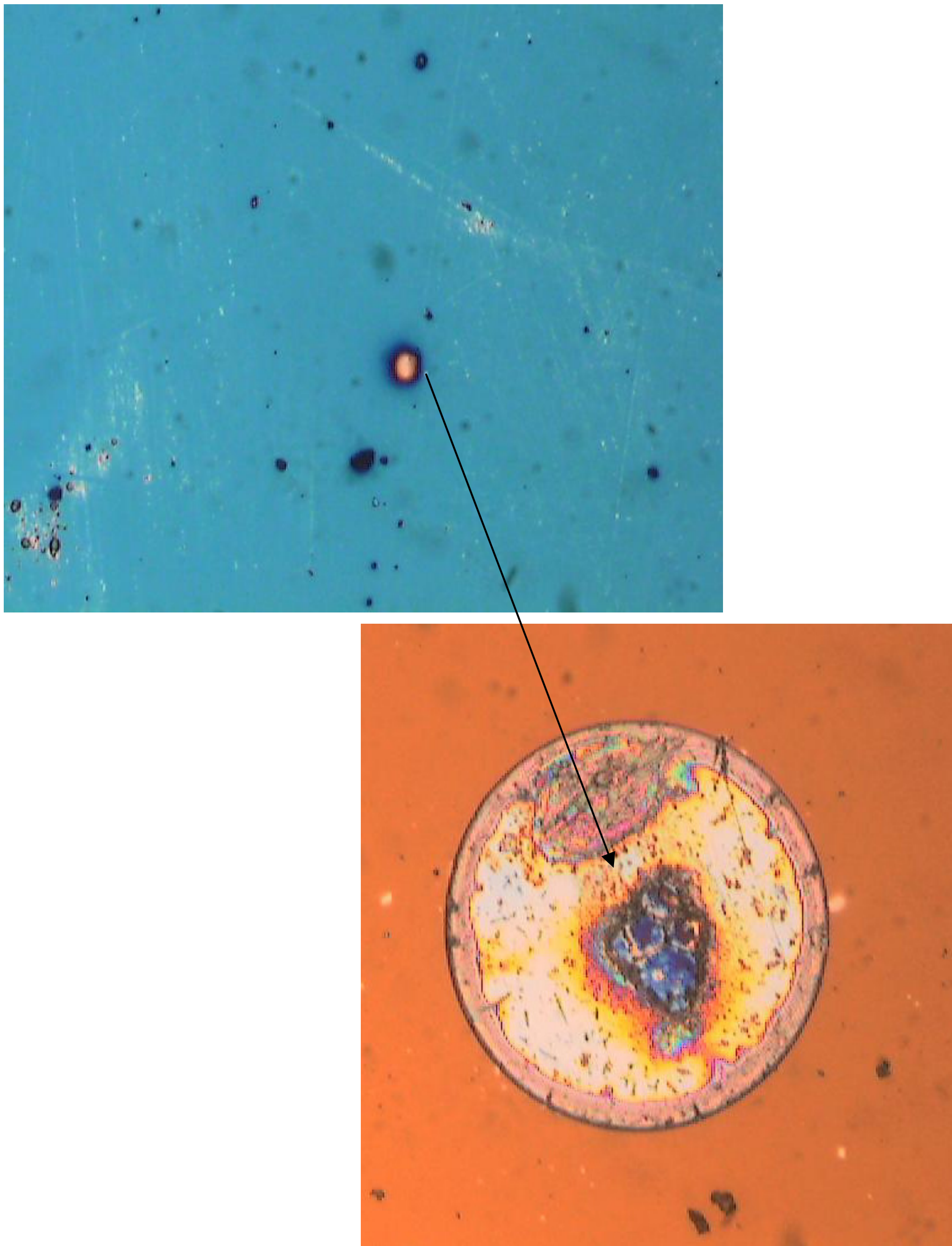

Figure 6.3.3 Optical microscopy characteristic appearance of an IZO film and high magnification image of a splash onto film's surface.

SEM analysis of the films showed that splashes are highly conductive and have a structured surface. An example of a splash is shown in figure 6.3.4.

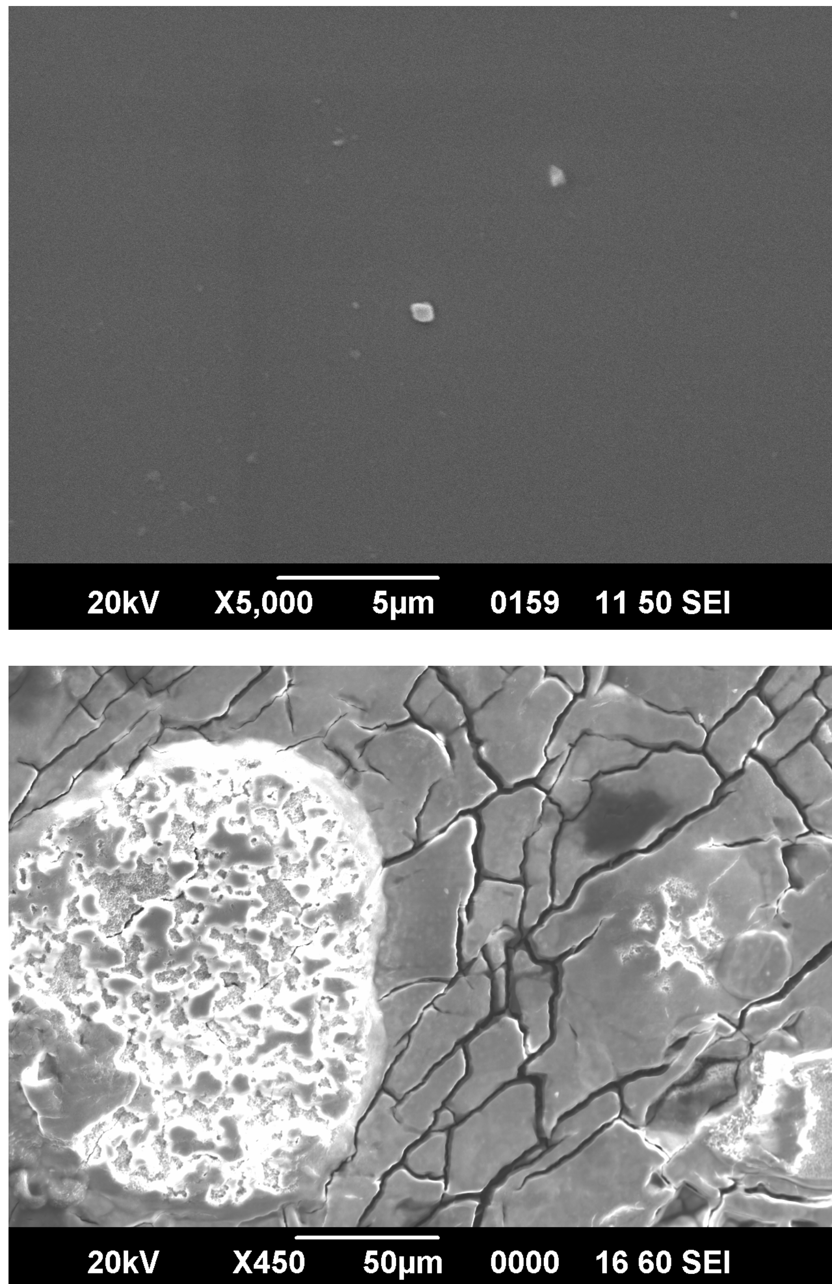

Figure 6.3.4 SEM characteristic appearance of an IZO film and high magnification image of a splash onto film's surface.

EDX analysis of films proved that the splashes contain islands of metallic In embedded in highly doped regions of ZnO and undoped ZnO. Images in figure 6.3.5 show a detail of In surface on a splash and the compositional spectrum of this region.

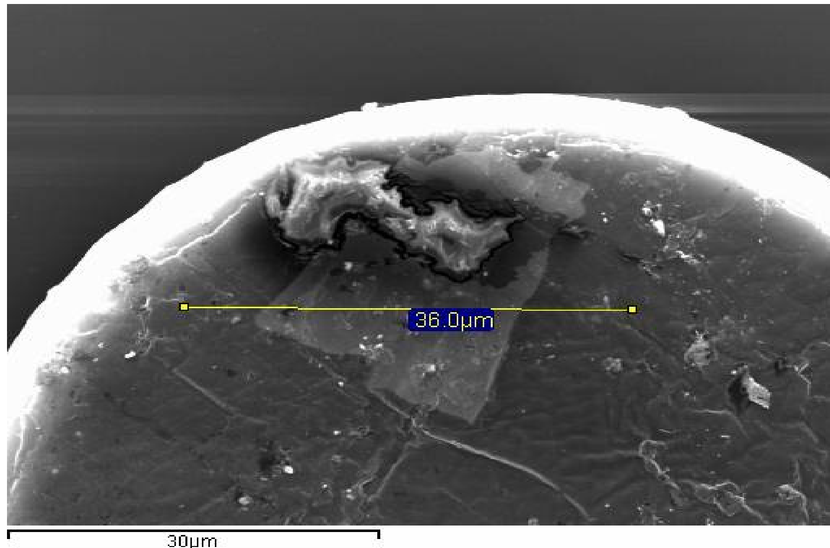

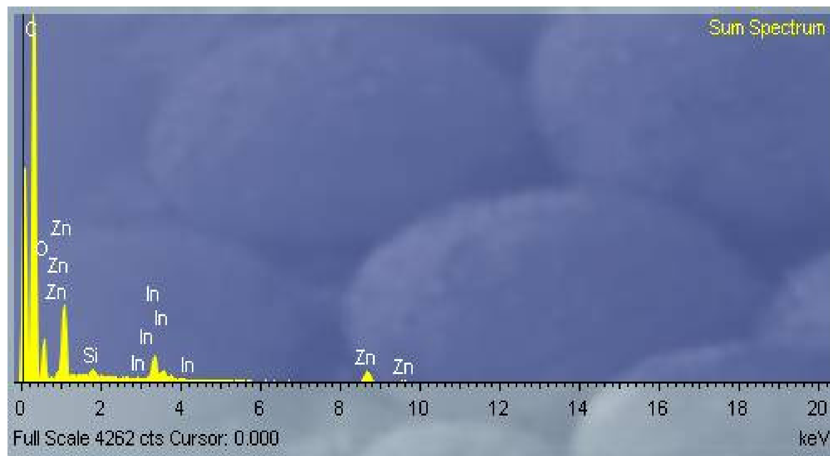

Figure 6.3.5 SEM image on a detail of In surface on a splash and the compositional spectrum of this region.

AFM characterization of the In:ZnO thin films grown by DC magnetron sputtering showed that these were very smooth between splashes, the z-range over the surface being smaller than 10nm, the respective features having a size of 10-50nm. 2x2µm AFM images are presented in figure 6.3.6, corresponding to films grown at different O_2:Ar plasma concentrations and two plasma current intensities (0.45 and 0.25 A). It is observed that for both current intensities, the surface grain size increases as the oxygen content decreases. This behavior correlates with the corresponding decrease in the growth rate. At the lower plasma current intensity, the grains are bigger, their dimension increasing as the Ar concentration increases.

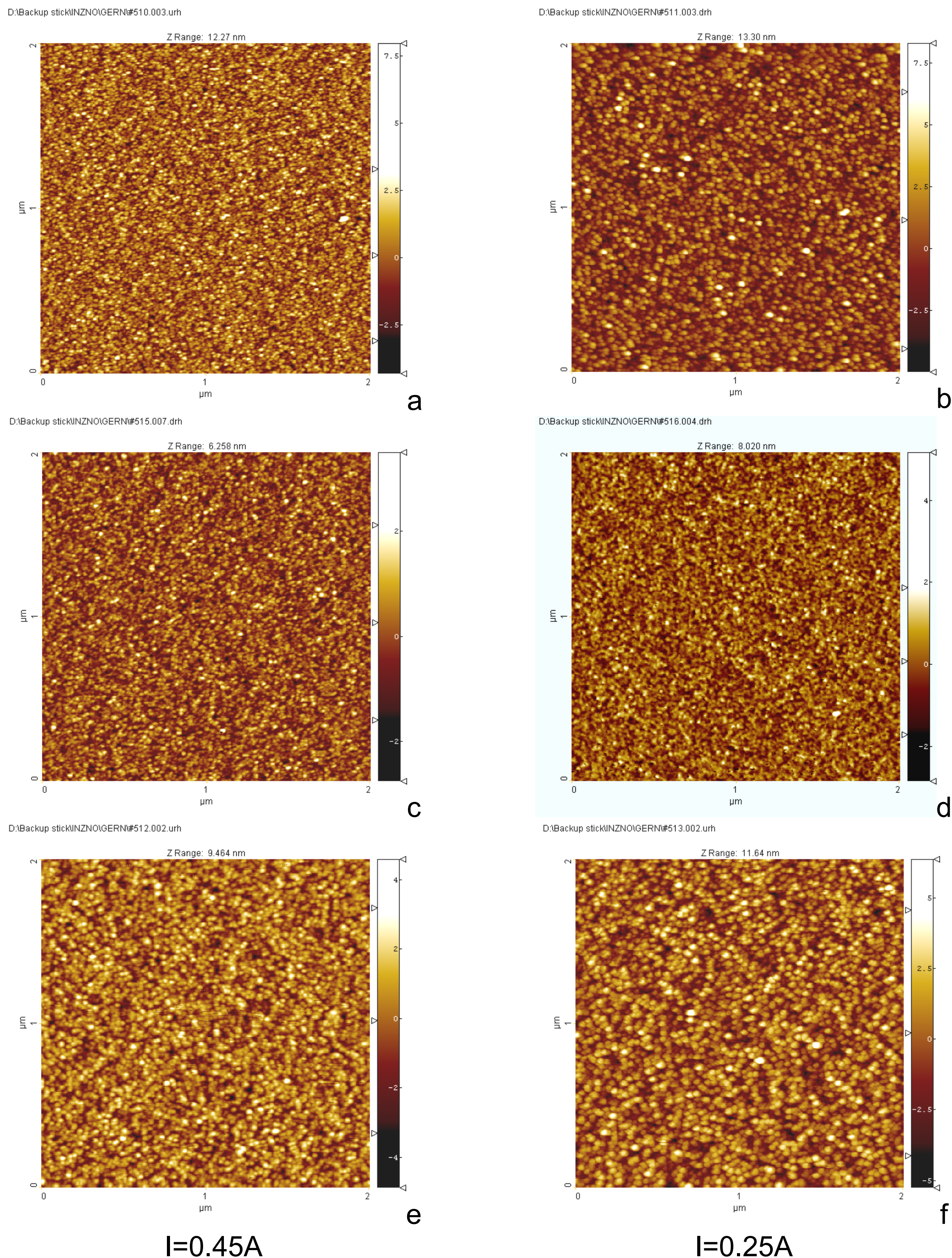

Figure 6.3.6 2x2μm AFM images are presented, corresponding to films grown at different O_2:Ar plasma concentrations and two plasma current intensities (0.45 and 0.25 A).

Surface parameters estimated from AFM measurements using the SPIP software will be presented in detail in the chapter regarding surface correlation.

Optical Properties

UV-Vis absorption spectra of In:ZnO films indicated that the films are highly transparent in the visible spectral region, their transmission approaching 90%. As shown in figure 6.3.7, under this experimental conditions, the growth parameters does not affect significantly the optical transmittance of the films.

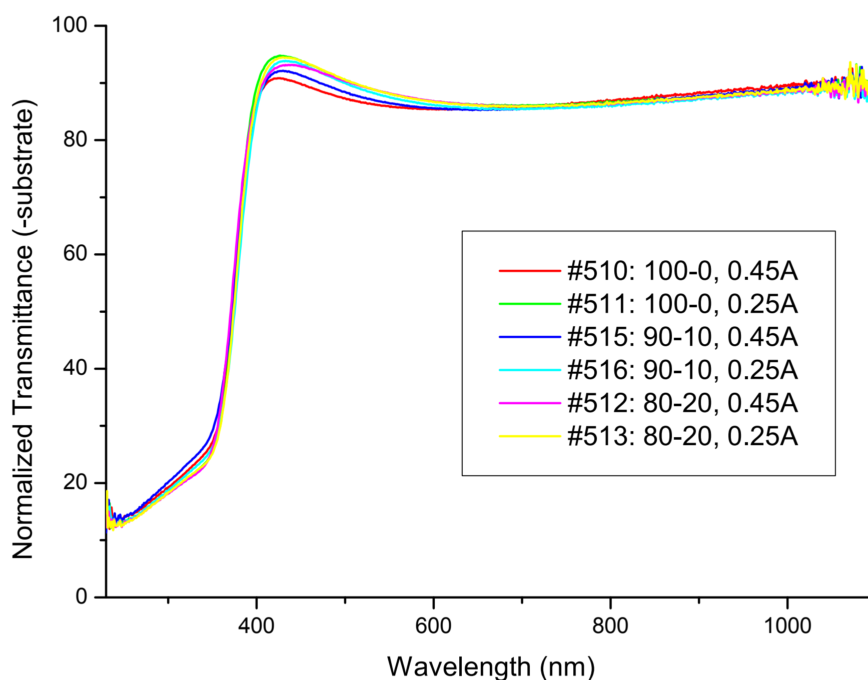

Figure 6.3.7 Typical UV-Vis spectra of In:ZnO grown at different O_2:Ar ratios and the two plasma currents.

Conductivity changes under UV exposure and ozone oxidation were also studied as a function of the O_2/Ar ratio. Conductivity variations are shown in figure 6.3.8 for two current series, discussed also above. Larger plasma current leads to slightly higher conductivity values. The largest sensing response was recorded for films grown in 100% O_2 atmosphere in both cases.

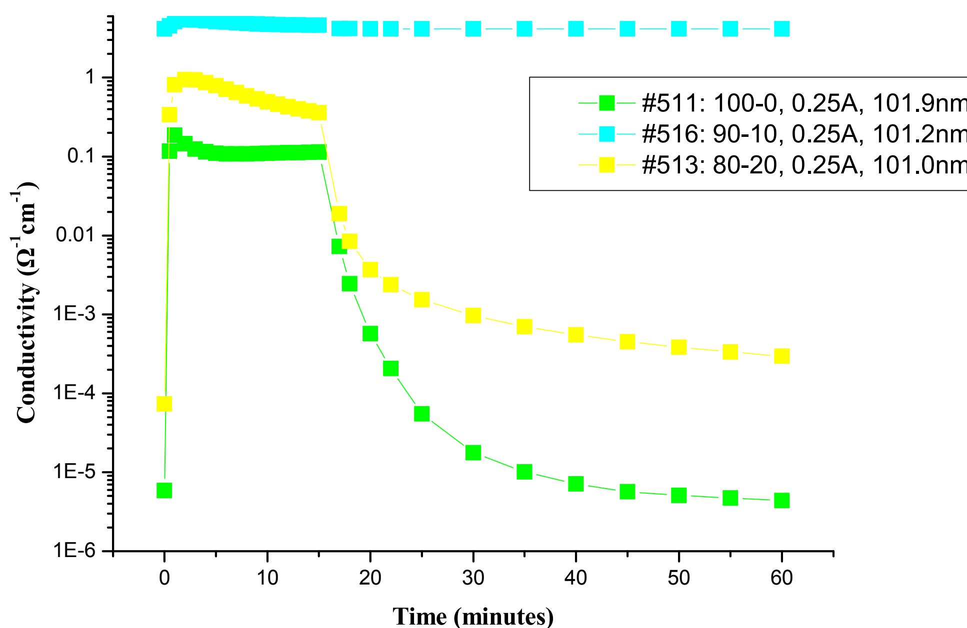

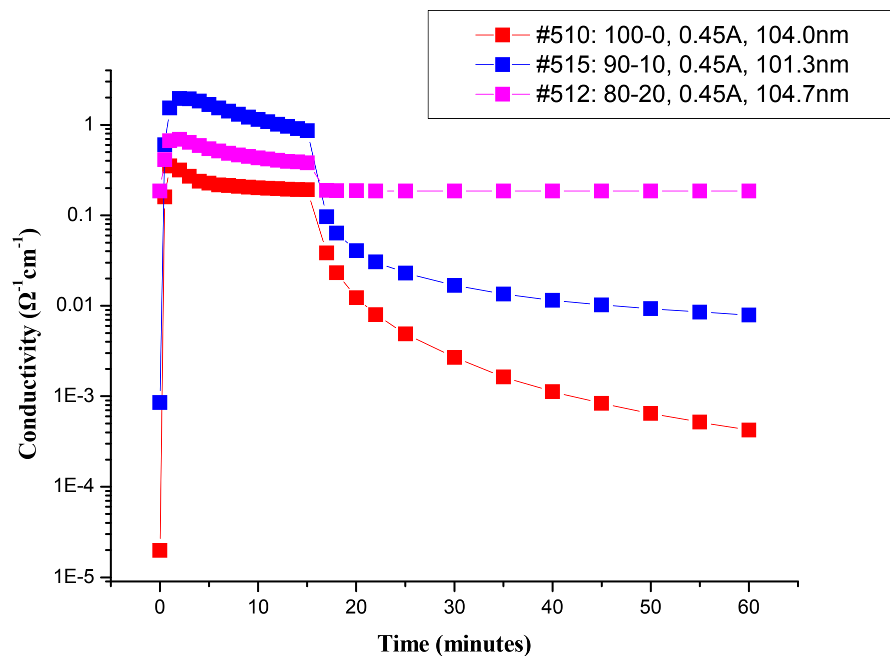

Figure 6.3.8 Conductivity changes under UV exposure and ozone oxidation were also studied as a function of the O_2/Ar ratio. a for films grown at 0.25A and 0.45A plasma current intensity.

Correlations of the surface parameters with the conductivity changes under photoreduction and ozone oxidation will be presented in the next chapter.

6.4 Conclusions

- Al, In, AlSi doped zinc oxide transparent thin films were prepared by DC magnetron sputtering using metallic and ceramic targets onto silicon and Corning glass substrates under identical deposition conditions and were compared with the undoped ZnO also grown by DC magnetron sputtering.

- Generally, for all doped samples, structural investigations carried out by AFM and XRD showed a strong influence of doping on the films structural properties, the film roughness (RMS), the grain shape and the feature dimensions correlating with the target material. XRD measurements proved that all doped films were polycrystalline. Moreover, AFM analysis of films sputtered from a ceramic target indicated a different surface behavior than that for films grown from a metallic target. The physical properties of the films are strongly influenced by the presence of the dopant, as was shown in the optical and electrical measurements. The target composition has a strong influence on the film characteristics.

- Surface topology studied by AFM of ZAO thin films deposited at room temperature from metallic and ceramic targets, under varying O_2:Ar plasma ratios, showed that the grain size and the surface RMS are determined by growth conditions for each specific target and they can be controlled and reproduced for a specific application. Comparison with ZnO films showed that ZAO films have a smoother surface and a smaller grain size than the pure ZnO films grown under similar conditions. An increase of the [002] peak intensity was also observed, a fact which may be associated with an improvement of the crystallinity. All films were exhibiting a transmittance higher than 80% in the visible spectral region and a sharp absorption edge. The optical band gap was estimated to be in the range of 3.31 to 3.35 eV for the ZnO films and from 3.35 to 3.43 eV for the ZAO films. Moreover, Al-doping was observed to lead to an increased optical transmittance for both metallic and ceramic targets. As deposited conductivity was found to increase with Al doping while conductivity change under photoreduction-oxidation treatment was found smaller as compared with that of pure ZnO films grown under similar conditions.

- Si:ZAO thin films were grown from 2% Al_2O_3 and 1000 ppm Si-doped zinc oxide ceramic target. All films had a [002] texture and improved crystallinity, as compared with that of ZAO films grown under similar conditions. Surface topology studied by AFM of films deposited at room temperature under varying O_2/Ar plasma ratios showed that grain size and surface RMS are determined by the growth conditions and they can be controlled and reproduced towards a specific application. All films were exhibiting a transmittance of about 90% in the visible spectral region and a sharp absorption edge. Even for a thickness larger than 1 μm, the optical transmittance remained quite high, indicating that Si co-doping can lead to an increased optical transmittance. Although the as deposited conductivity was found to increase with the Si co-doping present, the conductivity

change under photoreduction-oxidation treatment was significantly smaller than that of the ZAO films grown under similar conditions. Finally, Al,Si:ZnO thin films exhibited interesting physical properties which might be enhanced significantly by the control of the film's deposition parameters.

- In:ZnO films were deposited onto silicon and glass substrates from ZnIn5 (5% In-doped Zn) metallic target under different growth conditions, in an oxygen-argon atmosphere, at two different current intensities. The films were highly transparent and highly resistive (109 Ω). Surface characterization revealed that the films are very smooth and nanostructured, with features of about 50nm. Moreover, metallic "splashes" from the target were detected on all films, and because of these, no further experiments were performed. As future possibilities, growth optimization may open perspectives on use of In:ZnO as ozone sensor, based on the fact that In doping modify films physical properties in an apparently favorable way. This affirmation is sustained by the correlation of the surface parameters, from the AFM measurements, with the conductivity which will be presented in details in the next chapter of this thesis.

The general conclusion on the effect of dopants on the ZnO thin films grown by DC magnetron sputtering in different conditions is that the presence of dopants modifies the films surface morphology and consequently its sensing behavior.

References

- ✓ Suchea, M., Christoulakis, S., Moschovis, K., Katsarakis, N., Kiriakidis, G. "Nanostructured ZnO and ZAO transparent thin films by sputtering-surface characterization" (2005) *Reviews on Advanced Materials Science*, 10 (4), pp. 335-340. Cited 9 times.
- ✓ Suchea, M., Christoulakis, S., Katsarakis, N., Kitsopoulos, T., Kiriakidis, G. "Comparative study of zinc oxide and aluminum doped zinc oxide transparent thin films grown by direct current magnetron sputtering" (2007) *Thin Solid Films*, 515 (16 SPEC. ISS.), pp. 6562-6566. Cited 3 times.

***Annex 6A: Growth parameters for doped ZnO thin films grown by DC magnetron sputtering*.**

RUN	MATERIAL	% O2	pO2 (mbar)	ISP (A)	timp(sec)	t (°C)	d (nm)	growth rate
1	ZAO2	100.00	8.00E-03	0.44	420	47	97.4	2.32E-01
2	ZAO2	100.00	8.00E-03	0.45	360	47.5	109.8	3.05E-01
3	ZAO2	100.00	8.00E-03	0.25	720	50	109.3	1.52E-01
4	ZAO2	80.00	8.00E-03	0.44	260	41.5	108.5	4.17E-01
5	ZAO2	80.00	8.00E-03	0.24	570	40	109.4	1.92E-01
6	ZAO2	75.00	8.00E-03	0.44	240	42.5	110.4	4.60E-01
7	ZAO2	75.00	8.00E-03	0.25	550	37.5	107.6	1.96E-01
8	ZAO2C	0.00	8.00E-03	0.45	120	42	109.5	9.13E-01
9	ZAO2C	0.00	8.00E-03	0.25	240	38	107.6	4.48E-01
10	ZAO2C	15.00	8.00E-03	0.45	150	39	114	7.60E-01
11	ZAO2C	15.00	8.00E-03	0.24	360	37.5	113.5	3.15E-01
RUN	MATERIAL	% O2	pO2 (mbar)	ISP (A)	timp(sec)	t (°C)	d (nm)	growth rate
1	ZAO2D	0	8.00E-03	0.45	140	43.5	102	7.29E-01
2	ZAO2D	0	8.00E-03	0.25	300	38.5	100.4	3.35E-01
3	ZAO2D	0	8.00E-03	0.45	1140	58.5	1008	8.84E-01
4	ZAO2D	0	8.00E-03	0.45	300	45.5	203.6	6.79E-01
5	ZAO2D	0	8.00E-03	0.45	730	61	503.6	6.90E-01
6	ZAO2D	10	8.00E-03	0.45	180	43	102.2	5.68E-01
7	ZAO2D	20	8.00E-03	0.45	150	41	102.7	6.85E-01
8	ZAO2D	0	8.00E-03	0.25	360	34.5	101.5	2.82E-01
RUN	MATERIAL	% O2	pO2 (mbar)	ISP (A)	timp(sec)	t (°C)	d (nm)	growth rate
1	I5ZO	100	8.00E-03	0.45	320	RT	104	3.25E-01
2	I5ZO	100	8.00E-03	0.25	630	RT	101.9	1.62E-01
3	I5ZO	80	8.00E-03	0.45	260	RT	104.7	4.03E-01
4	I5ZO	80	8.00E-03	0.25	500	RT	101	2.02E-01
5	I5ZO	90	8.00E-03	0.45	230	RT	101.3	4.40E-01
6	I5ZO	90	8.00E-03	0.25	500	RT	101.2	2.02E-01

Chapter 7

Correlations

Outlines

- **Detailed explanations for the surface characterization method and the parameters considered for each film**
- **Correlation of data regarding thin films surface and ozone sensing response, collected in the work and presented in the previous chapters.**
- **Presentation of 3D graphical correlations of the most significant parameters of the thin film photo- and ozone sensing responses**
- **Sketching an experimental data based model for the dependence of the sensor response on the film surface structure and topology**
- **Presentation of particular observations for each material, method and parameters group.**
- **Annex 7A: SPIP surface roughness parameters – definitions**
- **Annex 7B: SPIP shape measurement parameters.**
- **Annex 7C Experimental data for In_2O_{3-x} grown by DC magnetron sputtering.**
- **Annex 7D Experimental data for ZnO grown by DC magnetron sputtering.**
- **Annex 7E Experimental data for ZnO grown by PLD.**
- **Annex 7F Experimental data for doped ZnO grown by DC magnetron sputtering.**

7. Correlations

As was already discussed in Chapter 1, the existing models for the sensing mechanism of metal oxide thin films refer to particular cases only and are contradictive in some cases. Given that in the case of film based sensors, the sensing effect is limited to the surface of the film, it is obvious that its morphology and microstructure can in principle play a crucial role. Qualitative information regarding the influence of the structural and the textural parameters (e.g. grain size, interconnectivity of the grains, surface to volume ratio, porosity and film thickness) was obtained for particular cases (i.e for specific materials, grown in specific conditions, using a particular technique) and some rather schematic models are available in literature. However, each of those parameters is not independent from all others and practically, it is impossible to consider only one neglecting the others. Since the change in the conductivity of the sensing material is limited to the exterior regions of the grains, the conductivity changes should be strongly connected with the grain parameters and, at the same time, with the grain distribution onto the surface. In the case of a film with given thickness, the presence of intergrain spacing, pores or channels will enable the gas access to a larger active surface. Then the grains "packing" should also play an essential role in the sensor response. Experimental results presented in Chapters 3, 4, 5 and 6 proved this in a systematical way for each material and growth technique used, at least for the particular cases where one growth parameter was varied. As a general observation from the results presented for particular film series, we can say that the domain of conductivity variation for films with smaller grains is larger than the one for films with larger grains. Also, the increase of the surface to volume ratio (SDR) was proved to affect positively the films sensing response, for a specific grain size range (SDR is connected with active sensing area as well as with film's porosity and agglomerations present). Film texture and fine features present onto the film's surface were also "measured" using fractal dimension and roughness parameters. All those are directly connected with the available sites for gas-sensor interaction and are determined by the specific growth conditions for each technique used.

The rigorous evaluation of those parameters is possible using the AFM techniques but yet, a systematic routine method for surface characterization of films is not generally adopted. Most of the researchers use partial characterization and limit their measurements at few parameters, not always significant for the purpose of their application, even if surface metrology standards are available for many years. The first section in this chapter is dedicated to the description of the methodology for the correlation of surface properties with sensing response and the definition and the evaluation of the required parameters using the available AFM possibilities for thin films.

7.1 Surface parameters evaluation from AFM measurement using SPIP software

For each grown film and characterized as presented in the previous four chapters, AFM measurements were performed in a very detailed way. SPIP software facilities were carefully used.

As an example a step by step film characterization will be presented.

The first step for a proper AFM characterization is the correct selection of the scanned areas, so that one can to have representative results for the specific sample. Due to the fact that the active film surface is generally few cm^2 while the surface features and AFM scan sizes are of the order of tens to hundreds nm and few µm respectively, the choice of the proper scan area on the sample plays crucial role. After finding the proper image, representative for the whole surface of the film, it is also very important to determine accurate data for this. This requires scan optimization for each surface and choice of proper scan size for each measurement according to the purpose of the analysis. This means that in the evaluation of the surface roughness parameters, a large scan size (but having very clear records of surface features) would give more accurate results while for shape analysis, a smaller scan size would reveal important details. The following figure presents scan size selection for a 200nm thick PLD deposed ZnO film where nanorods are present on the surface.

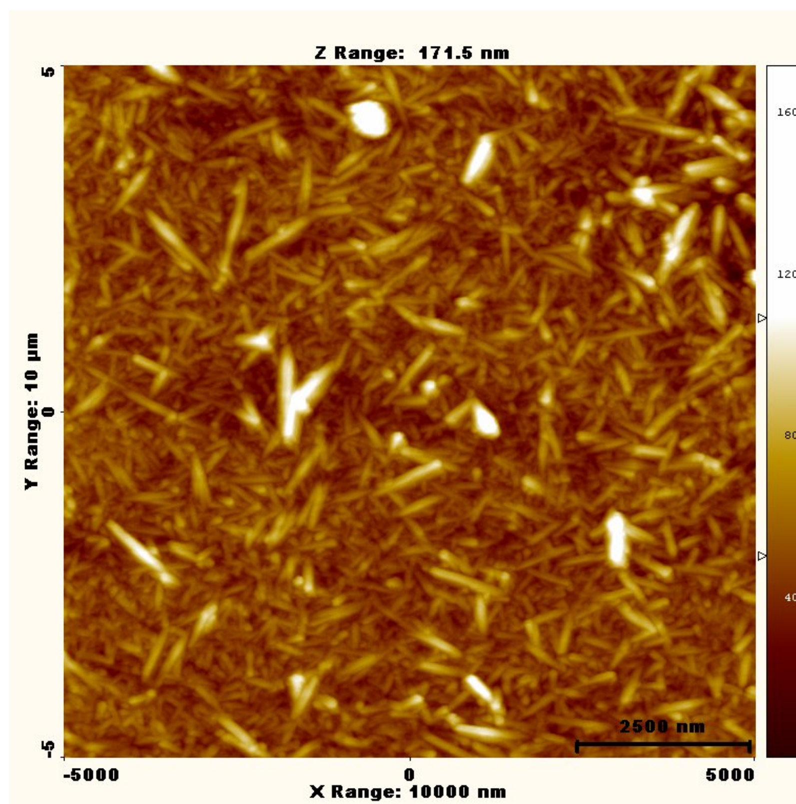

As shown in this figure, large (10x10 µm) scan sizes include the most significant features characteristic for the whole surface of the film, presenting very clear shapes, and perfect for evaluation of the roughness parameters.

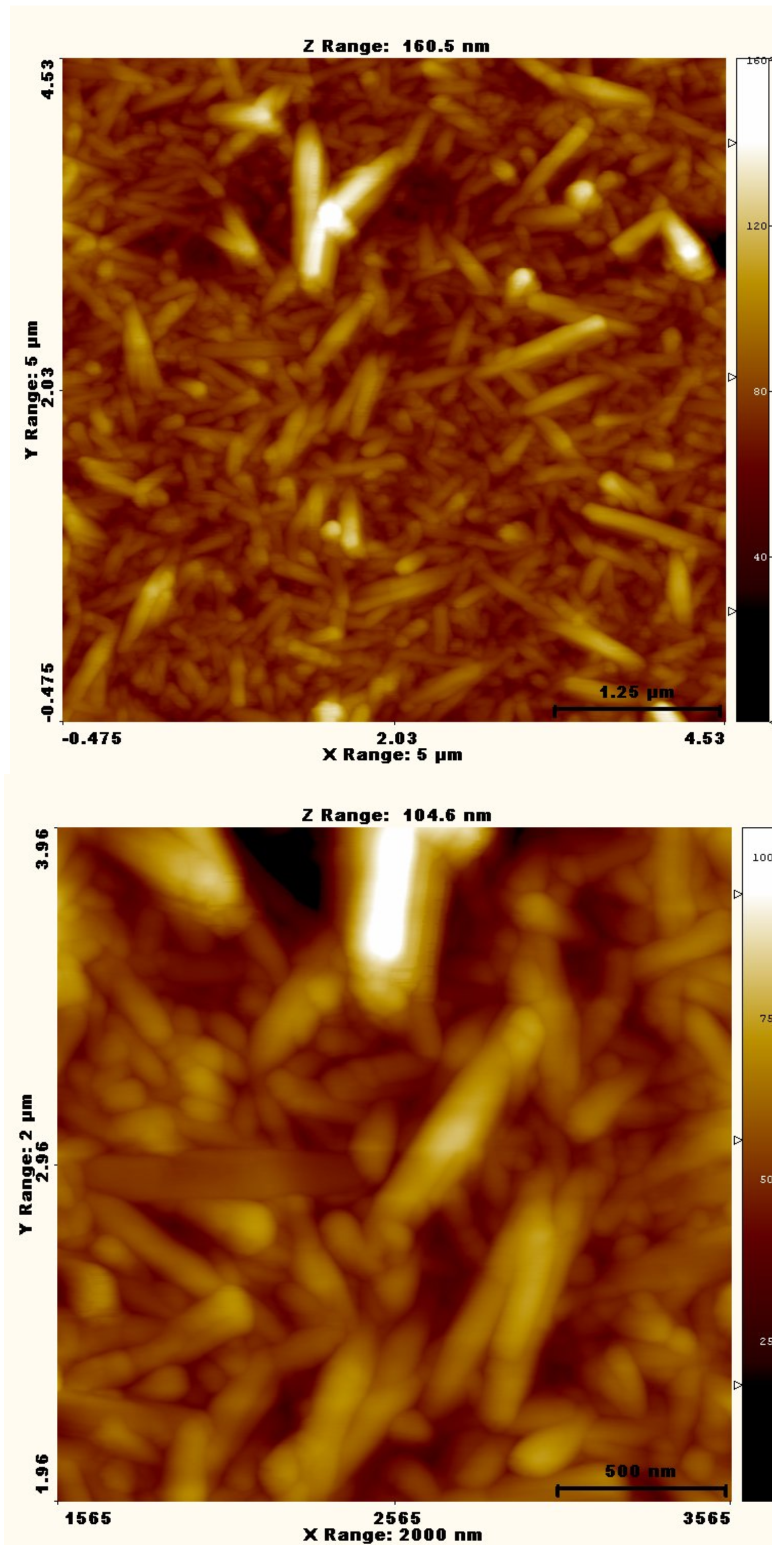

In contrast, smaller scan sizes can give better information for the surface features dimensions.

Having the proper information from the direct AFM scans onto the surface, using the proper software, a complete surface metrology can be performed. In this work we used the SPIP software, presented already in the chapter regarding experimental techniques. As an example, the surface parameters estimation for a

ZnO thin film grown by DC magnetron sputtering with granular surface structure will be presented.

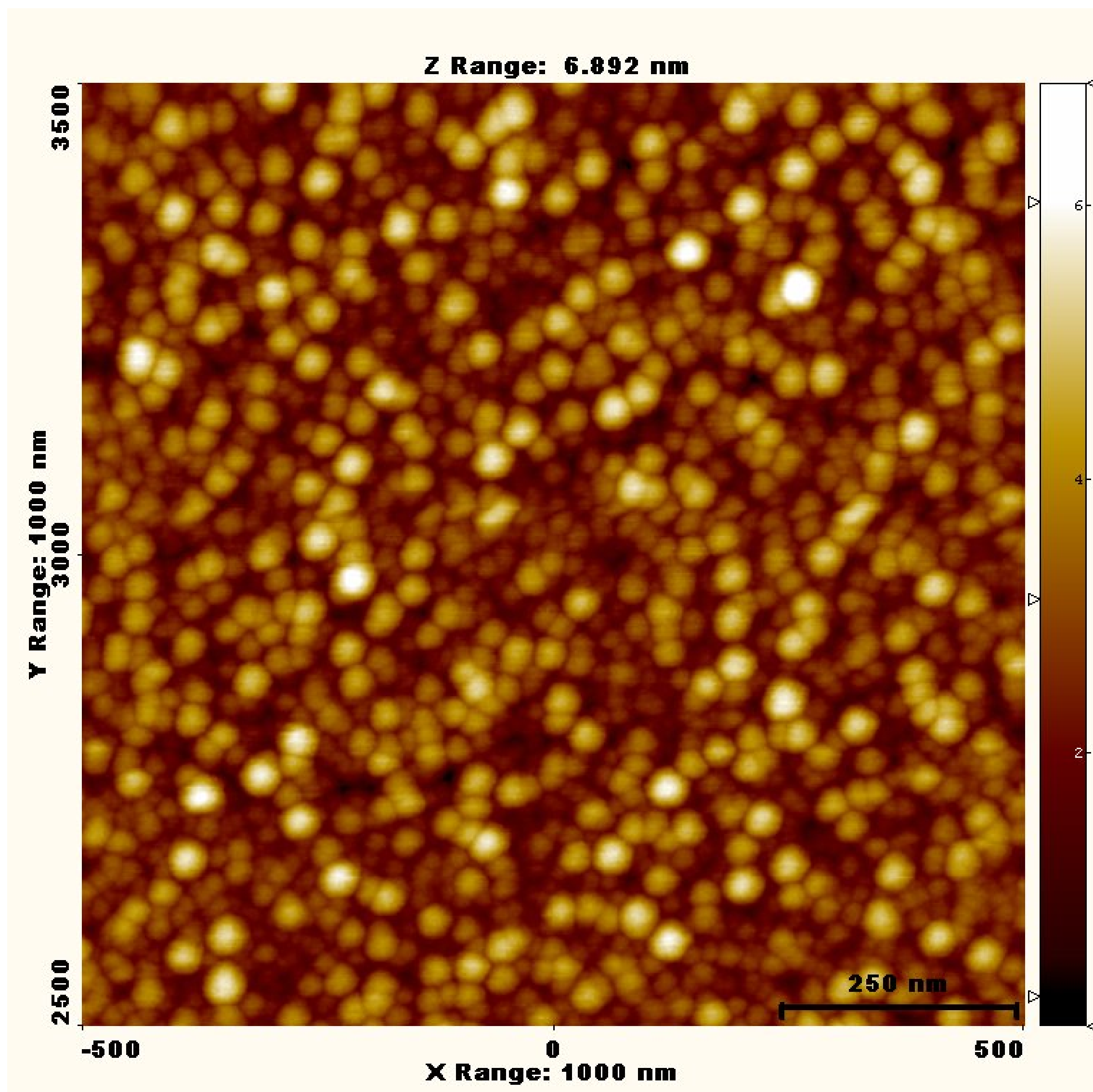

Due to small size of the grains and the fact that the z-range was bellow 7nm (see the above figure), a 1x1µm scan size can be used for the surface parameters evaluation. A height distribution histogram for the features present onto this surface is shown in next figure.

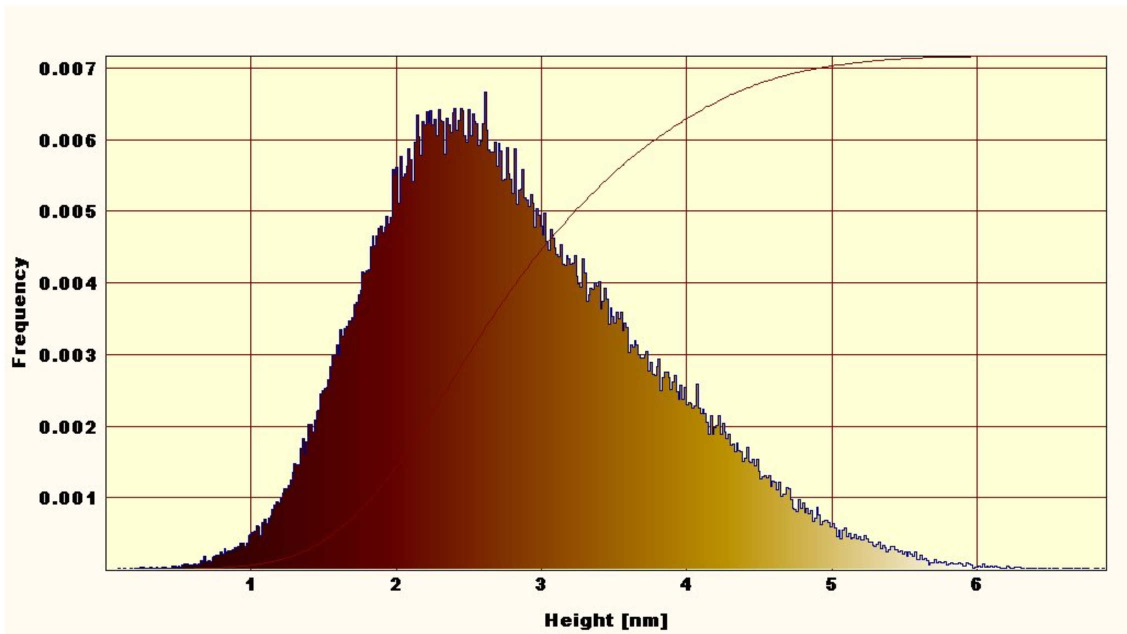

The roughness parameters for this film, determined by the SPIP software, are presented as table in the next table and as a histogram in the following figure.

Roughness Data Calculated by SPIP V4.6.1.0
File: D:\Date\afm data\MIRELA\THIKZNO\571BF.002.drh
Plane Correction: Subtract 1st Order Plane

Name	Value	Unit
Sa	0.75875	nm
Sq	0.94226	nm
Ssk	0.52645	
Sku	2.9967	
Sy	6.8917	nm
St	6.8917	nm
Sz	6.8917	nm
S10z	6.6319	nm
Sz_tph	6.6319	nm
Sds	3888	1/µm²
Ssc	0.052428	1/nm
Sv	2.8179	nm
Sp	4.0738	nm
Smean	5.3692E-009	nm
Sdq	0.13673	
Sdq6	0.13457	
Sdr	0.93015	%
S2A	1E+006	nm²
S3A	1.0093E+006	nm²

Name	Value	Unit
Sbi	0.5416	
Sci	1.8033	
Svi	0.08046	
Spk	1.2339	nm
Sk	2.2753	nm
Svk	0.50975	nm
Std	177.26	degree
Stdi	0.87252	
Srw	163.29	nm
Srwi	0.1979	
Shw	27.027	nm
Sfd	2.7786	
Scl20	19.569	nm
Str20	0.83333	
Scl37	17.612	nm
Str37	0.9	
SDC0_5	2.3341	nm
SDC5_10	0.41433	nm
SDC10_50	1.464	nm

The definitions of these parameters from SPIP software can be found in the Annex 7A at the end of this chapter.

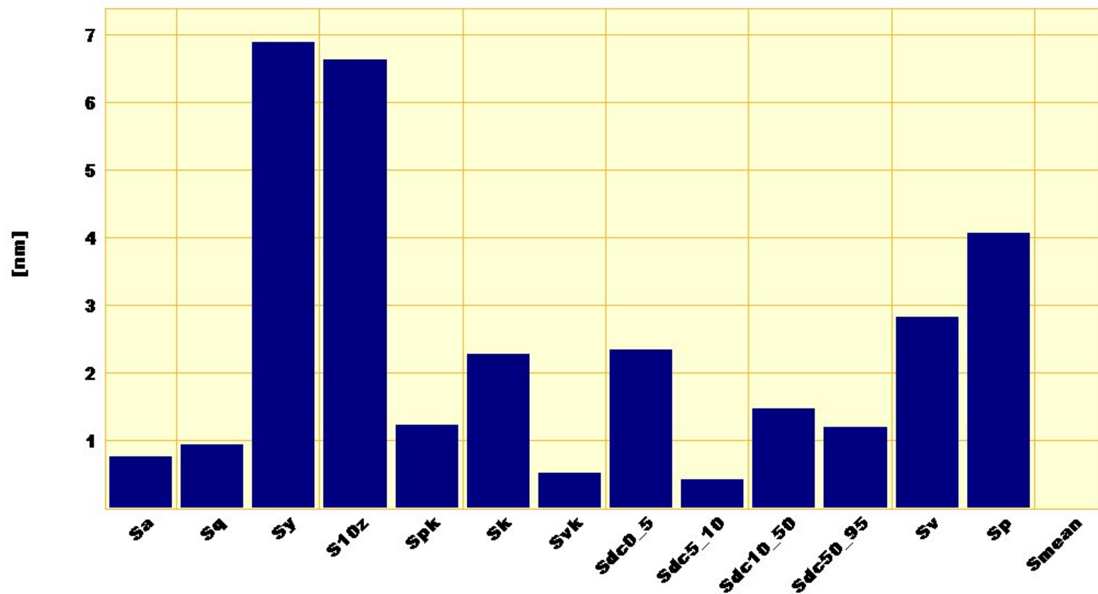

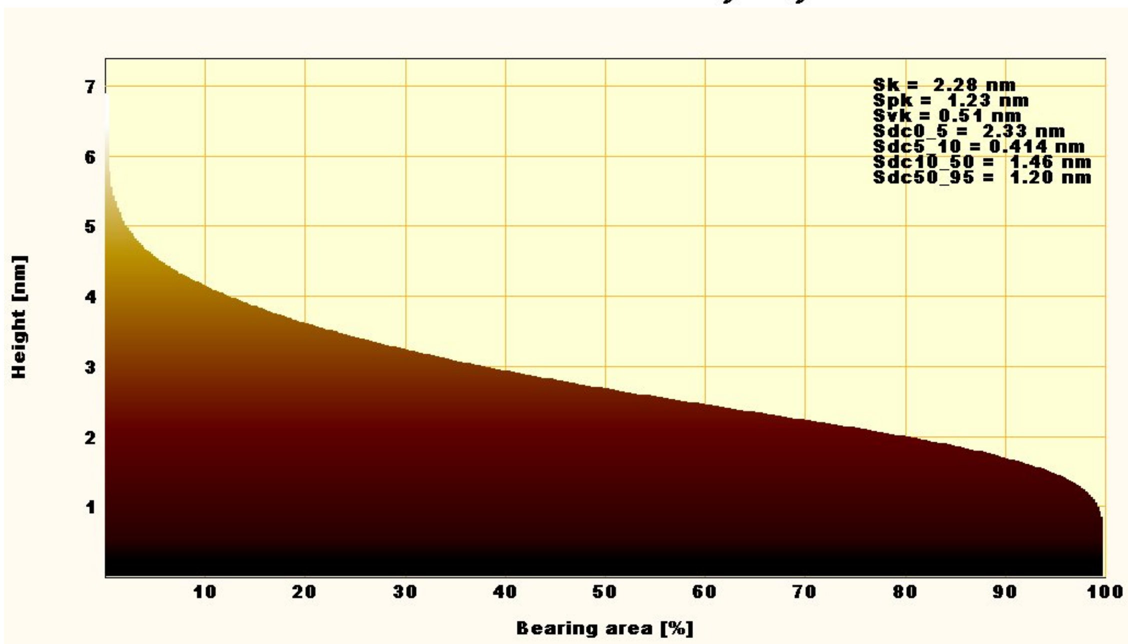

The above image shows the surface bearing curve for the same film.
The Correlation Length parameters *Scl20* and *Scl37,* defined as the horizontal distance of the areal autocorrelation function that has the fastest decay to 20% and 37% respectively (37% is equivalent to 1/e), and the Texture Aspect Ratio Parameters, *Str20 and Str37*, used to identify texture strength (uniformity of texture aspect), defined as the ratio of the fastest to slowest decay to 20% and 37% of the autocorrelation function respectively, are presented in the following two figures.

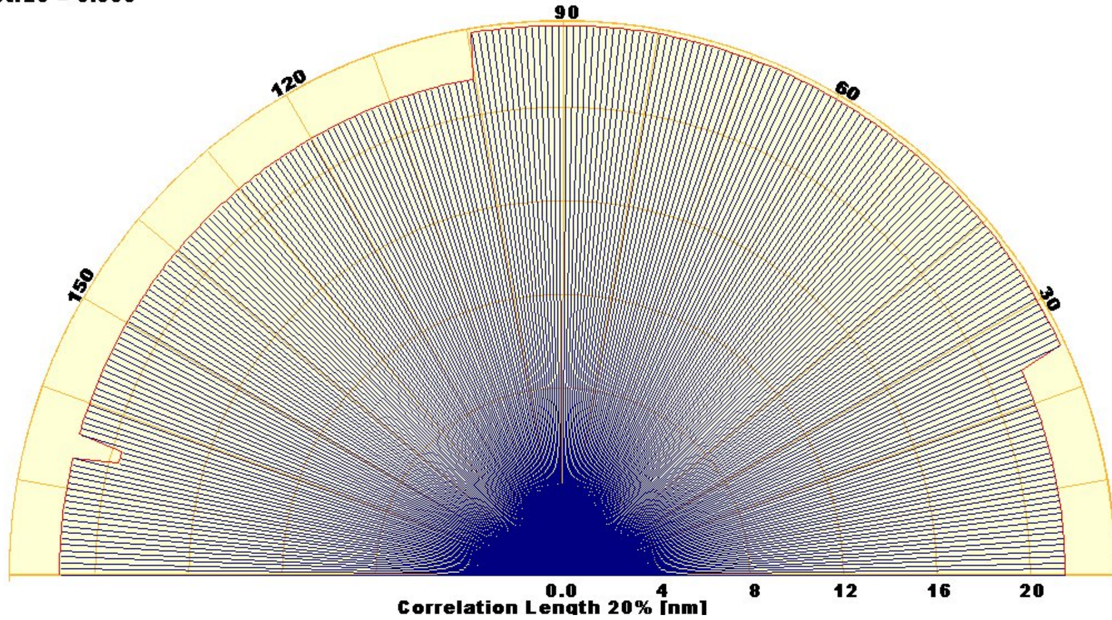

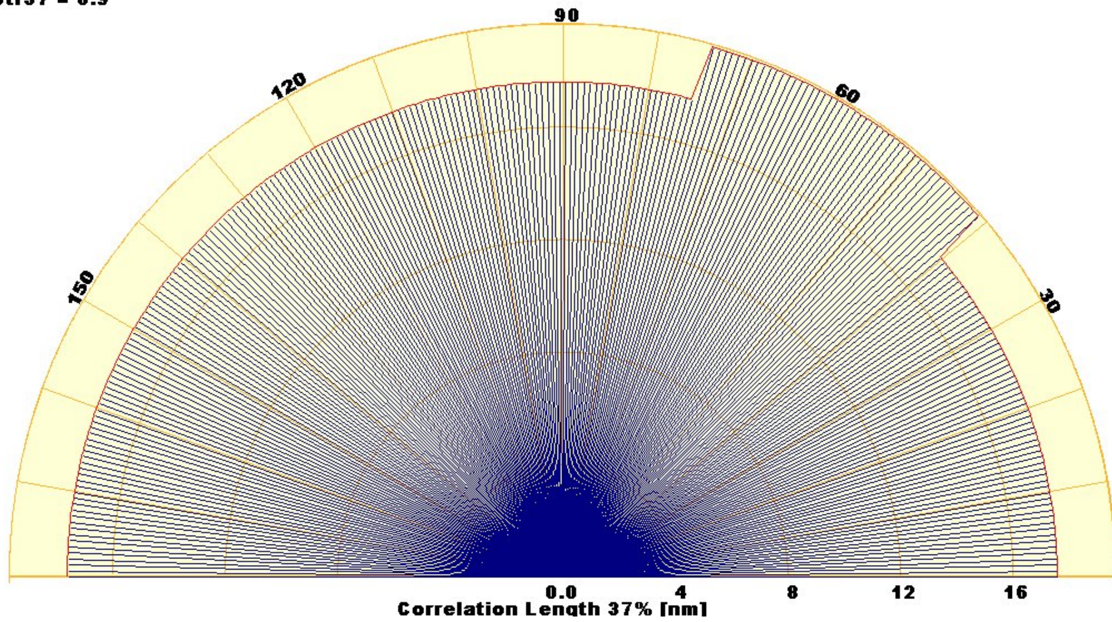

For an anisotropic surface, the correlation length is in a direction perpendicular to the surface layer. In principle, the texture aspect ratio has a value between 0 and 1. For a surface with a dominant layer, the parameters will approach 0.00, whereas, a spatially isotropic texture will result in a Str value of 1.00

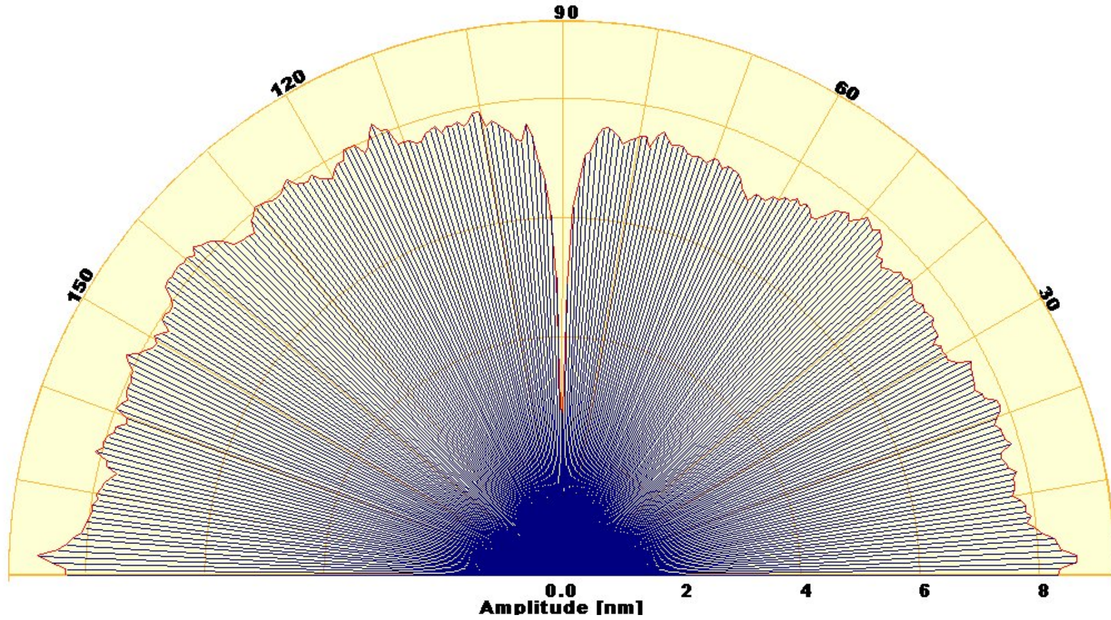

The Texture Direction Index, *Stdi*, for the current film is a measure of how dominant the dominating direction is, and is defined as the average amplitude sum divided by the amplitude sum of the dominating direction: *Stdi* value is always between 0 and 1. Surfaces with very dominant directions will have *Stdi* values close to zero and if the amplitude sum of all direction is similar, *Stdi* is close to 1.

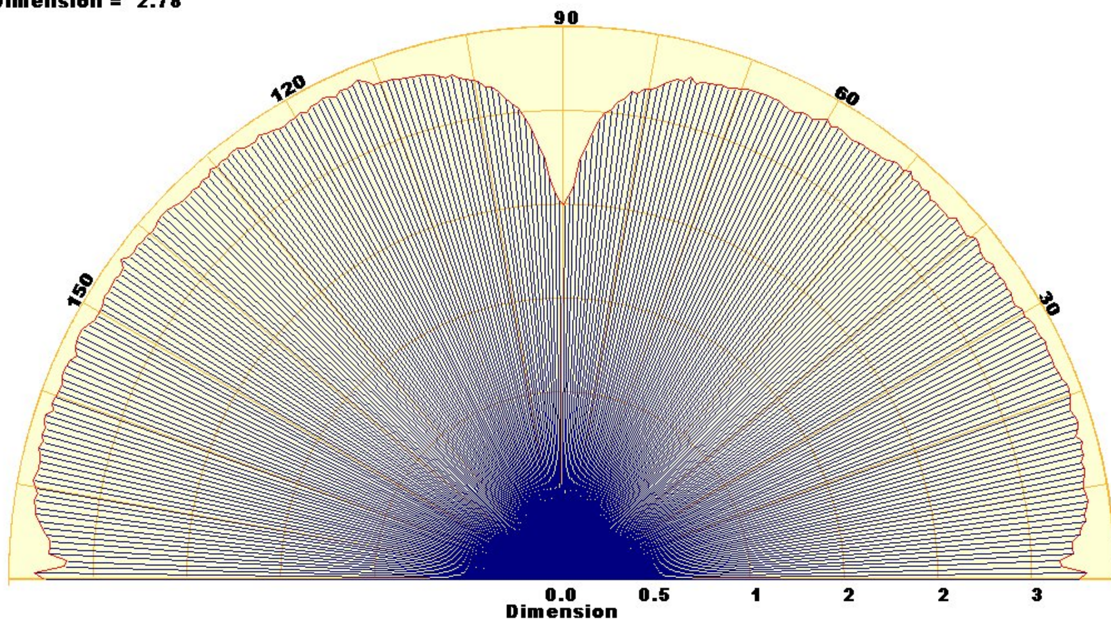

For this film the Mean Fractal Dimension is 2.78 being the average of *Sfd* (surface fractal dimension) which is calculated for different angles by analyzing the Fourier amplitude spectrum.

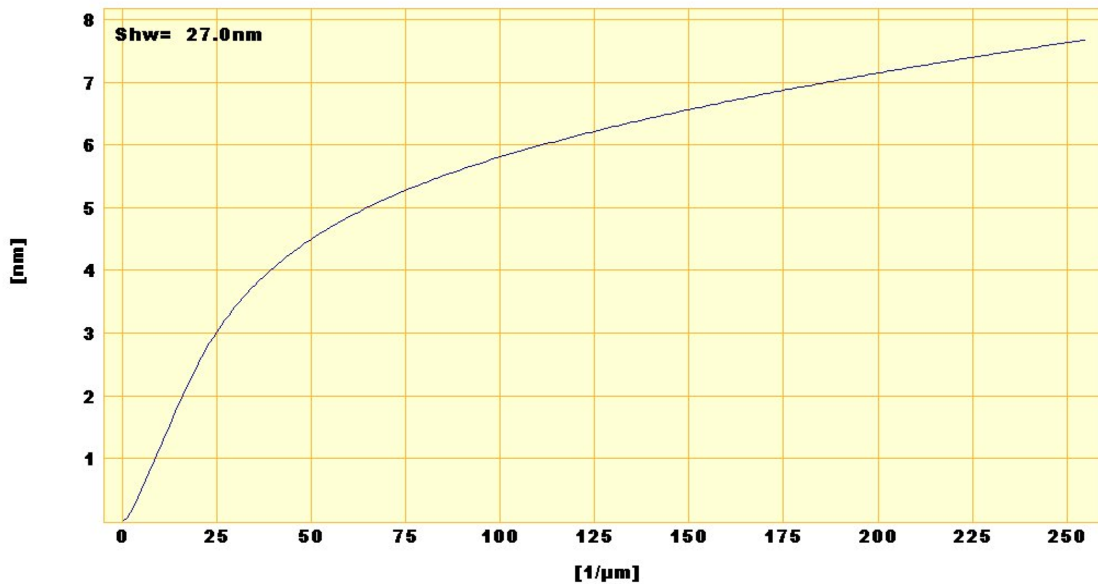

The Mean Half Wavelength, *Shw*, is derived from the integrated radial spectrum. For this film the *Shw* is 27nm.

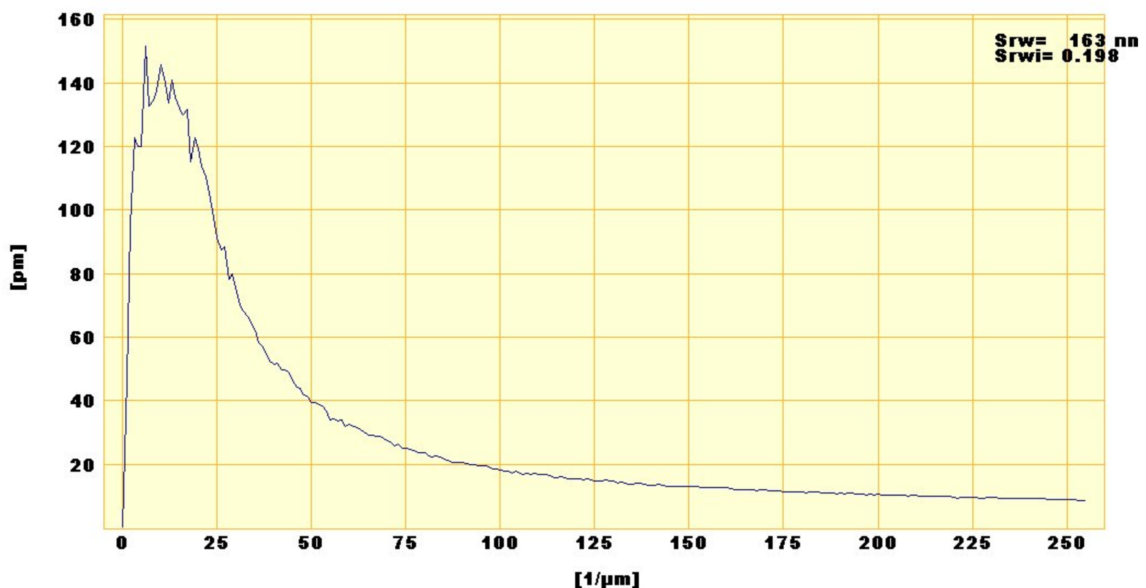

As shown in the above figure, the Dominating Radial Wavelength, *Srw*, corresponds to the semicircle with radius, *rmax*, having the highest amplitude sum, b*max.* And for this specific film has a value of 163nm. The Radial Wave Index, *Srwi*, is a measure of how dominant the dominating radial wavelength is, and is defined as the average amplitude sum divided by the amplitude sum of the dominating wavelength. For the above considered case it has a value of 0.198.

Grain parameters were also determined using The Particle and Pore Analysis module of the SPIP software, which offers four image feature detection methods based on two different segmentation principles: threshold segmentation and watershed segmentation. The two segmentation principles will be now explained in more details.

Threshold Segmentation

To explain the detection method, it is useful to regard an image as a topographic landscape. Then, the detection methods can be described by considering the behavior of water in this landscape. To get a clear idea of the term topographic landscapes, one can see the example below. At the left is an image in normal 2D view. At the right you see a projection of the topographic representation.

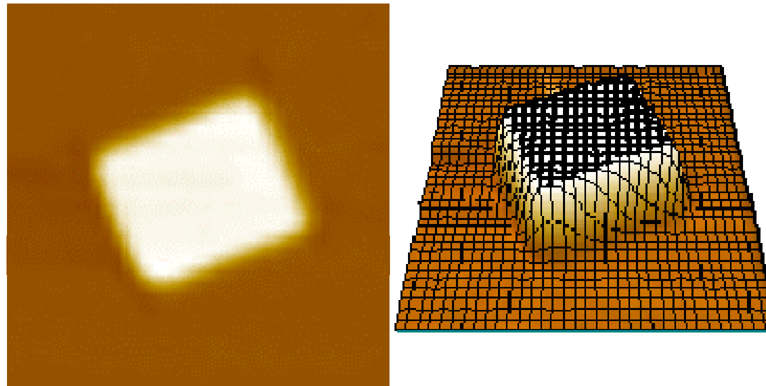

This metaphor applies whether the image is a true topographic image, for example an SPM image, or the image is a conventional optical image or any other type of image.
For the Threshold Segmentation method, one can define Particles and Pores based on a threshold level using the analogy of water flooding a landscape: Particles are the islands left when the landscape is flooded to the threshold level, while Pores are all below the surface of the water.
Consider the 1-Dimensional example represented by the upper curve in the following figure. When a threshold is chosen, indicated by the red horizontal dashed line, a binary condition is imposed. Only the parts of the signal above the threshold are considered as Particles. Correspondingly, in the lower curve, the parts below the Pore Threshold Level, indicated by the blue dashed line, are considered as Pores.

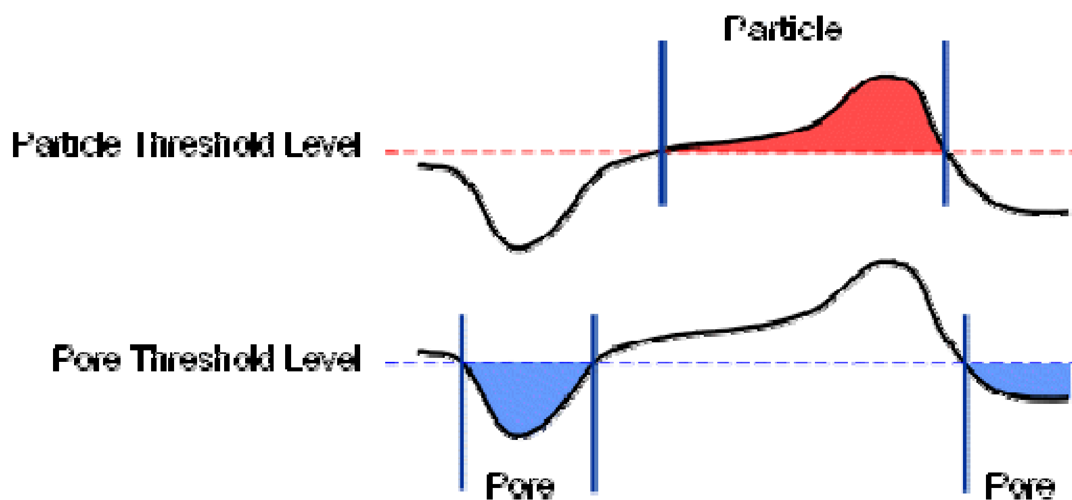

Watershed Segmentation

Basic watershed segmentation can be provided by the Watershed – Packed Features Detect Method. This method can also be explained by a metaphor based on the behavior of water in a landscape. When it rains, drops of water falling in different regions will follow the landscape downhill. The water will end up at the bottom of valleys. In this case we do not consider the depth of the resulting lakes in the valleys. So the Shapes are defined as: for each valley there will be a region where all the water will drain into it. In other words, each valley is associated with a catchments basin, and each point in the landscape belongs to exactly one unique basin.

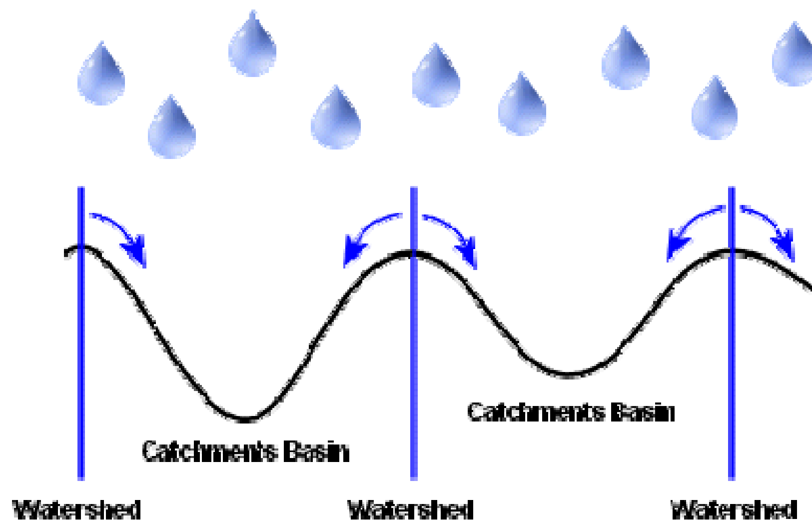

All generated Shapes are by definition *Pores*. In Particle mode the image is inversed behind the scenes, which is the case in the example below:

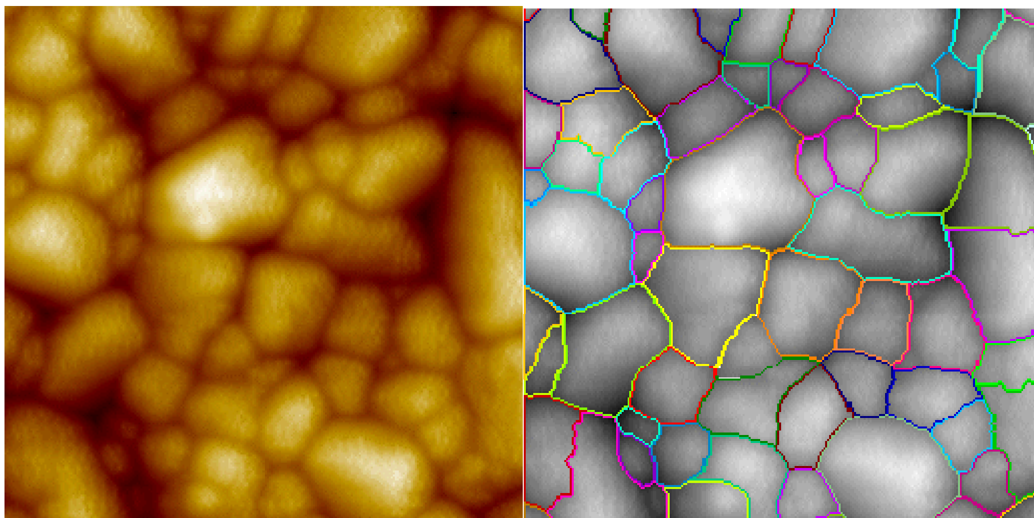

Avoiding over segmentation – Slope noise reduction
As any local maximum in the image will generate a Shape boundary (or part of), it is obvious that watershed segmentation has a strong potential for over segmentation, if not for other reasons, then because of noise. In order to compensate this, there is a built in noise reduction scheme – the Slope Noise Reduction filter. This filter eliminates small ridges that could otherwise trigger detection of Shape borders. The filter will exchange pixels with interpolated values using the following criteria.
1) The pixel has a Z value that is either larger or smaller than its two neighbor pixels in the X direction or its two neighbor pixels in the Y direction.
2) The slope to its neighbor pixels is smaller than the entered percentage of the maximum slope. In contrast to a Median filter, this filter will only affect the smaller corrugations.

Watershed – Packed Features
When the image is fully covered by adjoining features of the same type, i.e. Pores or Particles, with no spacing in between, the the Watershed – Packed Features method can be used. as for example the grain structure of a rough surface. Watershed segmentation works after the following principle: using the analogy of water flooding a landscape, water coming as rain water will drain into the bottom of all valleys. Hence, every valley is associated with a catchment area, from where all rain will run into the same drain. Shapes are generated from these catchment areas (or basins). All features are by definition Pores. In Particle mode, the image is inversed behind the scenes.

For all ZnO thin films prepared by DC magnetron sputtering, the grain size parameters were determined using the watershed method. Segment optimization of surface was done manually. Surface segmentation for the film presented above is shown in the figure:

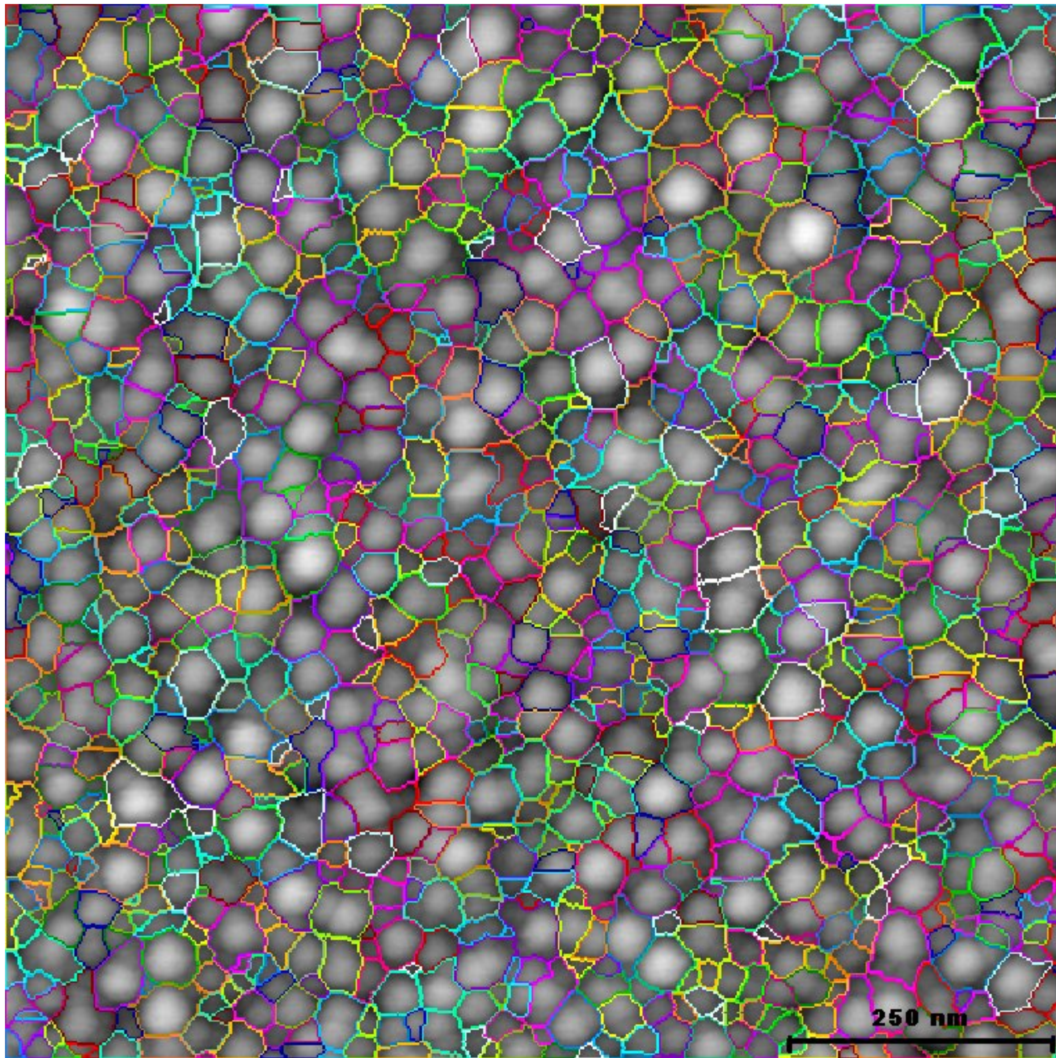

In this image, the color code associates to equivalent grains. Once the segmentation is done in the proper way to avoid overlap of boundaries or "agglomerations", grain parameters can be estimated for each family of grains. Then, mean values for each parameter are calculated taking into account the size frequency onto surface. Errors are also evaluated. An example of datasheet for the above film is attached below and shows the list of grain geometrical parameters and the statistical data for the estimation of each parameter evaluated.

Grain Distribution Analysis Calculated by SPIP
Date: 2009 07 23 16:44
File: D:\Date\afm data\MIRELA\THIKZNO\571BF.002.drh
Detected Segments: 1021
Mode Normalized Segments: 3026
Mean Area: 983 nm^2
Segments per um^2: 1021
Coverage : 100
X Range: 1000.0 nm
Y Range: 1000.0 nm

ID	Area nm^2	Length nm	Width nm	Size nm	Perim nm	Aspect	Diam nm	Volume nm^3	VolAbs nm^3
0	264.25	25.515	10.356	21.526	74.364	2.4638	18.343	44.349	595.19
1	892.31	51.368	17.371	41.096	164.38	2.9571	33.706	390.49	2390.7
2	195.31	31.857	6.1309	31.311	78.278	5.1961	15.77	52.475	523.58
3	1665.9	63.503	26.233	52.838	211.35	2.4207	46.055	1105.3	5023.1
4	520.83	48.924	10.646	46.967	125.24	4.5956	25.752	84.482	1048.8
5	157.02	19.569	8.0235	17.613	58.708	2.439	14.139	17.292	340.41
6	1099.1	55.385	19.845	46.967	180.04	2.7909	37.409	406.25	2915
7	241.27	60.791	3.9688	60.665	136.99	15.317	17.527	209.11	925.09
8	762.1	55.696	13.683	52.838	140.9	4.0704	31.15	576.2	2423.7
9	1171.9	48.61	24.108	41.096	156.56	2.0163	38.627	1097.7	3915.1
10	57.445	19.957	2.8784	19.569	50.881	6.9333	8.5522	4.4785	122.89
11	202.97	28.019	7.244	27.397	82.192	3.8679	16.076	35.264	471.62
12	1049.3	45.853	22.885	39.139	152.64	2.0036	36.552	323.8	2286.3
13	405.94	33.21	12.223	25.44	101.76	2.717	22.735	88.121	910.54
14	2454.8	72.169	34.015	60.665	242.66	2.1217	55.907	2907.2	9144
15	1309.7	67.564	19.385	66.536	195.69	3.4854	40.836	638.41	3413.2
[illegible]6	[illegible]	23.565	9.4259	19.569	70.45	[illegible]	[illegible]	29.664	[illegible]
[illegible]	[illegible]	[illegible]	7.9316	[illegible]	[illegible]	[illegible]	[illegible]	[illegible]	[illegible]
[illegible]	[illegible]	[illegible]	[illegible]	[illegible]	117.42	[illegible]	[illegible]	[illegible]	[illegible]
1010	375.3	36.559	10.266	[illegible]	105.68	3.5612	21.86	74.662	919.54
1011	202.97	21.077	9.63	19.569	66.536	2.1887	16.076	69.979	689.55
1012	206.8	27.467	7.529	27.397	82.192	3.6481	16.227	47.127	488.37
1013	160.84	21.879	7.3515	21.526	66.536	2.9762	14.311	25.463	421.97
1014	103.4	18.462	5.6008	15.656	50.881	3.2963	11.474	14.254	224.56
1015	191.48	29.419	6.5087	29.354	78.278	4.52	15.614	49.183	637.76
1016	65.104	12.531	5.1956	9.7847	35.225	2.4118	9.1046	2.4918	181.63
1017	103.4	19.957	5.1812	19.569	54.795	3.8519	11.474	6.7115	184.89
1018	176.16	31.857	5.5299	31.311	82.192	5.7609	14.977	60.696	468.1
1019	160.84	31.555	5.0973	31.311	74.364	6.1905	14.311	30.957	358.04
1020	103.4	29.614	3.4916	29.354	74.364	8.4815	11.474	10.926	233.92

	Area nm^2	Length nm	Width nm	Size nm	Perim nm	Aspect	Diam nm	Volume nm^3	VolAbs nm^3
Mean	983.27	45.723	19.012	42.142	154.97	2.5739	33.057	759.03	2770.7
SD	712.13	16.607	8.1052	15.866	61.525	0.8585	12.623	942.85	2371.1
Maximum	4266.2	97.396	49.935	91.977	360.08	15.317	73.702	7994.6	17023
Minimum	15.319	6.1884	2.3367	5.8708	19.569	1.5835	4.4164	0.2874	10.925
Median	771.45	43.253	17.669	39.105	144.49	2.3874	31.36	350.95	1982.2
Mode	331.82	32.26	16.726	32.876	110.46	2.3394	28.64	0.2874	1061.3
Total	1.00E+06	46683	19411	43027	1.58E+05	2628	33751	7.75E+05	2.83E+06

Grain parameters, for the same film, are presented as surface frequency histograms in the following figures:

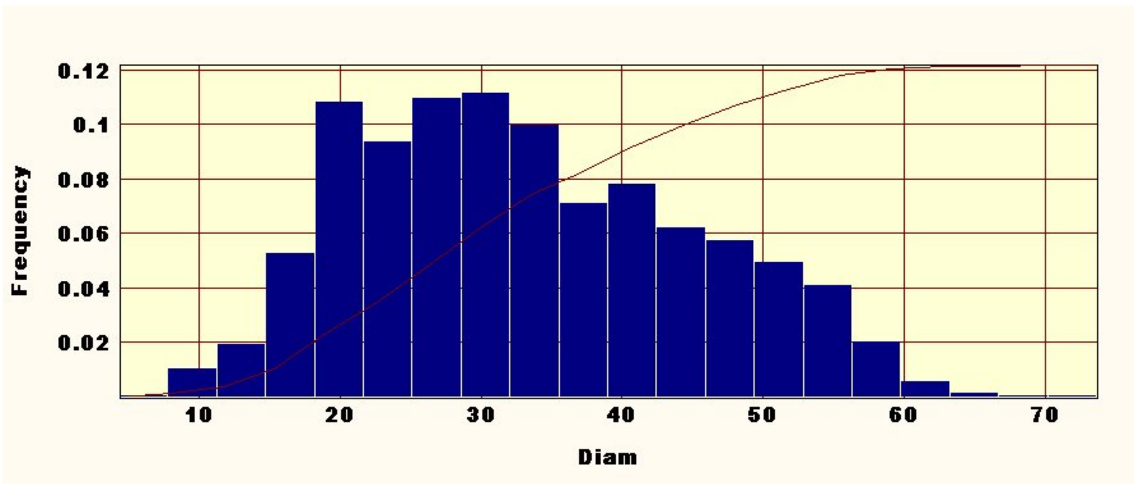
Frequency
0.12
0.1
0.08
0.06
0.04
0.02
10
20
30
40
50
60
70
Diam

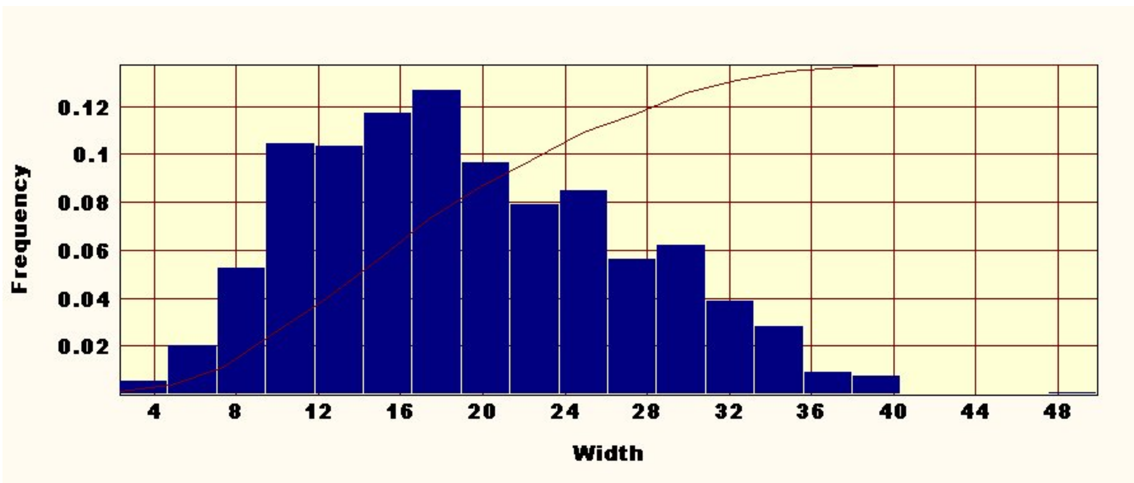
Frequency
0.12
0.1
0.08
0.06
0.04
0.02
4
8
12
16
20
24
28
32
36
40
44
48
Width

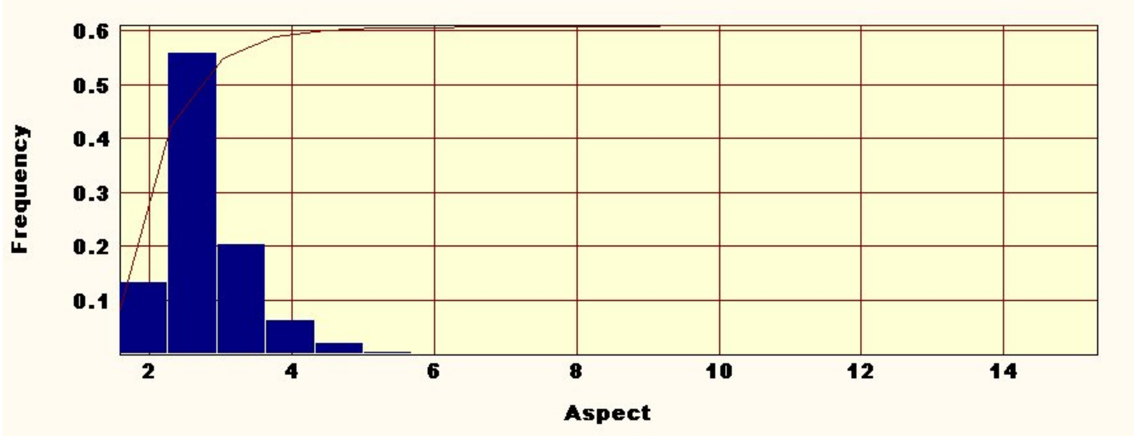
Frequency
0.6
0.5
0.4
0.3
0.2
0.1
2
4
6
8
10
12
14
Aspect

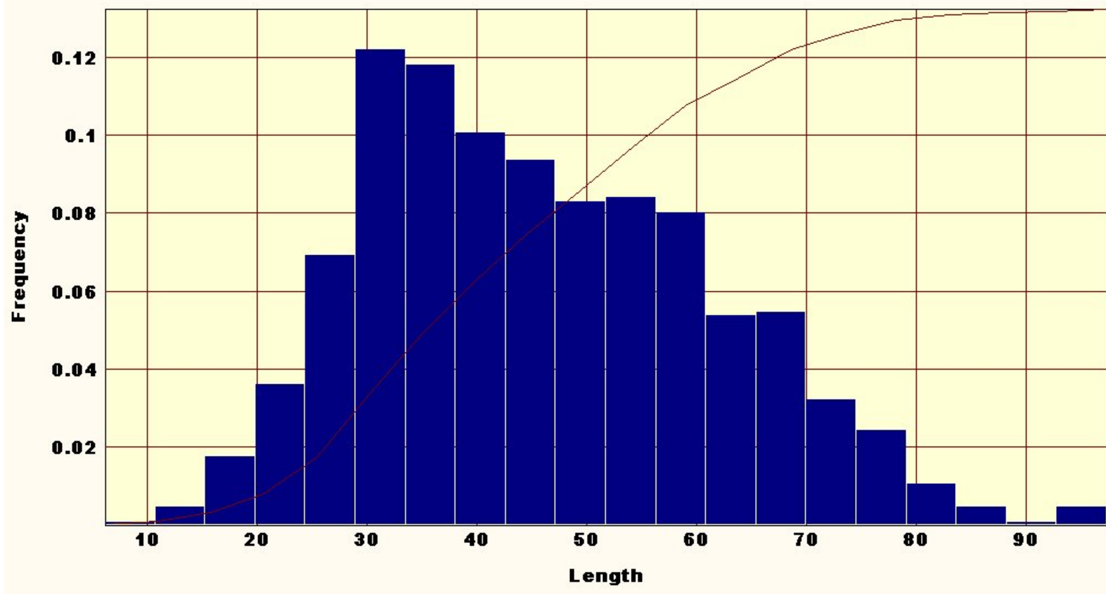

Frequency
0.12
0.1
0.08
0.06
0.04
0.02
10 20 30 40 50 60 70 80 90
Length

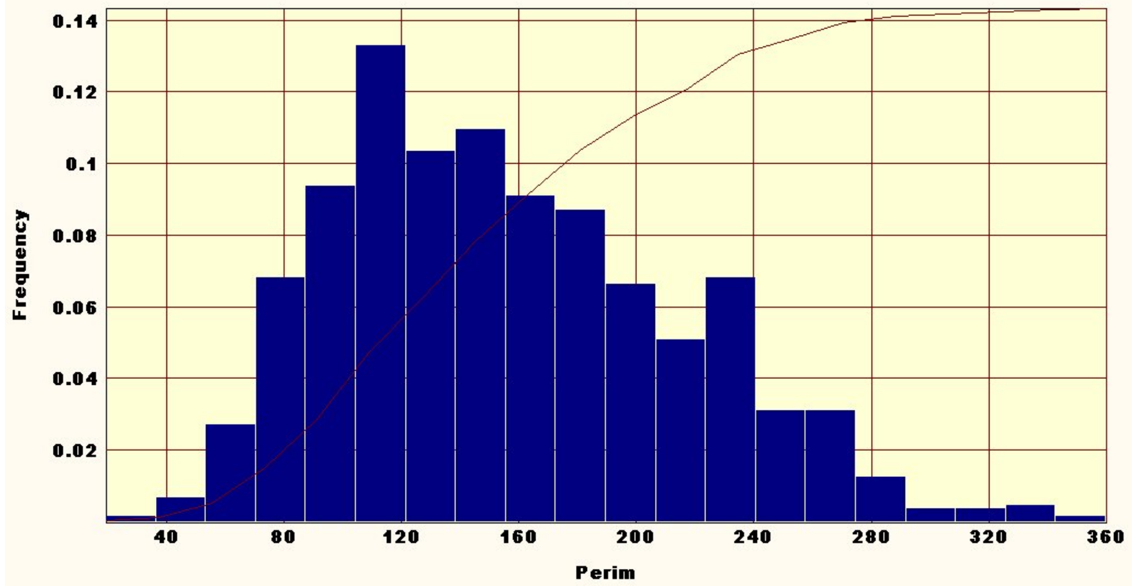

Frequency
0.14
0.12
0.1
0.08
0.06
0.04
0.02
40 80 120 160 200 240 280 320 360
Perim

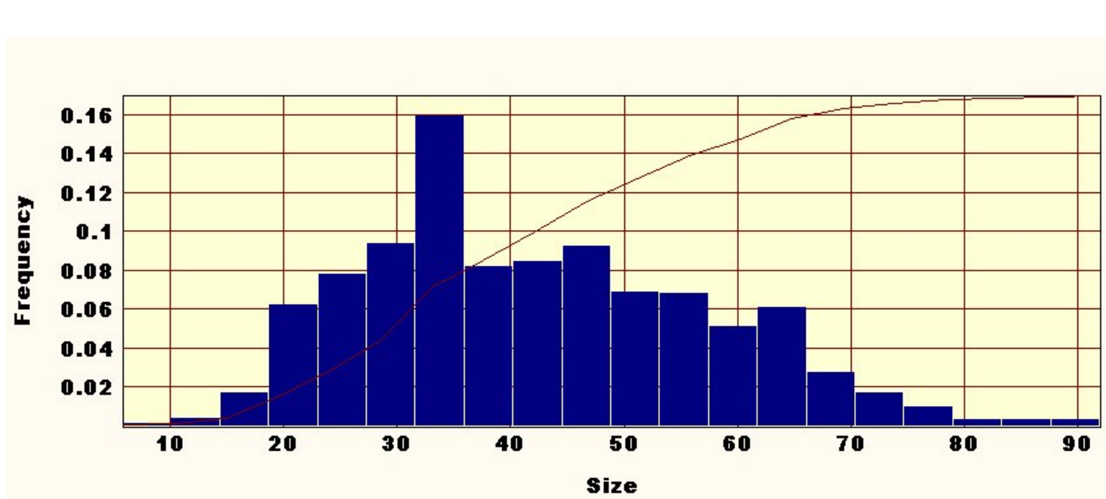

Frequency
0.16
0.14
0.12
0.1
0.08
0.06
0.04
0.02
10 20 30 40 50 60 70 80 90
Size

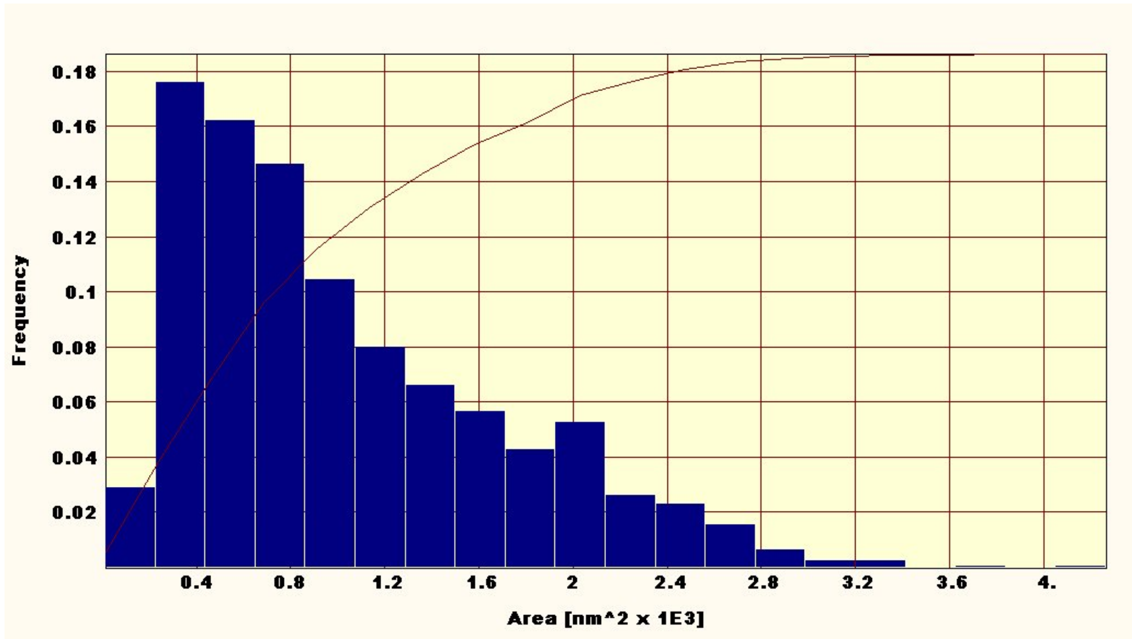

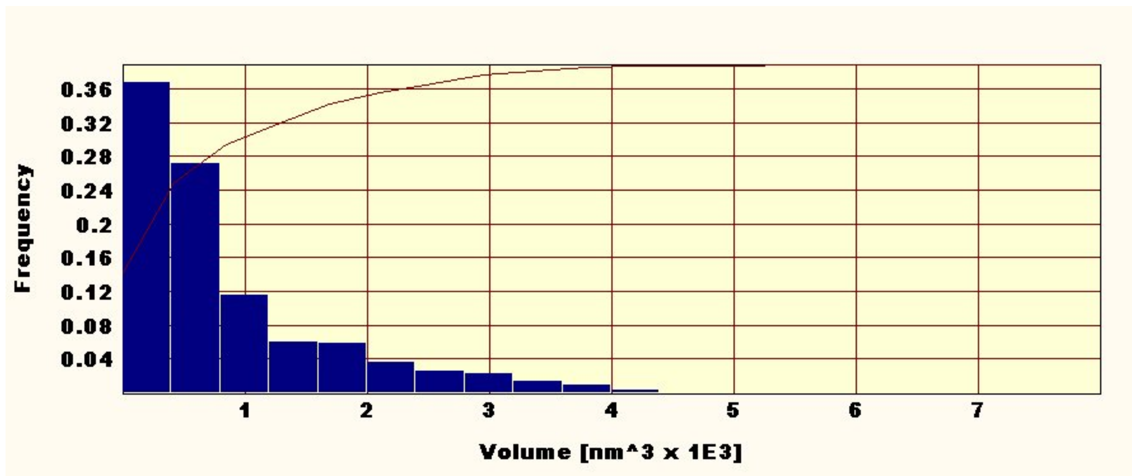

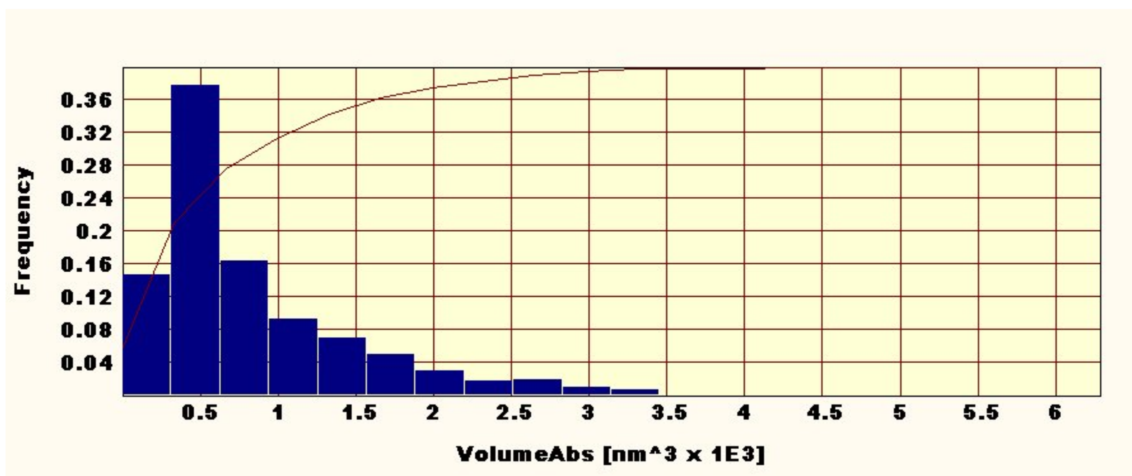

The results of this characterization for each film became a part of a large table-matrix, where all growth parameters were included together with the conductivity values: as deposited conductivity, the saturation conductivity in reduced state,

saturation conductivity after ozone oxidation and the ratio of the conductivities photoreduced/as deposited and photoreduced/oxidized.
The explanations and the concrete significance of each of the parameters presented above can be found in details in the annex 7B attached at the end of this chapter.

7.2 Considerations for modeling

The tables containing all parameters for each film are attached at the end of this chapter as annexes 7C, 7D, 7E and 7F.
A general model based on experimental results for estimation of surface topography influence on sensing properties of metal oxide thin films can be developed. This model may be a lifetime work due tot the fact that the number of independent variables involved in the discussion is huge and powerful computational skills and infrastructure must be involved.
The model should consider three groups of variables:

- Growth parameters characteristic to growth technique
- Surface parameters: roughness parameters and grain parameters
- Sensing involved parameters (the conductivities)

All these are strongly material connected.
In order to keep realistic limits and the need of generality on parameter considerations, optical parameters, required for the fact that film activation in this case is with UV light, are not included in the matrix. Thus the model can be used also for other types of activation.
Deterministic parameters during growth by DC magnetron sputtering growth technique are gas pressure, plasma composition, flow rates, plasma currents, and substrate temperature during growth, growth rate and film thickness.
Growth rate is a parameter depending on most of the others. Considering the growth rate as measured using a thickness monitor during deposition from species arriving to substrate, the only parameter not influencing this is the substrate temperature during growth. Thickness is also deduced from this growth rate multiplied by deposition time. Based on this, we can limit the independent parameters number from growth at two: substrate temperature and growth rate.
In the case of PLD deposition the equivalent of those can be considered substrate temperature and thickness/number of pulses. In our case thickness measurements using alpha step showed the direct proportionality of this with pulse number and we will consider the pulse number as independent variable. It must be mentioned that in all PLD depositions laser parameters were kept constant as well as pressure, plasma compositions, target, and substrate-target distance.
From surface associated parameters based on careful estimation of dependencies and on experimental results for particular series as shown in previous chapters, will be considered for correlation SDR and SFD from surface roughness and grain perimeter – as contour related parameter – and grain volume – including height contribution – as representative among grain parameters.
The experimental conductivity parameters are: as-deposited conductivity ($G_{as\ dep}$), the maximum equilibrium conductivity after photoreduction ($G_{max}=G_{photo}$) and the minimum conductivity after ozone oxidation ($G_{min}=G_{oxi}$). Film sensing is defined by changes of conductivities between an on and an off state. The sensor activation is controlled by $G_{photo}/G_{as\ dep}$ ratio while sensing response by G_{photo}/G_{oxi} ratio. From conductivity parameters the two ratios include both photoreduction and sensing response contributions.
To limit the discussion to these eight parameters (growth related: growth rate – GR and growth temperature – T; surface related: active surface ratio – SDR and surface fractal dimension – SFD; grain related: grain volume – V and grain

perimeter – P; sensing related: photo ratio and sensing response) also some optimization tests were performed using statistical methods.

7.3 Sketch of a model

As shown in the previous chapters, the growth process controls the surface formation and structuring. Therefore, it is not possible to neglect the influence of growth condition on the measured surface parameters, since the growth parameters are responsible for all important physical and chemical properties of the material itself. The characteristic growth conditions for each growth technique determine the values of specific parameters like: material density, grain structure and crystallinity, carrier densities, electrical mobility and optical constants, all having significant contribution and role in the sensing application. Although all these have been included in existing sensing models exclusively, there is no model that takes in to account deirectly measurable surface parameters, which are esential to describe accurately the sensing behavior of metal oxide thin films. A realistic model should be based on the simultaneous consideration of two functions: one function that coralates the sensing response with physical and chemical properties of the material and another function that correlates the sensing response with the surface parameters. The grown conditions are deterministic for the elements of a surface function (S) described by the measured surface parameters as well as for the physical and chemical sensing related properties. The convolution of these two functions can describe the sensor response.
Schematically this can be presented in a mathematical form as:

Sensor response = [$f_{Material}$ (growth conditions)] X [$S_{surface}$ (surface parameters, growth parameter)]

Where $f_{Material}$ (growth conditions) denotes a matrix containing all measurable material related physical and chemical parameters and it is the function usually considered in the literature as contribution to semiconductor material electrical related behavior. $S_{surface}$ (surface parameters, growth parameter) describes the surface contribution to sensing response, the surface contribution depending on the growth parameters.

This correlation method can, in principle, lead to a very general model, since the sensor response may include different stimuli acting on the film's surface (thermal, light or chemical stimuli) with a correct consideration of each parameter involved in the specific interaction.

Accurate evaluation of the material related parameters, according to growth conditions for each growth technique used, is an almost routine work nowadays. Prediction of the sensing response according to these parameters is possible and quite well understood in metal oxide sensors based on bulk related sensing phenomena. The challenging problem is the second function, which becomes dominant in the case of systems with at least one geometric dimension in nanoscale range.

The work included in this study provides a set of hypotheses for elaboration of this model. This study containes the parameters needed for the accurate evaluation of the involved functions. The experiments were done in such a way so that the

surface contribution in the sensing response is enhanced. UV photoreduction and ozone atmosphere for oxidation were used in order to obtaine extreme sensing response for the films under investigation. The use of direct current measurements at 1V fixed voltage assures that the samples included in the study are homogeneous and compact semiconductive thin films. The UV photoreduction in vacuum give the guarantee of an organic contamination free process. As a result, the experimentally determined values represent the maximum possible sensing response to oxidizing gases of a film with a specifically structured surface.
The UV photoreduction mechanism can be explained in terms of oxygen depleted surface, due to the UV action. The lamp used for photoreduction has the intensity maximum at a wavelength of 254 nm, which corresponds to a much higher energy than the optical bang gap for both materials. Under UV irradiation a charge separation occurs, the electrons being promoted to the conduction band and leaving holes in the valence band. The O^- from the metal oxide latice recombines with the photogenerated holes, forming radicals. The oxygen radicals can recombine with the the electrons from the conduction band or between them forming O_2 molecules. The oxygen molecules diffuse towards the surface. Due to vacuum in the chamber during photoreduction, the oxygen loss from the surface occurs, forcing the oxygen diffusion from the bulk towards the surface. This process induces a lowering of Schotky barriers existing at the grain boundaries (see chapter 1) and decreasing of the depletion layer at the grain boundaries, resulting in a dramatic increase of the films conductivity. Once the diffusion attains the steady state, the electron concentration in the conduction band reaches a maximum, corresponding to a maximum conductivity value, which remains constant with time, in vacuum, even in the absence of UV light. Oxidation in ozone takes place by the chemisorption of O_3 molecules on the grains surface. After the ozone molecules dissociation $O^{\bullet}$ radicals are forming. The radicals react with the electrons from the conduction band. This will cause a decrease of the conductivity, generally at values higher than “as deposited” ones due to an irreversible removal of contaminations. The conductivity changes during a photoreduction-oxidation process are directly related to chemisorption of species on the surface and bulk diffusion processes. Bulk diffusion is a very slow process and it can be neglected in the case of very thin films. In films with larger thickness, the bulk contribution to the film conductivity can be fairly considered constant and it can be modeled as a parallel fixed resistance connected to the variable resistance of the surface.

Using the already defined ratio G_{photo}/G_{oxi} (i.e. the ratio between maximum and minimum conductivity in the photoreduced and the oxidized states) as the maximum sensing response, this can be described and correlated with surface and growth parameters.
The surface function $S_{surface}$ (surface parameters, growth parameter) can be practically computed from experimental data, considering the sensor response as a superposition of bi-dimensional functions having as arguments a surface parameter and a growth parameter.

This can be written as:
$S_{surface}$ (surface parameters, growth parameter) = $\sum a_{kl}F_{kl}$ (s_i, g_j), where a_{kl} are coefficients, s_i=each of the surface measured parameters, g_j= any of the growth parameters influencing the surface formation. F_{kl} (s_i, g_j) functions are describing

the surfaces in the (s_i, g_j, sensor response) 3D-space. "k" is the term index and "l" is an index defining the (si, gj) pair variation in the (s_i, g_j, sensor response) space.
In the concrete case of DC magnetron sputtering and PLD grown films included in this work, considering the eight significant variables presented in the section 7.2, $S_{surface}$ (surface parameters, growth parameters) can be written as:

$S_{surface}$ (surface parameters, growth parameters)= $a_{1l}F_{1l}$ (P,GR)+ $a_{2l}F_{2l}$ (P,T)+ $a_{3l}F_{3l}$ (V,GR)+ $a_{4l}F_{4l}$ (V,T)+ $a_{5l}F_{5l}$ (SFD,GR)+ $a_{6l}F_{6l}$ (SFD,T)+ $a_{7l}F_{7l}$ (SDR,GR)+ $a_{8l}F_{8l}$ (SDR,T).

Each of the F_{kl} functions is described by families of surfaces as represented in the following graphical representations. The l index is determined by the [$f_{Material}$ (growth conditions)] and the a_{kl} coefficients.

Some of the F_{kl} surfaces are represented as generated using custom made software based on the voxel model. Surface detection was done by slicing algorithm. The end criterion is the convergence limit. The surface was forced to pass trough at least 90% of "voxels" surrounding a family of experimental points slicing along one median plan at least 50% of them. A family consists of points for which the spatial separation is under 10 voxels. For doped ZnO films the number of experimental values was to low for this algorithm. Alternative solution was not found based on the fact that sensing response was quite small for these films which are not of major interest for this thesis.

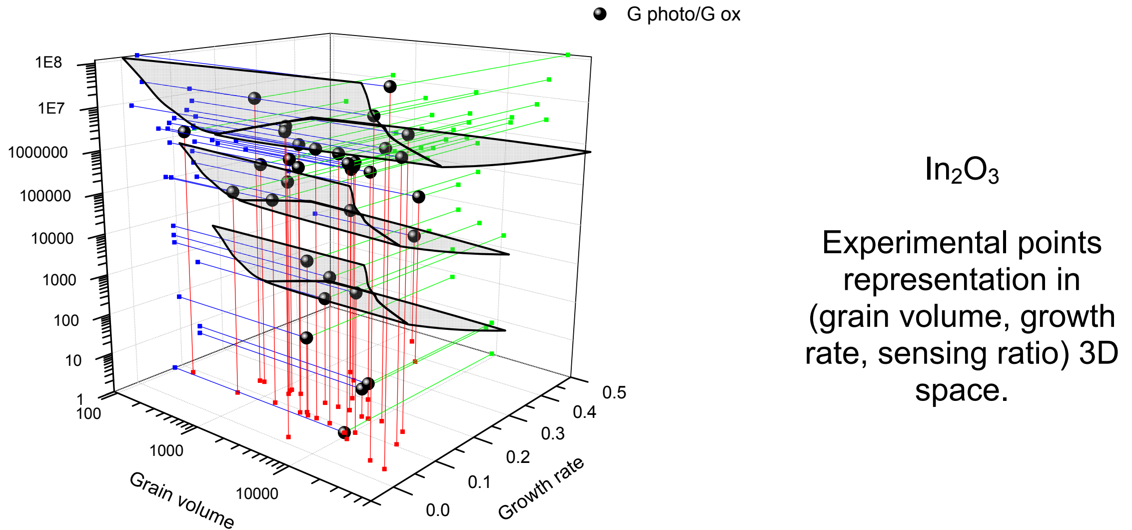

In_2O_3

Experimental points representation in (grain volume, growth rate, sensing ratio) 3D space.

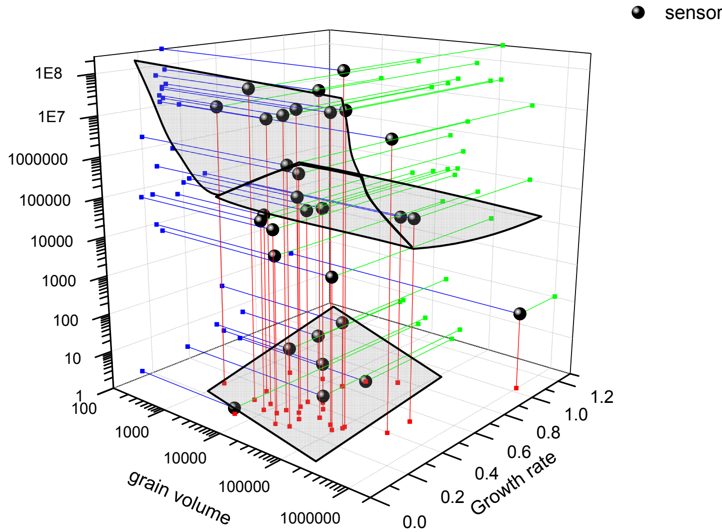

ZnO sputtering

Experimental points representation in (grain volume, growth rate, sensing ratio) 3D space.

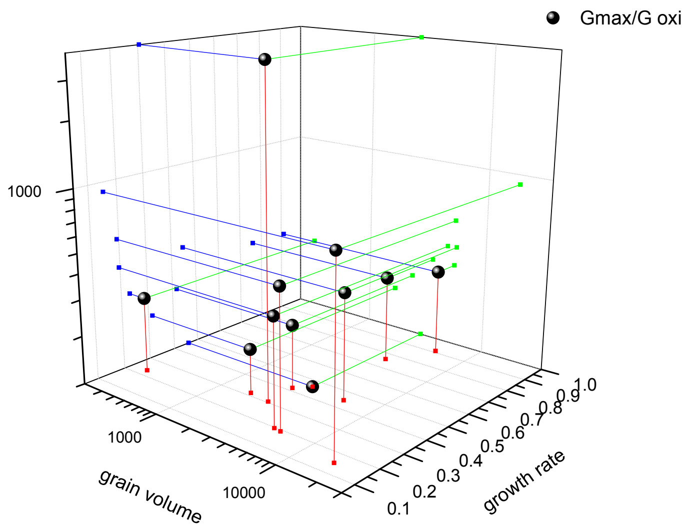

ZAO2

Experimental points representation in (grain volume, growth rate, sensing ratio) 3D space.

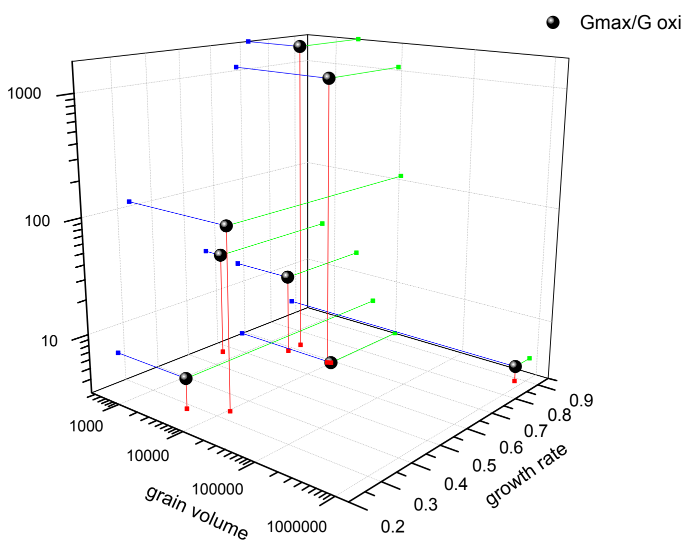

ZAO2D

Experimental points representation in (grain volume, growth rate, sensing ratio) 3D space.

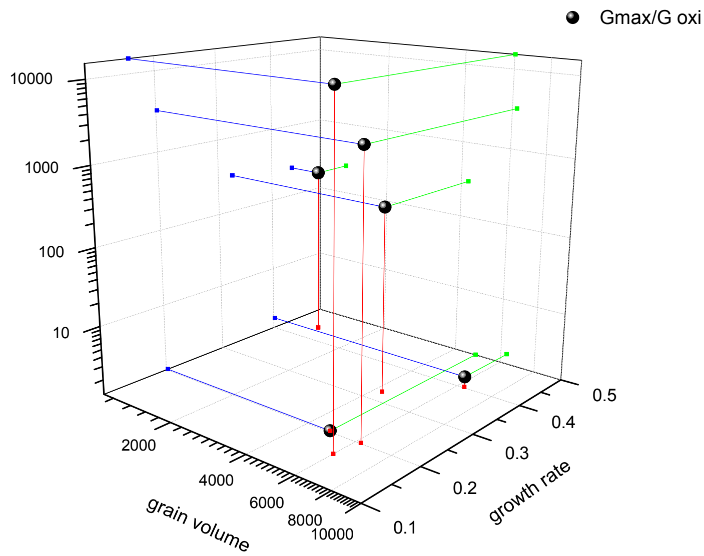

IZO

Experimental points representation in (grain volume, growth rate, sensing ratio) 3D space.

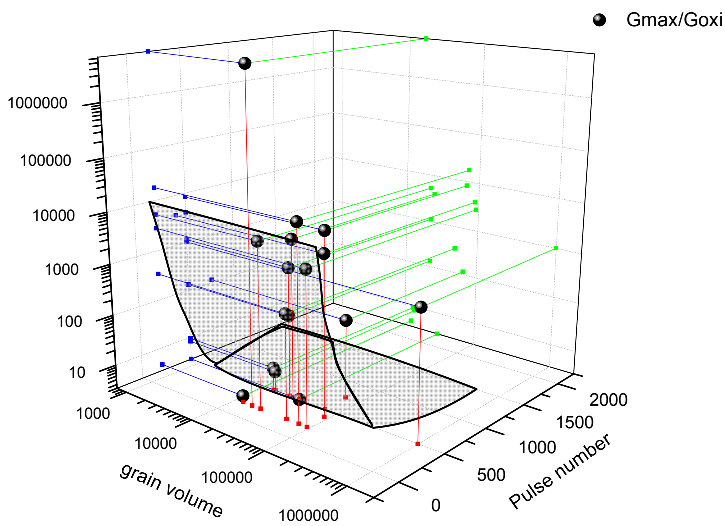

ZnO PLD

Experimental points representation in (grain volume, pulse number, sensing ratio) 3D space.

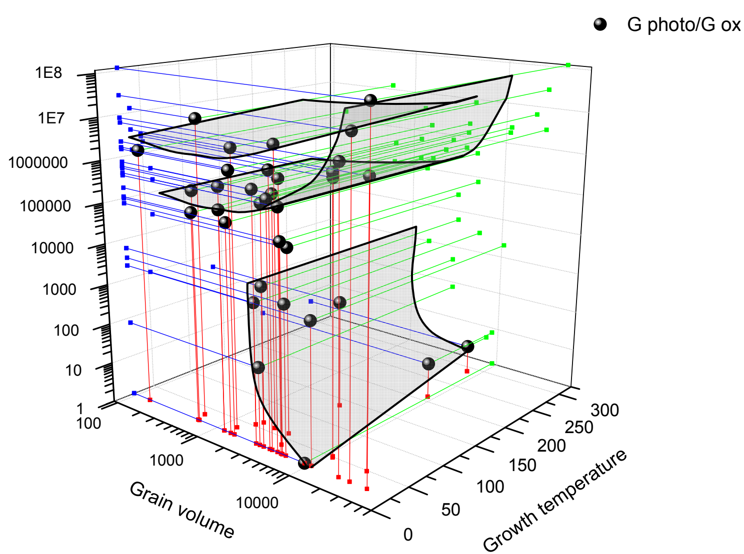

In2O3

Experimental points representation in (grain volume, growth temperature, sensing ratio) 3D space.

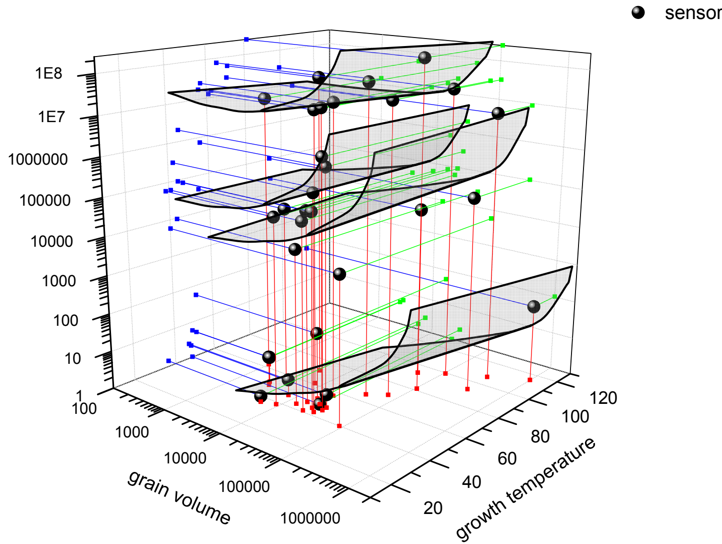

ZnO sputtering

Experimental points representation in (grain volume, growth temperature, sensing ratio) 3D space.

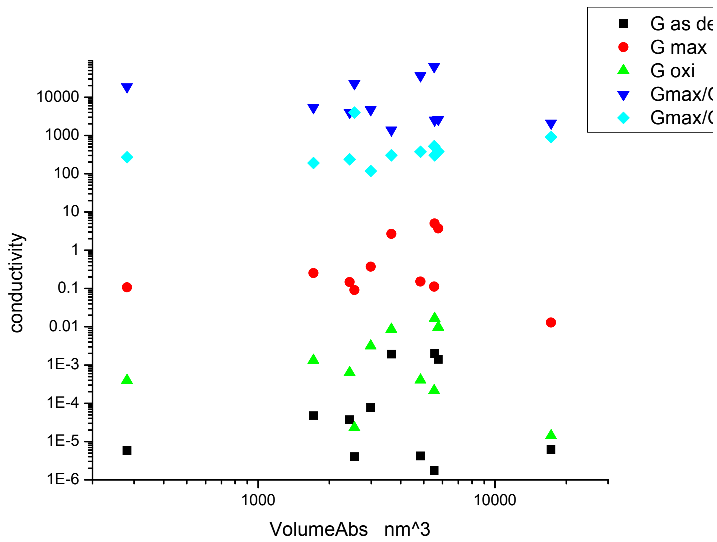

ZAO2

Experimental points representation in (grain volume, growth temperature, sensing ratio) 3D space.

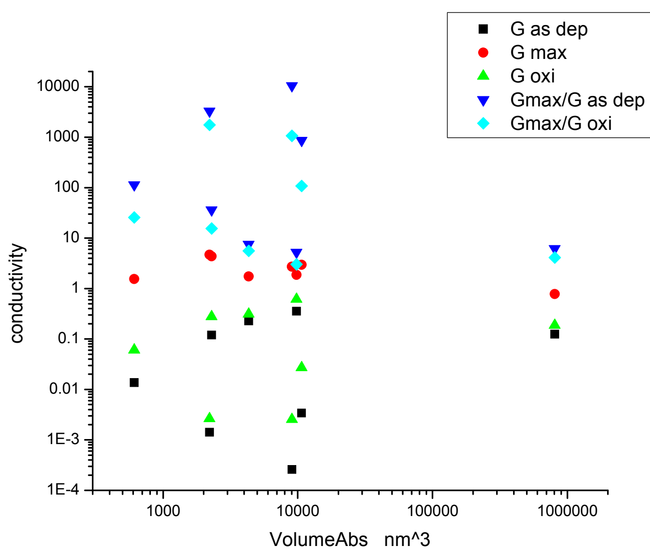

ZAO2D

Experimental points representation in (grain volume, growth temperature, sensing ratio) 3D space.

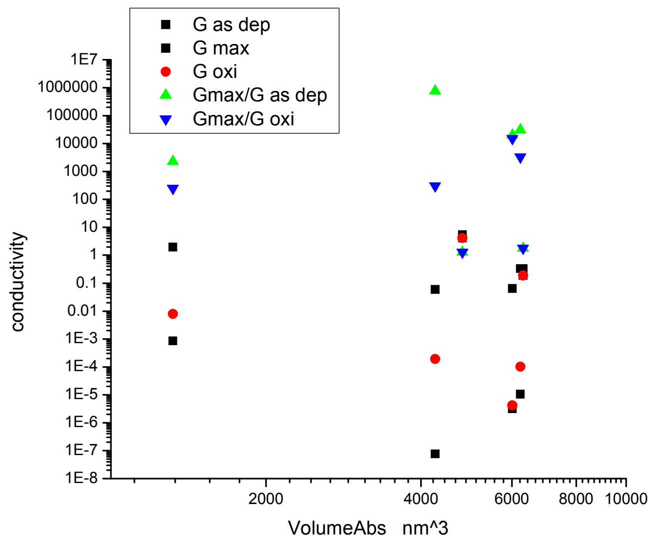

IZO

Experimental points representation in (grain volume, growth temperature, sensing ratio) 3D space.

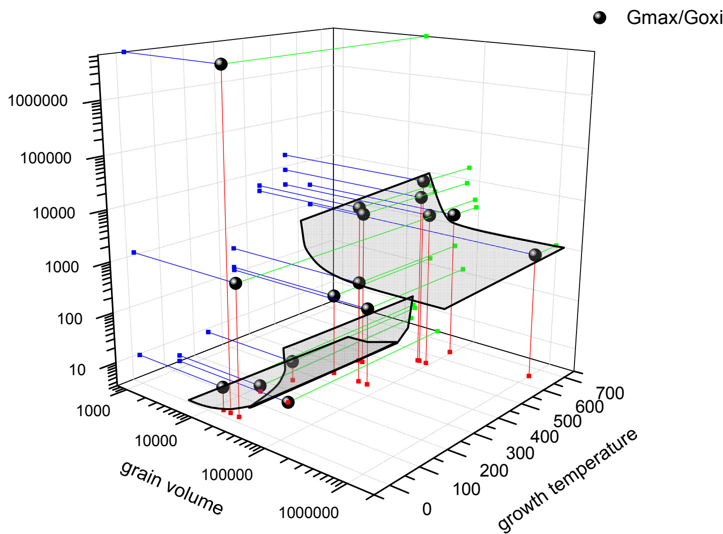

ZnO PLD

Experimental points representation in (grain volume, growth temperature, sensing ratio) 3D space.

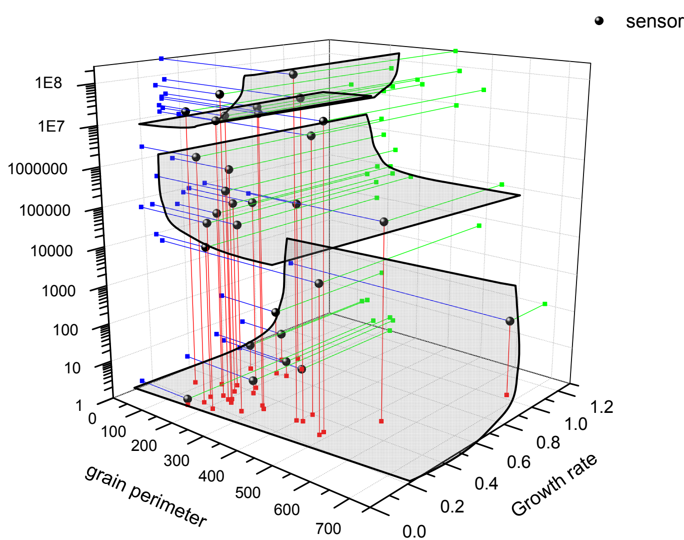

In_2O_3

Experimental points representation in (grain perimeter, growth rate, sensing ratio) 3D space.

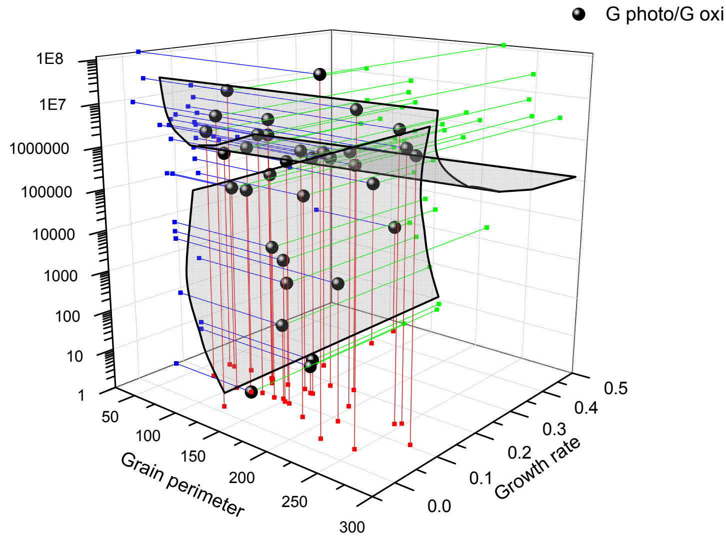

ZnO sputtering

Experimental points representation in (grain perimeter, growth rate, sensing ratio) 3D space.

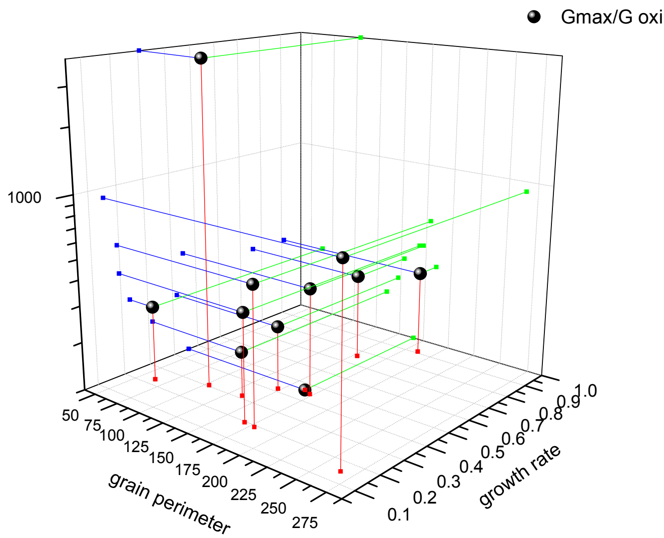

ZAO2

Experimental points representation in (grain perimeter, growth rate, sensing ratio) 3D space.

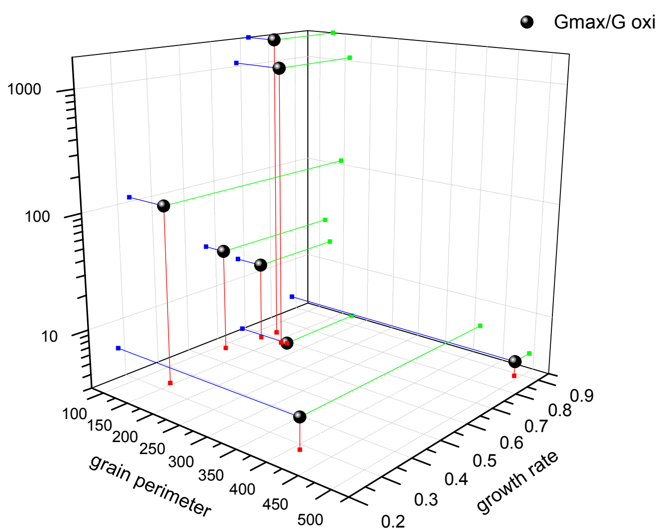

ZAO2D

Experimental points representation in (grain perimeter, growth rate, sensing ratio) 3D space.

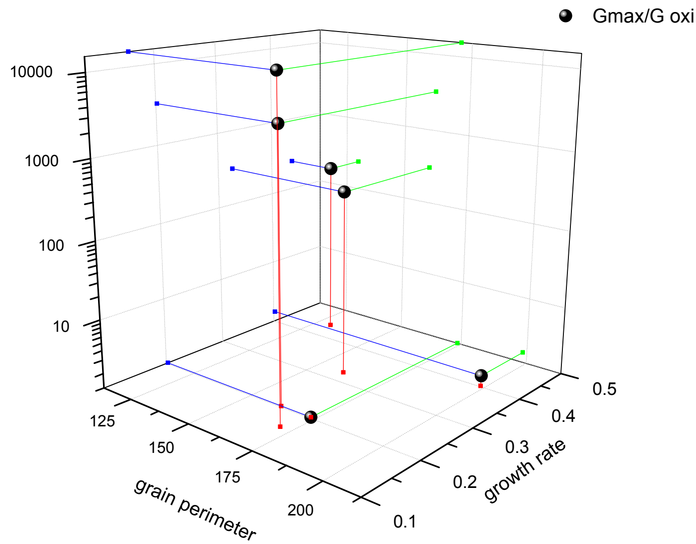

IZO

Experimental points representation in (grain perimeter, growth rate, sensing ratio) 3D space.

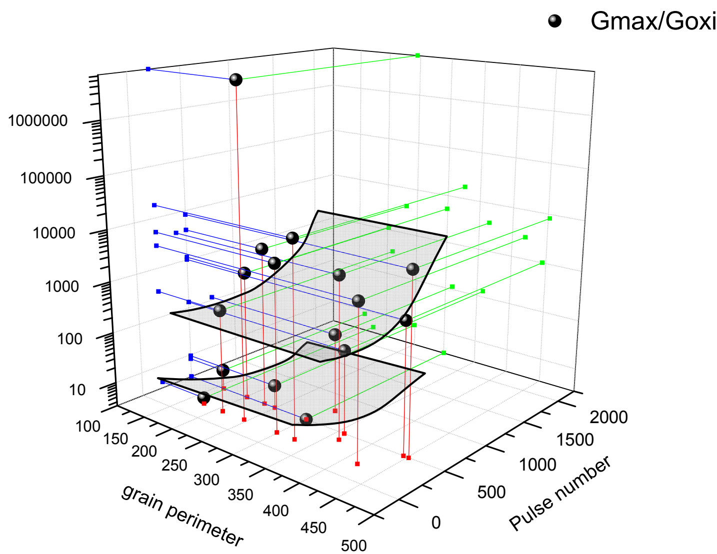

ZnO PLD

Experimental points representation in (grain perimeter, pulse number, sensing ratio) 3D space.

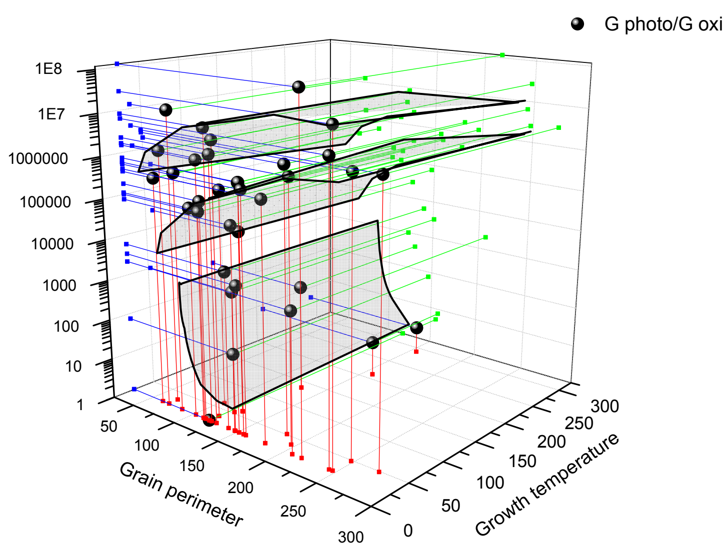

In_2O_3

Experimental points representation in (grain perimeter, growth temperature, sensing ratio) 3D space.

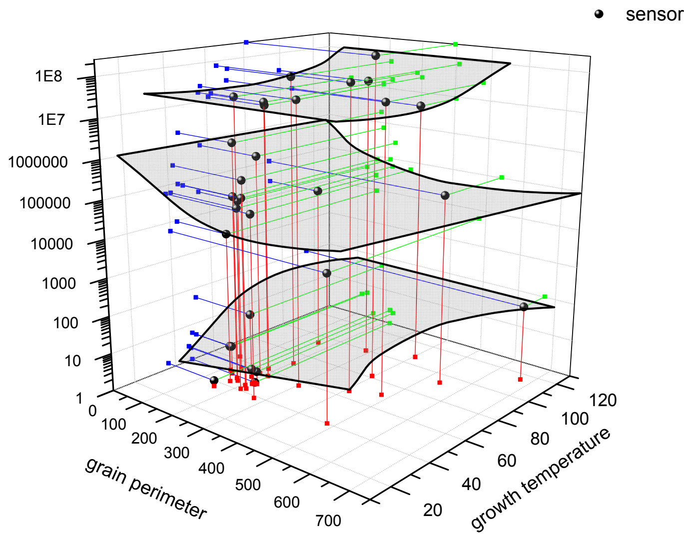

ZnO sputtering

Experimental points representation in (grain perimeter, growth temperature, sensing ratio) 3D space.

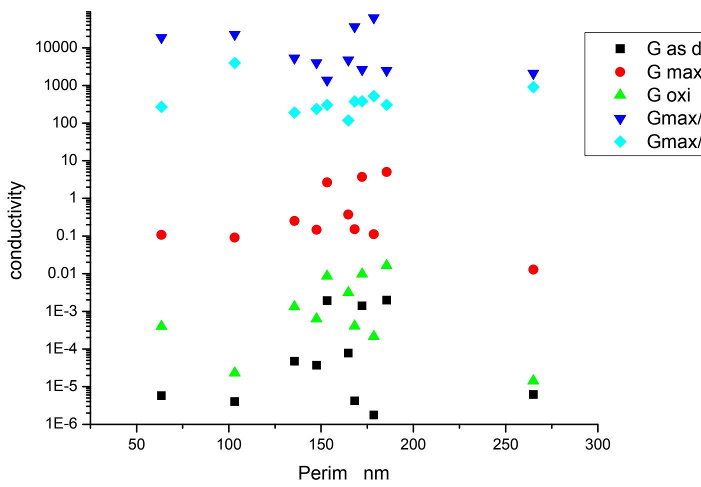

ZAO2

Experimental points representation in (grain perimeter, sensing ratio) 2D space. All the films were grown at RT.

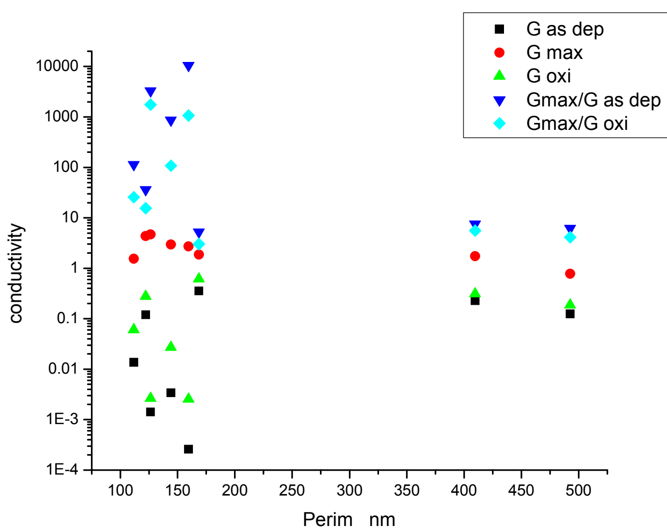

ZAO2D

Experimental points representation in (grain perimeter, sensing ratio) 2D space. All the films were grown at RT.

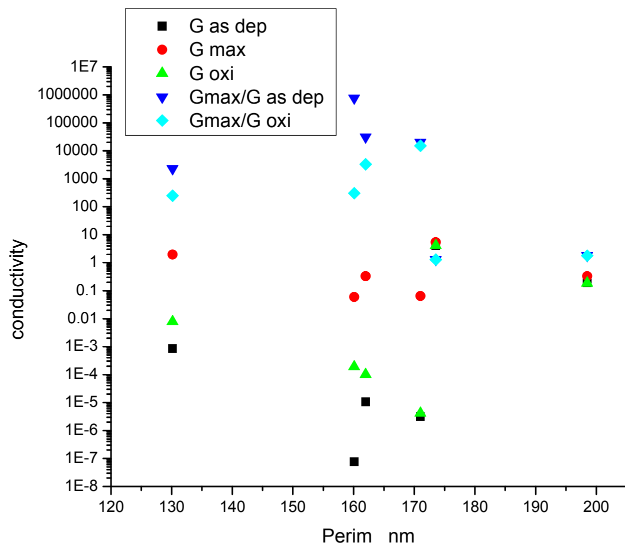

IZO

Experimental points representation in (grain perimeter, sensing ratio) 2D space. All the films were grown at RT.

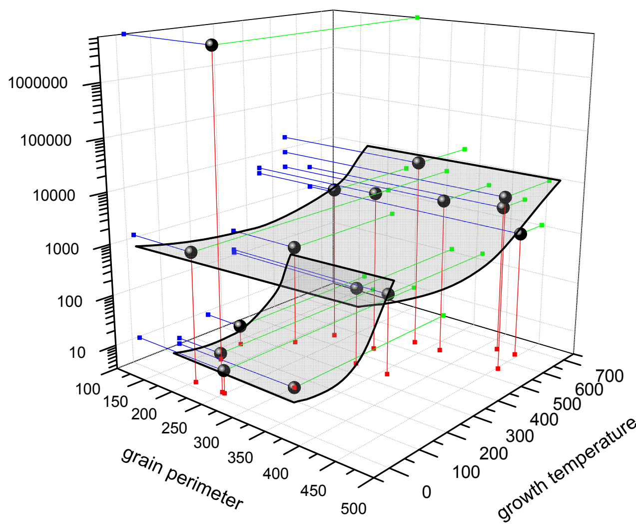

ZnO PLD

Experimental points representation in (grain perimeter, growth temperature, sensing ratio) 3D space.

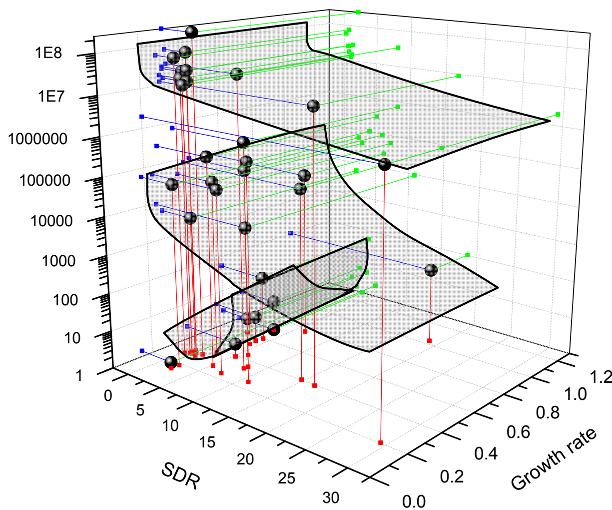

In_2O_3

Experimental points representation in (SDR, growth rate, sensing ratio) 3D space.

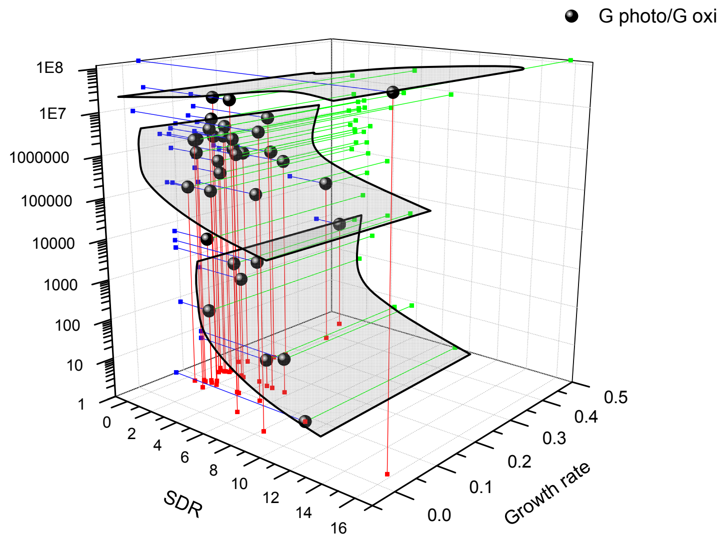

ZnO sputtering

Experimental points representation in (SDR, growth rate, sensing ratio) 3D space.

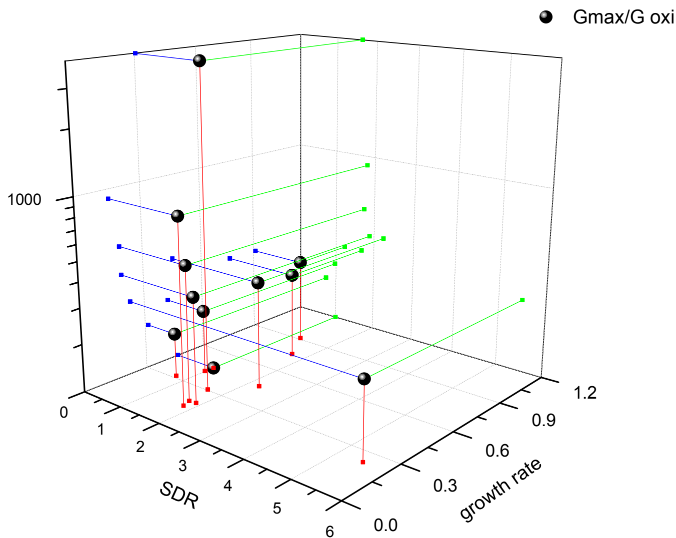

ZAO2

Experimental points representation in (SDR, growth rate, sensing ratio) 3D space.

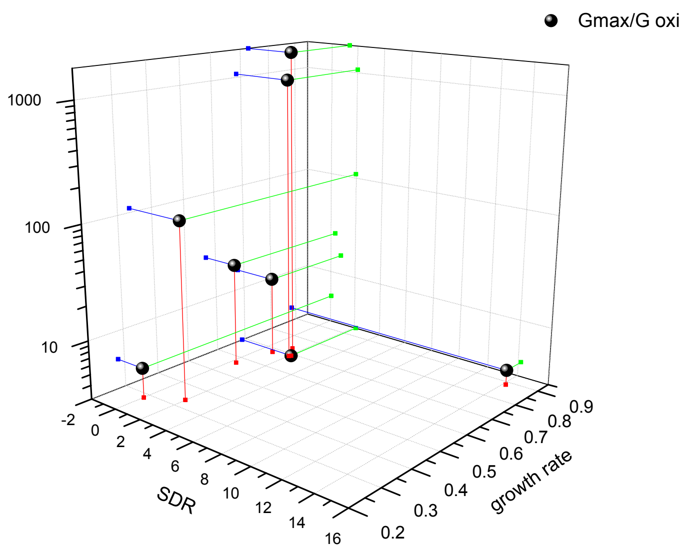

ZAO2D

Experimental points representation in (SDR, growth rate, sensing ratio) 3D space.

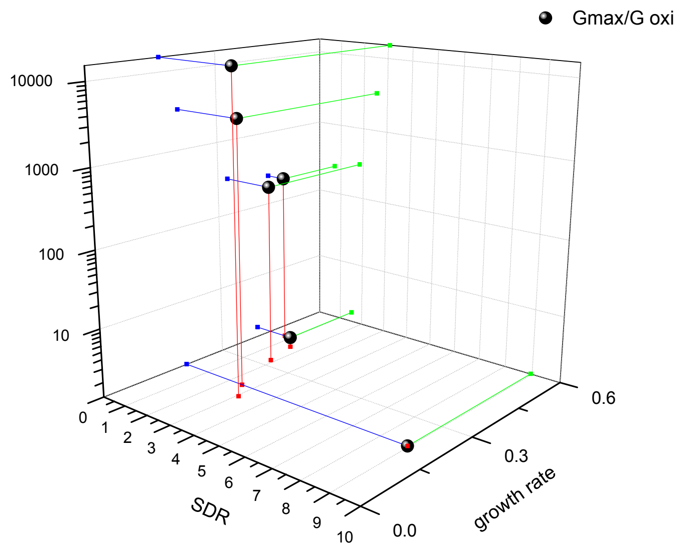

IZO

Experimental points representation in (SDR, growth rate, sensing ratio) 3D space.

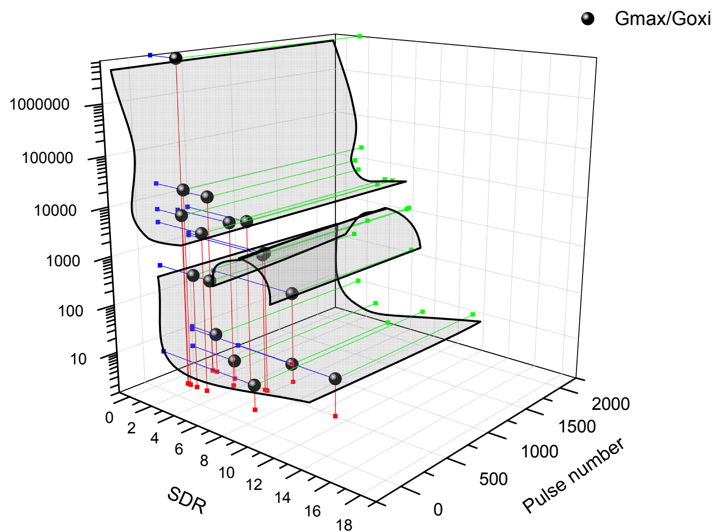

ZnO PLD

Experimental points representation in (SDR, pulse number, sensing ratio) 3D space.

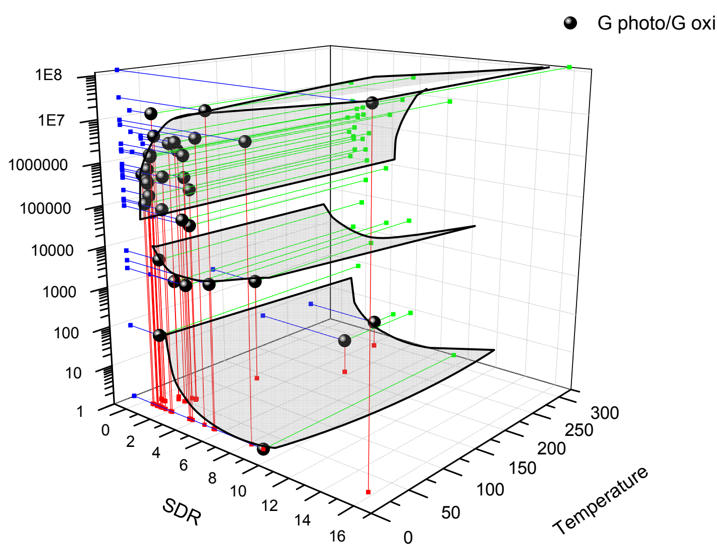

In_2O_3

Experimental points representation in (SDR, growth temperature, sensing ratio) 3D space.

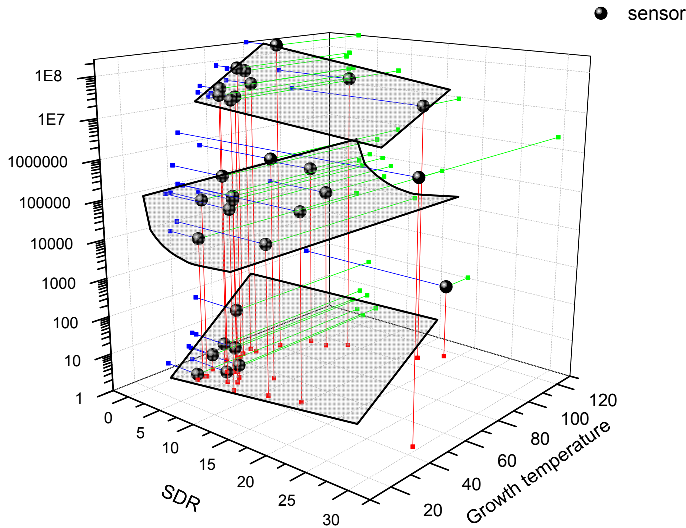

ZnO sputtering

Experimental points representation in (SDR, growth temperature, sensing ratio) 3D space.

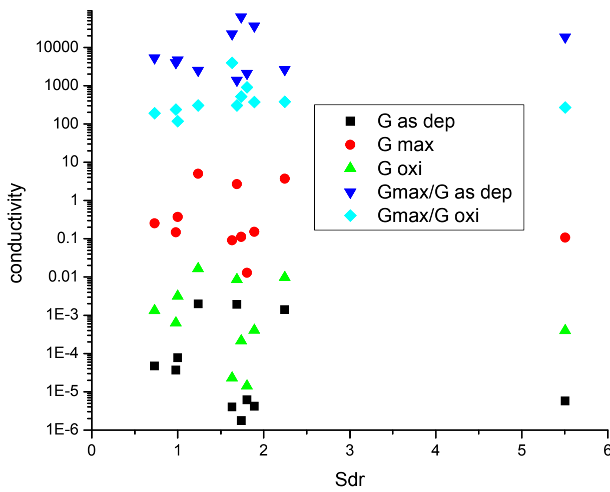

ZAO2

Experimental points representation in (SDR, sensing ratio) 2D space. All the films were grown at RT.

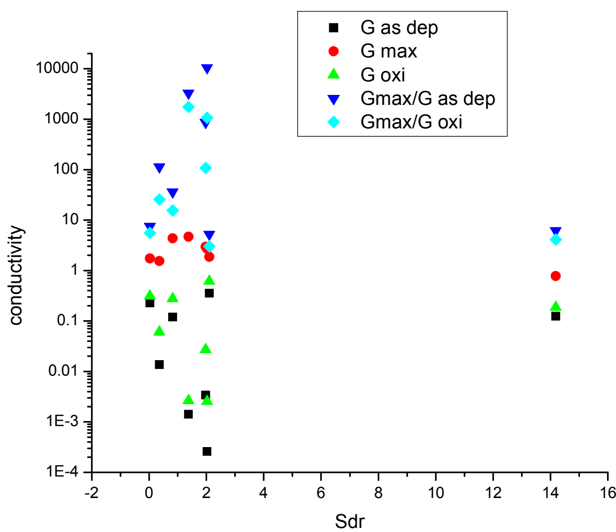

ZAO2D

Experimental points representation in (SDR, sensing ratio) 2D space. All the films were grown at RT.

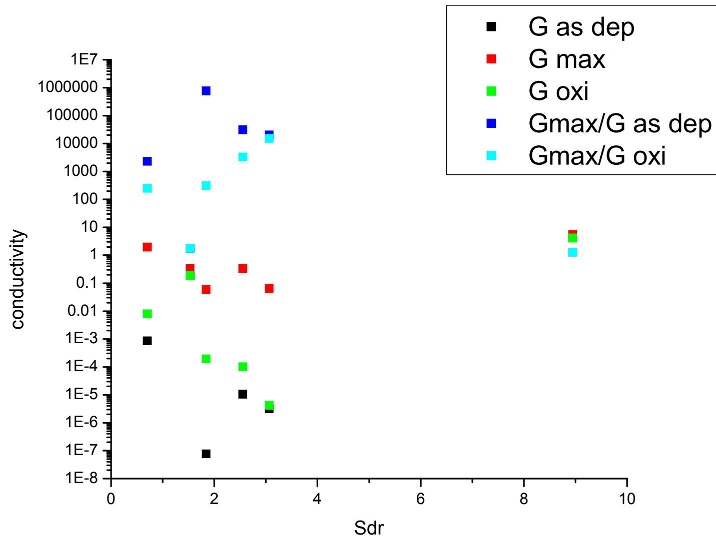

IZO

Experimental points representation in (SDR, sensing ratio) 2D space. All the films were grown at RT.

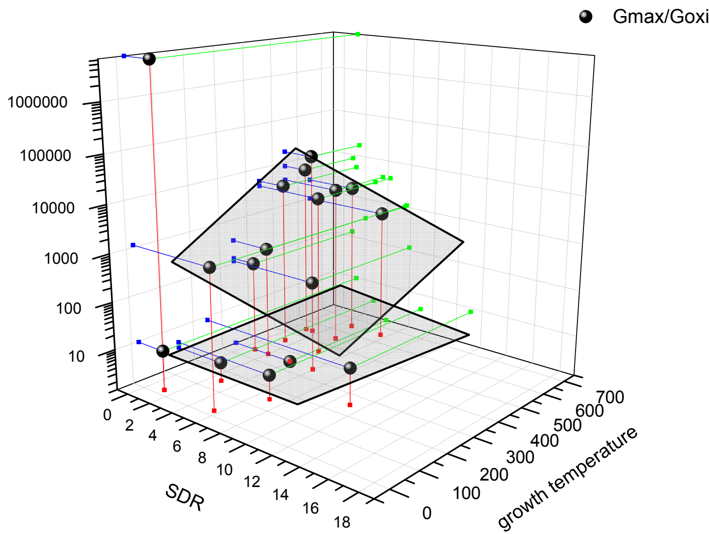

ZnO PLD

Experimental points representation in (SDR, growth temperature, sensing ratio) 3D space.

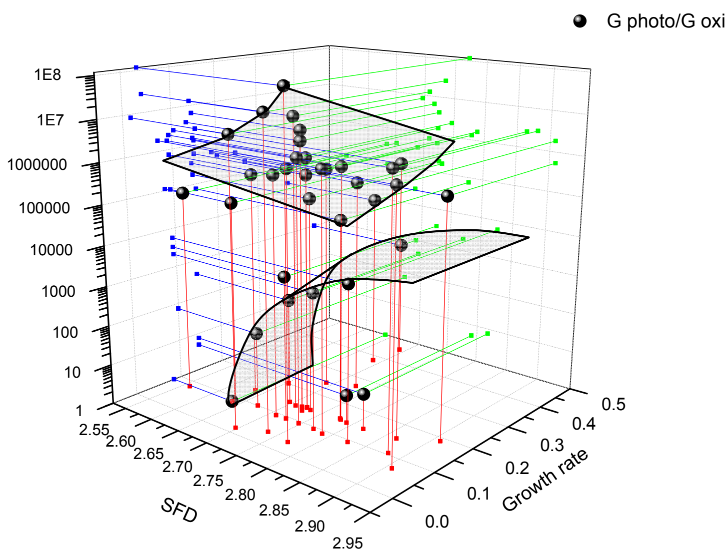

In_2O_3

Experimental points representation in (SFD, growth rate, sensing ratio) 3D space.

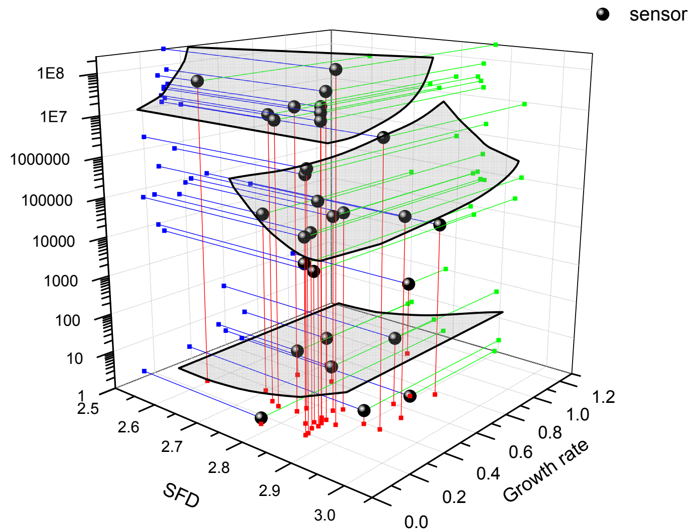

ZnO sputtering

Experimental points representation in (SFD, growth rate, sensing ratio) 3D space.

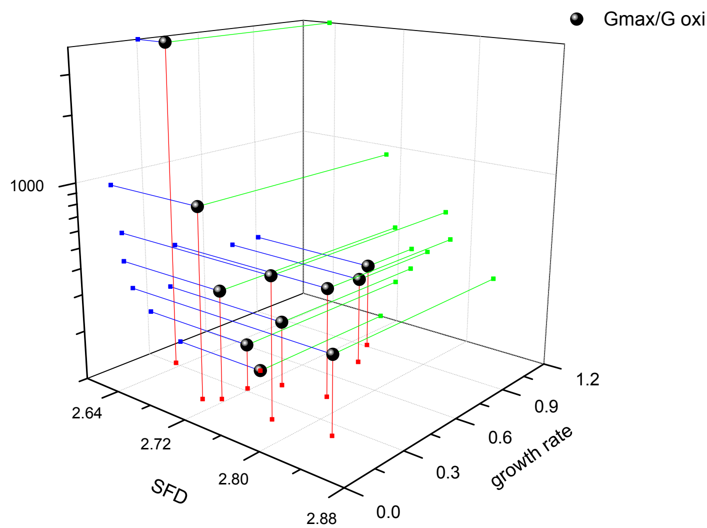

ZAO2

Experimental points representation in (SFD, growth rate, sensing ratio) 3D space.

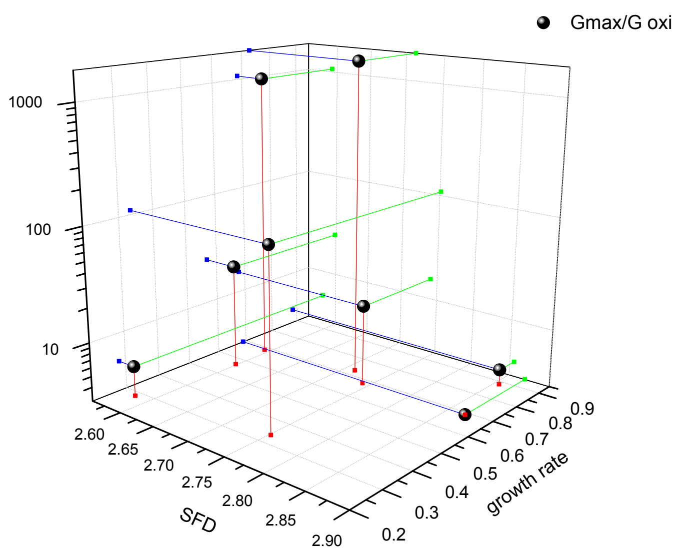

ZAO2D

Experimental points representation in (SFD, growth rate, sensing ratio) 3D space.

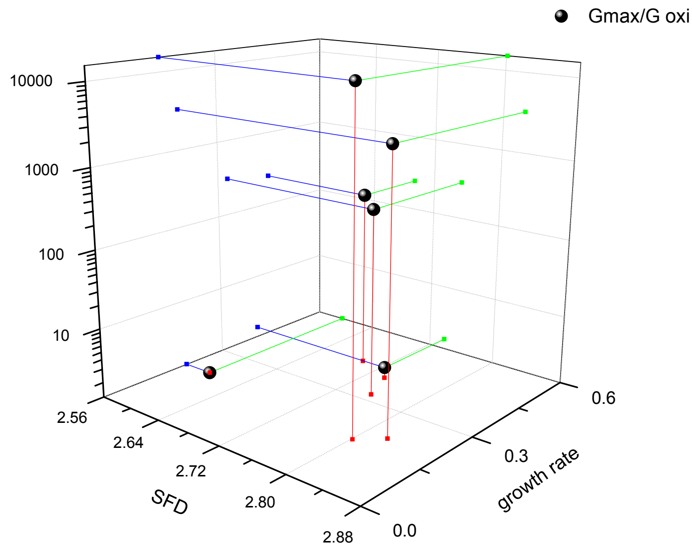

IZO

Experimental points representation in (SFD, growth rate, sensing ratio) 3D space.

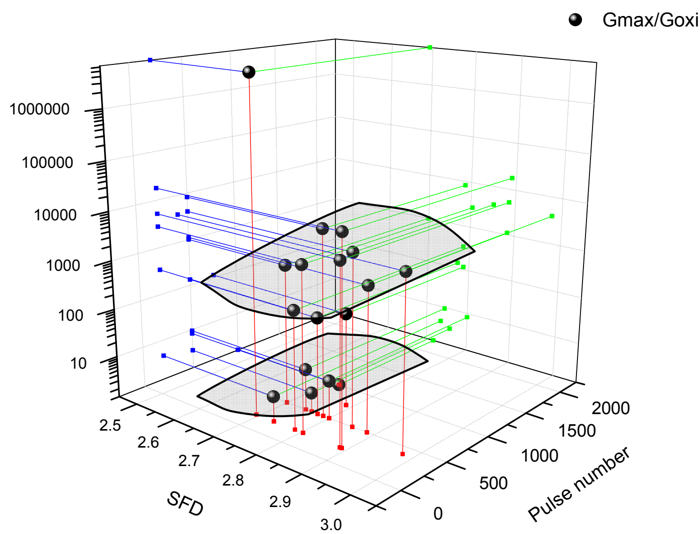

ZnO PLD

Experimental points representation in (SFD, pulse number, sensing ratio) 3D space.

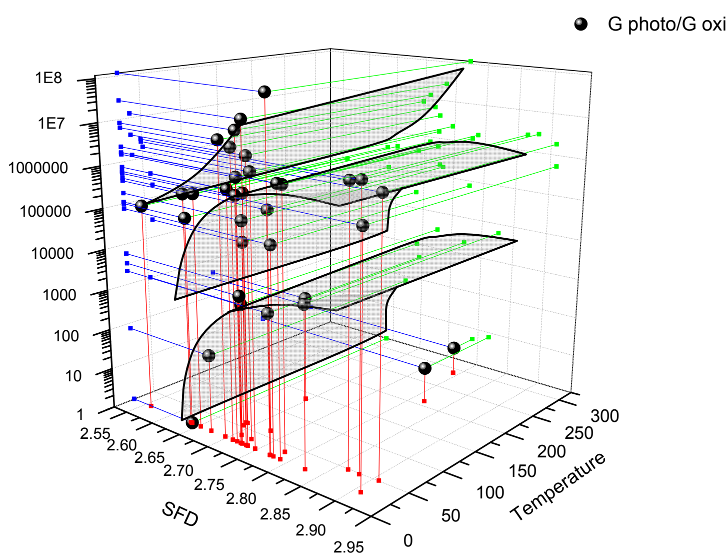

In_2O_3

Experimental points representation in (SFD, growth temperature, sensing ratio) 3D space.

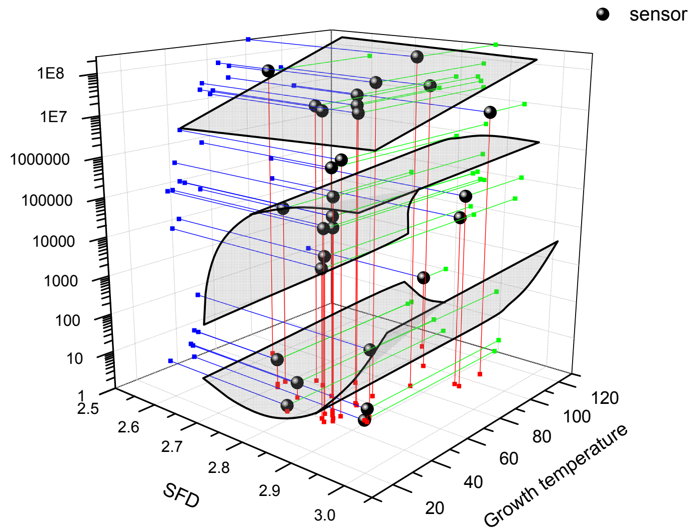

ZnO sputtering

Experimental points representation in (SFD, growth temperature, sensing ratio) 3D space.

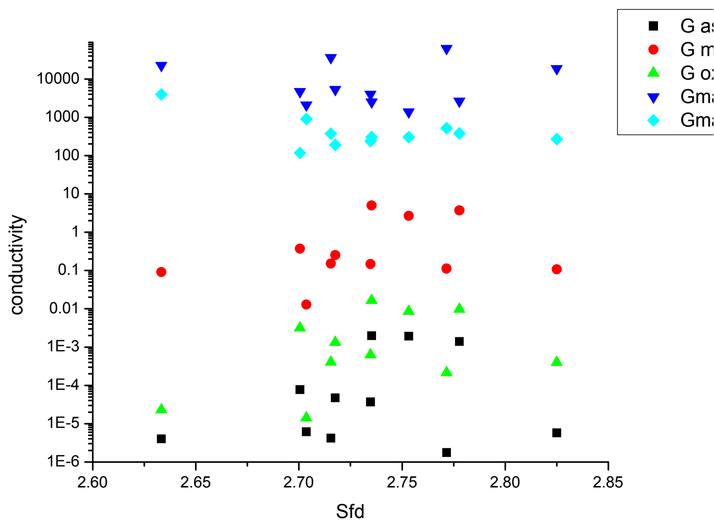

ZAO2

Experimental points representation in (SFD, sensing ratio) 2D space. All the films were grown at RT.

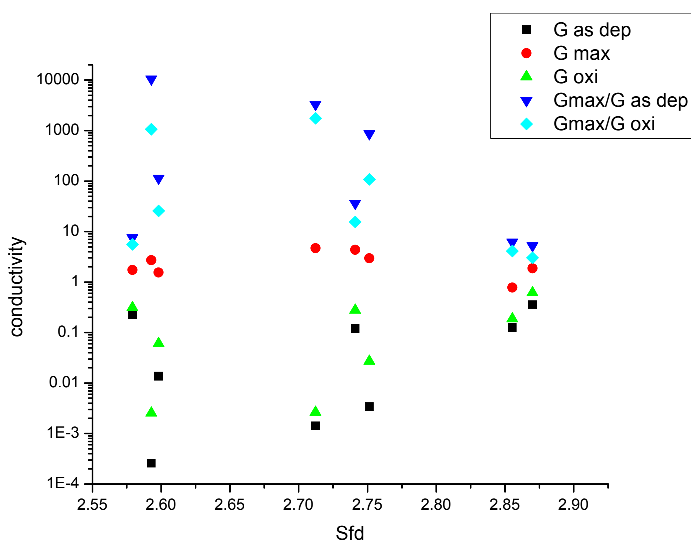

ZAO2D

Experimental points representation in (SFD, sensing ratio) 2D space. All the films were grown at RT.

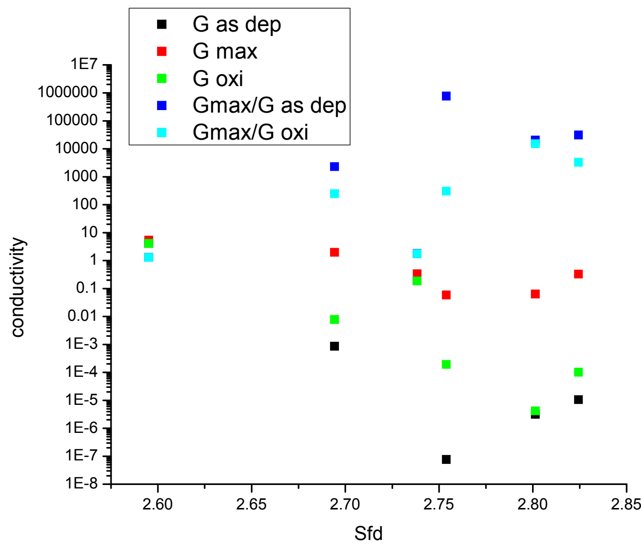

IZO

Experimental points representation in (SFD, sensing ratio) 2D space. All the films were grown at RT.

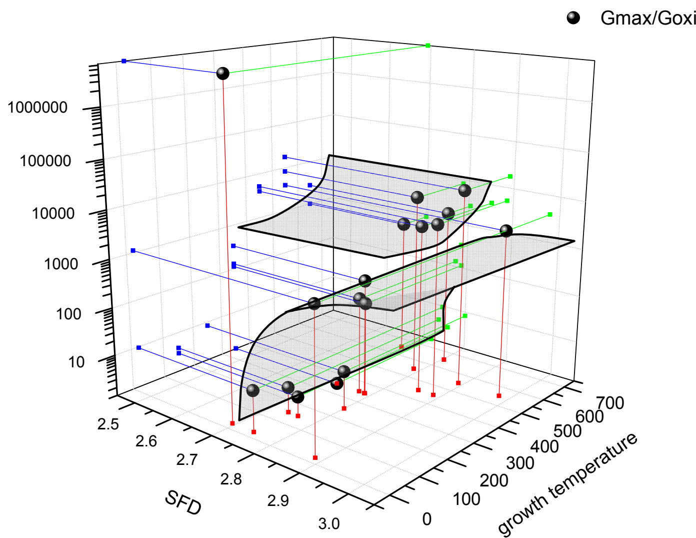

ZnO PLD

Experimental points representation in (SFD, growth temperature, sensing ratio) 3D space.

It is obvious, from these plots, that individual involvement of surface parameters and growth parameters to sensing answer follows different trends, which depends on other parameters, splitting data points in a group of surfaces which can be summarized as following:
Each surface follows data points associated to films series grown in some specific conditions with specific values of different surface parameters.
The surface appearance in the 3D specific space (shape, curvature etc.) is following the specific growth conditions and surface parameters.
The role of each of the four studied surface parameters (grain volume, grain perimeter, SDR and SFD) on sensing response seems to be equally important.

Mathematical evaluation of the F_{kl} functions and estimations of a_{kl} coefficients, can be done using, in addition, the equivalent representations in (s_i, g_j, photo-response) 3D space. The photo ratio shows a different dependence than sensing ratio on considered parameters due to the fact that it connects stronger with the contribution of $f_{Material}$ (growth conditions).
The representations for the photo ratio experimental values included in this work are presented bellow:

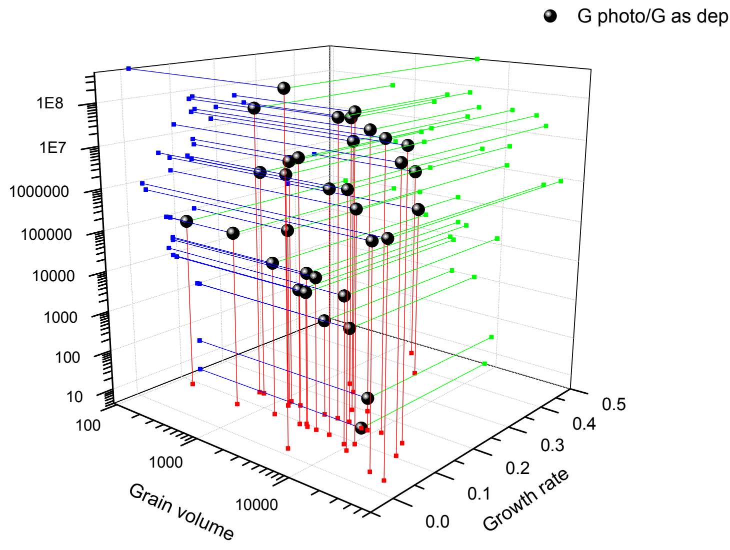

In_2O_3

Experimental points representation in (grain volume, growth rate, photo ratio) 3D space.

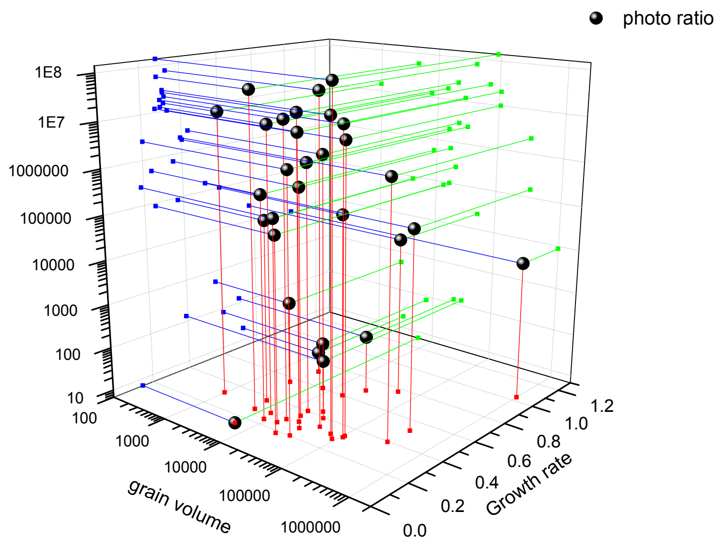

ZnO sputtering

Experimental points representation in (grain volume, growth rate, photo ratio) 3D space.

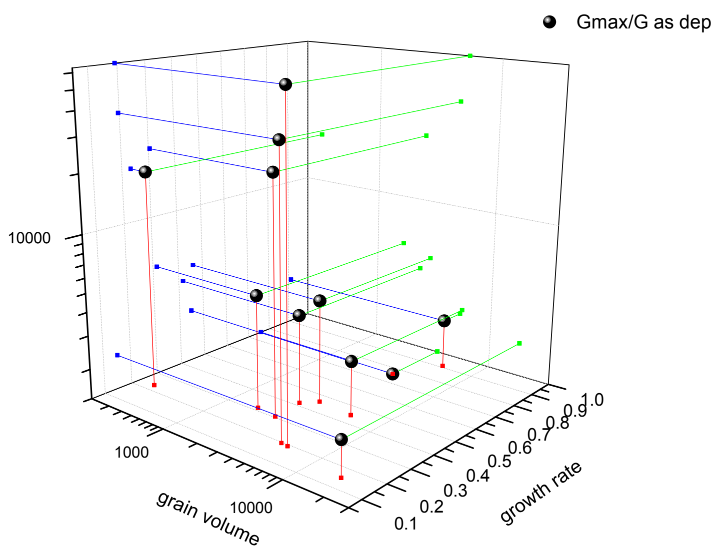

ZAO2

Experimental points representation in (grain volume, growth rate, photo ratio) 3D space.

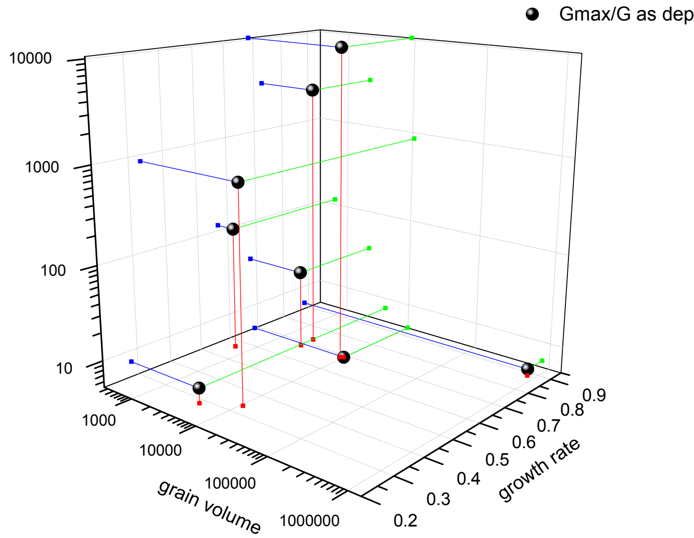

ZAO2D

Experimental points representation in (grain volume, growth rate, photo ratio) 3D space.

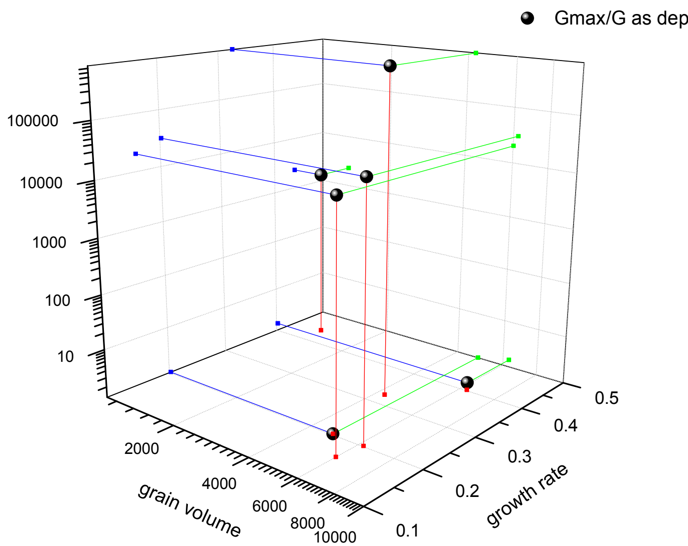

IZO

Experimental points representation in (grain volume, growth rate, photo ratio) 3D space.

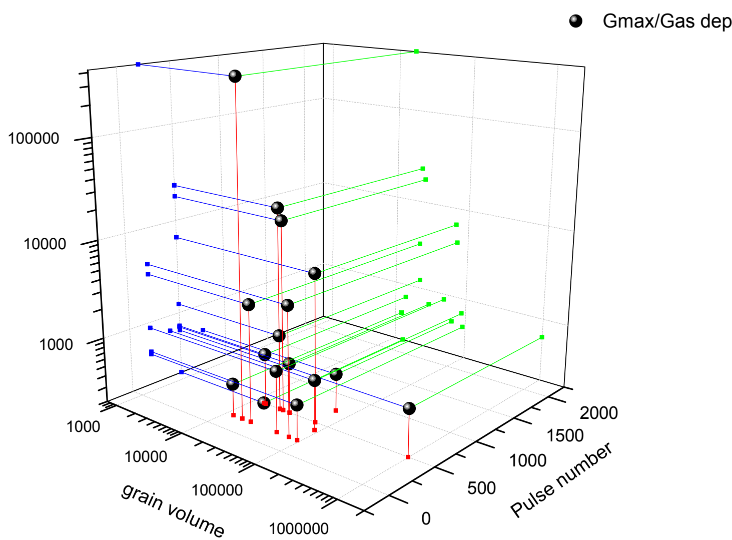

ZnO PLD

Experimental points representation in (grain volume, pulse number, photo ratio) 3D space.

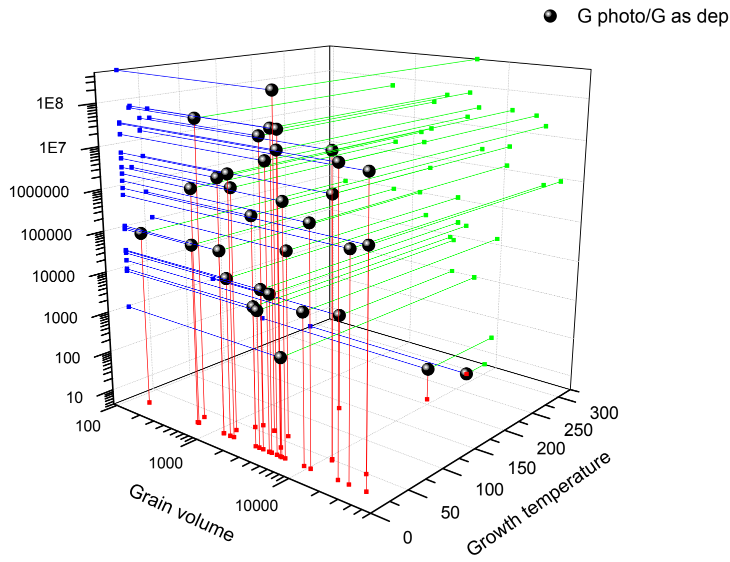

In_2O_3

Experimental points representation in (grain volume, growth temperature, photo ratio) 3D space.

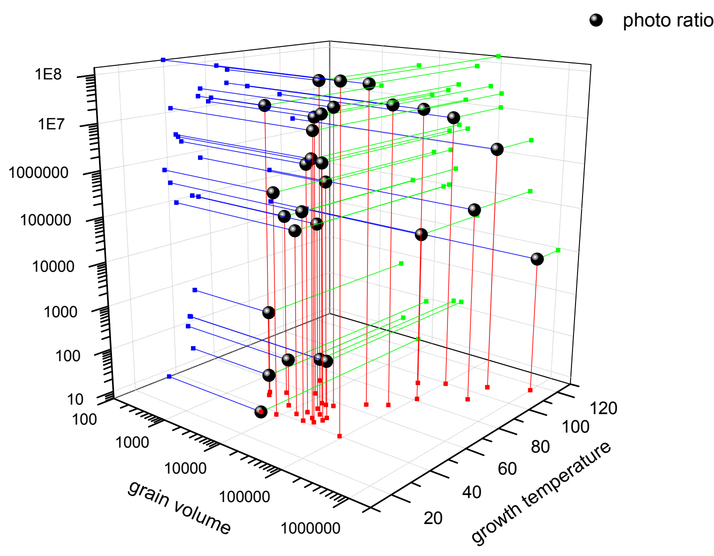

ZnO sputtering

Experimental points representation in (grain volume, growth temperature, photo ratio) 3D space.

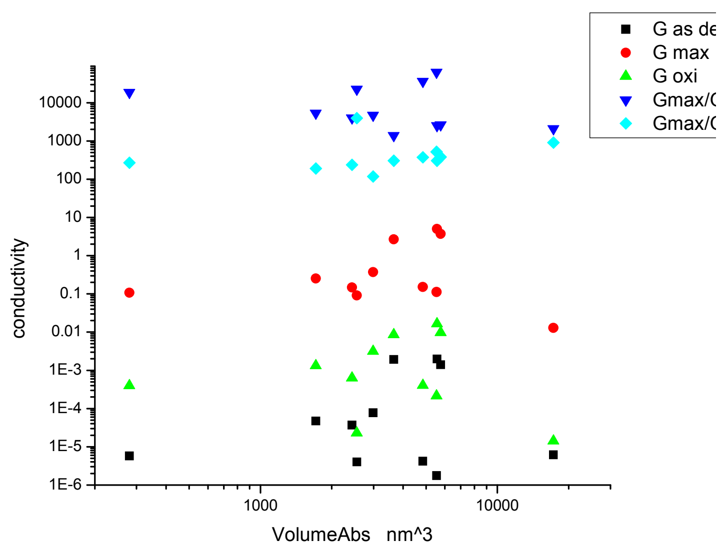

ZAO2

Experimental points representation in (grain volume, growth temperature, photo ratio) 3D space.

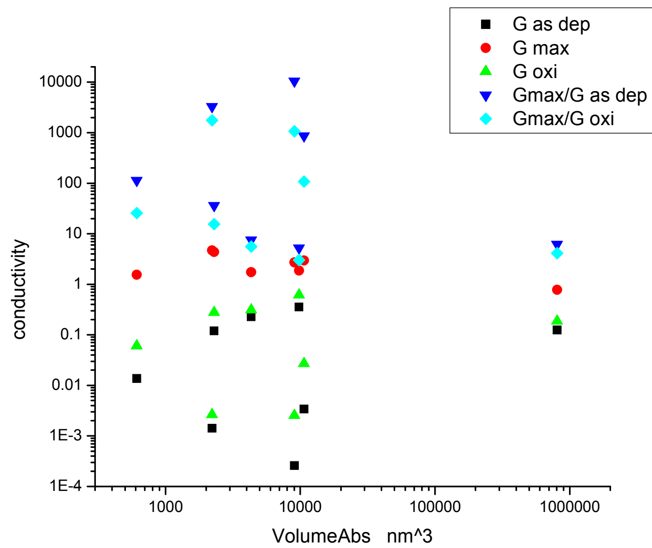

ZAO2D

Experimental points representation in (grain volume, growth temperature, photo ratio) 3D space.

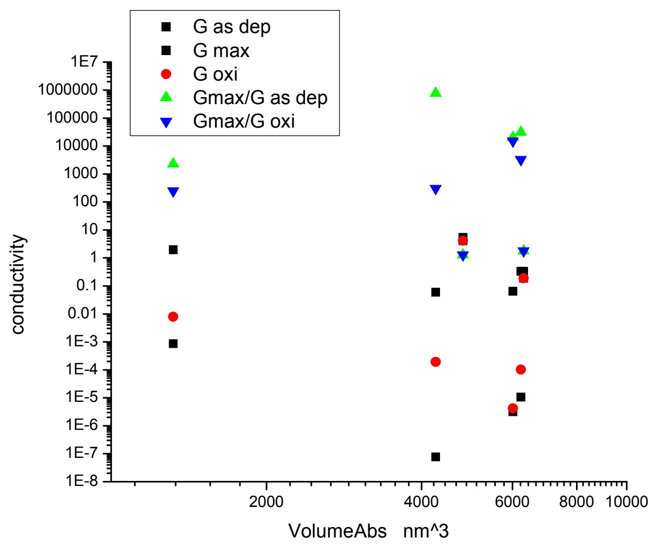

IZO

Experimental points representation in (grain volume, growth temperature, photo ratio) 3D space.

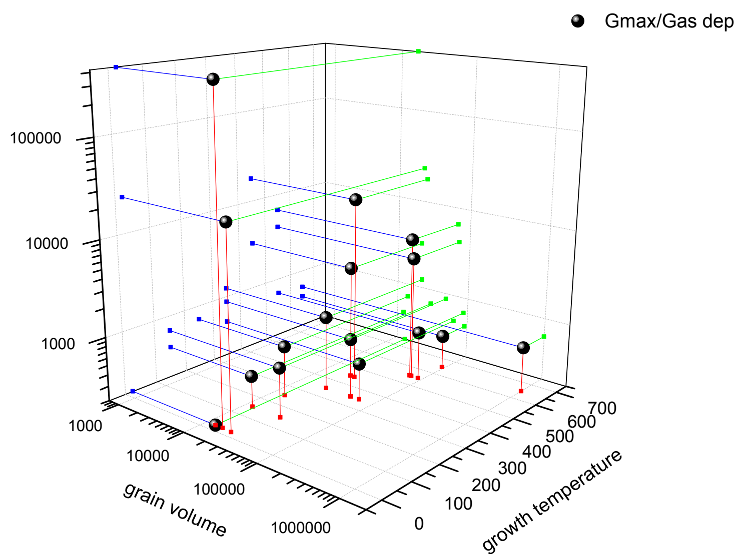

ZnO PLD

Experimental points representation in (grain volume, growth temperature, photo ratio) 3D space.

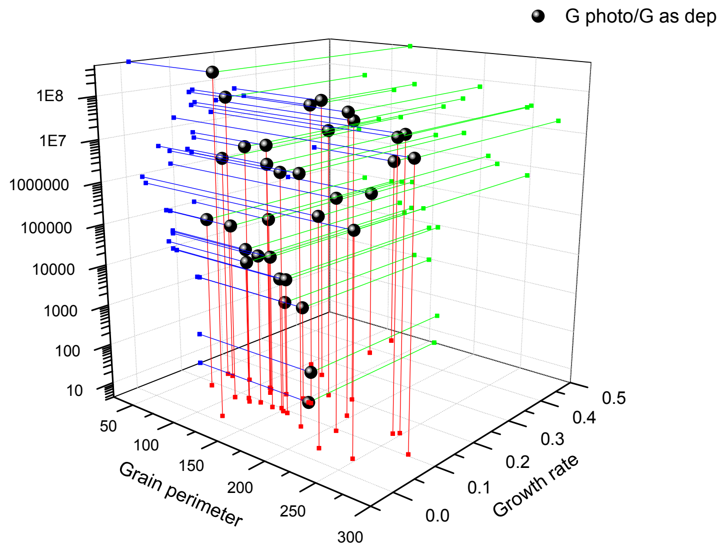

In_2O_3

Experimental points representation in (grain perimeter, growth rate, photo ratio) 3D space.

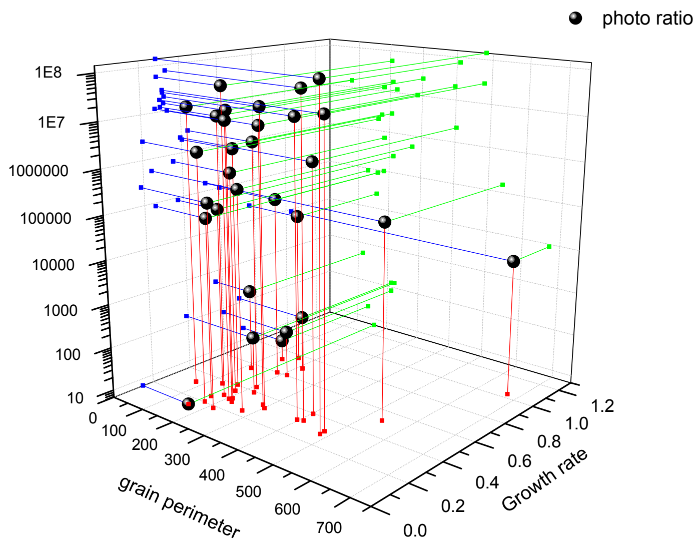

ZnO sputtering

Experimental points representation in (grain perimeter, growth rate, photo ratio) 3D space.

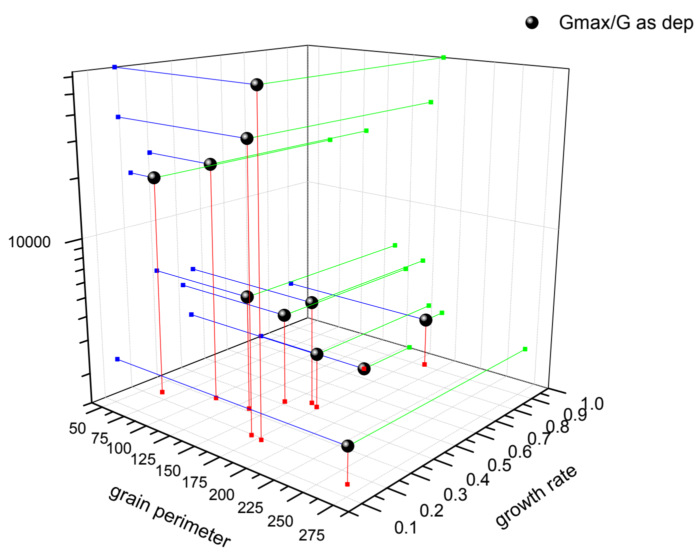

ZAO2

Experimental points representation in (grain perimeter, growth rate, photo ratio) 3D space.

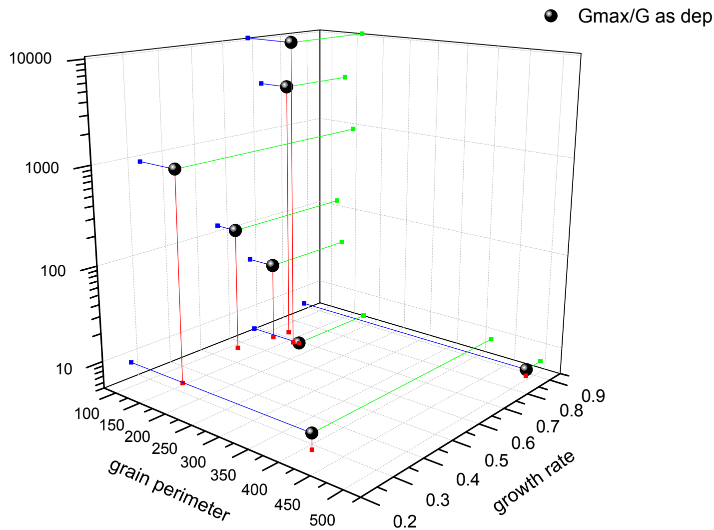

ZAO2D

Experimental points representation in (grain perimeter, growth rate, photo ratio) 3D space.

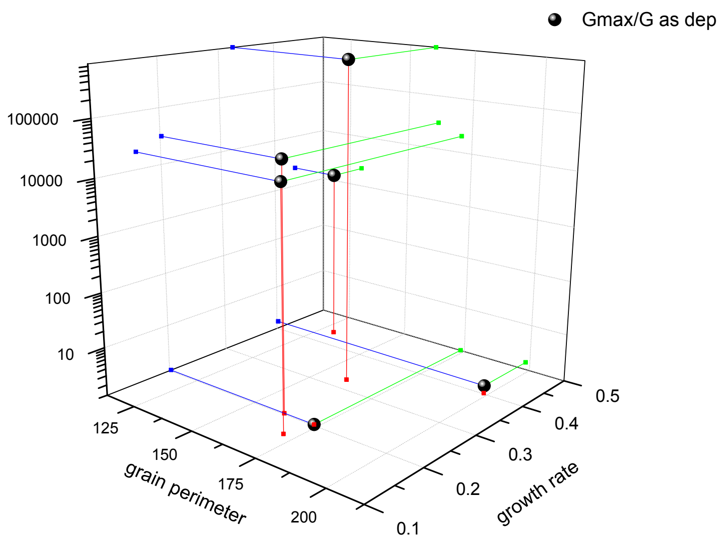

IZO

Experimental points representation in (grain perimeter, growth rate, photo ratio) 3D space.

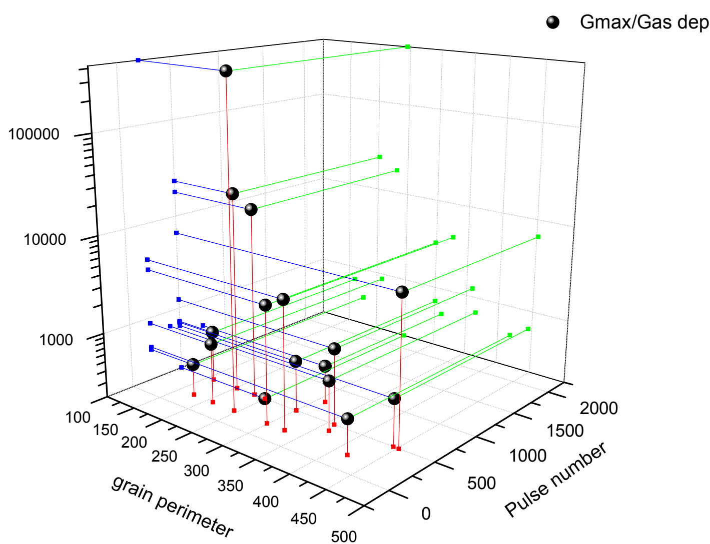

ZnO PLD

Experimental points representation in (grain perimeter, pulse number, photo ratio) 3D space.

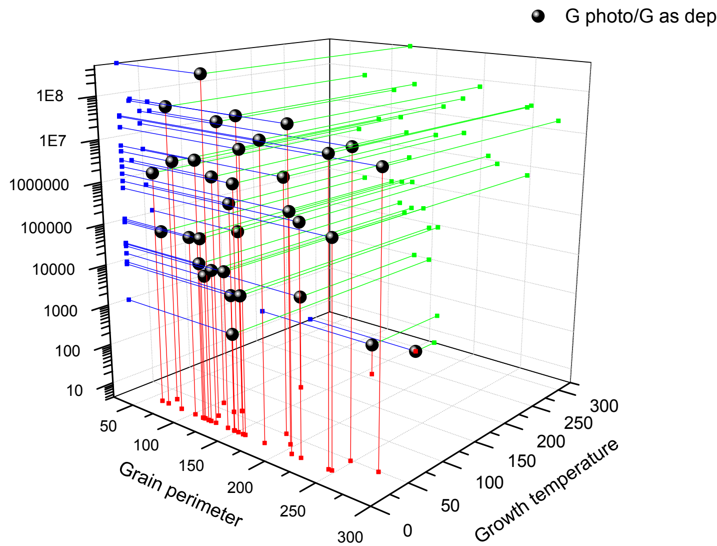

In_2O_3

Experimental points representation in (grain perimeter, growth temperature, photo ratio) 3D space.

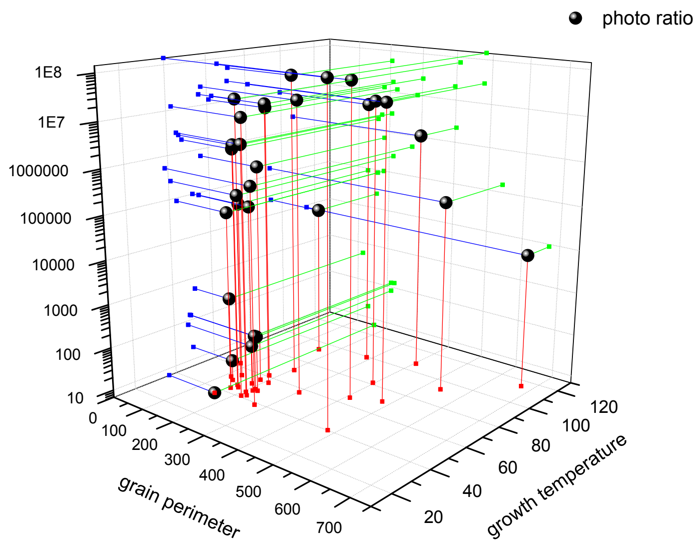

ZnO sputtering

Experimental points representation in (grain perimeter, growth temperature, photo ratio) 3D space.

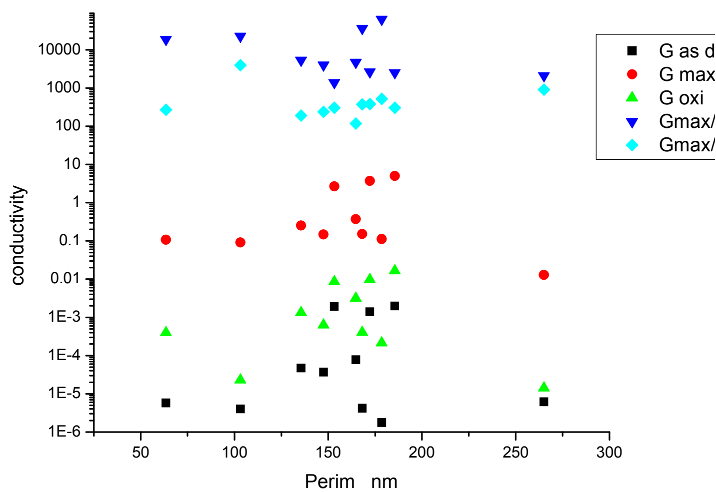

ZAO2

Experimental points representation in (grain perimeter, photo ratio) 2D space. All the films were grown at RT.

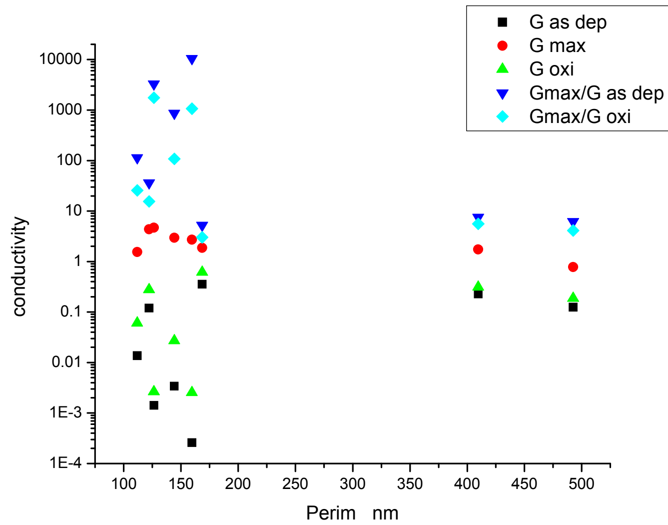

ZAO2D

Experimental points representation in (grain perimeter, photo ratio) 2D space. All the films were grown at RT.

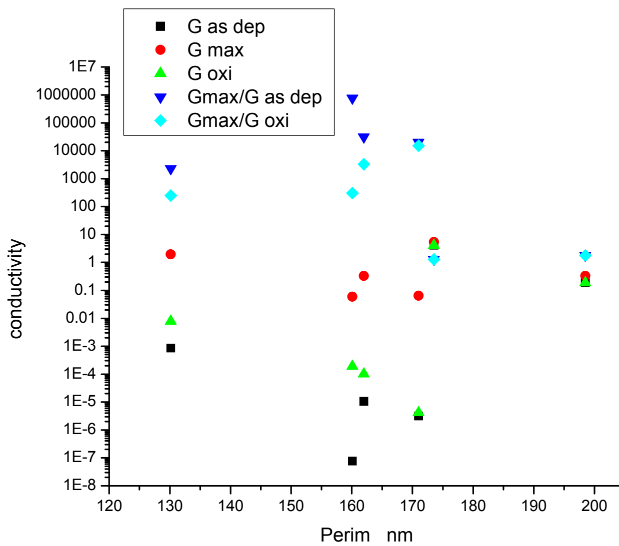

IZO

Experimental points representation in (grain perimeter, photo ratio) 2D space. All the films were grown at RT.

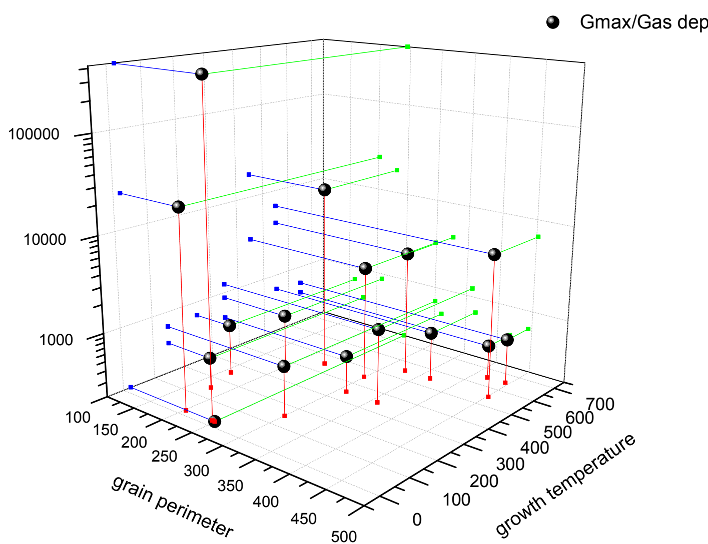

ZnO PLD

Experimental points representation in (grain perimeter, growth temperature, photo ratio) 3D space.

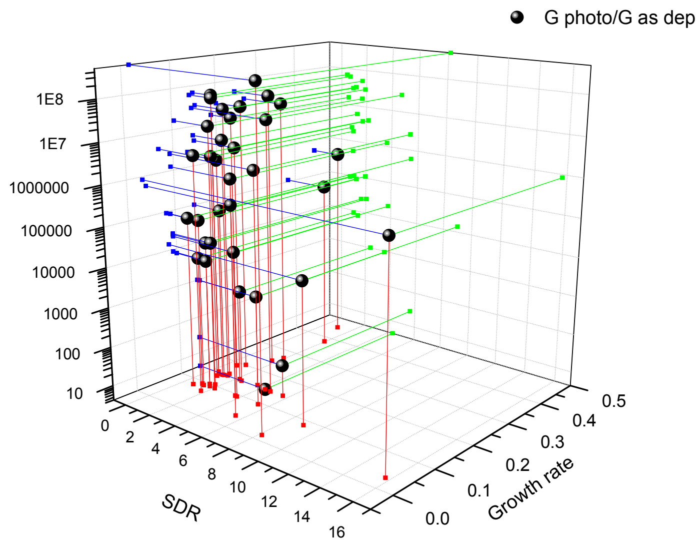

In_2O_3

Experimental points representation in (SDR, growth rate, photo ratio) 3D space.

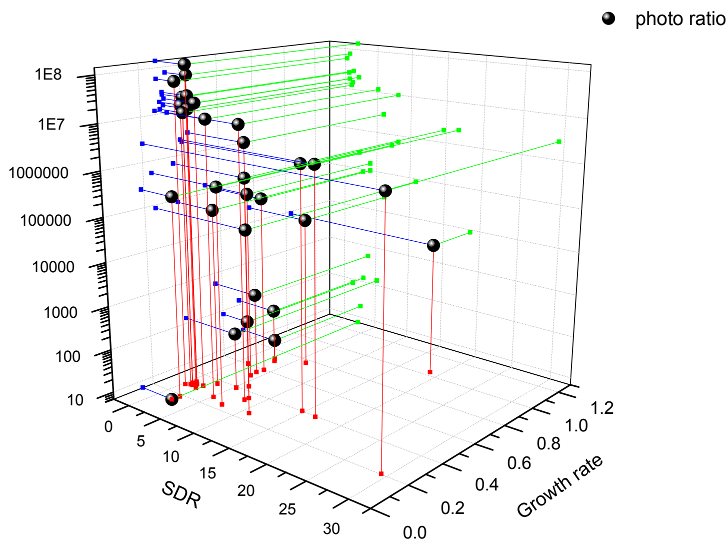

ZnO sputtering

Experimental points representation in (SDR, growth rate, photo ratio) 3D space.

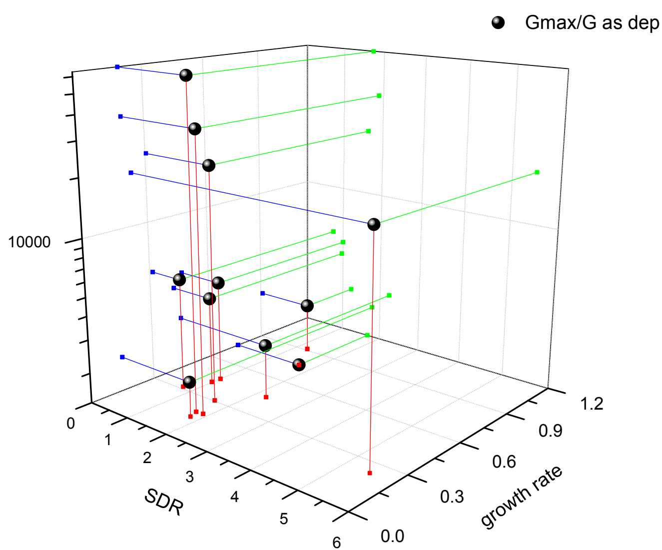

ZAO2

Experimental points representation in (SDR, growth rate, photo ratio) 3D space.

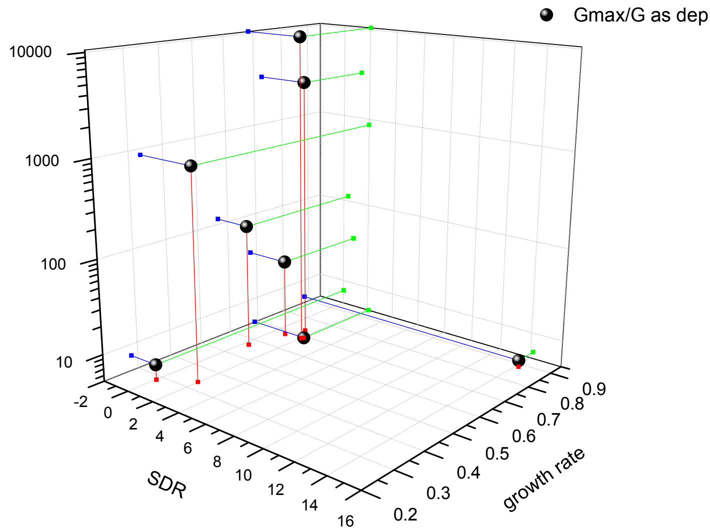

ZAO2D

Experimental points representation in (SDR, growth rate, photo ratio) 3D space.

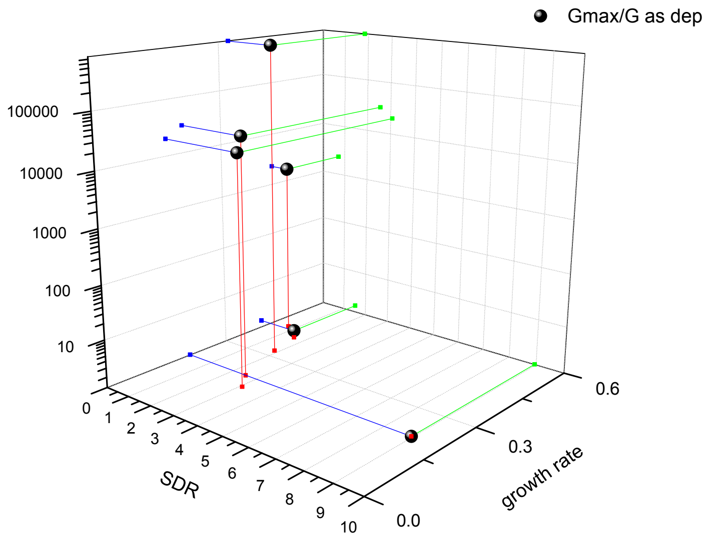

IZO

Experimental points representation in (SDR, growth rate, photo ratio) 3D space.

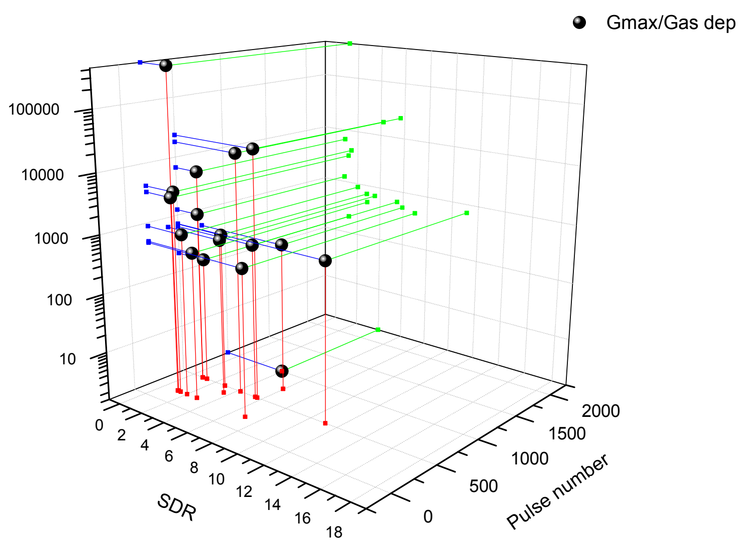

ZnO PLD

Experimental points representation in (SDR, pulse number, photo ratio) 3D space.

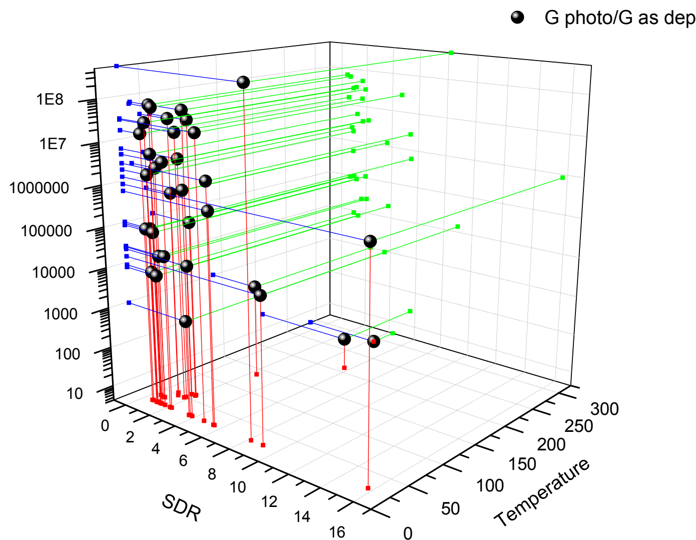

In_2O_3

Experimental points representation in (SDR, growth temperature, photo ratio) 3D space.

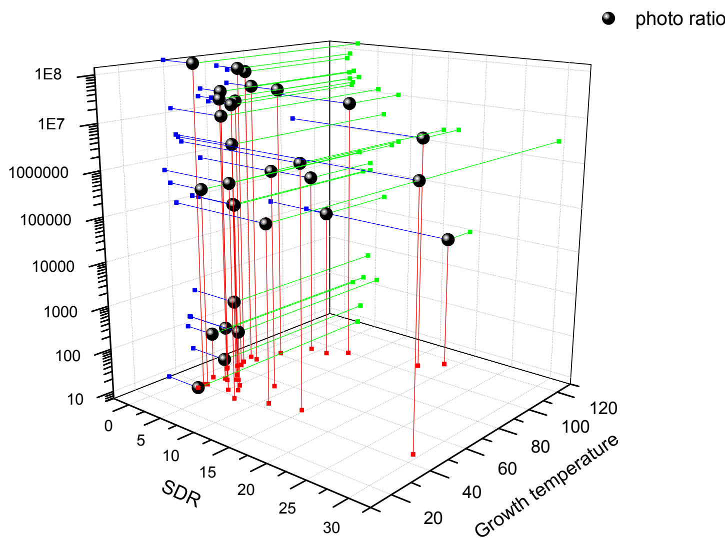

ZnO sputtering

Experimental points representation in (SDR, growth temperature, photo ratio) 3D space.

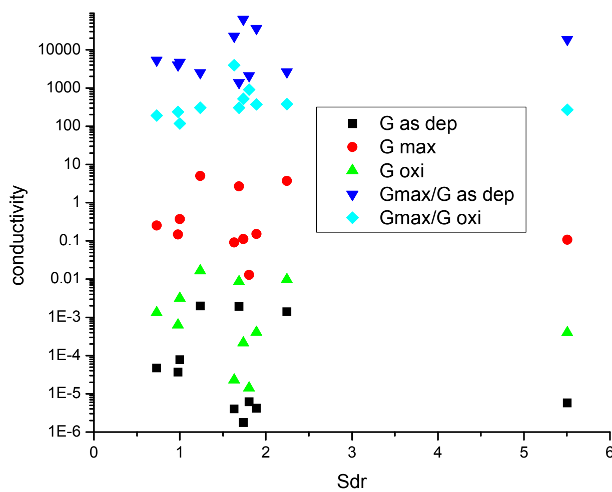

ZAO2

Experimental points representation in (SDR, photo ratio) 2D space. All the films were grown at RT.

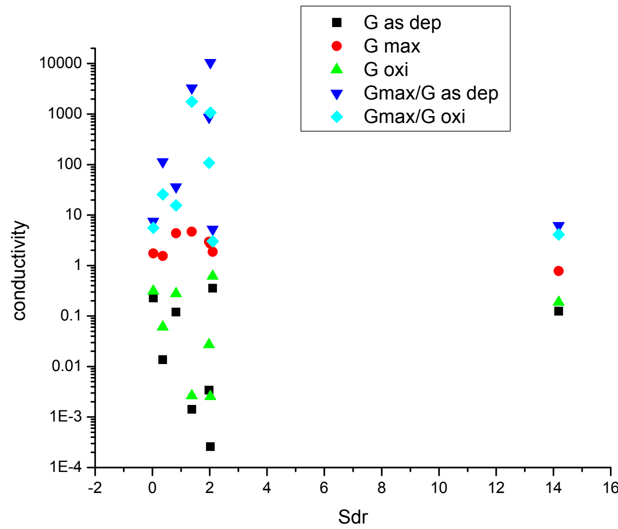

ZAO2D

Experimental points representation in (SDR, photo ratio) 2D space. All the films were grown at RT.

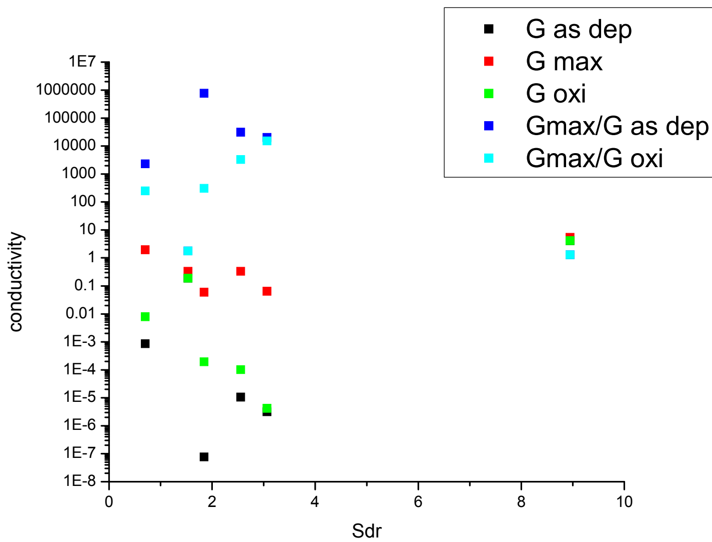

IZO

Experimental points representation in (SDR, photo ratio) 2D space. All the films were grown at RT.

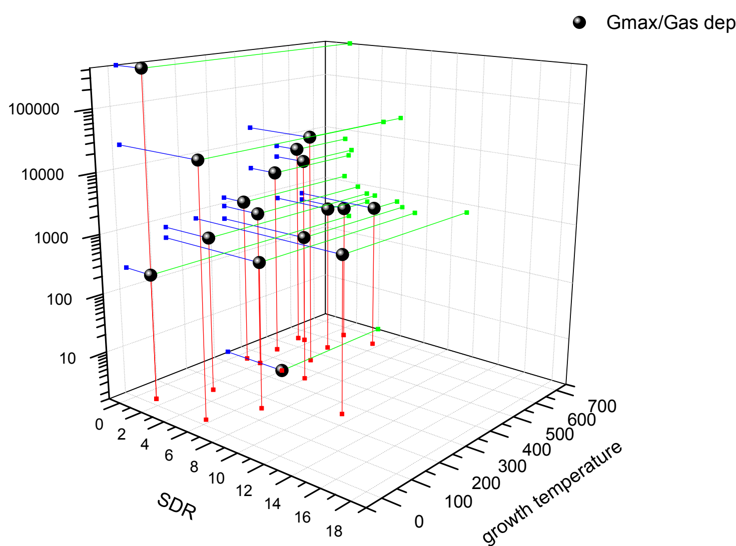

ZnO PLD

Experimental points representation in (SDR, growth temperature, photo ratio) 3D space.

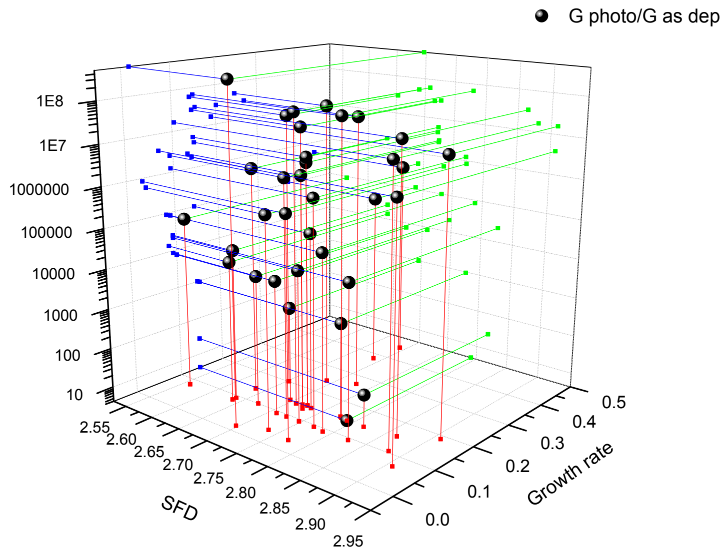

In_2O_3

Experimental points representation in (SFD, growth rate, photo ratio) 3D space.

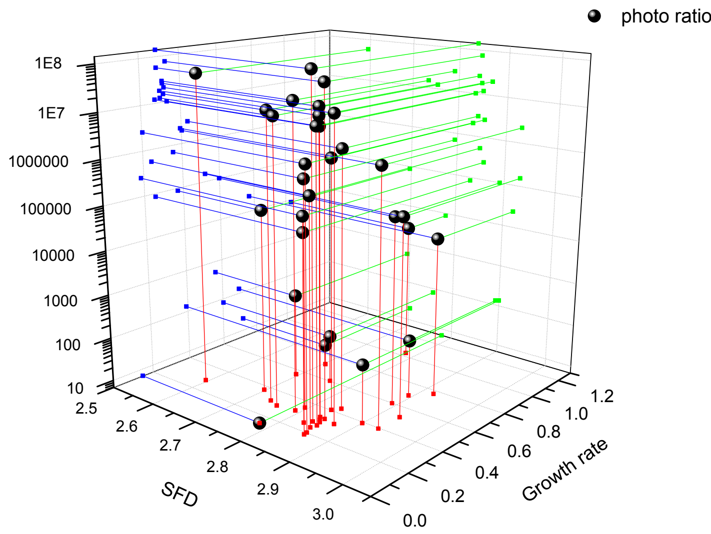

ZnO sputtering

Experimental points representation in (SFD, growth rate, photo ratio) 3D space.

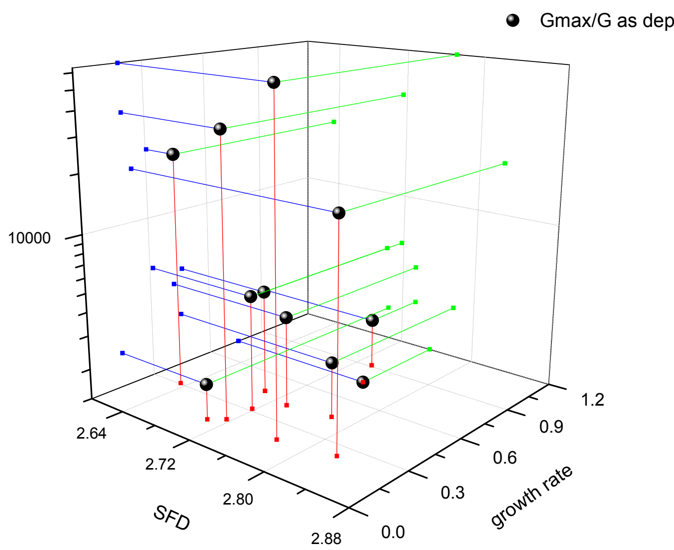

ZAO2

Experimental points representation in (SFD, growth rate, photo ratio) 3D space.

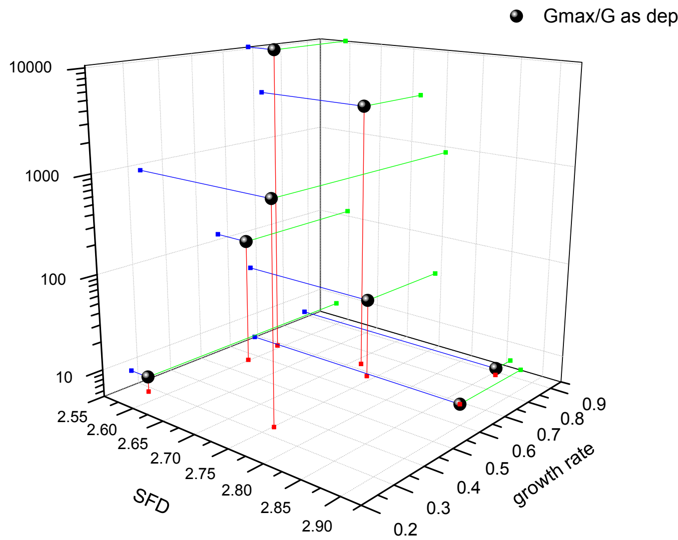

ZAO2D

Experimental points representation in (SFD, growth rate, photo ratio) 3D space.

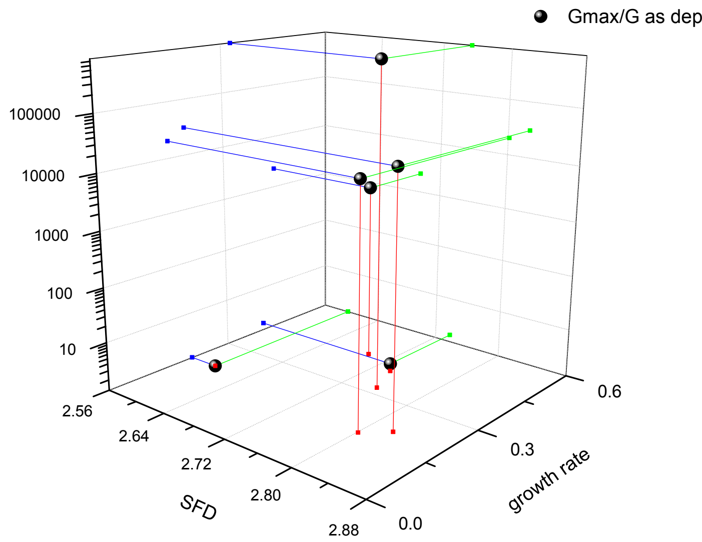

IZO

Experimental points representation in (SFD, growth rate, photo ratio) 3D space.

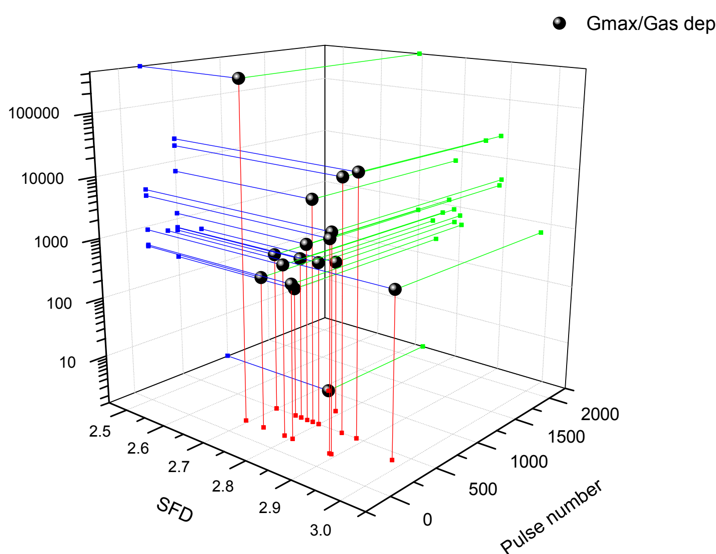

ZnO PLD

Experimental points representation in (SFD, pulse number, photo ratio) 3D space.

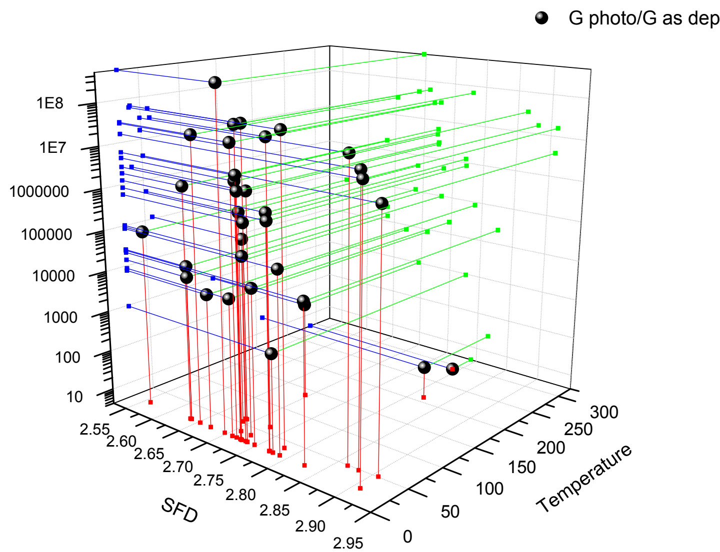

In_2O_3

Experimental points representation in (SFD, growth temperature, photo ratio) 3D space.

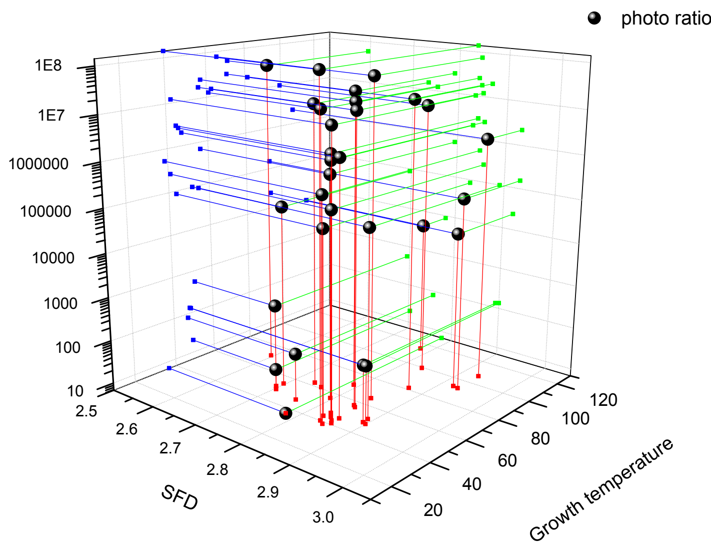

ZnO sputtering

Experimental points representation in (SFD, growth temperature, photo ratio) 3D space.

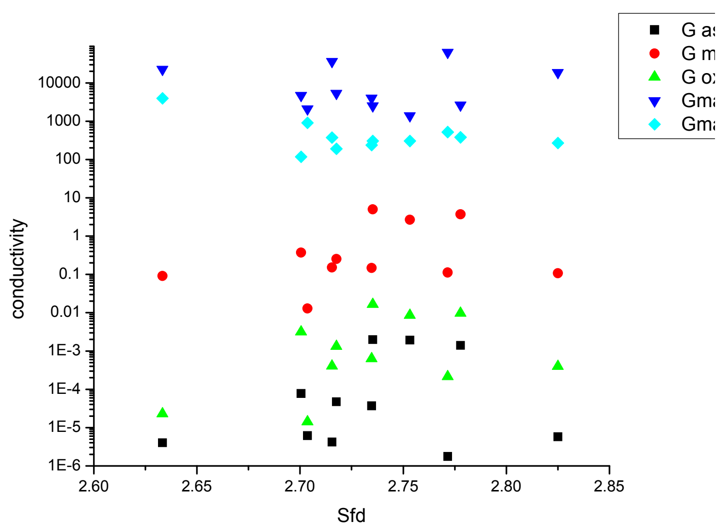

ZAO2

Experimental points representation in (SFD, photo ratio) 2D space. All the films were grown at RT.

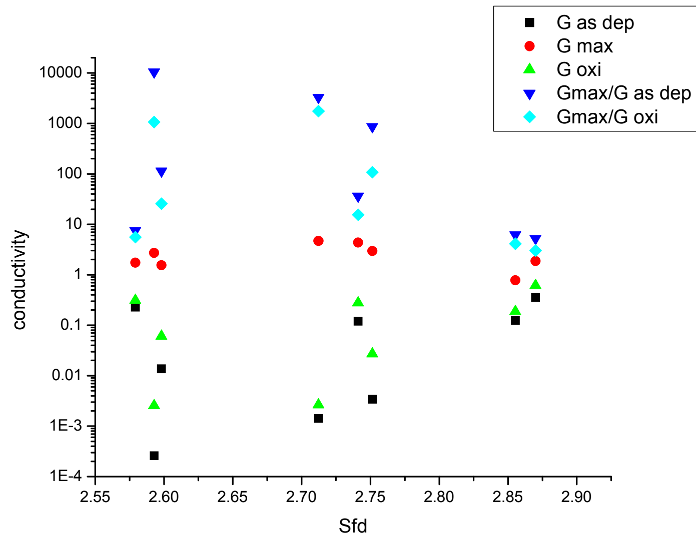

ZAO2D

Experimental points representation in (SFD, photo ratio) 2D space. All the films were grown at RT.

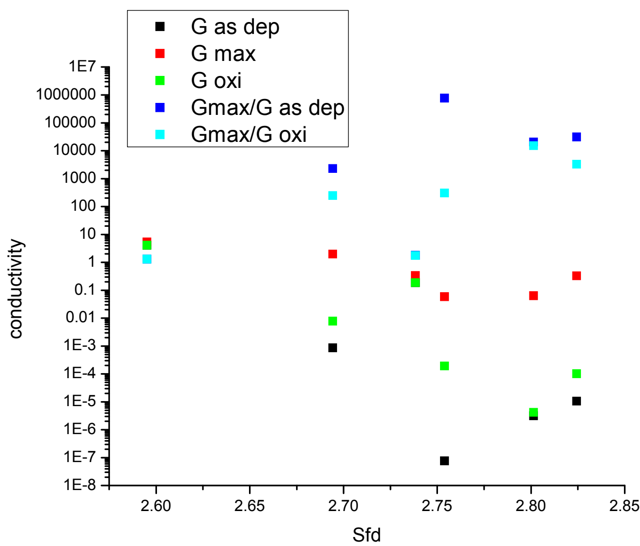

IZO

Experimental points representation in (SFD, photo ratio) 2D space. All the films were grown at RT.

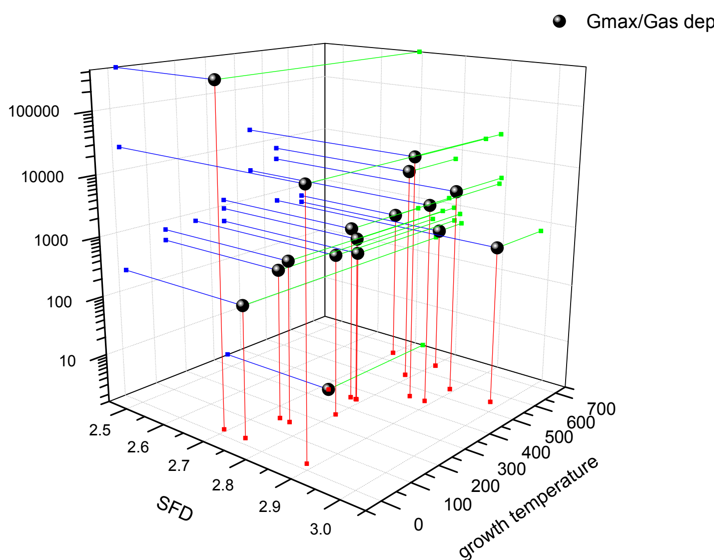

ZnO PLD

Experimental points representation in (SFD, growth temperature, photo ratio) 3D space.

A comparative analysis of photo-ratios representations with the equivalent ones of sensing response for each of the studied materials using adequate computational facilities for evaluation of local maxima for each F_{kl} member of the surfaces family

in both representations gives the optimization of sensing response for specific growth parameters. The local conditions for maxima detection should be the first partial derivative of each F_{kl} function with respect each of the variable equal zero and second partial derivatives sign change in the previous equation's solution point.
This means:

$$\left.\frac{\partial F_{kl}(s_i,g_j)}{\partial s_i}\right|_{g_j} ds_i = 0$$

$$\left.\frac{\partial F_{kl}(s_i,g_j)}{\partial g_j}\right|_{s_i} dg_j = 0$$

Solutions for this equations system for local maxima will lead to an analytic formula for the F_{kl} functions in the completion of the mathematical model.
Considering only the experimental points a raw analysis brings up the following general conclusions:
In the 3D representations involving growth rate and temperature, the sensing response per surface in the corresponding F_k family seems to decrease as grain volume increases for both In_2O_3 and ZnO grown by both growth techniques. The points corresponding to the maximum sensing response appeared for In_2O_3 and ZnO grown by DC magnetron sputtering for a grain volume of about 10000nm^3 grown at RT with small GR, which correspond to a grain radius of about 15nm. The influence of the grain perimeter on the sensing response seems to be different for films grown at temperatures lower than 50˚C and films grown at higher temperature. For low temperatures, the sensing response increases as perimeter increases while for higher temperatures the opposite was evident. An optimum sensing response of films grown by DC magnetron sputtering appeared for a mean grain perimeter of about 100-150nm, the value becoming around 200nm for ZnO grown by PLD. Increase of SDR resulted in a local decrease of the sensing response. An SDR value of about two seems to favor the sensing response for both materials and techniques.
A SFD value of about 2.65-2.7 appeared to optimize locally the sensing response. Generally, as SFD increases, the sensor response appeared to be improved. These are observations that apply for films grown by both techniques and for both materials, a fact that confirms the validity of the choice of the most significant parameters, among the measured ones (included in the tables).

7.4 Conclusions

This chapter regarding correlations brought together all experimental information collected during the work presented in chapters 3-6.

- A complete database containing enough experimental points for establishing the premises for an experimental realistic model for surface contribution to sensing response of thin films metal oxide based sensing layers was provided for DC magnetron sputtering grown In_2O_3 and ZnO grown by DC magnetron sputtering and PLD techniques. They were also included complete data sets for some doped ZnO thin films presented in chapter 6: ZAO2, ZAO2D and I5ZO.
- Rigorous surface characterization methodology using AFM and AFM related software was described and all analyzed parameters were described and explained.
- From detailed analysis of experimental results database, a set of six significant parameters with highest contribution to sensing response was defined, in addition to the two sensing related ratios, photo response and sensing response, they define a set of eight significant parameters for a general model elaboration.
- Sensing response and photo ratio evolutions in 3D spaces determined by the combinations of these parameters were graphically analyzed.
- A functional general expression of sensor response in connection with the defined parameters was suggested.
- It was sketched an algorithm for generation of an analytical expression for surface function contribution to sensor response based on experimental results.

Particular observations of experimental plots revealed the following:

- In the 3D representations involving growth rate and temperature, the sensing response per surface in the corresponding F_k family seems to decrease as grain volume increases for both In_2O_3 and ZnO grown by the two growth techniques.
- The points corresponding to the maximum sensing response appeared for In_2O_3 and ZnO grown by DC magnetron sputtering for a grain volume of about 10000nm^3 grown at RT with small GR, which correspond to a grain radius of about 15nm.
- The influence of the grain perimeter on the sensing response seems to be different for films grown at temperatures lower than 50˚C and films grown at higher temperature. For low temperatures, the sensing response increases as perimeter increases while for higher temperatures the opposite was evident. An optimum sensing response of films grown by DC magnetron sputtering appeared for a mean grain perimeter of about 100-150nm, the value becoming approximately 200nm for ZnO grown by PLD.
- Increase of SDR resulted in a local decrease of the sensing response. An SDR value of about two seems to favor the sensing response for both materials and techniques.
- A SFD value of about 2.65-2.7 appeared to optimize locally the sensing response. Generally, as SFD increases, the sensor response appeared improved.

Annex 7A Roughness Parameters

This section describes the surface roughness parameters implemented in the SPIP software. All parameters recommended in the European BCR Project “Scanning tunneling microscopy methods for roughness and micro hardness measurements” are implemented together with several other parameters applied by SPIP users.

Symbol	Name	2D standard	Default Unit	3D reference
Amplitude parameters:				
Sa	Roughness Average	DIN 4768 ASME B46.1	[nm]	ISO/DIS 25178-2 ASME B46.1
Sq	Root Mean Square (RMS)	ISO 4287/1 ASME B46.1	[nm]	ISO/DIS 25178-2 ASME B46.1
Ssk	Surface Skewness	ISO 4287/1 ASME B46.1		ISO/DIS 25178-2 ASME B46.1
Sku	Surface Kurtosis	ANSI B.46.1 ASME B46.1		ISO/DIS 25178-2 ASME B46.1
Sz	Peak-Peak	ISO 4287/1	[nm]	ISO/DIS 25178-2
St	Peak-Peak	ASME B46.1	[nm]	ASME B46.1
Sy	Peak-Peak (old SPIP term)		[nm]	[6]
S10z	Ten Point Height	ANSI B.46.1	[nm]	ISO/DIS 25178-2 ASME B46.1
Sv	Max Valley Depth	ASME B46.1		ISO/DIS 25178-2 ASME B46.1
Sp	Max Peak Height	ASME B46.1		ISO/DIS 25178-2 ASME B46.1
Smean	Mean Value			
Hybrid Parameters:				
Ssc	Mean Summit Curvature		[1/nm]	[6]
Sti	Texture Index			[7]
Sdq	Root Mean Square Gradient			ISO/DIS 25178-2
Sdq6	Area Root Mean Square Slope			ASME B46.1

Sdr	Surface Area Ratio			ISO/DIS 25178-2
S2A	Projected Area		nm^2	
S3A	Surface Area		nm^2	
Functional Parameters:				
Sbi	Surface Bearing Index			[6]
Sci	Core Fluid Retention Index			[6]
Svi	Valley Fluid Retention Index			[6]
Spk	Reduced Summit Height	DIN 4776	[nm]	
Sk	Core Roughness Depth	DIN 4776	[nm]	
Svk	Reduced Valley Depth	DIN 4776	[nm]	
SDCl-h	l-h% height intervals of Bearing Curve.	ISO 4287	[nm]	
Spatial Parameters:				
Sds	Density of Summits		$[1/\mu m^2]$	ASME B46.1 [6]
Std	Texture Direction		[deg]	[6]
Stdi	Texture Direction Index			[7]
Srw	Dominant Radial Wave Length		[nm]	[7]
Srwi	Radial Wave Index			[7]
dShw	Mean Half Wavelength		[nm]	
Sfd	Fractal Dimension			
Scl20	Correlation Length at 20%			
Scl37	Correlation Length at 37%			
Str20	Texture Aspect Ratio at 20%			
Str37	Texture Aspect Ratio at 37%			

The table lists the roughness parameters by their symbol, name, corresponding 2D standard and unit.

Most parameters are general and valid for any *M ´ N* rectangular image. However, for some parameters, related to the Fourier transform, we assume that the image is quadrangular (*M=N*).
Before the calculation of the roughness parameters is recommended to carry out a slope correction by a 2nd or 3rd order polynomial plane fit. Note also that the roughness values depend strongly on the measurement conditions, especially the scan range and the sample density. It is therefore important to refer to the measurement conditions when reporting roughness data.

Some of these parameters depend on the definition of a local minimum and a local maximum. A local minimum is defined as a pixel where all eight neighboring pixels are higher and a local maximum as a pixel where all eight neighboring pixels are lower.

As there are no pixels outside the borders of the image, there are no local minimums or local maximums on the borders. Note that parameters based on local minimums and/or local maximums may be more sensitive to noise than other parameters.

Amplitude parameters

The amplitude properties can be described by six parameters, which can give information about the statistical average properties, the shape of the height distribution histogram and about extreme properties. All the amplitude parameters are based on two-dimensional standards that are extended to three dimensions.

The Roughness Average, ***Sa***, is defined as:

$$S_a = \frac{1}{MN} \sum_{k=0}^{M-1} \sum_{l=0}^{N-1} |z(x_k, y_l)| \qquad \text{R 1}$$

The Root Mean Square (RMS) parameter *Sq*, is defined as:

$$S_q = \sqrt{\frac{1}{MN} \sum_{k=0}^{M-1} \sum_{l=0}^{N-1} \left[z(x_k, y_l) \right]^2} \qquad \text{R 2}$$

The Surface Skewness, *Ssk*, describes the asymmetry of the height distribution histogram, and is defined as:

$$S_{sk} = \frac{1}{MNS_q^3} \sum_{k=0}^{M-1} \sum_{l=0}^{N-1} \left[(z(x_k, y_l) \right]^3 \qquad \text{R 3}$$

If *Ssk* = 0, a symmetric height distributions is indicated, such as a Gaussian like distribution. *Ssk* < 0 indicates a bearing surface with holes while *Ssk* > 0 corresponds to a flat surface with peaks. Values numerically greater than 1.0 may indicate extreme holes or peaks on the surface.

The Surface Kurtosis, *Sku*, describes the “peakedness” of the surface topography, and is defined as:

$$S_{ku} = \frac{1}{MNS_q^4} \sum_{k=0}^{M-1} \sum_{l=0}^{N-1} \left[z(x_k, y_l) \right]^4 \qquad \text{R 4}$$

For Gaussian height distributions *Sku* approaches 3.0 with increasing number of pixels. Smaller values of *Sku* indicate broader height distributions, the opposite appearing for values greater than 3.0.

The **Peak-Peak Height** is denoted by three parameter names, ***Sz, St, Sy***, according to ISO, ASME and reference [6]. They are defined as the height difference between the highest and lowest pixel in the image.

$$S_z = S_t = S_y = z_{max} - z_{min} \qquad \text{R 5}$$

The Ten Point Height, *S10z*, is defined as the average height of the five highest local maxima plus the average height of the five lowest local minima:

$$S_{10z} = \frac{\sum_{i=1}^{5} |z_{pi}| + \sum_{i=1}^{5} |z_{vi}|}{5}, \qquad \text{R 6}$$

where *zpi* and z*vi* are the height of the ith highest local maximums and the ith lowest local minimums respectively. When there are less than five valid maximums or minimums, this parameter is not defined.

Maximum Valley Depth *Sv*: is defined as the largest valley depth value.

Maximum Peak Height *Sp*: is defined as the largest peak height value.

Hybrid parameters

There are three hybrid parameters. These parameters reflect the slope gradients and their calculations are based on local z-slopes.

The Mean Summit Curvature, *Ssc*, is the average of the principal curvature of the local maximums on the surface, and is defined as:

$$S_{sc} = \frac{-1}{2n} \sum_{i=1}^{n} \left(\frac{\delta^2 z(x,y)}{\delta x^2} \right) + \left(\frac{\delta^2 z(x,y)}{\delta y^2} \right) \quad \text{for all local maximums} \qquad \text{R 7}$$

where d*x* and d*y* are the pixel separation distances.

The Root Mean Square Gradient, *Sdq*, is the RMS-value of the surface slope within the sampling area, and is defined as:

$$S_{dq} = \sqrt{\frac{1}{(M-1)(N-1)} \sum_{k=0}^{M-1} \sum_{l=0}^{N-1} \left(\frac{z(x_k, y_l) - z(x_{k-1}, y_l)}{\delta x} \right)^2 + \left(\frac{z(x_k, y_l) - z(x_k, y_{l-1})}{\delta y} \right)^2} \qquad \text{R 8}$$

The Area Root Mean Square Slope, *Sdq6*, is similar to the *Sdq* but includes more neighbor pixels in the calculation of the slope for each pixel.

$$S_{dq6} = \frac{1}{(N-6)(M-6)} \sum_{k=3}^{N-3} \sum_{l=3}^{M-3} \Delta^2(x_k, y_l) \qquad \text{R 9}$$

$$\Delta^2(x_k, y_l) = \left(\left\{ \frac{1}{60\Delta x} \left[-z(x_{k-3}, y_l) + 9z(x_{k-2}, y_l) - 45z(x_{k-1}, y_l) + 45z(x_{k+1}, y_l) - 9z(x_{k+2}, y_l) + z(x_{k+3}, y_l) \right] \right\}^2 + \left\{ \frac{1}{60\Delta y} \left[-z(x_k, y_{l-3}) + 9z(x_k, y_{l-2}) - 45z(x_k, y_{l-1}) + 45z(x_k, y_{l+1}) - 9z(x_k, y_{l+2}) + z(x_k, y_{l+3}) \right] \right\}^2 \right)^{1/2}$$

The Surfaces Area Ratio, *Sdr*, expresses the increment of the interfacial surface area relative to the area of the projected (flat) x,y plane:

$$S_{dr} = \frac{\left(\sum_{k=0}^{M-2}\sum_{l=0}^{N-2} A_{kl}\right) - (M-1)(N-1)\delta x\delta y}{(M-1)(N-1)\delta x\delta y} 100\% \qquad \text{R 10a}$$

where Akl is defined as:

$$A_{kl} = \frac{1}{4}\left(\sqrt{\delta y^2 + (z(x_k,y_l) - z(x_k,y_{l+1}))^2} + \sqrt{\delta y^2 + (z(x_{k+1},y_l) - z(x_{k+1},y_{l+1}))^2}\right)\cdot \left(\sqrt{\delta x^2 + (z(x_k,y_l) - z(x_{k+1},y_l))^2} + \sqrt{\delta x^2 + (z(x_k,y_{l+1}) - z(x_{k+1},y_{l+1}))^2}\right) \qquad \text{R 10b}$$

For a totally flat surface, the surface area and the area of the xy plane are the same and *Sdr* = 0 %.

The Projected Area, *S2A*, expresses the area of the flat x,y plane as given in the denominator of R9.
The Surface Area, *S3A*, expresses the area of the surface area taking into account the z height as given in the numerator of R9.

Functional parameters for characterizing bearing and fluid retention properties
The functional parameters for characterizing bearing and fluid retention properties are described by six parameters. All six parameters are defined from the surface bearing area ratio curve shown in the figures below.

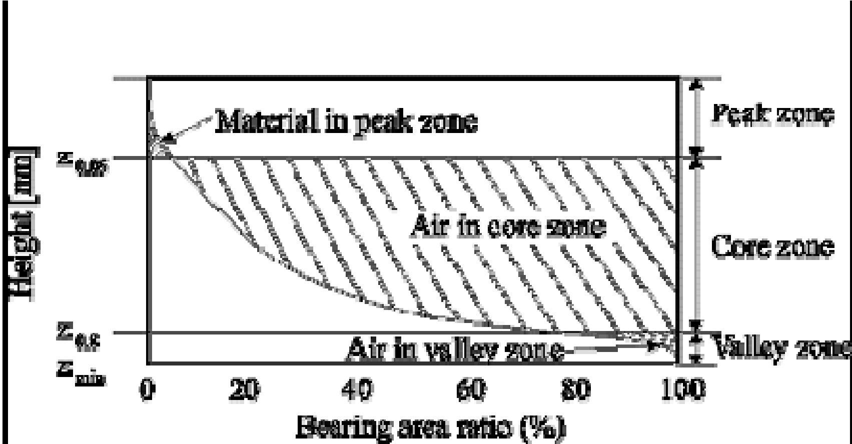

Figure 1: Bearing curve illustrating the calculation of Surface Bearing Index, Core Fluid Retention Index and Valley Fluid Retention Index

The surface bearing area ratio curve, which is also called the Abbott curve, is calculated by the accumulation of the height distribution histogram and the subsequent inversion. Both the histogram and the bearing curves should be divided into 1000 intervals, except for images having less than 10000 pixels, where the intervals are equal to 10% of the total pixels.

The hybrid parameters can be described graphically using the above figure. Horizontal lines are drawn through the bearing area ratio curve at ratio values of 5% and 80%. These lines are marked *Z*0.05 and *Z*0.8 and the three zones created are called the peak, the core and the valley zone. Three parameters are calculated based on this figure:

The Surface Bearing Index, *Sbi*, is defined as:

$$S_{bi} = \frac{S_q}{Z_{0.05}} \quad \text{R 11}$$

where *Z*.05 is the distance from the top of the surface to the height at 5% bearing area. For a Gaussian height distribution *Sbi* approaches 0.608 with increasing number of pixels. Large *Sbi* indicates a good bearing property.

The Core Fluid Retention Index, *Sci*, is defined as:

$$S_{ci} = \frac{V_v(h_{0.05}) - V_v(h_{0.80})}{(M-1)(N-1)\delta x \delta y} / S_q \quad \text{R 12}$$

where *Vv*(*Zx*), is the void area over the bearing area ratio curve and under the horizontal line *Zx*. For a Gaussian height distribution *Sci* approaches 1.56 with increasing number of pixels. Large values of *Sci* indicate that the void volume in the core zone is large. For all surfaces, *Sci* is between 0 and 0.75 (*Z*0.05 -*Z*0.80) / *Sq* . .

The Valley Fluid Retention Index, *Svi*, is defined as:

$$S_{ci} = \frac{V_v(h_{0.80})}{(M-1)(N-1)\delta x \delta y} / S_q \quad \text{R 13}$$

For a Gaussian height distribution *Svi* approaches 0.11 with increasing number of pixels. Large values of *Svi* indicate large void volumes in the valley zone. For all surfaces, *Svi* is between 0 and 0.2 (*Z*0.80 -*Z*min)/ *Sq* .

Parameters associated with the two-dimensional DIN 4776 standard can be also calculated based on the bearing area ratio curve. First, one has to draw the least mean squares line fitting to the 40% segment of the curve that results in the lowest decline (see figure below). Then, he has to extend this line so that it cuts the vertical axes for 0% and 100% bearing area ratio and draw horizontal lines at the intersection points. Finally, he has to draw a straight line that starts from the intersection point between the bearing area ratio curve and the upper horizontal line and ends at the 0% axis, so that the area of this triangle is the same as that between the horizontal line and the bearing area ratio curve. Using the same principle, he has to draw a line between the lower horizontal line and the 100% axis.

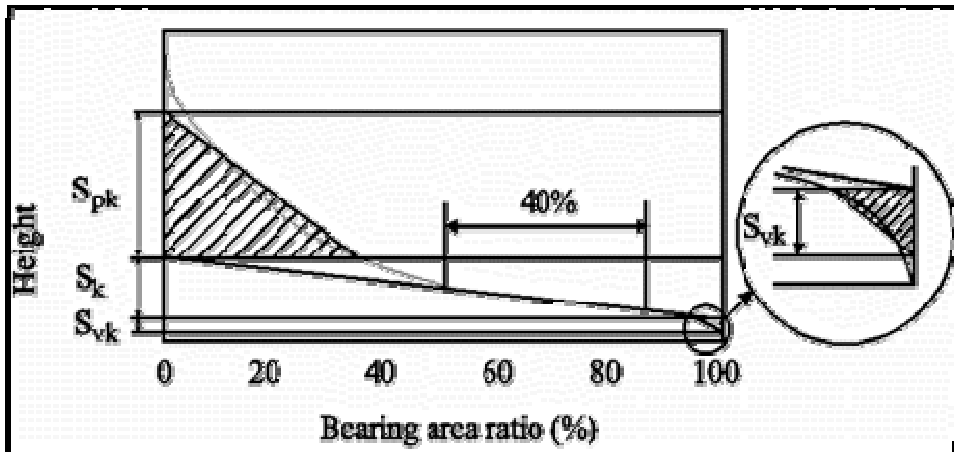

Figure 2: Bearing curve illustrating the calculation of Reduced Summit Height, Reduced Valley Height and Core Roughness Depth

The Reduced Summit Height, *Spk*, is the height of the upper left triangle.
The Core Roughness Depth, *Sk*, is the height difference between the intersection points of the found least mean square line.
The Reduced Valley Depth, *Svk*, is the height of the triangle drawn at 100%.

l-h% Height Intervals of Bearing Curve, *S*DC*l-h* this is a set of parameters describing height differences between certain bearing area ratios; *l* and *h* denotes the lower and upper bearing area ratios of the interval. *S*DC*l* is the height value at bearing area ratio of *l* % and *S*DC*h* is the bearing area ratio at *h* % and *S*DC*l-h* denotes their height difference *S*DC*l* - *S*DC*h.*
Currently SPIP calculates Sd0-5, SDC5-10, SDC10-50, SDC50-95 and SDC50-100.

Spatial parameters
The spatial properties can be described using five spatial parameters: density of summits, texture direction, dominating wavelength and two index parameters. The first parameter can be calculated directly from the image, while the others are based on the Fourier spectrum. For these parameters, the images are required to be quadratic.

The Density of Summits, ***Sds***, is the number of local maximums per area:

$$S_{ds} = \frac{\text{Number of local maximums}}{(M-1)(N-1)\delta x \delta y}, \qquad \text{R 14}$$

Because, the parameter is sensitive to noisy peaks, it should be interpreted carefully.

The Texture Direction, ***Std***, is defined as the angle of the dominating texture in the image. For images consisting of parallel ridges, the texture direction is parallel to the direction of the ridges. If the ridges are perpendicular to the X-scan direction *Std* = 0. If the angle of the ridges is turned clockwise, the angle is positive and if

the angle of the ridges is turned anti-clockwise, the angle becomes negative. This parameter is only meaningful if there is a dominating direction on the sample.
Std is calculated from the Fourier spectrum. The relative amplitudes of different angles are found by summation of the amplitudes along *M* equiangularly separated radial lines, as shown in the figure below. The result is called the angular spectrum. Note that the Fourier spectrum is translated so that the DC component is at (*M*/2,*M*/2). The angle, a , of the i-th line is a = p/ *M* , where i=0, 1, .., *M*-1. The amplitude sum, A(a) , at a line with the angle, a , is defined as:

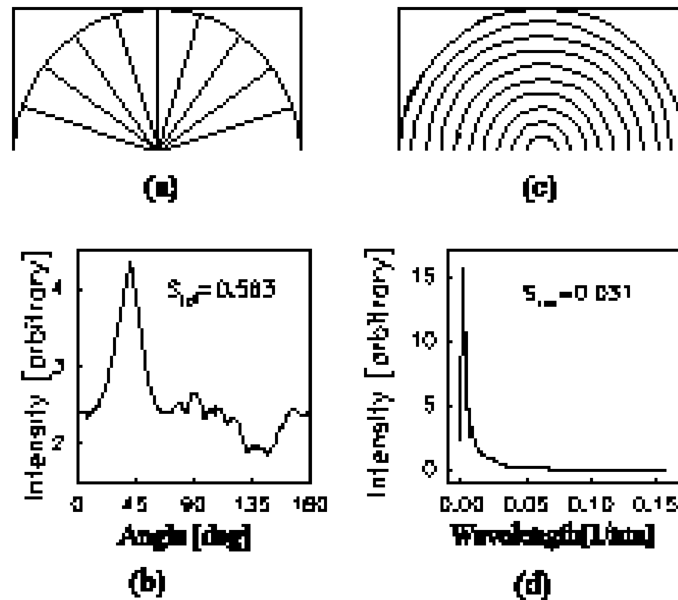

Figure 3: Fourier spectrum and the angular and radial spectrums (Modified from ***[6]***). a) Equidistant lines used for calculation of the angular spectrum shown in b). c) Equidistant semicircles used for calculation of the radial spectrum.

The angular spectrum is calculated by the following formula:

$$A(\alpha) = \sum_{i=1}^{M/2-1} \left| \ F(u(M/2+i \ \cos(\alpha)), \ \ v(M/2+i \ \sin(\alpha))) \ \right| \qquad \text{R 15}$$

For non-integer values of $p = M/(2+i\cos(\alpha))$ and $q = M/(2+i\sin(\alpha))$, the value of *F*(*u*(*p*),*v*(*q*)) is found by linear interpolation between the values of *F*(*u*(*p*),*v*(*q*)) in the 2x2 neighboring pixels. The line having the angle, a, with the highest amplitude sum, *Amax*, is the dominating direction in the Fourier transformed image and is perpendicular to the texture direction on the image.
Note that due to 1/f noise often a dominating direction parallel to the x-axis is found.

The Texture Direction Index, ***Stdi***, is a measure of how dominant the dominating direction is, and is defined as the average amplitude sum divided by the amplitude sum of the dominating direction:

$$S_{tdi} = \frac{\sum_{i=0}^{M-1} A(i\pi / M)}{M \ A_{\max}} \ , \qquad \text{R 16}$$

With this definition the *Stdi* value is always between 0 and 1. Surfaces with very dominant directions will have *Stdi* values close to zero and if the amplitude sum for all directions is similar, *Stdi* is close to 1.

The Radial Wavelength, ***Srw***, is the dominating wavelength found in the radial spectrum. The radial spectrum is calculated by summation of amplitude values around *M*/(2 -1) equidistantly separated semicircles as indicated in sub figure (b). The radius measured in pixels of the semicircles, *r*, is in the range *r* = 1, 2,.., *M*/(2 -1). The amplitude sum, b(*r*) , along a semicircle with the radius, *r*, is

The radial spectrum is calculated by the following formula:

$$\beta(r) = \sum_{i=1}^{M-1} \left| F(u(M/2 + r\cos(i\pi/M)),\ v(M/2 + r\sin(i\pi/M))) \right| \qquad \text{R 17}$$

Again the amplitude for non-integer values of

p=*M*/2 +*r* cos (*i* p/*M*) and *q*=*M*/2 +*r* sin (*i* p/*M*)

is calculated by linear interpolation between the values of *F*(*u*(*p*),*v*(*q*)) in the 2x2 neighboring pixels.

The **Dominating Radial Wavelength,** ***Srw***, corresponds to the semicircle with radius, *rmax* , having the highest amplitude sum, b*max*:

$$S_{rw} = \frac{\delta x(M-1)}{r_{\max}}, \qquad \text{R 18}$$

The **Radial Wave Index**, ***Srwi***, is a measure of how dominant the dominating radial wavelength is, and is defined as the average amplitude sum divided by the amplitude sum of the dominating wavelength:

$$S_{rwi} = \frac{2}{M\beta_{\max}} \sum_{i=1}^{M/2-1} \beta(i), \qquad \text{R 19}$$

With this definition, *Srwi* is always between 0 and 1. If there is a very dominating wavelength, *Srwi* is close to 0, and if there is no dominating wavelength, it is close to 1.

The **Mean Half Wavelength,** ***Shw***, is based on the integrated radial spectrum $\beta_i(r)$:

$$\beta_i(r) = \sum_{j=1}^{r} \beta(j) \qquad \text{R 20}$$

Shw corresponds to the radius *r 0.5* where:

$$\frac{\beta_i(r_{0.5})}{\beta_i(M/2-1)} = 0.5 \qquad \text{R 21}$$

Having found r 0.5*, Shw* is calculated using:

$$S_{hw} = \frac{\delta x(M-1)}{r_{0.5}} \qquad \text{R 22}$$

The **Fractal Dimension, *Sfd*** is calculated for different angles by analyzing the Fourier amplitude spectrum; for different angles, the Fourier profile is extracted and the logarithm of the frequency and amplitude coordinates is calculated. The fractal dimension for each direction is then calculated as 2.0 minus the slope of the log - log curves. The fractal dimension can be also evaluated from 2D Fourier spectra by application of the Log Log function. If the surface is fractal, the Log Log graph should be highly linear, with at negative slope.

The **Correlation Length parameters *Scl20* and *Scl37*** are defined as the horizontal distance of the areal autocorrelation function that has the fastest decay to 20% and 37% respectively (37% is equivalent to 1/e). For an anisotropic surface, the correlation length is in a direction perpendicular to the surface layer.

The **Texture Aspect Ratio Parameters, *Str20 and Str37*,** are used to identify texture strength (uniformity of texture aspect). They are defined as the ratio of the fastest to slowest decay to 20% and 37% of the autocorrelation function respectively. In principle, the texture aspect ratio has a value between 0 and 1. For a surface with a dominant layer, the parameters will approach 0.00, whereas, a spatially isotropic texture will result in a Str value of 1.00.

Annex 7B Shape Measurement Parameters

In this section, all calculated parameters related to the grain properties and included in the data tables are described in details.
The SPIP software used for the analysis has two options for shape analysis:
manually drawn Measure Shapes, using the Measure Shape tools (Type = User defined)
Shapes generated by the Particle & Pore Analysis module.
In the case of the thin films analyzed in this work, based on the SPIP 4.0 Version used, a combination of both methods was used. The calculated parameters were the same for manually drawn Measure Shapes using Measure Shape tools (Type = User defined) and for Shapes generated by the Particle & Pore Analysis module.
For a Line Measure Shape, which covers no area, all area and volume parameters are naturally not calculated. For an Ellipse/Circle Measure Shape (which are described by their major and minor axes), parameters were calculated from analytical geometrical formulas when possible. For a Polygon Measure Shape, parameters were calculated from their contour points and from the enclosed image points (pixels).

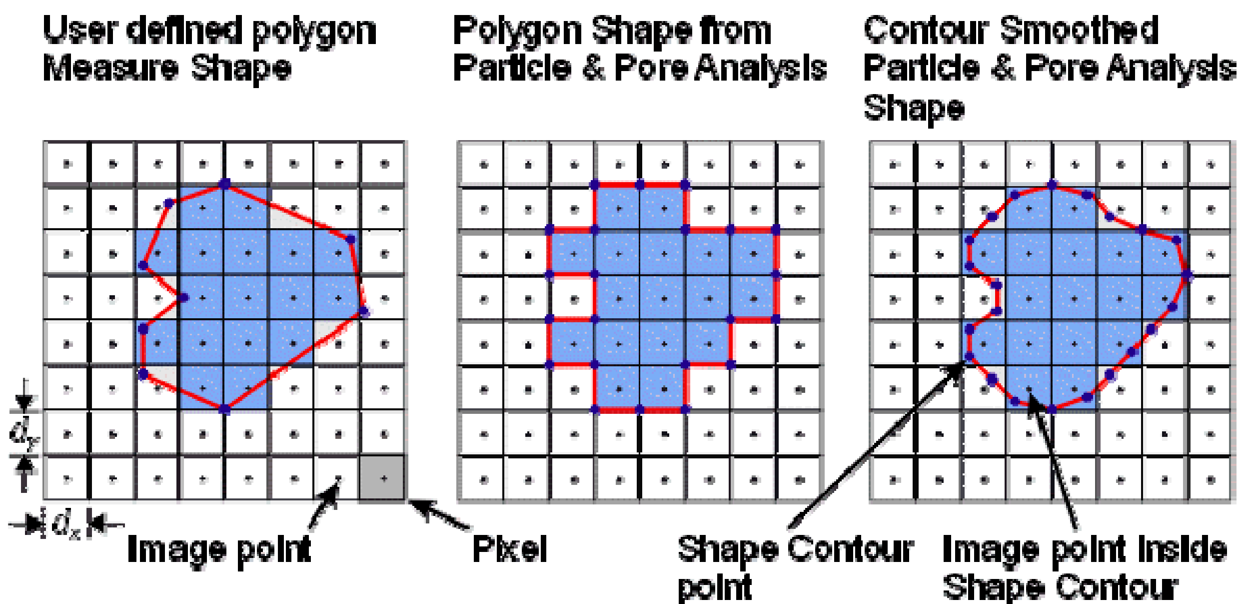

The above picture shows the difference between "handmade", i.e. User defined, Polygon Measure Shapes and Polygon Shapes generated by the Particle & Pore Analysis module. Handmade Measure Shapes have Contour points at the places where the user had clicked on the image (typically few). Particle & Pore Analysis Shapes have Contour points at all pixel corners of the feature boundary. Finally, note that the effect of Contour Smoothing is a shorter perimeter (contour length), but also a slight shrinkage of the Shape.
All Measure Shapes have an ID number. The lowest ID number is 1, the highest number equals to the number of Shapes.
Based on the shape contour correct definition, various areal, length and distance, height and volume parameters can be evaluated using the software. The formulas used in the computation of these parameters are presented bellow.

Areal Parameter

The **Area** is calculated from the shapes periphery, i.e. the closed polygon that surrounds the feature. The area is calculated using:

$$Area(polygon) = \frac{\sum_{i \in Contour} (x_i + x_{i-1}) \cdot (y_i - y_{i-1})}{2}$$

$$Area(ellipse) = \pi \cdot ab$$

Where *a* and *b* are the major and minor axes of the ellipse.

Length and Distance Parameters

The **diameter** (or Heywood diameter) is expressed as the diameter of a circle having an area equivalent to the shape's area.

$$Diameter = \sqrt{\frac{4}{\pi} \cdot Area}$$

Length is defined as the longest string along the angle Q given by the moment's axis with respect to the x-axis. In other words, if we rotated the shape so that the moment's axis becomes parallel to the x-axis, then Length is the extension of the bounding rectangle in the horizontal direction.

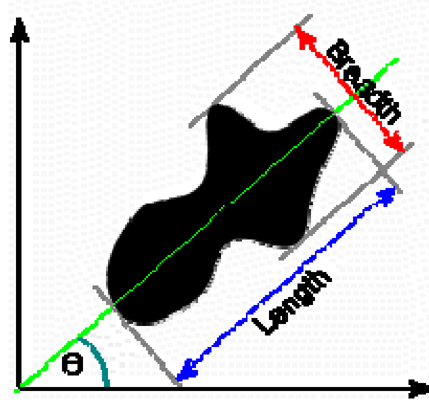

For lines, Length is the distance between the most distant points of the line.
For circles it equals the diameter
For ellipses it equals the length of the major axis, *a*.
Breadth (or width) is defined as the longest string perpendicular to the angle Q given by the moment's axis with respect to the x-axis. In other words, if the Shape was rotated so that the moment's axis becomes parallel to the x-axis, then Breadth is the extension of the bounding rectangle in the vertical direction. For ellipses it equals the length of the minor axis, *b*.
Radius is defined as half the size of the (Heywood) Diameter described above.
For Polygon Shapes the **Perimeter** is calculated from the Shape's contour as:

$$P = \sum_i \sqrt{(x_i - x_{i-1})^2 + (y_i - y_{i-1})^2}$$

Circular feature detected as a Polygon Shape by Particle & Pore Analysis

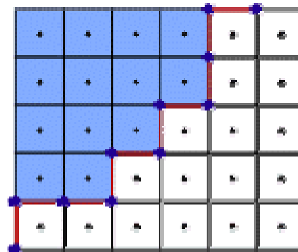

No Contour Smoothing:

P* = 4 x *d

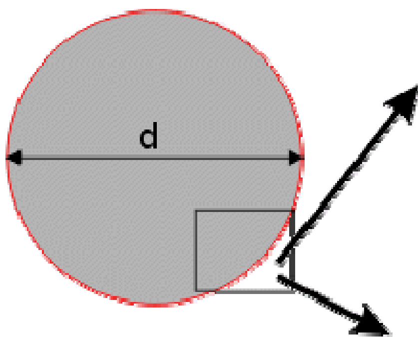

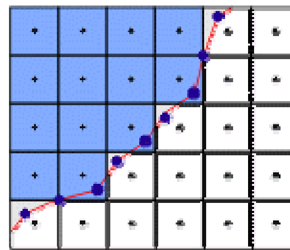

With Contour Smoothing:

P* ≈ π x *d

Example of the effect of Contour Smoothing can be seen in Figure ??: if a circular feature is detected by the Particle & Pore Analysis module, the perimeter of the generated polygon Shape will be the same as a square with the same side lengths as the diameter of the circle. Smoothing the Contour will bring the calculated Perimeter, *P*, closer to the expected result, namely p·*d.*

For ellipsoidal Shapes with major and minor axes *a* and *b*, respectively, the perimeter is calculated using the following formula (Ramanujan 1914):

$$P = \pi(a+b)\left(1 + \frac{3}{10 + \sqrt{4 - 3h}}\right) \quad , \quad h = \frac{(a-b)^2}{(a+b)^2}$$

Height and Volume Parameters

Raw Z values (reference Z=0)

Z Minimum, which is the minimum Z value of all points inside the Shape Contour.

Z Maximum, which is the maximum Z value of all points inside the Shape Contour.

Z Range = Z Maximum – Z Minimum

Z Mean is the average of the Z values of all points inside the Shape Contour:

$$Z\,Mean = \frac{\sum_{\{Z(x,y) \in Shape\}} Z(x,y)}{\sum_{\{Z(x,y) \in Shape\}} 1}$$

Z Median is the median of the Z values of all points inside the Shape Contour, i.e. the Z value above (or below) which, 50% of the points inside the Shape can be found.
Z Std. Dev. is the standard deviation of the Z values of all points inside the Shape Contour.
Z Volume is the maximum of Z Material Volume and Z Void Volume (see below)
Z Material Volume is the volume of all pixels inside the Shape's Contour with a Z value greater than or equal to zero:

$$Z\,MaterialVolume = \sum_{\{Z(x,y)\in Shape|Z\geq 0\}} Z(x,y)\cdot dxdy$$

where *dx* and *dy* are the point spacing in the X and Y directions of the image, respectively.
Z Void Volume is the volume of all pixels inside the Shape's Contour with a Z value lower than or equal to zero:

$$ZVoidVolume = \sum_{\{Z(x,y)\in Shape|Z\leq 0\}} Z(x,y)\cdot dxdy$$

where *dx* and *dy* are the point spacing in the X and Y directions of the image, respectively.
Z Net Volume = Z Material Volume – Z Void Volume
Minimum Contour Height is the minimum Z value (relative to Z=0) of the Shape's contour points. The local Z values are calculated using bi-linear interpolation at each Contour point. In the case of User defined Shapes (manually drawn) and Ellipse/Circle Shapes, the Contour is sampled at less than Ö2 pixel spacing by adding temporary Contour points.
Maximum Contour Height is the maximum Z value (relative to Z=0) of the Shape's contour points. The local Z values are calculated using bi-linear interpolation at each Contour point. In the case of User defined Shapes (manually drawn) and Ellipse/Circle Shapes the Contour is sampled at less than Ö2 pixel spacing by adding temporary Contour points.
Mean Contour Height is the average Z value (relative to Z=0) of the Shape's contour points. The local Z values are calculated using bi-linear interpolation at each Contour point. In the case of User defined Shapes (manually drawn) and Ellipse/Circle Shapes the Contour is sampled at less than Ö2 pixel spacings by adding temporary Contour points.
Parameters Relative to Mean Contour Height
These parameters are Z values relative to the Mean Contour Height, Z_{MCH}. All "height" parameters are for Z values higher than or equal to the Mean Contour Height. All "Depth" parameters are for Z values lower than or equal to the Mean Contour Height. In the following the following abbreviation is used:

$\mathbf{Z_{MCH}}$ = Mean Contour Height

Maximum Height

$$MaximumHeight = Max\{Z(x,y)\in Shape \mid Z\geq Z_{MCH}\} - Z_{MCH}$$

Mean Height is the average of Z values (relative to the Mean Contour Height) of all points inside a Shape having Z ≤ Z_{MCH}.

$$MeanHeight = \frac{\sum_{\{Z(x,y)\in Shape|Z\geq Z_{MCH}\}} \left(Z(x,y)-Z_{MCH}\right)}{\sum_{\{Z(x,y)\in Shape|Z\geq Z_{MCH}\}} 1}$$

Std. Dev. of Height is the standard deviation of Z values (relative to the Mean Contour Height) of all points inside a Shape having Z ≤ Z_{MCH}.
Median Height is the median of Z-Z_{MCH} of all points inside the Shape Contour with Z ≤ Z_{MCH}.

Maximum Depth

$$MaximumDepth = Z_{MCH} - Min\{Z(x,y)\in Shape \mid Z \leq Z_{MCH}\}$$

Mean Depth is the average of Z values (relative to the Mean Contour Height) of all points inside a Shape having Z ≤Z_{MCH}.

$$MeanDepth = \frac{\sum_{\{Z(x,y)\in Shape|Z\leq Z_{MCH}\}} \left(Z_{MCH}-Z(x,y)\right)}{\sum_{\{Z(x,y)\in Shape|Z\leq Z_{MCH}\}} 1}$$

Volume is the maximum of the found Material Volume and Void Volumes:
Volume = Max{Material Volume, Void Volume}
The **Material Volume** equals the volume of all points having a Z value higher than the Mean Contour Height:

$$MaterialVolume = \sum_{\{Z(x,y)\in Shape|Z\geq Z_{MCH}\}} (Z(x,y)-Z_{MCH})\cdot dxdy$$

The **Void Volume** equals the volume of all points having a Z value lower than the Mean Contour Height. This value will always be positive:

$$VoidVolume = \sum_{\{Z(x,y)\in Shape|Z\leq Z_{MCH}\}} (Z_{MCH}-Z(x,y))\cdot dxdy$$

The **Net Volume** is calculated as
Net Volume = Material Volume - Net Volume

Shape and Orientation Parameters
Aspect Ratio is defined as Length over Breadth. From this definition, the aspect ration will always be greater than or equal to 1.0. The aspect ratio of both a circle and a square is 1.0, whereas other shapes will have a value less than 1.0.

$$AspectRatio = \frac{Length}{Breadth}$$

Annex 7C Experimental data for In_2O_{3-x} grown by DC magnetron sputtering.

RUN	% O_2	PO_2 (mbar)	ISP (A)	time (s)	T (°C)	d (nm)	growth rate	Sa	Sq	Ssk	Sku
1	100	0.008	0.60	1260	300	151.4	0.12	1.37	1.74	0.42	3.40
2	100	0.008	0.60	1257	138	151.7	0.12	1.01	1.27	0.30	2.92
3	100	0.008	0.60	1225	200	152	0.12	1.24	1.53	0.04	2.75
4	100	0.008	0.60	1260	165	151.8	0.12	1.26	1.56	-0.01	2.83
5	100	0.008	0.60	1296	25	151.9	0.12	1.22	1.52	0.09	2.90
6	100	0.008	0.60	1262	100	151.7	0.12	1.46	1.82	0.03	2.82
7	100	0.008	0.45	4320	25	405.4	0.09	1.40	1.79	0.36	3.44
8	100	0.008	0.44	6600	25	615	0.09	1.55	1.97	0.30	3.25
9	100	0.008	0.44	1080	25	100.5	0.09	0.83	1.06	0.04	3.93
10	100	0.015	0.45	1200	25	100.5	0.08	1.48	1.84	0.20	3.01
11	100	0.050	0.45	1020	25	101.6	0.10	0.69	0.87	0.08	3.15
12	100	0.030	0.45	2550	25	100.8	0.04	2.15	2.71	0.03	3.02
13	100	0.050	0.45	3075	25	100.5	0.03	3.41	4.26	-0.14	2.97
14	100	0.008	0.45	540	25	48.3	0.09	0.70	0.86	0.03	2.71
15	100	0.008	0.45	240	25	19.4	0.08	0.28	0.35	-0.08	3.10
16	100	0.008	0.45	2100	25	195.9	0.09	1.11	1.40	0.03	3.15
17	100	0.008	0.45	1080	25	100.3	0.09	0.62	0.78	0.24	3.22
18	100	0.008	0.45	1200	25	110.8	0.09	0.62	0.78	0.21	3.43
19	100	0.015	0.15	5700	25	94	0.02	1.55	1.98	0.15	3.66
20	100	0.006	0.44	540	25	101.7	0.19	0.61	0.75	-0.14	2.72
21	100	0.007	0.44	516	25	103.6	0.20	0.68	1.02	2.24	13.38
22	100	0.008	0.44	720	25	103.1	0.14	0.52	0.66	0.22	3.16
23	100	0.008	0.44	480	25	70	0.15	0.55	0.70	0.01	3.07
24	100	0.008	0.44	900	25	133	0.15	0.79	0.99	0.13	3.07
25	100	0.008	0.44	240	25	34	0.14	0.33	0.44	0.63	11.12
26	100	0.008	0.44	1800	25	270.1	0.15	1.29	1.61	-0.05	2.95
27	100	0.015	0.45	900	25	129.9	0.14	1.82	2.44	0.60	5.12
28	100	0.015	0.45	900	137	130.6	0.15	0.94	1.18	0.37	3.27
29	100	0.015	0.45	900	210	130.7	0.15	2.25	2.87	0.56	3.55
30	100	0.015	0.45	900	290	130.2	0.14	2.04	2.61	0.56	3.67
31	100	0.015	0.45	240	37	31.8	0.13	0.46	0.61	1.14	7.89
32	100	0.015	0.45	480	37	67.4	0.14	0.47	0.60	0.37	3.66
33	100	0.015	0.45	900	38	133	0.15	0.65	0.84	0.30	3.47
34	100	0.015	0.45	1800	49	274	0.15	1.13	1.42	0.28	3.11
35	100	0.030	0.45	900	49	94.1	0.10	1.59	2.01	0.05	3.29
36	100	0.050	0.45	1500	51	104.3	0.07	1.82	2.30	0.23	3.20
37	100	0.015	0.15	660	35	41.3	0.06	0.50	0.63	0.40	3.38
38	100	0.015	0.45	570	58	132.9	0.23	0.77	0.97	0.14	2.97
39	100	0.015	0.45	570	110	133.7	0.23	0.80	1.00	0.42	3.32
40	100	0.015	0.45	570	154	135.7	0.24	1.18	1.50	0.43	3.41
41	100	0.015	0.45	540	206	134.7	0.25	2.52	3.28	0.66	4.27
42	100	0.015	0.45	570	250	137.6	0.24	2.07	2.59	0.52	3.27
43	100	0.015	0.45	600	290	137.6	0.23	1.27	1.65	0.88	4.12
44	100	0.008	0.44	600	59	147.4	0.25	0.72	0.90	-0.20	2.91
45	80	0.008	0.44	540	61	145.1	0.27	0.78	0.98	-0.02	2.93
46	60	0.008	0.44	390	59	148.4	0.38	0.69	0.87	0.02	3.19
47	40	0.008	0.44	330	53	150	0.45	0.46	0.58	0.18	3.33

RUN	Sy	St	Sz	S10z	Sz_tph	Sds	Ssc	Sv	Sp	Smean	Sdq
1	14.85	14.85	14.85	13.99	13.99	3423.00	0.11	5.95	8.89	-6.38E-09	0.40
2	9.40	9.40	9.40	9.08	9.08	3638.00	0.11	4.40	5.01	-1.71E-09	0.27
3	11.79	11.79	11.79	11.36	11.36	5468.00	0.22	5.85	5.95	-4.14E-10	0.49
4	12.44	12.44	12.44	12.12	12.12	7199.00	0.31	6.28	6.16	-4.01E-09	0.54
5	12.21	12.21	12.21	11.45	11.45	7082.00	0.27	5.84	6.37	-2.09E-09	0.45
6	18.52	18.52	18.52	14.38	14.38	5605.00	0.26	6.69	11.83	8.27E-11	0.49
7	14.95	14.95	14.95	14.50	14.50	5540.00	0.14	6.79	8.16	-2.99E-09	0.27
8	16.43	16.43	16.43	15.14	15.14	5433.00	0.17	6.65	9.77	-1.93E-09	0.34
9	11.15	11.15	11.15	9.95	9.95	4132.00	0.08	4.47	6.68	4.67E-09	0.18
10	25.22	25.22	25.22	15.81	15.81	6633.00	0.24	16.80	8.42	1.12E-08	0.44
11	7.46	7.46	7.46	7.03	7.03	8103.00	0.11	3.72	3.74	2.31E-10	0.17
12	20.88	20.88	20.88	19.86	19.86	4438.00	0.18	11.15	9.73	-1.22E-08	0.34
13	34.16	34.16	34.16	32.14	32.14	2943.00	0.28	20.48	13.67	7.66E-08	0.58
14	6.41	6.41	6.41	6.06	6.06	6199.00	0.08	2.92	3.49	-8.21E-10	0.16
15	3.03	3.03	3.03	2.93	2.93	15236.00	0.08	1.57	1.47	-2.48E-09	0.12
16	12.38	12.38	12.38	11.55	11.55	4077.00	0.11	6.57	5.81	-1.78E-09	0.28
17	7.04	7.04	7.04	6.72	6.72	9987.00	0.15	3.07	3.98	1.22E-08	0.20
18	7.05	7.05	7.05	6.69	6.69	12263.00	0.09	3.20	3.84	-4.89E-09	0.14
19	20.36	20.36	20.36	19.42	19.42	8132.00	0.31	8.67	11.69	3.45E-09	0.41
20	5.67	5.67	5.67	5.37	5.37	2303.00	0.03	3.07	2.60	9.08E-09	0.11
21	14.81	14.81	14.81	13.60	13.60	2379.30	0.04	4.03	10.78	3.86E-09	0.14
22	5.33	5.33	5.33	5.05	5.05	4068.00	0.06	2.37	2.97	-6.66E-09	0.15
23	6.37	6.37	6.37	5.94	5.94	3955.00	0.06	3.24	3.14	-4.95E-10	0.16
24	8.42	8.42	8.42	7.82	7.82	3769.00	0.07	3.86	4.56	1.51E-08	0.21
25	9.22	9.22	9.22	6.35	6.35	7122.00	0.07	3.68	5.54	8.07E-10	0.14
26	13.19	13.19	13.19	12.26	12.26	4489.00	0.10	6.34	6.85	6.43E-09	0.27
27	22.31	22.31	22.31	21.71	21.71	10596.00	0.25	9.67	12.63	1.45E-08	0.31
28	9.51	9.51	9.51	9.19	9.19	7491.00	0.16	4.38	5.13	-3.96E-09	0.22
29	23.69	23.69	23.69	21.99	21.99	4517.00	0.18	8.82	14.87	3.36E-08	0.34
30	20.53	20.53	20.53	19.59	19.59	6972.00	0.17	7.83	12.70	5.12E-09	0.30
31	7.53	7.53	7.53	6.99	6.99	5747.00	0.06	2.45	5.08	3.63E-09	0.13
32	6.28	6.28	6.28	5.51	5.51	6683.00	0.07	2.56	3.73	-4.03E-09	0.12
33	6.45	6.45	6.45	6.32	6.32	6335.00	0.05	2.80	3.64	-3.63E-09	0.10
34	10.02	10.02	10.02	9.89	9.89	3013.00	0.06	4.92	5.10	1.95E-08	0.15
35	16.46	16.46	16.46	15.45	15.45	2760.00	0.07	8.56	7.90	-2.58E-08	0.18
36	17.28	17.28	17.28	16.74	16.74	2104.00	0.06	8.28	9.00	-6.63E-09	0.19
37	6.03	6.03	6.03	5.36	5.36	4844.00	0.07	2.23	3.80	2.26E-09	0.14
38	8.08	8.08	8.08	7.57	7.57	5406.00	0.10	3.81	4.28	-3.52E-09	0.19
39	8.79	8.79	8.79	7.97	7.97	6591.00	0.12	3.51	5.28	-6.13E-09	0.21
40	12.26	12.26	12.26	11.22	11.22	4894.00	0.14	5.30	6.96	6.59E-09	0.24
41	29.25	29.25	29.25	27.68	27.68	3234.00	0.13	11.77	17.47	1.66E-08	0.38
42	19.44	19.44	19.44	18.83	18.83	7583.00	0.15	7.65	11.79	-2.28E-08	0.27
43	14.21	14.21	14.21	12.55	12.55	12659.00	0.17	6.09	8.12	-8.00E-09	0.25
44	7.08	7.08	7.08	6.53	6.53	9264.00	0.11	3.91	3.17	-1.20E-08	0.18
45	7.56	7.56	7.56	7.17	7.17	5903.00	0.10	3.88	3.68	-6.41E-09	0.20
46	10.76	10.76	10.76	8.37	8.37	8269.00	0.10	5.37	5.39	2.95E-09	0.20
47	5.85	5.85	5.85	5.43	5.43	7617.00	0.08	2.66	3.19	-2.25E-09	0.14

RUN	Sdq6	Sdr	S2A	S3A	Sbi	Sci	Svi	Spk	Sk	Svk	Std	Stdi
1	0.39	7.57	1.00E+06	1.08E+06	0.57	1.71	0.10	2.37	4.30	1.27	76.71	0.91
2	0.26	3.48	1.00E+06	1.03E+06	0.57	1.71	0.10	1.50	3.25	0.87	82.37	0.91
3	0.48	11.16	1.00E+06	1.11E+06	0.61	1.58	0.11	1.51	4.13	1.22	4.69	0.90
4	0.52	13.89	1.00E+06	1.14E+06	0.61	1.57	0.11	1.54	4.17	1.35	6.81	0.93
5	0.43	9.70	1.00E+06	1.10E+06	0.59	1.63	0.11	1.64	3.97	1.28	66.26	0.93
6	0.48	11.26	1.00E+06	1.11E+06	0.61	1.58	0.11	2.09	4.83	1.50	64.78	0.89
7	0.26	3.64	1.00E+06	1.04E+06	0.58	1.68	0.10	2.38	4.37	1.40	81.22	0.83
8	0.32	5.40	1.00E+06	1.05E+06	0.57	1.68	0.10	2.60	4.91	1.52	82.06	0.76
9	0.18	1.63	1.00E+06	1.02E+06	0.66	1.44	0.12	1.33	2.60	1.10	83.04	0.81
10	0.42	8.99	1.00E+06	1.09E+06	0.59	1.64	0.11	2.15	4.84	1.61	83.01	0.87
11	0.15	1.38	1.00E+06	1.01E+06	0.60	1.60	0.11	0.99	2.17	0.80	83.74	0.82
12	0.32	5.48	1.00E+06	1.05E+06	0.60	1.60	0.11	2.92	6.78	2.47	112.50	0.86
13	0.56	15.72	1.00E+06	1.16E+06	0.62	1.53	0.12	3.79	11.09	4.12	115.39	0.87
14	0.15	1.24	1.00E+06	1.01E+06	0.61	1.56	0.11	0.85	2.36	0.67	89.64	0.62
15	0.10	0.69	1.00E+06	1.01E+06	0.61	1.55	0.12	0.36	0.88	0.35	94.39	0.79
16	0.27	3.78	1.00E+06	1.04E+06	0.60	1.60	0.12	1.57	3.49	1.35	59.31	0.85
17	0.18	2.04	1.00E+06	1.02E+06	0.59	1.65	0.10	0.97	1.96	0.64	95.73	0.84
18	0.12	1.02	1.00E+06	1.01E+06	0.60	1.60	0.11	1.00	1.97	0.67	98.18	0.86
19	0.38	8.15	1.00E+06	1.08E+06	0.61	1.57	0.11	2.50	4.85	1.88	71.40	0.88
20	0.11	0.58	1.00E+06	1.01E+06	0.63	1.49	0.12	0.65	1.99	0.68	80.71	0.88
21	0.13	0.93	4.00E+06	4.04E+06	0.60	1.69	0.08	2.46	1.76	0.64	85.07	0.88
22	0.14	1.05	1.00E+06	1.01E+06	0.58	1.65	0.11	0.80	1.64	0.53	80.73	0.89
23	0.16	1.28	1.00E+06	1.01E+06	0.61	1.57	0.12	0.78	1.78	0.65	109.95	0.85
24	0.21	2.18	1.00E+06	1.02E+06	0.59	1.61	0.11	1.13	2.54	0.84	75.35	0.83
25	0.14	0.97	1.00E+06	1.01E+06	0.61	1.60	0.11	0.73	1.01	0.39	76.82	0.82
26	0.26	3.54	1.00E+06	1.04E+06	0.62	1.54	0.12	1.60	4.21	1.48	1.52	0.88
27	0.27	4.71	1.00E+06	1.05E+06	0.61	1.58	0.11	3.91	5.36	2.26	0.00	0.80
28	0.20	2.42	1.00E+06	1.02E+06	0.56	1.72	0.10	1.54	2.93	0.88	104.51	0.83
29	0.33	5.63	1.00E+06	1.06E+06	0.55	1.77	0.09	4.13	6.92	1.78	178.64	0.76
30	0.28	4.30	1.00E+06	1.04E+06	0.55	1.78	0.09	3.88	6.31	1.73	177.71	0.82
31	0.13	0.85	1.00E+06	1.01E+06	0.61	1.62	0.09	1.05	1.37	0.45	106.12	0.77
32	0.11	0.72	1.00E+06	1.01E+06	0.58	1.68	0.10	0.86	1.46	0.51	80.92	0.82
33	0.09	0.46	1.00E+06	1.00E+06	0.58	1.67	0.10	1.12	2.02	0.71	73.46	0.83
34	0.15	1.18	1.00E+06	1.01E+06	0.57	1.69	0.10	1.72	3.55	1.12	101.69	0.81
35	0.18	1.67	1.00E+06	1.02E+06	0.61	1.58	0.11	2.36	4.99	1.91	0.00	0.80
36	0.18	1.73	1.00E+06	1.02E+06	0.58	1.67	0.10	2.77	5.78	1.88	1.02	0.74
37	0.14	1.04	1.00E+06	1.01E+06	0.57	1.70	0.09	0.86	1.59	0.45	71.72	0.86
38	0.18	1.73	1.00E+06	1.02E+06	0.59	1.64	0.11	1.12	2.46	0.81	77.94	0.87
39	0.20	2.21	1.00E+06	1.02E+06	0.57	1.72	0.09	1.36	2.52	0.68	85.19	0.74
40	0.23	2.92	1.00E+06	1.03E+06	0.57	1.71	0.10	2.02	3.72	1.08	60.42	0.83
41	0.37	6.87	1.00E+06	1.07E+06	0.56	1.75	0.09	5.28	7.59	2.39	106.86	0.84
42	0.25	3.58	1.00E+06	1.04E+06	0.55	1.78	0.08	3.57	6.50	1.56	178.32	0.69
43	0.22	3.06	1.00E+06	1.03E+06	0.52	1.89	0.08	2.77	3.53	0.96	117.60	0.82
44	0.16	1.67	1.00E+06	1.02E+06	0.64	1.48	0.12	0.80	2.33	0.90	85.44	0.86
45	0.19	1.92	1.00E+06	1.02E+06	0.60	1.58	0.11	1.01	2.50	0.90	99.10	0.88
46	0.18	1.95	1.00E+06	1.02E+06	0.61	1.57	0.12	1.06	2.18	0.85	85.70	0.88
47	0.13	0.94	1.00E+06	1.01E+06	0.59	1.63	0.11	0.72	1.47	0.49	85.53	0.77

RUN	Srw	Srwi	Shw	Sfd	Scl20	Str20	Scl37	Str37	Sdc0_5	Sdc5_10	Sdc10_50
1	95.61	0.28	21.28	2.76	13.70	1.00	9.78	0.83	5.83	0.80	2.41
2	110.57	0.27	22.73	2.76	13.70	0.88	11.74	1.00	2.77	0.55	1.79
3	41.64	0.39	16.67	2.57	7.83	0.67	7.83	0.80	3.43	0.54	2.01
4	50.16	0.42	15.87	2.52	9.78	0.83	7.83	1.00	3.59	0.57	2.02
5	85.78	0.35	17.54	2.60	11.74	0.86	9.78	1.00	3.79	0.61	2.03
6	83.71	0.34	18.87	2.64	11.74	0.86	9.78	0.83	8.83	0.63	2.41
7	90.11	0.19	27.03	2.77	21.53	0.79	17.61	0.82	5.06	0.81	2.43
8	134.34	0.20	25.00	2.73	17.61	0.60	13.70	0.58	6.35	0.89	2.63
9	147.80	0.21	27.03	2.83	19.57	0.83	13.70	0.78	5.07	0.36	1.23
10	129.07	0.27	20.00	2.64	15.66	0.80	11.74	0.75	5.31	0.71	2.53
11	109.21	0.22	23.26	2.67	19.57	0.83	15.66	0.80	2.29	0.34	1.14
12	222.31	0.17	27.78	2.74	25.44	0.72	21.53	0.79	5.19	1.09	3.52
13	124.43	0.18	27.78	2.77	21.53	0.73	17.61	0.75	6.78	1.44	5.41
14	357.29	0.20	23.26	2.79	52.84	0.11	27.40	0.06	2.08	0.30	1.13
15	75.60	0.29	18.18	2.56	13.70	0.78	9.78	0.71	0.90	0.13	0.44
16	97.86	0.25	23.26	2.75	15.66	0.80	11.74	0.75	3.47	0.55	1.84
17	357.24	0.27	20.00	2.64	15.66	0.62	11.74	0.60	2.65	0.32	1.04
18	244.04	0.21	25.64	2.71	25.44	0.93	19.57	1.00	2.54	0.32	1.00
19	120.95	0.25	22.73	2.70	17.61	0.82	13.70	0.88	8.44	0.78	2.53
20	150.11	0.19	30.30	2.91	21.53	0.85	17.61	0.90	1.41	0.24	0.92
21	166.05	0.27	37.74	2.65	31.31	0.73	23.48	0.75	9.08	0.74	1.13
22	59.81	0.29	21.74	2.73	13.70	0.88	9.78	0.83	1.84	0.28	0.89
23	105.50	0.29	21.28	2.72	11.74	0.75	9.78	0.83	1.99	0.27	0.89
24	100.67	0.27	22.22	2.72	13.70	0.78	11.74	0.86	2.90	0.39	1.32
25	285.04	0.31	17.54	2.64	9.78	0.71	7.83	0.80	4.82	0.18	0.57
26	109.29	0.23	25.00	2.78	17.61	0.75	13.70	0.78	4.26	0.56	2.04
27	357.80	0.12	29.41	2.72	50.88	0.46	35.23	0.72	8.67	1.16	2.95
28	146.40	0.22	23.81	2.70	21.53	0.79	15.66	0.73	3.03	0.55	1.64
29	310.73	0.16	30.30	2.82	29.35	0.42	23.48	0.80	9.68	1.42	4.03
30	328.94	0.13	30.30	2.79	39.14	0.31	27.40	0.67	7.94	1.40	3.62
31	237.97	0.24	22.73	2.73	15.66	0.57	11.74	0.60	4.07	0.29	0.78
32	197.79	0.23	25.00	2.71	15.66	0.73	13.70	0.88	2.68	0.28	0.81
33	307.29	0.15	33.33	2.78	27.40	0.67	21.53	0.69	2.20	0.39	1.10
34	233.52	0.14	34.48	2.86	27.40	0.82	21.53	0.79	2.61	0.60	1.99
35	295.18	0.14	35.71	2.88	31.31	0.76	23.48	0.71	4.59	0.82	2.51
36	165.77	0.11	38.46	2.91	37.18	0.76	29.35	0.83	5.02	0.97	3.15
37	93.15	0.28	21.74	2.72	13.70	0.88	11.74	1.00	2.69	0.29	0.87
38	155.10	0.23	23.26	2.72	17.61	0.82	13.70	0.78	2.62	0.41	1.28
39	101.02	0.26	23.81	2.73	13.70	0.64	11.74	0.67	3.50	0.46	1.39
40	166.08	0.19	26.32	2.77	21.53	0.69	15.66	0.67	4.32	0.69	2.06
41	136.97	0.16	31.25	2.86	27.40	0.70	19.57	0.63	11.60	1.82	4.40
42	330.87	0.13	32.26	2.79	33.27	0.46	25.44	0.52	7.05	1.29	3.74
43	168.33	0.18	26.32	2.71	25.44	0.50	19.57	0.53	4.96	0.94	2.51
44	185.16	0.21	23.26	2.69	19.57	0.63	15.66	0.67	1.76	0.30	1.08
45	77.20	0.26	23.26	2.73	17.61	0.90	13.70	0.88	2.06	0.38	1.24
46	138.02	0.24	22.22	2.69	15.66	0.57	11.74	0.60	3.97	0.32	1.12
47	107.97	0.26	22.73	2.69	15.66	0.89	11.74	0.86	2.21	0.23	0.77

RUN	Sdc50_9!	Area nm^:	Length nm	Width nm	Size nm	Perim nm	Aspect	Diam nm
1	2.50	456.12	31.84	13.21	29.22	105.17	2.48	23.03
2	1.85	626.67	37.58	15.55	34.23	123.28	2.55	27.10
3	2.43	364.93	28.12	12.20	25.62	93.63	2.38	20.82
4	2.52	341.82	27.21	11.80	24.79	91.49	2.37	20.14
5	2.37	366.26	28.66	11.72	26.07	95.47	2.52	20.57
6	2.90	419.70	30.66	12.61	27.79	101.08	2.51	22.08
7	2.61	1554.10	61.19	22.34	57.23	207.42	2.98	41.35
8	3.00	864.70	47.38	15.57	44.55	151.30	3.25	30.35
9	1.81	750.31	44.45	15.38	41.58	139.48	3.06	29.21
10	2.83	535.42	35.47	13.53	32.80	117.84	2.74	24.56
11	1.38	816.19	43.54	16.50	40.44	146.51	2.82	30.00
12	4.39	2261.10	74.26	27.40	70.25	247.09	2.90	50.50
13	7.19	1789.50	65.68	25.27	60.46	216.95	2.75	45.66
14	1.39	207.68	23.05	7.79	21.26	69.62	3.21	14.95
15	0.58	377.84	30.51	10.71	28.11	102.07	3.00	20.23
16	2.21	631.00	38.46	14.88	35.30	125.90	2.73	26.81
17	1.17	470.44	33.05	12.47	30.43	112.31	2.75	22.75
18	1.21	866.94	46.65	15.70	43.67	156.36	3.24	30.16
19	3.14	542.95	36.21	13.35	33.36	120.63	2.83	24.63
20	1.32	1022.30	50.35	18.28	46.85	158.82	2.98	33.90
21	1.04	1270.00	54.05	20.46	49.41	179.36	2.73	37.29
22	0.99	512.73	34.59	13.57	31.77	113.97	2.66	24.29
23	1.14	489.72	34.00	13.39	31.25	111.22	2.65	23.93
24	1.54	315.60	27.13	10.06	24.95	85.72	2.88	18.49
25	0.61	166.40	19.56	7.42	17.83	62.13	2.74	13.51
26	2.67	837.30	44.52	17.07	41.09	147.23	2.79	30.86
27	3.58	2036.30	67.54	25.56	62.63	243.89	2.82	46.52
28	1.72	682.01	39.37	14.00	36.94	130.18	2.98	26.24
29	3.99	987.14	46.97	17.53	43.42	158.35	2.84	32.11
30	3.62	961.61	46.31	16.22	42.84	155.97	3.10	30.58
31	0.81	540.61	36.73	13.13	34.26	118.12	2.89	24.62
32	0.89	215.06	22.24	7.28	20.29	68.67	3.23	14.18
33	1.28	1448.70	59.71	19.36	56.11	196.17	3.35	37.97
34	2.09	2307.90	76.09	27.55	71.74	247.74	2.96	51.22
35	3.23	2884.80	84.89	30.54	80.45	273.95	2.99	56.95
36	3.46	1331.50	57.84	18.09	54.17	181.51	3.61	35.95
37	0.91	518.02	34.36	13.83	31.63	113.54	2.59	24.45
38	1.54	358.16	29.08	10.22	26.83	92.55	3.02	19.28
39	1.44	373.76	30.29	9.84	28.24	93.68	3.27	19.26
40	2.16	281.84	26.34	8.44	24.44	80.14	3.26	16.62
41	4.51	1148.60	53.95	17.82	50.35	168.56	3.30	34.60
42	3.47	462.64	32.13	10.11	29.79	102.63	3.35	20.03
43	1.97	457.57	32.01	10.98	29.42	108.80	3.05	20.96
44	1.57	588.81	39.65	12.63	36.76	126.28	3.38	24.96
45	1.62	430.31	32.21	11.61	29.93	103.33	2.99	21.62
46	1.40	613.27	38.85	14.01	35.16	125.94	2.93	26.13
47	0.88	592.28	37.98	14.02	35.09	122.05	2.89	25.82

RUN	Volume nm^3	VolumeAbs	G as dep	G max	G oxi	G photo/G as dep	G photo/G oxi
1	638.23	2715.60					
2	669.30	2754.80					
3	533.82	2133.10					
4	511.13	2145.70					
5	463.57	2139.60					
6	645.83	2808.60					
7	2257.80	10546.00	1.62E-06	2.02E+00	9.57E-04	1.25E+06	2.11E+03
8	1279.70	5754.20	5.05E-07	1.34E+00	4.04E-04	2.66E+06	3.32E+03
9	592.66	3357.40	5.05E-04	1.21E+01	2.08E-03	2.39E+04	5.81E+03
10	791.51	8994.90	1.25E-02	1.77E+02	1.77E+02	1.41E+04	1.00E+00
11	558.71	3036.00	1.05E-03	7.84E+00	1.07E-01	7.48E+03	7.34E+01
12	5576.80	25210.00	3.26E-04	1.87E+02	6.83E-06	5.74E+05	2.74E+07
13	7309.20	36657.00	9.70E-05	8.12E+01	6.93E-07	8.37E+05	1.17E+08
14	80.77	145.43	7.65E-05	6.42E+00	3.83E-06	8.39E+04	1.68E+06
15	92.50	592.66	1.31E-05	1.20E+00	1.09E-05	9.17E+04	1.09E+05
16	740.84	4144.80	1.83E-04	3.90E+00	1.71E-06	2.14E+04	2.28E+06
17	260.82	1442.80	1.18E-04	3.01E+00	3.01E-05	2.54E+04	1.00E+05
18	462.86	2778.30	8.60E-05	7.41E-01	9.97E-07	8.62E+03	7.44E+05
19	760.93	4704.70	1.06E-07	5.11E+01	6.17E-06	4.80E+08	8.28E+06
20	609.51	3901.60	1.67E-07	2.67E+00	5.01E-06	1.60E+07	5.32E+05
21	796.17	5119.90	1.16E-07	3.47E+00	8.49E-06	3.00E+07	4.09E+05
22	267.99	1214.40	9.52E-07	9.52E-02	5.33E-07	1.00E+05	1.79E+05
23	280.43	1584.20	1.43E-07	8.43E-01	5.57E-07	5.90E+06	1.51E+06
24	223.63	1217.00	7.69E-08	3.33E-01	5.61E-07	4.33E+06	5.94E+05
25	48.05	611.70	6.79E-08	1.27E-01	3.57E-07	1.87E+06	3.56E+05
26	1095.80	5307.60	1.18E-03	1.10E+00	1.48E-05	9.35E+02	7.44E+04
27	3445.40	19692.00	2.62E-06	7.38E+01	1.16E-05	2.82E+07	6.36E+06
28	617.85	2987.20	2.38E-01	2.42E+02	5.62E-01	1.01E+03	4.30E+02
29	1831.50	8702.60	3.15E+00	8.46E+01	1.14E+01	2.68E+01	7.43E+00
30	1482.70	7530.70	3.35E+01	1.43E+02	2.92E+01	4.28E+00	4.89E+00
31	241.85	1323.80	2.22E-07	5.31E-01	1.33E-07	2.39E+06	3.98E+06
32	70.15	549.74	2.11E-07	1.29E+01	1.00E-06	6.09E+07	1.29E+07
33	830.61	4061.10	7.52E-08	5.04E+00	3.83E-06	6.70E+07	1.31E+06
34	2771.10	11351.00	2.45E-06	7.88E+01	3.14E-05	3.22E+07	2.51E+06
35	4977.10	24701.00	1.26E-06	2.07E+01	7.26E-06	1.65E+07	2.86E+06
36	1905.90	11024.00	7.04E-06	2.74E+01	1.48E-05	3.89E+06	1.85E+06
37	264.55	1154.10					
38	226.00	1363.40					
39	262.08	1313.00					
40	222.38	1493.10					
41	2704.40	13521.00					
42	577.95	3540.30					
43	378.26	2786.00					
44	347.48	2302.50	3.39E-09	1.70E-01	4.41E-07	5.00E+07	3.85E+05
45	293.36	1669.90	3.45E-09	1.03E-01	5.17E-07	3.00E+07	2.00E+05
46	397.33	3291.40	9.91E-06	1.11E+00	4.04E-05	1.12E+05	2.75E+04
47	259.74	1573.30	9.73E-06	5.00E+00	5.00E-03	5.14E+05	1.00E+03

Annex 7D Experimental data for ZnO grown by DC magnetron sputtering.

RUN	% O2	pressure (mbar)	timp(sec)	medium temp	thickness (nm)	growth rate nm/sec	Sa	Sq	Ssk	Sku
1	100	8.00E-03	4800	93.5	3700	7.71E-01	6.29	8.32	0.16	4.13
2	100	8.00E-03	8460	99.5	2800	3.31E-01	6.09	7.54	0.24	2.77
3	80	8.00E-03	3900	107	1540	3.95E-01	9.57	11.95	-0.04	3.02
4	100	8.00E-03	1800	25	881	4.89E-01	4.83	6.05	0.23	2.95
5	80	8.00E-03	1620	66	1002	6.19E-01	4.01	5.09	0.02	3.22
6	100	8.00E-03	300	56	106	3.53E-01	2.41	3.02	-0.18	2.97
7	100	8.00E-03	570	41	106	1.86E-01	2.10	2.66	-0.33	3.21
8	73.40	8.00E-03	300	54.5	111	3.70E-01	1.14	1.50	0.77	4.33
9	73.40	8.00E-03	540	45.5	110	2.04E-01	4.38	5.51	-0.41	3.22
10	61.67	8.00E-03	270	47	108.8	4.03E-01	3.11	3.89	-0.14	2.94
11	61.67	8.00E-03	375	43.5	95.5	2.55E-01	2.47	3.10	-0.14	3.04
12	50.85	8.00E-03	190	51	106.8	5.62E-01	0.97	1.23	0.23	4.04
13	50.85	8.00E-03	420	38.5	101.7	2.42E-01	3.10	5.10	3.10	19.15
14	0	8.00E-03	150	49	107.7	7.18E-01	0.92	1.17	0.24	3.17
15	0	8.00E-03	720	36.5	106.1	1.47E-01	1.13	1.41	-0.13	2.93
16	10	8.00E-03	180	51.5	107.6	5.98E-01	3.06	3.95	0.68	3.58
17	10	8.00E-03	80	40	22.7	2.84E-01	2.51	3.04	-0.17	2.43
18	20	8.00E-03	180	47	108.5	6.03E-01	0.86	1.19	0.91	6.81
19	0	8.00E-03	150	48.5	104.5	6.97E-01	3.12	4.02	-0.02	3.24
20	10	8.00E-03	270	48	105.9	3.92E-01	3.50	4.56	0.53	4.35
21	50.85	8.00E-03	240	44.5	104.5	4.35E-01	2.37	3.00	-0.34	3.14
22	50.85	8.00E-03	390	42.5	105.6	2.71E-01	2.24	2.82	-0.35	3.18
23	100	8.00E-03	680	40.5	102	1.50E-01	1.52	1.90	0.04	2.91
24	100	8.00E-03	150	36.5	22.4	1.49E-01	1.13	2.11	1.97	17.97
25	100	8.00E-03	340	35.5	51.8	1.52E-01	1.94	2.82	1.69	8.63
26	100	8.00E-03	960	45.5	152.7	1.59E-01	8.34	11.01	0.38	3.53
27	100	8.00E-03	1260	48	202	1.60E-01	4.08	6.23	0.56	7.45
28	100	8.00E-03	1690	36	301.7	1.79E-01	1.10	1.40	0.27	3.22
29	100	8.00E-03	3070	55.5	502.5	1.64E-01	4.88	6.28	0.60	3.58
30	100	1.50E-02	670	44.5	102.6	1.53E-01	4.60	5.78	-0.26	3.08
31	100	3.00E-02	870	43	102.2	1.17E-01	3.83	4.79	-0.09	2.92
32	100	5.00E-02	1220	44	102.2	8.38E-02	4.97	6.46	0.12	4.05
33	100	8.00E-03	4800	115	4960	1.03E+00	14.40	17.98	0.12	2.82
34	100	8.00E-03	4800	93	2498	5.20E-01	7.96	9.81	0.12	2.59
35	100	8.00E-03	300	48.5	95.3	3.18E-01	0.68	0.86	0.52	3.33
36	90	8.00E-03	300	109.5	101.7	3.39E-01	0.56	0.71	0.54	3.47
37	80	8.00E-03	240	40	102.9	4.29E-01	0.23	0.30	0.11	3.42
38	70	8.00E-03	240	40	100.3	4.18E-01	1.20	1.55	0.39	5.33
39	100	1.00E-02	360	56	106.7	2.96E-01	1.10	1.56	1.14	9.41
40	100	1.00E-02	700	61	208	2.97E-01	1.01	1.29	0.23	3.59
41	100	1.00E-02	990	62.5	311.4	3.15E-01	0.91	1.17	0.39	3.90
42	100	1.00E-02	1620	70.5	504	3.11E-01	1.42	1.82	0.37	3.48
43	100	1.00E-02	3180	81.5	1012	3.18E-01	3.48	4.51	0.72	4.41
44	100	1.00E-02	360	71	101.9	2.83E-01	0.43	0.55	0.27	6.02
45	100	1.00E-02	500	57	155.5	3.11E-01	1.27	1.60	0.37	4.23
46	100	1.00E-02	780	65.5	256.1	3.28E-01	1.48	1.86	-0.05	2.98
47	100	1.00E-02	340	119	108.2	3.18E-01	0.53	0.67	0.09	3.66
48	100	1.00E-02	620	132	206.7	3.33E-01	0.96	1.26	0.79	4.46
49	100	1.00E-02	360	202.5	106.6	2.96E-01	0.82	1.42	11.26	306.32

RUN	Sy	St	Sz	S10z	Sz_tph	Sds	Ssc	Sv	Sp	Smean	Sdq	Sdq6	Sdr	S2A
1	67.08	67.08	67.08	61.59	61.59	2641	0.15	31.81	35.27	-7.75E-09	0.36	0.35	6.22	1.00E+06
2	46.83	46.83	46.83	44.80	44.80	6216	0.34	22.65	24.18	1.26E-07	0.41	0.35	8.12	1.00E+06
3	87.11	87.11	87.11	83.60	83.60	2339	0.25	46.82	40.29	6.55E-09	0.60	0.57	16.65	1.00E+06
4	43.83	43.83	43.83	40.00	40.00	2722	0.14	22.14	21.69	-3.37E-08	0.35	0.33	5.81	1.00E+06
5	40.85	40.85	40.85	38.06	38.06	1909	0.10	21.05	19.80	-2.45E-08	0.31	0.30	4.78	1.00E+06
6	22.88	22.88	22.88	22.17	22.17	2513	0.24	12.54	10.34	3.49E-08	0.41	0.40	8.22	1.00E+06
7	21.05	21.05	21.05	18.68	18.68	3116	0.09	12.12	8.93	3.55E-08	0.22	0.21	2.32	1.00E+06
8	13.52	13.52	13.52	13.00	13.00	7929	0.15	5.90	7.61	9.39E-09	0.24	0.22	2.89	1.00E+06
9	45.67	45.67	45.67	41.97	41.97	1289	0.14	26.03	19.64	-4.18E-08	0.82	0.82	29.39	1.00E+06
10	28.32	28.32	28.32	27.44	27.44	1416	0.19	14.99	13.33	3.28E-08	0.56	0.55	14.66	1.00E+06
11	24.50	24.50	24.50	23.35	23.35	1280	0.16	13.14	11.36	-1.24E-08	0.48	0.48	10.88	1.00E+06
12	12.92	12.92	12.92	12.37	12.37	5217	0.16	4.83	8.09	1.12E-08	0.28	0.26	3.79	1.00E+06
13	51.86	51.86	51.86	49.76	49.76	2128	0.20	14.89	36.97	3.78E-10	0.46	0.43	7.24	1.00E+06
14	9.63	9.63	9.63	9.10	9.10	5306	0.11	4.42	5.22	-3.98E-09	0.23	0.22	2.64	1.00E+06
15	11.06	11.06	11.06	10.22	10.22	5216	0.11	5.91	5.15	-2.23E-08	0.21	0.20	2.23	1.00E+06
16	28.04	28.04	28.04	27.15	27.15	3338	0.10	11.60	16.44	-9.98E-09	0.29	0.28	4.01	1.00E+06
17	17.68	17.68	17.68	17.15	17.15	5960	0.11	9.62	8.06	-2.97E-09	0.20	0.18	1.97	1.00E+06
18	12.63	12.63	12.63	11.95	11.95	8098	0.09	4.71	7.92	3.53E-09	0.17	0.15	1.39	1.00E+06
19	28.65	28.65	28.65	27.25	27.25	4151	0.10	13.87	14.79	-4.17E-08	0.25	0.24	3.11	1.00E+06
20	39.49	39.49	39.49	36.47	36.47	3387	0.11	16.05	23.43	-3.51E-08	0.33	0.32	5.21	1.00E+06
21	23.07	23.07	23.07	20.79	20.79	1965	0.10	13.35	9.72	2.01E-08	0.35	0.35	6.00	1.00E+06
22	23.72	23.72	23.72	20.69	20.69	1744	0.10	14.84	8.88	1.95E-08	0.32	0.32	5.11	1.00E+06
23	15.63	15.63	15.63	14.32	14.32	825	0.03	7.57	8.05	7.91E-09	0.16	0.16	1.31	4.00E+06
24	28.44	28.44	28.44	27.35	27.35	10513	0.11	11.13	17.31	-2.26E-09	0.19	0.17	1.67	1.00E+06
25	32.08	32.08	32.08	30.93	30.93	1087	0.05	10.74	21.35	5.27E-09	0.23	0.23	2.64	4.00E+06
26	101.17	101.17	101.17	63.83	63.83	385	0.03	60.88	40.30	-2.54E-08	0.25	0.25	3.16	4.00E+06
27	76.41	76.41	76.41	54.44	54.44	996.75	0.04	44.35	32.06	3.40E-08	0.19	0.18	1.78	4.00E+06
28	11.45	11.45	11.45	11.04	11.04	1062.5	0.03	5.47	5.98	1.21E-08	0.18	0.18	1.54	4.00E+06
29	53.60	53.60	53.60	43.58	43.58	463.75	0.03	28.00	25.60	-3.25E-08	0.22	0.22	2.42	4.00E+06
30	42.76	42.76	42.76	38.11	38.11	638.25	0.04	21.96	20.79	-4.58E-08	0.23	0.23	2.70	4.00E+06
31	35.86	35.86	35.86	33.60	33.60	3782	0.24	21.00	14.86	-8.36E-09	0.49	0.46	11.02	1.00E+06
32	56.31	56.31	56.31	55.73	55.73	4276	0.21	28.56	27.75	-1.64E-08	0.45	0.42	9.33	1.00E+06
33	123.63	123.63	123.63	110.81	110.81	2707	0.28	59.36	64.28	3.09E-07	0.65	0.55	18.71	4.00E+06
34	60.16	60.16	60.16	57.47	57.47	1051	0.09	29.99	30.17	2.61E-08	0.29	0.25	3.99	4.00E+06
35	7.85	7.85	7.85	7.12	7.12	2080	0.03	3.24	4.61	5.69E-09	0.12	0.12	0.75	4.00E+06
36	5.72	5.72	5.72	5.57	5.57	1653.8	0.02	2.51	3.21	-1.15E-09	0.10	0.09	0.45	4.00E+06
37	2.87	2.87	2.87	2.44	2.44	19134	0.06	1.45	1.42	-5.02E-09	0.07	0.06	0.25	1.00E+06
38	19.40	19.40	19.40	18.40	18.40	5089	0.15	7.44	11.96	1.58E-08	0.35	0.32	5.41	1.00E+06
39	19.74	19.74	19.74	19.29	19.29	1127.8	0.03	8.04	11.70	7.30E-09	0.12	0.12	0.74	4.00E+06
40	12.55	12.55	12.55	11.55	11.55	1355.5	0.03	5.70	6.86	5.72E-09	0.14	0.14	1.01	4.00E+06
41	10.34	10.34	10.34	9.63	9.63	9556	0.10	3.96	6.38	9.44E-09	0.16	0.14	1.19	1.00E+06
42	16.95	16.95	16.95	15.17	15.17	1444.3	0.04	8.41	8.54	-1.29E-08	0.17	0.14	1.33	4.00E+06
43	41.40	41.40	41.40	36.42	36.42	599.5	0.04	16.77	24.63	-3.29E-08	0.21	0.20	2.15	4.00E+06
44	9.46	9.46	9.46	8.35	8.35	2544.3	0.02	2.79	6.67	1.75E-09	0.08	0.07	0.28	4.00E+06
45	18.28	18.28	18.28	14.81	14.81	871.5	0.02	6.04	12.24	6.82E-09	0.11	0.11	0.63	4.00E+06
46	13.69	13.69	13.69	13.17	13.17	979	0.03	6.91	6.77	2.54E-09	0.12	0.12	0.74	4.00E+06
47	11.51	11.51	11.51	8.43	8.43	5681	0.07	8.85	2.65	2.83E-09	0.13	0.12	0.75	1.00E+06
48	10.89	10.89	10.89	10.54	10.54	7577	0.09	4.14	6.75	1.16E-08	0.18	0.16	1.50	1.00E+06
49	56.85	56.85	56.85	29.94	29.94	488.44	0.01	9.67	47.18	-9.65E-09	0.11	0.10	0.59	2.50E+07

RUN	S3A	Sbi	Sci	Svi	Spk	Sk	Svk	Std	Stdi	Srw	Srwi	Shw	Sfd	Scl20	Str20	Scl37	Str37
1	1.06E+06	0.60	1.58	0.12	12.47	18.07	8.97	178.56	0.55	465.02	0.07	41.67	2.92	86.11	0.28	68.49	0.51
2	1.08E+06	0.56	1.72	0.10	8.52	19.34	5.43	178.36	0.66	426.88	0.08	47.62	2.84	70.45	0.68	56.75	0.78
3	1.17E+06	0.62	1.53	0.11	11.60	31.21	10.68	1.48	0.58	175.90	0.10	45.46	2.93	52.84	0.71	43.05	0.76
4	1.06E+06	0.56	1.71	0.10	6.78	14.93	4.68	0.00	0.54	447.53	0.09	45.46	2.92	54.79	0.65	43.05	0.79
5	1.05E+06	0.60	1.57	0.12	5.59	12.59	5.01	0.00	0.41	279.09	0.10	43.48	2.95	48.92	0.60	39.14	0.67
6	1.08E+06	0.63	1.50	0.12	2.65	7.74	3.03	0.00	0.73	141.68	0.17	28.57	2.79	21.53	0.79	17.61	0.82
7	1.02E+06	0.65	1.43	0.13	2.37	6.65	3.02	0.00	0.62	165.48	0.13	38.46	2.86	39.14	0.91	29.35	0.88
8	1.03E+06	0.53	1.86	0.09	2.57	3.23	1.09	108.40	0.82	120.58	0.19	26.32	2.70	21.53	0.73	15.66	0.67
9	1.29E+06	0.66	1.40	0.14	4.38	13.90	6.49	80.25	0.85	122.61	0.21	27.78	2.86	17.61	0.75	15.66	0.89
10	1.15E+06	0.62	1.51	0.12	3.57	9.97	3.85	79.58	0.85	97.32	0.20	29.41	2.83	17.61	0.69	13.70	0.70
11	1.11E+06	0.63	1.50	0.12	3.03	7.87	3.14	101.24	0.76	141.37	0.20	27.78	2.83	15.66	0.53	11.74	0.50
12	1.04E+06	0.64	1.51	0.11	1.61	3.11	1.11	97.71	0.81	163.01	0.25	21.74	2.69	17.61	0.82	13.70	0.78
13	1.07E+06	0.74	1.40	0.07	12.37	7.49	3.13	93.04	0.75	352.35	0.10	37.04	2.85	54.79	0.74	41.10	0.72
14	1.03E+06	0.57	1.69	0.10	1.45	2.88	0.97	85.19	0.81	145.13	0.24	23.26	2.70	15.66	0.73	11.74	0.67
15	1.02E+06	0.62	1.53	0.12	1.31	3.63	1.40	178.41	0.90	137.77	0.20	26.32	2.78	23.48	0.86	17.61	0.82
16	1.04E+06	0.51	1.91	0.09	6.32	8.95	2.33	0.00	0.75	238.86	0.11	38.46	2.89	41.10	0.70	31.31	0.70
17	1.02E+06	0.64	1.48	0.11	1.84	8.80	2.37	1.34	0.70	169.91	0.10	41.67	2.84	45.01	0.85	37.18	0.90
18	1.01E+06	0.61	1.59	0.11	2.17	2.41	1.14	85.15	0.77	171.99	0.16	29.41	2.76	27.40	0.61	21.53	0.65
19	1.03E+06	0.59	1.61	0.12	4.95	9.03	4.27	0.00	0.45	307.55	0.09	38.46	2.89	52.84	0.73	43.05	0.79
20	1.05E+06	0.62	1.57	0.10	7.27	10.76	3.61	178.26	0.70	192.98	0.11	38.46	2.90	43.05	0.73	35.23	0.86
21	1.06E+06	0.65	1.44	0.13	2.55	7.34	3.53	178.29	0.83	165.11	0.17	31.25	2.84	23.48	0.63	17.61	0.64
22	1.05E+06	0.66	1.42	0.13	2.32	7.15	3.18	66.62	0.82	198.06	0.16	32.26	2.85	23.48	0.67	17.61	0.64
23	4.05E+06	0.60	1.59	0.11	1.99	4.94	1.64	80.87	0.78	292.29	0.22	52.63	2.81	35.23	0.75	27.40	0.70
24	1.02E+06	0.83	1.19	0.13	4.68	2.02	3.07	0.00	0.57	253.86	0.11	34.48	2.80	56.75	0.85	43.05	0.85
25	4.11E+06	0.51	1.96	0.08	6.56	4.84	2.04	104.44	0.77	298.03	0.20	50.00	2.79	39.14	0.59	31.31	0.62
26	4.13E+06	0.53	1.83	0.11	16.51	20.89	10.52	178.34	0.53	618.74	0.09	86.96	2.98	117.42	0.48	97.85	0.64
27	4.07E+06	0.57	1.69	0.14	12.73	8.57	8.46	0.00	0.38	550.98	0.10	74.07	2.88	148.73	0.90	117.42	0.94
28	4.06E+06	0.57	1.71	0.10	1.77	3.42	1.16	64.68	0.79	341.32	0.29	40.82	2.73	23.48	0.67	19.57	0.71
29	4.10E+06	0.52	1.86	0.09	9.59	13.72	4.62	0.00	0.64	485.66	0.11	80.00	2.95	86.11	0.59	70.45	0.78
30	4.11E+06	0.64	1.47	0.13	5.37	14.49	6.27	0.46	0.68	797.02	0.10	68.97	2.95	148.73	0.52	101.76	0.70
31	1.11E+06	0.61	1.56	0.12	4.51	12.33	4.54	1.60	0.79	341.34	0.15	34.48	2.84	35.23	0.86	27.40	0.88
32	1.09E+06	0.62	1.54	0.12	8.50	15.13	6.31	0.00	0.66	196.54	0.11	38.46	2.86	48.92	0.81	39.14	0.83
33	4.75E+06	0.58	1.64	0.11	18.60	45.30	15.55	0.65	0.57	712.91	0.10	74.07	2.78	117.42	0.58	93.93	0.67
34	4.16E+06	0.58	1.65	0.10	9.27	25.58	7.10	0.00	0.50	791.10	0.09	86.96	2.93	129.16	0.52	97.85	0.61
35	4.03E+06	0.55	1.77	0.09	1.18	2.11	0.55	93.58	0.78	196.07	0.31	37.74	2.64	23.48	0.67	19.57	0.71
36	4.02E+06	0.53	1.83	0.09	1.04	1.65	0.51	93.78	0.83	180.07	0.32	39.22	2.67	23.48	0.86	19.57	0.83
37	1.00E+06	0.59	1.63	0.11	0.38	0.73	0.29	80.18	0.82	199.94	0.16	20.00	2.58	31.31	0.57	23.48	0.55
38	1.05E+06	0.63	1.55	0.11	2.07	3.80	1.34	99.74	0.71	126.91	0.24	22.22	2.72	13.70	0.54	11.74	0.60
39	4.03E+06	0.64	1.55	0.10	2.76	3.05	1.52	74.27	0.80	532.72	0.16	52.63	2.85	66.54	0.55	43.05	0.73
40	4.04E+06	0.61	1.59	0.11	1.71	3.16	1.16	78.80	0.86	289.91	0.29	45.46	2.76	27.40	0.78	19.57	0.71
41	1.01E+06	0.61	1.57	0.11	1.73	2.82	0.98	0.00	0.50	246.51	0.15	27.78	2.73	37.18	0.49	27.40	0.78
42	4.05E+06	0.56	1.72	0.10	2.56	4.32	1.54	88.30	0.73	287.99	0.17	58.82	2.79	58.71	0.83	43.05	0.79
43	4.09E+06	0.56	1.76	0.09	6.96	10.31	3.01	178.58	0.81	603.70	0.13	71.43	2.87	70.45	0.86	54.79	0.82
44	4.01E+06	0.66	1.45	0.12	0.86	1.36	0.55	76.59	0.81	465.17	0.27	38.46	2.60	23.48	0.55	19.57	0.56
45	4.03E+06	0.62	1.57	0.10	2.09	4.13	1.23	0.00	0.85	625.41	0.19	60.61	2.84	43.05	0.92	35.23	0.90
46	4.03E+06	0.61	1.54	0.12	1.88	4.64	1.82	73.81	0.85	211.11	0.17	62.50	2.85	43.05	0.79	35.23	0.75
47	1.01E+06	0.59	1.64	0.12	0.76	1.69	0.70	81.38	0.77	148.64	0.22	25.00	2.72	17.61	0.69	13.70	0.64
48	1.02E+06	0.55	1.78	0.09	2.10	2.88	0.86	0.00	0.76	115.02	0.17	31.25	2.78	25.44	0.76	19.57	0.71
49	2.51E+07	0.95	1.07	0.10	3.58	2.42	1.25	104.00	0.84	753.04	0.31	74.63	2.54	68.49	0.54	39.14	0.50

RUN	Sdc0_5	Sdc5_10	Sdc10_50	Sdc50_95	Area nm^2	Length nm	Width nm	Size nm	Perim nm	Aspect
1	21.51	4.30	9.41	13.44	1624.50	50.84	16.56	46.69	161.05	2.90
2	10.70	3.28	10.79	11.26	4605.10	82.65	29.62	77.71	286.45	3.19
3	21.12	4.02	15.01	19.55	6876.10	128.36	44.35	119.91	403.67	3.56
4	10.98	2.55	8.70	8.70	2173.00	71.92	24.47	66.48	230.81	3.21
5	11.38	1.96	6.47	8.43	2053.00	69.79	24.37	64.16	220.80	3.24
6	5.55	0.96	3.76	5.18	1356.60	57.71	21.48	53.96	184.24	2.88
7	4.85	0.84	3.12	4.72	1752.00	66.08	22.50	61.75	213.78	3.31
8	4.77	0.92	2.11	1.92	656.58	39.08	13.54	36.28	131.50	3.06
9	11.35	1.56	6.41	10.07	1236.40	54.85	21.12	51.50	175.63	2.81
10	7.09	1.36	4.82	6.64	1071.40	51.02	19.54	47.48	164.07	2.79
11	6.43	1.08	3.78	5.30	1029.70	54.25	17.46	51.61	163.92	3.26
12	6.16	0.44	1.50	1.97	530.89	36.79	12.46	34.20	117.15	3.17
13	30.04	3.12	4.47	5.09	2884.80	83.43	30.20	78.21	272.35	2.97
14	3.17	0.52	1.60	1.76	660.04	41.22	14.40	38.49	135.20	3.01
15	2.88	0.49	1.77	2.39	951.58	48.34	17.55	44.80	156.83	2.94
16	8.71	2.42	5.84	5.11	1467.70	56.47	19.63	52.49	183.53	3.26
17	3.29	0.89	3.79	5.21	9295.50	141.35	52.59	133.27	480.61	3.05
18	5.97	0.63	1.39	1.70	1606.30	63.12	22.11	58.60	213.21	3.03
19	7.98	1.84	4.88	7.00	1678.80	67.95	19.39	63.95	213.14	3.89
20	16.06	2.14	5.46	6.81	1957.00	71.09	21.13	66.46	223.01	3.81
21	5.09	0.97	3.51	5.46	1745.90	66.39	23.56	59.96	207.17	3.08
22	4.61	0.86	3.28	4.99	1926.90	70.27	25.50	64.48	222.30	2.95
23	4.89	0.69	2.51	3.07	3455.80	94.43	33.14	87.64	299.96	3.01
24	14.76	1.25	1.42	2.56	765.76	41.88	14.16	39.06	139.32	3.17
25	15.82	2.57	3.41	3.02	1786.30	65.04	23.59	60.62	206.21	2.84
26	19.47	5.68	16.22	16.22	6550.90	116.15	40.55	107.30	370.60	3.00
27	21.13	4.75	6.58	9.19	3601.50	92.75	30.68	86.66	294.00	3.17
28	3.51	0.64	1.93	2.07	1533.90	61.81	22.59	55.41	198.70	2.82
29	13.64	3.33	9.56	8.06	5181.50	106.79	37.49	98.80	345.11	3.04
30	11.74	1.97	6.85	10.20	2129.20	74.43	23.18	68.73	228.73	3.51
31	6.97	1.80	6.11	7.98	3127.50	85.52	33.30	80.77	282.70	2.82
32	17.38	2.71	7.79	10.27	5426.60	111.31	42.10	104.15	367.27	2.98
33	33.45	6.69	25.02	28.24	16802.00	197.27	61.99	186.62	671.91	3.55
34	13.26	3.50	13.99	15.19	11312.00	164.28	55.11	151.08	539.23	3.19
35	3.05	0.39	1.27	1.15	1237.90	55.86	18.98	51.77	178.11	3.08
36	1.88	0.38	1.03	0.96	1306.30	55.72	20.64	51.09	178.64	2.86
37	0.91	0.13	0.39	0.45	183.77	20.64	7.26	18.76	70.82	2.89
38	9.49	0.58	1.94	2.37	531.17	37.89	12.20	35.52	116.34	3.24
39	9.26	0.75	1.90	1.82	1812.90	65.67	24.00	60.52	210.33	2.88
40	4.73	0.53	1.64	2.01	1365.90	57.98	20.17	53.31	181.73	3.10
41	4.47	0.50	1.45	1.80	248.62	24.11	7.71	22.14	75.63	3.20
42	5.30	0.92	2.48	2.65	8436.30	144.72	48.71	136.39	478.88	3.28
43	16.51	2.32	6.31	5.97	6235.50	125.07	42.06	116.86	396.30	3.19
44	5.84	0.19	0.64	0.91	1619.20	62.13	21.56	57.18	205.10	3.03
45	9.63	0.59	2.09	2.49	3538.00	96.02	32.02	89.68	301.72	3.41
46	3.73	0.69	2.36	3.15	6112.10	127.21	42.77	120.00	409.49	3.21
47	1.52	0.28	0.90	1.01	338.02	28.42	9.27	26.15	88.59	3.26
48	4.48	0.70	1.72	1.64	2061.40	71.47	24.94	67.42	237.73	3.05
49	45.69	0.34	1.25	1.71	1620.80	61.47	23.27	54.95	189.37	2.71

RUN	Diam nm	Volume nm^3	VolumeAbs nm^3	G as dep	G max	G oxi	photo ratio	sensing ratio
1	32.27	6.23E+03	5.17E+04	9.13E-08	2.19E-03	8.06E-08	2.40E+04	2.71E+04
2	55.08	2.67E+04	1.04E+05	3.13E-10	3.13E-03	9.38E-11	1.00E+07	3.33E+07
3	83.69	6.72E+04	3.22E+05	1.25E-09	2.81E-03	3.13E-10	2.25E+06	9.00E+06
4	46.70	7.23E+03	4.81E+04					
5	45.91	5.95E+03	4.32E+04					
6	39.37	3.52E+03	1.70E+04	6.60E-07	4.62E-01	6.42E-07	7.00E+05	7.21E+05
7	43.00	3.01E+03	2.12E+04	8.49E-07	2.22E-01	3.68E-06	2.61E+05	6.03E+04
8	25.71	6.17E+02	3.88E+03	1.44E-06	1.26E-01	2.97E-06	8.75E+04	4.24E+04
9	38.07	6.35E+03	3.22E+04	9.01E-08	2.34E-01	1.17E-07	2.60E+06	2.00E+06
10	35.35	3.62E+03	1.61E+04	9.26E-08	1.85E-01	2.31E-06	2.00E+06	8.00E+04
11	34.39	2.73E+03	1.35E+04	1.05E-06	8.90E-02	9.42E-06	8.50E+04	9.44E+03
12	23.90	4.62E+02	2.56E+03	1.47E-03	7.96E-01	1.69E-01	5.41E+02	4.72E+00
13	56.15	8.46E+03	8.93E+03	1.18E-06	6.39E-01	1.06E-05	5.42E+05	6.02E+04
14	27.21	5.48E+02	2.92E+03	5.20E-01	1.06E+01	1.85E+00	2.03E+01	5.70E+00
15	32.58	1.02E+03	5.62E+03	3.30E+01	2.26E+02	1.59E+02	6.86E+00	1.42E+00
16	37.08	3.68E+03	1.70E+04	5.74E-06	5.74E-01	1.06E-02	1.00E+05	5.39E+01
17	96.11	2.92E+04	8.94E+04	1.09E-07	1.52E+01	2.61E-03	1.40E+08	5.83E+03
18	41.76	1.31E+03	7.57E+03	1.17E-01	9.26E+00	3.61E+00	7.94E+01	2.56E+00
19	40.12	3.38E+03	2.33E+04	1.20E-01	1.55E+01	1.55E+01	1.29E+02	1.00E+00
20	42.81	5.19E+03	3.14E+04	1.19E-01	1.60E+01	7.26E+00	1.35E+02	2.21E+00
21	44.20	4.70E+03	2.33E+04	4.78E-08	1.44E-01	1.53E-06	3.00E+06	9.38E+04
22	47.36	4.91E+03	2.86E+04	9.47E-09	1.14E-01	3.79E-07	1.20E+07	3.00E+05
23	62.57	5.21E+03	2.62E+04					
24	27.22	6.91E+02	8.52E+03					
25	43.91	3.27E+03	1.92E+04					
26	76.44	3.89E+04	3.99E+05					
27	59.47	8.70E+03	1.60E+05					
28	41.91	1.61E+03	8.39E+03					
29	70.68	1.94E+04	1.45E+05					
30	46.21	4.59E+03	4.68E+04					
31	59.62	1.34E+04	6.57E+04					
32	76.33	3.14E+04	1.55E+05					
33	123.11	2.08E+05	9.97E+05	3.89E-06	3.41E-02	3.29E-04	8.76E+03	1.03E+02
34	106.21	6.36E+04	3.39E+05	1.76E-07	2.70E-02	2.61E-07	1.53E+05	1.04E+05
35	36.40	7.34E+02	4.01E+03					
36	37.96	6.55E+02	3.28E+03					
37	13.72	1.96E+01	2.66E+02					
38	24.02	5.75E+02	3.95E+03					
39	44.43	1.56E+03	1.46E+04	9.37E-10	1.69E-02	9.37E-10	1.80E+07	1.80E+07
40	38.20	1.18E+03	7.78E+03	4.81E-10	6.06E-03	4.81E-10	1.26E+07	1.26E+07
41	15.19	1.18E+02	9.85E+02	3.21E-10	4.78E-03	3.21E-10	1.49E+07	1.49E+07
42	93.66	1.12E+04	7.09E+04	1.98E-10	5.69E-03	1.98E-10	2.87E+07	2.87E+07
43	80.94	1.78E+04	1.05E+05	1.19E-09	2.45E-02	9.88E-11	2.07E+07	2.48E+08
44	40.95	6.12E+02	4.52E+03	1.81E-10	1.05E-02	1.81E-10	5.79E+07	5.79E+07
45	61.63	4.05E+03	2.14E+04	6.43E-11	1.67E-03	6.43E-11	2.59E+07	2.59E+07
46	82.41	8.99E+03	4.23E+04	3.90E-11	2.96E-03	3.90E-11	7.57E+07	7.57E+07
47	18.12	1.34E+02	2.99E+03					
48	47.20	2.05E+03	8.54E+03					
49	42.44	1.01E+03	1.57E+04					

Annex 7E Experimental data for ZnO grown by PLD.

run	dts	ts	ss	fluence	puls no.	Sa	Sq	Ssk	Sku	Sy	St	Sz	S10z	Sz_tph
1	47	360	8	21	5.4E+03	34.85	44.69	0.03	3.38	366.91	366.91	366.91	348.89	348.89
2	47	360	8	22	5.4E+03	91.05	113.69	-0.23	2.94	823.77	823.77	823.77	783.36	783.36
3	47	360	8	23	5.4E+03	78.92	100.41	0.29	3.08	701.90	701.90	701.90	654.00	654.00
4	48	360	8	24	6.0E+03	88.85	111.38	-0.33	3.03	840.63	840.63	840.63	760.28	760.28
5	48	360	8	24	6.0E+03	56.96	70.13	-0.11	2.67	454.95	454.95	454.95	443.84	443.84
6	48	360	8	24	6.0E+03	40.77	52.08	-0.43	3.57	441.61	441.61	441.61	406.29	406.29
7	48	350	8	24	1.0E+03	10.15	14.03	1.59	8.64	171.53	171.53	171.53	151.57	151.57
8	48	350	6	31	5.0E+02	1.33	1.67	0.62	3.45	12.43	12.43	12.43	12.04	12.04
9	48	350	6	31	5.0E+02	2.01	2.53	-0.03	3.13	23.13	23.13	23.13	19.36	19.36
10	48	350	8	24	7.5E+02	3.43	4.45	0.53	4.71	50.41	50.41	50.41	35.28	35.28
11	48	350	8	24	7.5E+02	2.57	3.27	0.17	3.27	30.07	30.07	30.07	26.99	26.99
12	48	350	10	19	4.0E+02	4.58	5.79	0.32	3.27	47.11	47.11	47.11	43.29	43.29
13	48	350	10	19	4.0E+02	2.34	2.97	0.33	3.35	24.57	24.57	24.57	22.16	22.16
14	48	350	7	23	2.0E+03	7.89	9.91	0.07	3.00	72.86	72.86	72.86	70.72	70.72
15	48	350	7	23	2.0E+02	1.72	3.07	1.44	21.64	61.97	61.97	61.97	50.41	50.41
16	48	350	8	24	5.0E+01	0.26	0.33	0.14	3.25	3.27	3.27	3.27	3.08	3.08
17	48	23	8	24	2.0E+02	1.24	1.62	0.55	4.72	17.60	17.60	17.60	15.91	15.91
18	48	150	8	24	2.0E+02	2.32	2.92	0.54	3.38	24.42	24.42	24.42	23.16	23.16
19	48	23	8	24	5.0E+02	1.25	1.59	0.46	3.48	13.27	13.27	13.27	12.86	12.86
20	48	450	8	24	2.0E+02	1.51	1.90	0.26	3.05	14.68	14.68	14.68	13.61	13.61
21	48	550	8	24	4.0E+02	3.24	4.14	-0.03	3.36	31.13	31.13	31.13	30.04	30.04
22	48	550	8	24	2.0E+02	2.25	3.24	1.76	16.79	48.80	48.80	48.80	46.90	46.90
23	48	650	8	24	2.0E+02	2.49	3.18	0.35	3.43	28.49	28.49	28.49	26.82	26.82
24	48	350	8	24	1.0E+03	3.26	4.07	0.06	2.92	31.20	31.20	31.20	28.91	28.91
25	48	350	6	31	5.0E+02	2.39	3.02	0.23	3.21	24.64	24.64	24.64	24.13	24.13
26	48	450	10	19	5.0E+02	2.87	3.60	0.13	3.09	30.71	30.71	30.71	27.79	27.79
27	48	450	10	19	5.0E+02	3.86	4.88	0.32	3.16	37.54	37.54	37.54	36.33	36.33
28	48	110	10	21	5.0E+02	2.54	3.17	0.18	2.90	22.51	22.51	22.51	21.97	21.97
29	48	100	10	21	5.0E+02	1.88	2.40	0.14	3.45	23.51	23.51	23.51	18.85	18.85
30	48	21	8	24	5.0E+02	1.62	2.05	-0.14	3.14	16.25	16.25	16.25	15.01	15.01
31	48	21	8	24	5.0E+02	2.71	3.41	-0.10	3.10	27.24	27.24	27.24	25.17	25.17
32	48	150	8	24	5.0E+02	1.49	1.86	0.29	3.04	13.81	13.81	13.81	13.24	13.24
33	48	150	8	24	5.0E+02	1.92	2.39	0.00	2.84	17.76	17.76	17.76	16.48	16.48
34	48	250	8	24	5.0E+02	1.89	2.37	0.35	3.05	19.50	19.50	19.50	17.83	17.83
35	48	250	8	24	5.0E+02	2.95	3.72	0.27	3.09	28.32	28.32	28.32	27.25	27.25
36	48	450	8	24	5.0E+02	2.82	3.56	0.26	3.30	27.30	27.30	27.30	26.08	26.08
37	48	450	8	24	5.0E+02	2.33	2.90	0.11	2.92	21.96	21.96	21.96	20.51	20.51
38	48	550	8	24	5.0E+02	1.82	2.32	0.28	3.44	21.00	21.00	21.00	20.37	20.37
39	48	550	8	24	5.0E+02	3.01	3.73	-0.01	2.82	27.68	27.68	27.68	26.07	26.07
40	48	650	8	24	5.0E+02	3.94	5.28	-0.64	30.24	229.53	229.53	229.53	146.42	146.42
41	48	350	8	24	1.0E+03	3.30	4.19	0.07	2.94	30.31	30.31	30.31	27.11	27.11
42	48	350	8	24	5.0E+02	4.71	5.83	-0.02	2.73	42.46	42.46	42.46	40.36	40.36
43	48	350	8	24	5.0E+02	2.71	3.39	0.16	2.94	25.42	25.42	25.42	24.70	24.70
44	51	350	8	22.5	1.0E+03	4.24	5.40	0.19	3.54	56.89	56.89	56.89	51.92	51.92
45	51	350	8	22.5	1.0E+03	3.27	4.08	0.01	2.92	31.83	31.83	31.83	28.86	28.86

run	Sds	Ssc	Sv	Sp	Smean	Sdq	Sdq6	Sdr	S2A	S3A	Sbi	Sci	Svi	Spk
1	131.36	0.10	203.89	163.02	-4.19E-08	0.71	0.68	22.08	2.5E+07	3.05E+07	0.59	1.61	0.12	51.83
2	56.57	0.06	446.20	377.57	-1.54E-06	0.99	0.93	41.51	1.0E+08	1.42E+08	0.63	1.48	0.13	96.46
3	60.16	0.06	333.30	368.61	-1.11E-06	0.91	0.86	36.41	1.0E+08	1.36E+08	0.54	1.77	0.10	129.85
4	10.99	0.02	484.99	355.64	-1.47E-06	1.06	1.05	47.24	1.0E+08	1.47E+08	0.66	1.42	0.13	92.71
5	11.88	0.02	248.05	206.90	2.59E-07	0.86	0.86	32.65	1.0E+08	1.33E+08	0.63	1.52	0.11	56.99
6	20.36	0.01	278.62	162.98	-2.24E-07	0.67	0.67	20.75	1.0E+08	1.21E+08	0.65	1.43	0.14	45.77
7	79.81	0.01	49.77	121.76	-9.97E-08	0.29	0.28	3.97	1.0E+08	1.04E+08	0.55	1.82	0.07	28.58
8	1324.50	0.03	4.65	7.79	3.31E-10	0.13	0.12	0.81	4.0E+06	4.03E+06	0.55	1.79	0.08	2.37
9	4484.00	0.15	12.11	11.02	-4.24E-09	0.36	0.34	6.12	1.0E+06	1.06E+06	0.62	1.55	0.12	2.77
10	1141.00	0.08	17.59	32.81	-7.05E-08	0.35	0.34	5.93	4.0E+06	4.24E+06	0.59	1.65	0.10	6.75
11	6712.00	0.17	15.90	14.18	5.75E-09	0.38	0.36	6.89	1.0E+06	1.07E+06	0.58	1.67	0.11	4.01
12	923.50	0.10	18.69	28.42	4.56E-08	0.48	0.47	10.92	4.0E+06	4.44E+06	0.58	1.67	0.10	7.48
13	7565.00	0.28	11.96	12.62	-8.82E-09	0.37	0.33	6.51	1.0E+06	1.07E+06	0.58	1.67	0.10	3.80
14	360.75	0.06	36.63	36.24	2.76E-08	0.61	0.60	17.00	4.0E+06	4.68E+06	0.60	1.59	0.11	10.59
15	2790.30	0.07	30.60	31.38	2.66E-09	0.20	0.19	2.02	4.0E+06	4.08E+06	0.73	1.37	0.11	7.25
16	21373.00	0.11	1.39	1.88	-1.98E-09	0.14	0.12	0.98	1.0E+06	1.01E+06	0.61	1.58	0.11	0.41
17	1824.30	0.04	7.00	10.61	9.37E-09	0.16	0.15	1.22	4.0E+06	4.05E+06	0.61	1.60	0.11	2.51
18	5928.00	0.27	9.90	14.53	9.74E-09	0.38	0.34	7.00	1.0E+06	1.07E+06	0.55	1.76	0.09	3.96
19	852.75	0.04	5.29	7.98	1.37E-09	0.16	0.15	1.22	4.0E+06	4.05E+06	0.58	1.69	0.09	2.17
20	526.75	0.02	6.25	8.43	1.14E-08	0.15	0.15	1.17	4.0E+06	4.05E+06	0.58	1.67	0.10	2.28
21	1524.00	0.08	16.41	14.73	-2.63E-08	0.27	0.26	3.55	1.0E+06	1.04E+06	0.61	1.55	0.12	4.50
22	856.75	0.03	16.50	32.31	2.73E-08	0.17	0.17	1.42	4.0E+06	4.06E+06	0.69	1.44	0.10	5.97
23	1407.50	0.06	14.51	13.98	-2.99E-08	0.24	0.22	2.88	4.0E+06	4.12E+06	0.57	1.70	0.10	4.18
24	1140.80	0.06	16.35	14.86	2.55E-08	0.23	0.22	2.48	4.0E+06	4.10E+06	0.59	1.61	0.11	4.27
25	3017.00	0.10	11.75	12.89	-3.66E-08	0.24	0.24	2.93	1.0E+06	1.03E+06	0.58	1.65	0.10	3.67
26	3486.00	0.31	16.09	14.63	4.71E-08	0.42	0.40	8.56	1.0E+06	1.09E+06	0.59	1.63	0.11	4.10
27	2628.70	0.32	18.23	19.31	-1.68E-08	0.45	0.43	9.69	1.0E+06	1.10E+06	0.57	1.71	0.10	6.20
28	4264.00	0.22	11.47	11.04	4.34E-08	0.36	0.34	6.28	1.0E+06	1.06E+06	0.59	1.63	0.10	3.43
29	1096.80	0.03	12.66	10.85	-1.03E-08	0.16	0.16	1.32	4.0E+06	4.05E+06	0.60	1.59	0.11	2.96
30	5242.00	0.10	9.16	7.09	6.43E-09	0.19	0.18	1.80	1.0E+06	1.02E+06	0.61	1.56	0.12	2.04
31	2244.00	0.12	14.24	13.00	6.22E-08	0.34	0.34	5.64	1.0E+06	1.06E+06	0.63	1.51	0.12	3.42
32	5042.00	0.09	6.11	7.71	1.13E-08	0.15	0.13	1.05	1.0E+06	1.01E+06	0.57	1.70	0.10	2.27
33	6535.00	0.16	9.28	8.48	-6.79E-09	0.24	0.22	2.83	1.0E+06	1.03E+06	0.60	1.58	0.11	2.29
34	3349.00	0.17	8.12	11.38	3.80E-08	0.39	0.37	7.11	1.0E+06	1.07E+06	0.56	1.73	0.09	3.00
35	4020.00	0.27	13.59	14.73	-1.16E-08	0.51	0.48	11.13	1.0E+06	1.11E+06	0.58	1.67	0.10	4.55
36	2724.00	0.13	11.24	16.06	-9.19E-09	0.29	0.28	4.21	1.0E+06	1.04E+06	0.59	1.63	0.10	4.27
37	2903.00	0.12	10.97	10.99	1.86E-08	0.27	0.26	3.63	1.0E+06	1.04E+06	0.60	1.61	0.10	3.03
38	1215.50	0.04	8.92	12.08	1.01E-08	0.13	0.12	0.85	4.0E+06	4.03E+06	0.57	1.70	0.10	3.11
39	2213.00	0.10	14.54	13.14	6.70E-08	0.27	0.26	3.59	1.0E+06	1.04E+06	0.62	1.54	0.11	3.65
40	2152.00	0.10	128.93	100.60	3.92E-08	0.68	0.41	5.46	4.0E+06	4.22E+06	0.73	1.35	0.17	9.67
41	2278.00	0.13	15.92	14.39	-6.99E-08	0.43	0.41	7.84	1.0E+06	1.08E+06	0.58	1.65	0.11	4.71
42	1236.00	0.14	21.47	20.99	1.98E-08	0.56	0.55	15.12	4.0E+06	4.60E+06	0.61	1.55	0.11	5.39
43	802.50	0.06	12.58	12.84	2.40E-08	0.31	0.31	4.72	4.0E+06	4.19E+06	0.59	1.63	0.10	3.76
44	4433.00	0.25	23.94	32.95	5.45E-08	0.57	0.53	13.20	1.0E+06	1.13E+06	0.60	1.61	0.11	7.07
45	2636.00	0.15	16.14	15.69	-6.76E-09	0.38	0.37	7.03	1.0E+06	1.07E+06	0.61	1.56	0.11	4.21

run	Sk	Svk	Std	Stdi	Srw	Srwi	Shw	Sfd	Scl20	Str20	Scl37	Str37	Sdc0_5	Sdc5_10
1	104.69	45.56	0.00	0.61	1621.80	0.12	166.67	2.81	234.83	0.73	195.69	0.87	87.50	18.38
2	295.86	120.86	0.00	0.69	2250.60	0.12	322.58	2.79	489.24	0.78	391.39	0.91	198.10	37.97
3	241.78	82.04	0.75	0.73	2600.60	0.13	312.50	2.78	371.82	0.35	293.54	0.47	184.27	49.23
4	287.09	127.13	0.00	0.76	2496.70	0.13	344.83	2.91	391.39	0.95	273.97	0.88	186.99	33.69
5	190.93	61.48	0.00	0.72	1320.50	0.18	312.50	2.92	234.83	0.75	176.13	0.75	94.82	22.79
6	126.97	65.38	0.00	0.78	1410.50	0.16	285.71	2.87	273.97	0.88	195.69	0.83	83.19	17.70
7	27.22	8.00	0.00	0.79	1669.90	0.24	217.39	2.72	215.26	0.85	156.56	0.89	96.25	8.94
8	4.27	0.82	3.57	0.83	222.70	0.22	52.63	2.77	39.14	0.63	31.31	0.67	4.73	0.82
9	6.42	2.46	0.00	0.69	100.60	0.21	27.78	2.77	23.48	0.86	19.57	0.91	6.91	0.93
10	10.42	3.65	0.00	0.78	401.14	0.19	51.28	2.79	66.54	0.68	39.14	0.83	25.25	2.02
11	8.07	2.95	0.00	0.75	154.03	0.14	30.30	2.79	33.27	0.81	25.44	0.81	8.50	1.39
12	14.59	4.41	112.40	0.89	341.54	0.23	52.63	2.76	39.14	0.91	27.40	0.78	18.41	2.45
13	7.28	2.34	1.35	0.80	329.91	0.14	27.78	2.71	33.27	0.53	25.44	0.62	7.48	1.28
14	25.26	8.79	114.30	0.84	377.36	0.17	62.50	2.88	46.97	0.67	35.23	0.64	19.71	3.80
15	3.71	3.46	0.00	0.63	535.03	0.15	54.05	2.79	74.36	0.73	58.71	0.88	27.20	2.11
16	0.84	0.29	92.81	0.77	140.20	0.30	16.95	2.50	13.70	0.78	11.74	0.86	1.34	0.12
17	3.82	1.38	79.73	0.81	494.71	0.20	43.48	2.69	35.23	0.47	27.40	0.50	7.94	0.74
18	7.09	1.87	178.47	0.84	167.03	0.17	29.41	2.74	31.31	0.94	23.48	0.92	9.25	1.32
19	3.90	1.08	100.60	0.80	415.14	0.23	47.62	2.74	31.31	0.67	23.48	0.67	5.21	0.69
20	4.77	1.43	109.87	0.78	195.39	0.19	55.56	2.89	31.31	0.62	23.48	0.60	5.15	0.79
21	10.18	4.42	177.64	0.75	254.26	0.11	43.48	2.98	45.01	0.70	35.23	0.69	7.99	1.56
22	6.47	3.01	178.35	0.79	334.93	0.14	66.67	2.89	70.45	0.86	50.88	0.87	27.58	1.37
23	7.64	2.57	86.37	0.73	392.28	0.16	64.52	2.80	46.97	0.80	35.23	0.75	8.39	1.43
24	10.46	3.44	111.33	0.85	407.70	0.16	58.82	2.80	74.36	0.90	54.79	0.82	8.00	1.56
25	7.52	2.45	0.00	0.65	238.57	0.11	37.04	2.91	37.18	0.56	29.35	0.63	7.70	1.23
26	9.19	3.05	178.38	0.75	157.90	0.16	32.26	2.79	23.48	0.63	19.57	0.67	8.49	1.48
27	11.99	3.65	0.88	0.70	252.46	0.15	35.78	2.84	35.29	0.64	27.45	0.78	10.68	2.18
28	8.23	2.40	73.00	0.77	211.23	0.15	31.25	2.79	27.40	0.56	21.53	0.58	5.68	1.22
29	5.90	2.24	100.58	0.85	323.28	0.15	55.56	2.80	54.79	0.82	39.14	0.77	6.88	0.99
30	5.08	2.06	0.00	0.77	192.69	0.13	34.48	2.84	39.14	0.83	29.35	0.79	3.71	0.78
31	8.72	3.35	1.94	0.85	193.15	0.15	33.33	2.89	29.35	0.71	23.48	0.75	7.59	1.15
32	4.75	1.37	176.82	0.79	303.66	0.10	40.00	2.82	45.01	0.66	37.18	0.83	4.43	0.83
33	6.29	2.10	0.00	0.53	169.10	0.14	32.26	2.76	37.18	0.79	29.35	0.79	4.52	0.85
34	5.98	1.61	80.41	0.81	130.81	0.21	26.32	2.78	19.57	0.71	15.66	0.73	7.15	1.06
35	9.27	2.85	0.00	0.76	197.80	0.15	28.57	2.80	29.35	0.83	21.53	0.79	8.29	1.59
36	8.84	2.83	178.27	0.74	176.25	0.13	37.04	2.85	39.14	0.77	29.35	0.79	10.01	1.42
37	7.53	2.37	0.82	0.75	253.38	0.15	35.71	2.84	35.23	0.90	29.35	1.00	6.12	1.06
38	5.61	1.98	0.00	0.79	466.86	0.15	74.07	2.79	50.88	0.72	39.14	0.77	7.99	1.09
39	9.93	3.12	0.00	0.67	247.33	0.11	43.48	2.91	41.10	0.78	31.31	0.76	7.10	1.33
40	11.72	7.49	90.99	0.48	778.04	0.12	62.50	2.70	78.28	0.63	62.62	0.80	93.38	1.38
41	9.93	3.84	0.00	0.61	202.77	0.15	35.71	2.91	33.27	0.89	25.44	0.87	7.17	1.76
42	15.55	4.90	65.80	0.91	213.47	0.26	46.51	2.73	35.23	1.00	27.40	1.00	11.49	2.04
43	8.72	2.72	61.61	0.82	181.80	0.23	48.78	2.75	31.31	0.67	23.48	0.67	7.08	1.32
44	13.33	4.94	0.97	0.77	189.83	0.13	30.30	2.78	39.14	0.80	29.35	0.79	23.94	2.17
45	10.61	3.61	0.00	0.71	191.41	0.13	34.48	2.87	35.23	0.82	27.40	0.82	8.99	1.53

run	Sdc10_50	Sdc50_95	Area nm^2	Length nm	Width nm	Size nm	Perim nm	Aspect	Diam nm
1	58.82	70.59	6.31E+04	372.83	127.66	349.10	1246.90	3.10	243.14
2	138.67	198.10	5.55E+05	1151.70	402.01	1087.90	3992.60	3.07	760.59
3	140.66	151.91	3.62E+05	903.69	320.60	838.80	3177.90	3.25	599.19
4	129.72	202.16	1.79E+05	674.75	223.87	624.13	2108.40	3.51	432.09
5	88.44	118.52	1.13E+05	536.91	179.99	500.41	1666.00	3.34	346.63
6	59.29	93.81	5.12E+04	350.30	123.22	322.63	1095.00	3.08	231.93
7	18.91	15.47							
8	2.42	2.19	4.82E+03	104.81	41.80	97.22	359.38	2.60	74.27
9	3.20	4.22	1.84E+03	65.81	26.06	61.41	220.07	2.67	46.37
10	5.86	6.36	3.70E+03	91.37	36.70	84.50	310.96	2.57	64.99
11	4.46	5.00	2.32E+03	78.87	25.96	75.42	252.88	3.24	50.46
12	7.93	8.59	4.07E+03	97.82	37.51	91.10	331.64	2.72	67.86
13	4.09	4.33	1.86E+03	66.06	23.86	61.01	229.80	2.93	44.37
14	13.00	15.92	7.40E+03	135.62	49.16	125.31	444.69	2.85	91.47
15	2.48	2.73	1.63E+03	61.14	23.48	56.15	209.05	2.67	42.50
16	0.43	0.52	9.15E+02	47.01	17.65	43.64	171.28	2.79	32.28
17	2.01	2.40	2.37E+03	74.73	27.54	68.61	245.46	2.84	50.83
18	4.31	3.92	1.25E+03	51.01	20.47	47.41	175.98	2.67	36.22
19	2.21	2.26	2.49E+03	78.65	28.62	73.53	249.39	2.85	53.16
20	2.62	2.85	3.48E+03	95.23	33.34	88.41	298.76	3.00	63.07
21	5.24	6.68	5.40E+03	117.34	39.39	110.60	365.23	3.28	76.00
22	3.62	4.11	4.36E+03	101.00	36.27	93.92	326.07	2.99	67.69
23	4.45	4.45	6.36E+03	131.19	42.74	124.54	418.85	3.35	83.50
24	5.44	6.38	3.14E+03	86.72	30.27	79.56	280.49	3.06	57.23
25	4.10	4.59	2.21E+03	77.47	24.03	72.79	241.76	3.52	48.07
26	4.80	5.54	1.82E+03	65.86	23.93	60.55	219.60	2.98	44.41
27	6.85	7.07	1.99E+03	68.65	24.59	64.54	223.86	3.05	45.87
28	4.29	4.87	1.59E+03	65.04	19.78	61.88	203.32	3.64	39.94
29	3.06	3.72	5.12E+03	114.90	39.14	108.12	368.88	3.11	74.95
30	2.57	3.45	3.24E+03	91.44	30.22	86.74	302.11	3.25	58.65
31	4.26	5.68	1.57E+03	62.08	22.77	57.27	201.87	2.91	42.01
32	2.57	2.77	3.85E+03	93.25	34.58	87.29	315.69	2.96	63.39
33	3.13	3.88	3.29E+03	89.41	32.93	82.49	300.10	2.92	60.70
34	3.36	3.44	7.97E+02	44.46	15.98	41.44	142.92	2.95	29.81
35	5.05	5.62	1.03E+03	50.73	17.10	47.59	160.20	3.16	32.89
36	4.81	5.47	2.22E+03	71.65	25.75	67.29	232.06	3.26	47.80
37	3.92	4.53	2.94E+03	81.21	32.71	76.27	274.68	2.75	57.61
38	3.16	3.41	7.63E+03	131.13	50.36	121.33	452.21	2.90	90.93
39	4.72	6.16	3.34E+03	94.25	30.11	89.31	290.64	3.84	59.11
40	5.98	9.20	7.71E+03	125.28	43.05	117.45	444.92	3.50	81.56
41	5.53	6.74	1.61E+03	59.68	21.61	55.92	192.06	3.15	40.00
42	7.49	9.70	2.63E+03	76.33	31.01	70.38	257.04	2.57	54.61
43	4.58	5.20	2.80E+03	82.70	30.71	75.76	267.76	2.81	56.50
44	7.07	8.44	2.18E+03	71.31	25.75	67.16	236.90	3.04	47.84
45	5.23	6.63	1.86E+03	66.53	23.78	62.21	214.30	2.94	44.48

run	Volume nm^3	VAbs nm^3	G as dep	G max	G oxi	Gmax/Gas dep	Gmax/Goxi
1	1.98E+06	1.29E+07					
2	5.28E+07	2.47E+08					
3	2.77E+07	1.21E+08					
4	1.46E+07	8.69E+07					
5	5.95E+06	2.80E+07					
6	1.59E+06	1.43E+07					
7			1.04E+02	1.56E+02	1.15E+02	1.50E+00	1.36E+00
8	6.46E+03	2.24E+04	3.90E-02	4.85E+01	3.65E-01	1.24E+03	1.33E+02
9	4.35E+03	2.23E+04					
10	1.19E+04	6.50E+04	8.53E-02	4.36E+01	3.79E-01	5.11E+02	1.15E+02
11	6.25E+03	3.69E+04					
12	1.88E+04	7.60E+04					
13	3.86E+03	2.21E+04					
14	6.50E+04	2.72E+05					
15	1.92E+03	4.97E+04	1.32E-01	1.15E+02	3.40E-01	8.70E+02	3.38E+02
16	2.56E+02	1.27E+03					
17	2.60E+03	1.66E+04	8.75E-05	3.70E+01	5.85E-06	4.22E+05	6.32E+06
18	2.81E+03	1.23E+04	7.50E-01	3.36E+02	7.53E+01	4.48E+02	4.47E+00
19	3.05E+03	1.32E+04	4.48E-01	9.50E+01	1.01E+01	2.12E+02	9.45E+00
20	5.35E+03	2.18E+04	4.15E-02	1.36E+02	2.61E-02	3.28E+03	5.21E+03
21	2.03E+04	8.86E+04	2.63E-01	1.78E+02	4.48E-02	6.78E+02	3.98E+03
22	9.23E+03	7.20E+04	2.90E-02	1.22E+02	6.88E-03	4.19E+03	1.77E+04
23	1.49E+04	9.23E+04	3.00E-01	1.43E+02	5.10E-02	4.78E+02	2.81E+03
24	7.02E+03	5.12E+04					
25	4.86E+03	2.61E+04					
26	5.58E+03	2.93E+04					
27	7.34E+03	3.62E+04					
28	3.97E+03	1.83E+04					
29	9.23E+03	6.49E+04					
30	5.28E+03	2.97E+04					
31	3.72E+03	2.24E+04	2.07E-03	4.86E+01	4.34E-02	2.35E+04	1.12E+03
32	5.60E+03	2.35E+04					
33	6.48E+03	3.05E+04	1.33E-01	9.17E+01	2.71E+01	6.89E+02	3.38E+00
34	1.37E+03	6.47E+03					
35	2.67E+03	1.40E+04	3.70E-02	2.62E+01	3.21E+00	7.08E+02	8.16E+00
36	5.88E+03	2.49E+04	2.12E-03	3.80E+01	9.40E-03	1.79E+04	4.04E+03
37	7.57E+03	3.23E+04					
38	1.33E+04	6.81E+04	5.86E-03	3.88E+01	4.68E-03	6.62E+03	8.29E+03
39	9.91E+03	4.85E+04					
40	2.59E+04	9.94E+05	3.89E-02	2.46E+01	2.44E-02	6.32E+02	1.01E+03
41	5.20E+03	2.55E+04					
42	1.27E+04	5.64E+04					
43	7.81E+03	3.53E+04					
44	8.98E+03	5.20E+04					
45	5.82E+03	2.99E+04					

Annex 7F Experimental data for doped ZnO grown by DC magnetron sputtering.

RUN	MATERIAL	% O2	pO2 (mbar)	ISP (A)	timp(sec)	t (°C)	d (nm)	growth rate	Sa	Sq
1	ZAO2	100.00	8.00E-03	0.44	420	47	97.4	2.32E-01	1.49	1.88
2	ZAO2	100.00	8.00E-03	0.45	360	47.5	109.8	3.05E-01	1.00	1.27
3	ZAO2	100.00	8.00E-03	0.25	720	50	109.3	1.52E-01	1.55	2.02
4	ZAO2	80.00	8.00E-03	0.44	260	41.5	108.5	4.17E-01	0.51	0.65
5	ZAO2	80.00	8.00E-03	0.24	570	40	109.4	1.92E-01	0.92	1.16
6	ZAO2	75.00	8.00E-03	0.44	240	42.5	110.4	4.60E-01	0.49	0.61
7	ZAO2	75.00	8.00E-03	0.25	550	37.5	107.6	1.96E-01	0.78	0.98
8	ZAO2C	0.00	8.00E-03	0.45	120	42	109.5	9.13E-01	0.66	0.85
9	ZAO2C	0.00	8.00E-03	0.25	240	38	107.6	4.48E-01	0.95	1.21
10	ZAO2C	15.00	8.00E-03	0.45	150	39	114	7.60E-01	0.85	1.07
11	ZAO2C	15.00	8.00E-03	0.24	360	37.5	113.5	3.15E-01	0.41	0.51
RUN	MATERIAL	% O2	pO2 (mbar)	ISP (A)	timp(sec)	t (°C)	d (nm)	growth rate	Sa	Sq
1	ZAO2D	0	8.00E-03	0.45	140	43.5	102	7.29E-01	0.63	0.82
2	ZAO2D	0	8.00E-03	0.25	300	38.5	100.4	3.35E-01	1.11	1.46
3	ZAO2D	0	8.00E-03	0.45	1140	58.5	1008	8.84E-01	17.14	21.22
4	ZAO2D	0	8.00E-03	0.45	300	45.5	203.6	6.79E-01	0.69	0.87
5	ZAO2D	0	8.00E-03	0.45	730	61	503.6	6.90E-01	1.41	1.88
6	ZAO2D	10	8.00E-03	0.45	180	43	102.2	5.68E-01	0.27	0.34
7	ZAO2D	20	8.00E-03	0.45	150	41	102.7	6.85E-01	0.84	1.18
8	ZAO2D	0	8.00E-03	0.25	360	34.5	101.5	2.82E-01	0.17	0.22
RUN	MATERIAL	% O2	pO2 (mbar)	ISP (A)	timp(sec)	t (°C)	d (nm)	growth rate	Sa	Sq
1	I5ZO	100	8.00E-03	0.45	320	RT	104	3.25E-01	0.78	0.98
2	I5ZO	100	8.00E-03	0.25	630	RT	101.9	1.62E-01	1.25	1.57
3	I5ZO	80	8.00E-03	0.45	260	RT	104.7	4.03E-01	0.84	1.05
4	I5ZO	80	8.00E-03	0.25	500	RT	101	2.02E-01	1.18	1.48
5	I5ZO	90	8.00E-03	0.45	230	RT	101.3	4.40E-01	0.45	0.57
6	I5ZO	90	8.00E-03	0.25	500	RT	101.2	2.02E-01	1.03	1.28

RUN	Ssk	Sku	Sy	St	Sz	S10z	Sz_tph	Sds	Ssc	Sv	Sp	Smean	Sdq
1	-0.08	3.15	16.97	16.97	16.97	15.13	15.13	4.38E+03	0.15	9.44	7.53	0.00	0.34
2	0.28	3.36	11.27	11.27	11.27	10.89	10.89	1.34E+03	0.04	5.05	6.22	0.00	0.18
3	0.97	4.87	17.67	17.67	17.67	16.57	16.57	1.83E+03	0.04	6.44	11.23	0.00	0.19
4	0.00	3.24	5.92	5.92	5.92	5.33	5.33	6.19E+03	0.07	2.92	3.00	0.00	0.14
5	0.27	3.43	10.11	10.11	10.11	9.80	9.80	4.57E+03	0.09	4.38	5.73	0.00	0.19
6	-0.09	2.97	5.25	5.25	5.25	4.80	4.80	7.88E+03	0.08	2.99	2.26	0.00	0.14
7	0.12	3.05	8.87	8.87	8.87	7.75	7.75	6.11E+03	0.11	4.55	4.32	0.00	0.20
8	-0.08	4.27	10.12	10.12	10.12	9.54	9.54	7.45E+03	0.09	4.37	5.75	0.00	0.16
9	0.14	3.20	10.34	10.34	10.34	9.52	9.52	4.72E+03	0.10	5.13	5.22	0.00	0.21
10	0.12	2.99	8.04	8.04	8.04	7.91	7.91	4.92E+03	0.09	3.86	4.17	0.00	0.18
11	0.03	3.09	4.96	4.96	4.96	4.31	4.31	9.04E+03	0.07	2.58	2.38	0.00	0.12

RUN	Ssk	Sku	Sy	St	Sz	S10z	Sz_tph	Sds	Ssc	Sv	Sp	Smean	Sdq
1	0.22	4.54	9.17	9.17	9.17	8.72	8.72	5.21E+03	0.08	3.64	5.53	0.00	0.17
2	-0.03	6.80	22.71	22.71	22.71	15.31	15.31	8.19E+03	0.13	13.64	9.07	0.00	0.20
3	-0.12	2.84	151.83	151.83	151.83	139.87	139.87	4.84E+02	0.13	75.25	76.59	0.00	0.56
4	-0.01	3.09	7.55	7.55	7.55	6.83	6.83	7.06E+03	0.08	4.01	3.53	0.00	0.13
5	0.65	6.46	22.22	22.22	22.22	19.46	19.46	2.57E+03	0.07	8.61	13.61	0.00	0.21
6	0.29	3.35	3.33	3.33	3.33	2.81	2.81	1.72E+04	0.06	1.36	1.97	0.00	0.08
7	1.62	12.02	23.97	23.97	23.97	19.14	19.14	1.64E+03	0.05	8.86	15.12	0.00	0.21
8	-0.07	3.02	2.02	2.02	2.02	1.77	1.77	3.90E+03	0.01	0.86	1.16	0.00	0.03

RUN	Ssk	Sku	Sy	St	Sz	S10z	Sz_tph	Sds	Ssc	Sv	Sp	Smean	Sdq
1	0.13	3.10	8.14	8.14	8.14	7.44	7.44	5.64E+03	0.09	4.32	3.82	0.00	0.19
2	0.34	3.35	13.41	13.41	13.41	12.63	12.63	4.02E+03	0.09	5.35	8.06	0.00	0.25
3	-0.04	2.98	9.30	9.30	9.30	8.20	8.20	6.90E+03	0.11	4.26	5.03	0.00	0.18
4	0.17	2.92	12.28	12.28	12.28	11.11	11.11	3.12E+03	0.10	6.06	6.22	0.00	0.23
5	0.25	3.20	5.05	5.05	5.05	4.71	4.71	6.84E+03	0.07	2.10	2.95	0.00	0.12
6	-0.80	3.02	8.02	8.02	8.02	7.86	7.86	9.84E+03	0.19	4.71	3.31	0.00	0.44

RUN	Sdq6	Sdr	S2A	S3A	Sbi	Sci	Svi	Spk	Sk	Svk	Std	Stdi	Srw	Srwi
1	0.33	5.50	1.E+06	1.06E+06	0.61	1.55	0.12	1.97	4.71	1.93	89.66	0.62	475.61	0.17
2	0.18	1.63	4.E+06	4.07E+06	0.58	1.66	0.10	1.68	3.13	1.02	71.54	0.80	117.69	0.35
3	0.18	1.80	4.E+06	4.07E+06	0.56	1.77	0.08	3.32	4.62	1.08	77.71	0.83	183.02	0.25
4	0.13	0.98	1.E+06	1.01E+06	0.60	1.58	0.12	0.76	1.61	0.65	94.01	0.76	120.50	0.24
5	0.18	1.74	1.E+06	1.02E+06	0.59	1.62	0.11	1.43	2.91	0.94	96.36	0.87	139.78	0.19
6	0.12	1.00	1.E+06	1.01E+06	0.62	1.53	0.12	0.61	1.59	0.59	94.16	0.80	145.27	0.24
7	0.18	1.89	1.E+06	1.02E+06	0.59	1.62	0.11	1.12	2.50	0.83	99.80	0.88	139.79	0.22
8	0.14	1.24	1.E+06	1.01E+06	0.67	1.42	0.13	1.01	2.09	0.93	94.27	0.84	177.06	0.23
9	0.20	2.25	1.E+06	1.02E+06	0.59	1.62	0.11	1.47	2.97	1.11	96.95	0.88	113.41	0.22
10	0.17	1.69	1.E+06	1.02E+06	0.59	1.63	0.11	1.20	2.72	0.90	83.56	0.87	124.08	0.19
11	0.10	0.73	1.E+06	1.01E+06	0.61	1.57	0.12	0.58	1.30	0.49	85.26	0.74	102.69	0.24

RUN	Sdq6	Sdr	S2A	S3A	Sbi	Sci	Svi	Spk	Sk	Svk	Std	Stdi	Srw	Srwi
1	0.16	1.37	1.E+06	1.01E+06	0.64	1.49	0.11	1.08	1.98	0.81	78.73	0.81	107.81	0.24
2	0.18	1.97	1.E+06	1.07E+06	0.62	1.55	0.11	2.00	3.43	1.43	0.00	0.78	354.35	0.17
3	0.54	14.19	4.E+06	4.57E+06	0.64	1.49	0.12	19.31	56.80	19.09	1.38	0.72	614.90	0.09
4	0.12	0.82	1.E+06	1.01E+06	0.60	1.58	0.12	0.92	2.17	0.86	0.00	0.84	237.30	0.18
5	0.20	2.10	1.E+06	1.02E+06	0.64	1.51	0.11	2.86	4.32	1.86	0.00	0.65	213.62	0.15
6	0.07	0.36	1.E+06	1.00E+06	0.59	1.64	0.10	0.45	0.86	0.27	92.90	0.83	164.32	0.19
7	0.20	2.02	4.E+06	4.08E+06	0.67	1.51	0.10	2.49	2.48	0.96	98.92	0.85	197.66	0.37
8	0.02	0.03	4.E+06	4.00E+06	0.62	1.55	0.11	0.24	0.57	0.21	0.82	0.87	299.23	0.19

RUN	Sdq6	Sdr	S2A	S3A	Sbi	Sci	Svi	Spk	Sk	Svk	Std	Stdi	Srw	Srwi
1	0.18	1.84	1.E+06	1.02E+06	0.59	1.63	0.11	1.14	2.44	0.90	93.77	0.86	138.16	0.23
2	0.24	3.07	1.E+06	1.03E+06	0.59	1.64	0.10	1.93	4.02	1.09	81.65	0.87	124.35	0.20
3	0.15	1.53	1.E+06	1.02E+06	0.61	1.57	0.11	1.13	2.73	0.96	93.14	0.85	142.69	0.18
4	0.21	2.55	1.E+06	1.03E+06	0.59	1.63	0.11	1.64	3.86	1.17	93.29	0.85	123.19	0.19
5	0.11	0.70	1.E+06	1.01E+06	0.58	1.66	0.10	0.72	1.42	0.44	106.30	0.90	88.43	0.25
6	0.42	8.95	1.E+06	1.09E+06	0.78	1.14	0.16	0.70	2.41	2.11	74.98	0.88	64.50	0.39

RUN	Shw	Sfd	Scl20	Str20	Scl37	Str37	Sdc0_5	Sdc5_10	Sdc10_50	Sdc50_95	Area nm^2
1	24.39	2.83	46.97	0.09	15.66	0.73	4.46	0.71	2.38	3.13	187.89
2	37.74	2.63	19.57	0.63	15.66	0.67	4.04	0.56	1.67	1.92	505.88
3	46.51	2.70	35.23	0.69	27.40	0.70	7.61	1.03	2.87	2.48	2677.10
4	25.00	2.73	15.66	0.89	13.70	0.88	1.92	0.26	0.83	1.06	835.21
5	27.03	2.77	21.53	0.79	17.61	0.90	3.77	0.47	1.56	1.76	1266.00
6	23.26	2.70	17.61	0.75	13.70	0.78	1.27	0.22	0.76	1.04	1000.90
7	23.81	2.72	19.57	0.91	15.66	0.89	2.67	0.39	1.30	1.55	1064.60
8	26.32	2.74	17.61	0.90	13.70	0.88	4.48	0.26	0.99	1.44	1272.40
9	26.32	2.78	17.61	0.82	13.70	0.78	3.17	0.52	1.58	1.91	1125.50
10	26.32	2.75	21.53	0.92	17.61	1.00	2.37	0.43	1.40	1.68	945.31
11	25.64	2.72	17.61	0.82	13.70	0.88	1.53	0.19	0.67	0.83	663.53
RUN	Shw	Sfd	Scl20	Str20	Scl37	Str37	Sdc0_5	Sdc5_10	Sdc10_50	Sdc50_95	Area nm^2
1	23.26	2.71	13.70	0.64	11.74	0.67	4.26	0.29	0.99	1.30	608.44
2	28.48	2.75	30.10	0.63	22.07	0.61	6.74	0.59	1.82	2.14	780.80
3	86.96	2.86	113.50	0.69	93.93	0.77	43.21	6.69	26.17	36.21	10708.00
4	26.32	2.74	25.44	0.87	19.57	0.83	2.09	0.33	1.13	1.42	571.71
5	32.26	2.87	35.23	0.90	25.44	0.87	10.69	0.76	2.27	2.81	1136.90
6	20.41	2.60	29.35	0.83	23.48	0.92	1.39	0.14	0.46	0.51	448.58
7	32.79	2.59	15.66	0.67	11.74	0.60	13.36	0.53	1.35	1.54	1021.00
8	39.22	2.58	58.71	0.71	46.97	0.80	0.80	0.08	0.28	0.36	5038.50
RUN	Shw	Sfd	Scl20	Str20	Scl37	Str37	Sdc0_5	Sdc5_10	Sdc10_50	Sdc50_95	Area nm^2
1	25.00	2.75	17.61	0.90	13.70	1.00	2.15	0.41	1.30	1.52	986.17
2	27.03	2.80	19.57	0.83	15.66	0.80	5.40	0.62	2.12	2.34	1124.20
3	28.57	2.74	21.53	0.79	17.61	0.82	3.30	0.39	1.36	1.71	1480.70
4	27.78	2.82	21.53	0.79	15.66	0.73	3.72	0.57	2.02	2.26	1028.60
5	23.26	2.69	15.66	0.80	11.74	0.75	1.97	0.24	0.76	0.86	628.23
6	16.39	2.60	7.83	0.57	7.83	0.80	1.67	0.27	1.04	2.88	1021.30

RUN	Length nm	Width nm	Size nm	Perim nm	Aspect	Diam nm	Volume nm^3	VAbs nm^3
1	21.01	7.24	19.04	63.48	3.11	13.78	1.72E+02	2.80E+02
2	33.66	11.90	30.25	103.14	2.98	22.40	3.89E+02	2.56E+03
3	79.68	29.34	74.10	265.06	2.84	54.18	3.97E+03	1.73E+04
4	46.43	16.42	43.55	147.50	3.11	30.81	4.51E+02	2.44E+03
5	52.78	21.84	48.62	178.55	2.59	38.03	1.29E+03	5.54E+03
6	49.37	18.52	45.25	164.70	2.81	33.88	5.19E+02	2.99E+03
7	49.65	19.65	46.22	168.16	2.65	35.02	9.16E+02	4.85E+03
8	54.88	21.31	50.94	185.57	2.73	38.30	9.27E+02	5.56E+03
9	52.11	20.00	48.30	172.25	2.74	36.16	1.19E+03	5.77E+03
10	46.41	18.20	43.30	153.24	2.79	32.51	8.46E+02	3.65E+03
11	43.56	13.21	41.22	135.51	3.63	26.68	2.36E+02	1.71E+03

RUN	Length nm	Width nm	Size nm	Perim nm	Aspect	Diam nm	Volume nm^3	VAbs nm^3
1	39.33	14.14	36.60	126.37	2.90	26.41	3.69E+02	2.21E+03
2	44.38	14.75	41.55	144.16	3.22	28.55	6.11E+02	1.07E+04
3	155.74	48.02	145.63	492.65	3.98	95.71	1.39E+05	8.06E+05
4	36.96	12.65	34.19	122.14	3.09	24.16	2.98E+02	2.29E+03
5	52.98	18.73	49.66	168.60	3.04	35.22	1.42E+03	9.79E+03
6	33.82	10.64	31.43	111.86	3.23	21.17	7.88E+01	6.12E+02
7	48.63	19.64	44.15	159.55	2.53	34.71	8.45E+02	9.04E+03
8	108.70	36.02	102.53	409.61	3.22	69.87	7.48E+02	4.32E+03

RUN	Length nm	Width nm	Size nm	Perim nm	Aspect	Diam nm	Volume nm^3	VAbs nm^3
1	47.93	19.14	44.25	160.10	2.62	33.96	8.23E+02	4.26E+03
2	52.11	20.01	48.58	171.00	2.74	36.17	1.49E+03	6.02E+03
3	60.07	22.45	55.64	198.50	2.85	41.08	1.24E+03	6.31E+03
4	51.14	18.01	48.19	161.98	3.06	33.92	1.18E+03	6.24E+03
5	38.71	14.56	35.77	130.17	2.82	26.59	2.71E+02	1.32E+03
6	48.89	19.41	45.14	173.53	2.60	34.58	1.41E+03	4.81E+03

RUN	G as dep	G max	G oxi	Gmax/G as dep	Gmax/G oxi
1	5.77E-06	1.08E-01	4.01E-04	1.87E+04	2.69E+02
2	4.00E-06	9.06E-02	2.31E-05	2.27E+04	3.93E+03
3	6.13E-06	1.29E-02	1.44E-05	2.10E+03	8.98E+02
4	3.69E-05	1.48E-01	6.27E-04	4.03E+03	2.37E+02
5	1.76E-06	1.11E-01	2.15E-04	6.31E+04	5.18E+02
6	7.79E-05	3.70E-01	3.16E-03	4.74E+03	1.17E+02
7	4.18E-06	1.52E-01	4.04E-04	3.63E+04	3.75E+02
8	1.99E-03	5.01E+00	1.65E-02	2.52E+03	3.03E+02
9	1.39E-03	3.70E+00	9.76E-03	2.65E+03	3.79E+02
10	1.91E-03	2.66E+00	8.68E-03	1.39E+03	3.06E+02
11	4.76E-05	2.54E-01	1.33E-03	5.34E+03	1.91E+02

RUN	G as dep	G max	G oxi	Gmax/G as dep	Gmax/G oxi
1	1.42E-03	4.67E+00	2.66E-03	3.28E+03	1.76E+03
2	3.40E-03	2.94E+00	2.71E-02	8.65E+02	1.08E+02
3	1.25E-01	7.74E-01	1.88E-01	6.17E+00	4.12E+00
4	1.19E-01	4.33E+00	2.79E-01	3.63E+01	1.55E+01
5	3.55E-01	1.86E+00	6.14E-01	5.24E+00	3.03E+00
6	1.36E-02	1.55E+00	6.06E-02	1.14E+02	2.56E+01
7	2.59E-04	2.72E+00	2.54E-03	1.05E+04	1.07E+03
8	2.29E-01	1.73E+00	3.11E-01	7.59E+00	5.57E+00

RUN	G as dep	G max	G oxi	Gmax/G as dep	Gmax/G oxi
1	7.69E-08	5.90E-02	1.92E-04	7.68E+05	3.07E+02
2	3.14E-06	6.38E-02	4.22E-06	2.03E+04	1.51E+04
3	1.87E-01	3.33E-01	1.88E-01	1.78E+00	1.77E+00
4	1.06E-05	3.31E-01	1.01E-04	3.12E+04	3.27E+03
5	8.54E-04	1.95E+00	7.90E-03	2.29E+03	2.48E+02
6	4.15E+00	5.39E+00	4.15E+00	1.30E+00	1.30E+00

Chapter 8

Outline

General conclusions

8. Conclusions

The development of a metal oxide based gas sensor with optimal operation characteristics is a very challenging field of study. In spite of the great technological possibilities, there is no generic procedure for the simultaneous optimization of all sensor parameters. This PhD study was related to the growth and the properties of In_2O_3 and pure or doped ZnO thin films, grown by DC magnetron sputtering and PLD techniques, with focus on the correlation between the surface parameters and the ozone sensing response. The conclusions of this study can be summarized as following

- The study of the deposition and the properties of In_2O_{3-x} films grown by DC magnetron sputtering under different growth conditions revealed that films grown at room temperature are nonstoichiometric, oxygen deficient. The In_2O_{3-x} films were amorphous in the early stages of the growth, becoming polycrystalline after a certain film thickness depending on growth temperature, having a columnar bulk structure and texturing on a preferential orientation [222] of bixbyite crystalline structure. All films had a homogenous surface with narrow grain size distribution and an RMS bellow 3 nm, even for films with large thickness. Growth conditions were found to control the surface texturing and roughening as well as the bulk crystallite growth. More specifically, increasing thickness, growth temperature and pressure in the chamber were observed to induce an increase of both RMS and grain radius. Regarding sensing, the films were found to exhibit a quite effective response, the ration $\sigma_{photo}/\sigma_{oxi}$ approaching a value of 10^7. The photoreduction with UV light and oxidation with ozone experiments indicated that the gas sensing was strongly related to surface properties. In particular, for films with various thicknesses, the sensing was found improving with increasing RMS value, the opposite appearing with increasing grain radius. In the case of varying temperature, the increasing of both RMS and grain radius was found to cause a decrease of sensing.

- Pure ZnO series were grown by DC magnetron sputtering using Zn metallic and ZnO ceramic targets and the influences of thickness, growth temperature, total pressure and oxygen:argon ratio during growth on the properties of the films was examined. It was proved that all films were polycrystalline (even the thinnest ones grown at room temperature) with columnar grains and textured with preferential orientation along the [002] crystalline direction of the wurzite structure. In addition, films grown from ceramic targets had always a higher stoichiometry than films grown from metallic ones. Increasing thickness and total pressure were observed to result in an increase of both RMS and SDR values, the opposite appearing with increasing growth temperature. Regarding the sensing response, this was found also very effective, similar to that for In_2O_3 and influenced by the surface morphology since increasing RMS and grain radius were found to improve sensing.

- The growth and the properties of pure ZnO thin films grown by PLD from sintered ceramic targets under various conditions were studied, the study

focused mainly on the influence of the thickness and the growth temperature on the properties of the films. The grown films were found to be polycrystalline (even the thinnest ones, or the ones grown at room temperature), exhibiting higher stoichiometry than the films grown by DC magnetron sputtering, having columnar grains and being textured with preferential orientation along [002] crystalline direction of the wurzite structure. Regarding the electrical properties of the as deposited films, increasing substrate temperature was found to induce a decrease in the conductivity, the opposite appearing with increasing thickness. Only films grown at RT of having quite small thickness were found to deviate from this behaviour. Finally, increasing growth temperature was found to enhance the sensing response, the opposite appearing with increasing thickness,

Al, In, AlSi doped zinc oxide transparent thin films were prepared by DC magnetron sputtering using metallic and ceramic targets onto silicon and Corning glass substrates under identical deposition conditions and their properties were compared with those of the undoped ZnO grown by the same technique. In all cases, the doped films were polycrystalline and a strong influence of doping on the structural properties of the films was observed. More specifically:

- ZAO thin films deposited at room temperature from metallic and ceramic targets, for various O_2:Ar plasma ratios, showed that their surface morphology is determined by the growth conditions. In general, the ZAO films were found to have smoother surface, smaller grain size, improved crystallinity and larger as deposited conductivity, as compared to the pure ZnO films. Moreover, Al-doping was observed to lead in an increased of the optical transmittance. However, the sensing response of the ZAO films was found weaker than that of the undoped ZnO ones.
- Si:ZAO thin films grown from 2% Al_2O_3 and 1000 ppm Si-doped zinc oxide ceramic target had a [002] texture and improved crystallinity, as compared with that of the ZAO films grown under similar conditions. Increasing thickness was found to induce an increase of their RMS value, the opposite appearing with increasing oxygen concentration. Regarding their sensing response, this was found quite weak, the films being not promising candidates for gas sensing.
- In:ZnO films deposited onto silicon and glass substrates from ZnIn5 (5% In-doped Zn) metallic target under different growth conditions were found to be highly transparent, highly resistive (109 Ω) and nanostructured, having features of about 50nm. However, because of the presence of metallic “splashes” on their surface, coming from the target, no further experiments were performed.

Based on particular correlations of the surface parameters with the sensing response for each material and technique used, a trial was performed for the development of a general model regarding the influence of the surface parameters on the sensing response. For the preparation and the confirmation of this model, a large database, containing enough experimental points for establishing a realistic model, was created, using the surface morphology and the sensing results for the In_2O_3 and ZnO films grown by the DC magnetron sputtering and the PLD techniques. Moreover, results regarding doped ZnO thin films were also included

in this database, so that a more general picture can be revealed. From the detailed analysis of the experimental results of this database, a set of six significant morphology parameters (photo response and sensing response) were used in order to define a final set of eight significant parameters (growth related: growth rate – GR and growth temperature – T; surface related: active surface ratio – SDR and surface fractal dimension – SFD and grain related: grain volume – V and grain perimeter – P) having the highest contribution to the sensing response was defined. In addition, the two sensing related ratios that can be used for the elaboration of a general model regarding the connection between the surface properties of any film with its sensing response. Then, the evolution of the sensing response and the photo ratios were graphically analyzed in 3D spaces determined by the combinations of the six morphology parameters. As a result, a general functional expression for describing the sensing response in connection with the defined parameters was denoted. Finally, an algorithm based on experimental results was sketched, for the generation of an analytical expression for the contribution of the surface function to the sensor response.

Particular observations of experimental plots revealed the following:

- In the 3D representations involving growth rate and temperature, the sensing response per surface seems to decrease as the grain volume increases for both In_2O_3 and ZnO grown by both growth techniques.
- In general, films grown with DC magnetron sputtering appeared to exhibit better sensing properties
- Maximum sensing response appeared for In_2O_3 and ZnO grown with a small growth rate at RT by DC magnetron sputtering for a grain volume of about $10^4 nm^3$, which correspond to a grain radius of about 15nm.
- The influence of the grain perimeter on the sensing response seems to be different for films grown at temperatures lower than 50°C and films grown at higher temperature. For low temperatures, the sensing response increases as perimeter increases while for higher temperatures the opposite was evident. The optimum sensing response of films grown by DC magnetron sputtering appeared for a mean grain perimeter of about 100-150nm, the value becoming around 200nm for ZnO grown by PLD.
- Increase of SDR resulted in a local decrease of the sensing response. A SDR value of about 2 seems to favour the sensing response for both materials and techniques.
- A SFD value of about 2.65-2.7 appeared to optimize locally the sensing response. Generally, an increase of SFD was found to improve the sensing response.

Acknowledgements

This Ph.D. work has been carried out at the Materials Group of the Institute of Electronic Structure & Laser (IESL)/Foundation for Research & Technology-Hellas (FORTH), under the supervision of Prof. G. Kiriakidis, at the Center of Materials and Laser at the Technological Educational Institute of Crete (TEI), under the supervision of Prof. E. Koudoumas and at the Chemistry Department of the University of Crete, under the supervision of Prof. T. Kitsopoulos, in the framework of PENED 2003 (project 03ED733), a Greek National and European co-founded project.

First, I would like to thank Professors T. Kitsopoulos, G. Kiriakidis and E Koudoumas, for their interest, concern and advice in this academic work.

I would like to express my deep gratitude to my friend and former colleague Savvas Christoulakis for providing me with valuable technical and scientific support, discussions and suggestions, all along this work.

It is a pleasure to acknowledge Prof. N. Katsarakis for valuable discussions concerning structural, electrical and optical measurements in semiconducting materials, Mrs. Katerina Tsagaraki from Microelectronics Group of IESL/FORTH for her constant support and advice in microscopy work and Sandra Siakouli from Biology Department of University of Crete, for technical support during SEM and TEM measurements.

I would like to express my deep thankfulness to Prof. John Stoemenos from Aristotelian University of Thessaloniki for XTEM and HRTEM characterization of the highest professional level. Also I would like to express my gratitude to Dr. G. Konstantinidis for a fellowship that was offered to me for the period between my admission in the postgraduate program in University of Crete and the PENED finance, as well as to Prof. P. Ditsas for providing me with his support for my residence permit for a legal stay in Greece for the same period of time.

I also want to give my thanks to Prof T. Eftimiopoulos from University of Patras for his valuable advices regarding the PLD technique.

I would like to thank my former colleagues, Dr. Michalis Katharakis and Dr. Dimitra Vernardou for their permanent availability for discussions and advice on experimental results and theoretical assumptions, and K. Moschovis, E. Gagaoudakis and I. Kortidis for the growth of some of the DC magnetron sputtering In_2O_3 samples and some sensing response measurements.

I am indebted to all my friends who stood by me along this work and had the power to support my stress and encourage me when I was down.